TECHNISCHE UNIVERSITÄT MÜNCHEN

Lehrstuhl für Numerische Mechanik

Computational Multiscale Methods for Turbulent Single and Two-Phase Flows

Ursula Rasthofer

Vollständiger Abdruck der von der Fakultät für Maschinenwesen der Technischen Universität München zur Erlangung des akademischen Grades eines

Doktor-Ingenieurs (Dr.-Ing.)

genehmigten Dissertation.

Vorsitzender:	Univ.-Prof. Dr.-Ing. habil. Hans-Jakob Kaltenbach
Prüfer der Dissertation:	
	1. TUM Junior Fellow Dr.-Ing. Volker Gravemeier
	2. Univ.-Prof. Dr. rer. nat. habil. Volker John Freie Universität Berlin
	3. Univ.-Prof. Dr.-Ing. Wolfgang A. Wall

Die Dissertation wurde am 13. Januar 2015 bei der Technischen Universität München eingereicht und durch die Fakultät für Maschinenwesen am 22. Juni 2015 angenommen.

Abstract

Novel and comprehensive computational multiscale methods for turbulent single- and two-phase flows are developed in this thesis. All numerical methods rely on the framework of the variational multiscale method motivated by their application to large-eddy simulation.

For large-eddy simulation of turbulent incompressible single-phase flow, an algebraic variational multiscale-multigrid-multifractal method (AVM^4) is proposed. In this approach, the subgrid-scale velocity is explicitly evaluated based on the multifractal subgrid-scale modeling approach. The multifractal subgrid-scale modeling approach requires the further separation of the resolved scales into larger and smaller ones which is accomplished via level-transfer operators from plain aggregation algebraic multigrid methods. The multifractal subgrid-scale modeling approach is eventually incorporated into the variational multiscale formulation, which is completed by accompanying residual-based multiscale terms to provide a stable numerical method. For application of the AVM^4 to wall-bounded turbulent flow, a near-wall limit of the multifractal subgrid-scale modeling approach is additionally derived. Moreover, the AVM^4 is further developed for large-eddy simulation of passive-scalar mixing in turbulent incompressible flow as well as of turbulent variable-density flow at low Mach number. In a variety of examples, comprising homogeneous isotropic turbulence, turbulent channel flow, turbulent flow past a square-section cylinder and over a backward-facing step, an excellent performance of the proposed method is shown.

Concerning the simulation of incompressible two-phase flow in general, a face-oriented stabilized Nitsche-type extended variational multiscale method is suggested. Based on a level-set description for the interface, an extended finite element method is developed to enable a sharp representation of the discontinuities in the flow field at the interface, which are related to surface-tension effects and large ratios of the physical parameters. To capture the discontinuities, jump enrichments are applied to both the velocity and the pressure field. Nitsche's method is then used to weakly impose the continuity of the velocity field at the interface. For a stable formulation on the entire domain, residual-based multiscale terms are supported by appropriate face-oriented ghost-penalty and fluid stabilization terms in the vicinity of the interface. Both face-oriented stabilization terms as well as interface terms related to Nitsche's method are extended in order to appropriately account for viscous- and convection-dominated transient flows. The proposed method is validated for various two- and three-dimensional numerical examples of increasing complexity: Rayleigh-Taylor instabilities, a collapsing water column, rising bubbles as well as a bubble coalescence. For all examples, excellent agreement with either analytical solutions or numerical and experimental reference data is shown, while the method proves to be robust for all flow regimes.

Eventually, the AVM^4 and the face-oriented stabilized Nitsche-type extended variational multiscale method are combined to a comprehensive approach to large-eddy simulation of turbulent two-phase flow. The resulting extended algebraic variational multiscale-multigrid-multifractal

method (XAVM^4) is successfully applied to turbulent channel flow carrying a single large bubble of the size of the channel half-width. The simulation of this flow problem rigorously demonstrates the high potential of the novel approach.

Zusammenfassung

In der vorliegenden Arbeit werden neuartige numerische Mehrskalenmethoden zur Berechnung turbulenter Ein- und Zweiphasenströmungen entwickelt, welche auf der variationellen Mehrskalenmethode basieren und im Rahmen von Grobstruktursimulationen zum Einsatz kommen sollen.

Zur Grobstruktursimulation turbulenter Einphasenströmungen wird eine sogenannte "Algebraic Variational Multiscale-Multigrid-Multifractal Method (AVM^4)" vorgestellt. Dabei wird zur direkten Approximation der nicht aufgelösten Subskalen ein multifraktaler Modellierungsansatz gewählt. Dieser Ansatz erfordert eine weitere explizite Aufspaltung der aufgelösten Skalen, welche mittels Transferoperatoren algebraischer Mehrgitterverfahren erfolgt. Residuenbasierte Mehrskalenterme, die die Stabilität der numerischen Methode sicherstellen, vervollständigen schließlich die Formulierung. Im Rahmen der Anwendung der AVM^4 auf wandbegrenzte Strömungen wird zusätzlich eine Wandkorrektur des multifraktalen Subskalenmodellierungsansatzes abgeleitet. Darüber hinaus erfolgt eine Weiterentwicklung der AVM^4 für passiven Skalartransport in turbulenten inkompressiblen Strömungen und für turbulente Strömungen variabler Dichte bei kleiner Machzahl. Die Validierung der Methode erfolgt anhand einer Vielzahl numerischer Beispiele. Diese umfassen die homogene, isotrope Turbulenz, die turbulente Kanalströmung, die turbulente Umströmung eines Quaders sowie die turbulente Stufenströmung.

Zur Simulation von Zweiphasenströmungen wird zunächst eine Nitsche-basierte angereicherte variationelle Mehrskalenmethode mit flächenbasierter Stabilisierung vorgestellt. Ausgehend von einer Level-Set-Beschreibung der Phasengrenze wird eine angereicherte Finite-Element-Methode hergeleitet, welche es erlaubt, die aus der Oberflächenspannung und den sich sprunghaft ändernden Materialparametern resultierenden Diskontinuitäten im Strömungsfeld explizit darzustellen. Dafür werden sowohl für das Geschwindigkeits- als auch für das Druckfeld Sprunganreicherungen verwendet. Die Nitsche-Methode sorgt dann an der Phasengrenze für eine schwache Kopplung der Geschwindigkeitsfelder. Um die Stabilität des Ansatzes im gesamten Gebiet zu gewährleisten, werden die residuenbasierten Mehrskalenterme durch geeignete flächenbasierte Phantomstrafterme und Fluidstabilisierungsterme im Nahbereich der Phasengrenze unterstützt. Die flächenbasierten Terme sowie die Grenzflächenterme der Nitsche-Methode werden in geeigneter Form für viskos- und konvektionsdominierte, instationäre Strömungen erweitert. Die Methode wird für zwei- und dreidimensionale Beispiele ansteigender Komplexität getestet. Zu diesen Beispielen zählen die Rayleigh-Taylor-Instablität, das Dammbruchproblem, aufsteigende Gasblasen und die Vereinigung von Gasblasen. Für alle Beispiele kann eine sehr gute Übereinstimmung mit analytischen, numerischen oder experimentellen Referenzlösungen gezeigt werden.

Die Zusammenführung der AVM^4 und der Nitsche-basierten angereicherten variationellen Mehrskalenmethode mit flächenbasierter Stabilisierung führt schließlich zur "Extended Variational Multiscale-Multigrid-Multifractal Method ($XAVM^4$)" für die Grobstruktursimulation turbulenter Zweiphasenströmungen. Diese Methode wird erfolgreich auf eine turbulente Kanalströmung mit einer Luftblase von der Größe der halben Kanalhöhe angewendet. Diese Grobstruktursimulation verdeutlicht anschaulich das große Potential der hier vorgestellten Methode.

Contents

Nomenclature **ix**

1 Introduction **1**
1.1 Motivation . . . 1
1.2 Contribution of this Work . . . 2
1.3 Outline . . . 4

I AVM^4 - The Algebraic Variational Multiscale-Multigrid-Multifractal Method **5**

2 From the Fundamentals of Turbulence to its Numerical Simulation **7**
2.1 The Incompressible Navier-Stokes Equations . . . 7
2.2 The Nature of Turbulent Incompressible Flow . . . 8
2.2.1 Vorticity Dynamics . . . 8
2.2.2 Energy Cascade . . . 10
2.3 Large-Eddy Simulation of Turbulent Flows . . . 11
2.3.1 The Filtered Navier-Stokes Equations . . . 12
2.3.2 A Review of Relevant Subgrid-Scale Models . . . 14

3 The Concept of the Variational Multiscale Method **17**
3.1 A Paradigm for Scale Separation in Large-Eddy Simulation . . . 17
3.2 Variational Multiscale Formulation of the Incompressible Navier-Stokes Equations 19
3.3 Residual-Based Subgrid-Scale Modeling . . . 23

4 Multifractal Subgrid-Scale Modeling within a Variational Multiscale Method **27**
4.1 Multifractals in Turbulent Flows . . . 27
4.2 Multifractal Subgrid-Scale Modeling . . . 30
4.2.1 General Idea of the Modeling Strategy . . . 30
4.2.2 Vorticity-Magnitude Cascade . . . 31
4.2.3 Vorticity-Orientation Cascade . . . 33
4.2.4 Subgrid-Scale Velocity Approximation . . . 35
4.2.5 Number of Cascade Steps . . . 36
4.3 Scale-Separation by Plain Aggregation Algebraic Multigrid . . . 37
4.4 Residual-Based Subgrid-Scale Modeling . . . 39
4.5 AVM^4 in a Nutshell . . . 40
4.6 The AVM^4 Flow Solver . . . 41
4.6.1 Overview of the Flow Solver . . . 41
4.6.2 Implementational Aspects of the AVM^4 . . . 42
4.7 Validation for Homogeneous Isotropic Turbulence . . . 43

4.8 Adaption for Wall-Bounded Turbulence . . . 45
4.8.1 Derivation of a Near-Wall Limit . . . 45
4.8.2 Validation for Turbulent Channel Flow . . . 47
4.9 Square-Section Cylinder . . . 59

5 Extension I: Passive-Scalar Mixing 67
5.1 A Brief Insight into Scalar Mixing . . . 68
5.1.1 The Convection-Diffusion Equation . . . 68
5.1.2 Transport Regimes . . . 68
5.2 Variational Multiscale Formulation of the Convection-Diffusion Equation . . . 70
5.3 Multifractal Subgrid-Scale Modeling for Passive Scalars . . . 72
5.3.1 Outline of the Modeling Procedure . . . 72
5.3.2 Scalar-Gradient-Magnitude Cascade . . . 73
5.3.3 Scalar-Gradient-Orientation Cascade . . . 75
5.3.4 Subgrid-Scale Scalar Approximation . . . 75
5.3.5 Relation of Cascades in Scalar and Velocity Field . . . 76
5.3.6 A Remark on the Near-Wall Behavior . . . 77
5.4 Residual-Based Subgrid-Scale Modeling . . . 78
5.5 AVM^4 for Passive Scalars . . . 78
5.6 Passive-Scalar Mixing in Turbulent Channel Flow . . . 79
5.6.1 Low-to-Moderate Schmidt-Number Mixing at Sc ≈ 1 . . . 79
5.6.2 High-Schmidt-Number Mixing at Sc $\gg 1$ . . . 90
5.6.3 Transfer Coefficient . . . 93

6 Extension II: Turbulent Variable-Density Flow at Low Mach Number 97
6.1 The Low-Mach-Number Equation System . . . 98
6.2 Variational Multiscale Formulation of the Low-Mach-Number Equation System 100
6.3 Impacts of the Weak Compressibility on the Multifractal Subgrid-Scale Modeling 102
6.4 AVM^4 for Active Scalars . . . 104
6.5 Numerical Examples . . . 106
6.5.1 Turbulent Channel Flow with a Heated and a Cooled Wall . . . 106
6.5.2 Backward-Facing Step with Heating . . . 119

II XAVM^4 - The EXtended Algebraic Variational Multiscale-Multigrid-Multifractal Method for Two-Phase Flows 131

7 Fluid Dynamics with Interfaces 133
7.1 Physics of Two-Phase Flows . . . 133
7.2 Simulating Flows with Moving Interfaces . . . 135

8 A Computational Framework for the Level-Set Method 137
8.1 The Level-Set Equation . . . 137
8.2 Reinitialization . . . 139
8.2.1 Common Techniques for Reinitization . . . 140

8.2.2 Geometric Reinitialization . . . 141
8.2.3 Elliptic Reinitialization . . . 142
8.3 A Hybrid Particle-Level-Set Method . . . 144
8.3.1 Mass Loss: Sources and Remedies . . . 144
8.3.2 Initialization Procedure . . . 145
8.3.3 Particle Transport . . . 147
8.3.4 Correction by Particles . . . 147
8.3.5 Reseeding . . . 149
8.3.6 Overview of the Algorithm . . . 150
8.4 Numerical Test Cases and Applications . . . 151
8.4.1 Zalesak's Disk . . . 151
8.4.2 Single Vortex Stretching . . . 153
8.4.3 Deformation of a Sphere . . . 154
8.4.4 Impact of a Drop . . . 155

9 A Nitsche-Type Extended Variational Multiscale Method for Two-Phase Flow 157
9.1 Problem Statement . . . 157
9.2 The Extended Finite Element Method . . . 159
9.2.1 The Extent of the XFEM . . . 159
9.2.2 Enrichment Strategy . . . 160
9.3 A Face-Oriented Stabilized Nitsche-Type Formulation . . . 163
9.3.1 "Nitsche's method is the most straightforward method to use" . . . 163
9.3.2 Enforcement of the Dirichlet-Type Interface Condition . . . 166
9.3.3 Face-Oriented Ghost-Penalty Stabilization . . . 167
9.4 The Final Coupled Formulation . . . 171
9.5 The Fluid-Level-Set Coupling Algorithm . . . 172
9.6 Numerical Examples for Laminar Two-Phase Flows . . . 176
9.6.1 Two-Dimensional Rayleigh-Taylor Instability . . . 176
9.6.2 Two-Dimensional Collapsing Water Column . . . 180
9.6.3 Three-Dimensional Rising Bubbles . . . 184
9.6.4 Three-Dimensional Bubble Coalescence . . . 187

10 Turbulent Two-Phase Flows 193
10.1 Towards New Challenges for Modeling Subgrid-Scale Features . . . 193
10.2 Bubble-Vortex Interaction . . . 194
10.3 Extending the AVM^4 . . . 197
10.4 Turbulent Two-Phase Bubbly Channel Flow . . . 198

11 Summary and Outlook 207

A Supplementary Data for Backward-Facing Step Flow with Heating 209

Bibliography 213

Nomenclature

Abbreviations

ALE	Arbitrary Lagrangian-Eulerian
AVM^4	Algebraic Variational Multiscale-Multigrid-Multifractal Method
BACI	Bavarian Advanced Computational Initiative
CFD	Computational Fluid Dynamics
CFL	Courant-Friedrichs-Lewy number
DES	Detached Eddy Simulation
DNS	Direct Numerical Simulation
DSM	Dynamic Smagorinsky Model
ENO/WENO	(Weighted) Essentially Non-Oscillatory schemes
FDM	Finite Difference Method
FEM	Finite Element Method
FFT	Fast Fourier Transformation
FVM	Finite Volume Method
HPLS	Hybrid Particle-Level-Set method
ILES	Implicit Large-Eddy Simulation
LES	Large-Eddy Simulation
LS	Level-Set
MFS	MultiFractal Subgrid-scale modeling
PA-AMG	Plain Aggregation Algebraic MultiGrid method
PSPG	Pressure Stabilized Petrov-Galerkin
RANS	Reynolds-Averaged Navier-Stokes
RBVMM	complete Residual-Based Variational Multiscale Method
REINIT	REINITialization
SPGSM	SUPG/PSPG/Grad-div Stabilized Method
SUPG	Streamline/Upwind Petrov-Galerkin
VMM	Variational Multiscale Method
VOF	Volume-of-Fluid method
XAVM^4	eXtended Algebraic Variational Multiscale-Multigrid-Multifractal Method
XFEM	eXtended Finite Element Method

Dimensionless Numbers

At	Atwood number
Eo	Eötvös number
Ma	Mach number
Mo	Morton number
Pe	Péclet number

Pr	Prandtl number
Re	Reynolds number
Sc	Schmidt number
St	Strouhal number
We	Weber number

Greek Symbols

α	coarsening factor
α	void fraction
α_{F}	time-integration parameter (generalized-α)
α_{M}	time-integration parameter (generalized-α)
α_{NP}	Nitsche parameter
α_{P}	penalty parameter elliptic reinitalization
γ	time-integration parameter (generalized-α)
γ	parameter for inertial-convective- and viscous-convective-range scaling
γ	surface-tension coefficient
$\gamma_{\mathrm{gp}}^{\mu}$	parameter of viscous face-oriented ghost-penalty stabilization term
γ_{gp}^{p}	parameter of pressure face-oriented ghost-penalty stabilization term
γ_{gp}^{t}	parameter of reactive face-oriented ghost-penalty stabilization term
γ^{div}	parameter of divergence face-oriented fluid stabilization term
$\gamma^{\mathbf{u}}$	parameter of convective face-oriented fluid stabilization term
$\Gamma_{\mathrm{D},\phi}$	Dirichlet boundary for convection-diffusion equation
$\Gamma_{\mathrm{D},\mathbf{u}}$	Dirichlet boundary for momentum equation
$\Gamma_{\mathrm{D},T}$	Dirichlet boundary for energy equation
$\Gamma_{\mathrm{N},\phi}$	Neumann boundary for convection-diffusion equation
$\Gamma_{\mathrm{N},\mathbf{u}}$	Neumann boundary for momentum equation
$\Gamma_{\mathrm{N},T}$	Neumann boundary for energy equation
$\Gamma_{\mathrm{N},\mathbf{u}}^{\mathrm{in}}$	inflow part of Neumann boundary for momentum equation
$\Gamma_{\mathrm{N},T}^{\mathrm{in}}$	inflow part of Neumann boundary for energy equation
$\Gamma_{\mathrm{N},\mathbf{u}}^{\mathrm{out}}$	outflow part of Neumann boundary for momentum equation
$\Gamma_{\mathrm{N},T}^{\mathrm{out}}$	outflow part of Neumann boundary for energy equation
Γ_{int}	interface
δ_{c}	channel half-width
δ_{ν}	viscous length scale
$\boldsymbol{\delta}$	stochastic-decorrelation increment
$\boldsymbol{\delta}^{*}$	modified stochastic-decorrelation increment
$\boldsymbol{\Delta}$	grid filter width
ε	dissipation rate
$\varepsilon_{\mathrm{sgs}}$	subgrid-scale dissipation
$\boldsymbol{\varepsilon}(\mathbf{u})$	rate-of-deformation tensor
$\boldsymbol{\varepsilon}^{*}(\mathbf{u})$	deviatoric part of rate-of-deformation tensor
η	Kolmogorov length scale
η_{B}	Batchelor length scale

η_{OC}	Obukhov-Corrsin length scale
θ	time-integration parameter (one-step-theta)
ι	imaginary unit
κ	diffusivity
κ	curvature
κ_{sgs}	subgrid diffusivity
λ	thermal conductivity
λ_κ	diffusive (or inner) length scale
λ_ν	viscous (or inner) length scale
μ	dynamic viscosity
μ_{sgs}	dynamic subgrid viscosity
ν	kinematic viscosity
ν_{sgs}	kinematic subgrid viscosity
$\boldsymbol{\xi}$	element coordinate vector
$\xi_1,\ \xi_2,\ \xi_3$	first, second and third element coordinate
ρ	density
ρ_∞	time-integration parameter (generalized-α)
ρ_{m}	mixture density
$\boldsymbol{\sigma}(\mathbf{u}, p)$	Cauchy-stress tensor
τ_{C}	stabilization parameter of grad-div term
τ_{CD}	stabilization parameter of SUPG term for convection-diffusion equation
τ_{E}	stabilization parameter of SUPG term for energy equation
τ_{LS}	stabilization parameter of SUPG term for level-set equation
τ_{M}	stabilization parameter of SUPG and PSPG term
τ_{W}	wall-shear stress
$\boldsymbol{\tau}_{\mathrm{C}}$	cross-stress tensor
$\boldsymbol{\tau}_{\mathrm{L}}$	Leonard-stress tensor
$\boldsymbol{\tau}_{\mathrm{R}}$	subfilter-scale Reynolds-stress tensor
$\boldsymbol{\tau}_{\mathrm{sfs}}$	subfilter-scale stress tensor
$\boldsymbol{\tau}^*_{\mathrm{sfs}}$	subfilter-scale stress tensor without Leonard-stress part
$\boldsymbol{\tau}_{\mathrm{sgs}}$	subgrid-scale stress tensor
$\boldsymbol{\tau}^*_{\mathrm{sgs}}$	subgrid-scale stress tensor without Leonard-stress part
ϕ	passive-scalar quantity
ϕ	level-set function
ϕ_τ	friction scalar
$\boldsymbol{\Phi}$	vector of scalar degrees of freedom
χ	diffusion rate
$\chi_-,\ \chi_+$	phase-indicator function
$\boldsymbol{\Psi}$	enrichment function
$\boldsymbol{\omega}$	vorticity vector
Ω	domain
$\partial\Omega$	domain boundary
$\overline{\Omega}$	closure of domain
Ω^e	element domain

Ω^*	union of all element interiors

Roman Symbols

a	thermal diffusivity
$\mathbf{a}$	advective velocity
A	node
$A(\cdot)$	area of specified domain
$\mathcal{A}^h$	aggregate
$\mathbf{A}$	convective matrix
b	rate of expansion
b_{min}	minimal distance of interface
b_{max}	maximal distance of interface
B	coefficient of multifractal subgrid-scale velocity
$\mathcal{B}_{\text{C}}(\{\cdot\};\{\cdot\})$	continuity part on left-hand side of variational form
$\mathcal{B}_{\text{C}}^{1,\text{lin}}(q^h;\hat{\mathbf{u}},\hat{T})$	variational form of linear terms in unresolved-scale quantities without convective part in particular form of continuity equation for variable-density flow at low Mach number
$\mathcal{B}_{\text{C}}^{2}(q^h;\mathbf{u}^h,\hat{\mathbf{u}},T^h,\hat{T})$	variational form of non-linear terms in unresolved-scale quantities in particular form of continuity equation for variable-density flow at low Mach number
$\mathcal{B}_{\text{CD}}(\{\cdot\};\{\cdot\})$	variational form comprising left-hand-side terms of convection-diffusion equation
$\mathcal{B}_{\text{CD}}^{1,\text{lin}}(w^h;\hat{\phi})$	variational form of linear terms in unresolved-scale quantities without convective part of convection-diffusion equation
$\mathcal{B}_{\text{E}}(w^h;\mathbf{u}^h,T^h)$	variational form comprising left-hand-side terms of energy equation
$\mathcal{B}_{\text{E}}^{1,\text{lin}}(w^h;\hat{T})$	variational form of linear terms in unresolved-scale quantities without convective part of energy equation
$\mathcal{B}_{\text{FOStab}}(\mathbf{v}^h,q^h;\mathbf{u}^h,p^h)$	compact form of face-oriented stabilizations terms
$\mathcal{B}_{\text{M}}(\{\cdot\};\{\cdot,\cdot\})$	momentum part on left-hand side of variational form
$\mathcal{B}_{\text{M}}^{1,\text{lin}}(\mathbf{v}^h;\hat{\mathbf{u}},\hat{p})$	variational form of linear terms in unresolved-scale quantities without convective part of momentum equation
$\mathcal{B}_{\text{Nit}}(\mathbf{v}^h,q^h;\mathbf{u}^h,p^h)$	compact form of interface terms of Nitsche's method
$\mathcal{B}_{\text{NS}}(\{\cdot,\cdot\};\{\cdot,\cdot\})$	variational form comprising left-hand-side terms of Navier-Stokes equations
$\mathcal{B}_{\text{NS}}^{1}(\{\cdot,\cdot\};\mathbf{u}^h,\hat{\mathbf{u}},\hat{p})$	variational form of linear terms in unresolved-scale quantities of Navier-Stokes equations
$\mathcal{B}_{\text{NS}}^{2}(\{\cdot\};\hat{\mathbf{u}})$	variational form of quadratic term in unresolved-scale quantities of Navier-Stokes equations
$\mathcal{B}_{\text{NS}}^{1,\text{lin}}(\mathbf{v}^h,q^h;\hat{\mathbf{u}},\hat{p})$	variational form of linear terms in unresolved-scale quantities without convective part of Navier-Stokes equations
$\mathcal{B}_{\text{RBStab}}(\mathbf{v}^h,q^h;\mathbf{u}^h,p^h)$	compact form of residual-based stabilizations terms
c_ν	proportionality constant of element-Reynolds-number scaling
c_p	specific heat capacity at constant pressure
C_{B}	Batchelor constant

C_{C}	scaling factor for mesh stretching parameter
C_{G}	mesh stretching parameter for refinement
C_{I}	constant depending on element topology
C_{K}	Kolmogorov constant
C_{M}	coefficient for global mass conservation
C_{OC}	Obukhov-Corrsin constant
C_{S}	Smagorinsky constant
$C_{\mathrm{sgs}}^{\mathrm{B}}$	model parameter of multifractal subgrid-scale velocity
$C_{\mathrm{sgs}}^{\mathrm{Bmw}}$	model parameter of multifractal subgrid-scale velocity including near-wall limit
$C_{\mathrm{sgs}}^{\mathrm{D}}$	model parameter of multifractal subgrid-scale scalar quantity
$C_{\mathrm{sgs}}^{\mathrm{Dc}}$	model parameter of multifractal subgrid-scale scalar quantity adapted to near-wall limit
$\mathcal{C}(\mathbf{v}^h; \mathbf{u}^h, \hat{\mathbf{u}})$	(variational) cross-stress terms
$\mathcal{C}_{\mathrm{CD}}(\mathbf{v}^h; \mathbf{u}^h, \hat{\mathbf{u}}, \phi^h, \hat{\phi})$	(variational) cross-stress terms of convection-diffusion equation
$\mathcal{C}_{\mathrm{E}}(\mathbf{v}^h; \mathbf{u}^h, \hat{\mathbf{u}}, T^h, \hat{T})$	(variational) cross-stress terms of energy equation
$\mathbf{C}$	matrix of cross-stress terms
$d^{\mathcal{A}^h}$	degree of freedom of root node
D	coefficient of multifractal subgrid-scale scalar quantity
D	diameter of sphere/circle or edge length of cube/square
$D_\chi(k)$	diffusion spectrum
e	element
$\mathbf{e}_{\boldsymbol{\omega}}$	unit orientation vector of vorticity
$\mathbf{e}_{\nabla\phi}$	unit orientation vector of scalar gradient
$E(\mathbf{k})$	kinetic energy at given wave-number vector
$E(k)$	three-dimensional kinetic-energy spectrum
$E_\phi(k)$	three-dimensional scalar-variance spectrum
$\mathcal{E}$	set of all nodes
$\mathcal{E}_{\mathrm{enr}}$	set of enriched nodes
f	mesh stretching function
f	face
f_{ai}	anisotropy factor
f_ϕ	source term convection-diffusion equation
$\mathbf{f}$	right-hand-side vector
$\mathbf{f}$	volume force vector
$\mathcal{F}$	set of element faces for face-oriented stabilization
g	magnitude of gravity force vector
$\mathbf{g}$	gravity force vector
$\mathcal{G}^h$	set of intersected elements
$\mathbf{G}$	covariant metric tensor
$\mathbf{G}$	gradient matrix
h	characteristic element length
h_f	length associated with element face
h_ϕ	Neumann boundary diffusive flux
h_T	Neumann boundary heat flux

$\mathbf{h_u}$	Neumann boundary momentum flux
H	geometric height
$H^1(\Omega)$	Sobolev space of square-integrable functions with square-integrable first derivatives
$\mathcal{I}_{\boldsymbol{\omega}}$	intermittency factor for vorticity field
$\mathcal{I}_{\nabla\phi}$	intermittency factor for scalar gradient field
$\mathbf{I}$	identity tensor
k	wave number
k_κ	diffusive (or inner) wave number
k_ν	viscous (or inner) wave number
k_h	wave number associated with discretization
$k_{\alpha h}$	wave number associated with coarser level
$\mathbf{k}$	wave-number vector
$\mathbf{K}$	summarized mass, convective and viscous matrix
ℓ	characteristic length
$\ell_{\mathrm{C}}(\{\cdot\})$	right-hand-side variational form of particular form of continuity equation for variable-density flow at low Mach number
$\ell_{\mathrm{CD}}(\{\cdot\})$	right-hand-side variational form of convection-diffusion equation
$\ell_{\mathrm{E}}(\{\cdot\})$	right-hand-side variational form of energy equation
$\ell_{\mathrm{M}}(\{\cdot\})$	right-hand-side variational form of momentum equation
$\ell_{\mathrm{NS}}(\{\cdot\})$	right-hand-side variational form of Navier-Stokes equations
L	geometric length
$L_2(\Omega)$	Hilbert space of square-integrable functions
$\mathcal{M}$	multiplier
$\mathbf{M}$	mass matrix
n_{B}	number of bubbles
n_{el}	number of elements
n_P	number of particles
n_{sc}	base of multiplicative process
n_{sd}	number of space dimensions
$\mathbf{n}$	outer unit normal vector on domain boundary
$\mathbf{n}(\phi)$	unit normal vector on level-set iso-contours
$\mathbf{n}_f$	unit normal vector on element face
$\mathbf{n}_{\mathrm{int}}$	unit normal vector on interface
N	shape function
N_{n}	number of sampling nodes
N_{s}	number of sampling time steps
$\mathcal{N}$	number of cascade steps
$\mathcal{N}_\phi$	number of cascade steps for scalar gradient field
$\mathcal{N}_{\mathbf{u}}$	number of cascade steps for vorticity field
$\mathbf{N}$	matrix containing shape functions
p	pressure
p_{hyd}	hydrodynamic pressure part
p_{kin}	kinematic pressure
p_{the}	thermodynamic pressure part

P	particle
$P(\mathcal{M})$	distribution of multipliers
$\mathcal{P}$	set of escaped particles
$\mathbf{P}$	vector of pressure degrees of freedom
$\mathbf{P}_{3h}^{h}$	prolongation operator matrix
q	pressure weighting function
q_{W}	wall heat flux
Q	enstrophy
$\mathcal{Q}_1(\Omega^e)$	set of trilinear functions
$r_{\max}$	maximal particle radius
$r_{\min}$	minimal particle radius
r_P	particle radius
r_{C}^{h}	discrete residual of continuity equation
r_{CD}^{h}	discrete residual of convection-diffusion equation
$\mathbf{r}_{\mathrm{E}}^{h}$	discrete residual of energy equation
$\mathbf{r}_{\mathrm{LS}}^{h}$	discrete residual of level-set equation
$\mathbf{r}_{\mathrm{M}}^{h}$	discrete residual of momentum equation
R	gas constant
R	bubble radius
Re_τ	friction Reynolds number
Re_h	element Reynolds number
$\mathrm{Re}_h^{\mathrm{R}}$	element Reynolds number based on resolved velocity
$\mathrm{Re}_h^{\mathrm{S}}$	element Reynolds number based on strain rate tensor
$\mathcal{R}(\mathbf{v}^h;\hat{\mathbf{u}})$	(variational) subgrid-scale Reynolds-stress term
$\mathcal{R}_{\mathrm{CD}}(\mathbf{v}^h;\hat{\mathbf{u}},\hat{\phi})$	(variational) subgrid-scale Reynolds-stress term of convection-diffusion equation
$\mathcal{R}_{\mathrm{E}}(\mathbf{v}^h;\hat{\mathbf{u}},\hat{T})$	(variational) subgrid-scale Reynolds-stress term of energy equation
$\mathbf{R}$	matrix of subgrid-scale Reynolds-stress term
$\mathbf{R}_h^{3h}$	restriction operator matrix
w	scalar weighting function
$w_-,\ w_+$	weights for averaging
S	Sutherland constant
$\mathcal{S}_\phi$	solution function space for scalar quantity
$\mathcal{S}_\phi^h$	finite-dimensional subspace for (resolved) scalar solution function
$\hat{\mathcal{S}}_\phi$	infinite-dimensional subspace for (subgrid) scalar solution function
$\mathcal{S}_p$	solution function space for pressure
$\mathcal{S}_p^h$	finite-dimensional subspace for (resolved) pressure solution function
$\hat{\mathcal{S}}_p$	infinite-dimensional subspace for (subgrid) pressure solution function
$\mathcal{S}_p^{h,\mathrm{enr}}$	finite-dimensional subspace for enriched pressure solution function
$\mathcal{S}_{\mathbf{u}}$	solution function space for velocity
$\mathcal{S}_{\mathbf{u}}^h$	finite-dimensional subspace for (resolved) velocity solution function
$\hat{\mathcal{S}}_{\mathbf{u}}$	infinite-dimensional subspace for (subgrid) velocity solution function
$\mathcal{S}_{\mathbf{u}}^{h,\mathrm{enr}}$	finite-dimensional subspace for enriched velocity solution function

$\mathcal{S}_T^h$	finite-dimensional subspace for (resolved) temperature solution function
$\mathbf{S}_h^{3h}$	scale-separation operator matrix
t	time
t_{end}	time period
Δt	time-step length
$\mathbf{t}_{\text{int}}$	unit tangential vector on interface
T	temperature
T_τ	friction temperature
$\mathcal{T}^h$	triangulation
u	scalar solution field for illustration purposes
u_{int}	interface velocity
u_τ	friction velocity
$\mathbf{u}$	velocity vector
$u_1,\ u_2,\ u_3$	first (streamwise), second (wall-normal) and third (spanwise) component of velocity vector
$\mathbf{u}^{(\boldsymbol{\omega})}$	rotational velocity component
$\mathbf{u}^{(\phi)}$	irrotational velocity component
U	characteristic velocity
$\mathbf{U}$	vector of velocity degrees of freedom
$\dot{\mathbf{U}}$	vector of nodal acceleration values
$\mathbf{v}$	velocity weighting function
$V(\cdot)$	volume of specified domain
$\mathcal{V}_\phi$	weighting function space for scalar quantity
$\mathcal{V}_\phi^h$	finite-dimensional subspace for (resolved) scalar weighting function
$\hat{\mathcal{V}}_\phi$	infinite-dimensional subspace for (subgrid) scalar weighting function
$\mathcal{V}_p$	weighting function space for pressure
$\mathcal{V}_p^h$	finite-dimensional subspace for (resolved) pressure weighting function
$\hat{\mathcal{V}}_p$	infinite-dimensional subspace for (subgrid) pressure weighting function
$\mathcal{V}_p^{h,\text{enr}}$	finite-dimensional subspace for enriched pressure weighting function
$\mathcal{V}_\mathbf{u}$	weighting function space for velocity
$\mathcal{V}_\mathbf{u}^h$	finite-dimensional subspace for (resolved) velocity weighting function
$\hat{\mathcal{V}}_\mathbf{u}$	infinite-dimensional subspace for (subgrid) velocity weighting function
$\mathcal{V}_\mathbf{u}^{h,\text{enr}}$	finite-dimensional subspace for enriched velocity weighting function
$\mathcal{V}_T^h$	finite-dimensional subspace for (resolved) temperature weighting function
$\mathbf{V}$	viscous matrix
x_{G}	location of inflection point for mesh stretching
$\mathbf{x}$	coordinate vector
$x_1,\ x_2,\ x_3$	first (streamwise), second (wall-normal/vertical) and third (spanwise) coordinate
X_{r}	mean recirculation/reattachment length
$Z_Q(k)$	enstrophy spectrum

Symbols, Subscripts, Superscripts and other Quantifiers

$(\cdot)^h$	resolved-scale quantity associated with finite-dimensional subspace
$(\cdot)^{\alpha h}$	larger resolved-scale quantity
$\delta(\cdot)^h$	smaller resolved-scale quantity
$\widehat{(\cdot)}$	subgrid-scale quantity associated with infinite-dimensional subspace
$\langle\cdot\rangle$	mean value
$(\cdot)'$	fluctuation
$\overline{(\cdot)}$	filtered quantity
$(\cdot)''$	subfilter-scale quantity
$\widehat{(\cdot)}$	Fourier transform
$\widehat{(\cdot)}^*$	conjugate complex of Fourier transform
$\widetilde{(\cdot)}$	related to enrichment
$(\cdot)_+$	quantity in domain defined by positive level-set values
$(\cdot)_-$	quantity in domain defined by negative level-set values
$(\cdot)_k$	identifier for fluid/subdomain in two-phase flow
$(\cdot)_0$	initial value
$(\cdot)_\infty$	free-stream value
$(\cdot)_{\mathrm{D}}$	Dirichlet boundary value
$(\cdot)_{\max}$	maximal value
$(\cdot)_{\min}$	minimal value
$(\cdot)_{\mathrm{ref}}$	reference value
$(\cdot)_{\mathrm{W}}$	value at the wall
$(\cdot)_A$	nodal value
$(\cdot)_h$	determined from discrete values
$(\cdot)_P$	corresponding to particle
$(\cdot)^+$	value in wall units
$(\cdot)^{\mathrm{corr}}$	corrected level-set value
$(\cdot)^{\mathrm{extr}}$	extrapolated field, function or domain
$\check{(\cdot)}$	integration variable
rms $(\cdot)$	root-mean-square value
sign$(\cdot)$	sign-function
tr$(\cdot)$	trace of matrix

Operators

$(\{\cdot\},\{\cdot\})_{\{\cdot\}}$	L_2-inner product on domain or boundary/interface specified by index
$\{\cdot\}_w,\ \langle\cdot\rangle_w$	weighted average
$[\![\cdot]\!]$	jump operator
$\nabla_\Gamma(\cdot)$	tangential derivative operator
$D^i(\cdot)$	normal derivative of order i

1 Introduction

1.1 Motivation

Although the first attempts to describe the phenomenon of turbulence may be traced back to drawings by Leonardo da Vinci about 500 years ago, turbulence has lost nothing of its fascination for scientists and still constitutes a field of extensive research. In a review article, Moin and Kim [222] stated: "Practically all the fluid flows that interest scientists and engineers are turbulent ones; turbulence is the rule, not the exception, in fluid dynamics." In fact, turbulent flows are ubiquitous in the natural environment and the technical field of engineering. Solar flares have their origins in the turbulence emerging on the surface of the sun. The knowledge of turbulent atmospheric flows involved in cloud formation allows for accurate weather forecasting. The design of efficient internal combustion engines strongly relies on the turbulent mixing of fuel and oxidizer. The drag acting on aircraft, cars and nautical vessels is controlled by turbulent boundary layers, to name but a few examples.

Owing to the continuous developments in computer technology and the related rapid increase of computing power, Computational Fluid Dynamics (CFD) has become an established and important tool for the investigation of fluid flows. Since the non-linear nature of turbulence, however, gives rise to an enormous range of length and time scales, Direct Numerical Simulation (DNS), which aims at resolving all features down to the smallest scales, remains still infeasible for all but the simplest turbulent flows. In contrast to DNS, approaches based on the Reynolds-Averaged Navier-Stokes (RANS) equations merely compute the statistical averages; that is, the time-averaged non-turbulent mean flow, leaving all turbulent features to a model. By merely computing the larger flow-dependent structures, Large-Eddy Simulation (LES) can be classified in between DNS and RANS modeling. The larger scales of turbulent flows are of particular relevance for science and engineering. For instance, they control turbulent mixing of momentum and heat and provoke aerodynamic noise. In contrast, high-frequent fluctuations are usually only of minor interest. The cost of LES is significantly reduced compared to DNS, while the necessary degree of modeling is kept notably lower than for RANS approaches. Extensive research has been conducted in the field of LES in the past decades; see, e.g., the review articles by Rogallo and Moin [268] in the 1980s, by Piomelli [247] in the 1990s as well as by Moin [221] in the 2000s.

In LES, the large scales are explicitly computed. However, non-linear interactions between all turbulent scales are involved in the evolution of turbulent flows. Therefore, the unresolved small-scale information is crucial for a physically correct behavior of the resolved scales. To incorporate the effect of the non-linear interaction between resolved and unresolved (or subgrid) scales, proper modeling is required. The development of efficient and accurate models constitutes a

major research challenge in LES. In a review article, Piomelli [247] summarized four requirements which a successful subgrid-scale model should fulfill: (i) predict the overall dissipation correctly, (ii) vanish in laminar flow, (iii) depend strongly on the smallest resolved scales rather than on the entire turbulent spectrum and (iv) predict the local energy transfer between resolved and subgrid scales. Moreover, the actual applicability of the overall approach to LES of practically relevant flows is also of particular relevance. In this respect, there are two further aspects that deserve closer attention and were also raised to some extent by Piomelli [247]: A promising approach to LES should not only include a subgrid-scale model satisfying the aforementioned prerequisites but also (v) allow for convenient application to complex geometries and (vi) remain computationally efficient.

This elaboration highlights the need for comprehensive approaches to LES, which thoroughly take into account physical aspects, practical demands and computational issues. Aiming at developing such an approach, LES of turbulent single-phase incompressible flow is first considered in this thesis. Further extensions of LES methods to turbulent mixing of scalar fields are also of practical relevance. Passive-scalar fields, occurring, for instance, in electrochemical processes, have no influence on the flow field. In contrast, active-scalar fields such as the temperature in weakly compressible flows, for example, encountered in turbulent combustion, may give rise to substantial density variations. For these applications, new length scales in the scalar field as well as additional physics have to be incorporated into the approach to LES.

Furthermore, LES of turbulent two-phase flows is considered in this thesis. Industrial interest in turbulent two-phase flows range from bubble columns in chemical processes to liquid jets in combustion devices. Two-phase flows typically exhibit density ratios of the order of one thousand. Since the interface separating the two fluids may be assumed infinitely thin, it appears as a discontinuity in the flow field. Moreover, a localized surface-tension force acts at the interface. The interface may also be subject to large and complex deformations. All these features render two-phase flow particularly challenging from a computational point of view, independent of whether it is laminar or turbulent. Therefore, a first step towards successful LES of turbulent two-phase flows consists of the development of a reliable approach which copes with the aforementioned aspects. Further progress towards LES constitute another field of active research, among other things, due to modeling issues emanating from the presence of the interface.

1.2 Contribution of this Work

The present thesis is related to a subproject of the Emmy Noether research group "Computational multiscale methods for turbulent combustion in complex geometries"[1], which was headed by Dr.-Ing. Volker Gravemeier at the Institute for Computational Mechanics of the Technische Universiät München.

The objective of the present subproject is the development of novel and comprehensive computational multiscale methods for LES of turbulent single- and two-phase flows. Therefore, the

[1]Support via the Emmy Noether Program of the Deutsche Forschungsgemeinschaft (DFG) is gratefully acknowledged.

Variational Multiscale Method (VMM; see Hughes *et al.* [153]), which provides a promising conceptual framework, is exploited. As already implied by the name of the research group, all developed methods are intended to be applied to flows in complex geometries and generally suitable for practically relevant configurations. All algorithms are implemented on the basis of a continuous Galerkin finite element method.

For the present thesis, three major achievements can by stated:

An Algebraic Variational Multiscale-Multigrid-Multifractal Method (AVM^4): The AVM^4 (see Rasthofer and Gravemeier [258]) is particularly tailored in order to meet the aforementioned six demands towards an accurate and efficient LES. It is therefore built up from the VMM, multifractal subgrid-scale modeling and scale separation by level-transfer operators from plain aggregation algebraic multigrid methods. To evaluate the subgrid-scale velocity, the multifractal subgrid-scale modeling approach (see Burton and Dahm [53, 54]) is incorporated. Multifractal subgrid-scale modeling requires the further separation of the resolved scales into larger and smaller ones, which is performed by level-transfer operators from plain aggregation algebraic multigrid methods (see Gravemeier *et al.* [125]). The variational multiscale formulation is finalized by additional appropriate residual-based multiscale terms to control the stability of the numerical method.

A Face-Oriented Stabilized Nitsche-Type Extended Variational Multiscale Method: This approach (see Rasthofer and Schott *et al.* [262]) constitutes, to the best of the authors' knowledge, the first stable extended VMM based on Nitsche's method derived for two-phase flow governed by the incompressible Navier-Stokes equations. The method is based on a level-set description for the interface separating the two fluids. It incorporates the eXtended Finite Element Method (XFEM) using jump enrichments for the velocity and pressure field to enable a sharp representation of the discontinuities in the flow field. A further developed Nitsche's method is used to weakly impose continuity of the velocity field at the interface. Specifically devised face-oriented ghost-penalty and fluid stabilization terms in the vicinity of the interface ensure stability for viscous- and convection-dominated transient flows independent of the interface position.

An Extended Algebraic Variational Multiscale-Multigrid-Multifractal Method (XAVM^4): The XAVM^4 combines the AVM^4 and the face-oriented stabilized Nitsche-type extended VMM to a novel and comprehensive approach to LES of turbulent two-phase flows. The XAVM^4 is successfully applied to LES of turbulent channel flow carrying a single large bubble of the size of the channel half-width. To the best of the author's knowledge, this investigation constitutes the most challenging XFEM application in the vast field of CFD to date.

Additionally, several further developments and scientific contributions can be identified:

- the first application of the multifractal subgrid-scale modeling approach to wall-bounded turbulent flow including the derivation of a near-wall limit (see Rasthofer and Gravemeier [258]),
- the extension of the AVM^4 to LES of passive-scalar mixing in turbulent incompressible flow (see Rasthofer *et al.* [260]),
- the extension of the AVM^4 to LES of turbulent variable-density flow at low Mach number (see Rasthofer *et al.* [261]),

- a hybrid particle-level-set method realized as an add-on for further improving the level-set method.

In summary, a variety of subtopics is addressed by the developments provided in this thesis. As indicated, major parts have already been published in peer-reviewed journals.

1.3 Outline

The present thesis is organized in two parts according to the two flow types already mentioned in its title: single- and two-phase flow. Both parts can be read independently from each other for the most part.

Part I is devoted to LES of turbulent single-phase flow, for which the AVM^4 is introduced. The first part is further subdivided into the following chapters. In Chapter 2, the fundamentals of turbulent incompressible flow are briefly addressed, and the basic concept of LES is summarized. Chapter 3 is devoted to the VMM. Chapter 4 reports on multifractal subgrid-scale modeling within a VMM for LES of turbulent incompressible flow, eventually leading to the AVM^4. An appropriate near-wall limit for the multifractal subgrid-scale modeling is derived for application of the AVM^4 to wall-bounded turbulent flows. Results from various numerical examples of increasing complexity are included throughout this chapter to validate the approach and to illustrate its performance. Chapter 5 further extends the AVM^4 to passive-scalar mixing in turbulent incompressible flow. Within the multifractal subgrid-scale modeling approach, the entire range from low to high Schmidt numbers is considered. The method is eventually validated for passive-scalar mixing in turbulent channel flow for a broad range of Schmidt numbers in between 1 and 1000. The extension of the AVM^4 to turbulent variable-density flow at low Mach number is shown in Chapter 6. Applications to turbulent channel flow with a heated and a cooled wall as well as turbulent flow over a backward-facing step with heating are presented.

Part II reports on the combined level-set extended finite element approach for two-phase flow and further extends the AVM^4 to LES of turbulent two-phase flows. The remainder of the second part is given as follows. A brief introduction into two-phase flow and its numerical simulation is given in Chapter 7. A computational framework for level-set approaches within a finite element method is provided in Chapter 8. This chapter summarizes the level-set method used for two-phase flow. Additionally, a hybrid particle-level-set method is adapted and thoroughly validated. In Chapter 9, the face-oriented stabilized Nitsche-type extended VMM for two-phase-flow problems is developed step-by-step; that is, the applied XFEM is presented, Nitsche's method is incorporated and appropriate face-oriented ghost-penalty and fluid stabilization terms in the region of enriched elements are devised. Various two- and three-dimensional numerical examples for validation of the proposed formulation are discussed. Chapter 10 brings together the AVM^4 and the face-oriented stabilized Nitsche-type extended VMM for LES of turbulent two-phase flow, resulting in the XAVM^4. LES of turbulent two-phase bubbly channel flow is elaborately investigated.

The present thesis is concluded in Chapter 11.

I

AVM^4 - The Algebraic Variational Multiscale-Multigrid-Multifractal Method

2

From the Fundamentals of Turbulence to its Numerical Simulation

The present chapter is devoted to the fundamentals of turbulent incompressible flow. First, the mathematical description of incompressible fluid flow is provided, and the origins of turbulence are identified. Except for Chapter 6, where turbulent variable-density flow at low Mach number is investigated, incompressible flow is exclusively considered in the present thesis. Continuity and momentum equation are thus merely presented in the respective form for incompressible flow. Furthermore, a brief insight into the dynamics inherent in turbulent flow is given. Finally, in consideration of the characteristics and challenges of turbulent flow, Large-Eddy Simulation (LES) is identified as an adequate method for its numerical simulation and addressed in some more detail.

2.1 The Incompressible Navier-Stokes Equations

Based on the continuum hypothesis, which allows for treating fluids as a continuous medium instead of an ensemble of individual molecules, conservation of mass and momentum constitute the fundamental principles of fluid motion; see, e.g., the textbook by Batchelor [20] as well as the elucidations in the context of turbulent flows in the textbooks by Pope [252] and Tennekes and Lumley [309]. Assuming Newtonian fluids, the Navier-Stokes momentum equation is obtained from linear momentum conservation. For incompressible flow, mass conservation degenerates to a divergence-free constraint on the velocity field. The resulting system of equations for incompressible flow, comprising the Navier-Stokes momentum equation, expressed in conservative form, and the continuity equation, is given by

$$\frac{\partial \mathbf{u}}{\partial t} + \nabla \cdot (\mathbf{u} \otimes \mathbf{u}) + \nabla p_{\text{kin}} - 2\nu \nabla \cdot \boldsymbol{\varepsilon}(\mathbf{u}) = \mathbf{f}, \tag{2.1}$$

$$\nabla \cdot \mathbf{u} = 0, \tag{2.2}$$

presuming constant density. Here, $\mathbf{u}(\mathbf{x}, t) = (u_1(\mathbf{x}, t), u_2(\mathbf{x}, t), u_3(\mathbf{x}, t))^{\mathrm{T}}$ denotes the velocity vector, $p_{\text{kin}}(\mathbf{x}, t)$ the kinematic pressure, imposing the divergence-free constraint, and ν the kinematic viscosity, assumed constant. The independent variables $\mathbf{x} = (x_1, x_2, x_3)^{\mathrm{T}}$ and t represent spatial coordinates in a Cartesian coordinate system and time, respectively. The rate-of-deformation tensor $\boldsymbol{\varepsilon}(\mathbf{u})$ is defined as

$$\boldsymbol{\varepsilon}(\mathbf{u}) = \frac{1}{2} \left(\nabla \mathbf{u} + (\nabla \mathbf{u})^{\mathrm{T}} \right). \tag{2.3}$$

For brevity, a potential (i.e., taken to be zero unless specified otherwise) volume force vector $\mathbf{f}$ is omitted in the remainder of this chapter. For a detailed derivation of the governing equations of fluid flow, the reader is referred to classical textbooks on fluid dynamics, e.g., Batchelor [20], Kundu and Cohen [176] as well as Panton [243].

It is the non-linear convective term of the momentum equation that causes the origins of turbulence. In case of predominating inertia forces compared to viscous ones, instabilities related to the non-linear term provoke the transition to turbulence. If these inherent instabilities are suppressed by predominating viscous forces, the flow remains laminar. This behavior may also be quantified in terms of the Reynolds number, which is defined via the ratio of inertia to viscous forces as

$$\mathrm{Re} = \frac{U\ell}{\nu}, \tag{2.4}$$

where U denotes a characteristic velocity of the flow and ℓ a characteristic length, for instance, related to the geometry of the considered problem. Turbulent flow is thus characterized by a high Reynolds number.

2.2 The Nature of Turbulent Incompressible Flow

Turbulence is driven by vorticity and its self-induced velocity field. The dynamics of turbulence are not self-sustaining and require a continuous supply of energy to compensate dissipation. Hence, vorticity dynamics and energy transfer play an essential role in the evolution of turbulent flows, and particular attention is payed to these issues in the present section. For an exhaustive description of these aspects as well as for further elaboration of the physics of turbulence, the reader is referred, e.g., to the textbooks on turbulent flows by Davidson [78], Pope [252] and Tennekes and Lumley [309].

2.2.1 Vorticity Dynamics

Turbulent flows are rotational and exhibit a spatially complex three-dimensional distribution of vortical structures. These vortical structures, which may be spherical, tubular, sheet-like or even more complex in shape, and their associated velocity field are usually referred to as turbulent eddies. Turbulent eddies are localized in space, occupying a region of a certain size which defines their associated length scale. The evolution of an eddy is governed by the velocity field induced by the eddy itself and by all the other vortical structures.

The vorticity $\boldsymbol{\omega}(\mathbf{x}, t)$ is defined as

$$\boldsymbol{\omega}(\mathbf{x}, t) = \nabla \times \mathbf{u}(\mathbf{x}, t). \tag{2.5}$$

The law of Biot-Savart enables the inversion of this relation, and the velocity field induced by vorticity is given by

$$\mathbf{u}(\mathbf{x}, t) = \frac{1}{4\pi} \int \boldsymbol{\omega}(\check{\mathbf{x}}, t) \times \frac{\mathbf{x} - \check{\mathbf{x}}}{\|\mathbf{x} - \check{\mathbf{x}}\|^3} \mathrm{d}\check{\mathbf{x}}; \tag{2.6}$$

see, e.g., the textbook by Panton [243] for derivation. By taking the curl of the momentum equation (2.1), the vorticity equation is obtained as

$$\frac{\partial \boldsymbol{\omega}}{\partial t} + \mathbf{u} \cdot \nabla \boldsymbol{\omega} = \boldsymbol{\omega} \cdot \nabla \mathbf{u} + \nu \Delta \boldsymbol{\omega}. \tag{2.7}$$

The first term on the right-hand side, which can be transformed into $\varepsilon(\mathbf{u})\boldsymbol{\omega}$, describes a modification of the vorticity vector in magnitude and orientation by the strain rate and is thus referred to as vortex-stretching term. A simplified process of vortex stretching is illustrated in Figure 2.1. A spherical vortical structure is elongated by the strain rate field of convergent streamlines, resulting in a shrinking cross-section area and, hence, in a decrease of the moment of inertia. Owing to the conservation of angular momentum, the magnitude of $\boldsymbol{\omega}$ increases. Hence, vortex stretching comes along with a change of the length scale. Since this process leads to a hierarchy of vortical structures of varying size, it is responsible for the multiscale character of turbulence. Vortex-stretching is exclusively linked to three dimensions, since the respective term vanishes for two-dimensional flows. The only non-zero component of $\boldsymbol{\omega}$ then behaves as a conserved scalar.

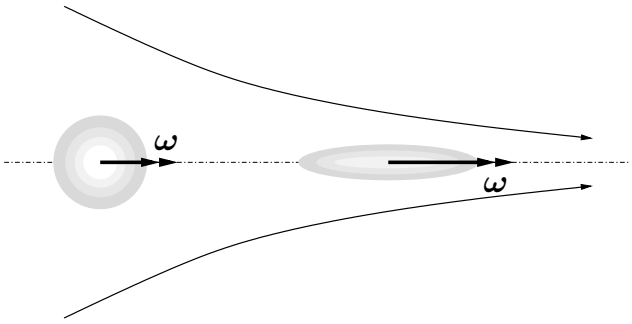

Figure 2.1: Vortex stretching by strain rate field of convergent streamlines (adapted from Davidson [78]).

The intensification of vorticity due to stretching may also be expressed via the enstrophy Q, which is defined as

$$Q = \boldsymbol{\omega} \cdot \boldsymbol{\omega}. \tag{2.8}$$

Taking the scalar product of the vorticity equation (2.7) with $\boldsymbol{\omega}$ yields the corresponding evolution equation:

$$\frac{\partial}{\partial t}\left(\frac{Q}{2}\right) + \mathbf{u} \cdot \nabla \left(\frac{Q}{2}\right) = \boldsymbol{\omega} \cdot (\boldsymbol{\omega} \cdot \nabla \mathbf{u}) - \nu \left(\nabla \times \boldsymbol{\omega}\right)^2 + \nu \nabla \cdot (\boldsymbol{\omega} \times (\nabla \times \boldsymbol{\omega})). \tag{2.9}$$

The first term on the right-hand side of the enstrophy equation corresponds to the generation and reduction of enstrophy by vortex stretching and compression, respectively. Since stretching outbalances compression, most of the enstrophy resides in the smallest structures. The second term on the right-hand side represents destruction of enstrophy by viscous effects. The derivations of equations (2.7) and (2.9) may be found, e.g., in the textbooks by Davidson [78] and Tennekes and Lumley [309].

2.2.2 Energy Cascade

Vortex stretching constitutes the primary mechanism of turbulence. It is accompanied by a transfer of energy to successively smaller scales, which manifests itself in Richardson's [265] picture of an energy cascade. The continuous distortion of the shape of the vortical structures, also named eddy break-up, proceeds until the vortical structures are sufficiently small to enforce dissipation. The entire energy-transfer process starts from the introduction of energy by turbulence production mechanisms acting on the largest flow scales and continues via an inviscid cascade passing energy to successively smaller scales until the energy is eventually dissipated at the smallest scales. Within this process, the production of energy equals its dissipation which in turn equals the rate at which energy is passed through the cascade.

A further specification of the various stages of the energy transfer and the involved scale ranges is enabled by the three hypotheses proposed by Kolmogorov [174]. For sufficiently high Reynolds numbers, Kolmogorov [174] hypothesized the existence of a universal equilibrium range containing the scales down the cascade as well as the ones affected by dissipation. The corresponding small-scale eddies are considered isotropic, independent of the flow and in equilibrium, as postulated in the hypothesis of local isotropy. The remaining anisotropic, large-scale structures, which possess the bulk of the energy, are comprised in the energy-containing range. According to the first similarity hypothesis, the turbulent structures belonging to the universal equilibrium range are exclusively determined by the dissipation rate ε, the kinematic viscosity ν and their associated length scale. Based on ε and ν, the Kolmogorov length scale

$$\eta = \left(\frac{\nu^3}{\varepsilon}\right)^{\frac{1}{4}} \tag{2.10}$$

is defined. Since the corresponding Reynolds number is unity and, hence, small enough for dissipation to be effective, the Kolmogorov length scale estimates the smallest scale of significance in turbulent flows. The universal equilibrium range is further divided into two subranges. Structures belonging to the dissipation range experience extensive viscous forces such that dissipation can be almost exclusively confined to this range. In contrast, the evolution of the eddies contained in the inertial subrange, which is addressed by the second similarity hypothesis, is unaffected by viscosity and mainly driven by inertial forces.

This feature of turbulent flow may be expressed in a more quantitative form via the three-dimensional kinetic-energy spectrum $E(k)$, which represents the involved scales as well as their associated kinetic energy in terms of the wave number k. Therefore, the velocity field $\mathbf{u}$ is transferred to Fourier space via

$$\widehat{\mathbf{u}}(\mathbf{k}, t) = \frac{1}{(2\pi)^3} \int \mathbf{u}(\mathbf{x}, t) \mathrm{e}^{-\iota \mathbf{k}\cdot\mathbf{x}} \mathrm{d}\mathbf{x}, \tag{2.11}$$

where $\mathbf{k} = (k_1, k_2, k_3)^{\mathrm{T}}$ is the wave-number vector with magnitude $k = \|\mathbf{k}\|$ and $\iota^2 = -1$. The conjugate complex of $\widehat{\mathbf{u}}$ is denoted by $\widehat{\mathbf{u}}^*$. Furthermore, the kinetic energy at a given wave-

number vector $\mathbf{k}$ is obtained as

$$E(\mathbf{k},t) = \frac{1}{2}\langle \widehat{\mathbf{u}}(\mathbf{k},t) \cdot \widehat{\mathbf{u}}^*(\mathbf{k},t)\rangle, \tag{2.12}$$

where $\langle\cdot\rangle$ denotes a mean value obtained from ensemble averaging. Assuming homogeneous isotropic turbulence with zero mean velocity and removing the directional information via integration of $E(\mathbf{k},t)$ over spherical shells with radius k leads to the three-dimensional kinetic-energy spectrum:

$$E(k,t) = \oint\limits_{\|\mathbf{k}\|=k} E(\mathbf{k},t)\mathrm{d}\mathbf{k}. \tag{2.13}$$

Kolmogorov's hypothesis of local isotropy implies a universal form of $E(k)$ in the equilibrium range; that is, the energy spectra of high-Reynolds-number flows coincide when nondimensionalization by ε and ν, as stated in the first similarity hypothesis, is applied. In the inertial subrange, the shape of the three-dimensional kinetic-energy spectrum is further determined by the second similarity hypothesis. Based on dimensional grounds, it is obtained as

$$E(k) = C_\mathrm{K}\varepsilon^{\frac{2}{3}}k^{-\frac{5}{3}}, \tag{2.14}$$

where C_K is the Kolmogorov constant. Figure 2.2 shows the three-dimensional kinetic-energy spectrum $E(k)$ for turbulent flows. Therein, the various scale ranges are marked, and the energy-transfer process is indicated. High-Reynolds-number flows are characterized by their distinctive inertial subrange, which is absent in the laminar case.

2.3 Large-Eddy Simulation of Turbulent Flows

Summarizing the previous section, turbulence is a multiscale problem, where the ratio of the length scale $\mathcal{L}$ associated with the largest and most energetic structures and the length scale η related to the smallest ones is estimated by the Reynolds number as

$$\frac{\mathcal{L}}{\eta} \sim \mathrm{Re}^{\frac{3}{4}}. \tag{2.15}$$

This dependency currently renders DNS inappropriate for practically relevant high-Reynolds-number flows. Hence, a certain level of modeling is unavoidable. Instead of modeling all turbulent features of the flow, as it is done for RANS approaches, Kolmogorov's hypothesis of local isotropy suggests restricting the modeling effort to the smaller scales. Due to their universal character, models accounting for these scales are supposed to be independent of the flow. The flow-dependent larger turbulent motions are then explicitly computed in LES. The corresponding scales usually comprise the entire energy-containing range as well as parts of the inertial subrange. An elaborate introduction into the framework of LES as well as a compilation of various modeling procedures may be found in the textbook by Sagaut [270]. More advanced approaches further extending the LES concept towards multiscale and multiresolution methods are provided

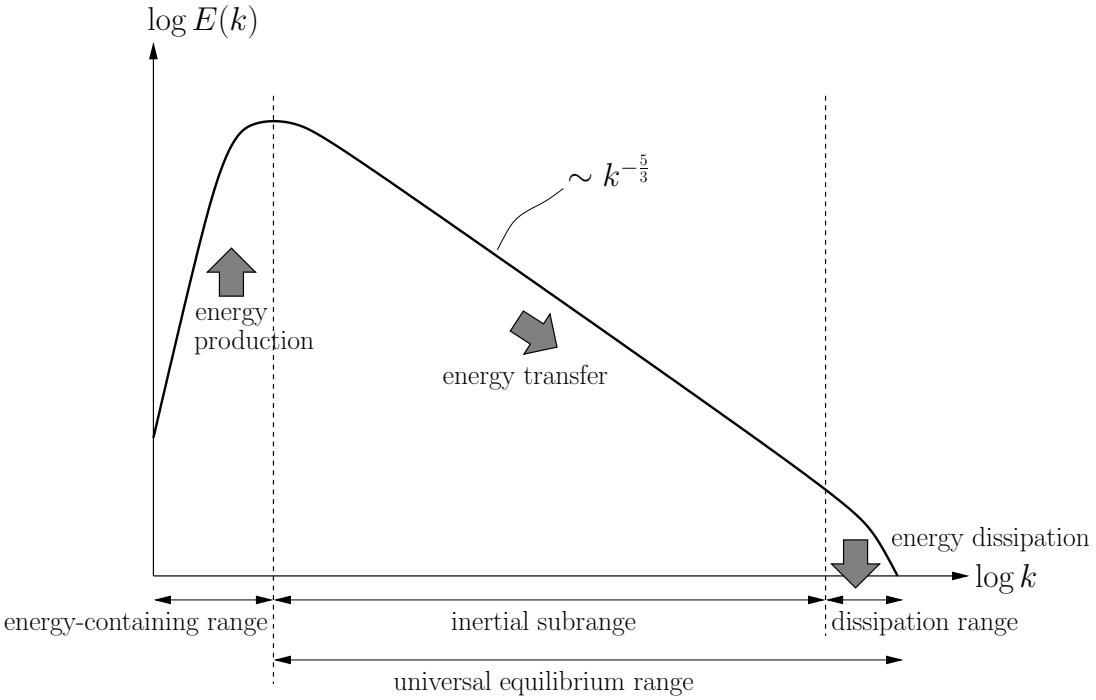

Figure 2.2: Three-dimensional kinetic-energy spectrum for turbulent flows.

in a second textbook by Sagaut *et al.* [271]. The textbook by Pope [252] also offers an introduction into LES. In addition to the monographs already mentioned in the introduction of this thesis, the review articles, e.g., by Fröhlich and Rodi [102], Georgiadis *et al.* [112], Guermond *et al.* [133] as well as Lesieur and Métais [186] give further insights into historical aspects, recent developments, practical issues as well as the related physical and mathematical theory of LES.

2.3.1 The Filtered Navier-Stokes Equations

To eliminate the small scales, Leonard [185] proposed the application of a spatial low-pass filtering operation, which is expressed as a convolution of the velocity field with a filter kernel G

$$\bar{\mathbf{u}}(\mathbf{x},t) = \int G(\mathbf{x}-\check{\mathbf{x}})\mathbf{u}(\check{\mathbf{x}},t)\mathrm{d}\check{\mathbf{x}}. \tag{2.16}$$

The filter kernel G is assumed homogeneous with normalization $\int G(\mathbf{x})\mathrm{d}\mathbf{x} = 1$. Here, the resolved large-scale part is denoted by $\bar{(\cdot)}$. The unresolved subfilter-scale part, marked by $(\cdot)''$, is obtained as

$$\mathbf{u}'' = \mathbf{u} - \bar{\mathbf{u}}. \tag{2.17}$$

Applying the filtering operation to the Navier-Stokes equations and assuming commutation with derivative operators, the filtered Navier-Stokes equations, governing the evolution of the resolved

scales, take the form

$$\frac{\partial \bar{\mathbf{u}}}{\partial t} + \nabla \cdot (\bar{\mathbf{u}} \otimes \bar{\mathbf{u}}) + \nabla \bar{p}_{\text{kin}} - 2\nu \nabla \cdot \boldsymbol{\varepsilon}(\bar{\mathbf{u}}) = -\nabla \cdot \boldsymbol{\tau}_{\text{sfs}}, \tag{2.18}$$

$$\nabla \cdot \bar{\mathbf{u}} = 0, \tag{2.19}$$

where the subfilter-scale stress tensor $\boldsymbol{\tau}_{\text{sfs}}$ is defined as

$$\boldsymbol{\tau}_{\text{sfs}} = \overline{\mathbf{u} \otimes \mathbf{u}} - \bar{\mathbf{u}} \otimes \bar{\mathbf{u}}. \tag{2.20}$$

Following Leonard [185], the subfilter-scale stress tensor $\boldsymbol{\tau}_{\text{sfs}}$ can be decomposed into two parts. The first part

$$\boldsymbol{\tau}_{\text{L}} = \overline{\bar{\mathbf{u}} \otimes \bar{\mathbf{u}}} - \bar{\mathbf{u}} \otimes \bar{\mathbf{u}} \tag{2.21}$$

comprises all terms that can be computed from the known filtered solution and is termed Leonard-stress tensor. Moreover, it characterizes the fluctuations of the interactions among the resolved scales. The second part, containing the subfilter scales, is given by

$$\boldsymbol{\tau}^{*}_{\text{sfs}} = \overline{\bar{\mathbf{u}} \otimes \mathbf{u}''} + \overline{\mathbf{u}'' \otimes \bar{\mathbf{u}}} + \overline{\mathbf{u}'' \otimes \mathbf{u}''} \tag{2.22}$$

and further subdivided as

$$\boldsymbol{\tau}_{\text{C}} = \overline{\bar{\mathbf{u}} \otimes \mathbf{u}''} + \overline{\mathbf{u}'' \otimes \bar{\mathbf{u}}}, \tag{2.23}$$

$$\boldsymbol{\tau}_{\text{R}} = \overline{\mathbf{u}'' \otimes \mathbf{u}''}. \tag{2.24}$$

The cross-stress tensor $\boldsymbol{\tau}_{\text{C}}$ reflects cross-correlations between the subfilter scales and the resolved scales, whereas the subfilter-scale Reynolds-stress tensor $\boldsymbol{\tau}_{\text{R}}$ represents the effect of autocorrelations between the subfilter scales. Since $\boldsymbol{\tau}^{*}_{\text{sfs}}$ is not exclusively defined in terms of the resolved velocity field, the filtered momentum equation is not closed. Closure is achieved by modeling the impact of the subfilter scales on the basis of the information contained in the resolved scales only. Incorporating the Leonard-stress tensor into the non-linear term yields an alternative form of the filtered momentum equation:

$$\frac{\partial \bar{\mathbf{u}}}{\partial t} + \nabla \cdot (\overline{\bar{\mathbf{u}} \otimes \bar{\mathbf{u}}}) + \nabla \bar{p}_{\text{kin}} - 2\nu \nabla \cdot \boldsymbol{\varepsilon}(\bar{\mathbf{u}}) = -\nabla \cdot \boldsymbol{\tau}^{*}_{\text{sfs}}. \tag{2.25}$$

Using this strategy based on an analytical filter, frequently termed explicit filtering, filtering and subfilter-scale modeling are assumed independent of the subsequent discretization of the filtered governing equations. As a consequence, the numerical scheme has to account for an accurate solution of the filtered governing equations. An alternative approach consists of considering the cumulative effect of the numerical treatment of the governing equations, in particular, the introduction of a computational grid and the application of discrete approximations of the derivative operators inherent in every flow simulation as an implicit filtering giving rise to the large-scale field. This approach, which is closely related to the volume-balance procedure suggested by Schumann [277], also implies that scale separation, discretization and modeling of the unresolved scales are not separated. As discussed, e.g., by Sagaut *et al.* [271] (see also Sagaut [270]), considering the alternative form (2.25) of the filtered momentum equation seems to be more

appropriate in this case, since the form $\bar{\mathbf{u}} \otimes \bar{\mathbf{u}}$ of the convective term causes unresolved scales which are truncated by the implicit filter, inevitably resulting in $\overline{\bar{\mathbf{u}} \otimes \bar{\mathbf{u}}}$. In the context of implicit filtering, it also seems to be more appropriate to refer to the unresolved scales as the subgrid scales rather than the subfilter scales and to the subfilter-scale stress tensor as the subgrid-scale stress tensor $\boldsymbol{\tau}^*_{\text{sgs}}$ (and $\boldsymbol{\tau}_{\text{sgs}}$, respectively). With regard to the subsequent application of the VMM, this notation is adopted for the remainder of this thesis.

To further identify the role of the subgrid scales, the transport equation governing the evolution of the kinetic energy

$$K = \frac{1}{2}\bar{\mathbf{u}} \cdot \bar{\mathbf{u}} \tag{2.26}$$

of the resolved scales is considered. Taking the scalar product of the filtered momentum equation (2.18) with $\bar{\mathbf{u}}$ yields

$$\frac{\partial K}{\partial t} + \bar{\mathbf{u}} \cdot \nabla K - \nabla \cdot (2\nu\boldsymbol{\varepsilon}(\bar{\mathbf{u}})\bar{\mathbf{u}} - \boldsymbol{\tau}_{\text{sgs}}\bar{\mathbf{u}} - \bar{p}_{\text{kin}}\bar{\mathbf{u}}) = -2\nu\boldsymbol{\varepsilon}(\bar{\mathbf{u}}) : \boldsymbol{\varepsilon}(\bar{\mathbf{u}}) + \boldsymbol{\tau}_{\text{sgs}} : \boldsymbol{\varepsilon}(\bar{\mathbf{u}}); \tag{2.27}$$

see, e.g., the textbooks by Pope [252] and Sagaut [270] for derivation. The last term on the left-hand side represents the transport of kinetic energy among the resolved scales and merely constitutes a redistribution of resolved kinetic energy. The two terms on the right-hand side describe the dissipation of energy by viscous effects acting on the resolved scales as well as the rate of energy transferred between the resolved and the unresolved scales, named subgrid-scale dissipation. The subgrid-scale dissipation, defined as

$$\varepsilon_{\text{sgs}} = -\boldsymbol{\tau}_{\text{sgs}} : \boldsymbol{\varepsilon}(\bar{\mathbf{u}}), \tag{2.28}$$

may be positive or negative. Whereas $\varepsilon_{\text{sgs}} > 0$ represents a transfer of energy to the subgrid scales, also referred to as forward scatter of energy, $\varepsilon_{\text{sgs}} < 0$ indicates reverse energy transfer or backscatter of energy, respectively. In the mean, the second term is negative such that energy is continuously passed to the unresolved scales in accordance with the picture of an energy cascade. With regard to subgrid-scale modeling in LES, this elaboration implies that interscale energy transfer constitutes an essential feature that has to be accounted for in an appropriate way.

2.3.2 A Review of Relevant Subgrid-Scale Models

According to Sagaut [270], two modeling strategies are usually distinguished in LES. On the one hand, functional models aim at modeling only the impact of the subgrid scales onto the evolution of the resolved scales, but not necessarily their structure. As presented in the previous section, their action is of dissipative nature in the mean. The subgrid-viscosity concept relies on the assumption that the related mechanism behaves similar to the dissipation by molecular motion. A general expression for the deviatoric part of the subgrid-scale stress tensor thus reads as

$$\boldsymbol{\tau}_{\text{sgs}} - \frac{1}{3}\text{tr}(\boldsymbol{\tau}_{\text{sgs}})\mathbf{I} = -2\nu_{\text{sgs}}\boldsymbol{\varepsilon}(\bar{\mathbf{u}}), \tag{2.29}$$

where ν_{sgs} denotes the subgrid viscosity. The Smagorinsky model [288], proposed in the 1960s, is among the most popular subgrid-viscosity models. In the meantime, various modifications and enhancements have been developed, for instance, its dynamic form introduced by Germano *et al.* [114] to adapt the involved model parameter to local flow structures. The underlying concept, which is based on the so-called Germano identity [113], evolved into a comprehensive procedure to determine otherwise tunable model parameters and was recently reviewed by Meneveau [212]. However, subgrid-viscosity models inherently assume that the subgrid-scale stress tensor is aligned with the resolved strain rate tensor. Indeed, the actual subgrid-scale stress tensor and the strain rate tensor are only weakly correlated; see, e.g., Liu *et al.* [197]. Furthermore, subgrid-viscosity models do not intend, by definition, to capture the phenomenon of inverse energy transfer from the subgrid scales to the resolved scales. Although energy is passed to the subgrid scales in the mean, backscatter can be quite significant and of the same magnitude as forward scatter; see, e.g., Piomelli *et al.* [248].

Structural models, on the other hand, intend to reconstruct the subgrid-scale stress tensor directly using information extracted from the resolved velocity field. Exploiting the similarity between the scales of adjacent ranges, Bardina's scale-similarity model [14, 15] calculates the subgrid-scale stress tensor from its definition as

$$\boldsymbol{\tau}_{\text{sgs}} \sim \overline{\bar{\mathbf{u}} \otimes \bar{\mathbf{u}}} - \bar{\bar{\mathbf{u}}} \otimes \bar{\bar{\mathbf{u}}}. \tag{2.30}$$

In general, scale invariance, which also enters the dynamic model mentioned above, constitutes a particularly important property for subgrid-scale modeling in LES, as pointed out in a review article by Meneveau and Katz [213]. The scale-similarity model may be interpreted as a particular case of the general class of deconvolution-type models. Deconvolution-type models, such as the approximate deconvolution model of Stolz and Adams [295], use an approximate inverse of the filtering operator to obtain information on the unresolved scales. Models of this category exhibit a notably high level of correlation with the actual subgrid-scale stress tensor. Moreover, forward scatter as well as backscatter of energy are represented naturally. However, these models often do not provide sufficient subgrid-scale dissipation. This issue is particularly addressed in a review article by Domaradzki and Adams [83]. To adequately capture the missing subgrid-scale dissipation, both physically and mathematically motivated approaches have been proposed; see, e.g., the textbook by Garnier *et al.* [108] for an overview. In the case of the scale-similarity model, an additional subgrid-viscosity term is frequently included, resulting in a so-called mixed model; see, e.g., Bardina *et al.* [14, 15], Zang *et al.* [338] and Singh and You [287]. Recently, Anderson and Domaradzki [4] further evaluated the scale-similarity model with respect to its subgrid-scale energy transfer and proposed a modification to circumvent those additional measures. For the approximate deconvolution method, a second step, the relaxation regularization, is applied to provide the necessary dissipation; see, e.g., Stolz *et al.* [296]. Structural models explicitly approximating the subgrid-scale velocity are, for instance, the velocity-estimation model (see Domaradzki and Loh [84] for a version appropriate for application in physical space) and the model by Scotti and Meneveau [279]. The velocity-estimation model interpolates the defiltered field on a finer grid to generate some smaller scales. Scotti and Meneveau [279] use fractal interpolation for the construction of a synthetic subgrid-scale velocity field. Subgrid-scale models based upon vorticity or vortex-based concepts have also been proposed in literature. Misra

and Pullin [218], for instance, presented a vortex-based subgrid-scale stress model where the subgrid-scale structures of turbulence are assumed to consist of stretched vortices.

3

The Concept of the Variational Multiscale Method

The Variational Multiscale Method (VMM) was established by Hughes *et al.* [153] as a general framework for computational mechanics, which particularly addresses problems exhibiting multiscale characteristics. By separating the scales of the underlying problem into a predefined number of scale groups, an individual numerical treatment of each scale group is enabled, which allows for designing advanced computational methods. Originally, the VMM was introduced by Hughes [150] to explain the origins of stabilized methods, as used in the Finite Element Method (FEM), by relating them to subgrid-scale models in general. A categorization of the VMM into the broad field of multiscale methods, taking into account applications both in fluid as well as in solid mechanics, may be found, e.g., in the overview article by Gravemeier *et al.* [124]. After identifying the VMM as a sound framework for LES, the derivation of an appropriate variational multiscale formulation is presented in this chapter. Eventually, residual-based subgrid-scale approximations leading to stabilized FEMs are introduced.

3.1 A Paradigm for Scale Separation in Large-Eddy Simulation

The variational multiscale concept offers a different perspective on the fundamental step of scale separation in LES. In the VMM, scale separation based on a variational projection of the governing equations is assumed. The variational projection, identifying the resolved and subgrid scales, emanates from the discretization of the governing equations (see, e.g., the review article by Gravemeier [119]), for instance, by using the FEM, which is applied in this thesis. Concerning the Galerkin FEM, the reader is referred, e.g., to the textbook by Gresho and Sani [129] for an exhaustive discussion of its mathematical interpretation as a projection. VMMs for LES are therefore inherently linked with approaches assuming implicit filtering. Although filtering might not be performed explicitly, the filtered formulation shown in Section 2.3.1 frequently serves as an analytical tool for devising and evaluating approaches to LES. Particularly for this case, the VMM enables a profound mathematical framework for LES. Due to implicit filtering, the VMM can be straightforwardly applied to arbitrary complex geometries. The VMM also allows for *a priori* separating an arbitrary number of scale ranges and provides an equation for each scale range, which governs the evolution of the respective scales; see, e.g., Collis [70] as well as the review article by Gravemeier [119]. By augmenting the number of separated scale groups beyond the established two-scale decomposition of LES, more advanced multilevel LES approaches may be consistently derived; see Sagaut *et al.* [271] for a classification of multilevel

methods in general as well as a compilation of various concepts. This opportunity gives further evidence of the multi-purpose framework provided by the VMM.

The VMM as a framework for LES was originally suggested by Hughes *et al.* [154]. In that study, a three-scale version of the VMM, as later clarified by Collis [70], was proposed that allows for incorporating a subgrid-viscosity term which acts only on the smaller resolved scales. The first applications to LES of decaying homogeneous isotropic turbulence and turbulent channel flow using a spectral method were reported by Hughes *et al.* [155] and Hughes *et al.* [156], respectively. Comprehensive overviews of the three-scale VMM may be found, e.g., in the review articles by Gravemeier [119] and John [162]. A crucial aspect of the three-scale VMM is the actual implementation of the further separation of the resolved scaled, as also emphasized by the authors of the aforementioned review articles. Jansen and Tejada-Martínez [157] extended the three-scale VMM to physical space using an FEM with hierarchical shape functions to perform scale separation based on the polynomial order. Also within an FEM, John and Kaya [163] introduced an L_2-projection-based scale separation, which formally allows for performing scale separation either based on the polynomial order of the shape functions or based on a coarser grid. For recent applications and developments of the L_2-projection-based three-scale VMM, the reader is referred, e.g., to Röhe and Lube [269], who introduced a grad-div stabilization term as a subgrid-scale model for the pressure, as well as to John and Kindl [164], who considered an adaptive large-scale space such that the direct influence of the subgrid-viscosity term may be increased or attenuated depending on the local flow structures. Despite its flexibility with respect to the way scale separation may be realized, the polynomial-order-based option was chosen for all the aforementioned L_2-projection-based three-scale VMMs. For grid-based scale separation, Gravemeier *et al.* [126] proposed the Algebraic Variational Multigrid-Multiscale Method (AVM^3), which is the predecessor method of the approach developed in the present thesis. In the AVM^3, level-transfer operators from plain aggregation algebraic multigrid methods are introduced to implement the separation between larger and smaller resolved scales, thus eluding any explicit construction of a coarser grid. Level-transfer operators from plain aggregation algebraic multigrid methods are also involved in the method derived in this thesis.

A residual-based two-scale version for LES of turbulent incompressible flow was presented, e.g., by Bazilevs *et al.* [22]. By using the residual together with an appropriate parameter to approximate the unresolved-scale quantities, that approach is closely related to stabilized methods and the original intention of the VMM. Time-dependent residual-based subgrid-scale approximations, as originally introduced by Codina *et al.* [68], were investigated for LES, e.g., by Gamnitzer *et al.* [107] and Principe *et al.* [255]. Furthermore, Masud and Calderer [210] used bubble functions defined on the element interior to devise a more sophisticated stabilization operator for residual-based two-scale VMMs. Recently, Oberai *et al.* [234] suggested a two-scale VMM based on a subgrid-viscosity approach acting on the entire range of resolved scales. In that study, the subgrid viscosity is determined using a residual-based approximation for the subgrid-scale velocity.

All aforementioned VMMs were realized within FEMs or spectral methods. The VMM however constitutes a theoretical framework for LES, which is not specifically related to these methods, in contrast to what these examples may imply. In fact, the VMM can be used as a framework within

other numerical methods as well. This issue was discussed by Gravemeier [119] in comprehensive from with a focus on Finite Volume Methods (FVMs) as well as additional hints concerning Finite Difference Methods (FDMs). Applications of the three-scale VMM using a small-scale subgrid-viscosity term and the residual-based two-scale VMM in FVMs may be found, e.g., in Gravemeier [118] and Calo [56], respectively.

In this thesis, the FEM is applied. Moreover, a two-scale variational multiscale formulation is exclusively considered and presented in the next section.

3.2 Variational Multiscale Formulation of the Incompressible Navier-Stokes Equations

Fluid motion in the domain Ω described by the incompressible Navier-Stokes equations is considered for a time period t_{end}:

$$\frac{\partial \mathbf{u}}{\partial t} + \mathbf{u} \cdot \nabla \mathbf{u} + \nabla p_{\text{kin}} - 2\nu \nabla \cdot \boldsymbol{\varepsilon}(\mathbf{u}) = \mathbf{f} \qquad \text{in } \Omega \times]0, t_{\text{end}}[\,, \quad (3.1)$$

$$\nabla \cdot \mathbf{u} = 0 \qquad \text{in } \Omega \times]0, t_{\text{end}}[\,, \quad (3.2)$$

$$\mathbf{u} = \mathbf{u}_{\text{D}} \qquad \text{on } \Gamma_{\text{D},\mathbf{u}} \times]0, t_{\text{end}}[\,, \quad (3.3)$$

$$\left.\begin{aligned} (-p_{\text{kin}}\mathbf{I} + 2\nu\boldsymbol{\varepsilon}(\mathbf{u})) \cdot \mathbf{n} &= \mathbf{h}_{\mathbf{u}} \quad \text{if } \mathbf{u} \cdot \mathbf{n} \geqslant 0 \\ -\mathbf{u}\,(\mathbf{u} \cdot \mathbf{n}) + (-p_{\text{kin}}\mathbf{I} + 2\nu\boldsymbol{\varepsilon}(\mathbf{u})) \cdot \mathbf{n} &= \mathbf{h}_{\mathbf{u}} \quad \text{if } \mathbf{u} \cdot \mathbf{n} < 0 \end{aligned}\right\} \quad \text{on } \Gamma_{\text{N},\mathbf{u}} \times]0, t_{\text{end}}[\,, \quad (3.4)$$

$$\mathbf{u} = \mathbf{u}_0 \qquad \text{in } \Omega \times \{0\}, \quad (3.5)$$

where the momentum equation is given in convective form. Furthermore, $\mathbf{I}$ is the identity tensor and $\mathbf{n}$ the outer unit normal vector on the boundary $\partial\Omega$ of the domain Ω. Dirichlet boundary conditions are imposed on the part $\Gamma_{\text{D},\mathbf{u}}$ of $\partial\Omega$ and Neumann boundary conditions on $\Gamma_{\text{N},\mathbf{u}}$, assuming $\Gamma_{\text{D},\mathbf{u}} \cap \Gamma_{\text{N},\mathbf{u}} = \emptyset$ and $\Gamma_{\text{D},\mathbf{u}} \cup \Gamma_{\text{N},\mathbf{u}} = \partial\Omega$. Neumann boundary conditions are prescribed differently on inflow and outflow parts of the Neumann boundary, as only the traction is prescribed on the outflow part $\Gamma^{\text{out}}_{\text{N},\mathbf{u}}(t) := \{\mathbf{x} \in \Gamma_{\text{N},\mathbf{u}} | \mathbf{u}(\mathbf{x},t) \cdot \mathbf{n}(\mathbf{x}) \geqslant 0\}$, but the total momentum flux on a potential inflow part $\Gamma^{\text{in}}_{\text{N},\mathbf{u}}(t) := \{\mathbf{x} \in \Gamma_{\text{N},\mathbf{u}} | \mathbf{u}(\mathbf{x},t) \cdot \mathbf{n}(\mathbf{x}) < 0\}$, with $\Gamma^{\text{out}}_{\text{N},\mathbf{u}} \cap \Gamma^{\text{in}}_{\text{N},\mathbf{u}} = \emptyset$ and $\Gamma^{\text{out}}_{\text{N},\mathbf{u}} \cup \Gamma^{\text{in}}_{\text{N},\mathbf{u}} = \Gamma_{\text{N},\mathbf{u}}$; see, e.g., Hughes and Wells [151]. Due to potentially arising eddies at the outflow boundary of the domain Ω, which may evoke (partial) inflow at the outlet, the Neumann boundary condition is split up as shown in equation (3.4). The inclusion of the resulting convective boundary term at the outlet of the domain is mandatory for ensuring stability at the outlet in such cases, meaning that potential eddies are indeed convected out of the domain, as observed, e.g., by Bazilevs *et al.* [23] as well as by Gravemeier and Wall [122]. The initial velocity field $\mathbf{u}_0$ is assumed divergence-free.

For the variational formulation of the Navier-Stokes equations, solution function spaces

$$\mathcal{S}_{\mathbf{u}} := \left\{ \mathbf{u} \in \left[H^1(\Omega)\right]^3 \mid \mathbf{u} = \mathbf{u}_{\text{D}} \text{ on } \Gamma_{\text{D},\mathbf{u}} \right\} \quad (3.6)$$

for $\mathbf{u}$ and

$$\mathcal{S}_p := \{p_{\text{kin}} \in L_2(\Omega)\} \tag{3.7}$$

for p_{kin} as well as weighting function spaces

$$\mathcal{V}_{\mathbf{u}} := \left\{\mathbf{v} \in \left[H^1(\Omega)\right]^3 \mid \mathbf{v} = \mathbf{0} \text{ on } \Gamma_{\text{D},\mathbf{u}}\right\} \tag{3.8}$$

for the velocity weighting function $\mathbf{v}$ and

$$\mathcal{V}_p := \{q \in L_2(\Omega)\} \tag{3.9}$$

for the pressure weighting function q are assumed. As usual, $L_2(\Omega)$ is the Hilbert space of square-integrable functions in the domain Ω and $H^1(\Omega) \subset L_2(\Omega)$ the Sobolev space of square-integrable functions with square-integrable first derivatives. The three-dimensional vectorial version of the space $H^1(\Omega)$, indicated by the respective exponent, is used for the velocity field. For pure Dirichlet problems (i.e., $\partial\Omega = \Gamma_{\text{D},\mathbf{u}}$), the pressure is only defined up to a constant, and the pressure solution and weighting function space have to be formally restricted to $\mathcal{S}_p/\mathbb{R}$ and $\mathcal{V}_p/\mathbb{R}$, grouping together functions which differ only by a constant. The system of equations (3.1) and (3.2) is multiplied by $\mathbf{v} \in \mathcal{V}_{\mathbf{u}}$ and $q \in \mathcal{V}_p$ and integrated over the domain Ω. Viscous and pressure term are integrated by parts, with boundary conditions (3.3) and (3.4) applied to the resulting boundary integrals. The variational formulation of the incompressible Navier-Stokes equations is given as follows: find $(\mathbf{u}, p_{\text{kin}}) \in \mathcal{S}_{\mathbf{u}} \times \mathcal{S}_p$ such that

$$\mathcal{B}_{\text{NS}}(\mathbf{v}, q; \mathbf{u}, p_{\text{kin}}) = \ell_{\text{NS}}(\mathbf{v}) \tag{3.10}$$

for all $(\mathbf{v}, q) \in \mathcal{V}_{\mathbf{u}} \times \mathcal{V}_p$. The form on the left-hand side is defined as

$$\mathcal{B}_{\text{NS}}(\mathbf{v}, q; \mathbf{u}, p_{\text{kin}}) := \mathcal{B}_{\text{M}}(\mathbf{v}; \mathbf{u}, p_{\text{kin}}) + \mathcal{B}_{\text{C}}(q; \mathbf{u}), \tag{3.11}$$

with the momentum part

$$\begin{aligned}\mathcal{B}_{\text{M}}(\mathbf{v}; \mathbf{u}, p_{\text{kin}}) := &\left(\mathbf{v}, \frac{\partial \mathbf{u}}{\partial t}\right)_{\Omega} + (\mathbf{v}, \mathbf{u} \cdot \nabla \mathbf{u})_{\Omega} - (\nabla \cdot \mathbf{v}, p_{\text{kin}})_{\Omega} \\ &+ (\boldsymbol{\varepsilon}(\mathbf{v}), 2\nu\boldsymbol{\varepsilon}(\mathbf{u}))_{\Omega} - (\mathbf{v}, \mathbf{u}\,(\mathbf{u} \cdot \mathbf{n}))_{\Gamma^{\text{in}}_{\text{N},\mathbf{u}}}\end{aligned} \tag{3.12}$$

and the continuity part

$$\mathcal{B}_{\text{C}}(q; \mathbf{u}) := (q, \nabla \cdot \mathbf{u})_{\Omega}\,. \tag{3.13}$$

The linear form $\ell_{\text{NS}}(\mathbf{v})$, including the Neumann boundary condition, is given as

$$\ell_{\text{NS}}(\mathbf{v}) := (\mathbf{v}, \mathbf{f})_{\Omega} + (\mathbf{v}, \mathbf{h}_{\mathbf{u}})_{\Gamma_{\text{N},\mathbf{u}}}\,. \tag{3.14}$$

The last term of the momentum part arises due to the aforementioned inflow part of the Neumann boundary condition. Since this term is not subject to the following scale separation, it is omitted in the subsequent derivations for brevity. Throughout this thesis, $(\cdot,\cdot)_{\Omega}$ and $(\cdot,\cdot)_{\Gamma}$ denote the usual L_2-inner product in a domain Ω and on a boundary or interface Γ, which may be further

specified by additional sub- or superscripts. The L_2-inner product in Ω is defined as

$$(\mathsf{a}, \mathsf{b})_\Omega := \int_\Omega \mathsf{a}\mathsf{b}\,\mathrm{d}\Omega \tag{3.15}$$

for scalar functions $\mathsf{a}, \mathsf{b} \in L_2(\Omega)$ and extends to the respective vector- and tensor-valued functions $\mathbf{a}$ and $\mathbf{b}$ as well as $\mathbf{A}$ and $\mathbf{B}$ as $(\mathbf{a}, \mathbf{b})_\Omega := \int_\Omega \mathbf{a} \cdot \mathbf{b}\,\mathrm{d}\Omega$ and $(\mathbf{A}, \mathbf{B})_\Omega := \int_\Omega \mathbf{A} : \mathbf{B}\,\mathrm{d}\Omega$, respectively.

For the variational multiscale formulation of the Navier-Stokes equations, the velocity is decomposed into resolved and unresolved (or subgrid) components as

$$\mathbf{u} = \mathbf{u}^h + \hat{\mathbf{u}}, \tag{3.16}$$

where resolved velocity scales are identified by a spatial discretization of characteristic element length h. The subgrid scales are denoted by $\hat{(\cdot)}$. Analogously, the pressure is decomposed as

$$p_{\text{kin}} = p^h_{\text{kin}} + \hat{p}_{\text{kin}}. \tag{3.17}$$

According to the decomposition of the solution functions, direct sum decompositions of the underlying function spaces into a finite-dimensional subspace of resolved scales and an infinite-dimensional subspace of unresolved scales in the form $\mathcal{S}_\mathbf{u} = \mathcal{S}^h_\mathbf{u} \oplus \hat{\mathcal{S}}_\mathbf{u}$ and $\mathcal{S}_p = \mathcal{S}^h_p \oplus \hat{\mathcal{S}}_p$, respectively, are assumed. Inserting the decomposition of velocity and pressure, (3.16) and (3.17), into the variational formulation (3.10) leads to

$$\mathcal{B}_{\text{NS}}(\mathbf{v}, q; \mathbf{u}^h, p^h_{\text{kin}}) + \mathcal{B}^1_{\text{NS}}(\mathbf{v}, q; \mathbf{u}^h, \hat{\mathbf{u}}, \hat{p}_{\text{kin}}) + \mathcal{B}^2_{\text{NS}}(\mathbf{v}; \hat{\mathbf{u}}) = \ell_{\text{NS}}(\mathbf{v}), \tag{3.18}$$

where

$$\begin{aligned}\mathcal{B}^1_{\text{NS}}(\mathbf{v}, q; \mathbf{u}^h, \hat{\mathbf{u}}, \hat{p}_{\text{kin}}) := &\left(\mathbf{v}, \frac{\partial \hat{\mathbf{u}}}{\partial t}\right)_\Omega + \left(\mathbf{v}, \mathbf{u}^h \cdot \nabla \hat{\mathbf{u}} + \hat{\mathbf{u}} \cdot \nabla \mathbf{u}^h\right)_\Omega - (\nabla \cdot \mathbf{v}, \hat{p}_{\text{kin}})_\Omega \\ &+ (\boldsymbol{\varepsilon}(\mathbf{v}), 2\nu\boldsymbol{\varepsilon}(\hat{\mathbf{u}}))_\Omega + (q, \nabla \cdot \hat{\mathbf{u}})_\Omega\end{aligned} \tag{3.19}$$

contains linear terms in the unresolved-scale quantities. The quadratic contribution from the convective term is given by

$$\mathcal{B}^2_{\text{NS}}(\mathbf{v}; \hat{\mathbf{u}}) := (\mathbf{v}, \hat{\mathbf{u}} \cdot \nabla \hat{\mathbf{u}})_\Omega\,. \tag{3.20}$$

For separating resolved and unresolved scales via a variational projection, direct sum decompositions of the weighting function spaces $\mathcal{V}_\mathbf{u} = \mathcal{V}^h_\mathbf{u} \oplus \hat{\mathcal{V}}_\mathbf{u}$ and $\mathcal{V}_p = \mathcal{V}^h_p \oplus \hat{\mathcal{V}}_p$, respectively, are also introduced. Accordingly, the weighting functions read as

$$\mathbf{v} = \mathbf{v}^h + \hat{\mathbf{v}}, \tag{3.21}$$

$$q = q^h + \hat{q}, \tag{3.22}$$

respectively. By this decomposition, the variational form of the Navier-Stokes equations is decoupled into a resolved- and an unresolved-scale equation, that is, variational form (3.18) is

separately weighted by the resolved- and the unresolved-scale part of the decomposed weighting functions. The equation projected onto the space of resolved scales reads as

$$\mathcal{B}_{\mathrm{NS}}(\mathbf{v}^h, q^h; \mathbf{u}^h, p^h_{\mathrm{kin}}) + \mathcal{B}^1_{\mathrm{NS}}(\mathbf{v}^h, q^h; \mathbf{u}^h, \hat{\mathbf{u}}, \hat{p}_{\mathrm{kin}}) + \mathcal{B}^2_{\mathrm{NS}}(\mathbf{v}^h; \hat{\mathbf{u}}) = \ell_{\mathrm{NS}}(\mathbf{v}^h) \tag{3.23}$$

for all $(\mathbf{v}^h, q^h) \in \mathcal{V}^h_{\mathbf{u}} \times \mathcal{V}^h_p$ and the equation projected onto the space of unresolved scales as

$$\mathcal{B}_{\mathrm{NS}}(\hat{\mathbf{v}}, \hat{q}; \mathbf{u}^h, p^h_{\mathrm{kin}}) + \mathcal{B}^1_{\mathrm{NS}}(\hat{\mathbf{v}}, \hat{q}; \mathbf{u}^h, \hat{\mathbf{u}}, \hat{p}_{\mathrm{kin}}) + \mathcal{B}^2_{\mathrm{NS}}(\hat{\mathbf{v}}; \hat{\mathbf{u}}) = \ell_{\mathrm{NS}}(\hat{\mathbf{v}}) \tag{3.24}$$

for all $(\hat{\mathbf{v}}, \hat{q}) \in \hat{\mathcal{V}}_{\mathbf{u}} \times \hat{\mathcal{V}}_p$. The resolved-scale equation is solved for $(\mathbf{u}^h, p^h_{\mathrm{kin}}) \in \mathcal{S}^h_{\mathbf{u}} \times \mathcal{S}^h_p$, while the unresolved-scale equation, yielding $(\hat{\mathbf{u}}, \hat{p}_{\mathrm{kin}}) \in \hat{\mathcal{S}}_{\mathbf{u}} \times \hat{\mathcal{S}}_p$, is usually omitted. Hence, the resolved-scale equation is not closed, and the unresolved-scale contributions have to be appropriately modeled. Eventually, the variational multiscale formulation (3.23) is split up as follows:

$$\mathcal{B}_{\mathrm{NS}}(\mathbf{v}^h, q^h; \mathbf{u}^h, p^h_{\mathrm{kin}}) + \mathcal{C}(\mathbf{v}^h; \mathbf{u}^h, \hat{\mathbf{u}}) + \mathcal{R}(\mathbf{v}^h; \hat{\mathbf{u}}) + \mathcal{B}^{1,\mathrm{lin}}_{\mathrm{NS}}(\mathbf{v}^h, q^h; \hat{\mathbf{u}}, \hat{p}_{\mathrm{kin}}) = \ell_{\mathrm{NS}}(\mathbf{v}^h), \tag{3.25}$$

where

$$\mathcal{C}(\mathbf{v}^h; \mathbf{u}^h, \hat{\mathbf{u}}) := \left(\mathbf{v}^h, \mathbf{u}^h \cdot \nabla\hat{\mathbf{u}} + \hat{\mathbf{u}} \cdot \nabla\mathbf{u}^h\right)_\Omega = \left(\mathbf{v}^h, \mathbf{u}^h \cdot \nabla\hat{\mathbf{u}}\right)_\Omega + \left(\mathbf{v}^h, \hat{\mathbf{u}} \cdot \nabla\mathbf{u}^h\right)_\Omega \tag{3.26}$$

is the projection of the cross-stress tensor and

$$\mathcal{R}(\mathbf{v}^h; \hat{\mathbf{u}}) := \mathcal{B}^2_{\mathrm{NS}}(\mathbf{v}^h; \hat{\mathbf{u}}) = \left(\mathbf{v}^h, \hat{\mathbf{u}} \cdot \nabla\hat{\mathbf{u}}\right)_\Omega \tag{3.27}$$

the projection of the subgrid-scale Reynolds-stress tensor onto the space of resolved scales. The form

$$\mathcal{B}^{1,\mathrm{lin}}_{\mathrm{NS}}(\mathbf{v}^h, q^h; \hat{\mathbf{u}}, \hat{p}_{\mathrm{kin}}) := \left(\mathbf{v}^h, \frac{\partial\hat{\mathbf{u}}}{\partial t}\right)_\Omega - \left(\nabla \cdot \mathbf{v}^h, \hat{p}_{\mathrm{kin}}\right)_\Omega + \left(\boldsymbol{\varepsilon}(\mathbf{v}^h), 2\nu\boldsymbol{\varepsilon}(\hat{\mathbf{u}})\right)_\Omega + \left(q^h, \nabla \cdot \hat{\mathbf{u}}\right)_\Omega \tag{3.28}$$

contains the remaining linear terms in the unresolved-scale quantities. The variational multiscale formulation (3.25) represents an analogue to the filtered Navier-Stokes equations and constitutes an alternative mathematical framework for LES. Converting the particularly relevant convective term as well as the cross- and subgrid-scale Reynolds-stress terms of the variational multiscale formulation into their respective filter-based form, they read as $\overline{\bar{\mathbf{u}} \cdot \nabla\bar{\mathbf{u}}}$, $\overline{\bar{\mathbf{u}} \cdot \nabla\mathbf{u}''} + \overline{\mathbf{u}'' \cdot \nabla\bar{\mathbf{u}}}$ and $\overline{\mathbf{u}'' \cdot \nabla\mathbf{u}''}$, respectively. These filtered terms may be compared to their counterparts in equation (2.25). The alternative form, specifically suggested for implicit filtering, is thus obtained naturally, with the notable difference that the assumption of commutation between partial derivatives and filter operation is not required (see also, e.g., Collis [70] and Vreman [325]). Concerning the variational counterpart of the transport equation (2.27) for the resolved kinetic energy, an equivalent expression is readily obtained from the variational multiscale formulation by replacing $\mathbf{v}^h$ by $\mathbf{u}^h$ and q^h by p^h_{kin}.

Eventually, basic ingredients of the FEM, which constitutes, as aforementioned, the numerical approach considered in this thesis, are summarized. For an elaborate survey of the FEM in general, the reader is referred, e.g., to the textbook by Hughes [149] and the collection by Zienkiewicz and Taylor [339], which also comprises aspects of the FEM in fluid dynamics. Intro-

ductory textbooks exclusively focusing on the FEM for flow problems are Donea and Huerta [85] and Gresho and Sani [129, 130]. For discretization, the domain Ω is partitioned into n_{el} non-overlapping elements e with domain Ω^e and characteristic element length h, i.e., $\overline{\Omega} := \bigcup_{e=1}^{n_{\text{el}}} \overline{\Omega}^e$, where the closure of Ω is defined as $\overline{\Omega} := \Omega \cup \partial\Omega$. The resulting triangulation is denoted by $\mathcal{T}^h$. The discrete solution functions are given in a usual finite element expansion by

$$\mathbf{u}^h(\mathbf{x}, t) = \sum_{A \in \mathcal{E}} N_A(\mathbf{x}) \mathbf{u}_A(t), \tag{3.29}$$

$$p^h_{\text{kin}}(\mathbf{x}, t) = \sum_{A \in \mathcal{E}} N_A(\mathbf{x}) p_{\text{kin},A}(t), \tag{3.30}$$

where $\mathcal{E}$ denotes the set of all nodes A of the discretization. Moreover, $\mathbf{u}_A$ and $p_{\text{kin},A}$ are the velocity and pressure degrees of freedom at node A. These nodal values are interpolated by shape functions N_A, each corresponding to a node A. Throughout this thesis, the shape functions are chosen to be trilinear Lagrangian polynomials. The same approximation is used for the weighting functions $\mathbf{v}^h$ and q^h. The associated finite element interpolation spaces, given by

$$\mathcal{S}^h_{\mathbf{u}} := \left\{ \mathbf{u}^h \in \left[H^1(\Omega)\right]^3 \mid \mathbf{u}^h|_{\Omega^e} \in \left[\mathcal{Q}_1(\Omega^e)\right]^3 \ \forall e \in \mathcal{T}^h \text{ and } \mathbf{u}^h = \mathbf{u}_{\text{D}} \text{ on } \Gamma_{\text{D},\mathbf{u}} \right\}, \tag{3.31}$$

$$\mathcal{V}^h_{\mathbf{u}} := \left\{ \mathbf{v}^h \in \left[H^1(\Omega)\right]^3 \mid \mathbf{v}^h|_{\Omega^e} \in \left[\mathcal{Q}_1(\Omega^e)\right]^3 \ \forall e \in \mathcal{T}^h \text{ and } \mathbf{v}^h = \mathbf{0} \text{ on } \Gamma_{\text{D},\mathbf{u}} \right\}, \tag{3.32}$$

$$\mathcal{S}^h_p := \left\{ p^h_{\text{kin}} \in L_2(\Omega) \mid p^h_{\text{kin}}|_{\Omega^e} \in \mathcal{Q}_1(\Omega^e) \ \forall e \in \mathcal{T}^h \right\}, \tag{3.33}$$

$$\mathcal{V}^h_p := \left\{ q^h \in L_2(\Omega) \mid q^h|_{\Omega^e} \in \mathcal{Q}_1(\Omega^e) \ \forall e \in \mathcal{T}^h \right\}, \tag{3.34}$$

may now be identified as the finite-dimensional subspaces of $\mathcal{S}_{\mathbf{u}}, \mathcal{S}_p, \mathcal{V}_{\mathbf{u}}$ and $\mathcal{V}_p$, introduced in the derivation of the variational multiscale formulation of the Navier-Stokes equations. Here, $\mathcal{Q}_1(\Omega^e)$ denotes the set of trilinear functions defined in the domain of hexahedral elements, which are used in this thesis.

3.3 Residual-Based Subgrid-Scale Modeling

Equation (3.24), governing the evolution of the unresolved scales, enables an approximation for the subgrid-scale quantities. Various strategies to estimate the subgrid-scale quantities from equation (3.24), ranging from the elementwise numerical solution of local subproblems to approximate analytical expressions for $\hat{\mathbf{u}}$ and $\hat{p}_{\text{kin}}$, have been proposed in literature; see, e.g., Hughes *et al.* [153] for an overview and the relationship between them. Rearranging equation (3.24) yields

$$\mathcal{B}^1_{\text{NS}}(\hat{\mathbf{v}}, \hat{q}; \mathbf{u}^h, \hat{\mathbf{u}}, \hat{p}_{\text{kin}}) + \mathcal{B}^2_{\text{NS}}(\hat{\mathbf{v}}; \hat{\mathbf{u}}) = -\left[\mathcal{B}_{\text{NS}}(\hat{\mathbf{v}}, \hat{q}; \mathbf{u}^h, p^h_{\text{kin}}) - \ell_{\text{NS}}(\hat{\mathbf{v}})\right], \tag{3.35}$$

where the projection of the resolved-scale residual onto the space of unresolved scales constitutes the right-hand side and drives the unresolved-scale equation (see Calo [56]).

Residual-based subgrid-scale modeling aims at providing an approximate analytical solution for $\hat{\mathbf{u}}$ and $\hat{p}_{\text{kin}}$; see, e.g., Bazilevs *et al.* [22], Calo [56] and Gamnitzer [106]. As a result, the subgrid-

scale parts of velocity and pressure are approximated in an elementwise manner as

$$\hat{\mathbf{u}} = -\tau_{\mathrm{M}} \mathbf{r}_{\mathrm{M}}^h, \tag{3.36}$$

$$\hat{p}_{\mathrm{kin}} = -\tau_{\mathrm{C}} r_{\mathrm{C}}^h, \tag{3.37}$$

where

$$\mathbf{r}_{\mathrm{M}}^h = \frac{\partial \mathbf{u}^h}{\partial t} + \mathbf{u}^h \cdot \nabla \mathbf{u}^h + \nabla p_{\mathrm{kin}}^h - 2\nu \nabla \cdot \boldsymbol{\varepsilon}(\mathbf{u}^h) - \mathbf{f}, \tag{3.38}$$

$$r_{\mathrm{C}}^h = \nabla \cdot \mathbf{u}^h \tag{3.39}$$

denote the discrete residual of momentum and continuity equation, respectively. The definitions for the stabilization parameters τ_{M} and τ_{C} as proposed by Taylor *et al.* [306] and Whiting and Jansen [333] are used in this thesis. They are given by

$$\tau_{\mathrm{M}} = \frac{1}{\sqrt{\frac{4}{\Delta t^2} + \mathbf{u}^h \cdot \mathbf{G} \mathbf{u}^h + C_{\mathrm{I}} \nu^2 \mathbf{G} : \mathbf{G}}}, \tag{3.40}$$

$$\tau_{\mathrm{C}} = \frac{1}{\tau_{\mathrm{M}} \mathrm{tr}(\mathbf{G})}, \tag{3.41}$$

where

$$G_{ij} = \sum_{k=1}^{3} \frac{\partial \xi_k}{\partial x_i} \frac{\partial \xi_k}{\partial x_j} \tag{3.42}$$

is the covariant metric tensor related to the mapping between global coordinates $\mathbf{x}$ and local element coordinates $\boldsymbol{\xi}$. The time-step length of the temporal discretization is denoted by Δt, and C_{I} is a positive constant independent of the characteristic element length, which is chosen to be 36.0 for trilinearly-interpolated hexahedral elements as exclusively used in this thesis.

Introducing the subgrid-scale approximations (3.36) and (3.37) into the unclosed terms (3.26) to (3.28) of the variational multiscale formulation (3.25), integrating by parts some terms and omitting some other terms, the following residual-based multiscale or stabilization terms are obtained:

$$\mathcal{C}(\mathbf{v}^h; \mathbf{u}^h, \hat{\mathbf{u}}) \approx \left(\mathbf{u}^h \cdot \nabla \mathbf{v}^h, \tau_{\mathrm{M}} \mathbf{r}_{\mathrm{M}}^h\right)_{\Omega^*} - \left(\mathbf{v}^h, \tau_{\mathrm{M}} \mathbf{r}_{\mathrm{M}}^h \cdot \nabla \mathbf{u}^h\right)_{\Omega^*}, \tag{3.43}$$

$$\mathcal{R}(\mathbf{v}^h; \hat{\mathbf{u}}) \approx -\left(\tau_{\mathrm{M}} \mathbf{r}_{\mathrm{M}}^h \cdot \nabla \mathbf{v}^h, \tau_{\mathrm{M}} \mathbf{r}_{\mathrm{M}}^h\right)_{\Omega^*}, \tag{3.44}$$

$$\mathcal{B}_{\mathrm{NS}}^{1,\mathrm{lin}}(\mathbf{v}^h, q^h; \hat{\mathbf{u}}, \hat{p}) \approx \left(\nabla \cdot \mathbf{v}^h, \tau_{\mathrm{C}} r_{\mathrm{C}}^h\right)_{\Omega^*} + \left(\nabla q^h, \tau_{\mathrm{M}} \mathbf{r}_{\mathrm{M}}^h\right)_{\Omega^*}. \tag{3.45}$$

To eliminate potential boundary terms arising from integration by parts, it is assumed that the subgrid-scale quantities vanish on the element boundaries; see, e.g., Hughes [150] for elaboration. Moreover, Ω^* represents the union of all element interiors, i.e., $\Omega^* := \bigcup_{e=1}^{n_{\mathrm{el}}} \Omega^e$, and $(\cdot,\cdot)_{\Omega^*} := \sum_{e \in \mathcal{T}^h} (\cdot,\cdot)_{\Omega^e}$. The first cross-stress term constitutes a Streamline/Upwind Petrov-Galerkin (SUPG) term. Moreover, a grad-div term, the first term of the modeled form of $\mathcal{B}_{\mathrm{NS}}^{1,\mathrm{lin}}(\mathbf{v}^h, q^h; \hat{\mathbf{u}}, \hat{p})$, and a Pressure Stabilizing Petrov-Galerkin (PSPG) term, the second term, arise. The transient and viscous term of $\mathcal{B}_{\mathrm{NS}}^{1,\mathrm{lin}}(\mathbf{v}^h, q^h; \hat{\mathbf{u}}, \hat{p})$ are neglected. With respect to the

transient term, this assumption leads to a so-called quasi-static subgrid-scale approximation, in contrast to a time-dependent subgrid-scale approximation as suggested by Codina *et al.* [68]. Owing to the use of trilinearly-interpolated hexahedral elements, the viscous term, including second derivatives of $\mathbf{v}^h$ after integration by parts, is considered negligible. Omitting the second cross-stress term as well as the subgrid-scale Reynolds-stress term yields a standard stabilized formulation merely containing the SUPG, PSPG and grad-div term. Independent of the VMM, these terms had already been proposed previously as means to account for instabilities inherent in the standard (or Bubnov-)Galerkin formulation for the incompressible Navier-Stokes equations. The SUPG term was originally proposed by Brooks and Hughes [41] to overcome numerical instabilities related to dominant convection by introducing dissipation in streamline direction. The PSPG term allows for circumventing the inf-sup condition (see, e.g., Brezzi and Fortin [39]), a mixed finite element formulation is subject to, and enables the convenient choice of equal-order interpolated elements for velocity and pressure. This term was first presented by Hughes *et al.* [152] for the Stokes equations. The grad-div term is addressed in comprehensive form, e.g., in the review article by De Mulder [79]. Among other things, the grad-div term provides improved discrete mass conservation, which comes along with an additional numerical dissipation; see, e.g., Olshanskii *et al.* [237]. The benefits and drawbacks related to the grad-div term are still discussed in current research efforts, both from a mathematical and an engineering point of view; see, e.g., Olshanskii *et al.* [237] and Masud and Calderer [210] for recent contributions to this discussion. Since these stabilization terms vanish for the exact solution, consistency is ensured for the overall approach. Deriving these terms in the context of the variational multiscale method gives rise to two further terms: the second cross-stress term as well as the subgrid-scale Reynolds-stress term. As analyzed by Hughes and Wells [151], the second cross-stress term enables global momentum conservation for the convective form of the momentum equation. The subgrid-scale Reynolds-stress term may be interpreted as a convective stabilization of the second cross-stress term, acting in a similar manner as the SUPG term for the standard Galerkin convective term. The formulation incorporating terms (3.43) to (3.45) constitutes a complete residual-based VMM: find $(\mathbf{u}^h, p^h_{\text{kin}}) \in \mathcal{S}^h_{\mathbf{u}} \times \mathcal{S}^h_p$ such that

$$\begin{aligned}
&\mathcal{B}_{\text{NS}}(\mathbf{v}^h, q^h; \mathbf{u}^h, p^h_{\text{kin}}) \\
&+ \left(\mathbf{u}^h \cdot \nabla \mathbf{v}^h, \tau_{\text{M}} \mathbf{r}^h_{\text{M}}\right)_{\Omega^*} - \left(\mathbf{v}^h, \tau_{\text{M}} \mathbf{r}^h_{\text{M}} \cdot \nabla \mathbf{u}^h\right)_{\Omega^*} - \left(\tau_{\text{M}} \mathbf{r}^h_{\text{M}} \cdot \nabla \mathbf{v}^h, \tau_{\text{M}} \mathbf{r}^h_{\text{M}}\right)_{\Omega^*} \\
&+ \left(\nabla q^h, \tau_{\text{M}} \mathbf{r}^h_{\text{M}}\right)_{\Omega^*} + \left(\nabla \cdot \mathbf{v}^h, \tau_{\text{C}} r^h_{\text{C}}\right)_{\Omega^*} = \ell_{\text{NS}}(\mathbf{v}^h)
\end{aligned} \tag{3.46}$$

for all $(\mathbf{v}^h, q^h) \in \mathcal{V}^h_{\mathbf{u}} \times \mathcal{V}^h_p$.

4 Multifractal Subgrid-Scale Modeling within a Variational Multiscale Method

Resuming Chapter 2 and Chapter 3, vorticity and local straining represent key features in the dynamics of turbulent flows. Structural subgrid-scale models promise high-fidelity LES, since they are generally able to appropriately estimate the subgrid-scale stress tensor and usually allow for forward as well as reverse transfer of energy. Moreover, the variational multiscale formulation provides a sound theoretical framework for LES that suggests directly modeling the cross- and subgrid-scale Reynolds-stress terms by a structural subgrid-scale velocity-estimation model. Recently, Burton and Dahm [53, 54] proposed multifractal subgrid-scale modeling to approximate the unresolved velocity in LES. This approach, which is built on the aforementioned physical aspects of turbulent flow, demonstrated excellent performance both in *a priori* and *a posteriori* evaluations. Based on this subgrid-scale modeling, a novel computational approach within the VMM is developed for LES of turbulent incompressible flow in this chapter.

After reviewing the occurrence of multifractal structures in turbulent flows, the multifractal subgrid-scale modeling approach is presented in comprehensive form. Then, level-transfer operators from plain aggregation algebraic multigrid methods are introduced to further separate the resolved scales, which is required within the multifractal subgrid-scale modeling approach. The multifractal subgrid-scale modeling is eventually embedded into a residual-based VMM, since the respective terms provide a stable numerical framework. After summarizing the complete modeled variational multiscale formulation, some implementational aspects are briefly addressed. Moreover, multifractal subgrid-scale modeling is further adapted for wall-bounded turbulent flows, which have not yet been addressed in any of the preceding studies on multifractal subgrid-scale modeling. Throughout this chapter, the proposed approach is evaluated for various numerical examples of increasing complexity. The present chapter is based on work published in Rasthofer and Gravemeier [258].

4.1 Multifractals in Turbulent Flows

The interface separating turbulent and non-turbulent parts of jet flows or the flame front in turbulent combustion processes, for instance, evolves into a complex and highly irregular shape. Analogously, the spatial distribution of the kinetic-energy dissipation rate shows significant intermittent features. Mathematically, these structures, which exhibit some form of self similarity, though, can be described by fractals and multifractals, respectively. An early concept for multifractals in turbulence was proposed by Mandelbrot [206]. The state-of-the-art mathematical basis was later introduced by Hentschel and Procaccia [142], Frisch and Parisi [101] and Halsey

et al. [135]. A comprehensive review of fractal and multifractal structures in turbulent flows including the related mathematical formalism was presented, e.g., by Sreenivasan [290]. Detailed introductions into the mathematical theory of fractals and multifractals in general may be found, e.g., in the textbooks by Falconer [93] and Peitgen *et al.* [245]. In this section, merely those aspects of multifractals that are essential for the subsequent derivation of the multifractal subgrid-scale modeling approach are summarized. Furthermore, the dynamics by which turbulent flows exhibit multifractal structures are outlined.

Multifractal structures originate from the repeated application of a scale-invariant multiplicative process on an initial field. These processes can be described by deterministic or stochastic multiplicative cascades. In consecutive cascade steps, the considered field is mapped from one cell to smaller subcells. The set of multipliers $\mathcal{M}$, with $0 < \mathcal{M} < 1$, which determines the (unequal) distribution of the field of interest contained in one cell among the corresponding subcells, can be either prescribed *a priori* or obtained randomly from a scale-invariant distribution $P(\mathcal{M})$, depending on whether a deterministic or stochastic cascade is considered. After a sufficient number of cascade steps, the resulting field becomes highly intermittent and displays multifractal scaling properties. Moreover, all fields generated by one multiplier distribution $P(\mathcal{M})$ are statistically indistinguishable from each other. Assuming an (integral) measure Θ, for instance, mass, the multiplicative cascade is mathematically expressed as

$$\Theta(\mathbf{x}) = \Theta_0 \prod_{n=1}^{\mathcal{N}} \mathcal{M}_n(\mathbf{x}), \tag{4.1}$$

where $\mathcal{N}$ denotes the number of cascade steps and Θ_0 the total amount of the measure to be distributed within the considered domain. In each step of the cascade, an n_{sd}-dimensional parent cell of size ϱ_{n-1} (i.e., the edge length for a square or a cube) is split into $n_{\text{sc}}^{n_{\text{sd}}}$ subcells of equal size ϱ_n, where n_{sc} is also referred to as the base of the process. After $\mathcal{N}$ steps, the size $\varrho_{\mathcal{N}}$ of the smallest subcells is related to the size ϱ_0 of the initial cell via

$$\frac{\varrho_0}{\varrho_{\mathcal{N}}} = n_{\text{sc}}^{\mathcal{N}}. \tag{4.2}$$

Expressed for a cell-averaged distributed measure ϑ (i.e., $\vartheta_n = \Theta_n/(\varrho_n)^{n_{\text{sd}}}$), for instance, density, the multiplicative cascade reads as

$$\vartheta(\mathbf{x}) = \vartheta_0 \left(n_{\text{sc}}^{\mathcal{N}}\right)^{n_{\text{sd}}} \prod_{n=1}^{\mathcal{N}} \mathcal{M}_n(\mathbf{x}). \tag{4.3}$$

For illustration, a one-dimensional stochastic binomial cascade, depicted in Figure 4.1, is considered. At each stage of the process, the measure contained in one cell is divided between two subcells, each half the size of the parent cell. The scale-invariant distribution of the multipliers is given in terms of δ-functions as

$$P(\mathcal{M}) = 0.5\,(\delta(\mathcal{M} - 0.4) + \delta(\mathcal{M} - 0.6)) \tag{4.4}$$

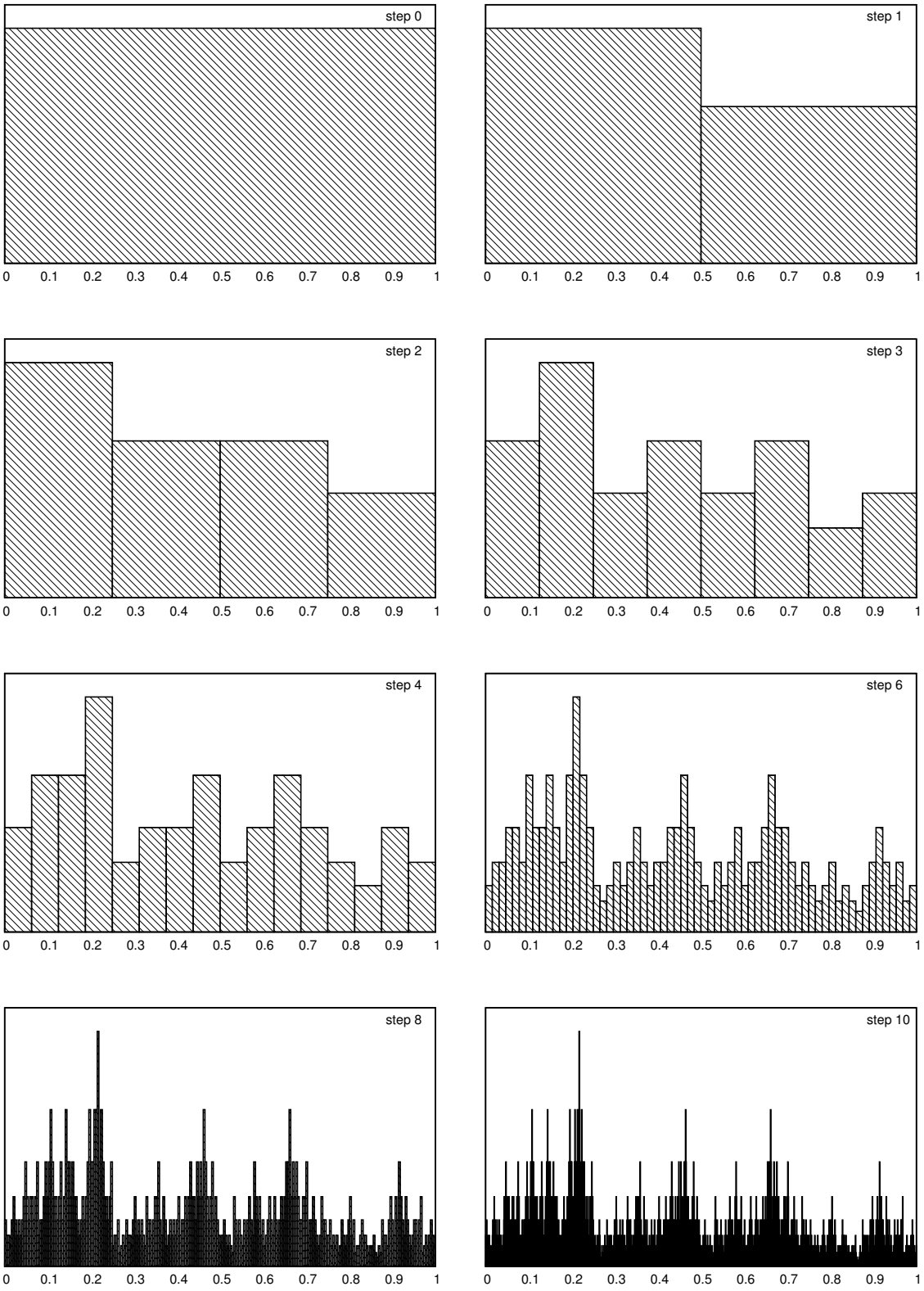

Figure 4.1: One-dimensional stochastic binomial cascade with imposed conservation of the measure: initial field as well as resulting fields after $\mathcal{N} = 1$, 2, 3, 4, 6, 8 and 10 cascade steps normalized by the respective maximum values.

such that only two values are possible for $\mathcal{M}$. Additionally, conservation of the measure is imposed in every cascade step by randomly selecting the multiplier $\mathcal{M}_n$ for the first subcell and assigning the multiplier $1 - \mathcal{M}_n$ to the second one. Figure 4.1 shows the initial field as well as the resulting fields after 1, 2, 3, 4, 6, 8 and 10 cascade steps. All fields are scaled by their maximum value. Passing through the cascade, the intermittency is increased, and the field becomes concentrated onto successively smaller parts of the domain.

In turbulent flows, it is the repeated stretching and folding mechanism of the vorticity and strain-rate field that causes multiplicative processes. Gradient-magnitude fields in high-Reynolds-number flows, such as the kinetic-energy dissipation rate, the enstrophy and the scalar-variance diffusion rate, are subject to these processes. As a result, they exhibit multifractal structures in the inertial subrange, where the required scale-invariance is naturally satisfied. Based on experimental data, Meneveau and Sreenivasan [214, 215], for instance, confirmed the multifractal scale-similarity scaling in the kinetic-energy dissipation-rate field. Further experimental investigations, e.g., by Prasad *et al.* [254], Sreenivasan and Prasad [292] as well as Frederiksen *et al.* [97] demonstrated that the scalar-variance diffusion rate exhibits multifractal scale-similarity properties as well. Concerning the enstrophy field, Burton [49] revealed multifractal structures within the inertial subrange by investigating DNS data of homogeneous isotropic turbulence, and Mullin and Dahm [227] evaluated experimental measurements to identify its multifractal properties.

4.2 Multifractal Subgrid-Scale Modeling

A structural subgrid-scale model providing the subgrid-scale velocity allows for directly evaluating the cross- and subgrid-scale Reynolds-stress terms, (3.26) and (3.27), of the variational multiscale formulation (3.25). The physical considerations on multifractal scale similarity inherent in the enstrophy field enable a novel approach to subgrid-scale modeling for LES of turbulent incompressible flow, as proposed by Burton and Dahm [53]. The multifractal subgrid-scale modeling approach presented in that study constitutes a further developed version of the modeling strategy originally introduced by Burton [49]. The application of the suggested method to homogeneous isotropic turbulence was shown in an accompanying work by Burton and Dahm [54].

4.2.1 General Idea of the Modeling Strategy

In the multifractal subgrid-scale modeling approach, the subgrid-scale velocity $\hat{\mathbf{u}}$ is evaluated using a multifractal reconstruction of the associated subgrid-scale vorticity $\hat{\boldsymbol{\omega}}$ over inertial-subrange scales. The subgrid-scale velocity field is then recovered via the Biot-Savart operator (2.6):

$$\hat{\mathbf{u}}(\mathbf{x}, t) = \frac{1}{4\pi} \int \hat{\boldsymbol{\omega}}(\check{\mathbf{x}}, t) \times \frac{\mathbf{x} - \check{\mathbf{x}}}{\|\mathbf{x} - \check{\mathbf{x}}\|^3} \mathrm{d}\check{\mathbf{x}}. \tag{4.5}$$

Burton and Dahm [53] argued that the evaluation of the subgrid-scale velocity field via integration of the directly modeled subgrid-scale vorticity field renders the resulting velocity field less sensitive to the details of the modeling of $\hat{\boldsymbol{\omega}}$.

The reconstruction of the subgrid-scale vorticity field, expressed by means of its magnitude $\|\hat{\boldsymbol{\omega}}\|(\mathbf{x},t)$ and orientation vector $\hat{\mathbf{e}}_{\boldsymbol{\omega}}(\mathbf{x},t)$ of unit length as

$$\hat{\boldsymbol{\omega}}(\mathbf{x},t) = \|\hat{\boldsymbol{\omega}}\|(\mathbf{x},t)\hat{\mathbf{e}}_{\boldsymbol{\omega}}(\mathbf{x},t), \tag{4.6}$$

consists of two steps. First, the magnitude $\|\hat{\boldsymbol{\omega}}\|$ of the subgrid-scale vorticity field is derived by a multiplicative cascade distributing the total subgrid-scale enstrophy within each element. In a second step, the orientation $\hat{\mathbf{e}}_{\boldsymbol{\omega}}$ of the subgrid-scale vorticity field is determined using an additive decorrelation cascade. Both cascades start at a scale of the size of the element length h and proceed down to the viscous (or inner) length scale λ_ν. The viscous length scale λ_ν defines the scale at which the competing effects of local strain rates and viscous diffusion are in equilibrium; see, e.g., Buch and Dahm [42] and Mullin and Dahm [227]. In contrast to the Kolmogorov length scale η (see equation (2.10)), which is determined by dimensional analysis, λ_ν is obtained based on physical grounds and about a factor of six larger than η (see, e.g., Mullin and Dahm [227]). Assuming that each parent element decays into two child elements per spatial direction, i.e., $n_{\text{sc}} = 2$, which is a reasonable value for turbulent flow (see, e.g., Frederiksen *et al.* [97] and Sreenivasan and Stolovitzky [293]), the number of steps $\mathcal{N}_{\mathbf{u}}$ of both cascades is determined by the ratio of the element length h to the viscous length scale λ_ν via

$$\mathcal{N}_{\mathbf{u}} = \log_2\left(\frac{h}{\lambda_\nu}\right), \tag{4.7}$$

which follows immediately from equation (4.2). The local element Reynolds number Re_h provides a scaling for the ratio of the element length to the viscous length scale as

$$\frac{h}{\lambda_\nu} \sim \text{Re}_h^{\frac{3}{4}}. \tag{4.8}$$

4.2.2 Vorticity-Magnitude Cascade

The magnitude of the subgrid-scale vorticity $\|\hat{\boldsymbol{\omega}}\|$ in each subelement of the size of the viscous length scale is derived from the distribution of the total subgrid-scale enstrophy contained in the considered element. Therefore, the average subgrid-scale enstrophy $\hat{Q}$ over the element is estimated using the inertial-subrange scaling of the enstrophy spectrum:

$$Z_Q(k) \sim \varepsilon^{\frac{2}{3}} k^{\frac{1}{3}}, \tag{4.9}$$

which follows from analogous arguments as those assumed for the inertial-subrange scaling of the energy spectrum (see Section 2.2.2). To eliminate the required proportionality constant in relation (4.9), $\hat{Q}$ is determined as a function of the average enstrophy δQ^h at the smaller resolved scales, i.e., a scale range between h and a larger length scale αh (i.e., $\alpha > 1$), which is assumed to be located in the inertial subrange. Accordingly, quantities corresponding to the larger

resolved scales are marked by $(\cdot)^{\alpha h}$ and quantities associated with the smaller resolved scales by $\delta(\cdot)^h$. Figure 4.2 displays the enstrophy spectrum, including the inertial-subrange scaling, as well as its decomposition according to the introduced scale ranges. Integrating the enstrophy

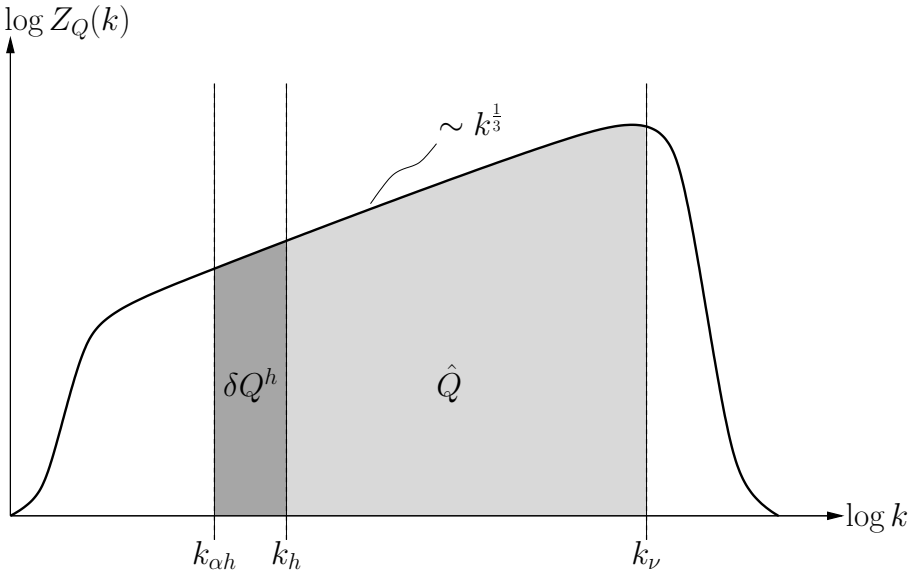

Figure 4.2: Decomposition of enstrophy spectrum.

spectrum both from the wave number k_h associated with the basic discretization to the viscous wave number k_ν,

$$\hat{Q} = \int_{k_h}^{k_\nu} c_Q \varepsilon^{\frac{2}{3}} k^{\frac{1}{3}} \mathrm{d}k, \tag{4.10}$$

where $c_Q > 0$ is the associated proportionality constant, and from the smaller wave number $k_{\alpha h}$ to k_h

$$\delta Q^h = \int_{k_{\alpha h}}^{k_h} c_Q \varepsilon^{\frac{2}{3}} k^{\frac{1}{3}} \mathrm{d}k, \tag{4.11}$$

enables a formulation for the subgrid-scale enstrophy depending on the enstrophy of the smaller resolved scales:

$$\hat{Q} = \left(1 - \alpha^{-\frac{4}{3}}\right)^{-1} \left[\left(\frac{k_\nu}{k_h}\right)^{\frac{4}{3}} - 1\right] \delta Q^h. \tag{4.12}$$

The enstrophy at the smaller resolved scales is determined from the resolved velocity field. Therefore, the resolved velocity $\mathbf{u}^h$ is further decomposed as

$$\mathbf{u} = \underbrace{\mathbf{u}^{\alpha h} + \delta \mathbf{u}^h}_{\mathbf{u}^h} + \hat{\mathbf{u}}, \tag{4.13}$$

where the larger resolved velocity scales $\mathbf{u}^{\alpha h}$ are obtained by explicitly separating the velocity field at a scale αh. By this decomposition, the enstrophy is formally split up as

$$Q = \boldsymbol{\omega}^{\alpha h} \cdot \boldsymbol{\omega}^{\alpha h} + \delta\boldsymbol{\omega}^{h} \cdot \delta\boldsymbol{\omega}^{h} + \hat{\boldsymbol{\omega}} \cdot \hat{\boldsymbol{\omega}} + 2\left(\boldsymbol{\omega}^{\alpha h} \cdot \delta\boldsymbol{\omega}^{h} + \boldsymbol{\omega}^{\alpha h} \cdot \hat{\boldsymbol{\omega}} + \delta\boldsymbol{\omega}^{h} \cdot \hat{\boldsymbol{\omega}}\right). \tag{4.14}$$

The enstrophies $Q^{\alpha h}$, δQ^{h} and $\hat{Q}$, associated with the three scale ranges, are identified as

$$Q^{\alpha h} = \boldsymbol{\omega}^{\alpha h} \cdot \boldsymbol{\omega}^{\alpha h}, \tag{4.15}$$

$$\delta Q^{h} = \delta\boldsymbol{\omega}^{h} \cdot \delta\boldsymbol{\omega}^{h}, \tag{4.16}$$

$$\hat{Q} = \hat{\boldsymbol{\omega}} \cdot \hat{\boldsymbol{\omega}}. \tag{4.17}$$

Averages over the cross terms are neglected due to the decorrelation of widely separated scales in the vorticity field.

A three-dimensional stochastic multiplicative cascade (4.3) distributes the average subgrid-scale enstrophy, as given in equation (4.12) with expressions (4.16) and (4.17) being introduced, over each element, leading to the following expression for the magnitude of the subgrid-scale vorticity in each subelement of the size of the viscous length scale:

$$\|\hat{\boldsymbol{\omega}}\|(\mathbf{x},t) = \left[\left(1-\alpha^{-\frac{4}{3}}\right)^{-1}\left(\left(\frac{k_\nu}{k_h}\right)^{\frac{4}{3}}-1\right)\left(2^{\mathcal{N}_\mathbf{u}}\right)^3\prod_{n=1}^{\mathcal{N}_\mathbf{u}}\mathcal{M}_n(\mathbf{x},t)\right]^{\frac{1}{2}}\|\delta\boldsymbol{\omega}^{h}\|. \tag{4.18}$$

For depiction of the corresponding scale-invariant distribution $\mathrm{P}(\mathcal{M})$ of the multipliers of the enstrophy field, the reader is referred to Burton [49] (see Figure 2.9 therein) as well as Mullin and Dahm [227] (see Figure 29 therein).

4.2.3 Vorticity-Orientation Cascade

Also the second cascade, which describes the reconstruction of the orientation $\hat{\mathbf{e}}_\omega$ of the subgrid-scale vorticity, is based on physical reasoning. Various experimental and computational studies indicate that the velocity fields of adjacent scale ranges are highly correlated; see, e.g, Bardina *et al.* [14, 15] for an early investigation of scale similarities in the context of LES, Liu *et al.* [197] for a comprehensive experimental study and Meneveau and Katz [213] for a review. Building on these findings, the orientation $\hat{\mathbf{e}}_\omega$ in the subgrid-scale vorticity field is taken to decorrelate at successively smaller scales from the local orientation $\delta\mathbf{e}_\omega^h$ of the smaller resolved scales. The additive cascade is then given as

$$\hat{\mathbf{e}}_\omega(\mathbf{x},t) = \delta\mathbf{e}_\omega^h(\mathbf{x},t) + \sum_{n=1}^{\mathcal{N}_\mathbf{u}}\boldsymbol{\delta}_n, \tag{4.19}$$

where $\boldsymbol{\delta}_n$ denotes stochastic-decorrelation increments between adjoining scale ranges. Consistent with the isotropy observed at the smallest scales in high-Reynolds-number flows, the cascade leads to an increasingly isotropic decorrelation of the subgrid-scale orientations from the element length scale to the viscous length scale. At each stage n of the cascade, $\boldsymbol{\delta}_n$ is defined by

two stochastic spherical decorrelation angles ψ and β. Figure 4.3 displays a single step of the additive decorrelation cascade leading to $\hat{\mathrm{e}}_{\boldsymbol{\omega},n}$ at the current stage n . Assuming $\hat{\mathrm{e}}_{\boldsymbol{\omega},n-1} = (0,0,1)^{\mathrm{T}}$ for the orientation vector of the preceding stage $n-1$, the components of $\boldsymbol{\delta}_n$ are given by

$$\boldsymbol{\delta}_n = \begin{pmatrix} \sin\psi\cos\beta \\ \sin\psi\sin\beta \\ \cos\psi - 1 \end{pmatrix}. \tag{4.20}$$

An isotropic probability distribution is assumed for β, as also implied in Figure 4.3, such that ψ quantifies the decorrelation of the vorticity orientation at two adjoining scales in the subgrid-scale field. Evaluation of DNS data by Burton and Dahm [53] revealed correlations between the

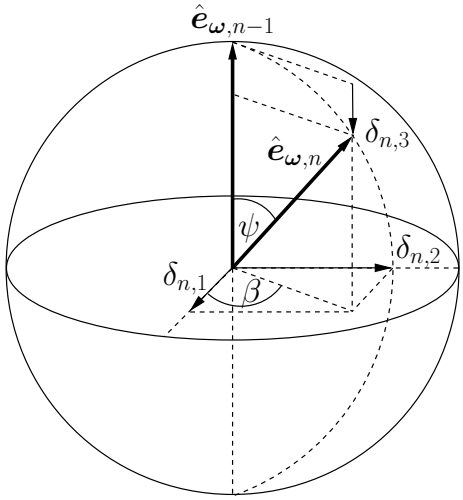

Figure 4.3: Single step of additive decorrelation cascade.

probability distribution of ψ and the value of the multiplier $\mathcal{M}_n$. While there is only a weak correlation between the orientation vectors at two successive scales for lower multiplier values, the vectors $\hat{\mathrm{e}}_{\boldsymbol{\omega},n-1}$ and $\hat{\mathrm{e}}_{\boldsymbol{\omega},n}$ are almost identical for higher ones. This behavior reflects the observation that the strongest vortical structures, which are identified by larger multiplier values, exhibit a preferred alignment with the local strain rate tensor over a relatively large range of scales.

As a result of these considerations, an intermittency factor $\mathcal{I}_\omega$ can be defined from a correlation between $\hat{\boldsymbol{\omega}}$ and $\delta\boldsymbol{\omega}^h$ as

$$\mathcal{I}_\omega = \frac{\int \hat{\boldsymbol{\omega}} \cdot \delta\boldsymbol{\omega}^h \mathrm{d}\mathbf{x}}{\int \|\hat{\boldsymbol{\omega}}\| \, \|\delta\boldsymbol{\omega}^h\| \mathrm{d}\mathbf{x}}, \tag{4.21}$$

where $\mathcal{I}_\omega$ is expected to depend on the number of cascade steps $\mathcal{N}_\mathbf{u}$ in the decorrelation cascade. The orientation of the subgrid-scale vorticity after $\mathcal{N}_\mathbf{u}$ cascade steps can then be reformulated using the intermittency factor $\mathcal{I}_\omega$:

$$\hat{\mathrm{e}}_\omega(\mathbf{x},t) = \mathcal{I}_\omega \delta\mathrm{e}^h_\omega(\mathbf{x},t) + (1-\mathcal{I}_\omega) \sum_{n=1}^{\mathcal{N}_\mathbf{u}} \boldsymbol{\delta}^*_n, \tag{4.22}$$

where $\boldsymbol{\delta}_n^*$ are modified decorrelation increments due to the introduction of the intermittency factor $\mathcal{I}_{\boldsymbol{\omega}}$, which will be further specified below.

4.2.4 Subgrid-Scale Velocity Approximation

Combining cascades (4.18) and (4.22) yields the subgrid-scale vorticity $\hat{\boldsymbol{\omega}}$, which is a stochastic field due to the stochastic nature of both the multipliers and the modified decorrelation increments. Assuming that (i) the correlations between $\mathcal{M}_n$ and $\boldsymbol{\delta}_n^*$ are sufficiently weak, (ii) the decorrelation cascade is isotropic (i.e., the expectation value of $\boldsymbol{\delta}_n^*$ vanishes) and (iii) the multipliers are statistically independent, the subgrid-scale vorticity $\hat{\boldsymbol{\omega}}$, which is taken to be approximately equal to its expectation value, may be simplified as

$$\hat{\boldsymbol{\omega}}(\mathbf{x},t) = \left[\left(1-\alpha^{-\frac{4}{3}}\right)^{-1}\left(\left(\frac{k_\nu}{k_h}\right)^{\frac{4}{3}}-1\right)\left(2^{\mathcal{N}_\mathbf{u}}\right)^3\right]^{\frac{1}{2}}\left\langle\mathcal{M}^{\frac{1}{2}}\right\rangle^{\mathcal{N}_\mathbf{u}}\mathcal{I}_{\boldsymbol{\omega}}\delta\boldsymbol{\omega}^h(\mathbf{x},t), \tag{4.23}$$

with the expectation value $\left\langle\mathcal{M}^{\frac{1}{2}}\right\rangle$ for the square root of the multipliers. After introducing expression (4.23) into the Biot-Savart operator (4.5), the subgrid-scale velocity can be computed as

$$\hat{\mathbf{u}}(\mathbf{x},t) = \left(1-\alpha^{-\frac{4}{3}}\right)^{-\frac{1}{2}}2^{\frac{3\mathcal{N}_\mathbf{u}}{2}}\left(2^{\frac{4\mathcal{N}_\mathbf{u}}{3}}-1\right)^{\frac{1}{2}}\left\langle\mathcal{M}^{\frac{1}{2}}\right\rangle^{\mathcal{N}_\mathbf{u}}\mathcal{I}_{\boldsymbol{\omega}}\delta\mathbf{u}^h(\mathbf{x},t), \tag{4.24}$$

where it is assumed that the distribution $\mathrm{P}(\mathcal{M})$ is independent of $\mathbf{x}$, and k_ν/k_h is replaced by using equation (4.7). In the high-Reynolds-number limit, a proper behavior of the model has to be ensured. Therefore, the subgrid-scale velocity $\hat{\mathbf{u}}$ should become independent of Re_h for $\mathrm{Re}_h \to \infty$ and, consequently, $\mathcal{N}_\mathbf{u} \to \infty$, implying the following scaling for the intermittency factor subject to $\mathcal{N}_\mathbf{u}$:

$$\mathcal{I}_{\boldsymbol{\omega}}(\mathcal{N}_\mathbf{u}) \sim 2^{-\left(\frac{2}{3}+\frac{3}{2}\right)\mathcal{N}_\mathbf{u}}\left\langle\mathcal{M}^{\frac{1}{2}}\right\rangle^{-\mathcal{N}_\mathbf{u}}. \tag{4.25}$$

Finally, the subgrid-scale velocity $\hat{\mathbf{u}}$ reads as

$$\hat{\mathbf{u}}(\mathbf{x},t) = B\delta\mathbf{u}^h(\mathbf{x},t), \tag{4.26}$$

where

$$B := C_{\mathrm{sgs}}^{\mathrm{B}}\left(1-\alpha^{-\frac{4}{3}}\right)^{-\frac{1}{2}}2^{-\frac{2\mathcal{N}_\mathbf{u}}{3}}\left(2^{\frac{4\mathcal{N}_\mathbf{u}}{3}}-1\right)^{\frac{1}{2}}. \tag{4.27}$$

The parameter $C_{\mathrm{sgs}}^{\mathrm{B}}$ is the associated proportionality constant. Burton and Dahm [53] first introduced $C_{\mathrm{sgs}}^{\mathrm{B}}$ as a universal constant and provided $C_{\mathrm{sgs}}^{\mathrm{B}} \approx 0.37$, resulting from *a priori* investigations of DNS data for forced homogeneous isotropic turbulence. Based on subsequent applications, including those by Burton and Dahm [54], Burton [50] later argued that $C_{\mathrm{sgs}}^{\mathrm{B}}$ is proportional to the subgrid-scale energy transfer and should exhibit a Reynolds number dependence. In particular, $C_{\mathrm{sgs}}^{\mathrm{B}}$ should obey a universal function of an appropriate Reynolds number Re; Burton [50] considered the Taylor micro-scale Reynolds number Re_λ (see, e.g., Pope [252] for definition), but Re_h or an average of it seems also conceivable. This function should approach a finite value in the high-Reynolds-number limit (i.e., $\mathrm{Re} \to \infty$) and tend to zero as $\mathrm{Re} \to 1$.

Using approximation (4.26), the modeled forms of the cross- and subgrid-scale Reynolds-stress terms, (3.26) and (3.27), read as

$$\mathcal{C}(\mathbf{v}^h;\mathbf{u}^h,\hat{\mathbf{u}}) \approx \left(\mathbf{v}^h, \mathbf{u}^h\cdot\nabla\left(B\delta\mathbf{u}^h\right) + B\delta\mathbf{u}^h\cdot\nabla\mathbf{u}^h\right)_{\Omega^*}, \tag{4.28}$$

$$\mathcal{R}(\mathbf{v}^h;\hat{\mathbf{u}}) \approx \left(\mathbf{v}^h, B\delta\mathbf{u}^h\cdot\nabla\left(B\delta\mathbf{u}^h\right)\right)_{\Omega^*}. \tag{4.29}$$

The remaining terms containing unresolved-scale quantities are not incorporated by multifractal subgrid-scale modeling.

4.2.5 Number of Cascade Steps

According to equation (4.7), the number of cascade steps is given by the ratio of the element length to the viscous length scale, which in turn can be approximated by the local element Reynolds number Re_h. The respective relation (4.8) requires a proper definition of Re_h as well as the introduction of a proportionality constant c_ν, i.e.,

$$\frac{h}{\lambda_\nu} = c_\nu \mathrm{Re}_h^{\frac{3}{4}}. \tag{4.30}$$

Two definitions for the element Reynolds number are considered in this thesis:

- based on the strain rate tensor, as suggested by Burton and Dahm [53],

$$\mathrm{Re}_h^{\mathrm{S}} = \frac{\left(\boldsymbol{\varepsilon}(\mathbf{u}^h):\boldsymbol{\varepsilon}(\mathbf{u}^h)\right)^{\frac{1}{2}} h^2}{\nu} \tag{4.31}$$

- and based on the resolved velocity

$$\mathrm{Re}_h^{\mathrm{R}} = \frac{\|\mathbf{u}^h\| h}{\nu}. \tag{4.32}$$

The element length h is approximated by the cubic root of the element volume $V(\Omega^e)$:

$$h = \left(V(\Omega^e)\right)^{\frac{1}{3}}. \tag{4.33}$$

Among others, the experimental study by Mullin and Dahm [227] aimed at estimating $1/c_\nu$ from direct measurements of the enstrophy field in a turbulent flow. In that study, a mean value of $\langle 1/c_\nu\rangle = 12.3$ was reported. In an earlier experimental work by Buch and Dahm [42], $\langle 1/c_\nu\rangle = 11.2$ was obtained indirectly from measurements in scalar fields.

Finally, Figure 4.4 illustrates the dependence of the coefficient B on the number of cascade steps $\mathcal{N}_\mathbf{u}$ according to equation (4.27). Since B approaches its asymptotic value already for $\mathcal{N}_\mathbf{u} > 4$, significant variations in B can merely occur for small $\mathcal{N}_\mathbf{u}$. According to Burton[1], this

[1] private communication

behavior reflects the decoupling of the subgrid scales from the resolved scales for increasing values of $\mathcal{N}_{\mathbf{u}}$.

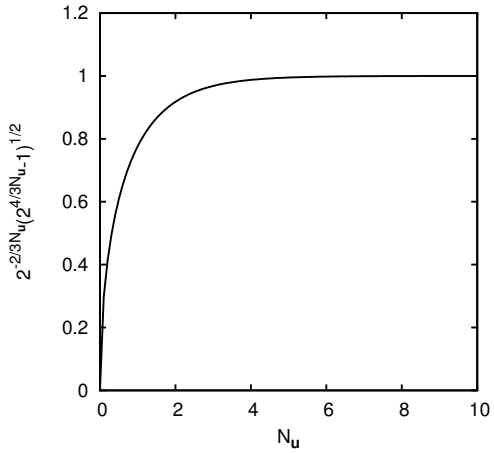

Figure 4.4: Dependence of parameter $B \sim 2^{-\frac{2\mathcal{N}_{\mathbf{u}}}{3}} \left(2^{\frac{4\mathcal{N}_{\mathbf{u}}}{3}} - 1\right)^{\frac{1}{2}}$ on number of cascade steps $\mathcal{N}_{\mathbf{u}}$.

4.3 Scale-Separation by Plain Aggregation Algebraic Multigrid

The multifractal subgrid-scale approximation includes scales between h and a larger length scale αh. To extract the required smaller resolved scales, level-transfer operators from Plain Aggregation Algebraic MultiGrid (PA-AMG) methods are used, as suggested by Gravemeier *et al.* [125] for separating scale groups within a three-scale VMM. Based on this concept, Gravemeier *et al.* [126] later introduced the AVM^3 for LES. From a computational point of view, level-transfer operators from PA-AMG are particularly attractive for scale separation in LES. Since they are obtained in a purely algebraic way, i.e., without explicitly generating a coarser grid, they can be computed for arbitrarily designed meshes without additional effort. Therefore, they are well suited for approaches intended to be applied to practically relevant problems involving complex geometries. Using the AVM^3, Comerford *et al.* [72] recently demonstrated the convenient applicability of the resulting scale-separating operator to such problem configurations in the context of LES of pulmonary airway flow. Usually, algebraic multigrid principles are applied in the context of solution methods for matrix systems arising from the discretization of partial differential equations. For these systems, multigrid approaches in general are among the most efficient algorithms. Multigrid methods combine simple iterative schemes, for instance, Gauss-Seidel relaxation, with a hierarchy of coarser resolution levels. For details on multigrid-based solution strategies, the reader is referred, e.g., to the textbooks by Briggs *et al.* [40], Hackbusch [134] and Trottenberg *et al.* [314]. As aforementioned, level-transfer operators from PA-AMG are applied for explicit scale separation in this thesis. Originally, PA-AMG was introduced

as a preliminary stage towards smooth aggregation algebraic multigrid methods, developed by Vaněk *et al.* [319].

To obtain a scale-separating operator, a prolongation operator matrix $\mathbf{P}_{3h}^{h} \in \mathbb{R}^{n_{\text{dof}}^{h} \times n_{\text{dof}}^{3h}} : \mathcal{S}^{3h} \rightarrow \mathcal{S}^{h}$, transferring the coarser solution field onto the actual (i.e., fine) discretization, is generated first. In the context of multigrid methods, it is common to refer to the larger resolved scales as the coarse scales. This notation is taken up in the remainder of this section when referring to multigrid methods. In the notations introduced above, coarsening by a factor of $\alpha = 3$, which is the usual value in aggregation-based algebraic multigrid methods (see, e.g., Vaněk *et al.* [319]) and also obtained from the strategy briefly described below, is already assumed. Moreover, n_{dof}^{h} denotes the number of degrees of freedom of the discretization, n_{dof}^{3h} the number of degrees of freedom on the coarser level, $\mathcal{S}^{3h}$ the function space associated with the coarser level and $\mathcal{S}^{h}$ the function space associated with the discretization. The construction of $\mathbf{P}_{3h}^{h}$ consists of two steps. First, its sparsity pattern is determined. Therefore, the degrees of freedom corresponding to the system matrix are grouped into a set of so-called aggregates $\mathcal{A}_{i}^{h}$ such that $\bigcup_{i=1}^{n_{\text{nb}}^{3h}} \mathcal{A}_{i}^{h} = \{1, ..., n_{\text{dof}}^{h}\}$ and $\mathcal{A}_{i}^{h} \cap \mathcal{A}_{j}^{h} = \emptyset$ for all $1 \leq i, j \leq n_{\text{nb}}^{3h}$ with $i \neq j$, where n_{nb}^{3h} is the number of nodal blocks on the coarser level. Each aggregate $\mathcal{A}_{i}^{h}$ is defined by its root node with all its associated degrees of freedom $d_{j}^{\mathcal{A}_{i}^{h}} \in \{1, ..., n_{\text{dof}}^{h}\}$ and all adjacent degrees of freedom that share a non-zero off-diagonal entry with $d_{j}^{\mathcal{A}_{i}^{h}}$. Second, the non-zero values of $\mathbf{P}_{3h}^{h}$ are calculated. Based on the near-null space $\mathbf{B}$ of the system matrix $\tilde{\mathbf{K}}$ without Dirichlet boundary conditions being applied (i.e., $\tilde{\mathbf{K}}\mathbf{B} \approx \mathbf{0}$), the prolongation operator matrix $\mathbf{P}_{3h}^{h}$ as well as a coarse-level representation of the near-null space are constructed simultaneously via a local aggregate-wise QR-factorization of $\mathbf{B}$ such that an exact prolongation of the near-null space is achieved. The restriction operator matrix $\mathbf{R}_{h}^{3h} \in \mathbb{R}^{n_{\text{dof}}^{3h} \times n_{\text{dof}}^{h}} : \mathcal{S}^{h} \rightarrow \mathcal{S}^{3h}$, which maps the solution field onto the coarser level, is chosen to be the transpose of the prolongation operator matrix, i.e.,

$$\mathbf{R}_{h}^{3h} = \left(\mathbf{P}_{3h}^{h}\right)^{\mathrm{T}}. \tag{4.34}$$

By construction via a local aggregate-wise QR-factorization, it holds

$$\mathbf{R}_{h}^{3h}\mathbf{P}_{3h}^{h} = \mathbf{I}, \tag{4.35}$$

where $\mathbf{I}$ denotes the identity matrix. A scale-separating operator matrix yielding the larger resolved scales $\mathbf{u}^{3h}$ is then defined as

$$\mathbf{S}_{h}^{3h} = \mathbf{P}_{3h}^{h}\mathbf{R}_{h}^{3h}. \tag{4.36}$$

Owing to equation (4.35), PA-AMG level-transfer operators enable projective scale-separating operators, i.e.,

$$\left(\mathbf{S}_{h}^{3h}\right)^{n} = \underbrace{\mathbf{S}_{h}^{3h} \circ \mathbf{S}_{h}^{3h} \circ ... \circ \mathbf{S}_{h}^{3h}}_{n \text{ times}} = \mathbf{S}_{h}^{3h}, \tag{4.37}$$

where $n \in \mathbb{N}^{+}$. More details of the presented derivations as well as further considerations and references concerning level-transfer operators from PA-AMG are provided in Gravemeier *et al.* [125] in conjunction with its application within a three-level VMM.

The scale-separating operator matrix is applied to the discrete (i.e., nodal) values of the resolved velocity field. The usual finite element expansion (3.29) of the resolved velocity field can also be written as

$$\mathbf{u}^h = \sum_{A \in \mathcal{E}} N_A \mathbf{u}_A = \mathbf{N}\mathbf{U}^h, \tag{4.38}$$

where $\mathbf{U}^h$ denotes the vector of resolved velocity degrees of freedom $\mathbf{u}_A$ and $\mathbf{N}$ a matrix containing the shape functions N_A. Using equation (4.36), the small-scale velocity field is obtained as

$$\delta\mathbf{u}^h = \sum_{\mathrm{A} \in \mathcal{E}} N_\mathrm{A} \delta\mathbf{u}_\mathrm{A}^h = \mathbf{N}\delta\mathbf{U}^h = \mathbf{N}\left[\mathbf{I} - \mathbf{S}_h^{3h}\right]\mathbf{U}^h, \tag{4.39}$$

where $\delta\mathbf{U}^h$ is the vector containing the nodal values $\delta\mathbf{u}_\mathrm{A}^h$ of the small-scale velocity field.

Figure 4.5 illustrates scale separation by level-transfer operators from PA-AMG for a one-dimensional problem with one degree of freedom per node. On the bottom, the discretization based on linearly-interpolated one-dimensional elements is shown, and the aggregates $\mathcal{A}_i^h$, further identified by their root node with associated degree of freedom $d^{\mathcal{A}_i^h}$, are visualized by grey boxes. The smaller resolved velocity δu^h, obtained from subtracting the larger resolved velocity u_h^{3h} from the solution field u^h, is depicted above. Applying $\mathbf{S}_h^{3h}$ to the vector of discrete values of u^h and interpolating with N_A yields the larger resolved velocity u_h^{3h} on the used discretization, which is here indicated by the additional subscript h.

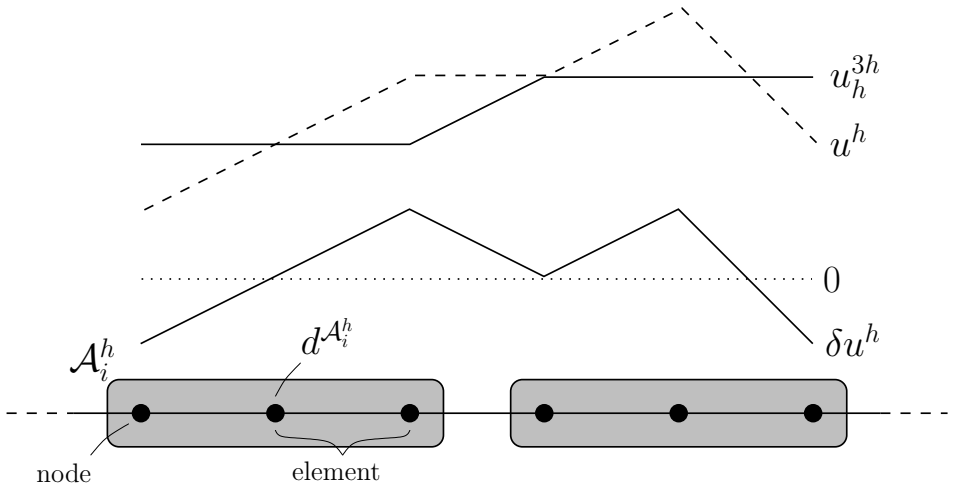

Figure 4.5: Scale separation by level-transfer operators from PA-AMG.

4.4 Residual-Based Subgrid-Scale Modeling

The multifractal subgrid-scale modeling approach introduced so far is based on physical reasoning. In particular, the multifractal subgrid-scale modeling approach aims at capturing the physical interaction that leads to the actual energy transfer between the larger and the smaller scales in

turbulent flows, i.e., the resolved and the subgrid scales in the respective LES. Therefore, it is not purely dissipative and allows for physical backscatter of energy, among other things. An introduction of additional artificial (or subgrid-scale) dissipation to also stabilize numerical schemes is not intended by the multifractal subgrid-scale modeling approach, and incorporating the multifractal subgrid-scale approximation into the variational multiscale formulation does generally not ensure the stability of the final numerical method. Therefore, potentially destabilizing effects induced by the numerical scheme have to be accounted for otherwise, as elaborately discussed by Burton and Dahm [54]. For the multifractal subgrid-scale modeling approach in its original form, a backscatter limiter was proposed by Burton and Dahm [54] and in a more advanced adaptive form by Burton [50] to overcome this limitation. By a reduction of those components of the inertial stress tensor $\overline{\bar{\mathbf{u}} \otimes \bar{\mathbf{u}}} + \boldsymbol{\tau}_{\text{sgs}}^{*}$ that contribute to backscatter, the control of spurious energy is accomplished. In the latter study, the resulting overall approach was referred to as non-linear LES (nLES).

Here, the multifractal subgrid-scale modeling approach is embedded into a residual-based variational multiscale formulation. A mathematically solid foundation, as outlined in Section 3.3, renders residual-based subgrid-scale approximations, which lead to stabilized methods, a reliable means for accounting for stability issues not addressed by the multifractal subgrid-scale modeling. Hence, the following solely numerically motivated stabilization terms are included:

$$\mathcal{B}_{\text{RBStab}}(\mathbf{v}^h, q^h; \mathbf{u}^h, p_{\text{kin}}^h) := \left(\mathbf{u}^h \cdot \nabla \mathbf{v}^h, \tau_{\text{M}} \mathbf{r}_{\text{M}}^h\right)_{\Omega^*} + \left(\nabla q^h, \tau_{\text{M}} \mathbf{r}_{\text{M}}^h\right)_{\Omega^*} + \left(\nabla \cdot \mathbf{v}^h, \tau_{\text{C}} r_{\text{C}}^h\right)_{\Omega^*} . \quad (4.40)$$

As shown in equation (3.45), the PSPG and grad-div term emanate from $\mathcal{B}_{\text{NS}}^{1,\text{lin}}(\mathbf{v}^h, q^h; \hat{\mathbf{u}}, \hat{p}_{\text{kin}})$, which has not been considered by the multifractal subgrid-scale modeling. The SUPG term, formally arsing from $\mathcal{C}(\mathbf{v}^h; \mathbf{u}^h, \hat{\mathbf{u}})$, as explained in Section 3.3, provides convective stabilization and, hence, the necessary dissipation on the subgrid-scale level. Since the terms given in equation (4.40) arise from a residual-based approximation of the subgrid scales, their inclusion may also be interpreted as a second subgrid-scale modeling step.

4.5 AVM^4 in a Nutshell

As developed in the previous sections, four features constitute the novel approach for LES:

- its derivation within the framework of the **V**ariational **M**ultiscale **M**ethod,
- the evaluation of the subgrid-scale velocity based on the **M**ultifractal subgrid-scale modeling approach,
- the identification of the required smaller resolved scales by level-transfer operators from plain aggregation **A**lgebraic **M**ultigrid methods and
- the inclusion of additional residual-based multiscale terms to primarily shield against potentially destabilizing effects due to the numerical scheme.

It is thus referred to as Algebraic Variational Multiscale-Multigrid-Multifractal Method - abbreviated by AVM^4. The respective modeled variational multiscale formulation is obtained by inserting expressions (4.28), (4.29) as well as (4.40) into equation (3.25): find $(\mathbf{u}^h, p_{\text{kin}}^h) \in \mathcal{S}_{\mathbf{u}}^h \times \mathcal{S}_p^h$

such that

$$\begin{aligned}&\mathcal{B}_{\text{NS}}(\mathbf{v}^h, q^h; \mathbf{u}^h, p^h_{\text{kin}}) \\ &+ \left(\mathbf{v}^h, \mathbf{u}^h \cdot \nabla \left(B\delta\mathbf{u}^h\right) + B\delta\mathbf{u}^h \cdot \nabla\mathbf{u}^h\right)_{\Omega^*} + \left(\mathbf{v}^h, B\delta\mathbf{u}^h \cdot \nabla \left(B\delta\mathbf{u}^h\right)\right)_{\Omega^*} \\ &+ \left(\mathbf{u}^h \cdot \nabla\mathbf{v}^h, \tau_{\text{M}}\mathbf{r}^h_{\text{M}}\right)_{\Omega^*} + \left(\nabla q^h, \tau_{\text{M}}\mathbf{r}^h_{\text{M}}\right)_{\Omega^*} + \left(\nabla \cdot \mathbf{v}^h, \tau_{\text{C}} r^h_{\text{C}}\right)_{\Omega^*} = \ell_{\text{NS}}(\mathbf{v}^h)\end{aligned} \tag{4.41}$$

for all $(\mathbf{v}^h, q^h) \in \mathcal{V}^h_{\mathbf{u}} \times \mathcal{V}^h_p$, with the multifractal subgrid-scale modeling terms in the second line (both terms) and the residual-based multiscale terms in the third line (first three terms).

4.6 The AVM^4 Flow Solver

All simulations presented in this thesis have been performed using the parallel multiphysics software platform "Bavarian Advanced Computational Initiative" (BACI; see Wall and Gee [326]). BACI is a flexible finite element software environment, which is continuously developed and maintained by the Institute for Computational Mechanics at the Technische Universität München. The object-oriented code is written in C++ and utilizes powerful open-source libraries provided by the Trilinos project (see, e.g., Heroux *et al.* [143]), including linear algebra, iterative solvers, and state-of-the-art algebraic multigrid preconditioners. BACI is composed of three major modules: the structure, the fluid and the scalar-transport module. This section first provides a brief overview of the solver for (single-phase) incompressible flow problems. Then, an efficient realization of the multifractal subgrid-scale modeling terms is presented.

4.6.1 Overview of the Flow Solver

As aforementioned, a finite element flow solver is used for the numerical investigation of the proposed method. Trilinearly-interpolated hexahedral elements are exclusively utilized in this thesis. Recently, it was argued by Löhner [198] that, with respect to the typical accuracy of engineering interest, trilinearly-interpolated elements are superior regarding error and work estimates when compared to higher-order elements for three-dimensional flow problems (with the same holding true, e.g., in the context of FDMs and FVMs).

For temporal discretization, the generalized-α time-integration scheme is applied to all examples in the first part of the present thesis. The generalized-α scheme was originally introduced by Chung and Hulbert [66] for problems of solid mechanics and later extended to flow problems described by the compressible Navier-Stokes equations by Jansen *et al.* [159]. In this thesis, generalized-α time integration is applied in the particular form presented by Gravemeier *et al.* [127] for the incompressible Navier-Stokes equations. The generalized-α time-integration scheme enables the crucial balance between damping of high temporal frequencies, which are often only marginally resolved in simulations and may provoke numerical instabilities, and leaving the dynamics of the well-resolved temporal scales unaffected by damping. This issue is particularly beneficial when integrating a wide range of temporal scales for a long time period, for instance, in turbulent flow problems. As introduced by Jansen *et al.* [159], the generalized-α

time-integration scheme is second-order accurate and unconditionally stable. The corresponding parameter $\rho_\infty \in [0,1]$ allows for precisely controlling the damping of high frequencies. Zero damping is obtained for $\rho_\infty = 1$. For evaluation, intermediate points in time between level n and $n+1$, defined by two parameters $\alpha_\mathrm{M}, \alpha_\mathrm{F} \in [0,1]$, which are subject to ρ_∞, are considered. Following Gravemeier *et al.* [127] for the incompressible Navier-Stokes equations, the matrix system of the standard Galerkin formulation (i.e., the formulation without multifractal subgrid-scale terms and residual-based multiscale terms) using the generalized-α scheme results in

$$\begin{bmatrix} \mathbf{M} & \mathbf{0} \\ \mathbf{0} & \mathbf{0} \end{bmatrix} \begin{bmatrix} \dot{\mathbf{U}}^h_{n+\alpha_\mathrm{M}} \\ \mathbf{0} \end{bmatrix} + \begin{bmatrix} \mathbf{A}(\mathbf{U}^h_{n+\alpha_\mathrm{F}}) + \mathbf{V} & \mathbf{G} \\ -\mathbf{G}^\mathrm{T} & \mathbf{0} \end{bmatrix} \begin{bmatrix} \mathbf{U}^h_{n+\alpha_\mathrm{F}} \\ \mathbf{P}^h_{n+\alpha_\mathrm{F}} \end{bmatrix} = \begin{bmatrix} \mathbf{f}_{n+\alpha_\mathrm{F}} \\ \mathbf{0} \end{bmatrix} \tag{4.42}$$

with

$$\mathbf{U}^h_{n+1} = \mathbf{U}^h_n + \gamma \Delta t \dot{\mathbf{U}}^h_{n+1} + (1-\gamma)\Delta t \dot{\mathbf{U}}^h_n, \tag{4.43}$$

$$\dot{\mathbf{U}}^h_{n+\alpha_\mathrm{M}} = \alpha_\mathrm{M} \dot{\mathbf{U}}^h_{n+1} + (1-\alpha_\mathrm{M}) \dot{\mathbf{U}}^h_n, \tag{4.44}$$

$$\mathbf{U}^h_{n+\alpha_\mathrm{F}} = \alpha_\mathrm{F} \mathbf{U}^h_{n+1} + (1-\alpha_\mathrm{F}) \mathbf{U}^h_n, \tag{4.45}$$

$$\mathbf{P}^h_{n+\alpha_\mathrm{F}} = \alpha_\mathrm{F} \mathbf{P}^h_{n+1} + (1-\alpha_\mathrm{F}) \mathbf{P}^h_n, \tag{4.46}$$

where $\mathbf{M}$, $\mathbf{A}(\mathbf{U}^h_{n+\alpha_\mathrm{F}})$, $\mathbf{V}$ and $\mathbf{G}$ are the matrices containing the transient, convective, viscous and pressure term of form $\mathcal{B}_\mathrm{M}(\mathbf{v}^h; \mathbf{u}^h, p^h)$. The non-linearity of the convective term is explicitly indicated. The negative transpose of $\mathbf{G}$ results from $\mathcal{B}_\mathrm{C}(q^h; \mathbf{u}^h)$, and the right-hand-side terms of $\ell(\mathbf{v})$, which may be time dependent, constitute the vector $\mathbf{f}_{n+\alpha_\mathrm{F}}$. Moreover, the vectors $\mathbf{U}^h$ and $\mathbf{P}^h$ contain the degrees of freedom for velocity and pressure, respectively; and vector $\dot{\mathbf{U}}^h$ comprises the acceleration values at the nodes. The parameters α_M, α_F and γ depend on ρ_∞ as

$$\alpha_\mathrm{M} = \frac{1}{2}\left(\frac{3-\rho_\infty}{1+\rho_\infty}\right), \tag{4.47}$$

$$\alpha_\mathrm{F} = \frac{1}{1+\rho_\infty}, \tag{4.48}$$

$$\gamma = \frac{1}{2} + \alpha_\mathrm{M} - \alpha_\mathrm{F}. \tag{4.49}$$

As proposed by Jansen *et al.* [159], ρ_∞ is set to 0.5 in this thesis. For further details on the inclusion of stabilization terms as well as the derivation of an incremental formulation to account for the non-linearity of the Navier-Stokes equations, the reader is referred to Gravemeier *et al.* [127].

4.6.2 Implementational Aspects of the AVM^4

To illustrate the implementation of the multifractal subgrid-scale modeling terms, while keeping the depiction as simple as possible, a generic matrix system, which is not assigned to any specific time-integration scheme, is assumed. Hence, all submatrices and -vectors have to be understood as generalized ones in the following, potentially including further contributions from time integration. The matrix system is iteratively solved for the increments

$\Delta\mathbf{U}^{h,i+1} = \mathbf{U}^{h,i+1} - \mathbf{U}^{h,i}$ and $\Delta\mathbf{P}^{h,i+1} = \mathbf{P}^{h,i+1} - \mathbf{P}^{h,i}$ based on a Picard (or fixed-point-like) iteration scheme. The linearized system results in

$$\begin{aligned}
&\begin{bmatrix} \mathbf{K}(\mathbf{U}^{h,i}) + \beta\left\{\mathbf{C}(\mathbf{U}^{h,i})[\mathbf{I} - \mathbf{S}_h^{3h}] + \mathbf{C}([\mathbf{I} - \mathbf{S}_h^{3h}]\mathbf{U}^{h,i}) + \mathbf{R}([\mathbf{I} - \mathbf{S}_h^{3h}]\mathbf{U}^{h,i})[\mathbf{I} - \mathbf{S}_h^{3h}]\right\} & \mathbf{G} \\ -\mathbf{G}^{\mathrm{T}} & \mathbf{0} \end{bmatrix} \begin{bmatrix} \Delta\mathbf{U}^{h,i+1} \\ \Delta\mathbf{P}^{h,i+1} \end{bmatrix} \\
&= \begin{bmatrix} \mathbf{f} - \mathbf{K}(\mathbf{U}^{h,i})\mathbf{U}^{h,i} - \mathbf{G}\mathbf{P}^{h,i} \\ \mathbf{G}^{\mathrm{T}}\mathbf{U}^{h,i} \end{bmatrix} \\
&+ \begin{bmatrix} -\left\{\mathbf{C}(\mathbf{U}^{h,i})[\mathbf{I} - \mathbf{S}_h^{3h}] + \mathbf{C}([\mathbf{I} - \mathbf{S}_h^{3h}]\mathbf{U}^{h,i}) + \mathbf{R}([\mathbf{I} - \mathbf{S}_h^{3h}]\mathbf{U}^{h,i})[\mathbf{I} - \mathbf{S}_h^{3h}]\right\}\mathbf{U}^{h,i} \\ \mathbf{0} \end{bmatrix}.
\end{aligned} \tag{4.50}$$

The matrix $\mathbf{K}(\mathbf{U}^{h,i})$ contains the transient, convective and viscous term. Multifractal subgrid-scale modeling for the cross- and subgrid-scale Reynolds-stress terms results in the matrices $\mathbf{C}$ and $\mathbf{R}$, respectively. Potential contributions from the residual-based multiscale terms to the sub-matrices and -vectors are again omitted for brevity. The parameter β is chosen to be either zero or one. The parameter β allows for distinguishing a Picard iteration scheme ($\beta = 1$) also for the cross- and subgrid-scale Reynolds-stress terms and a computationally more efficient fixed-point iteration ($\beta = 0$) for these two contributions, which is used for the numerical examples in this thesis. Choosing $\beta = 0$ avoids computationally expensive matrix-matrix products with matrix $\left[\mathbf{I} - \mathbf{S}_h^{3h}\right]$ and thereby circumvents more densely populated system matrices, as, e.g., discussed by Gravemeier *et al.* [126] in the context of the AVM^3. Matrix $\left[\mathbf{I} - \mathbf{S}_h^{3h}\right]$ is calculated only once in the beginning and then stored for the remaining simulation. Consequently, scale separation for obtaining the vector of small-scale velocity nodal values reduces to a matrix-vector product in each iterative solution step. To construct the prolongation operator matrix $\mathbf{P}_{3h}^h$, the "ML" multigrid software package (see Gee *et al.* [111]) is used.

4.7 Validation for Homogeneous Isotropic Turbulence

As a first test, the AVM^4 is applied to forced homogeneous isotropic turbulence in a $(2\pi)^3$-periodic box. To maintain a predefined three-dimensional kinetic energy spectrum, the right-hand-side term of the momentum equation has to be adjusted such that dissipation is compensated. The applied forcing, which only affects larger scales by construction, is given in spectral space through its Fourier coefficients $\widehat{\mathbf{f}}$ as

$$\widehat{\mathbf{f}}(\mathbf{k},t) = C_{\mathrm{F}}(k,t)\widehat{\mathbf{u}^h}(\mathbf{k},t), \tag{4.51}$$

where $\widehat{\mathbf{u}^h}(\mathbf{k},t)$ are the Fourier coefficients of the velocity solution obtained by using Fast Fourier Transformation (FFT). As suggested by Hickel *et al.* [146], the linear compensation factor C_{F} is calculated as

$$C_{\mathrm{F}}(k,t) = \begin{cases} -\dfrac{1}{2E^*(k,t)}\dfrac{\partial E^*(k,t)}{\partial t} & \text{if } k \leq k_{\mathrm{F}} \\ 0 & \text{otherwise,} \end{cases} \tag{4.52}$$

where k_F is a given threshold wave number and E^* an intermediate kinetic-energy spectrum obtained from first solving the Navier-Stokes equations without forcing at the current time level.

The initial velocity field, which is given in spectral space, is randomized to phase and exhibits an energy spectrum of the shape $E(k) \sim k^{-\frac{5}{3}}$. The Fourier coefficients of the initial velocity field, satisfying the continuity equation in spectral space, read as

$$\begin{aligned}
\widehat{u}_1(\mathbf{k}) &= \begin{cases} \alpha(\mathbf{k}) & \text{if } k_{12} = 0 \\ \dfrac{\alpha(\mathbf{k}) k k_2 + \beta(\mathbf{k}) k_1 k_3}{k k_{12}} & \text{otherwise,} \end{cases} \\
\widehat{u}_2(\mathbf{k}) &= \begin{cases} \beta(\mathbf{k}) & \text{if } k_{12} = 0 \\ \dfrac{\beta(\mathbf{k}) k_2 k_3 - \alpha(\mathbf{k}) k k_1}{k k_{12}} & \text{otherwise,} \end{cases} \\
\widehat{u}_3(\mathbf{k}) &= \begin{cases} 0 & \text{if } k_{12} = 0 \text{ and } k_3 = 0 \\ -\dfrac{\beta(\mathbf{k}) k_{12}}{k} & \text{if } k_{12} \neq 0 \text{ and } k_3 = 0 \\ -\dfrac{k_1 \widehat{u}_1 + k_2 \widehat{u}_2}{k_3} & \text{otherwise,} \end{cases}
\end{aligned} \tag{4.53}$$

where

$$\alpha(\mathbf{k}) = \sqrt{\frac{E(k)}{2\pi k^2}} \mathrm{e}^{\iota 2\pi\theta_1(\mathbf{k})} \cos(2\pi\varphi(\mathbf{k})), \tag{4.54}$$

$$\beta(\mathbf{k}) = \sqrt{\frac{E(k)}{2\pi k^2}} \mathrm{e}^{\iota 2\pi\theta_2(\mathbf{k})} \sin(2\pi\varphi(\mathbf{k})); \tag{4.55}$$

see, e.g., Collis [71] and Rogallo [267]. Here, $\iota = \sqrt{-1}$ and $\theta_1(\mathbf{k})$, $\theta_2(\mathbf{k})$, $\varphi(\mathbf{k}) \in [0, 1]$ denote the three random phase angles. Moreover, k_{12} is defined as $k_{12} = \sqrt{k_1^2 + k_2^2}$ and $k = \|\mathbf{k}\|$. Relations (4.53) are only evaluated for one half of the Fourier modes. The coefficients of the remaining half are determined by the symmetry condition $\widehat{\mathbf{u}}(\mathbf{k}) = \widehat{\mathbf{u}}^*(-\mathbf{k})$, ensuring that the resulting field is real in physical space. The constructed velocity field is transferred to physical space using inverse FFT. At each time level, the energy spectrum is obtained via

$$E(k) = \frac{1}{2} \sum_{k-\frac{1}{2} < \|\mathbf{k}\| \leq k+\frac{1}{2}} \widehat{\mathbf{u}^h}(\mathbf{k}) \cdot \widehat{\mathbf{u}^h}^*(\mathbf{k}), \tag{4.56}$$

where $k \in \mathbb{N}$.

For simulation, a Reynolds number $\mathrm{Re} = 1/\nu = 10^5$ is assumed. The computational domain is discretized using 32^3 and 64^3 uniformly-distributed elements. The time-step length is set to $\Delta t = 0.03$ for the coarser mesh and to 0.015 for the finer one. After an initial transient, samples of the energy spectrum are collected until convergence is observed. The threshold wave number is $k_\mathrm{F} = 4$. The parameters $C_\mathrm{sgs}^\mathrm{B}$ and c_ν of the multifractal subgrid-scale modeling are chosen to be 0.35 and 0.1. The element Reynolds number is defined based on the strain rate (see

equation (4.31)) for this problem. Figure 4.6 depicts the mean three-dimensional kinetic-energy spectrum $E(k)$ as well as the theoretical inertial-subrange scaling. Additionally, instantaneous velocity streamlines and vorticity magnitude iso-contours during the sampling period computed on 64^3 elements are shown. The kinetic-energy spectra for both grids coincide and follow the expected slope.

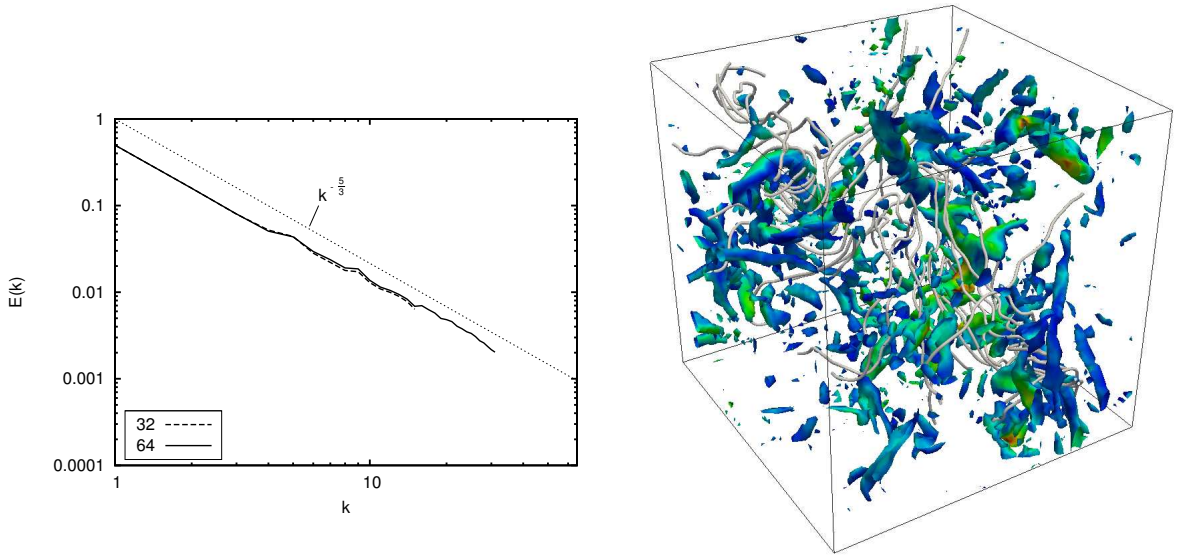

Figure 4.6: Mean three-dimensional kinetic-energy spectrum $E(k)$ for forced homogeneous isotropic turbulence at $\mathrm{Re} = 10^5$ using 32^3 and 64^3 elements as well as instantaneous vorticity magnitude iso-contours colored by kinetic energy (red color indicates high kinetic energy and blue color low kinetic energy) together with velocity streamlines using 64^3 elements.

4.8 Adaption for Wall-Bounded Turbulence

In this section, the multifractal subgrid-scale modeling approach, applied as a part of the AVM^4, is extended and analyzed for wall-bounded turbulent flow. To particularly account for near-wall effects, an enhancement of the multifractal subgrid-scale modeling, referred to as near-wall limit, is derived for wall-resolved LES. Eventually, a comprehensive investigation of the AVM^4 for turbulent channel flow at various friction Reynolds numbers is shown.

4.8.1 Derivation of a Near-Wall Limit

Important effects of wall-bounded turbulent flow are the decrease of the local element Reynolds number as the wall is approached as well as the higher anisotropy of the vorticity field in the near-wall region. The reduction in Re_h results in a decrease of the number of cascade steps.

The decrease of $\mathcal{N}_{\mathbf{u}}$ thus leads to a significant decrease of B towards the wall, if $\mathcal{N}_{\mathbf{u}}$ becomes sufficiently small, as discussed in the Section 4.2.5. As the local element Reynolds number should decrease towards the wall, definition (4.32) using the norm of the resolved velocity is considered particularly appropriate for this flow type.

In the near-wall region, the vorticity field becomes highly anisotropic. This strong anisotropy leads to strong correlations in the orientation of the subgrid-scale vorticity. The stronger correlations in the orientation of the subgrid-scale vorticity result in an increase of the intermittency factor $\mathcal{I}_{\boldsymbol{\omega}}$, which is defined from the correlation between the subgrid-scale vorticity and the vorticity of the smaller resolved scales. In equation (4.25), the intermittency factor $\mathcal{I}_{\boldsymbol{\omega}}$ has only been determined up to the proportionality constant $C_{\text{sgs}}^{\text{B}}$. Precisely this factor allows for modifying the derivation of the multifractal subgrid-scale modeling approach to provide a near-wall limit. Higher intermittency factors $\mathcal{I}_{\boldsymbol{\omega}}$ due to stronger correlations are associated with an increase of $C_{\text{sgs}}^{\text{B}}$. Therefore, $C_{\text{sgs}}^{\text{B}}$ becomes non-uniform and also depends on local flow features. Based on these considerations, $C_{\text{sgs}}^{\text{B}}$ is multiplied by an anisotropy factor f_{ai} for wall-bounded turbulent flow, yielding an enhanced proportionality coefficient $C_{\text{sgs}}^{\text{Bnw}}$:

$$C_{\text{sgs}}^{\text{Bnw}} = f_{\text{ai}} C_{\text{sgs}}^{\text{B}}. \tag{4.57}$$

As explained in Section 4.2.4, $C_{\text{sgs}}^{\text{B}}$ tends to a finite value as $\text{Re}_h \to \infty$, and to zero as $\text{Re}_h \to 1$. These limits have to be maintained by the enhanced parameter $C_{\text{sgs}}^{\text{Bnw}}$. The intermittency factor $\mathcal{I}_{\boldsymbol{\omega}}$ is bounded as $0 \leq \mathcal{I}_{\boldsymbol{\omega}} \leq 1$. Furthermore, the norm of the strain rate tensor is taken to be an appropriate measure for anisotropy. Combing all three requirements, the following form of the anisotropy factor for wall-bounded turbulent flow is suggested:

$$f_{\text{ai}} = \left(1 - \left(\text{Re}_h^{\text{S}}\right)^{-\frac{3}{16}}\right), \tag{4.58}$$

where the element Reynolds number according to equation (4.31) is used. The exponent $-3/16$ has turned out to work best for wall-bounded flow problems.

It is remarked that the anisotropy factor for wall-bounded turbulent flow introduces the element Reynolds number into the final proportionality coefficient $C_{\text{sgs}}^{\text{Bnw}}$ (see the discussion in Section 4.2.4) and, therefore, also integrates a certain dependence on the resolution into the definition of $C_{\text{sgs}}^{\text{Bnw}}$. This aspect contributes to the potential of choosing a fixed value for $C_{\text{sgs}}^{\text{B}}$ for a wide range of Reynolds numbers and resolutions. As a result of preliminary test investigations, the parameter $C_{\text{sgs}}^{\text{B}}$ is set to 0.25 for all turbulent flow examples examined in the remainder of this thesis and incorporating the near-wall limit. It is emphasized that even better results might be obtained when tuning $C_{\text{sgs}}^{\text{B}}$ towards an optimal value for the respective problem. However, it is refrained from exploiting this potential improvement within this thesis for the purposes of a modeling approach as simple as possible. Based on the measurements of Buch and Dahm [42] and Mullin and Dahm [227], $c_\nu = 0.1$ is assumed.

4.8.2 Validation for Turbulent Channel Flow

Overview. To verify the AVM^4 for wall-bounded flows, turbulent channel flow is studied at various friction Reynolds numbers. The friction Reynolds number

$$\mathrm{Re}_\tau = \frac{u_\tau \delta_\mathrm{c}}{\nu} \tag{4.59}$$

is defined based on the friction velocity

$$u_\tau = \sqrt{\tau_\mathrm{W}} \tag{4.60}$$

(for the present incompressible flow at unit density), where τ_W denotes the wall-shear stress, and the channel half-width δ_c. The results for the mean streamwise velocity and the root-mean-square values of the velocity fluctuations obtained with the AVM^4 are compared to results from DNS for $\mathrm{Re}_\tau = 395$ and 590 given by Moser *et al.* [224] and for $\mathrm{Re}_\tau = 950$ by del Álamo *et al.* [80], marked by "DNS MKM99" and "DNS AJZM04", respectively. To assess the dissipative properties of the proposed method, filtered DNS data for $\mathrm{Re}_\tau = 211$ taken from Härtel *et al.* [138] and marked by "DNS HKUF94" are also incorporated.

When evaluating the AVM^4, results obtained with the underlying approach without subgrid-scale model are also considered. Additionally, the results provided by the AVM^4 are compared to results obtained from implementations of other subgrid-scale models. Merely using the SUPG, PSPG and grad-div term as derived in Section 3.3 is considered here the approach with no (explicit) model, which may be viewed, for instance, as a form of an Implicit Large-Eddy Simulation (ILES) without explicit subgrid-scale model as summarized, e.g., in Sagaut [270]. Results obtained with the basic approach (i.e., the SUPG/PSPG/Grad-div Stabilized Method) are marked by "SPGSM" in the remainder of this thesis. By including also the second cross-stress term as well as the subgrid-scale Reynolds-stress term via the residual-based subgrid-scale modeling, as shown in Section 3.3, the (complete) Residual-Based Variational Multiscale Method, as suggested by Bazilevs *et al.* [22] and abbreviated by "RBVMM" in all numerical examples sections, is obtained. Furthermore, a form of the widely-used dynamic Smagorinsky model (see Germano *et al.* [114]) is taken into account for comparison. A subgrid-viscosity model of Smagorinsky type is obtained by modeling cross- and subgrid-scale Reynolds-stress terms by $(\boldsymbol{\varepsilon}(\mathbf{v}^h), 2\nu_\mathrm{sgs}\boldsymbol{\varepsilon}(\mathbf{u}^h))$, where $\nu_\mathrm{sgs} = (C_\mathrm{S}\Delta)^2(2\boldsymbol{\varepsilon}(\mathbf{u}^h) : \boldsymbol{\varepsilon}(\mathbf{u}^h))^{\frac{1}{2}}$ denotes the subgrid viscosity. The parameter $(C_\mathrm{S}\Delta)^2$, that is, the product of Smagorinsky constant C_S and grid filter width Δ, is determined dynamically using a box filter and a contraction according to Lilly [193]. Analogously to the other methods, SUPG, PSPG and grad-div term are included in the formulation since they constitute the basic approach. A similar method was used, e.g., by Tejada-Martínez and Jansen [308], who studied the interaction between the dynamic Smagorinsky model and a stabilized finite element approach in detail. Results provided by the Dynamic Smagorinsky Model are marked by "DSM".

Moreover, the AVM^4 is juxtaposed for the sake of comparison with the Adaptive Local Deconvolution Method (ALDM), a form of an ILES, for example, applied to wall-bounded turbulent flow by Hickel and Adams [145]. Results presented by Hickel and Adams [145] and obtained

with the ALDM-ILES are denoted by "ILES HA07". This comparison allows for classifying the AVM^4 for LES not only in terms of the present approaches, which are all realized within the basic finite element flow solver described in Section 4.6, but also, in some degree, with respect to other reliable methods for LES considered elsewhere.

Problem Setup. The channel dimensions are L_1 in streamwise, L_2 in wall-normal and L_3 in spanwise direction. The wall-normal extension of the channel is related to the channel half-width as $L_2 = 2\delta_\mathrm{c}$. As usual, δ_c is set to 1.0. No-slip boundary conditions are imposed at the top and the bottom wall. In the homogeneous streamwise and spanwise directions, periodic boundary conditions are applied. A constant pressure gradient in streamwise direction drives the flow. A parabolic velocity profile in streamwise direction with superimposed random perturbations constitutes the initial velocity field. In wall-normal direction, the distribution of the elements is refined towards the walls to obtain a better resolution in the vicinity of the walls. The hyperbolic mesh stretching function f is given as $f : [0, 2\delta_\mathrm{c}] \rightarrow [-\delta_\mathrm{c}, \delta_\mathrm{c}]$:

$$x_2 \mapsto f(x_2) = -\delta_\mathrm{c} \frac{\tanh\left(C_\mathrm{G}\left(\delta_\mathrm{c} - x_2\right)\right)}{\tanh(C_\mathrm{G}\delta_\mathrm{c})}, \tag{4.61}$$

where the constant parameter C_G defines the degree of refinement. Depending on the value of Re_τ, channel dimensions, number of elements, mesh stretching parameter and element lengths, given in non-dimensional form as

$$h_i^+ = \frac{h_i}{\delta_\nu}, \tag{4.62}$$

where

$$\delta_\nu = \frac{\nu}{u_\tau} \tag{4.63}$$

denotes the viscous length scale and $i = 1, 2, 3$ for the spatial directions, are summarized in Table 4.1. The time-step length, expressed in non-dimensional form as

$$\Delta t^+ = \frac{\Delta t u_\tau^2}{\nu} \tag{4.64}$$

(see, e.g., Choi and Moin [65]), is set to $\Delta t^+ = 0.7$. After the flow has reached a fully turbulent state, statistics are collected in homogeneous directions and in time during 5000 time steps. Statistical averages are denoted by $\langle\cdot\rangle$ and fluctuations by $(\cdot)'$. The root mean square, labeled by rms $(\cdot)$, is defined as $\mathrm{rms}\,(\cdot) := \langle((\cdot)')^2\rangle^{\frac{1}{2}} = (\langle(\cdot)^2\rangle - \langle(\cdot)\rangle^2)^{\frac{1}{2}}$. All velocity results are normalized by the friction velocity u_τ, as usual, and plotted in wall units x_2^+, i.e., as a function of the distance from the wall normalized by δ_ν.

A Posteriori Evaluation of the Near-Wall Limit. To illustrate the beneficial influence of the near-wall limit, turbulent channel flow at $\mathrm{Re}_\tau = 395$ is examined using the coarser discretization, and simulations with and without enhancement, labeled modified and basic MultiFractal Subgrid-scale (MFS) modeling, respectively, are considered. For the basic MFS, $C_\mathrm{sgs}^\mathrm{B}$ is adapted to the mean value of the enhanced coefficient $\langle C_\mathrm{sgs}^\mathrm{Bnw}\rangle$ as displayed in Figure 4.7. Additionally, Figure 4.7 illustrates mean values of the number of cascade steps $\langle\mathcal{N}_\mathbf{u}\rangle$ and the resulting parameter $\langle B\rangle$. As expected, $\langle\mathcal{N}_\mathbf{u}\rangle$ decreases as the wall is approached. Due to the higher anisotropy in the near-wall region, stronger correlations in the vorticity orientation are expected, yielding

Table 4.1: Mesh parameters for turbulent channel flow at $\mathrm{Re}_\tau = 211, 395, 590$ and 950: channel dimensions L_i, number of elements, mesh stretching parameter C_G and non-dimensional element lengths h_i^+.

Re_τ	L_1	L_2	L_3	no. elements	C_G	h_1^+	$h_{2,\mathrm{min}}^+$	$h_{2,\mathrm{max}}^+$	h_3^+
211	$2\pi\delta_\mathrm{c}$	$2\delta_\mathrm{c}$	$\frac{4}{3}\pi\delta_\mathrm{c}$	32^3	2.20	41.43	1.63	29.55	27.62
395	$2\pi\delta_\mathrm{c}$	$2\delta_\mathrm{c}$	$\frac{2}{3}\pi\delta_\mathrm{c}$	32^3	2.70	77.56	1.43	66.63	25.85
395	$2\pi\delta_\mathrm{c}$	$2\delta_\mathrm{c}$	$\frac{2}{3}\pi\delta_\mathrm{c}$	64^3	2.25	38.78	1.32	28.35	12.93
395	$2\pi\delta_\mathrm{c}$	$2\delta_\mathrm{c}$	$\frac{2}{3}\pi\delta_\mathrm{c}$	128^3	1.95	19.39	1.00	12.53	6.46
590	$2\pi\delta_\mathrm{c}$	$2\delta_\mathrm{c}$	$\pi\delta_\mathrm{c}$	64^3	2.50	57.92	1.34	46.62	28.96
950	$2\pi\delta_\mathrm{c}$	$2\delta_\mathrm{c}$	$\pi\delta_\mathrm{c}$	128^3	2.25	46.63	1.54	34.13	23.32

an increase of the intermittency factor. The resulting increase of $\langle C_\mathrm{sgs}^\mathrm{Bnw}\rangle$ is well reproduced by the proposed enhancement for the near-wall region. Due to the increase of $\langle C_\mathrm{sgs}^\mathrm{Bnw}\rangle$, the resulting parameter $\langle B\rangle$ also increases towards the wall and shows its maximum value very close to the wall. Without near-wall limit, $\langle B\rangle$ immediately falls off at the wall. Figure 4.8 depicts the mean

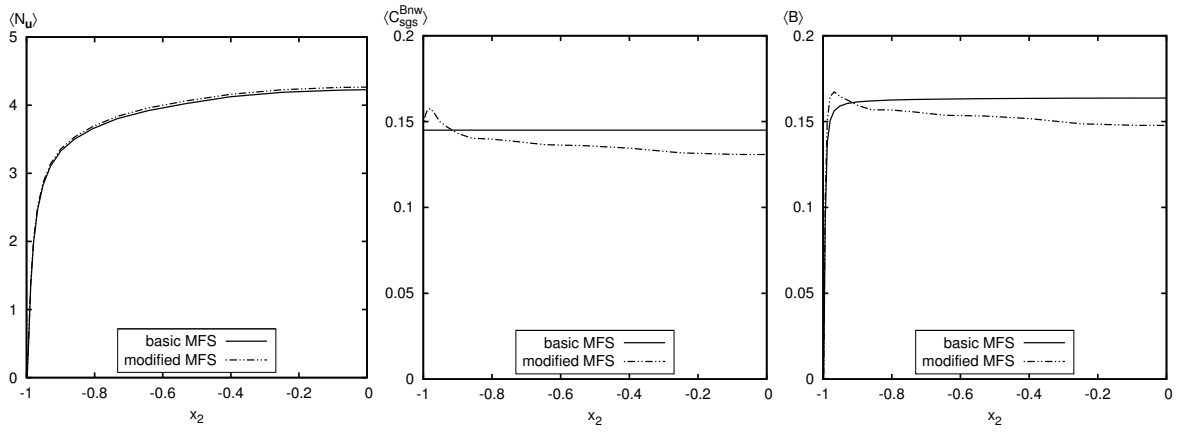

Figure 4.7: Mean values of the number of cascade steps $\langle \mathcal{N}_\mathbf{u}\rangle$, coefficient $\langle C_\mathrm{sgs}^\mathrm{Bnw}\rangle$ and parameter $\langle B\rangle$ with and without near-wall limit for turbulent channel flow at $\mathrm{Re}_\tau = 395$ using 32^3 elements.

streamwise velocity u_1^+ as well as all root-mean-square velocities rms u_i^+. Owing to the rather coarse discretization, the curves somewhat deviate from the DNS data. Comparing the results for the basic and modified MFS, marginal improvements are stated for the enhanced version. Using the basic MFS, the computed friction Reynolds number is 382.2, deviating from the target value by about 3%. In contrast, it is 393.2 for the modified version.

In LES, the mean total shear stress $\langle \tau_{12}\rangle$ of turbulent channel flow obeys the following decomposition:

$$\underbrace{-\frac{\nu}{u_\tau^2}\frac{\partial\langle u_1\rangle}{\partial x_2} + \frac{\langle u_1' u_2'\rangle}{u_\tau^2} + \frac{\langle \tau_{\mathrm{sgs},12}\rangle}{u_\tau^2}}_{-\frac{\langle\tau_{12}\rangle}{\tau_\mathrm{W}}} = \frac{x_2}{\delta_\mathrm{c}}, \tag{4.65}$$

where $\langle \tau_{\text{sgs},12} \rangle$ is the mean subgrid-scale shear stress. For the AVM^4, $\langle \tau_{\text{sgs},12} \rangle$ contains not only the cross- and subgrid-scale Reynolds-stress terms incorporated by the multifractal subgrid-scale modeling but also contributions from the residual-based multiscale terms. Figure 4.9 shows the decomposition of the mean total shear stress for the AVM^4 with basic and modified MFS. Using the basic MFS, the viscous stress $\nu \partial \langle u_1 \rangle / \partial x_2$ does not reach the total stress at the wall, causing the underprediction of the friction Reynolds number. Instead, $\langle \tau_{\text{sgs},12} \rangle$ is larger than zero at the wall. As can be observed, this behavior is corrected by the proposed near-wall limit, as $\langle \tau_{\text{sgs},12} \rangle$ tends to zero and $\nu / u_\tau^2 \partial \langle u_1 \rangle / \partial x_2$ to one as the wall is approached. Even though the overall behavior of the modified MFS does not show any substantial differences compared to the basic MFS, the near-wall limit is essential for correctly capturing the wall-shear stress. In particular, the increase of $\langle B \rangle$ towards the walls is supposed to be responsible for the improved near-wall accuracy.

Statistical Results. Next, turbulent channel flow at $\text{Re}_\tau = 395$ is further investigated. Three discretizations of increasing resolution are considered for a convergence study. The respective results for the mean streamwise velocity u_1^+ and the root-mean-square values rms u_i^+ are depicted in Figure 4.10, including the predictions provided by the SPGSM, RBVMM and DSM. For all methods, convergence to DNS is observed for u_1^+ as well as for all rms u_i^+. The AVM^4 provides by far the best results for both mean and root-mean-square velocity in streamwise direction. Indeed, the results obtained with the AVM^4 are already for the medium discretization quite close to the DNS results, and the improvement due to the finer discretization is only of small amount. In contrast, the SPGSM and RBVMM provide results which substantially deviate from the DNS data using the coarser and the medium discretization. Even with the finer discretization, there are notable deviations from the DNS results, while the AVM^4 results match them almost exactly. For all discretizations, the worst results are obtained with the DSM. For the root-mean-square velocities in wall-normal and spanwise direction, both the AVM^4 as well as the SPGSM and RBVMM, respectively, yield good approximations. While the AVM^4 as well as the SPGSM and RBVMM underpredict rms u_2^+ for the coarser and medium discretization, they overpredict the

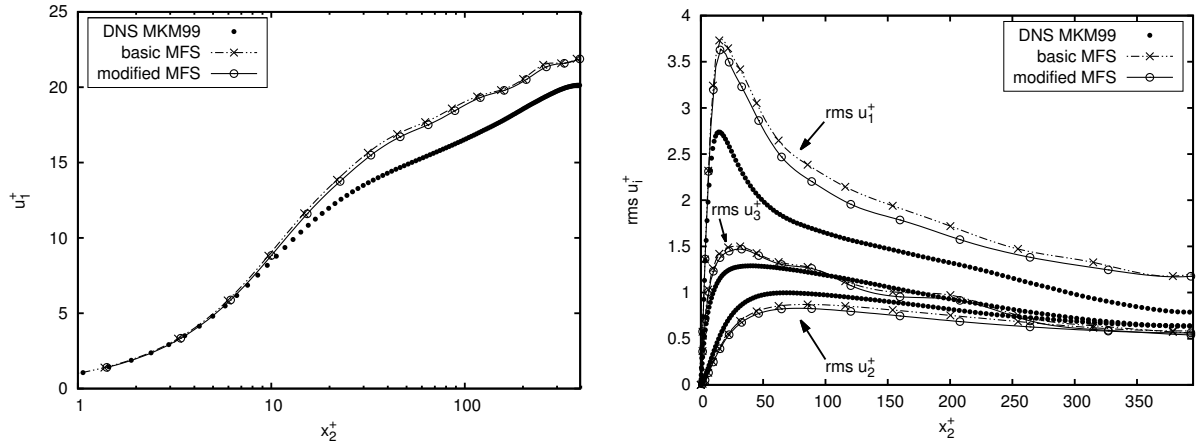

Figure 4.8: Mean streamwise velocity u_1^+ and root-mean-square velocities rms u_i^+ for turbulent channel flow at $\text{Re}_\tau = 395$ using 32^3 elements and the AVM^4 with and without near-wall limit.

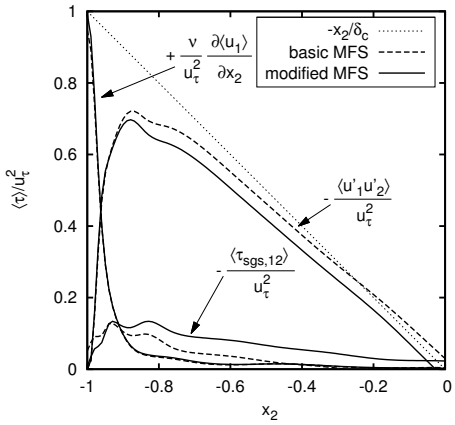

Figure 4.9: Decomposition of the mean total shear stress $\langle \tau_{12} \rangle$ obtained with the basic MFS and the modified form for turbulent channel flow at $\mathrm{Re}_\tau = 395$ using 32^3 elements.

maximum value of rms u_3^+. Both root-mean-square velocities are underestimated by the DSM for all discretizations. For all results, differences between the SPGSM and RBVMM are only marginal, indicating that the inclusion of the remaining cross- and subgrid-scale Reynolds-stress term into the residual-based formulation does not necessarily improve the results. The results for $\mathrm{Re}_\tau = 590$ and $\mathrm{Re}_\tau = 950$ are shown in Figures 4.11 and 4.12, respectively. They are in accordance with the previous findings for $\mathrm{Re}_\tau = 395$. Again, the AVM^4 provides the best approximations, especially for the mean and root-mean-square velocity in streamwise direction. The values rms u_2^+ and rms u_3^+ appear to be quite similar for the AVM^4, SPGSM and RBVMM, while the DSM notably underpredicts rms u_2^+.

Since the setup of the channel flow at $\mathrm{Re}_\tau = 950$ is fully comparable with respect to channel domain and resolution to the respective simulation by Hickel and Adams [145] using the ALDM-ILES, results taken from that study are also considered here for comparison. Being aware of the fact that the same resolution in streamwise direction, a slightly finer one in wall-normal and a coarser one in spanwise direction were used by Hickel and Adams [145] for $\mathrm{Re}_\tau = 395$, those results are included, too. Figure 4.13 illustrates the juxtaposition of the AVM^4 and ALDM-ILES. The AVM^4 and ALDM-ILES results are close to each other for $\mathrm{Re}_\tau = 395$: similar results are obtained for u_1^+, slightly better results for rms u_1^+ are shown by the ALDM-ILES, while the AVM^4 reveals better approximations for the other two root-mean-square values. Concerning the mean streamwise velocity, the AVM^4 and ALDM-ILES yield a similar approximation quality for $\mathrm{Re}_\tau = 950$. While the peak value of rms u_1^+ is better captured by the ALDM-ILES, an improved estimate for rms u_2^+ is produced by the AVM^4. For rms u_3^+, the ALDM-ILES notably underestimates the peak value, and the AVM^4 only slightly overestimates it. Overall, it can be stated that the AVM^4 provides results of similar quality for turbulent flow in a channel when being compared to the ALDM-ILES.

In summary, all findings indicate that the identified model parameters are sufficiently independent of the friction Reynolds number and also the spatial resolution. All statistical values are accurately predicted for a wide range of Re_τ. For a detailed depiction of the corresponding model

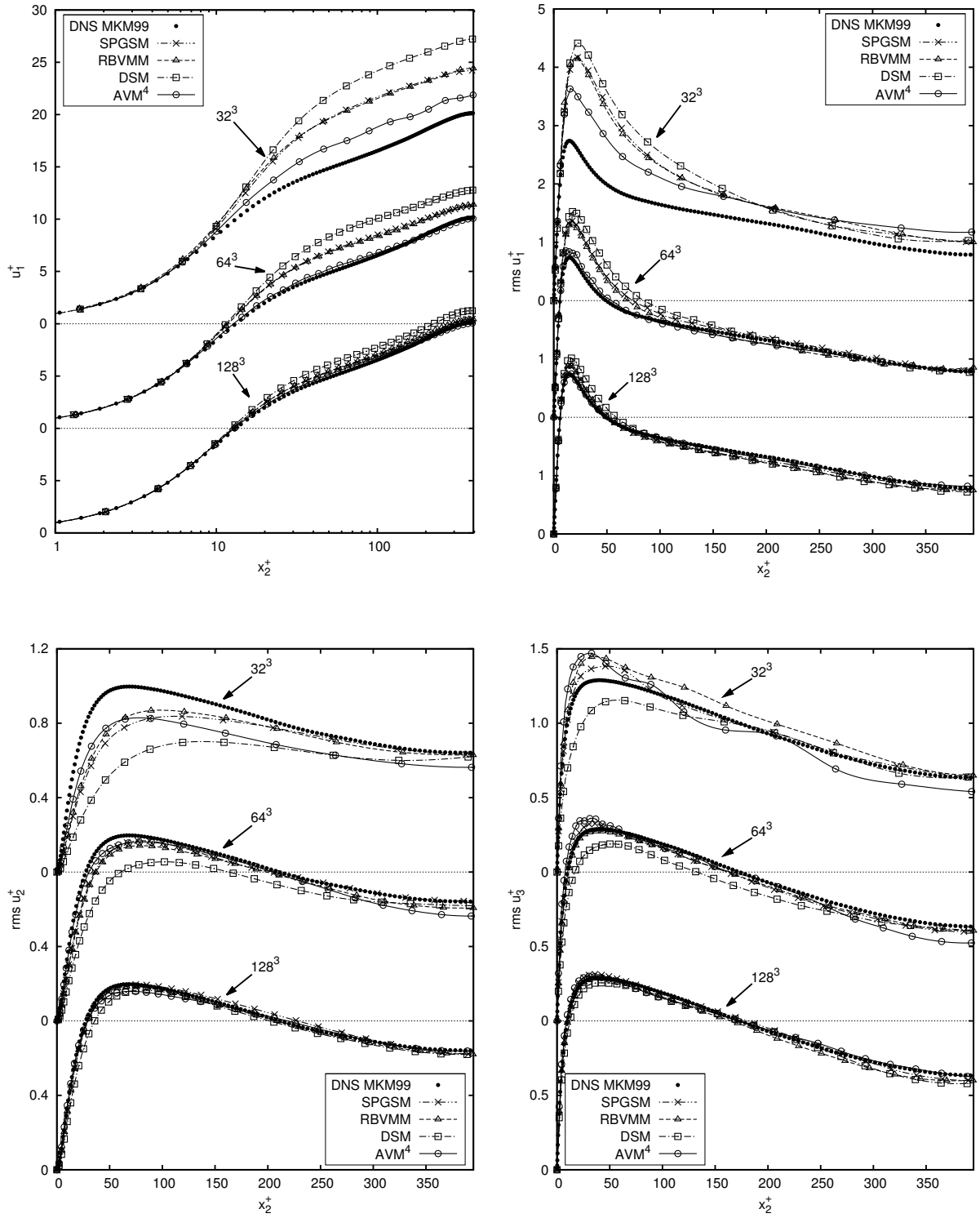

Figure 4.10: Convergence study of mean streamwise velocity u_1^+ and root-mean-square velocities rms u_i^+ for turbulent channel flow at $\mathrm{Re}_\tau = 395$ using 32^3, 64^3 and 128^3 elements.

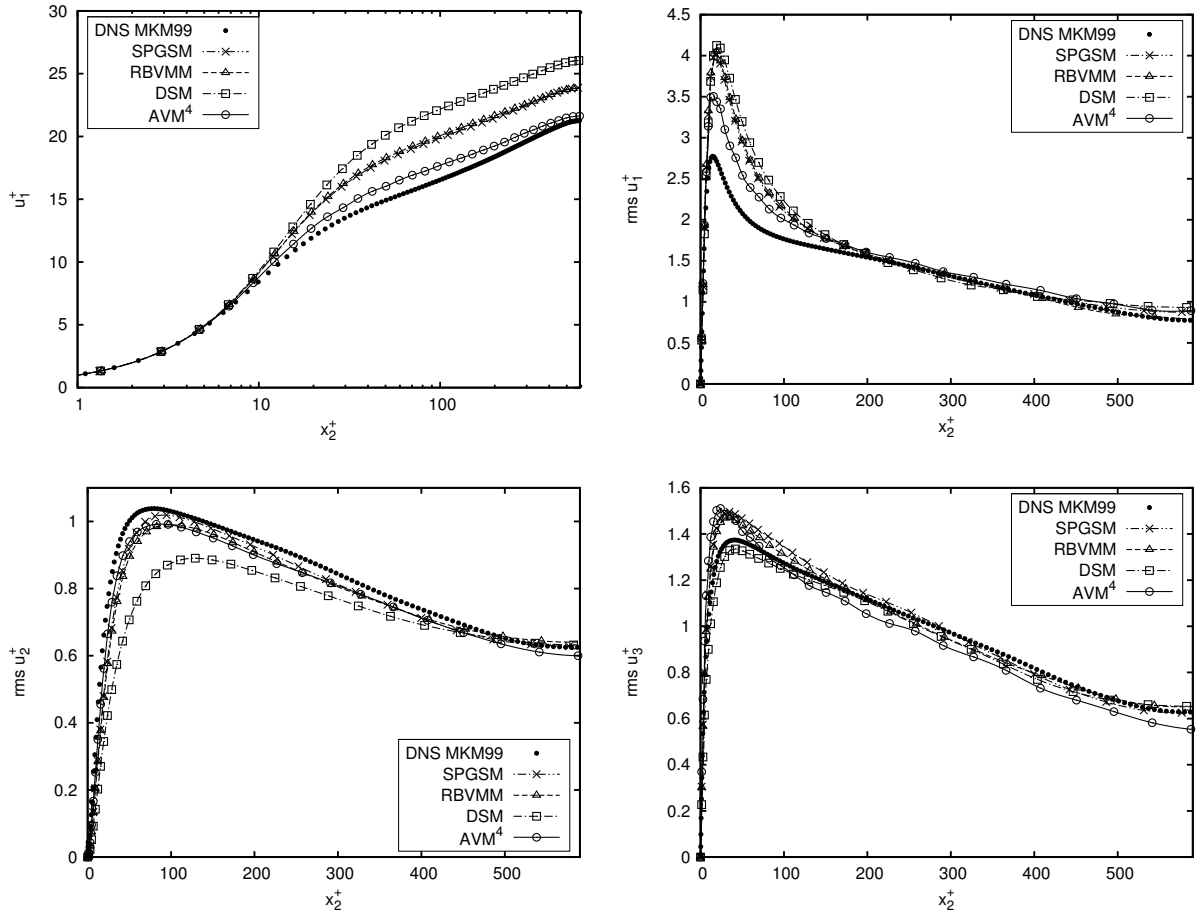

Figure 4.11: Mean streamwise velocity u_1^+ and root-mean-square velocities rms u_i^+ for turbulent channel flow at $\mathrm{Re}_\tau = 590$ using 64^3 elements.

parameters, which exhibit the expected behavior with respect to Re_τ and the resolution, the reader is referred to Rasthofer and Gravemeier [258]. Concerning the computational efficiency of the proposed method, the following computing times are observed. Setting the computing time of the SPGSM to 1.00, the relative computing times for the AVM^4, RBVMM and DSM are given by 1.02, 1.05 and 1.52. The slightly enhanced computing time of the AVM^4 compared to the SPGSM for this example is mainly caused by the computations on the element level, where the multifractal cross- and subgrid-scale Reynolds-stress terms are evaluated. Compared to the DSM, however, the computing time is substantially reduced. A major part of the additional computing time required by the DSM can be related to the involved filtering procedure.

Subgrid-scale dissipation. The subgrid-scale dissipation of the different methods is now analyzed in more detail and compared to each other. Similar evaluations of the dissipation introduced by stabilized FEMs were presented, e.g., by Gamnitzer [106], Gravemeier and Wall [122], Principe *et al.* [255] and Tejada-Martínez and Jansen [308]. Summarizing the contributions of the SUPG, PSPG and grad-div term constitutes the subgrid-scale dissipation $\varepsilon_{\mathrm{sp}}$ of the basic approach, i.e., the SPGSM. Therein, the individual dissipation due to the SUPG and grad-div term

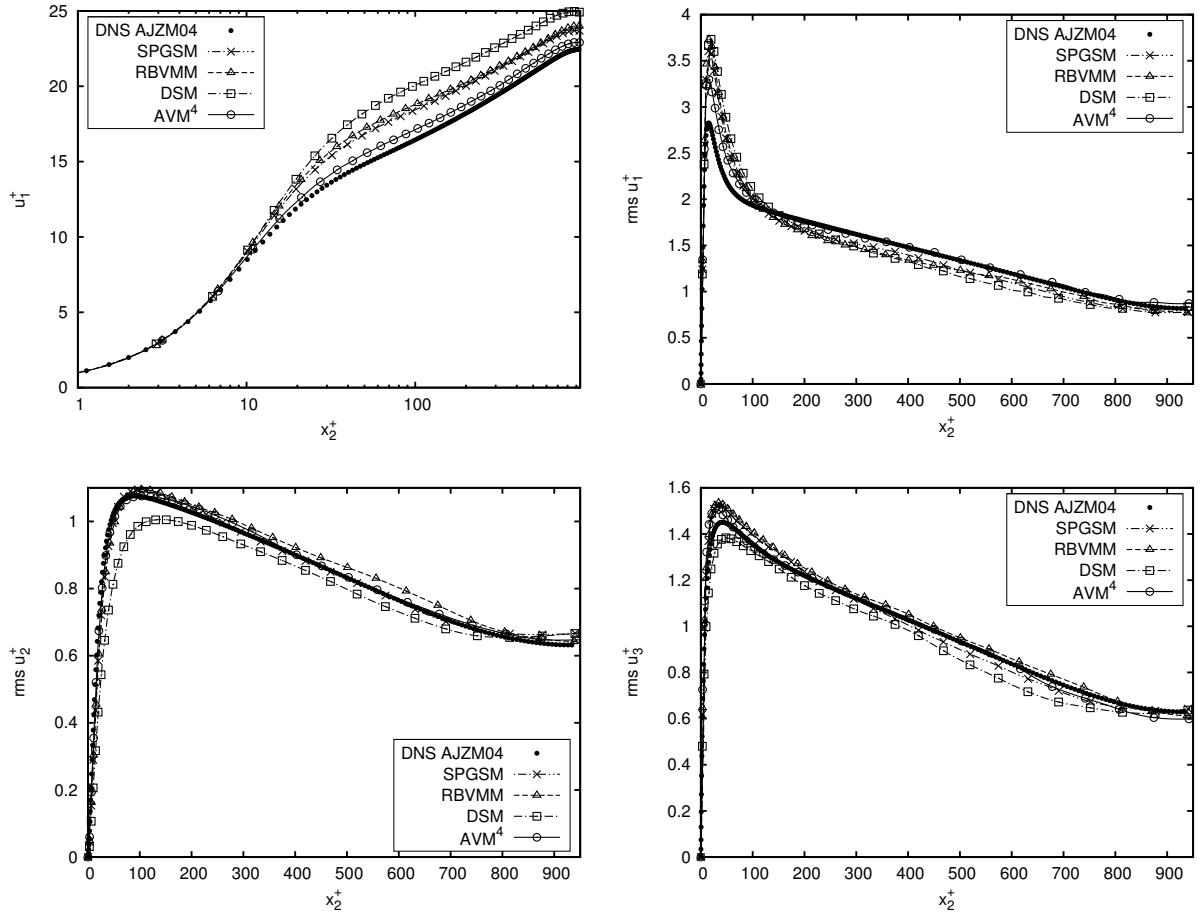

Figure 4.12: Mean streamwise velocity u_1^+ and root-mean-square velocities rms u_i^+ for turbulent channel flow at $\mathrm{Re}_\tau = 950$ using 128^3 elements.

read

$$\varepsilon_{\mathrm{su}} = \left(\tau_{\mathrm{M}} \mathbf{r}_{\mathrm{M}}^h \otimes \mathbf{u}^h\right) : \nabla \mathbf{u}^h, \tag{4.66}$$

$$\varepsilon_{\mathrm{gd}} = \tau_{\mathrm{C}} r_{\mathrm{C}}^h \mathbf{I} : \nabla \mathbf{u}^h = \tau_{\mathrm{C}} r_{\mathrm{C}}^h (\nabla \cdot \mathbf{u}^h). \tag{4.67}$$

As mentioned in Section 3.3, additional dissipation is introduced by the grad-div term, which should therefore be taken into account in the subgrid-scale dissipation of the methods, in contrast to the study by Tejada-Martínez and Jansen [308], where this contribution was neglected. An analogous measure for the dissipation introduced by the PSPG term is defined as

$$\varepsilon_{\mathrm{ps}} = \nabla p_{\mathrm{kin}}^h \cdot \tau_{\mathrm{M}} \mathbf{r}_{\mathrm{M}}^h, \tag{4.68}$$

which provides, in general, a contribution of negligible amount. For the subgrid-scale dissipation $\varepsilon_{\mathrm{av}}$ of the AVM^4, the dissipation owing to the cross- and subgrid-scale Reynolds-stress terms, $\varepsilon_{\mathrm{mc}}$ and $\varepsilon_{\mathrm{mr}}$, respectively, modeled by the multifractal subgrid-scale modeling approach, which

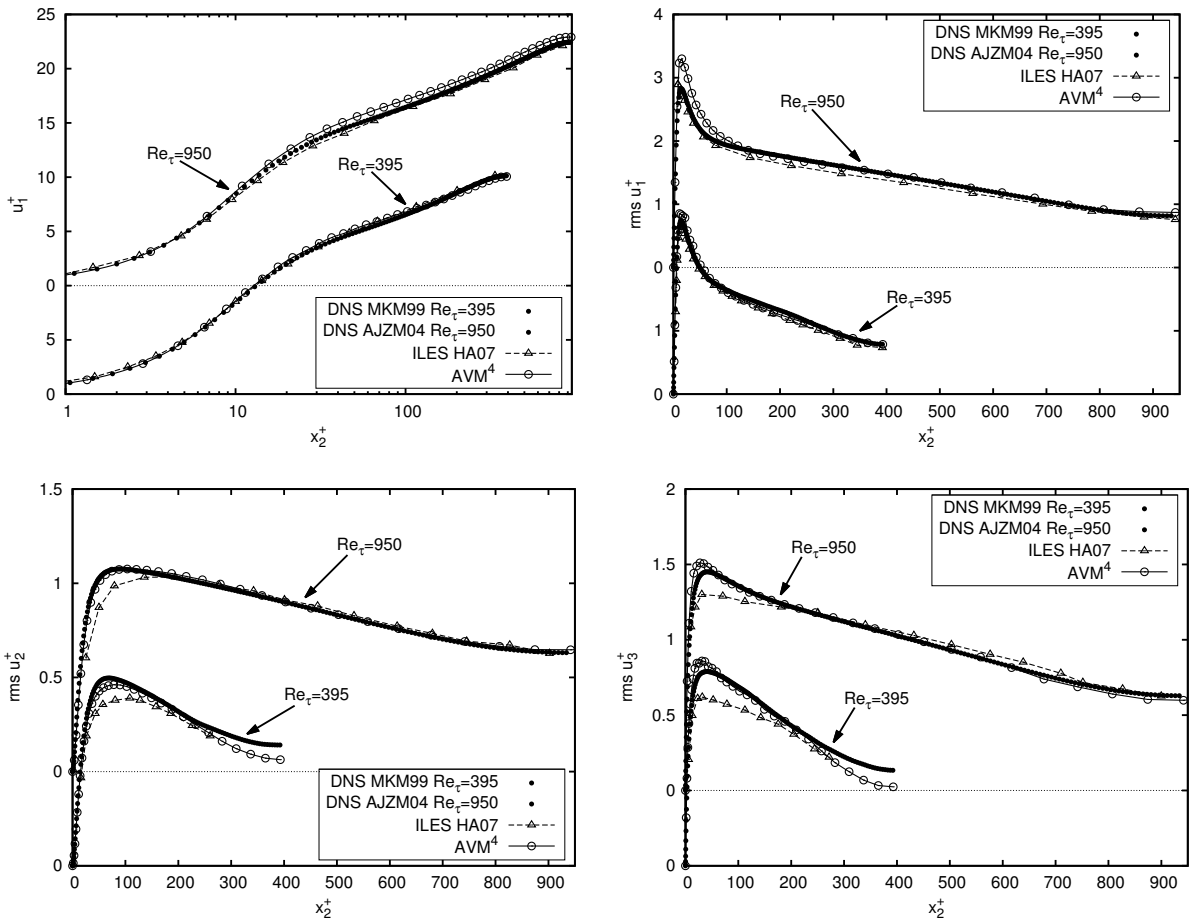

Figure 4.13: Comparison of the AVM^4 and the ALDM-ILES according to Hickel and Adams [145] for turbulent channel flow at $\mathrm{Re}_\tau = 395$ using 64^3 elements and at $\mathrm{Re}_\tau = 950$ using 128^3 elements. Results for the mean streamwise velocity u_1^+ and the root-mean-square velocities rms u_i^+ are shown.

are given as

$$\varepsilon_{\mathrm{mc}} = -\left(B\delta\mathbf{u}^h \otimes \mathbf{u}^h + \mathbf{u}^h \otimes B\delta\mathbf{u}^h\right) : \boldsymbol{\varepsilon}(\mathbf{u}^h), \tag{4.69}$$

$$\varepsilon_{\mathrm{mr}} = -\left(B\delta\mathbf{u}^h \otimes B\delta\mathbf{u}^h\right) : \boldsymbol{\varepsilon}(\mathbf{u}^h), \tag{4.70}$$

have to be included. The additional contribution of the subgrid-viscosity term of the DSM is obtained as

$$\varepsilon_{\mathrm{sv}} = 2\nu_{\mathrm{sgs}}\boldsymbol{\varepsilon}(\mathbf{u}^h) : \boldsymbol{\varepsilon}(\mathbf{u}^h). \tag{4.71}$$

The subgrid-scale dissipation of the DSM is then denoted by $\varepsilon_{\mathrm{ds}}$. The dissipation due to the remaining cross- and subgrid-scale Reynolds-stress term of the RBVMM are defined as

$$\varepsilon_{\mathrm{cr}} = \left(\mathbf{u}^h \otimes \tau_{\mathrm{M}}\mathbf{r}_{\mathrm{M}}^h\right) : \nabla\mathbf{u}^h, \tag{4.72}$$

$$\varepsilon_{\mathrm{re}} = -\left(\tau_{\mathrm{M}}\mathbf{r}_{\mathrm{M}}^h \otimes \tau_{\mathrm{M}}\mathbf{r}_{\mathrm{M}}^h\right) : \nabla\mathbf{u}^h, \tag{4.73}$$

resulting in the subgrid-scale dissipation $\varepsilon_{\mathrm{rb}}$ of the RBVMM.

Figure 4.14 depicts the mean subgrid-scale dissipation in non-dimensionalized form, given by

$$\varepsilon^{+} = \frac{\langle \varepsilon \rangle \nu}{u_{\tau}^{4}}, \tag{4.74}$$

in wall-normal direction for all methods and turbulent channel flow at $\mathrm{Re}_{\tau} = 395$. The results demonstrate a predominant subgrid-scale dissipation in the vicinity of the channel walls for the AVM^4. In the core region, the subgrid-scale dissipation is approximately zero. As shown in the closeup views, this increased subgrid-scale dissipation particularly occurs within the buffer layer of the channel flow with the peak value at approximately $x_2^{+} = 12$. Considering that the buffer layer constitutes the region of vigorous turbulence dynamics with the turbulent energy production rate reaching its maximum value at approximately $x_2^{+} = 12$ (see, e.g., Tennekes and Lumely [309]), a very intense dissipation has to be expected in that region, in accordance with, e.g., the analysis of DNS data by Härtel *et al.* [138]. The beneficial effect of subgrid-scale models introducing a substantial amount of subgrid-scale dissipation in the buffer-layer region of the channel for obtaining high-quality results was already observed, e.g., by Gravemeier [118] and for the AVM^3, i.e., the predecessor of the present AVM^4, in the context of variable-density flow at low Mach number by Gravemeier and Wall [122]. As observable, the proposed method provides this beneficial effect almost exactly at the theoretically expected location. In accordance with the increased range of resolved scales, the subgrid-scale dissipation of all methods decreases from the coarser via the medium to the finer discretization.

To further assess the dissipative properties of the proposed method, a direct comparison of the subgrid-scale dissipation introduced by the various methods and the subgrid-scale dissipation estimated from filtered DNS data in Härtel *et al.* [138] is given. In Härtel *et al.* [138], DNS of turbulent channel flow at $\mathrm{Re}_{\tau} = 211$ was examined to evaluate the energy transfer between resolved and unresolved scales in LES. To identify the subgrid-scale quantities, filtering corresponding to a resolution of 32×32 grid points in the homogeneous directions, resulting in $h_1^{+} = 75$ and $h_3^{+} = 39$, was applied. Figure 4.15 displays the distribution of the subgrid-scale dissipation in wall-normal direction introduced by the different methods for channel flow at $\mathrm{Re}_{\tau} = 211$ as well as the respective result from filtered DNS. Excellent agreement is observed between the AVM^4 and filtered DNS. The other methods provide considerably different curves in the buffer layer. Although the respective distributions exhibit their maximum values, which decrease from the DSM via the RBVMM to the SPGSM, in the near-wall region, these maximum values are clearly smaller and less pronounced than the peak value of the AVM^4 and filtered DNS. Moreover, compared to the filtered DNS, they are also somewhat shifted towards the upper bound of the buffer layer. Additionally, a higher subgrid-scale dissipation in the middle of the channel occurs, which is approximately equal for the SPGSM, RBVMM and DSM. Altogether, the distributions of the subgrid-scale dissipation in wall-normal direction due to the SPGSM, RBVMM and DSM show a quite similar behavior.

Further insight into the dissipative characteristics of the proposed method and the interaction of its constituents, i.e., the multifractal subgrid-scale modeling terms and the residual-based multiscale terms, is gained by analyzing the individual components. Figure 4.16 illustrates the dissipation introduced by the various modeling terms of the AVM^4. To demonstrate the interplay

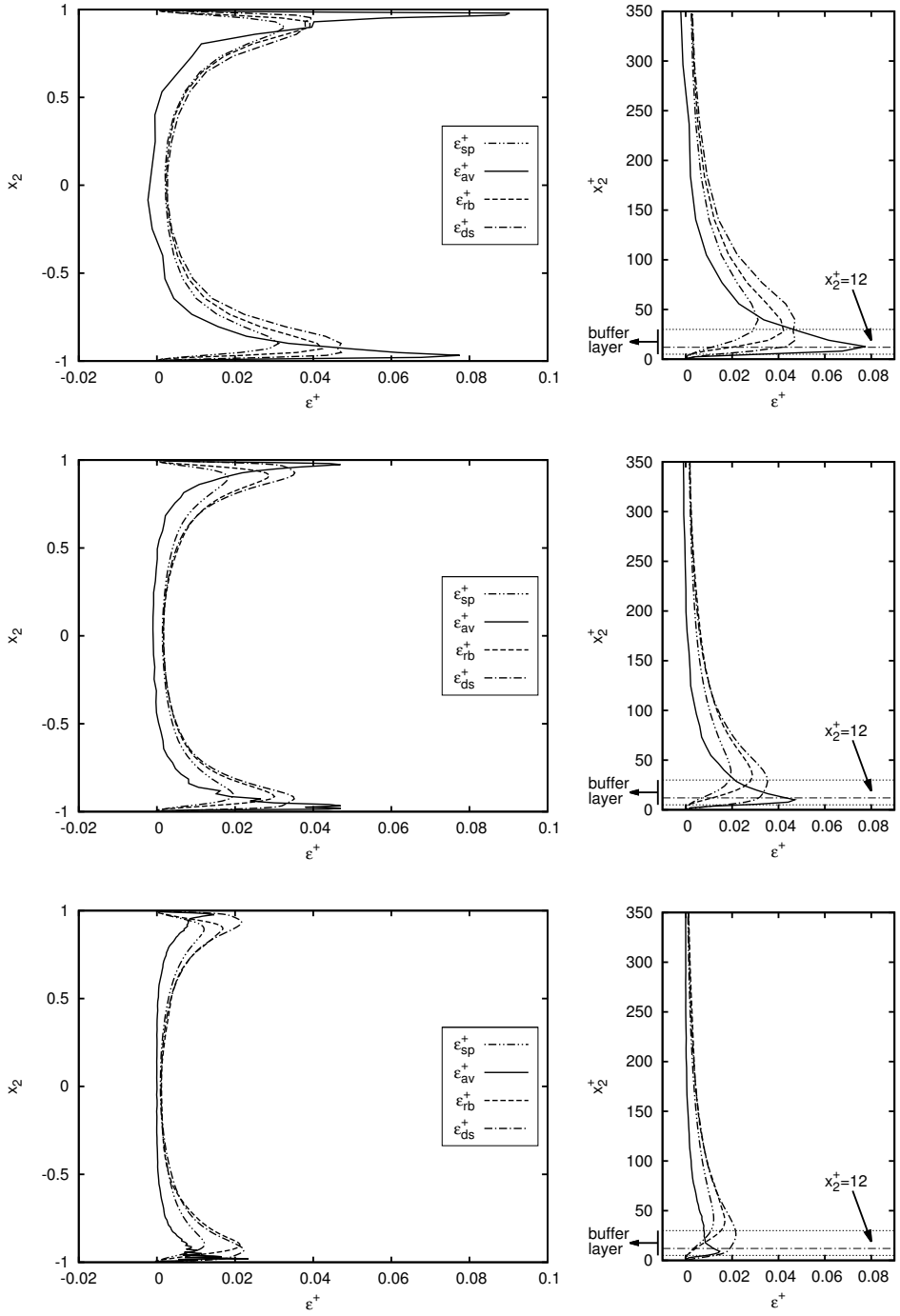

Figure 4.14: Mean subgrid-scale dissipation ε^+ for turbulent channel flow at $\mathrm{Re}_\tau = 395$ using (from top to bottom) 32^3, 64^3 and 128^3 elements including a closeup view of the near-wall region.

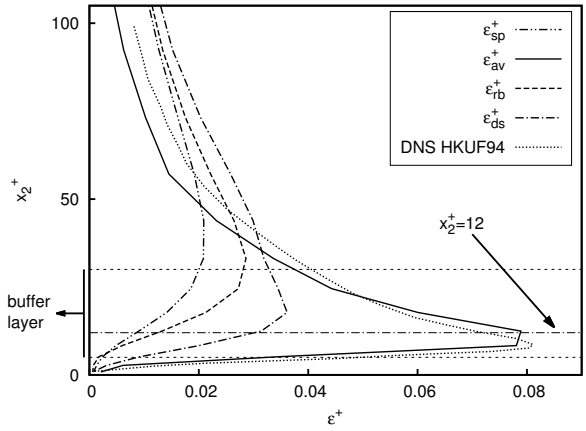

Figure 4.15: Mean subgrid-scale dissipation ε^+ for turbulent channel flow at $\mathrm{Re}_\tau = 211$ using 32^3 elements compared to the subgrid-scale dissipation from filtered DNS.

of the multifractal subgrid-scale modeling terms and the residual-based multiscale terms, the respective terms of the SPGSM are likewise included. First of all, the contributions by the multifractal subgrid-scale modeling terms are considered. The dissipation $\varepsilon_{\mathrm{mr}}^+$ due to the subgrid-scale Reynolds-stress term is small compared to the other contributions, but positive throughout the channel. Moreover, $\varepsilon_{\mathrm{mr}}^+$ exhibits a peak near the wall. The contribution $\varepsilon_{\mathrm{mc}}^+$ of the cross-stress terms displays positive and negative values and, therefore, incorporates backscatter of energy in parts of the channel. In particular, $\varepsilon_{\mathrm{mc}}^+$ provides a pronounced positive (i.e., forward energy transfer) peak in the vicinity of the wall, which is responsible for the excellent agreement between the subgrid-scale dissipation $\varepsilon_{\mathrm{av}}^+$ of the proposed method and the filtered DNS data in the buffer layer. The negative part in the core of the channel is also remarkable. This anti-dissipative contribution counterbalances the dissipation introduced by the residual-based multiscale terms, resulting in approximately zero subgrid-scale dissipation in the core of the channel. Comparing the individual parts of the residual-based multiscale terms of the AVM^4 and the SPGSM, the interaction of both modeling parts in the proposed method is obvious. While the grad-div term introduces only a somewhat higher dissipation than the SUPG term in the context of the SPGSM, it yields a notably higher one in the context of the AVM^4. Furthermore, the contribution of the SUPG term shows a sharper peak in the near-wall region for the AVM^4. Moreover, it is remarked that the contributions of the SUPG and grad-div term are considerably reduced for the purely dissipative DSM, which nevertheless results in the most dissipative method, as already indicated by the substantial overestimation of the mean streamwise velocity. For the RBVMM, additional dissipation is introduced by the second cross-stress term, while the contribution of the subgrid-scale Reynolds-stress term is negligible.

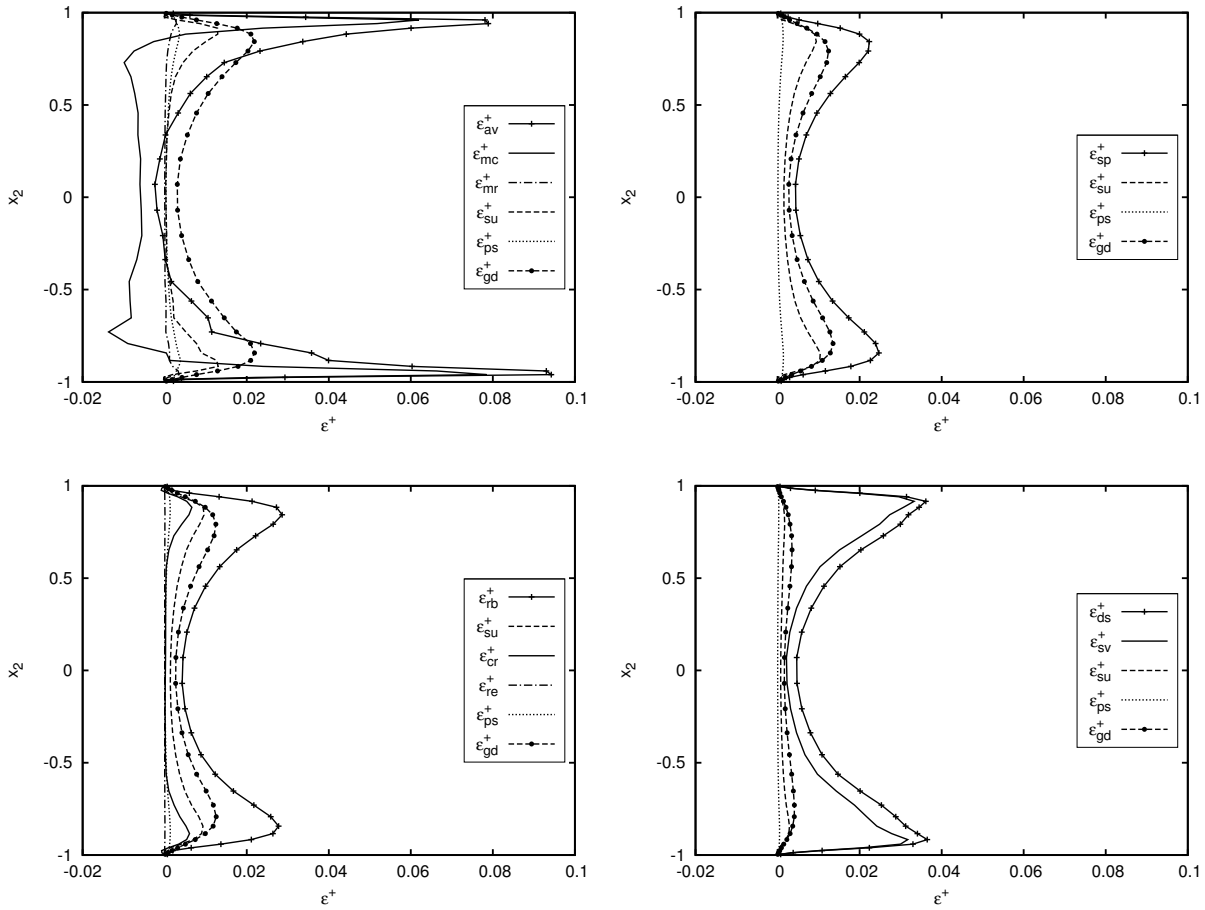

Figure 4.16: Contributions of the individual constituents of the (from left to right and from top to bottom) AVM^4, SPGSM, RBVMM and DSM to the mean subgrid-scale dissipation ε^+ for turbulent channel flow at $\mathrm{Re}_\tau = 211$ using 32^3 elements.

4.9 Square-Section Cylinder

Having validated the AVM^4 for two of the most important test cases for subgrid-scale modeling in LES, the proposed method is applied to substantially more complex examples to illustrate its behavior for realistic flow configurations. In this thesis, the investigations are restricted to turbulent flow past a square-section cylinder. The application of the AVM^4 to turbulent flow over a backward facing-step is not included here, since this flow problem is also examined in Chapter 6 in the context of turbulent-variable density flow at low Mach number. Results for the incompressible case using the AVM^4 can be found in comprehensive form in Rasthofer and Gravemeier [258] or in more compact form in Gravemeier and Rasthofer [120, 121].

Flow Description and Overview. Flows past bluff bodies are of particular engineering significance. For instance, drag prediction and control are among the major objectives in aerodynamics. Concerning civil engineering, tall buildings may be subject to large fluctuating forces transverse to the flow direction causing structural vibrations or even resonance. The square-section cylinder

constitutes a generic configuration to investigate the flow situations involved in the aforementioned examples. For sufficiently high Reynolds numbers, laminar, transitional and turbulent flow patterns are encountered in the flow past a square-section cylinder. In particular, Kelvin-Helmholtz instabilities within the separated shear layers, developing at the upstream edges of the square-section cylinder, trigger transition to turbulence and are coupled to the Von Kármán instability in the near-wake region. The wake itself is spatially complex and includes both intense vortices as well as enclosed irrotational flow. Altogether, turbulent flow past a square-section cylinder exhibits several challenging phenomena for LES methods: the separation of the flow on the body surface, the formation of a near-wake region and the alternating vortex street. Therefore, this flow configuration was numerically examined in exhaustive form in two workshops. The results of those workshops were published in Rodi *et al.* [266] and Voke [324]. Moreover, Fureby *et al.* [104] as well as Sohankar *et al.* [289] used this example for evaluating the performance of various subgrid-scale models for LES. DNS of turbulent flow past a square-section cylinder was briefly addressed by Verstappen and Veldman [320]. Experimental data for this flow example were provided, e.g., by Lyn and Rodi [203] and Lyn *et al.* [204]. Particularly, these data frequently serve as a reference. Recently, this flow configuration was exhaustively examined both experimentally and numerically via LES by Minguez *et al.* [217].

Problem Setup. Based on the free-stream velocity U_∞ and the edge length D of the cylinder, the Reynolds number is defined as

$$\mathrm{Re} = \frac{U_\infty D}{\nu}. \tag{4.75}$$

In accordance with the aforementioned studies, the Reynolds number considered here is $\mathrm{Re} = 22\,000$. The flow domain, which is the same as in Rodi *et al.* [266] and Voke [324], is depicted in Figure 4.17. At the inflow boundary $x_1 = -5D$, a constant free-stream velocity $U_\infty = 1.0\,\mathrm{m/s}$ in x_1-direction is prescribed. A zero-traction Neumann boundary condition is assumed at the outflow boundary $x_1 = 15.0D$. No-slip boundary conditions are prescribed on all surfaces of the square-section cylinder. In the homogeneous x_3-direction, periodic boundary conditions are imposed. At the top and the bottom boundary, slip boundary conditions are assumed. The cylinder edge length is set to $D = 1.0\,\mathrm{m}$ such that the kinematic viscosity amounts to $\nu = 4.545 \cdot 10^{-5}\,\mathrm{m^2/s}$. A time-step length $\Delta t = 0.0375\,\mathrm{s}$ is applied. After the flow has developed, statistics are collected during 2400 time steps, representing approximately 12 periods of vortex shedding. Samples are collected in homogeneous direction and in time. The spatial discretization is refined towards the cylinder surfaces. The refinement is realized inside a box with dimensions $5D \times 5D$ in the x_1x_2-plane. The x_3-axis of the box is aligned with the x_3-axis of the coordinate system (see Figure 4.17). For the refinement from the surface of the box to the cylinder surface, 30 elements are used. The smallest element length orthogonal to the cylinder surface is $(h/D)_{\mathrm{min}} = 0.008$ at each cylinder surface, as applied by Sohankar *et al.* [289]. Along each cylinder surface, 20 elements are uniformly distributed. Outside the box, the element lengths in x_1- and x_2-direction are chosen identical to the one in x_3-direction. In x_3-direction, 16 elements with a uniform element length $h/D = 0.25$ are used. Overall, the discretization consists of 103 680 elements, resulting in approximately 450 000 degrees of freedom. Apart from experimental and numerical data provide elsewhere, the results obtained with the AVM^4 are also compared to predictions by the RBVMM and DSM. Concerning the multifractal subgrid-scale modeling, the strain-rate-based definition (4.31) of the element Reynolds number together with

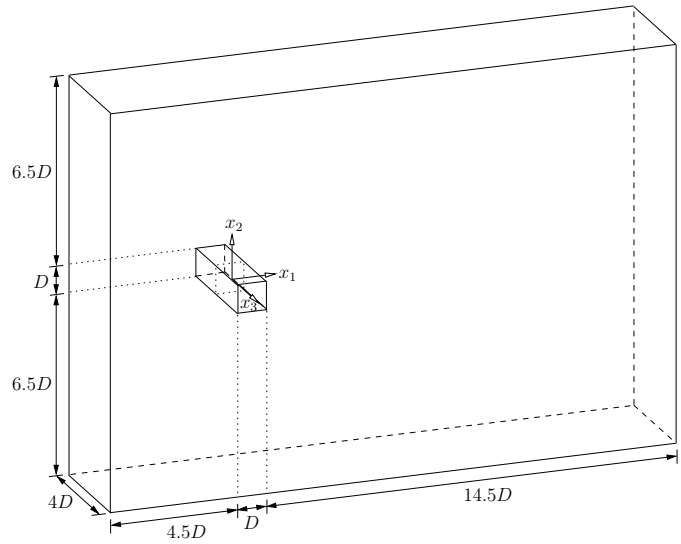

Figure 4.17: Geometry of square-section cylinder.

a proportionality constant $c_\nu = 0.01$ is chosen for the present configuration with free-stream regions. As identified for wall-bounded flows, the parameter $C_{\text{sgs}}^{\text{B}}$ is set to 0.25, and the near-wall limit is included. The evaluation of the computational cost for this problem reveals the following numbers. Setting the computing time for the RBVMM to 1.00, the relative computing time required by the AVM^4 and DSM are 1.15 and 1.72, respectively. The increased computational cost of the DSM compared to the other methods is attributed to the filtering procedure, on the one hand, and to the fact that the DSM requires more linear iterations to convergence, on the other hand.

Discussion of the Results. A visualization of the complex flow is provided in Figure 4.18 via instantaneous pressure iso-contours. Moreover, a closeup view of the near-cylinder region shows streamlines in the x_1x_2-centerplane. Figure 4.19 depicts the mean streamwise velocity $\langle u_1 \rangle / U_\infty$ downstream and above the cylinder as well as closeup views of the near-cylinder region, and Figure 4.20 displays the streamwise and vertical root-mean-square velocities, rms u_1/U_∞ and rms u_2/U_∞, respectively, downstream of the cylinder. All velocity results are normalized by the free-stream velocity. Experimental data taken from Lyn and Rodi [203] and Lyn *et al.* [204], denoted by "Exp LR94/95", are included for comparison. As may also be seen in most of the aforementioned reports of numerical results, all methods overestimate the velocity in the wake of the cylinder compared to the experimental results. In particular, the AVM^4 substantially overpredicts the velocity. Concerning the negative peak in the near-cylinder area, which is often underestimated, the AVM^4 provides a more accurate approximation than the DSM and RBVMM. In addition, experimental results reported by Durão *et al.* [88], who examined flow past a square-section cylinder at Re $= 14\,000$, are included, as they indicate potentially higher velocities in the wake. The respective data are named "Exp DHP88". Concerning the streamwise velocity on top of the upper surface of the cylinder, all methods yield almost the same curve, which is close to the experimental data, and differences between them are merely identifiable from the closeup view of the near-cylinder region, where the AVM^4 again appropriately captures the experimental data. The root-mean-square values in x_1-direction are overpredicted by all methods, except for

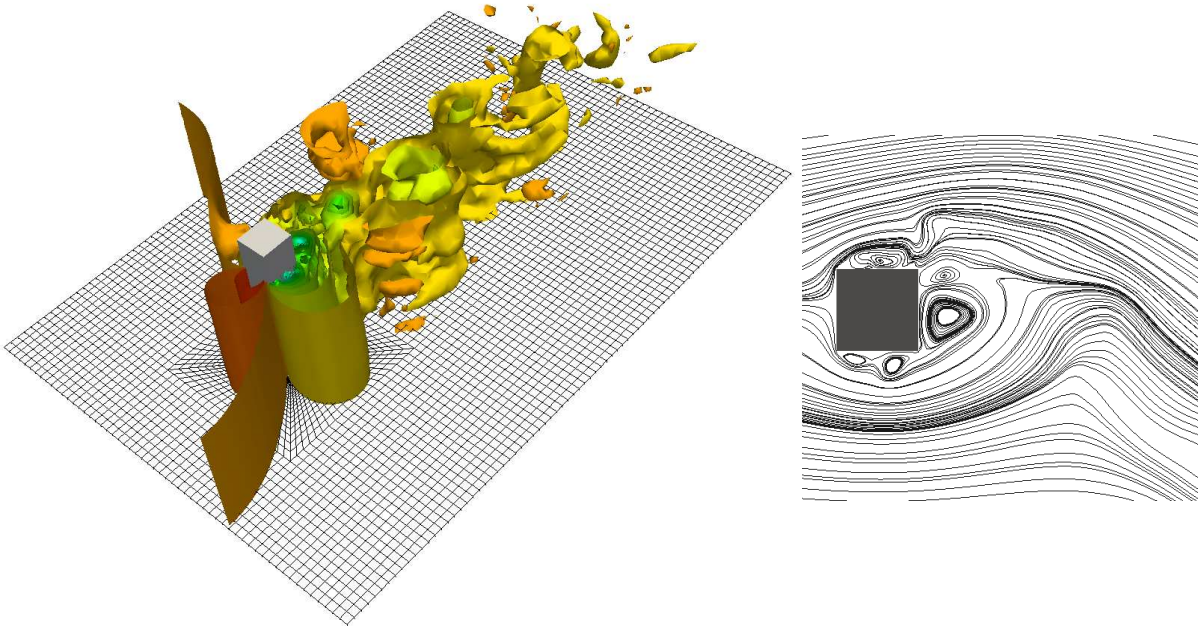

Figure 4.18: Instantaneous pressure iso-contours (red color indicates high pressure and blue color low pressure) including the grid in the background (left) and streamlines in the near-cylinder region in the x_1x_2-centerplane (right) for flow past a square-section cylinder. Results obtained with the AVM^4 are shown during the sampling period.

the AVM^4, which provides a very good prediction in the near-cylinder region. Further downstream, it underpredicts the root-mean-square values. With respect to rms u_2, all methods shift the maximum value closer to the cylinder. While the RBVMM and DSM quite accurately approximate the peak value, the AVM^4 significantly underpredicts it. However, immediately behind the cylinder, the AVM^4 yields a better approximation than the other methods.

Figure 4.21 illustrates the pressure coefficient C_p along the upper, back and lower cylinder surface. The coordinate x_cyl runs in clockwise direction along the cylinder surface, starting and ending at the lower left corner. The pressure coefficient is defined as

$$C_\mathrm{p} = \frac{\langle p_\mathrm{kin} \rangle - p_{\mathrm{kin},\infty}}{\frac{1}{2}U_\infty^2}, \tag{4.76}$$

where $p_{\mathrm{kin},\infty}$ is the mean kinematic pressure at $x_2 = 0$ on the inflow boundary. The results are compared to experimental data measured by Lee [180] and Bearman and Obasaju *et al.* [24] and marked by "Exp L75" and "Exp BO82", respectively. Those data are included here in the form presented in Rodi *et al.* [266]. The only results located at least partly between the two experimental curves are the ones provided by the AVM^4. Both the RBVMM and the DSM are entirely below the lower experimental curve.

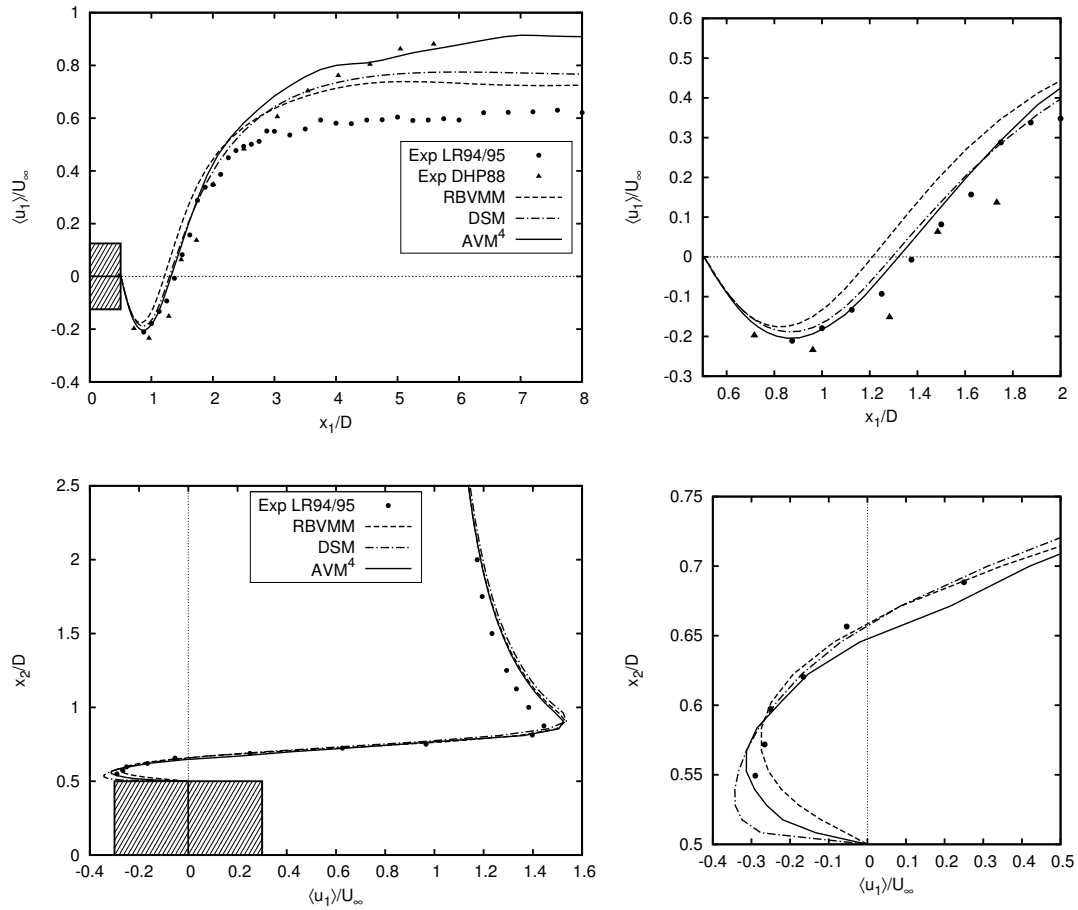

Figure 4.19: Mean streamwise velocity $\langle u_1 \rangle / U_\infty$ downstream (top) and above (bottom) the square-section cylinder at $x_2 = 0$ and $x_1 = 0$ including closeup views of the near-cylinder region.

Table 4.2 summarizes the values obtained for the Strouhal number, defined as

$$\mathrm{St} = \frac{D f_{\mathrm{vs}}}{U_\infty}, \tag{4.77}$$

where f_{vs} denotes the frequency of vortex shedding, the mean drag coefficient, defined as

$$C_{\mathrm{D}} = \frac{\langle F_1 \rangle}{\frac{1}{2} U_\infty^2 A_D}, \tag{4.78}$$

where F_1 is the x_1-component of the force acting on the cylinder and A_D the area of the front surface of the cylinder, the root-mean-square values of drag and lift coefficient, $C_{\mathrm{D,rms}}$ and $C_{\mathrm{L,rms}}$, respectively, the mean base suction $-C_{\mathrm{pb}}$, which is the pressure coefficient at the centerline of the back surface, and the mean recirculation length X_{r}/D. The lift coefficient C_{L} is defined analogously to C_{D} with F_1 being replaced by the resulting force in x_2-direction, i.e., F_2. The location of zero mean streamwise velocity downstream of the cylinder marks the recirculation length. For comparison, results from various numerical and experimental studies are included. In addition to

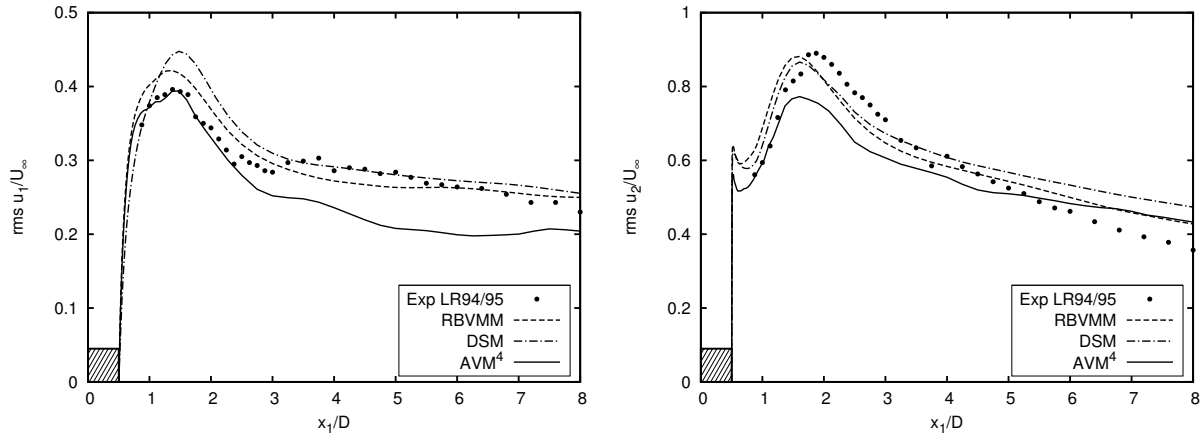

Figure 4.20: Root-mean-square velocities rms u_1/U_∞ and rms u_2/U_∞ downstream of the square-section cylinder at $x_2 = 0$.

the aforementioned studies, experimental data taken from Luo *et al.* [202] are also considered. For all methods, the Strouhal number is in good agreement with the numerical and experimental results. More pronounced differences between the methods are observed for the remaining values. The values reported by the participants of the two workshops exhibit a broad range. It is therefore focused on a comparison of the present results to the experimental data. Numerical results from other works are additionally taken into account to some extent. Only the AVM^4 provides a drag coefficient within the range of the experimental results, matching the one reported by Bearman and Obasaju [24]. The values obtained with the RBVMM and DSM notably overpredict C_D, with the RBVMM performing somewhat better than the DSM. The same behavior is observed for $-C_\mathrm{pb}$; that is, higher values are observed for the RBVMM and DSM, while the value predicted by the AVM^4 fits into the range of experimental results. The root-mean-square

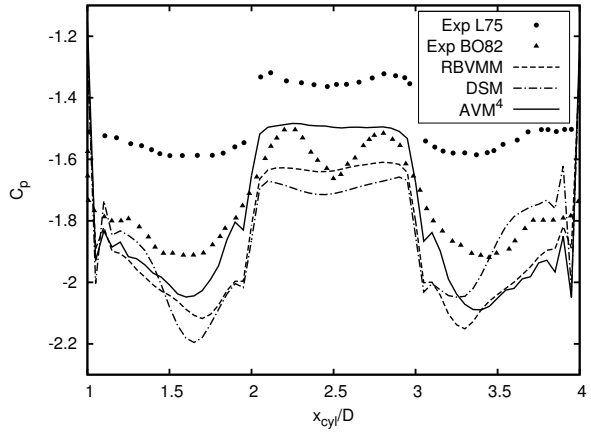

Figure 4.21: Pressure coefficient C_p along the upper, back and lower cylinder surface. The coordinate x_cyl runs in clockwise direction along the cylinder surface, starting and ending at the lower left corner.

values for the drag coefficient are close to the experimental and numerical results ranging from 0.16 to 0.23. The results from the workshops are not considered here for the aforementioned reason. Compared to the experimental data, the AVM^4 only slightly underpredicts $C_{\mathrm{L,rms}}$. In contrast, the RBVMM and DSM yield substantially higher values fitting into the range of numerical results reported by Sohankar *et al.* [289] and almost matching the value given by Verstappen and Veldman [320]. The recirculation length produced by the AVM^4 is the closest to the only experimental value available, while the RBVMM and DSM yield smaller values.

Table 4.2: Strouhal number St, mean drag coefficient C_{D}, root-mean-square values of drag and lift coefficient, $C_{\mathrm{D,rms}}$ and $C_{\mathrm{L,rms}}$, mean base suction $-C_{\mathrm{pb}}$ and mean recirculation length X_{r}/D of flow past a square-section cylinder from present simulations and other numerical and experimental studies. The values labeled by Exp LR94/95 are extracted from [266], Exp L75 from [324] (C_{D}, $C_{\mathrm{D,rms}}$) and [289] ($-C_{\mathrm{pb}}$) and Exp BO82 as well as Exp LYCL94 from [175].

	St	C_{D}	$C_{\mathrm{D,rms}}$	$C_{\mathrm{L,rms}}$	$-C_{\mathrm{pb}}$	$\frac{X_{\mathrm{r}}}{D}$
present results						
AVM^4	0.15	2.28	0.15	1.17	1.50	1.32
RBVMM	0.14	2.41	0.22	1.49	1.63	1.21
DSM	0.14	2.50	0.27	1.43	1.71	1.29
numerical results						
workshop RFBP97 [266]	0.07-0.15	1.66-2.77	0.10-0.27	0.38-1.79	-	0.89-2.96
workshop V97 [324]	0.13-0.16	2.03-2.79	0.12-0.36	1.01-1.68	-	1.02-1.61
LES FTWG00 [104]	0.13	2.00-2.20	0.17-0.20	1.29-1.34	-	1.23-1.37
LES SDN00 [289]	0.13	2.03-2.32	0.16-0.20	1.23-1.54	1.30-1.63	-
LES MBPS11 [217]	0.14	2.20	-	-	1.30	-
DNS VV97 [320]	0.13	2.09	0.18	1.45	-	-
experimental results						
Exp LR94/95 [203, 204]	0.13	2.10	-	-	-	1.38
Exp L75 [180]	-	2.05	0.23	-	1.33	-
Exp BO82 [24]	0.13	2.28	-	1.20	1.60	-
Exp LYCL94 [202]	0.13	2.21	0.18	1.21	1.52	-
Exp MBPS11 [217]	0.13	2.10	-	-	1.30	-

5

Extension I: Passive-Scalar Mixing

Turbulent mixing of passive-scalar fields is important for a wide range of environmental and engineering applications, such as ocean chemistry (see, e.g., Scalo *et al.* [274]) and electrochemical processes (see, e.g., Bauer *et al.* [21]). These examples already indicate that turbulent mixing constitutes a complex process, which is also reflected in LESs of the respective situations. Passive-scalar mixing brings in additional challenges due to the substantially different length scales that may occur in the flow and the scalar field depending on the Schmidt number. An introduction into LES of passive-scalar mixing in turbulent flow, including a survey of selected subgrid-scale models further developed for that purpose, may be found, e.g., in the textbook by Sagaut [270].

Applications of the VMM to turbulent flow including passive-scalar mixing are so far barely considered in literature. Bauer *et al.* [21] used a residual-based two-scale version of the VMM for a specific passive high-Schmidt-number problem. Also within a residual-based two-scale form, Codina *et al.* [69] focused on thermally coupled flows using the Bousinessq approximation. Among others, they also showed one example of turbulent incompressible flow with passive-scalar mixing.

In this chapter, the AVM^4 is extended to LES of passive-scalar mixing in turbulent incompressible flow. The first extension of multifractal subgrid-scale modeling to passive-scalar mixing problems was derived by Burton [50]. The complete approach, termed nLES method (see Section 4.4), was further applied to high-Schmidt-number mixing in a turbulent jet flow by Burton [51]. In this thesis, the multifractal subgrid-scale modeling approach for passive-scalar fields is further developed. By explicitly taking into account the relation between velocity and scalar field with respect to their individual resolutions, the multifractal reconstruction process within the scalar field is refined. Moreover, it is focused on wall-bounded turbulent flow in the context of passive-scalar mixing, which has not yet been addressed in any of the preceding studies on multifractal subgrid-scale modeling for scalar fields and which is particularly relevant for industrial and environmental applications. First, a short introduction into passive-scalar mixing in turbulent flow is provided in this chapter, and the variational multiscale formulation of the convection-diffusion equation is outlined. Then, multifractal subgrid-scale modeling for scalar quantities is derived. After briefly addressing the residual-based subgrid-scale modeling step to obtain a stable numerical scheme, the resulting AVM^4 for passive-scalar mixing is summarized. Finally, passive-scalar mixing in turbulent channel flow for Schmidt numbers up to 1000 is thoroughly investigated, demonstrating an excellent performance of the AVM^4. All derivations and numerical results presented in this chapter were previously published in Rasthofer *et al.* [260].

5.1 A Brief Insight into Scalar Mixing

This section is devoted to the fundamentals of scalar mixing in turbulent flow. First, the mathematical description is presented. Then, important characteristics of a scalar field evolving in a turbulent flow are addressed. For an elaborate description of the dynamics of passive-scalar mixing in turbulent flow, the reader is referred, e.g., to the textbooks by Davidson [78] and Tennekes and Lumely [309].

5.1.1 The Convection-Diffusion Equation

Scalar transport is mathematically governed by the convection-diffusion equation as

$$\frac{\partial \phi}{\partial t} + \nabla \cdot (\mathbf{u}\phi) - \kappa \Delta \phi = 0, \tag{5.1}$$

where $\phi(\mathbf{x}, t)$ denotes a scalar quantity, for instance, concentration, and κ, which is assumed constant, the diffusivity. Via the velocity $\mathbf{u}(\mathbf{x}, t)$, this equation is coupled to the incompressible Navier-Stokes equations. If the scalar field has no influence on the fluid field, it is referred to as passive.

Similar to the Reynolds number, the Péclet number is defined as

$$\mathrm{Pe} = \frac{U\ell}{\kappa}, \tag{5.2}$$

based on a characteristic velocity U and length ℓ, and quantifies the ratio between convective and diffusive transport. A relation between the smallest length scales in the velocity and scalar field may be obtained from the Schmidt number, which is defined as the ratio of kinematic viscosity ν and diffusivity κ:

$$\mathrm{Sc} = \frac{\nu}{\kappa}. \tag{5.3}$$

5.1.2 Transport Regimes

The passive-scalar field is subject to different transport regimes, which originate from the difference between the length scale characterizing the dissipation range of the velocity field and the length scale identifying the diffusive range of the scalar field. In the following, homogeneous isotropic turbulence is assumed with a Reynolds number sufficiently high such that the three-dimensional kinetic-energy spectrum of the underlying velocity field develops an inertial subrange. Depending on the Schmidt number, different ranges are distinguished for the three-dimensional scalar-variance spectrum, which is defined in a similar way as the kinetic-energy spectrum (see, e.g., Tennekes and Lumley [309]).

First, small Schmidt numbers, i.e., $\mathrm{Sc} \leq 1$, are considered. For high Péclet numbers, the scalar-variance spectrum exhibits an inertial-convective range, where scalar fluctuations are convected

and unaffected by diffusivity. The shape of the scalar-variance spectrum corresponding to the inertial-convective range was independently determined by Obukhov [235] and Corrsin [74]. From dimensional arguments, it follows as

$$E_\phi(k) = C_{\mathrm{OC}} \chi \varepsilon^{-\frac{1}{3}} k^{-\frac{5}{3}}, \tag{5.4}$$

where C_{OC} is the Obukhov-Corrsin constant and χ the diffusion rate. Analogously to the Kolmogorov scale η (see equation (2.10)) for the velocity field, the Obukhov-Corrsin scale

$$\eta_{\mathrm{OC}} = \left(\frac{\kappa^3}{\varepsilon} \right)^{\frac{1}{4}} \tag{5.5}$$

estimates the scale associated with the smallest structures in the scalar field. The ratio of these scales depends on Sc as

$$\frac{\eta_{\mathrm{OC}}}{\eta} = \mathrm{Sc}^{-\frac{3}{4}}. \tag{5.6}$$

For $\mathrm{Sc} \ll 1$, a further range emerges within the inertial subrange of the kinetic-energy spectrum. Since scalar fluctuations already become sufficiently small to suffer from diffusion within the inertial subrange in this case, this range is thus referred to as inertial-diffusive range.

Schmidt numbers much larger than unity, i.e., $\mathrm{Sc} \gg 1$, exhibit a more complex situation, as two distinct inertial ranges exist for the scalar-variance spectrum. For scales within the inertial subrange of the kinetic-energy spectrum, that is, scales much larger than the Kolmogorov scale, an inertial-convective range, similar to $\mathrm{Sc} \leq 1$, develops. At smaller scales, velocity fluctuations are already affected by dissipation, while diffusivity is not yet effective. Therefore, a second inertial range, the viscous-convective range, emerges in the scalar-variance spectrum. In this range, the strain rate progressively reduces the scales of scalar fluctuations. As derived by Batchelor [19], the scalar-variance spectrum is determined as

$$E_\phi(k) = C_{\mathrm{B}} \chi \nu^{\frac{1}{2}} \varepsilon^{-\frac{1}{2}} k^{-1} \tag{5.7}$$

within this range. Here, C_{B} denotes the Batchelor constant. The viscous-diffusive range, where diffusion eventually acts on the scalar fluctuations, is identified by the Batchelor scale which is given by

$$\eta_{\mathrm{B}} = \left(\frac{\nu \kappa^2}{\varepsilon} \right)^{\frac{1}{4}}. \tag{5.8}$$

The ratio of the Batchelor scale to the Kolmogorov scale is obtained as

$$\frac{\eta_{\mathrm{B}}}{\eta} = \mathrm{Sc}^{-\frac{1}{2}}. \tag{5.9}$$

Figure 5.1 depicts the three-dimensional scalar-variance spectrum $E_\phi(k)$ for passive-scalar mixing in turbulent flow. Both $\mathrm{Sc} \ll 1$ and $\mathrm{Sc} \gg 1$ are considered, and the various scale ranges are marked. Additionally, the three-dimensional kinetic-energy spectrum $E(k)$ is included.

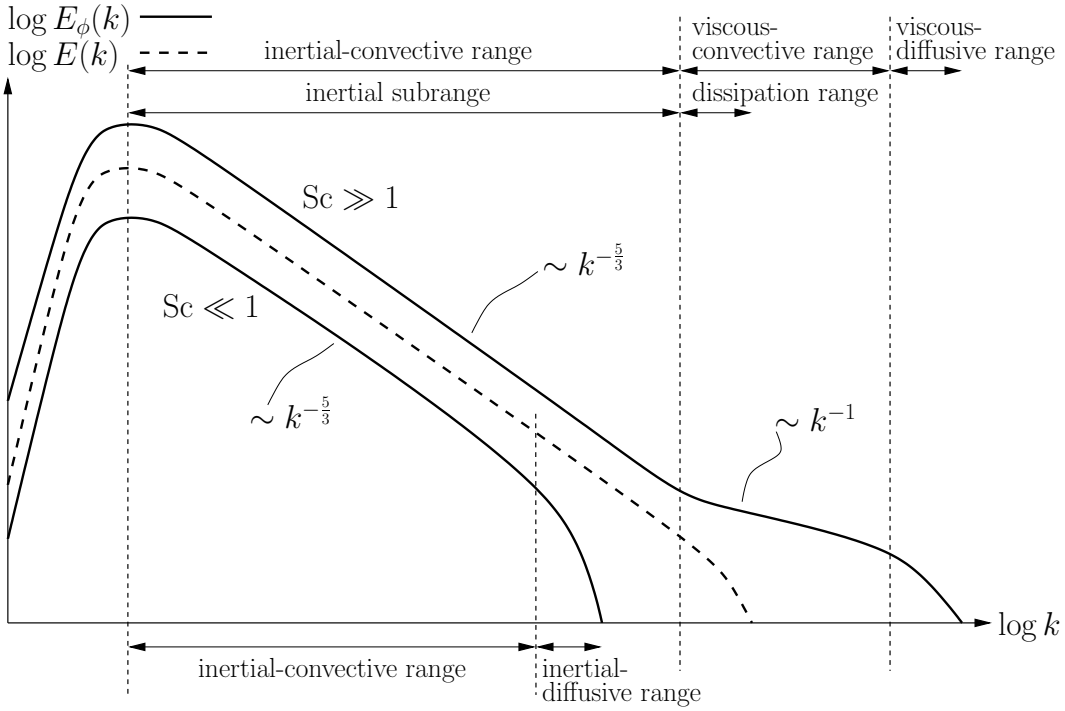

Figure 5.1: Three-dimensional scalar-variance spectrum for Sc $\ll 1$ and Sc $\gg 1$.

5.2 Variational Multiscale Formulation of the Convection-Diffusion Equation

Passive-scalar mixing in the domain Ω described by the convection-diffusion equation, given in convective form, is considered for a time period t_{end}:

$$\frac{\partial \phi}{\partial t} + \mathbf{u} \cdot \nabla \phi - \kappa \Delta \phi = f_\phi \qquad \text{in } \Omega \times]0, t_{\text{end}}[\,, \tag{5.10}$$

$$\phi = \phi_{\text{D}} \qquad \text{on } \Gamma_{\text{D},\phi} \times]0, t_{\text{end}}[\,, \tag{5.11}$$

$$\kappa \nabla \phi \cdot \mathbf{n} = h_\phi \qquad \text{on } \Gamma_{\text{N},\phi} \times]0, t_{\text{end}}[\,, \tag{5.12}$$

$$\phi = \phi_0 \qquad \text{in } \Omega \times \{0\}. \tag{5.13}$$

Dirichlet boundary conditions are provided on the part $\Gamma_{\text{D},\phi}$ of the boundary $\partial\Omega$, while Neumann boundary conditions are imposed on $\Gamma_{\text{N},\phi}$, assuming $\Gamma_{\text{D},\phi} \cap \Gamma_{\text{N},\phi} = \emptyset$ and $\Gamma_{\text{D},\phi} \cup \Gamma_{\text{N},\phi} = \partial\Omega$. Additionally, a potential source term f_ϕ is included, which is taken to be zero unless otherwise specified. Initially, the scalar field ϕ_0 is prescribed. The velocity field $\mathbf{u}$ is obtained from the incompressible Navier-Stokes equations.

Assuming an appropriate solution function space $\mathcal{S}_\phi$ for ϕ as well as a weighting function space $\mathcal{V}_\phi$ for the scalar weighting function w (i.e., the scalar counterparts of the vector spaces defined in Section 3.2 for the velocity) the convection-diffusion equation (5.10) is multiplied by $w \in \mathcal{V}_\phi$ and integrated over the domain Ω. The diffusive term is integrated by parts, with

boundary conditions (5.11) and (5.12) applied to the resulting boundary integral. The variational formulation of the convection-diffusion equation is thus given as follows: find $\phi \in \mathcal{S}_\phi$ such that

$$\mathcal{B}_{\mathrm{CD}}(w;\phi) = \ell_{\mathrm{CD}}(w) \tag{5.14}$$

for all $w \in \mathcal{V}_\phi$, where the form on the left-hand side is given as

$$\mathcal{B}_{\mathrm{CD}}(w;\phi) := \left(w, \frac{\partial \phi}{\partial t}\right)_\Omega + (w, \mathbf{u}\cdot\nabla\phi)_\Omega + (\nabla w, \kappa\nabla\phi)_\Omega \,. \tag{5.15}$$

The linear form on the right-hand side, including the Neumann boundary condition, is given as

$$\ell_{\mathrm{CD}}(w) := (w, f_\phi)_\Omega + (w, h_\phi)_{\Gamma_{\mathrm{N},\phi}} \,. \tag{5.16}$$

For the variational multiscale formulation of the convection-diffusion equation, the scalar quantity is decomposed into a resolved and subgrid-scale component as

$$\phi = \phi^h + \hat{\phi}, \tag{5.17}$$

implying a direct sum decomposition of the underlying function space in the form $\mathcal{S}_\phi = \mathcal{S}_\phi^h \oplus \hat{\mathcal{S}}_\phi$. Based on the variational multiscale concept, a variational projection for separating resolved and unresolved scales is assumed. Therefore, a direct sum decomposition of weighting function space $\mathcal{V}_\phi = \mathcal{V}_\phi^h \oplus \hat{\mathcal{V}}_\phi$ is introduced. Accordingly, the weighting function is decomposed as

$$w = w^h + \hat{w}. \tag{5.18}$$

Inserting decomposition (5.17) into the variational form (5.14), weighting separately by the resolved and the subgrid-scale part of the decomposed weighting function (5.18) and omitting the equation projected onto the space of unresolved scales, the variational multiscale formulation of the convection-diffusion equation is obtained as follows:

$$\mathcal{B}_{\mathrm{CD}}(w^h;\phi^h) + \mathcal{C}_{\mathrm{CD}}(w^h;\mathbf{u}^h,\hat{\mathbf{u}},\phi^h,\hat{\phi}) + \mathcal{R}_{\mathrm{CD}}(w^h;\hat{\mathbf{u}},\hat{\phi}) + \mathcal{B}_{\mathrm{CD}}^{\mathrm{1,lin}}(w^h;\hat{\phi}) = \ell_{\mathrm{CD}}(w^h) \tag{5.19}$$

for all $w^h \in \mathcal{V}_\phi^h$, where

$$\mathcal{C}_{\mathrm{CD}}(w^h;\mathbf{u}^h,\hat{\mathbf{u}},\phi^h,\hat{\phi}) := \left(w^h, \mathbf{u}^h\cdot\nabla\hat{\phi} + \hat{\mathbf{u}}\cdot\nabla\phi^h\right)_\Omega \tag{5.20}$$

and

$$\mathcal{R}_{\mathrm{CD}}(w^h;\hat{\mathbf{u}},\hat{\phi}) := \left(w^h, \hat{\mathbf{u}}\cdot\nabla\hat{\phi}\right)_\Omega \tag{5.21}$$

are the projections of the subgrid-scale flux vectors onto the space of resolved scales. Since these terms are analogous to the cross- and subgrid-scale Reynolds-stress terms of the momentum equation, they are likewise referred to as cross-stress terms and subgrid-scale Reynolds-stress term, respectively. The form

$$\mathcal{B}_{\mathrm{CD}}^{\mathrm{1,lin}}(w^h;\hat{\phi}) := \left(w^h, \frac{\partial\hat{\phi}}{\partial t}\right)_\Omega + \left(\nabla w^h, \kappa\nabla\hat{\phi}\right)_\Omega \tag{5.22}$$

contains the remaining linear terms in the unresolved-scale quantity. To solve the variational multiscale formulation for $\phi^h \in \mathcal{S}_\phi^h$, the cross- and subgrid-scale Reynolds-stress terms as well as $\mathcal{B}_{\mathrm{CD}}^{\mathrm{l,lin}}(w^h;\hat{\phi})$ have to be modeled. Since passive-scalar mixing in turbulent incompressible flow constitutes a one-way-coupled problem, subgrid-scale modeling in the incompressible Navier-Stokes equations remains unaffected.

5.3 Multifractal Subgrid-Scale Modeling for Passive Scalars

The reconstruction of the subgrid-scale scalar quantity, presented in this section, basically follows, with further enhancements concerning the relation between velocity and scalar field, the idea for a multifractal development of $\hat{\phi}$ suggested by Burton [50]. In particular, the model parameters are evaluated with respect to low- and high-Schmidt-number mixing, and the near-wall behavior of the multifractal subgrid-scale modeling for passive-scalar mixing in wall-resolved LES is considered.

5.3.1 Outline of the Modeling Procedure

For passive-scalar mixing, the subgrid-scale scalar field is explicitly calculated from its gradient field $\nabla\hat{\phi}(\mathbf{x},t)$ via integration based on Green's function for the Laplacian:

$$\hat{\phi}(\mathbf{x},t) = \frac{1}{4\pi}\int \frac{\nabla\cdot(\nabla\hat{\phi}(\check{\mathbf{x}},t))}{\|\mathbf{x}-\check{\mathbf{x}}\|}\mathrm{d}\check{\mathbf{x}}, \tag{5.23}$$

representing the scalar analogue to the law of Biot-Savart (2.6). The subgrid-scale scalar gradient field is decomposed into its magnitude $\|\nabla\hat{\phi}\|(\mathbf{x},t)$ and orientation vector $\hat{\mathbf{e}}_{\nabla\phi}(\mathbf{x},t)$ of unit length as

$$\nabla\hat{\phi}(\mathbf{x},t) = \|\nabla\hat{\phi}\|(\mathbf{x},t)\hat{\mathbf{e}}_{\nabla\phi}(\mathbf{x},t). \tag{5.24}$$

Analogously to the subgrid-scale vorticity field, the subgrid-scale scalar gradient field is reconstructed within each element by a two-step cascade process, separately recovering $\|\nabla\hat{\phi}\|$ and $\hat{\mathbf{e}}_{\nabla\phi}$. In the scalar field, the diffusive (or inner) length scale λ_κ, which is established by the equilibrium between the competing effects of local strain rate and molecular diffusion (see, e.g., Buch and Dahm [42]), represents the smallest scales considered in the cascades. Accordingly, the required number of cascade steps $\mathcal{N}_\phi$ in the subgrid-scale scalar gradient cascade is determined by the ratio of the element length h to the diffusive length scale λ_κ via

$$\mathcal{N}_\phi = \log_2\left(\frac{h}{\lambda_\kappa}\right). \tag{5.25}$$

As already implied by the elaborations given in Section 5.1.2, the different transport regimes have also to be taken into account in the subgrid-scale modeling procedure. Figure 5.2 illustrates the various modeling situations encountered in LES of passive-scalar mixing by means of the scalar-variance spectrum $E_\phi(k)$ and the kinetic-energy spectrum $E(k)$. The particular

case Sc ≈ 1 is additionally included. In the depicted diagrams, the diffusive wave number is denoted by k_κ and the viscous one by k_ν. The wave number associated with the discretization is k_h. While in LES of passive-scalar mixing at low Schmidt numbers both velocity and scalar field are usually underresolved, two different situations need to be distinguished in the high-Schmidt-number case. If k_h lies within the inertial-convective range (marked by the additional index "ic" in the right diagram of Figure 5.2), the same modeling situation as for Sc ≤ 1 occurs. A different situation is encountered if k_h is located within the viscous-convective range (marked by the additional index "vc"). This case constitutes a simulation in which the velocity is resolved, and subgrid-scale modeling is merely needed in the scalar field. Consequently, different approaches are required depending on the Schmidt-number regime, the resolution of velocity and scalar field as well as the corresponding physical mechanisms driving the subgrid-scale scalar field.

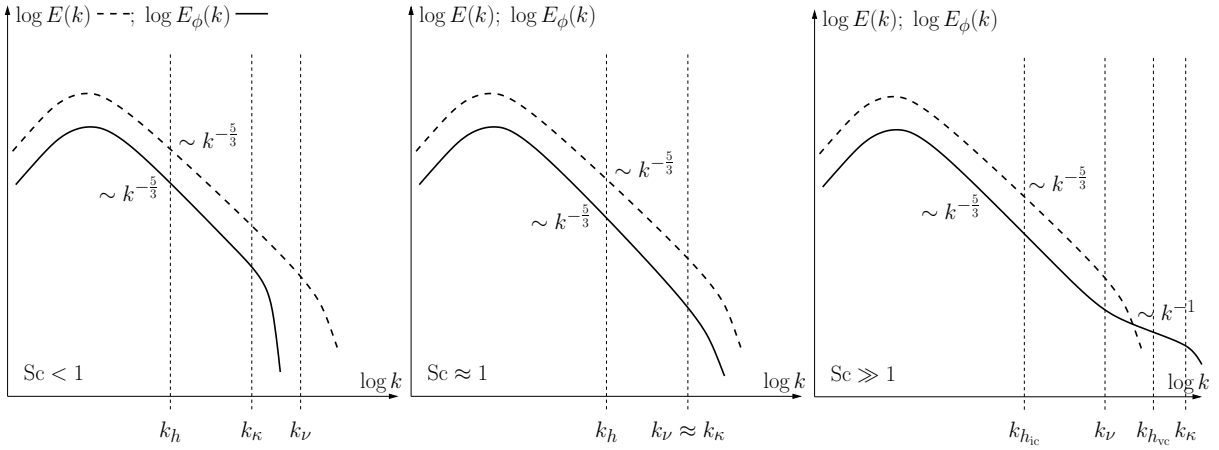

Figure 5.2: Modeling situations in LES of passive-scalar mixing.

5.3.2 Scalar-Gradient-Magnitude Cascade

As outlined in Section 4.1, several studies confirmed that the diffusion-rate field of a passive-scalar quantity exhibits multifractal scale similarity. The multiplicative cascade therefore distributes the total subgrid-scale diffusion within each element to obtain a multifractal expression for the magnitude $\|\nabla\hat{\phi}\|$ of the gradient of the subgrid-scale scalar quantity. The scalar-variance diffusion is defined as

$$\chi = \kappa \nabla\phi \cdot \nabla\phi, \tag{5.26}$$

and the diffusion spectrum $D_\chi(k)$ associated with the aforementioned transport regimes scales as

$$D_\chi(k) \sim k^\gamma, \tag{5.27}$$

where $\gamma = 1/3$ at inertial-convective scales and $\gamma = 1$ at viscous-convective scales, which follows directly from the scaling of the scalar-variance spectrum (see Section 5.1.2). The average subgrid-scale diffusion $\hat{\chi}$ is determined depending on the average diffusion $\delta\chi^h$ at smaller

resolved scales. Further decomposing the resolved scalar field ϕ^h as

$$\phi = \underbrace{\phi^{\alpha h} + \delta\phi^h}_{\phi^h} + \hat{\phi}, \tag{5.28}$$

the diffusion rates associated with the smaller resolved scales and the subgrid scales are given by

$$\delta\chi^h = \kappa \nabla\delta\phi^h \cdot \nabla\delta\phi^h, \tag{5.29}$$

$$\hat{\chi} = \kappa \nabla\hat{\phi} \cdot \nabla\hat{\phi}. \tag{5.30}$$

Depending on the Schmidt number, the length scale αh is assumed to be located in the inertial-convective or the viscous-convective range. The diffusion spectrum is integrated both from the wave number k_h to the diffusive wave number k_κ,

$$\hat{\chi} = \int_{k_h}^{k_\kappa} c_\chi k^\gamma \mathrm{d}k, \tag{5.31}$$

where $c_\chi > 0$ is the associated proportionality constant, and from $k_{\alpha h}$ to k_h,

$$\delta\chi^h = \int_{k_{\alpha h}}^{k_h} c_\chi k^\gamma \mathrm{d}k, \tag{5.32}$$

yielding an expression for the subgrid-scale diffusion depending on the diffusion at the smaller resolved scales:

$$\hat{\chi} = \left(1 - \alpha^{-(\gamma+1)}\right)^{-1} \left[\left(\frac{k_\kappa}{k_h}\right)^{(\gamma+1)} - 1\right] \delta\chi^h. \tag{5.33}$$

A constant exponent γ is implicitly assumed for integration, such that it can be performed without further distinguishing whether Sc ≤ 1 or Sc $\gg 1$ and $k_h = k_{h_{\mathrm{vc}}}$. For Sc $\gg 1$ and $k_h = k_{h_{\mathrm{ic}}}$, exponent γ is discontinuous, resulting in a potential separate integration for both ranges. This issue is not further considered here, but will be addressed in Section 5.3.5. Applying the multiplicative cascade to the resulting average subgrid-scale diffusion and introducing equations (5.29) and (5.30) leads to the following expression for the magnitude of the subgrid-scale scalar gradient:

$$\|\nabla\hat{\phi}\|(\mathbf{x},t) = \left[\left(1 - \alpha^{-(\gamma+1)}\right)^{-1} \left(\left(\frac{k_\kappa}{k_h}\right)^{(\gamma+1)} - 1\right) \left(2^{\mathcal{N}_\phi}\right)^3 \prod_{n=1}^{\mathcal{N}_\phi} \mathcal{M}_n(\mathbf{x},t)\right]^{\frac{1}{2}} \|\nabla\delta\phi^h\|. \tag{5.34}$$

For illustration of the corresponding scale-invariant distribution of multipliers $P(\mathcal{M})$, the reader is referred, e.g., to Frederiksen *et al.* [97] (see Figure 18 therein).

5.3.3 Scalar-Gradient-Orientation Cascade

To determine the orientation $\hat{\mathbf{e}}_{\nabla\phi}$ of the gradient of the subgrid-scale scalar field, an additive decorrelation cascade is set up analogously to the one for the subgrid-scale vorticity field:

$$\hat{\mathbf{e}}_{\nabla\phi}(\mathbf{x},t) = \mathcal{I}_{\nabla\phi}\delta\mathbf{e}^h_{\nabla\phi}(\mathbf{x},t) + (1-\mathcal{I}_{\nabla\phi})\sum_{n=1}^{\mathcal{N}_\phi}\boldsymbol{\delta}^*_n, \tag{5.35}$$

based on the orientation $\delta\mathbf{e}^h_{\nabla\phi}$ of the gradient of the smaller resolved scales and the (modified) stochastic-decorrelation increments $\boldsymbol{\delta}^*_n$. The scalar-gradient intermittency factor $\mathcal{I}_{\nabla\phi}$ is defined from the relative orientation of $\nabla\hat{\phi}$ and $\nabla\delta\phi^h$ as

$$\mathcal{I}_{\nabla\phi} = \frac{\int \nabla\hat{\phi}\cdot\nabla\delta\phi^h \mathrm{d}\mathbf{x}}{\int \|\nabla\hat{\phi}\|\,\|\nabla\delta\phi^h\|\mathrm{d}\mathbf{x}}. \tag{5.36}$$

5.3.4 Subgrid-Scale Scalar Approximation

After combining cascades (5.34) and (5.35) and introducing the resulting subgrid-scale scalar gradient $\nabla\hat{\phi}$, which is assumed approximately equal to its expectation value, into equation (5.23), the subgrid-scale scalar field is calculated as

$$\hat{\phi}(\mathbf{x},t) = \left(1-\alpha^{-(\gamma+1)}\right)^{-\frac{1}{2}} 2^{\frac{3\mathcal{N}_\phi}{2}} \left(2^{(\gamma+1)\mathcal{N}_\phi}-1\right)^{\frac{1}{2}} \left\langle \mathcal{M}^{\frac{1}{2}}\right\rangle^{\mathcal{N}_\phi} \mathcal{I}_{\nabla\phi}\delta\phi^h(\mathbf{x},t), \tag{5.37}$$

where assumptions analogous to the ones discussed in Section 4.2.4 for the subgrid-scale vorticity are incorporated. Moreover, k_κ/k_h is replaced by relation (5.25). The necessary independence of $\hat{\phi}$ from $\mathcal{N}_\phi$ as $\mathcal{N}_\phi\to\infty$, i.e., the high-Reynolds-number limit, constrains $\mathcal{I}_{\nabla\phi}$ as

$$\mathcal{I}_{\nabla\phi} \sim 2^{-\left(\frac{\gamma+1}{2}+\frac{3}{2}\right)\mathcal{N}_\phi}\left\langle \mathcal{M}^{\frac{1}{2}}\right\rangle^{-\mathcal{N}_\phi}. \tag{5.38}$$

Hence, the subgrid-scale scalar $\hat{\phi}$ reads

$$\hat{\phi}(\mathbf{x},t) = D\delta\phi^h(\mathbf{x},t), \tag{5.39}$$

where

$$D := C^{\mathrm{D}}_{\mathrm{sgs}}\left(1-\alpha^{-(\gamma+1)}\right)^{-\frac{1}{2}} 2^{-\frac{(\gamma+1)\mathcal{N}_\phi}{2}}\left(2^{(\gamma+1)\mathcal{N}_\phi}-1\right)^{\frac{1}{2}}. \tag{5.40}$$

The required proportionality constant is denoted by $C^{\mathrm{D}}_{\mathrm{sgs}}$. Parameter $C^{\mathrm{D}}_{\mathrm{sgs}}$ should exhibit a universal dependence on the Reynolds number and satisfy the same characteristics as discussed for $C^{\mathrm{B}}_{\mathrm{sgs}}$ in Section 4.2.4. Based on the evaluations of Burton [50], $C^{\mathrm{D}}_{\mathrm{sgs}}$ is expected to be approximately equal to or somewhat higher than $C^{\mathrm{B}}_{\mathrm{sgs}}$ depending on the Reynolds number. A potentially higher value of $C^{\mathrm{D}}_{\mathrm{sgs}}$ correlates with the higher intermittency of the scalar field, which is consistent with studies on turbulent mixing of passive-scalar quantities (see, e.g., the review articles by Sreenivasan and Antonia [291] and Warhaft [332]).

Eventually, the cross- and subgrid-scale Reynolds-stress terms, (5.20) and (5.21), are modeled as follows:

$$\mathcal{C}_{\mathrm{CD}}(w^h; \mathbf{u}^h, \hat{\mathbf{u}}, \phi^h, \hat{\phi}) \approx \left(w^h, \mathbf{u}^h \cdot \nabla \left(D\delta\phi^h\right) + B\delta\mathbf{u}^h \cdot \nabla\phi^h\right)_{\Omega^*}, \tag{5.41}$$

$$\mathcal{R}_{\mathrm{CD}}(w^h; \hat{\mathbf{u}}, \hat{\phi}) \approx \left(w^h, B\delta\mathbf{u}^h \cdot \nabla \left(D\delta\phi^h\right)\right)_{\Omega^*}. \tag{5.42}$$

5.3.5 Relation of Cascades in Scalar and Velocity Field

With respect to low- and high-Schmidt-number passive-scalar mixing and the resulting transport regimes, it is crucial to explicitly distinguish between the number of cascade steps $\mathcal{N}_{\mathbf{u}}$ in the vorticity cascade and the number of cascade steps $\mathcal{N}_{\phi}$ in the scalar gradient cascade. Recalling Figure 5.2, different levels of resolution need to be considered in the velocity and scalar field for $\mathrm{Sc} \neq 1$. Therefore, a potentially different number of cascade steps in both cascades is expected. The number of cascade steps $\mathcal{N}_{\mathbf{u}}$ in the vorticity cascade is estimated via the ratio of the element length h to the viscous length scale λ_ν according to relation (4.7). As given in equation (4.30), the ratio of h to λ_ν is approximated using the local element Reynolds number Re_h. The ratio of λ_κ to λ_ν may be estimated based on the Schmidt number:

$$\frac{\lambda_\kappa}{\lambda_\nu} = \mathrm{Sc}^{-\varphi}, \tag{5.43}$$

where $\varphi = 3/4$ for $\mathrm{Sc} \leq 1$ and $\varphi = 1/2$ for $\mathrm{Sc} \gg 1$, as outlined in Section 5.1.2. Combining this relation with equation (4.30) yields an approximation for the ratio of h to λ_κ:

$$\frac{h}{\lambda_\kappa} = c_\nu \mathrm{Re}_h^{\frac{3}{4}} \mathrm{Sc}^{\varphi}, \tag{5.44}$$

resulting in a higher number of steps $\mathcal{N}_{\phi}$ in the scalar gradient cascade than in the vorticity cascade for $\mathrm{Sc} \gg 1$ and vice versa for $\mathrm{Sc} < 1$. The case $\mathrm{Sc} \gg 1$ requires particular attention, as already indicated in Section 5.3.2. First, it is assumed that k_h is located within the inertial-convective range. Since scales of adjacent ranges are particularly coupled, it is reasonable to consider the unresolved scales of the inertial-convective range to influence the evolution of the resolved scales, while scales belonging to the viscous-convective range have only minor influence on them. Therefore, the same subgrid-scale modeling as for the case $\mathrm{Sc} \leq 1$ is used, if k_h is located within the inertial-convective range. Hence, the exponent γ in the definition (5.40) of the parameter D is set to $1/3$. The exponent φ of the inner-scale scaling (5.43) remains unchanged and thus equal to $1/2$. This approximation might be interpreted as an extrapolation of the inertial-convective scaling down to the Batchelor scale. More sophisticated estimations may be obtained by separately considering the inertial- and viscous-convective range within the integration procedure of the diffusion spectrum. Due to the aforementioned relation between scale ranges, it is however expected that further improvements may be difficult to achieve. Therefore, it is refrained from examining further refinements to this strategy. If k_h is located within the viscous-convective range, the velocity field is fully resolved such that $\mathrm{Re}_h \to 1$ and $\mathcal{N}_{\mathbf{u}} \approx 0$. Due to the multiplication of Re_h by Sc, $\mathcal{N}_{\phi}$ does not vanish, resulting solely in a subgrid-scale

scalar field. These considerations may easily be verified using equations (4.7), (4.30), (5.25) and (5.44).

Figure 5.3 displays the influence of $\mathcal{N}_\phi$, γ and α on D, defined in equation (5.40). The left diagram demonstrates that D reaches its asymptotic value for $\gamma = 1$ already at $\mathcal{N}_\phi > 3$, whereas it is reached at $\mathcal{N}_\phi > 4$ for $\gamma = 1/3$. This behavior reflects an earlier decoupling of the scalar subgrid scales from the resolved scales for scales in the viscous-convective range. If the factor containing the scale-separation parameter α is also included (see the right diagram of Figure 5.3), $\gamma = 1/3$ and $\gamma = 1$ provide almost the same dependence of D on $\mathcal{N}_\phi$ for $\mathcal{N}_\phi < 2$. For $\mathcal{N}_\phi > 2$, $\gamma = 1/3$ leads to a somewhat higher asymptotic value.

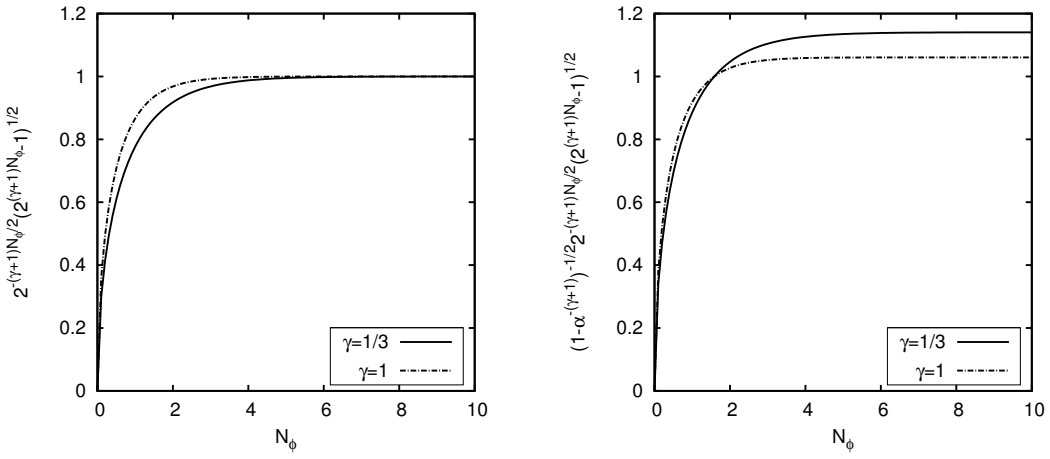

Figure 5.3: Dependence of parameter $D \sim 2^{-\frac{(\gamma+1)\mathcal{N}_\phi}{2}} \left(2^{(\gamma+1)\mathcal{N}_\phi} - 1\right)^{\frac{1}{2}}$ on number of cascade steps $\mathcal{N}_\phi$ for k_h in the inertial-convective ($\gamma = 1/3$) and viscous-convective ($\gamma = 1$) range. The right diagram shows the inclusion of the scale-separation-dependent coefficient $\left(1 - \alpha^{-(\gamma+1)}\right)^{-\frac{1}{2}}$ with parameter $\alpha = 3$ as chosen for scale separation by PA-AMG.

5.3.6 A Remark on the Near-Wall Behavior

Wall-bounded turbulent flow with passive-scalar mixing requires an adequate near-wall behavior of the multifractal subgrid-scale modeling approach. Therefore, the near-wall limit, derived in Section 4.8.1, is applied to the velocity field. The velocity field acts on the scalar field by convecting it. If the anisotropy of the velocity field is appropriately captured, as it is done by the near-wall limit, the scalar field is able to directly respond to the anisotropy via the convective term. As a result, directly coupling the parameter $C_{\text{sgs}}^{\text{D}}$ of the subgrid-scale scalar field to the parameter $C_{\text{sgs}}^{\text{Bnw}}$ obtained from the near-wall limit for the subgrid-scale velocity field is taken to be sufficient to adequately incorporate the near-wall dynamics in the scalar field. Therefore, $C_{\text{sgs}}^{\text{D}}$ is set to the mean value of $C_{\text{sgs}}^{\text{Bnw}}$, yielding a modified parameter $C_{\text{sgs}}^{\text{Dc}}$:

$$C_{\text{sgs}}^{\text{Dc}} = \langle f_{\text{ai}} \rangle C_{\text{sgs}}^{\text{B}}. \tag{5.45}$$

In doing so, a Reynolds-number dependence is also introduced into $C_{\text{sgs}}^{\text{Dc}}$. In addition, except for the vicinity of the wall, where $C_{\text{sgs}}^{\text{Bnw}}$ increases due to the higher anisotropy, $C_{\text{sgs}}^{\text{Dc}}$ is approximately equal to or somewhat higher than $C_{\text{sgs}}^{\text{Bnw}}$, consistent with the preceding considerations.

5.4 Residual-Based Subgrid-Scale Modeling

As discussed in Section 4.4 in the context of the Navier-Stokes equations, the multifractal subgrid-scale modeling terms are embedded into a residual-based variational multiscale formulation of the convection-diffusion equation to ensure proper stabilization of the numerical method. To obtain an appropriate accompanying residual-based multiscale term, the subgrid-scale part $\hat{\phi}$ of the scalar quantity is approximated in an elementwise manner based on the resolved-scale part:

$$\hat{\phi} = -\tau_{\text{CD}} r_{\text{CD}}^h. \tag{5.46}$$

The discrete residual of the convection-diffusion equation reads as

$$r_{\text{CD}}^h = \frac{\partial \phi^h}{\partial t} + \mathbf{u}^h \cdot \nabla \phi^h - \kappa \Delta \phi^h - f_\phi. \tag{5.47}$$

Analogously to τ_{M} for the momentum equation (see equation (3.40)), the stabilization parameter τ_{CD} is defined as

$$\tau_{\text{CD}} = \frac{1}{\sqrt{\frac{4}{\Delta t^2} + \mathbf{u}^h \cdot \mathbf{G}\mathbf{u}^h + C_{\text{I}} \kappa^2 \mathbf{G} : \mathbf{G}}}. \tag{5.48}$$

As outlined for the subgrid-scale velocity in Section 3.3, approximation (5.46) may be derived from the equation projected onto the space of unresolved scales, which governs the evolution of $\hat{\phi}$.

Introducing approximation (5.46) into the first cross-stress term, omitting the second cross-stress term, integrating by parts and assuming that subgrid scales vanish on element boundaries leads to the SUPG term for the convection-diffusion equation, which provides convective stability:

$$\mathcal{C}_{\text{CD}}(w^h; \mathbf{u}^h, \hat{\mathbf{u}}, \phi^h, \hat{\phi}) \approx \left(\mathbf{u}^h \cdot \nabla w^h, \tau_{\text{CD}} r_{\text{CD}}^h \right)_{\Omega^*}. \tag{5.49}$$

The second cross-stress term as well as the subgrid-scale Reynolds-stress term are only incorporated by the residual-based subgrid-scale modeling in a complete residual-based VMM. The terms summarized in the compact form $\mathcal{B}_{\text{CD}}^{1,\text{lin}}(w^h; \hat{\phi})$ are neglected for the same reasons as given for the respective terms of the variational multiscale formulation of the momentum equation.

5.5 AVM^4 for Passive Scalars

The final modeled variational multiscale formulation of the convection-diffusion equation is obtained by inserting expressions (5.41) and (5.42) into equation (5.19) and adding term (5.49):

find $\phi^h \in \mathcal{S}_\phi^h$ such that

$$\begin{aligned}&\mathcal{B}_{\mathrm{CD}}(w^h;\phi^h) + \left(w^h, \mathbf{u}^h\cdot\nabla\left(D\delta\phi^h\right) + B\delta\mathbf{u}^h\cdot\nabla\phi^h\right)_{\Omega^*} + \left(w^h, B\delta\mathbf{u}^h\cdot\nabla\left(D\delta\phi^h\right)\right)_{\Omega^*}\\ &+ \left(\mathbf{u}^h\cdot\nabla w^h, \tau_{\mathrm{CD}} r_{\mathrm{CD}}^h\right)_{\Omega^*} = \ell_{\mathrm{CD}}(w^h)\end{aligned} \tag{5.50}$$

for all $w^h \in \mathcal{V}_\phi^h$. The multifractal subgrid-scale modeling terms can be found in the first line (second and third term). The residual-based multiscale term is given in the second line on the left-hand side. Using level-transfer operators from PA-AMG for scale separation as described in Section 4.3 for the velocity field, the small-scale scalar field is obtained as

$$\delta\phi^h = \sum_{A\in\mathcal{E}} N_A \delta\phi_A^h = \mathbf{N}\delta\mathbf{\Phi}^h = \mathbf{N}\left[\mathbf{I} - \mathbf{S}_h^{3h}\right]\mathbf{\Phi}^h, \tag{5.51}$$

where $\mathbf{\Phi}^h$ is the vector of resolved scalar degrees of freedom ϕ_A and $\delta\mathbf{\Phi}^h$ the vector of nodal values $\delta\phi_A^h$ of the small-scale scalar field.

5.6 Passive-Scalar Mixing in Turbulent Channel Flow

The proposed method is validated for passive-scalar mixing in turbulent channel flow for a broad range of Schmidt numbers in between 1 and 1000, including some supportive results for forced homogeneous isotropic turbulence at higher Schmidt number. In particular, the subgrid-scale scalar-variance transfer is analyzed to evaluate the influence of the multifractal subgrid-scale modeling. Furthermore, the near-wall behavior of the AVM^4 is investigated via the transfer coefficient. Trilinearly-interpolated hexahedral elements are utilized for the subsequent simulations, and a generalized-α time-integration scheme with $\rho_\infty = 0.5$ is applied. For wall-bounded turbulent flow, the parameters of the multifractal subgrid-scale modeling are chosen as listed in Section 4.8.1.

5.6.1 Low-to-Moderate Schmidt-Number Mixing at $\mathrm{Sc} \approx 1$

Problem Setup. Turbulent channel flow at friction Reynolds number $\mathrm{Re}_\tau = 180$ with passive-scalar mixing is examined for two Schmidt numbers, $\mathrm{Sc} = 1$ and 25. A DNS study for $\mathrm{Sc} = 1$, 3, 10, 25 and 49 and $\mathrm{Re}_\tau = 180$ was reported by Schwertfirm and Manhart [278]. LES studies for passive-scalar mixing in turbulent channel flow at $\mathrm{Re}_\tau = 180$ and $\mathrm{Sc} = 1$ a well as 25 may be found, e.g., in Hickel *et al.* [147] and You and Moin [336]. In the latter study, DNS was also performed for these Schmidt numbers. The channel dimensions are $2\pi\delta_\mathrm{c} \times 2\delta_\mathrm{c} \times \pi\delta_\mathrm{c}$ in streamwise, wall-normal and spanwise direction, respectively. The channel half-width δ_c is 1.0 as usual. The channel dimensions are chosen according to the respective dimensions used by Schwertfirm and Manhart [278], Hickel *et al.* [147] and You and Moin [336]. No-slip boundary conditions for the velocity field are applied at the top and bottom wall. For the scalar field, a constant value $\phi_\mathrm{D} = 1.0$ is prescribed at the top wall and $\phi_\mathrm{D} = -1.0$ at the bottom wall. In the homogeneous streamwise and spanwise directions, periodic boundary conditions are assumed for the flow and

the scalar field. A randomly perturbed parabolic velocity profile in streamwise direction constitutes the initial velocity field. The scalar field is initialized with a linear distribution from -1.0 to 1.0 in wall-normal direction. A constant pressure gradient in streamwise direction drives the flow, and a constant time-step length $\Delta t^+ = 0.72$ in non-dimensional form (4.64) is applied. After flow and scalar field have developed, statistics are collected in homogeneous directions and in time during 5000 time steps.

In wall-normal direction, the distribution of the elements is refined towards the wall using the hyperbolic mesh stretching function (4.61) with $C_{\mathrm{G}} = 2.5$ to obtain a better resolution of the near-wall region. The resolution requirements for the diffusive sublayer relative to the requirements for the viscous sublayer increase with the square root of the Schmidt number. Three different spatial discretizations with 32, 48 and 64 elements in each spatial direction are used for both Schmidt numbers. The refinement of the elements is performed such that the same discretizations can be used for $\mathrm{Sc} = 1$ and 25. The resulting non-dimensional element lengths h_i^+ in non-dimensional form (4.62) are summarized in Table 5.1. For LES of turbulent incompressible flow only, wall resolutions with $h_{2,\mathrm{min}}^+ < 1$ are not necessary.

Table 5.1: Mesh parameters for passive-scalar mixing at $\mathrm{Sc} = 1$ and 25 in turbulent channel flow: number of elements and non-dimensional element lengths h_i^+.

no. elements	h_1^+	$h_{2,\mathrm{min}}^+$	$h_{2,\mathrm{max}}^+$	h_3^+
32^3	35.34	0.89	28.28	17.67
48^3	23.56	0.56	18.94	11.78
64^3	17.67	0.41	14.22	8.84

The results obtained with the proposed method are compared to the SPGSM, RBVMM and DSM as well as to various DNS and LES data provided in literature. The SPGSM is extended to passive-scalar mixing by merely using the SUPG term for the convection-diffusion equation. In the RBVMM, all cross- and subgrid-scale Reynolds-stress terms arising in the variational multiscale formulation of the convection-diffusion equation are incorporated via a residual-based subgrid-scale modeling of the velocity and scalar quantity. For the DSM, which was further developed for compressible flow including scalar mixing by Moin *et al.* [223], the aforementioned cross- and subgrid-scale Reynolds-stress terms are modeled by $(\nabla w^h, \kappa_{\mathrm{sgs}} \nabla \phi^h)$, where $\kappa_{\mathrm{sgs}} = \nu_{\mathrm{sgs}}/\mathrm{Sc}_{\mathrm{t}}$ denotes the subgrid diffusivity and Sc_{t} the turbulent Schmidt number, which is determined dynamically (see also Section 4.8.2). As explained in Section 4.8.2 in the context of the Navier-Stokes equations, the subgrid-diffusivity term is applied together with the SUPG term. DNS data extracted from Schwertfirm and Manhart [278] are denoted by "DNS SM07" and from You and Moin [336] by "DNS YM09". You and Moin [336] used two different discretizations for their LES. Here, the results obtained with the finer one of the two discretizations, which consisted of $48 \times 64 \times 48$ grid points, are included, since the corresponding wall resolution $h_{2,\mathrm{min}}^+ = 0.60$ is comparable to the one of the present medium discretization. LES data taken from that study are denoted by "LES YM09". Hickel *et al.* [147], who extended the ALDM-ILES (see Section 4.8.2) to passive-scalar mixing, used a discretization equivalent to the present medium discretization. Results taken from that study are marked by "ILES HAM07".

Analysis of Model Parameters. Before the statistical results are discussed, the parameters of the multifractal subgrid-scale modeling are evaluated with respect to their expected behavior. Figure 5.4 illustrates the mean values of the number of cascade steps $\langle \mathcal{N}_{\mathbf{u}} \rangle$ and $\langle \mathcal{N}_{\phi} \rangle$, the coefficients $\langle C_{\text{sgs}}^{\text{Bnw}} \rangle$ and $\langle C_{\text{sgs}}^{\text{Dc}} \rangle$ as well as the resulting parameters $\langle B \rangle$ and $\langle D \rangle$. For Sc $= 1$, $\langle \mathcal{N}_{\phi} \rangle$ is equal to $\langle \mathcal{N}_{\mathbf{u}} \rangle$. In accordance with the higher resolution of the velocity field compared to the scalar field for Sc $= 25$, more cascade steps are required in the scalar gradient cascade. Moreover, $\langle \mathcal{N}_{\mathbf{u}} \rangle$ and $\langle \mathcal{N}_{\phi} \rangle$ decrease with increasing resolution as expected. It is remarked that, except for the first layers of elements from the walls of the medium and finer discretization, $\langle \mathcal{N}_{\mathbf{u}} \rangle$ is non-zero for all discretizations. Related to the increasing resolution requirements with increasing Schmidt number, $\langle \mathcal{N}_{\phi} \rangle$ does not vanish within these layers for Sc $= 25$. Therefore, k_h is almost exclusively located within the inertial-convective range also for Sc $= 25$, and both scalar field as well as velocity field are underresolved. Hence, it is proceeded as described in Section 5.3.5. Since passive-scalar mixing has no influence on the velocity field, $\langle C_{\text{sgs}}^{\text{Dc}} \rangle$, which is the mean value of the respective parameter of the velocity field adapted by the near-wall limit, i.e., $C_{\text{sgs}}^{\text{Bnw}}$, is constant and equal for both Schmidt numbers. Due to the near-wall limit, $\langle C_{\text{sgs}}^{\text{Bnw}} \rangle$ shows a peak near the wall, reflecting the higher anisotropy in this region. The near-wall limit does not only bring in a modification of $\langle C_{\text{sgs}}^{\text{Bnw}} \rangle$ near the wall, but also comes along with a Reynolds number dependence of $\langle C_{\text{sgs}}^{\text{Bnw}} \rangle$ that allows for setting $C_{\text{sgs}}^{\text{B}}$ and, hence, also $C_{\text{sgs}}^{\text{D}}$ irrespective of the resolution. The near-wall behavior of $\langle C_{\text{sgs}}^{\text{Bnw}} \rangle$ is incorporated in the final parameter $\langle B \rangle$. In contrast, $\langle D \rangle$ is almost constant in the middle of the channel and falls off at the walls. A steeper gradient at the wall and a higher value in the middle of the channel is observed for Sc $= 25$ than for Sc $= 1$. The higher value immediately follows from the increased number of cascade steps. The steeper gradient correlates with the smaller diffusion zone for the higher Schmidt number, where scalar transport is governed by diffusion rather than by convection.

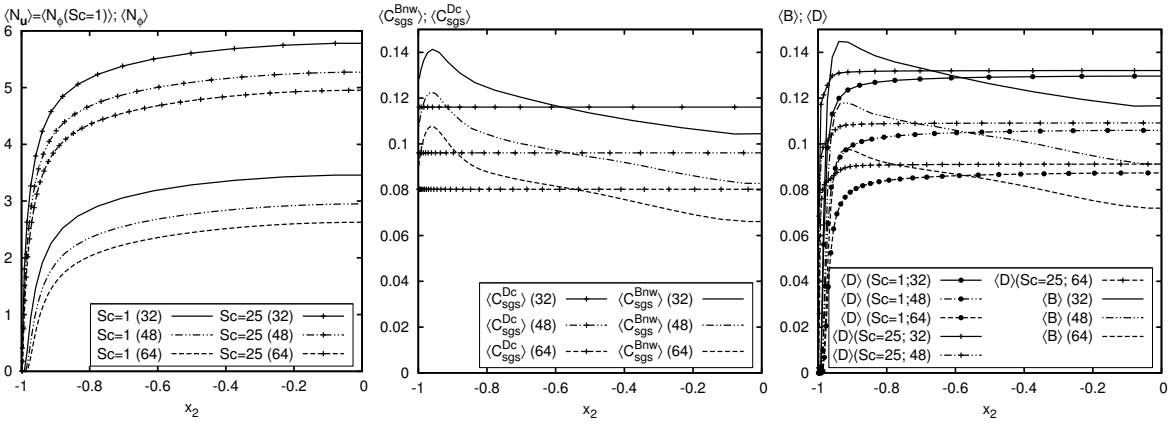

Figure 5.4: Mean values of the number of cascade steps $\langle \mathcal{N}_{\mathbf{u}} \rangle$ and $\langle \mathcal{N}_{\phi} \rangle$, coefficients $\langle C_{\text{sgs}}^{\text{Bnw}} \rangle$ and $\langle C_{\text{sgs}}^{\text{Dc}} \rangle$ as well as parameters $\langle B \rangle$ and $\langle D \rangle$ for passive-scalar mixing at Sc $= 1$ and 25 in turbulent channel flow using 32^3, 48^3 and 64^3 elements.

Statistical Results. Since the fluid field remains unaffected by the inclusion of the scalar field, merely the mean streamwise velocity u_1^+ and the root-mean-square values rms u_i^+ of the velocity fluctuations obtained with the medium discretization are displayed in Figure 5.5. All statistical

results are normalized by the friction velocity u_τ (see equation (4.60)) and the friction scalar

$$\phi_\tau = \frac{c_\mathrm{W}}{u_\tau}, \tag{5.52}$$

respectively, where $c_\mathrm{W} = \kappa(\partial\langle\phi\rangle/\partial x_2)|_\mathrm{W}$ is the diffusive flux in wall-normal direction at the wall. As usual, statistical results are depicted in wall units x_2^+. For the AVM^4, good agreement with the DNS data of turbulent incompressible flow taken from Moser *et al.* [224], marked by "DNS MKM99", is observed. The SPGSM, RBVMM and DSM still deviate from DNS for this discretization, particularly for u_1^+ and rms u_1^+.

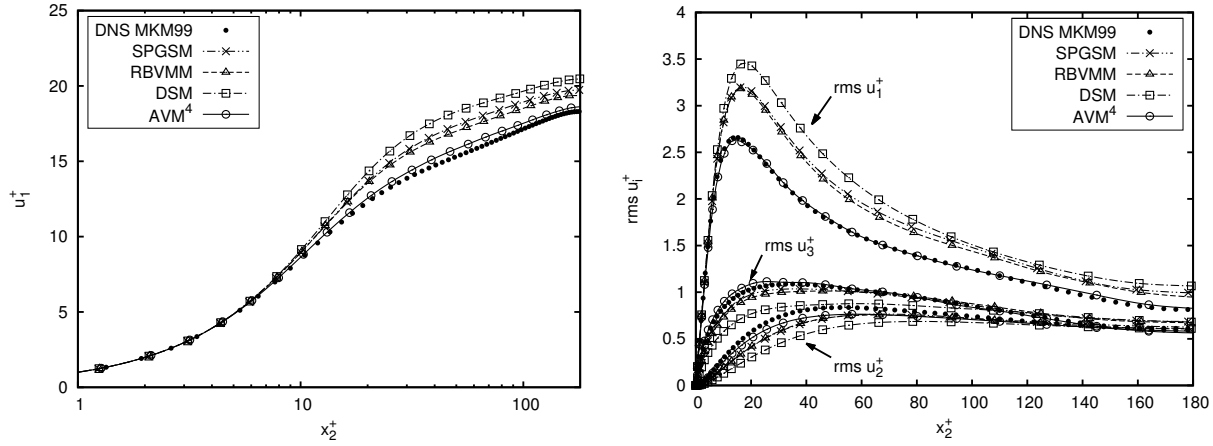

Figure 5.5: Mean streamwise velocity u_1^+ and root-mean-square velocities rms u_i^+ for turbulent channel flow at $\mathrm{Re}_\tau = 180$ using 48^3 elements.

Figures 5.6 and 5.7 depict the scalar statistics obtained with the proposed method, comparing them to the respective data presented in the aforementioned studies. For both Schmidt numbers, the mean scalar ϕ^+, the root-mean-square scalar rms ϕ^+ as well as the correlations of streamwise and wall-normal velocity and scalar fluctuations, $\langle u_1'\phi'\rangle^+$ and $\langle u_2'\phi'\rangle^+$, respectively, are shown. Here, merely the results obtained with the medium discretization are displayed. The DNS data by Schwertfirm and Manhart [278] and You and Moin [336] are in overall good agreement. Differences are observed for the wall-normal velocity-scalar fluctuations $\langle u_2'\phi'\rangle^+$ in the core of the channel. Here, the DNS presented by You and Moin [336] predicts lower values than the one by Schwertfirm and Manhart [278]. The curve obtained with the AVM^4 tends towards the data reported by You and Moin [336]. Further differences are observable for rms ϕ^+ and $\mathrm{Sc} = 1$, where the two DNS data again deviate in the core of channel. For this value, the results predicted by the AVM^4 are located between the two DNS data curves. Except for a slight underestimation of the peak value of $\langle u_1'\phi'\rangle^+$ for both Schmidt numbers, all statistical results provided by the AVM^4 agree well with the DNS data. Concerning the other LES data, it is stated that all LES curves almost match, and the AVM^4 captures the DNS data as accurately as the ALDM-ILES method by Hickel *et al.* [147] and the dynamic global-coefficient subgrid-scale model by You and Moin [336].

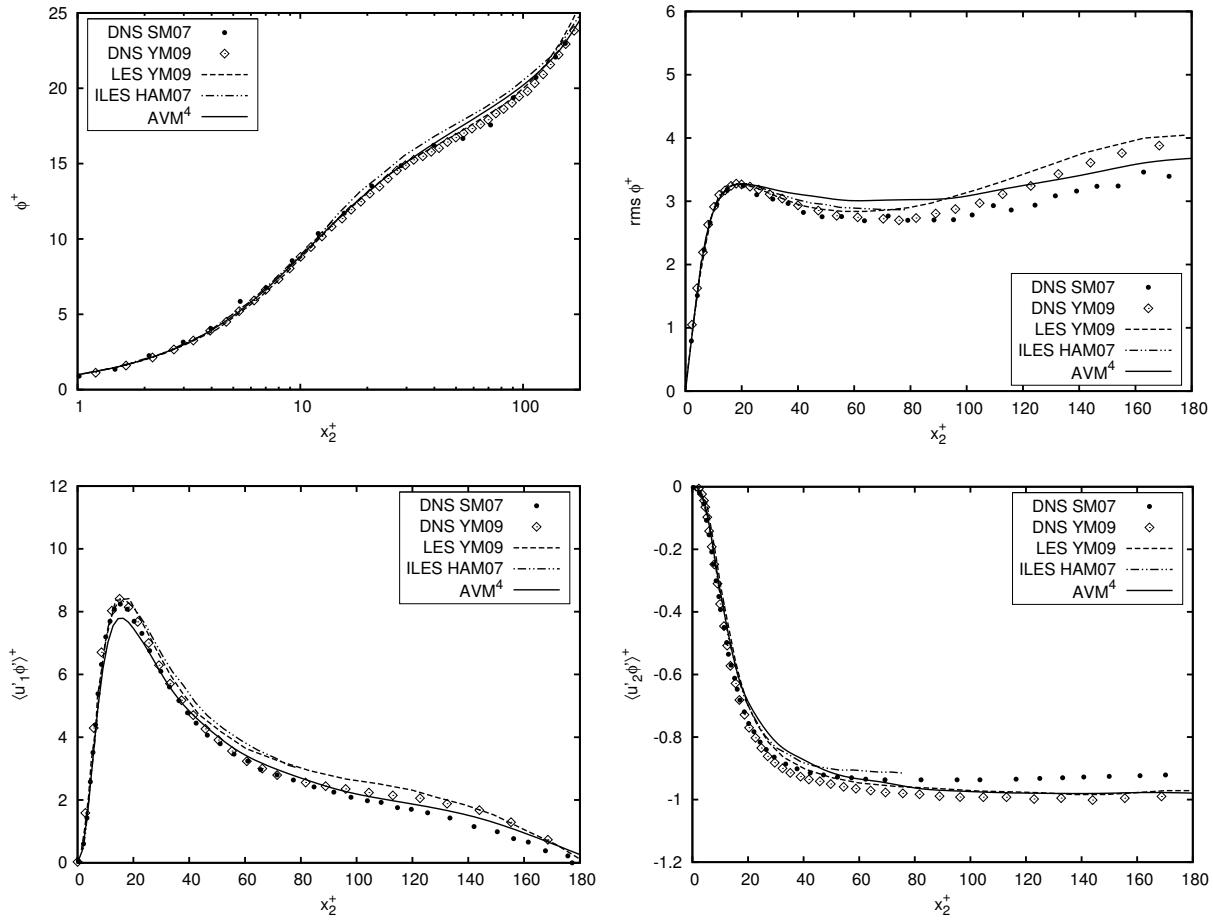

Figure 5.6: Mean scalar ϕ^+, root-mean-square scalar rms ϕ^+, streamwise velocity-scalar fluctuations $\langle u_1'\phi'\rangle^+$ and wall-normal velocity-scalar fluctuations $\langle u_2'\phi'\rangle^+$ obtained with the AVM^4 for passive-scalar mixing at Sc $= 1$ in turbulent channel flow using 48^3 elements. Various LES data taken from literature are included for comparison.

Figures 5.8 and 5.9 show a convergence study for Sc $= 1$ and 25, including results obtained with the SPGSM, RBVMM and DSM. As reference data, merely the DNS data presented by You and Moin [336] are included. Results for the mean scalar quantity, the root-mean-square value as well as the velocity-scalar fluctuations are provided. All methods converge towards the DNS data with increasing resolution. However, notable differences in the accuracy are observable between the various methods. For all discretizations, the AVM^4 yields by far the best approximations for both Schmidt numbers. As previously stated, the results obtained with the AVM^4 are already for the medium discretization notably close to DNS, and the improvement due to the finer discretization is only of small amount. In contrast, the SPGSM and RBVMM provide results which substantially deviate from the DNS data using the coarser and the medium discretization. Even with the finer discretization, there are notable deviations from the DNS results for most of the displayed quantities, while the results of the AVM^4 match all of them almost exactly. The differences in the results provided by the SPGSM and RBVMM are small, with the RBVMM showing overall slightly improved results. The largest deviations from DNS are ob-

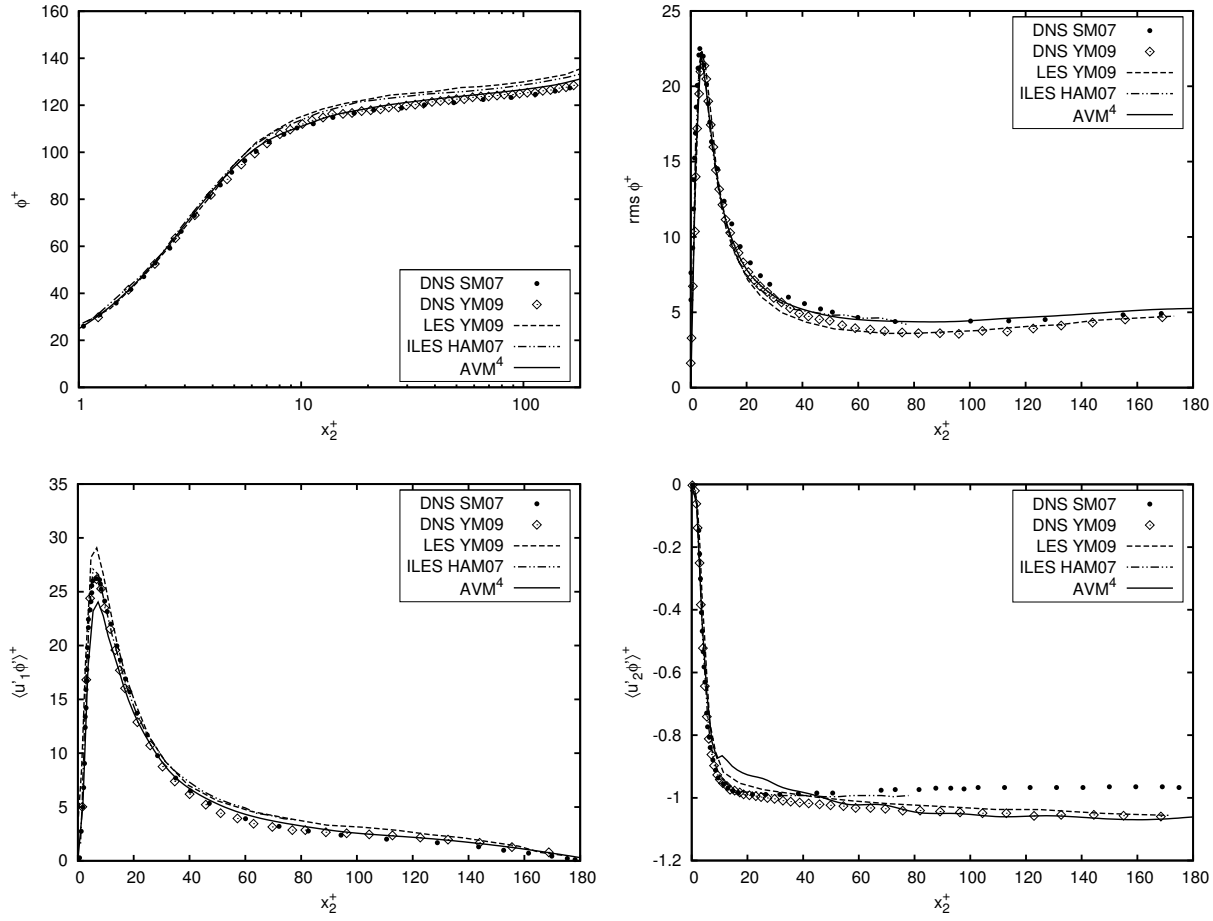

Figure 5.7: Mean scalar ϕ^+, root-mean-square scalar rms ϕ^+, streamwise velocity-scalar fluctuations $\langle u_1'\phi'\rangle^+$ and wall-normal velocity-scalar fluctuations $\langle u_2'\phi'\rangle^+$ obtained with the AVM^4 for passive-scalar mixing at Sc $= 25$ in turbulent channel flow using 48^3 elements. Various LES data taken from literature are included for comparison.

served for the DSM. Also when using the finer discretization, the DSM substantially deviates from DNS for both Schmidt numbers as well as all quantities. Concerning ϕ^+, the results obtained with the AVM^4 for both Schmidt numbers perfectly match the DNS data already for the medium discretization. When using the finer discretization, the SPGSM and RBVMM still deviate from DNS for Sc $= 25$, while the DSM significantly overpredicts ϕ^+ for both Schmidt numbers. The differences between the methods are particularly pronounced for $\langle u_1'\phi'\rangle^+$. For both Schmidt numbers, the approximations provided by the SPGSM and RBVMM using the finer discretization are comparable with the one obtained by the AVM^4 using the coarser discretization. The DSM notably overestimates the peak value for all discretizations. Similarly, the maximum value of rms ϕ^+ is captured more accurately by the AVM^4 than by the other three methods, since the SPGSM and RBVMM as well as in particular the DSM overpredict the peak near the wall for all discretizations. For Sc $= 1$, all methods differ from the DNS values by You and Moin [336] towards the channel center, where also the DNS data deviate from each other. Taking the deviating DNS data also for the correlation $\langle u_2'\phi'\rangle^+$ into consideration, the AVM^4 as

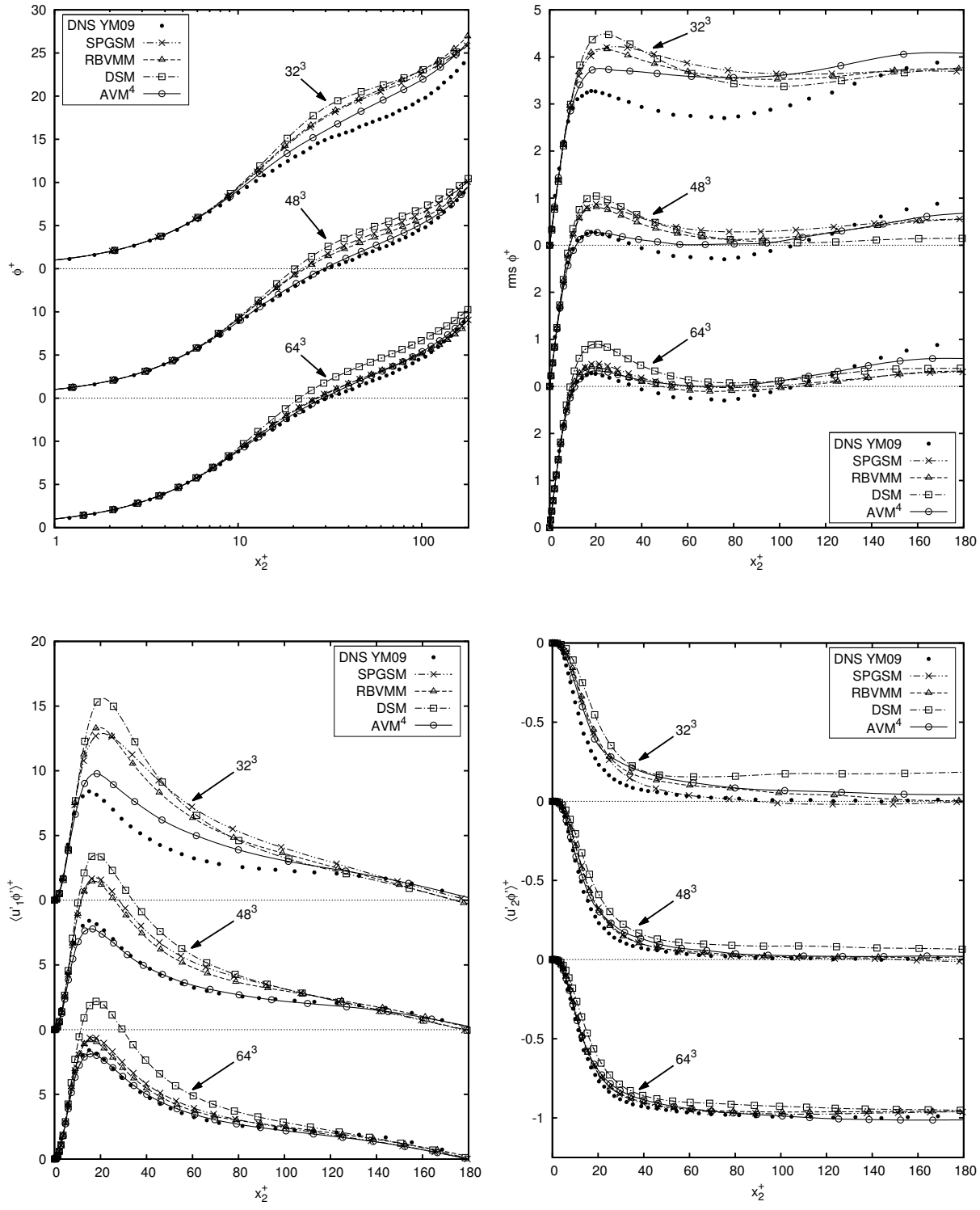

Figure 5.8: Convergence study of mean scalar ϕ^+, root-mean-square scalar rms ϕ^+, streamwise velocity-scalar fluctuations $\langle u_1'\phi'\rangle^+$ and wall-normal velocity-scalar fluctuations $\langle u_2'\phi'\rangle^+$ for passive-scalar mixing at $\mathrm{Sc} = 1$ in turbulent channel flow using 32^3, 48^3 and 64^3 elements.

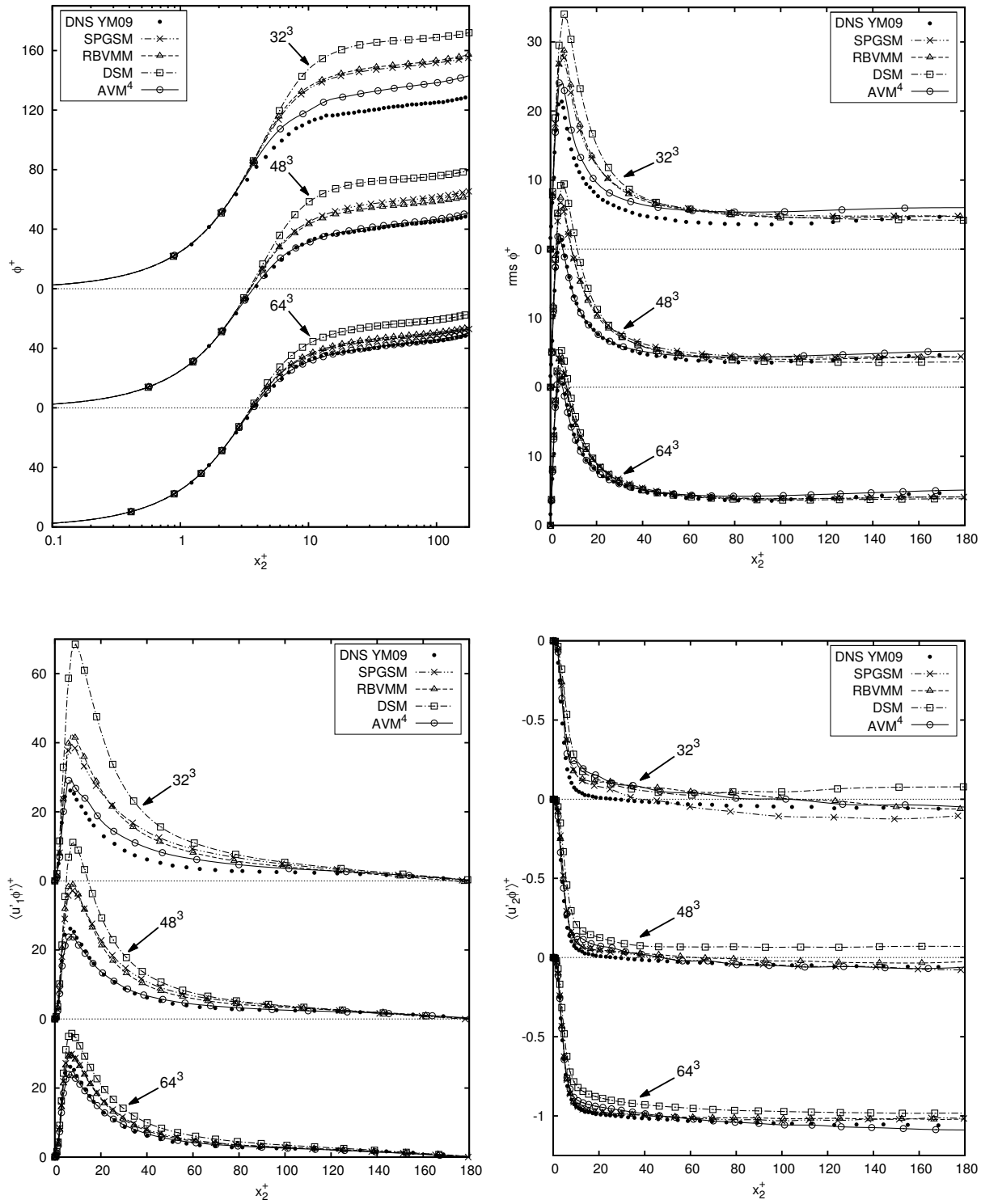

Figure 5.9: Convergence study of mean scalar ϕ^+, root-mean-square scalar rms ϕ^+, streamwise velocity-scalar fluctuations $\langle u_1'\phi'\rangle^+$ and wall-normal velocity-scalar fluctuations $\langle u_2'\phi'\rangle^+$ for passive-scalar mixing at $\mathrm{Sc} = 25$ in turbulent channel flow using 32^3, 48^3 and 64^3 elements.

well as the SPGSM and RBVMM provide good approximations for both Schmidt numbers when using the medium and finer discretization. The DSM yields somewhat shifted curves. To further quantify the computational efficiency of the proposed method, computing times are evaluated. The convection-diffusion equation is iteratively solved within each time step. A computationally efficient implementation of the proposed method is realized by using a fixed-point iteration for the cross- and subgrid-scale Reynolds-stress terms, (5.41) and (5.42); that is, merely the right-hand-side contributions of these terms are evaluated, as explained in Section 4.6.2 in the context of the Navier-Stokes equations. Setting the computing time of the SPGSM to 1.00, the relative computing times required by the AVM^4, RBVMM and DSM amount to 1.22, 1.23 and 1.65, respectively. Taking also the only slightly increased computational cost for the AVM^4 compared to the SPGSM into account, an overall excellent computational performance is stated for the AVM^4.

Subgrid-Scale Scalar-Variance Diffusion. Next, the subgrid-scale diffusion introduced by the different methods is analyzed in more detail, analogously to the investigations of the subgrid-scale dissipation in Section 4.8.2. The contribution of the SUPG term alone constitutes the subgrid-scale diffusion χ_{sp} of the basic approach SPGSM:

$$\chi_{\text{su}} = \tau_{\text{CD}} r_{\text{CD}}^h \mathbf{u}^h \cdot \nabla \phi^h. \tag{5.53}$$

For the subgrid-scale diffusion χ_{av} of the AVM^4, the diffusion due to the cross- and subgrid-scale Reynolds-stress terms, χ_{mc} and χ_{mr}, respectively, modeled by the multifractal subgrid-scale modeling approach have to be considered in addition to the contribution of the SUPG term. They are given by

$$\chi_{\text{mc}} = -(D\delta\phi^h \mathbf{u}^h + \phi^h B \delta \mathbf{u}^h) \cdot \nabla \phi^h, \tag{5.54}$$

$$\chi_{\text{mr}} = -(D\phi^h B \delta \mathbf{u}^h) \cdot \nabla \phi^h. \tag{5.55}$$

The subgrid-scale diffusion of the DSM is denoted by χ_{ds}. The contribution of the subgrid-diffusivity term

$$\chi_{\text{sd}} = \kappa_{\text{sgs}} \nabla \phi^h \cdot \nabla \phi^h \tag{5.56}$$

has to be included for χ_{ds}. The diffusion introduced by the second cross-stress term and the subgrid-scale Reynolds-stress term of the RBVMM is defined as

$$\chi_{\text{cr}} = \phi^h \tau_{\text{M}} \mathbf{r}_{\text{M}}^h \cdot \nabla \phi^h, \tag{5.57}$$

$$\chi_{\text{re}} = -\tau_{\text{CD}} r_{\text{CD}}^h \tau_{\text{M}} \mathbf{r}_{\text{M}}^h \cdot \nabla \phi^h, \tag{5.58}$$

resulting together with χ_{su} in the subgrid-scale diffusion χ_{rb} of the RBVMM. The investigation of the subgrid-scale diffusion was conducted for all methods, discretizations and both Schmidt numbers. Here, merely the results obtained with the medium discretization are depicted, since the conclusions drawn from these results can be extended to both coarser and finer discretization.

Figure 5.10 illustrates the mean subgrid-scale diffusion of the various methods. The mean subgrid-scale diffusion is given in non-dimensional form as

$$\chi^+ = \frac{\langle \chi \rangle \kappa}{\phi_\tau^2 u_\tau^2} \tag{5.59}$$

and displayed in wall-normal direction. You and Moin [336] filtered their DNS data for Sc $= 1$ in streamwise and spanwise direction to estimate the required subgrid-scale diffusion for their coarser discretization with 32 elements in the respective directions. Due to deviating procedures,

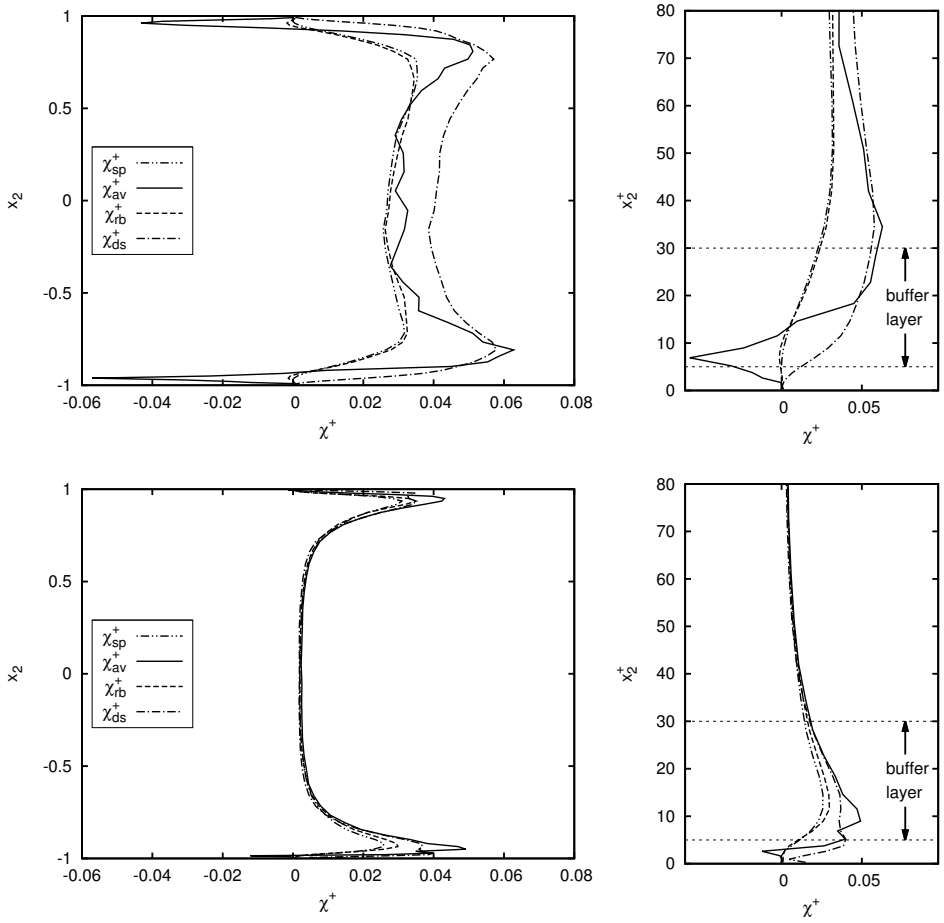

Figure 5.10: Mean subgrid-scale diffusion χ^+ for passive-scalar mixing at Sc $= 1$ (top) and Sc $= 25$ (bottom) in turbulent channel flow using 48^3 elements including a closeup view of the near-wall region with marked buffer layer of the underlying velocity field.

a quantitative comparison to those data is not possible. Therefore, the present results are merely qualitatively compared to the subgrid-scale diffusion determined from filtered DNS data and displayed in Figure 2 of the study by You and Moin [336]. The distribution of the subgrid-scale diffusion given in the work by You and Moin [336] shows a peak near the wall and then falls off to an almost constant value in the middle of the channel. With respect to the present methods, the scalar-variance transfer can be captured more accurately by the inclusion of the multifractal

subgrid-scale modeling terms. While the distributions of subgrid-scale diffusion corresponding to the SPGSM and RBVMM are almost uniform after increasing from the walls, the distributions of the DSM and in particular the AVM^4, which both include an explicit subgrid-scale model, exhibit a peak in the vicinity of the wall. The tendency of the SPGSM to unphysically flatten the distribution of the subgrid-scale diffusion has also been observed in Section 4.8.2 for the mean subgrid-scale dissipation of turbulent incompressible channel flow in the form of a notably smaller peak in the buffer layer compared to, for instance, the AVM^4. Although the filtered DNS data suggest a positive averaged subgrid-scale diffusion throughout the channel height, the subgrid-scale diffusion of the AVM^4 shows a thin negative peak close to the wall. A closeup of the near-wall region reveals the occurrence of the negative and positive peak value of χ_{av}^{+} within the buffer layer of the underlying velocity field, which is known to be the region of intensified turbulence activity (see, e.g., Pope [252] and Tennekes and Lumely [309]). The gain of scalar variance is related to the ability of the AVM^4 to account for local backscatter of energy, which is another already mentioned advantage of the AVM^4 compared to, for instance, subgrid-diffusivity models such as the DSM, which are usually purely diffusive. The SPGSM and RBVMM also introduce a very small negative contribution at the same location. Comparing both Schmidt number cases, it is stated that subgrid-scale diffusion is introduced throughout the channel for $\mathrm{Sc} = 1$, while the distribution of the subgrid-scale diffusion for all methods is almost zero in the core of the channel and has a significant peak near the wall for $\mathrm{Sc} = 25$. From the closeup view, it is observed that the peak is still located within the buffer layer of the underlying velocity field, but moves towards the wall. Since the gradient of the scalar field, which determines the diffusion from the fluxes, increases at the wall and approaches zero in the core of the channel with increasing Schmidt number, both the more pronounced peak as well as its shift towards the wall have to be expected. Again, the distributions of subgrid-scale diffusion corresponding to the SPGSM and RBVMM are almost the same, while the ones of the AVM^4 and DSM provide higher peak values due to the explicit subgrid-scale modeling. Transferring the observation from $\mathrm{Sc} = 1$ to $\mathrm{Sc} = 25$, this behavior reflects the improvements due to the multifractal subgrid-scale modeling terms. Again, the AVM^4 shows a very small negative peak close to the buffer layer.

Further insight into the diffusive properties of the proposed method is gained by analyzing its constituents. Figure 5.11 displays the diffusion introduced by the various modeling terms of the AVM^4 for $\mathrm{Sc} = 1$ as well as 25. The contribution χ_{mr}^{+} of the subgrid-scale Reynolds-stress term is positive throughout the channel and of negligible amount for both Schmidt numbers. The contribution χ_{mc}^{+} of the cross-stress terms shows positive and negative values. Hence, these terms allow for backscatter of energy as already observed for incompressible flow in Section 4.8.2. Due to the presence of the cross-stress terms, the contribution of the SUPG term for $\mathrm{Sc} = 1$ is reduced in the core of the channel compared to the SPGSM in Figure 5.10, which only contains this term. For $\mathrm{Sc} = 25$, diffusion is mainly introduced by the SUPG term. While the SUPG term is active throughout the channel, the cross-stress terms mainly act in the near-wall region by increasing the subgrid-scale diffusion χ_{av}^{+}.

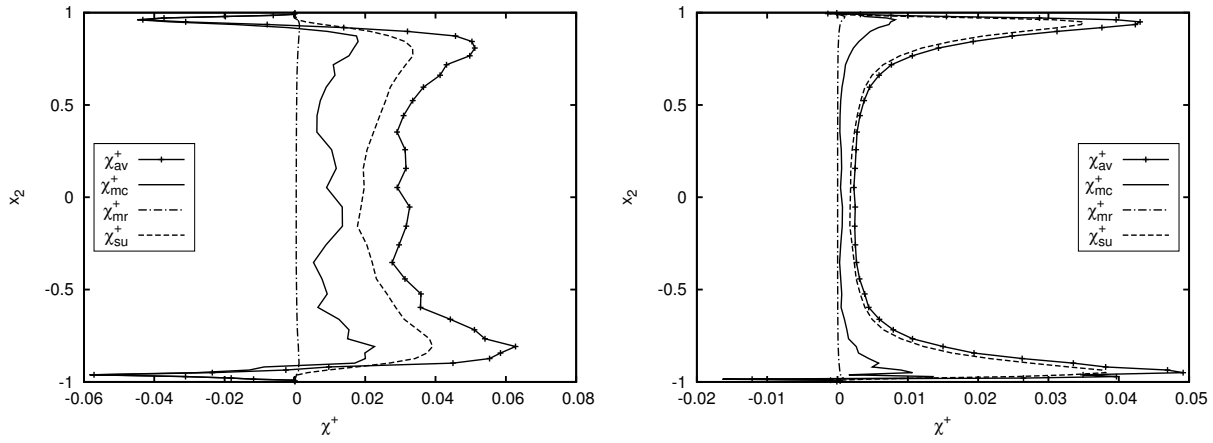

Figure 5.11: Contributions of the individual constituents of the AVM^4 to the mean subgrid-scale diffusion χ^+_{av} for passive-scalar mixing at $\text{Sc} = 1$ (left) and $\text{Sc} = 25$ (right) in turbulent channel flow using 48^3 elements.

5.6.2 High-Schmidt-Number Mixing at $\text{Sc} \gg 1$

Preliminary Investigations. For high-Schmidt-number mixing, there is a lack of numerical and experimental examples providing reference data in literature, particularly for wall-bounded flows due to enormous resolution requirements to appropriately capture the diffusive sublayer. Therefore, aside from turbulent channel flow with passive-scalar mixing, results from preliminary investigations of the proposed method for forced homogeneous isotropic turbulence with passive-scalar mixing at $\text{Sc} = 400$ and $\text{Re} = 20$, where the Reynolds number is defined as $\text{Re} = 1/\nu$, are also shown here for the high-Schmidt-number mixing. An elaborate investigation of the performance of the multifractal subgrid-scale modeling approach for passive-scalar mixing in homogeneous isotropic turbulence was conducted by Burton [50] in the context of the nLES method.

Forced homogeneous isotropic turbulence is computed in a periodic box of size $2\pi \times 2\pi \times 2\pi$, which is discretized using 32 uniformly distributed elements in each spatial direction. A source term on the right-hand side of the momentum equation (3.1) and the convection-diffusion equation (5.10) accounts for dissipation and diffusion, such that the shape of the spectra is preserved. Forcing is constructed such that only large scales (i.e., $k \leq 2$) are affected. The initial velocity and scalar field are randomized to phase and consistent with an $E(k) \sim k^{-5/3}$ and $E_\phi(k) \sim k^{-1}$ scaling, respectively; see also Section 4.7 for further details on the initialization and forcing of the velocity field, which may be readily transferred to the scalar field. The time-step length Δt is set to 0.1. After an initial transient, samples of the three-dimensional kinetic-energy spectrum and the scalar-variance spectrum are collected until they are converged. Concerning the AVM^4, the near-wall limit is not required for the present configuration, and $C^{\text{B}}_{\text{sgs}}$ and $C^{\text{D}}_{\text{sgs}}$ are set to 0.1. The element Reynolds number is estimated based on the resolved velocity, and $c_\nu = 0.1$ is assumed, as usual. As illustrated in Figure 5.12, the kinetic-energy spectrum is fully resolved. The scalar-variance spectrum shows the expected viscous-convective range scaling, which is also indicated in the diagram.

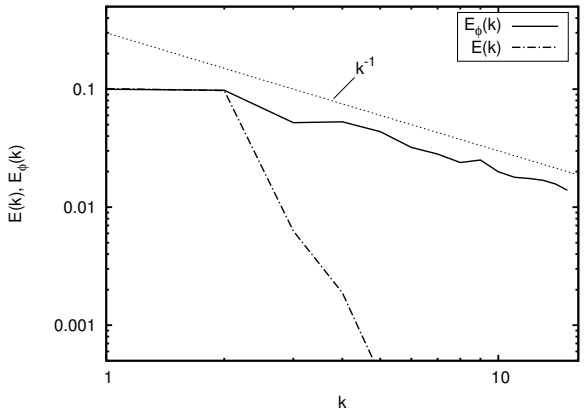

Figure 5.12: Mean three-dimensional kinetic-energy spectrum $E(k)$ and scalar-variance spectrum $E_\phi(k)$ for passive-scalar mixing at Sc $=$ 400 in forced homogeneous isotropic turbulence at Re $= 20$.

Problem Setup. Turbulent channel flow at $\mathrm{Re}_\tau = 180$ and Sc $=$ 1000 is considered an appropriate wall-bounded test for mixing at high Schmidt number. With respect to domain size, initial and boundary conditions, time-step length as well as sampling, the problem setup is chosen analogously to the one of the low-to-moderate Schmidt-number examples. However, due to the higher resolution requirements near the walls, different spatial discretizations are used compared to the previous configurations. Here, two discretizations with 64 and 128 elements in each spatial direction are considered. Parameter C_G of the hyperbolic mesh stretching function (4.61) is set to 2.9. A summary of the details of the discretizations is provided in Table 5.2. For the finer discretization, it is expected that the velocity field is almost resolved.

Table 5.2: Mesh parameters for passive-scalar mixing at Sc $= 1000$ in turbulent channel flow: number of elements and non-dimensional element lengths h_i^+.

no. elements	h_1^+	$h_{2,\mathrm{min}}^+$	$h_{2,\mathrm{max}}^+$	h_3^+
64^3	17.67	0.22	16.37	8.84
128^3	8.84	0.10	8.20	4.42

Analysis of Model Parameters. The model parameters of the multifractal subgrid-scale modeling are also investigated first for this high-Schmidt-number case. Therefore, the mean values of the number of cascade steps $\langle \mathcal{N}_\mathbf{u} \rangle$ and $\langle \mathcal{N}_\phi \rangle$, the coefficients $\langle C_\mathrm{sgs}^\mathrm{Bnw} \rangle$ and $\langle C_\mathrm{sgs}^\mathrm{Dc} \rangle$ as well as the resulting parameters $\langle B \rangle$ and $\langle D \rangle$ are displayed in Figure 5.13. Again, $\langle \mathcal{N}_\mathbf{u} \rangle$ and $\langle \mathcal{N}_\phi \rangle$ decrease with increasing resolution. Near the wall, $\langle \mathcal{N}_\mathbf{u} \rangle$ approaches zero, then increasing towards the middle of the channel. The region of vanishing $\langle \mathcal{N}_\mathbf{u} \rangle$ increases when refining the resolution. Due to the higher near-wall resolution of the discretization with 64 elements in each spatial direction for this configuration compared to the one used for the low-to-medium-Schmidt-number configurations, $\langle \mathcal{N}_\mathbf{u} \rangle$ is able to vanish throughout the near-wall region. In contrast, $\langle \mathcal{N}_\phi \rangle$ increases, starting right from the wall. This means that, in the near-wall region, the velocity is fully re-

solved, and k_h is located in the viscous-convective range. Towards the channel center, k_h enters the inertial-convective range, meaning that both resolutions are explicitly covered by this configuration. For $\langle C_{\text{sgs}}^{\text{Bnw}} \rangle$ and $\langle C_{\text{sgs}}^{\text{Dc}} \rangle$, the same statements as for the low-to-medium-Schmidt-number configurations hold. Analogously to $\langle \mathcal{N}_{\mathbf{u}} \rangle$, $\langle B \rangle$ vanishes in the near-wall region. In contrast to the low-to-medium-Schmidt-number cases, $\langle D \rangle$ does not fall off at the walls, but shows a constant level, where $\langle B \rangle$ goes to zero. This behavior is related to the relatively high values for $\langle \mathcal{N}_{\phi} \rangle$ at the wall owing to $\text{Sc} = 1000$. The two levels in the curve for $\langle D \rangle$ reflect the occurrence of the viscous-convective range near the wall and the inertial-convective range towards the channel center in the subgrid-scale modeling procedure, since $\gamma = 1/3$ leads to a higher asymptotic value for $\langle D \rangle$ than $\gamma = 1$, as displayed in Figure 5.3.

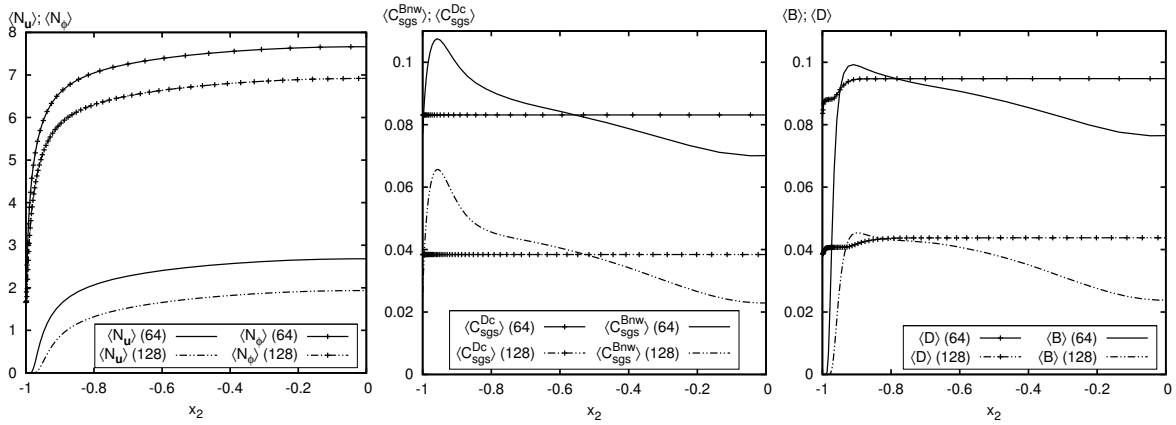

Figure 5.13: Mean values of the number of cascade steps $\langle \mathcal{N}_{\mathbf{u}} \rangle$ and $\langle \mathcal{N}_{\phi} \rangle$, coefficients $\langle C_{\text{sgs}}^{\text{Bnw}} \rangle$ and $\langle C_{\text{sgs}}^{\text{Dc}} \rangle$ as well as parameters $\langle B \rangle$ and $\langle D \rangle$ for passive-scalar mixing at $\text{Sc} = 1000$ in turbulent channel flow using 64^3 and 128^3 elements.

Statistical Results. With respect to the subsequent discussion of the statistical results for the scalar field, the mean streamwise velocity and the root-mean-square velocities are displayed in Figure 5.14 for the finer discretization. Although the DSM still slightly deviates from DNS, all methods are overall quite close to the reference data, as expected. Figure 5.15 shows ϕ^+, rms ϕ^+, $\langle u_1' \phi' \rangle^+$ and $\langle u_2' \phi' \rangle^+$ for both discretizations and all methods. For the coarser discretization, notable differences between the methods, as already observed for the low-to-moderate Schmidt-number cases, occur. As before, the AVM^4 provides more accurate results for ϕ^+, rms ϕ^+ and $\langle u_1' \phi' \rangle^+$ than the SPGSM and RBVMM, which in turn yield better values than the DSM. Again, the DSM also shows a less steep gradient for $\langle u_2' \phi' \rangle^+$ than the other methods, which provide very similar results for this value. Except for $\langle u_2' \phi' \rangle^+$, which is still somewhat underpredicted by the DSM, the results obtained with the different methods are relatively close to each other for the finer discretization, indicating that all methods are almost converged. Hence, these results are considered as reference values for the subsequent investigation. The advantage of the AVM^4 becomes apparent by directly comparing the results for the AVM^4 obtained with the two discretizations as given in Figure 5.16. This juxtaposition of the results reveals that the AVM^4 is able to reliably capture all statistical quantities already for the coarser discretization, in contrast to the methods included for comparison.

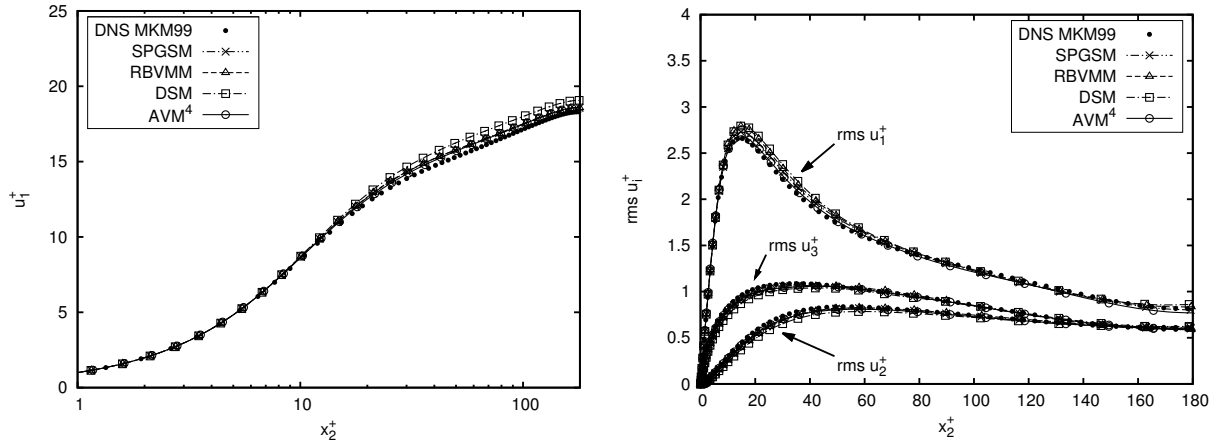

Figure 5.14: Mean streamwise velocity u_1^+ and root-mean-square velocities rms u_i^+ for turbulent channel flow at $\mathrm{Re}_\tau = 180$ using 128^3 elements.

5.6.3 Transfer Coefficient

The evaluation of the non-dimensional transfer coefficient, which describes the transfer of a scalar quantity from the wall to the fluid, constitutes an essential test to validate the performance of a subgrid-scale modeling approach for passive-scalar mixing in the near-wall region of the flow. The non-dimensional transfer coefficient is defined as

$$K^+ = \frac{\kappa \frac{\partial \langle \phi \rangle}{\partial x_2}\big|_\mathrm{W}}{u_\tau \left(|\phi_\mathrm{W}| - \phi_\mathrm{C} \right)} = \frac{\phi_\tau}{|\phi_\mathrm{W}|}, \tag{5.60}$$

where ϕ_C is the mean centerline scalar quantity and ϕ_W its value at the wall. To assess the near-wall behavior of the AVM^4, investigations analogous to the ones presented by Hickel *et al.* [147] are conducted. Apart from the evaluation of the turbulent transfer of a scalar quantity from the walls to the fluid, the transfer coefficient also allows for examining the asymptotic behavior of a subgrid-scale modeling approach towards the high-Schmidt-number regime and, thereby, constitutes another possible means to validate the modeling approach for high Schmidt numbers. The results obtained with the AVM^4 are compared to correlations for high Schmidt numbers deduced from experimental results and theoretical considerations. From a theoretical point of view, a correlation of the form

$$K^+ \sim \mathrm{Sc}^{-\frac{2}{3}} \quad \text{or} \quad \sim \mathrm{Sc}^{-\frac{3}{4}}$$

can be derived; see, e.g., Shaw and Hanratty [286] and references therein. A comprehensive experimental study was presented by Shaw and Hanratty [286]. In that study, turbulent pipe flow with scalar mixing at $693 \leq \mathrm{Sc} \leq 37\,200$ was considered for Reynolds numbers ranging from $\mathrm{Re} = 16\,400$ to $34\,000$. Shaw and Hanratty [286] provided the correlations

$$K^+ = 0.0649\,\mathrm{Sc}^{-\frac{2}{3}} \quad \text{and} \quad K^+ = 0.132\,\mathrm{Sc}^{-\frac{3}{4}}$$

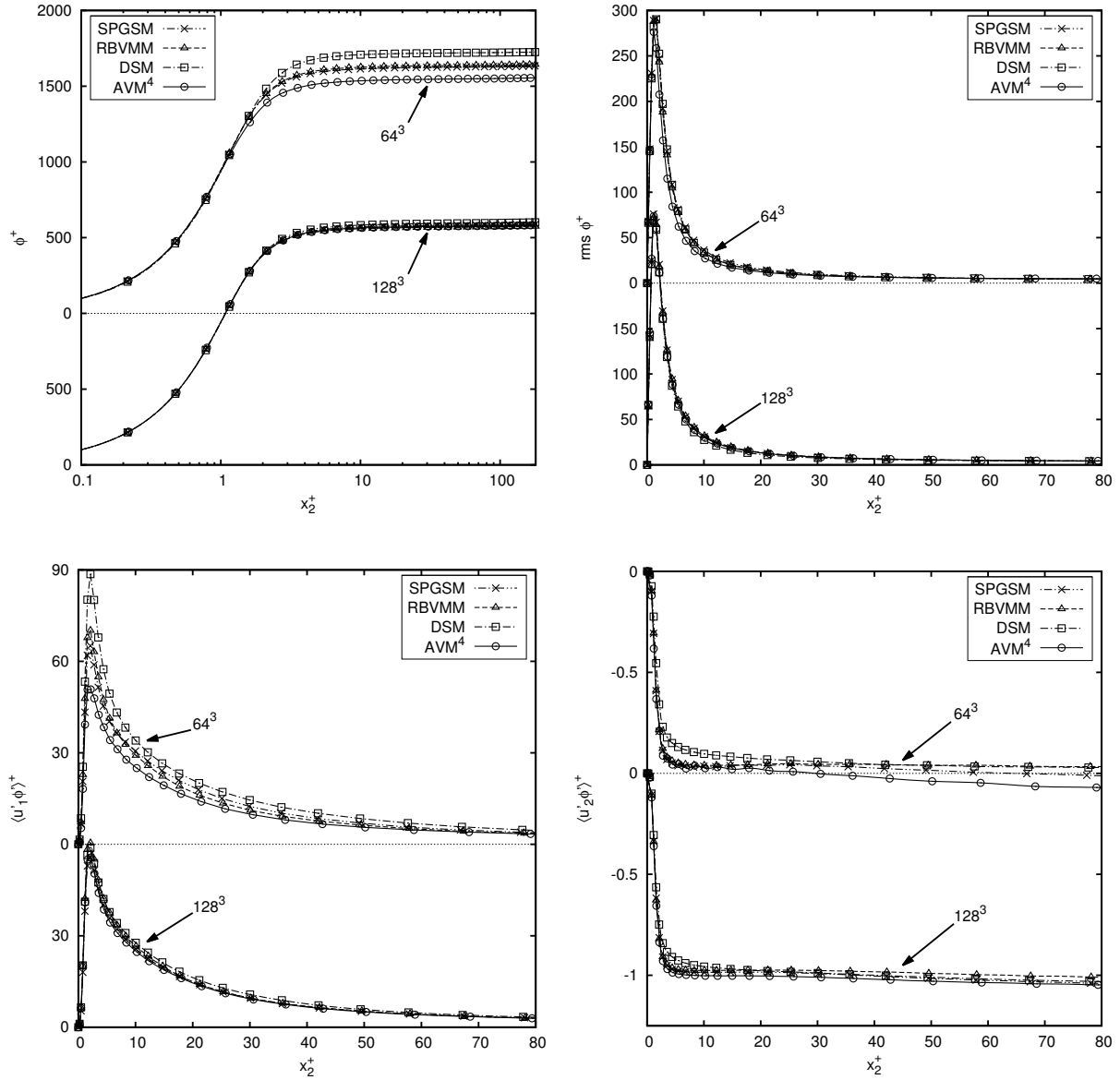

Figure 5.15: Convergence study of mean scalar ϕ^+, root-mean-square scalar rms ϕ^+, streamwise velocity-scalar fluctuations $\langle u_1'\phi'\rangle^+$ and wall-normal velocity-scalar fluctuations $\langle u_2'\phi'\rangle^+$ for passive-scalar mixing at $\mathrm{Sc} = 1000$ in turbulent channel flow using 64^3 and 128^3 elements.

for the two theoretical exponents. However, it was found in that study that the dependence

$$K^+ = 0.0889\,\mathrm{Sc}^{-0.704},$$

where the exponent lies between $-2/3$ and $-3/4$, gave a better approximation of the measurements. Here, the results obtained with the AVM^4 are compared to both the correlation suggested by Shaw and Hanratty [286] as well as the alternative fit to the theoretical exponent -2/3, which is also strongly supported in literature (see, e.g., Kader and Yaglom [166]). The given correla-

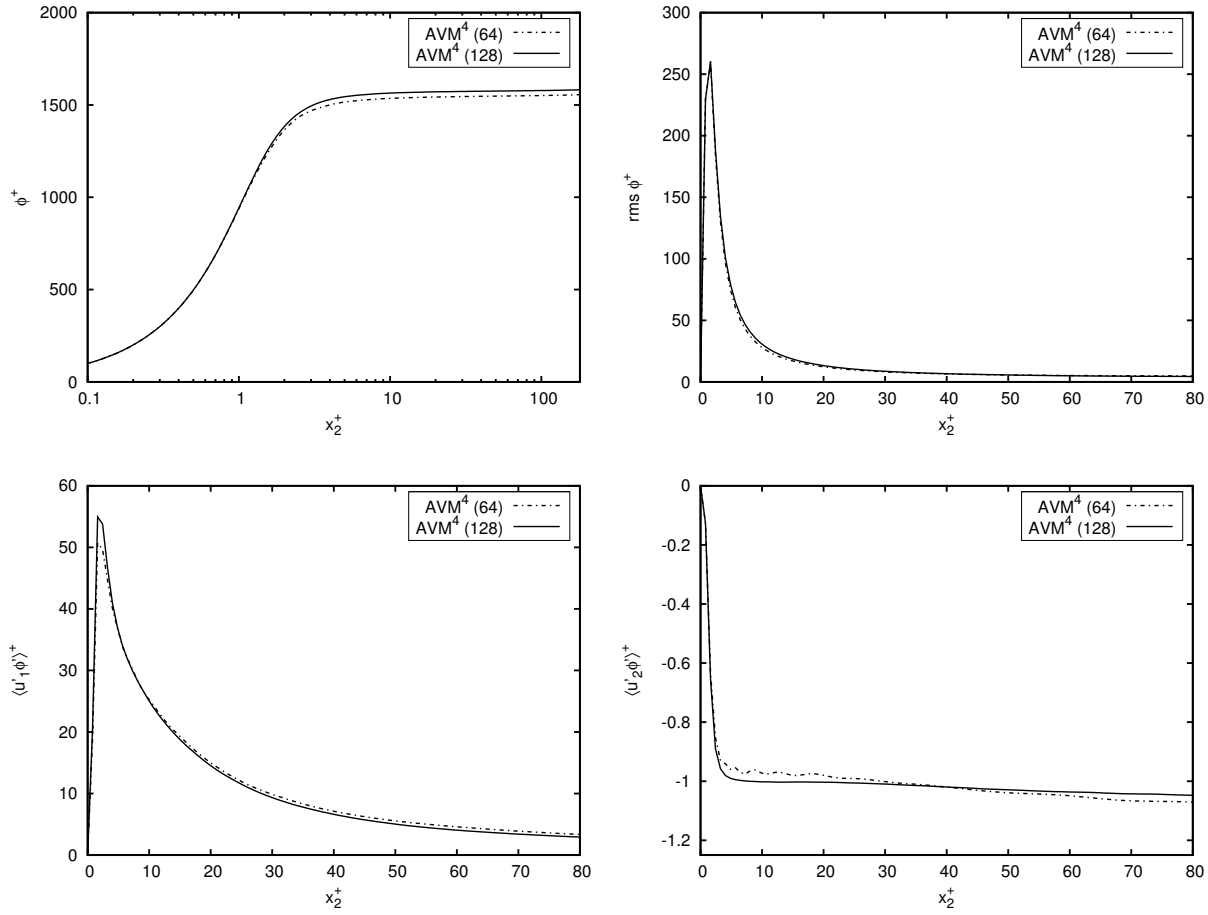

Figure 5.16: Separate convergence study for the AVM^4 of mean scalar ϕ^+, root-mean-square scalar rms ϕ^+, streamwise velocity-scalar fluctuations $\langle u'_1\phi'\rangle^+$ and wall-normal velocity-scalar fluctuations $\langle u'_2\phi'\rangle^+$ for passive-scalar mixing at Sc $= 1000$ in turbulent channel flow using 64^3 and 128^3 elements.

tions are only valid for moderate and high Schmidt numbers, since, for low Schmidt numbers, K^+ is also affected by the Reynolds number (see, e.g., Schwertfirm and Manhart [278] as well as Kader and Yaglom [166]). Again, Schmidt numbers up to 1000 are considered. All simulations are conducted with the medium discretization of Section 5.6.1, which is similar to the one used by Hickel *et al.* [147] and allows for a direct comparison. The transfer coefficient depending on the Schmidt number is depicted in Figure 5.17. Besides DNS data given in Schwertfirm and Manhart [278], reference data, which were additionally used in Hickel *et al.* [147] and indicated therein to originate from semi-DNS for Sc $= 100$ and 1000 provided by Schwertfirm and Manhart, are also shown. They are marked by "sDNS SM05". Furthermore, results from several other numerical studies are also included for comparison in Figure 5.17. In a study by Calmet and Magnaudet [55], LES of passive-scalar mixing in a turbulent channel flow at a higher friction Reynolds number $\mathrm{Re}_\tau = 640$ was performed. Therein, a somewhat higher resolution was used, and Schmidt numbers Sc $= 1$, 100 and 200 were investigated. Results extracted from that study are marked by "LES CM97". A Lagrangian technique was used by Papavassiliou

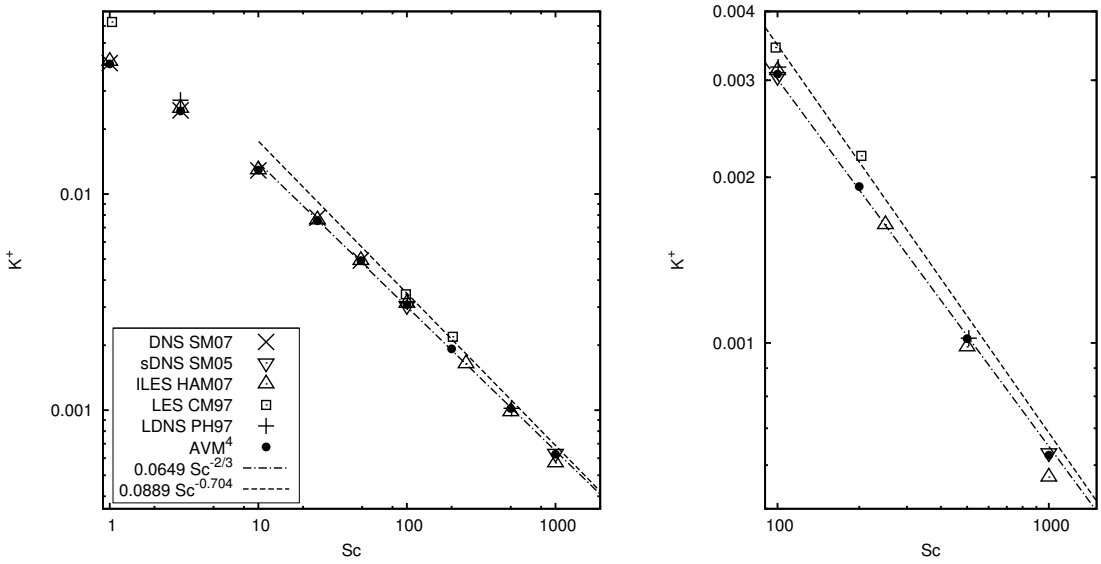

Figure 5.17: Transfer coefficient K^+ of passive-scalar mixing at various Schmidt numbers in turbulent channel flow obtained with the AVM^4 using 48^3 elements including a closeup view of the high-Schmidt-number values.

and Hanratty [244] to simulate passive-scalar mixing at various Schmidt numbers in turbulent channel flow at $\mathrm{Re}_\tau = 150$, which is relatively close to the present one. Papavassiliou and Hanratty [244] discretized the channel domain of size $4\pi\delta_\mathrm{c} \times 2\delta_\mathrm{c} \times 2\pi\delta_\mathrm{c}$ by $128 \times 65 \times 128$ grid cells and applied therefore a higher resolution than the present one. The respective results are denoted by "LDNS PH97". For Schmidt numbers $\mathrm{Sc} \leq 10$, K^+ deviates from the correlations as expected, since the transfer coefficient also depends on the Reynolds number in this Schmidt number range. While more advanced correlations taking also low Schmidt numbers into account (see, e.g., Schwertfirm and Manhart [278] and Kader and Yaglom [166]) predict decreasing transfer coefficients with increasing Reynolds numbers, the value extracted from the study of Calmet and Magnaudet [55] for $\mathrm{Re}_\tau = 640$ suggests the opposite trend with respect to the AVM^4 and the value taken from Papavassiliou and Hanratty [244]. All results obtained with the AVM^4 agree well with the DNS and semi-DNS data and perfectly reproduce the experimental correlation based on the theoretical exponent for the higher Schmidt numbers up to $\mathrm{Sc} = 1000$. In contrast, Hickel *et al.* [147] stated that the ALDM-ILES followed the correlation only up to $\mathrm{Sc} = 500$, as may also be seen from Figure 5.17. The observed agreement for the AVM^4 with the semi-DNS value as well as the correlation at $\mathrm{Sc} = 1000$ is particularly remarkable, since, for this high Schmidt number, the medium discretization, which nearly resolves the velocity field in the viscous sublayer, is rather coarse with respect to the scalar field and hardly allows for resolving the mean scalar gradient at the wall. This high-Schmidt-number behavior further confirms the excellent performance of the AVM^4 for $\mathrm{Sc} \gg 1$ already observed in Section 5.6.2. In summary, the presented results demonstrate that the proposed method yields accurate results for wall-bounded turbulent flow with passive-scalar mixing within the considered Schmidt number range. As explained in Section 5.3.6, an additional modification for wall-bounded flow is not required in the scalar field to obtain reasonable results, since the anisotropy is already sufficiently captured by the velocity field.

6

Extension II: Turbulent Variable-Density Flow at Low Mach Number

The low-Mach-number limit of the compressible Navier-Stokes equations may be used to describe a variety of turbulent variable-density flows, which cover a wide range of challenging applications such as turbulent combustion phenomena (see, e.g., the textbooks by Cant and Mastorakos [57] and Peters [246]). A comprehensive derivation of the equation system may be found, e.g., in Fedorchenko [95], Müller [226] and Rehm and Baum [263] and with emphasis on combustion, e.g., in Majda and Sethian [205]. Applications of LES using the low-Mach-number limit of the compressible Navier-Stokes equations or an alternative description, for instance, the mixture-fraction formulation, to simulate non-reactive and/or reactive variable-density flows are rather rarely considered in literature; see, e.g., Desjardins *et al.* [81], Lessani and Papalexandris [187] and Wang *et al.* [327]. Applications of the VMM to LES of turbulent variable-density flow at low Mach number can be found based on a three-scale separation, e.g., in Gravemeier and Wall [122] and based on a residual-based two-scale formulation, e.g., in Gravemeier and Wall [123]. Recently, another residual-based VMM with time-dependent subgrid scales and incorporation of those subgrid scales into all non-linear terms arising in the VMM, including the evaluation of the physical parameters, was proposed by Avila *et al.* [10].

The present chapter develops the AVM^4 for LES of turbulent variable-density flow at low Mach number. For this purpose, the generalization and application of the multifractal subgrid-scale modeling approach to turbulent variable-density flow is discussed. In contrast to the study by Burton [52], where the multifractal subgrid-scale modeling approach was applied within a mixture-fraction formulation to examine turbulent Rayleigh-Taylor instabilities, the present chapter reports on the first application of the multifractal subgrid-scale modeling approach to the low-Mach-number limit of the compressible Navier-Stokes equations based on a temperature formulation of the energy equation. The remainder of this chapter is organized as follows. First, the low-Mach-number equation system and its variational multiscale formulation are presented. Then, subgrid-scale modeling for LES of weakly compressible turbulent flow is addressed, and impacts on the multifractal subgrid-scale modeling approach are discussed. Based on these considerations, the AVM^4 for LES of turbulent variable-density flow at low Mach number is derived. Finally, the proposed method is validated for two numerical examples. The results obtained for turbulent flow in a channel with a heated and a cooled wall indicate the excellent prediction quality achievable by the proposed method also for turbulent variable-density flow at low Mach number. The investigation of turbulent flow over a backward-facing step with heating demonstrates its applicability to a substantially more demanding configuration. This chapter summarizes work published in Rasthofer *et al.* [261].

6.1 The Low-Mach-Number Equation System

The Mach number is defined as

$$\mathrm{Ma} = \frac{U}{c}, \tag{6.1}$$

where U is a characteristic velocity of the flow and c the speed of sound in the fluid, and provides a relation between inertia and compressibility forces. The low-Mach-number limit of the compressible Navier-Stokes equations is obtained by an asymptotic expansion of the problem variables as power series of the parameter $\gamma \mathrm{Ma}^2 \ll 1$, which depends on the specific heat ratio γ and the Mach number and is assumed small. This procedure leads to a decomposition of the pressure such that a thermodynamic pressure $p_{\mathrm{the}}(t)$ and a hydrodynamic pressure $p_{\mathrm{hyd}}(\mathbf{x}, t)$ are explicitly distinguished. The thermodynamic pressure is constant in space, but may vary in time. Analogously to the pressure in incompressible flow, the hydrodynamic pressure imposes a constraint on the divergence of the velocity and is thus determined by the continuity equation. Moreover, this process includes the removal of acoustic effects. As a result, the low-Mach-number limit of the compressible Navier-Stokes equations allows for substantial density variations in the presence of large temperature differences, while exhibiting the same mathematical structure as the incompressible Navier-Stokes equations, such that the respective equations can be solved by the same numerical methods. Variable-density flow at low Mach number in the domain Ω is thus governed by the following form of the conservation equations of mass, momentum and energy, the latter expressed in terms of temperature:

$$\frac{\partial \rho}{\partial t} + \nabla \cdot (\rho \mathbf{u}) = 0 \qquad \text{in } \Omega \times]0, t_{\mathrm{end}}[\,, \tag{6.2}$$

$$\rho \frac{\partial \mathbf{u}}{\partial t} + \rho \mathbf{u} \cdot \nabla \mathbf{u} + \nabla p_{\mathrm{hyd}} - \nabla \cdot (2\mu \boldsymbol{\varepsilon}^*(\mathbf{u})) = \rho \mathbf{f} \qquad \text{in } \Omega \times]0, t_{\mathrm{end}}[\,, \tag{6.3}$$

$$\rho \frac{\partial T}{\partial t} + \rho \mathbf{u} \cdot \nabla T - \nabla \cdot \left(\frac{\lambda}{c_p} \nabla T \right) = \frac{1}{c_p} \frac{\mathrm{d} p_{\mathrm{the}}}{\mathrm{d} t} \qquad \text{in } \Omega \times]0, t_{\mathrm{end}}[\,. \tag{6.4}$$

Momentum and energy equation are given here in convective form. The end of the considered time period is specified by t_{end}. Furthermore, $\rho(\mathbf{x}, t)$ denotes the density, $\mathbf{u}(\mathbf{x}, t)$ the velocity, $\mu(\mathbf{x}, t)$ the dynamic viscosity, $\mathbf{f}$ a potential volume force vector, $T(\mathbf{x}, t)$ the temperature, $\lambda(\mathbf{x}, t)$ the thermal conductivity and c_p the specific heat capacity at constant pressure, which is assumed constant. The deviatoric part of the rate-of-deformation tensor $\boldsymbol{\varepsilon}(\mathbf{u})$ (see equation (2.3)) is defined as

$$\boldsymbol{\varepsilon}^*(\mathbf{u}) = \boldsymbol{\varepsilon}(\mathbf{u}) - \frac{1}{3} (\nabla \cdot \mathbf{u}) \mathbf{I}, \tag{6.5}$$

where $\mathbf{I}$ is the identity tensor.

At time $t = 0$, velocity field $\mathbf{u}$ and temperature field T are prescribed as

$$\mathbf{u} = \mathbf{u}_0 \qquad \text{in } \Omega \times \{0\}, \tag{6.6}$$

$$T = T_0 \qquad \text{in } \Omega \times \{0\}. \tag{6.7}$$

On the boundary $\partial\Omega$, Dirichlet and Neumann boundary conditions for the momentum equation (6.3) are given as

$$\mathbf{u} = \mathbf{u}_{\mathrm{D}} \qquad \text{on } \Gamma_{\mathrm{D},\mathbf{u}} \times]0, t_{\mathrm{end}}[\,, \tag{6.8}$$

$$\left.\begin{aligned} (-p_{\mathrm{hyd}}\mathbf{I} + 2\mu\boldsymbol{\varepsilon}^*(\mathbf{u})) \cdot \mathbf{n} &= \mathbf{h}_{\mathbf{u}} \quad \text{if } \mathbf{u}\cdot\mathbf{n} \geqslant 0 \\ -\rho\mathbf{u}\,(\mathbf{u}\cdot\mathbf{n}) + (-p_{\mathrm{hyd}}\mathbf{I} + 2\mu\boldsymbol{\varepsilon}^*(\mathbf{u})) \cdot \mathbf{n} &= \mathbf{h}_{\mathbf{u}} \quad \text{if } \mathbf{u}\cdot\mathbf{n} < 0 \end{aligned}\right\} \quad \text{on } \Gamma_{\mathrm{N},\mathbf{u}} \times]0, t_{\mathrm{end}}[\,, \tag{6.9}$$

and for the energy equation (6.4) as

$$T = T_{\mathrm{D}} \qquad \text{on } \Gamma_{\mathrm{D},T} \times]0, t_{\mathrm{end}}[\,, \tag{6.10}$$

$$\left.\begin{aligned} \tfrac{\lambda}{c_p}\nabla T \cdot \mathbf{n} &= h_T \quad \text{if } \mathbf{u}\cdot\mathbf{n} \geqslant 0 \\ -\rho T\,(\mathbf{u}\cdot\mathbf{n}) + \tfrac{\lambda}{c_p}\nabla T \cdot \mathbf{n} &= h_T \quad \text{if } \mathbf{u}\cdot\mathbf{n} < 0 \end{aligned}\right\} \quad \text{on } \Gamma_{\mathrm{N},T} \times]0, t_{\mathrm{end}}[\,, \tag{6.11}$$

where $\mathbf{n}$ is the outer unit normal vector on the boundary $\partial\Omega$. Moreover, for each equation, it is assumed that $\Gamma_{\mathrm{D}} \cap \Gamma_{\mathrm{N}} = \emptyset$ and $\Gamma_{\mathrm{D}} \cup \Gamma_{\mathrm{N}} = \partial\Omega$. To account for locally recirculating flow that may occur at the outflow boundary of the domain Ω for turbulent flows, inflow and outflow parts of the Neumann boundary have to be distinguished as described in Section 3.2 for the momentum equation. Analogously for the energy equation, the diffusive flux is prescribed on the outflow part $\Gamma^{\mathrm{out}}_{\mathrm{N},T}(t) := \{\mathbf{x} \in \Gamma_{\mathrm{N},T} | \mathbf{u}(\mathbf{x},t)\cdot\mathbf{n}(\mathbf{x}) \geqslant 0\}$ and the total flux on a potential inflow part $\Gamma^{\mathrm{in}}_{\mathrm{N},T}(t) := \{\mathbf{x} \in \Gamma_{\mathrm{N},T} | \mathbf{u}(\mathbf{x},t)\cdot\mathbf{n}(\mathbf{x}) < 0\}$, with $\Gamma^{\mathrm{out}}_{\mathrm{N},T} \cap \Gamma^{\mathrm{in}}_{\mathrm{N},T} = \emptyset$ and $\Gamma^{\mathrm{out}}_{\mathrm{N},T} \cup \Gamma^{\mathrm{in}}_{\mathrm{N},T} = \Gamma_{\mathrm{N},T}$.

Continuity and momentum equation are coupled to the energy equation via the equation of state for an ideal gas,

$$\rho = \frac{p_{\mathrm{the}}}{RT}, \tag{6.12}$$

determining the density ρ. The gas constant is denoted by R. Using the equation of state (6.12), the continuity equation (6.2) may be reformulated as

$$\nabla\cdot\mathbf{u} - \frac{1}{T}\left(\frac{\partial T}{\partial t} + \mathbf{u}\cdot\nabla T\right) = -\frac{1}{p_{\mathrm{the}}}\frac{\mathrm{d}p_{\mathrm{the}}}{\mathrm{d}t} \qquad \text{in } \Omega \times]0, t_{\mathrm{end}}[\,. \tag{6.13}$$

Moreover, the dynamic viscosity μ is assumed to depend on T according to Sutherland's law:

$$\mu = \left(\frac{T}{T_{\mathrm{ref}}}\right)^{\frac{3}{2}}\left(\frac{T_{\mathrm{ref}} + S}{T + S}\right)\mu_{\mathrm{ref}}, \tag{6.14}$$

where T_{ref} is a reference temperature, S the Sutherland constant and μ_{ref} a reference dynamic viscosity. The thermal conductivity λ, likewise depending on T, can be expressed as

$$\lambda = \frac{c_p\mu}{\mathrm{Pr}}, \tag{6.15}$$

where Pr denotes the Prandtl number, which is assumed constant. The Prandtl number estimates the ratio of kinematic viscosity $\nu = \mu/\rho$ and thermal diffusivity $a = \lambda/(\rho c_p)$ and is the analog to the Schmidt number in the context of heat transfer.

Concerning the determination of the thermodynamic pressure, several situations need to be distinguished in general. If the considered system is open to the ambient, p_{the} is also constant in time and equal to the external pressure. For closed systems that do not experience the external pressure, the thermodynamic pressure depends on t and may be determined from global conservation principles over the domain Ω, exploiting that p_{the} is constant in space. Whether a system is considered as open or closed depends on the boundary conditions for the momentum equation. Open systems exhibit a Neumann boundary (i.e., $\Gamma_{\text{N},\mathbf{u}} \neq \emptyset$), whereas closed systems possess a pure Dirichlet boundary (i.e., $\Gamma_{\text{N},\mathbf{u}} = \emptyset$). With respect to the numerical examples considered in this thesis, the evaluation of p_{the} is restricted to two particular configurations: an open system with Neumann outflow boundary and a closed system without in- or outflow. Since the total mass has to remain constant in the latter case, p_{the} may be obtained at each time via an integral form of the equation of state (6.12):

$$p_{\text{the}} = \frac{R \int\limits_{\Omega} \rho_0 \mathrm{d}\Omega}{\int\limits_{\Omega} T^{-1} \mathrm{d}\Omega}, \tag{6.16}$$

where $\rho_0 = \rho(T_0, p_{\text{the},0})$ denotes the initial density. For both cases, the thermodynamic pressure is initially set to $p_{\text{the}}(t = 0) = p_{\text{the},0}$. For further discussion on the evaluation of p_{the} depending on the encountered situation, the reader is referred, e.g., to Beccantini *et al.* [25], Gravemeier and Wall [123] and Lessani and Papalexandris [187] as well as references therein.

6.2 Variational Multiscale Formulation of the Low-Mach-Number Equation System

The derivation of the variational multiscale formulation of the low-Mach-number equation system, considered here in the form using equations (6.13), (6.3) and (6.4), parallels the ones for the incompressible Navier-Stokes equations and the convection-diffusion equation, thoroughly presented in Sections 3.2 and 5.2, respectively. Therefore, merely the basic steps are outlined in the following. For a step-by-step derivation, the reader is referred to Rasthofer *et al.* [261].

Hydrodynamic pressure, velocity and temperature are decomposed via a variational projection into resolved and unresolved parts as

$$p_{\text{hyd}} = p_{\text{hyd}}^h + \hat{p}_{\text{hyd}}, \tag{6.17}$$

$$\mathbf{u} = \mathbf{u}^h + \hat{\mathbf{u}}, \tag{6.18}$$

$$T = T^h + \hat{T}. \tag{6.19}$$

Proceeding as described in Sections 3.2 and 5.2 and assuming appropriate finite element solution function spaces $\mathcal{S}_p^h$ for p_{hyd}^h, $\mathcal{S}_{\mathbf{u}}^h$ for $\mathbf{u}^h$ and $\mathcal{S}_T^h$ for T^h as well as finite element weighting function spaces $\mathcal{V}_p^h$ for the discrete pressure weighting function q^h, $\mathcal{V}_{\mathbf{u}}^h$ for the discrete velocity weighting function $\mathbf{v}^h$ and $\mathcal{V}_T^h$ for the discrete temperature weighting function w^h, the variational multiscale

formulation of the low-Mach-number equation system is obtained as follows:

$$\mathcal{B}_{\mathrm{C}}(q^h;\mathbf{u}^h,T^h)+\mathcal{B}_{\mathrm{C}}^{1,\mathrm{lin}}(q^h;\hat{\mathbf{u}},\hat{T})+\mathcal{B}_{\mathrm{C}}^{2}(q^h;\mathbf{u}^h,\hat{\mathbf{u}},T^h,\hat{T})=\ell_{\mathrm{C}}(q^h), \tag{6.20}$$

$$\mathcal{B}_{\mathrm{M}}(\mathbf{v}^h;\mathbf{u}^h,p_{\mathrm{hyd}}^h)+\mathcal{C}(\mathbf{v}^h;\mathbf{u}^h,\hat{\mathbf{u}})+\mathcal{R}(\mathbf{v}^h;\hat{\mathbf{u}})+\mathcal{B}_{\mathrm{M}}^{1,\mathrm{lin}}(\mathbf{v}^h;\hat{\mathbf{u}},\hat{p}_{\mathrm{hyd}})=\ell_{\mathrm{M}}(\mathbf{v}^h), \tag{6.21}$$

$$\mathcal{B}_{\mathrm{E}}(w^h;\mathbf{u}^h,T^h)+\mathcal{C}_{\mathrm{E}}(w^h;\mathbf{u}^h,\hat{\mathbf{u}},T^h,\hat{T})+\mathcal{R}_{\mathrm{E}}(w^h;\hat{\mathbf{u}},\hat{T})+\mathcal{B}_{\mathrm{E}}^{1,\mathrm{lin}}(w^h;\hat{T})=\ell_{\mathrm{E}}(w^h) \tag{6.22}$$

for all $(q^h,\mathbf{v}^h,w^h)\in\mathcal{V}_p^h\times\mathcal{V}_{\mathbf{u}}^h\times\mathcal{V}_T^h$. The second, third and potential fourth term on the left-hand side of each equation are not closed and have to be modeled to solve formulations (6.20) to (6.22) for $(p_{\mathrm{hyd}}^h,\mathbf{u}^h,T^h)\in\mathcal{S}_p^h\times\mathcal{S}_{\mathbf{u}}^h\times\mathcal{S}_T^h$. The compact forms $\mathcal{B}_{\mathrm{C}}(q^h;\mathbf{u}^h,T^h)$, $\mathcal{B}_{\mathrm{M}}(\mathbf{v}^h;\mathbf{u}^h,p_{\mathrm{hyd}}^h)$ and $\mathcal{B}_{\mathrm{E}}(w^h;\mathbf{u}^h,T^h)$ comprise the left-hand-side standard Galerkin terms of continuity, momentum as well as energy equation and are defined as

$$\mathcal{B}_{\mathrm{C}}(q^h;\mathbf{u}^h,T^h):=\left(q^h,\nabla\cdot\mathbf{u}^h\right)_{\Omega}-\left(q^h,\frac{1}{T^h}\frac{\partial T^h}{\partial t}\right)_{\Omega}-\left(q^h,\frac{1}{T^h}\mathbf{u}^h\cdot\nabla T^h\right)_{\Omega}, \tag{6.23}$$

$$\begin{aligned}\mathcal{B}_{\mathrm{M}}(\mathbf{v}^h;\mathbf{u}^h,p_{\mathrm{hyd}}^h):=&\left(\mathbf{v}^h,\rho_h\frac{\partial\mathbf{u}^h}{\partial t}\right)_{\Omega}+\left(\mathbf{v}^h,\rho_h\mathbf{u}^h\cdot\nabla\mathbf{u}^h\right)_{\Omega}-\left(\nabla\cdot\mathbf{v}^h,p_{\mathrm{hyd}}^h\right)_{\Omega}\\&+\left(\boldsymbol{\varepsilon}(\mathbf{v}^h),2\mu_h\boldsymbol{\varepsilon}^{*}(\mathbf{u}^h)\right)_{\Omega}-\left(\mathbf{v}^h,\rho_h\mathbf{u}^h\left(\mathbf{u}^h\cdot\mathbf{n}\right)\right)_{\Gamma_{\mathrm{N},\mathbf{u}}^{\mathrm{in}}},\end{aligned} \tag{6.24}$$

$$\begin{aligned}\mathcal{B}_{\mathrm{E}}(w^h;\mathbf{u}^h,T^h):=&\left(w^h,\rho_h\frac{\partial T^h}{\partial t}\right)_{\Omega}+\left(w^h,\rho_h\mathbf{u}^h\cdot\nabla T^h\right)_{\Omega}+\left(\nabla w^h,\frac{\lambda_h}{c_p}\nabla T^h\right)_{\Omega}\\&-\left(w^h,\rho_h T^h\left(\mathbf{u}^h\cdot\mathbf{n}\right)\right)_{\Gamma_{\mathrm{N},T}^{\mathrm{in}}}.\end{aligned} \tag{6.25}$$

The last term of the momentum and energy part arises due to the aforementioned inflow part of the respective Neumann boundary condition. The linear forms $\ell_{\mathrm{C}}(q^h)$, $\ell_{\mathrm{M}}(\mathbf{v}^h)$ and $\ell_{\mathrm{E}}(w^h)$ on the right-hand side, including the usual contributions from the Neumann boundary conditions, are given as

$$\ell_{\mathrm{C}}(q^h):=-\left(q^h,\frac{1}{p_{\mathrm{the}}}\frac{\mathrm{d}p_{\mathrm{the}}}{\mathrm{d}t}\right)_{\Omega}, \tag{6.26}$$

$$\ell_{\mathrm{M}}(\mathbf{v}^h):=\left(\mathbf{v}^h,\rho_h\mathbf{f}\right)_{\Omega}+\left(\mathbf{v}^h,\mathbf{h}_{\mathbf{u}}\right)_{\Gamma_{\mathrm{N},\mathbf{u}}}, \tag{6.27}$$

$$\ell_{\mathrm{E}}(w^h):=\left(w^h,\frac{1}{c_p}\frac{\mathrm{d}p_{\mathrm{the}}}{\mathrm{d}t}\right)_{\Omega}+\left(w^h,h_T\right)_{\Gamma_{\mathrm{N},T}}. \tag{6.28}$$

Moreover,

$$\mathcal{C}(\mathbf{v}^h;\mathbf{u}^h,\hat{\mathbf{u}}):=\left(\mathbf{v}^h,\rho_h\left(\mathbf{u}^h\cdot\nabla\hat{\mathbf{u}}+\hat{\mathbf{u}}\cdot\nabla\mathbf{u}^h\right)\right)_{\Omega}, \tag{6.29}$$

$$\mathcal{C}_{\mathrm{E}}(w^h;\mathbf{u}^h,\hat{\mathbf{u}},T^h,\hat{T}):=\left(w^h,\rho_h\left(\mathbf{u}^h\cdot\nabla\hat{T}+\hat{\mathbf{u}}\cdot\nabla T^h\right)\right)_{\Omega}, \tag{6.30}$$

are the cross-stress terms and

$$\mathcal{R}(\mathbf{v}^h;\hat{\mathbf{u}}):=\left(\mathbf{v}^h,\rho_h\hat{\mathbf{u}}\cdot\nabla\hat{\mathbf{u}}\right)_{\Omega}, \tag{6.31}$$

$$\mathcal{R}_{\mathrm{E}}(w^h;\hat{\mathbf{u}},\hat{T}):=\left(w^h,\rho_h\hat{\mathbf{u}}\cdot\nabla\hat{T}\right)_{\Omega}, \tag{6.32}$$

the subgrid-scale Reynolds-stress terms of the momentum and energy equation. The forms

$$\mathcal{B}_{\mathrm{C}}^{1,\mathrm{lin}}(q^h;\hat{\mathbf{u}},\hat{T}) := \left(q^h,\nabla\cdot\hat{\mathbf{u}}\right)_\Omega - \left(q^h,\frac{1}{T^h}\frac{\partial\hat{T}}{\partial t}\right)_\Omega, \tag{6.33}$$

$$\mathcal{B}_{\mathrm{M}}^{1,\mathrm{lin}}(\mathbf{v}^h;\hat{\mathbf{u}},\hat{p}_{\mathrm{hyd}}) := \left(\mathbf{v}^h,\rho_h\frac{\partial\hat{\mathbf{u}}}{\partial t}\right)_\Omega - \left(\nabla\cdot\mathbf{v}^h,\hat{p}_{\mathrm{hyd}}\right)_\Omega + \left(\boldsymbol{\varepsilon}(\mathbf{v}^h),2\mu_h\boldsymbol{\varepsilon}^*(\hat{\mathbf{u}})\right)_\Omega, \tag{6.34}$$

$$\mathcal{B}_{\mathrm{E}}^{1,\mathrm{lin}}(w^h;\hat{T}) := \left(w^h,\rho_h\frac{\partial\hat{T}}{\partial t}\right)_\Omega + \left(\nabla w^h,\frac{\lambda_h}{c_p}\nabla\hat{T}\right)_\Omega \tag{6.35}$$

contain the remaining linear terms in the unresolved-scale quantities. The non-linear contributions (i.e., terms resembling the cross- and subgrid-scale Reynolds-stress terms) in the continuity equation are separately given by

$$\mathcal{B}_{\mathrm{C}}^{2}(q^h;\mathbf{u}^h,\hat{\mathbf{u}},T^h,\hat{T}) := -\left(q^h,\frac{1}{T^h}\left(\hat{\mathbf{u}}\cdot\nabla T^h+\mathbf{u}^h\cdot\nabla\hat{T}+\hat{\mathbf{u}}\cdot\nabla\hat{T}\right)\right)_\Omega. \tag{6.36}$$

Density, viscosity and thermal conductivity are evaluated using the resolved temperature T^h in the equation of state (6.12) and the material laws (6.14) and (6.15). The usage of a subscript instead of a superscript illustrates that the respective quantity does not belong to any solution space $\mathcal{S}^h$, but is evaluated from the resolved temperature field T^h belonging to $\mathcal{S}_T^h$.

6.3 Impacts of the Weak Compressibility on the Multifractal Subgrid-Scale Modeling

In the multifractal subgrid-scale modeling approach for turbulent incompressible flow, derived in Chapter 4, the subgrid-scale vorticity field is recovered by a two-step cascade process and inserted into the Biot-Savart operator to obtain an expression for $\hat{\mathbf{u}}$. In incompressible flow, the law of Biot-Savart constitutes a sufficient relation to calculate the total velocity field from its derivatives. In variable-density or compressible flow in general, according to Helmholtz's decomposition, only the rotational but divergence-free part of a velocity field can be recovered by the law of Biot-Savart. Following Helmholtz's decomposition, the subgrid-scale velocity field may be divided into two parts:

$$\hat{\mathbf{u}} = \hat{\mathbf{u}}^{(\phi)} + \hat{\mathbf{u}}^{(\omega)}, \tag{6.37}$$

where $\hat{\mathbf{u}}^{(\phi)}$ is the irrotational (or potential) component and $\hat{\mathbf{u}}^{(\omega)}$ the rotational component, accounting for the complete subgrid-scale vorticity $\hat{\boldsymbol{\omega}}$:

$$\nabla\times\hat{\mathbf{u}} = \nabla\times\hat{\mathbf{u}}^{(\omega)} = \hat{\boldsymbol{\omega}}, \tag{6.38}$$

$$\nabla\times\hat{\mathbf{u}}^{(\phi)} = \mathbf{0}. \tag{6.39}$$

Moreover, the requirement of being a solenoidal field is imposed on the rotational part $\hat{\mathbf{u}}^{(\omega)}$, assigning the expansion of the flow to the irrotational component:

$$\nabla \cdot \hat{\mathbf{u}} = \nabla \cdot \hat{\mathbf{u}}^{(\phi)} = \hat{b}, \tag{6.40}$$

$$\nabla \cdot \hat{\mathbf{u}}^{(\omega)} = 0, \tag{6.41}$$

where $\hat{b}$ denotes the subgrid-scale rate of expansion (or source distribution). The rotational component $\hat{\mathbf{u}}^{(\omega)}$ is obtained from the subgrid-scale vorticity $\hat{\boldsymbol{\omega}}$ via the Biot-Savart operator (2.6), representing the solution of equation (6.38):

$$\hat{\mathbf{u}}^{(\omega)}(\mathbf{x}, t) = \frac{1}{4\pi} \int \hat{\boldsymbol{\omega}}\left(\check{\mathbf{x}}, t\right) \times \frac{\mathbf{x} - \check{\mathbf{x}}}{\|\mathbf{x} - \check{\mathbf{x}}\|^3} \mathrm{d}\check{\mathbf{x}}. \tag{6.42}$$

Analogously, the irrotational component $\hat{\mathbf{u}}^{(\phi)}$ is calculated from the subgrid-scale rate of expansion $\hat{b}$ via the solution of equation (6.40):

$$\hat{\mathbf{u}}^{(\phi)}(\mathbf{x}, t) = \frac{1}{4\pi} \int \hat{b}\left(\check{\mathbf{x}}, t\right) \frac{\mathbf{x} - \check{\mathbf{x}}}{\|\mathbf{x} - \check{\mathbf{x}}\|^3} \mathrm{d}\check{\mathbf{x}}; \tag{6.43}$$

see, e.g., the textbook by Panton [243]. For turbulent incompressible flow, where $\hat{b} = 0$ as well as $\hat{\mathbf{u}}^{(\phi)} = 0$, $\hat{\mathbf{u}}^{(\omega)}$ represents the total subgrid-scale velocity field. Helmholtz's decomposition (6.37) suggests that the multifractal reconstruction of the subgrid-scale velocity in turbulent compressible flow in general should consist of two parts, recovering separately both components, $\hat{\mathbf{u}}^{(\omega)}$ as well as $\hat{\mathbf{u}}^{(\phi)}$.

Subgrid-scale modeling for LES of turbulent compressible flow is discussed in exhaustive form, e.g., in the textbook by Garnier *et al.* [108]. While additional physical phenomena, such as acoustic effects and entropy fluctuations, might come into play for turbulent compressible flows, the physics of turbulence in the low-Mach-number limit of the compressible Navier-Stokes equations are rather comparable to the ones of turbulent incompressible flow, where turbulence is exclusively driven by vorticity and local straining. In particular, turbulent variable-density flows at low Mach number are only weakly compressible and do not account for acoustic effects, since they are explicitly removed from the governing equations. The hydrodynamic pressure complies with a constraint on the divergence of the velocity similar to incompressible flow, and the equation of state degenerates to a "material law" for the density. Density variations are therefore directly linked to temperature variations. In this context, the reader is also referred to the review article by Lele [184] on turbulent compressible flow, where it was explicitly distinguished between compressibility effects associated with volume changes due to pressure changes and variable inertia effects related to heat transfer. Based on these considerations and in accordance with the literature, where variable-density extensions and modifications of models developed for turbulent incompressible flow are usually applied to low-speed flows (see, e.g., the textbook by Garnier *et al.* [108] and, in the context of RANS, the review article by Chassaing [59]), a variable-density enhancement of the AVM^4 should constitute an appropriate approach to LES of turbulent variable-density flow at low Mach number.

Therefore, recovering merely the rotational component of the subgrid-scale velocity might be considered as the essential part of the multifractal subgrid-scale velocity reconstruction procedure and is proposed for turbulent variable-density flow at low Mach number:

$$\hat{\mathbf{u}} \approx \hat{\mathbf{u}}^{(\omega)} = B\delta\mathbf{u}^h, \tag{6.44}$$

as derived in Section 4.2. Moreover, the multifractal subgrid-scale approximation for a scalar quantity $\hat{\phi}$, developed in Section 5.3, is directly transferred to $\hat{T}$:

$$\hat{T} = D\delta T^h; \tag{6.45}$$

see equations (4.27) and (5.40) for the definitions of coefficients B and D. For the sake of completeness, the following rather self-evident remarks are added:

- The element Reynolds numbers $\mathrm{Re}_h^{\mathrm{R}}$ and $\mathrm{Re}_h^{\mathrm{S}}$ involved in the multifractal subgrid-scale modeling approach extend to variable-density flow as

$$\mathrm{Re}_h^{\mathrm{R}} = \frac{\rho_h \|\mathbf{u}^h\| h}{\mu_h} \tag{6.46}$$

  and

$$\mathrm{Re}_h^{\mathrm{S}} = \frac{\rho_h \left(\boldsymbol{\varepsilon}(\mathbf{u}^h) : \boldsymbol{\varepsilon}(\mathbf{u}^h)\right)^{\frac{1}{2}} h^2}{\mu_h}; \tag{6.47}$$

  see Section 4.2.5

- The Prandtl number replaces the Schmidt number in the estimation of the number of cascade steps; see Section 5.3.5.

6.4 AVM^4 for Active Scalars

Inserting the multifractal subgrid-scale approximations for $\hat{\mathbf{u}}$ and $\hat{T}$, (6.44) and (6.45), respectively, into the cross- and subgrid-scale Reynolds-stress terms, (6.29) to (6.32), of the variational multiscale formulations (6.21) and (6.22) for the momentum and energy equation and incorporating appropriate accompanying residual-based multiscale terms, the modeled formulation is obtained as: find $(p_{\mathrm{hyd}}^h, \mathbf{u}^h, T^h) \in \mathcal{S}_p^h \times \mathcal{S}_{\mathbf{u}}^h \times \mathcal{S}_T^h$ such that

$$\begin{aligned} &\mathcal{B}_{\mathrm{C}}(q^h; \mathbf{u}^h, T^h) \\ &+ \left(\nabla q^h, \tau_{\mathrm{M}} \mathbf{r}_{\mathrm{M}}^h\right)_{\Omega^*} = \ell_{\mathrm{C}}(q^h), \end{aligned} \tag{6.48}$$

$$
\begin{aligned}
&\mathcal{B}_{\mathrm{M}}(\mathbf{v}^h;\mathbf{u}^h,p^h_{\mathrm{hyd}})\\
&+\left(\mathbf{v}^h,\rho_h\left(\mathbf{u}^h\cdot\nabla\left(B\delta\mathbf{u}^h\right)+B\delta\mathbf{u}^h\cdot\nabla\mathbf{u}^h\right)\right)_{\Omega^*}+\left(\mathbf{v}^h,\rho_h B\delta\mathbf{u}^h\cdot\nabla\left(B\delta\mathbf{u}^h\right)\right)_{\Omega^*} \qquad (6.49)\\
&+\left(\rho_h\mathbf{u}^h\cdot\nabla\mathbf{v}^h,\tau_{\mathrm{M}}\mathbf{r}^h_{\mathrm{M}}\right)_{\Omega^*}+\left(\nabla\cdot\mathbf{v}^h,\tau_{\mathrm{C}}r^h_{\mathrm{C}}\right)_{\Omega^*}=\ell_{\mathrm{M}}(\mathbf{v}^h),\\
&\mathcal{B}_{\mathrm{E}}(w^h;\mathbf{u}^h,T^h)\\
&+\left(w^h,\rho_h\left(\mathbf{u}^h\cdot\nabla\left(D\delta T^h\right)+B\delta\mathbf{u}^h\cdot\nabla T^h\right)\right)_{\Omega^*}+\left(w^h,\rho_h B\delta\mathbf{u}^h\cdot\nabla\left(D\delta T^h\right)\right)_{\Omega^*} \qquad (6.50)\\
&+\left(\rho_h\mathbf{u}^h\cdot\nabla w^h,\tau_{\mathrm{E}}r^h_{\mathrm{E}}\right)_{\Omega^*}=\ell_{\mathrm{E}}(w^h),
\end{aligned}
$$

for all $(q^h,\mathbf{v}^h,w^h)\in\mathcal{V}^h_p\times\mathcal{V}^h_{\mathbf{u}}\times\mathcal{V}^h_T$. The multifractal subgrid-scale modeling terms are given in the second line of equations (6.49) and (6.50). As a particular feature of the AVM^4, the smaller resolved scales $\delta\mathbf{u}^h$ and δT^h are obtained from the resolved scales $\mathbf{u}^h$ and T^h via scale separation based on level-transfer operators from PA-AMG as derived in Section 4.3. The residual-based multiscale terms are summarized on the left-hand side in the last line of each equation. The residual-based multiscale procedure giving rise to the PSPG term in equation (6.48), the SUPG term in equations (6.49) and (6.50) (first term in the last line of each equation) and the grad-div term in equation (6.49) (second term in the last line) is not presented in detail here, since it proceeds analogously to the derivations provided for the continuity and momentum equation in Section 3.3 and the convection-diffusion equation in Section 5.4. For elaboration in the context of the low-Mach-number equation system, the reader is referred to Rasthofer *et al.* [261]. In the residual-based multiscale terms, the discrete residuals of continuity, momentum and energy equation read

$$
r^h_{\mathrm{C}}=\nabla\cdot\mathbf{u}^h-\frac{1}{T^h}\left(\frac{\partial T^h}{\partial t}+\mathbf{u}^h\cdot\nabla T^h\right)+\frac{1}{p_{\mathrm{the}}}\frac{\mathrm{d}p_{\mathrm{the}}}{\mathrm{d}t}, \qquad (6.51)
$$

$$
\mathbf{r}^h_{\mathrm{M}}=\rho_h\frac{\partial\mathbf{u}^h}{\partial t}+\rho_h\mathbf{u}^h\cdot\nabla\mathbf{u}^h+\nabla p^h_{\mathrm{hyd}}-\nabla\cdot\left(2\mu_h\boldsymbol{\varepsilon}^*(\mathbf{u}^h)\right)-\rho_h\mathbf{f}, \qquad (6.52)
$$

$$
r^h_{\mathrm{E}}=\rho_h\frac{\partial T^h}{\partial t}+\rho_h\mathbf{u}^h\cdot\nabla T^h-\nabla\cdot\left(\frac{\lambda_h}{c_p}\nabla T^h\right)-\frac{1}{c_p}\frac{\mathrm{d}p_{\mathrm{the}}}{\mathrm{d}t}. \qquad (6.53)
$$

The definitions for the stabilization parameters τ_{M} and τ_{CD} (see equations (3.40) and (5.48), respectively), which corresponds to τ_{E}, are adapted for variable-density flow:

$$
\tau_{\mathrm{M}}=\frac{1}{\sqrt{\left(\frac{2\rho_h}{\Delta t}\right)^2+(\rho_h\mathbf{u}^h)\cdot\mathbf{G}(\rho_h\mathbf{u}^h)+C_{\mathrm{I}}\mu_h^2\mathbf{G}:\mathbf{G}}}, \qquad (6.54)
$$

$$
\tau_{\mathrm{E}}=\frac{1}{\sqrt{\left(\frac{2\rho_h}{\Delta t}\right)^2+(\rho_h\mathbf{u}^h)\cdot\mathbf{G}(\rho_h\mathbf{u}^h)+C_{\mathrm{I}}\left(\frac{\lambda_h}{c_p}\right)^2\mathbf{G}:\mathbf{G}}}. \qquad (6.55)
$$

Parameter τ_{C} depends on τ_{M} as given in equation (3.41). Concerning subgrid-scale modeling in the formulation for the continuity equation, it is remarked that $\mathcal{B}^2_{\mathrm{C}}(q^h;\mathbf{u}^h,\hat{\mathbf{u}},T^h,\hat{T})\approx 0$ is assumed in equation (6.48).

6.5 Numerical Examples

The AVM^4 is examined for turbulent channel flow with a heated and a cooled wall as well as for turbulent flow over a backward-facing step with heating.[1] Furthermore, the following statements apply to both numerical examples:

- Trilinearly-interpolated hexahedral elements are used for the numerical investigations.
- A generalized-α time-integration scheme with $\rho_\infty = 0.5$ is applied (see also Section 4.6.1 and Gravemeier and Wall [122] in the context of variable-density flow at low Mach number).
- In each time step, it is first solved for the energy equation, then for the continuity and momentum equation and another time for the energy equation. Depending on prescribed tolerances, further iterations between the two fields may be performed (see Gravemeier and Wall [122] for further details).
- For both examples, the near-wall limit developed in Section 4.8.1 is applied to the multifractal subgrid-scale modeling approach. As given in Section 4.8.1, the parameters $C_{\text{sgs}}^{\text{B}}$ and c_ν are set to 0.25 and 0.1, respectively. According to Section 5.3.6, $C_{\text{sgs}}^{\text{D}}$ is adapted to $C_{\text{sgs}}^{\text{B}}$.

The results obtained with the proposed method are compared to results obtained with the RBVMM extended to turbulent variable-density flow at low Mach number by Gravemeier and Wall [123] and the DSM. A subgrid-scale model of Smagorinsky type for variable-density flow at low Mach number is obtained by modeling cross- and subgrid-scale Reynolds-stress terms in the momentum and energy equation, (6.49) and (6.50), respectively, by $(\boldsymbol{\varepsilon}(\mathbf{v}^h), 2\mu_{\text{sgs}}\boldsymbol{\varepsilon}^*(\mathbf{u}^h))$, where $\mu_{\text{sgs}} = \rho_h(C_{\text{S}}\Delta)^2(2\boldsymbol{\varepsilon}(\mathbf{u}^h) : \boldsymbol{\varepsilon}(\mathbf{u}^h))^{\frac{1}{2}}$ denotes the subgrid viscosity, and by $(\nabla w^h, (\lambda/c_p)_{\text{sgs}}\nabla T^h)$, where $(\lambda/c_p)_{\text{sgs}} = \mu_{\text{sgs}}/\text{Pr}_{\text{t}}$ denotes the subgrid diffusivity and Pr_{t} the turbulent Prandtl number. Parameter $(C_{\text{S}}\Delta)^2$, that is, the product of Smagorinsky constant C_{S} and grid-filter width Δ, as well as Pr_{t} are determined dynamically using a box filter and a contraction according to Lilly [193]. SUPG (both for the momentum and the energy equation), PSPG and grad-div term are additionally included in the formulation. With respect to the dynamic Smagorinsky model proposed for LES of turbulent compressible flow by Moin *et al.* [223], it is remarked that, owing to the present weakly compressible flows, a model for the isotropic part of the subgrid-scale stress tensor in the form $(\boldsymbol{\varepsilon}(\mathbf{v}^h), -1/3q_{\text{sgs}}^2\mathbf{I})$, where $q_{\text{sgs}}^2 = 2\rho_h(C_{\text{Y}}\Delta)^2(2\boldsymbol{\varepsilon}(\mathbf{u}^h) : \boldsymbol{\varepsilon}(\mathbf{u}^h))$ is the subgrid-scale energy and $(C_{\text{Y}}\Delta)^2$ the product of coefficient C_{Y} and grid-filter width Δ, as originally proposed by Yoshizawa [335], is not included, meaning that the isotropic part of the subgrid-scale stress tensor is assumed to be added to the hydrodynamic pressure.

6.5.1 Turbulent Channel Flow with a Heated and a Cooled Wall

Overview. Turbulent variable-density flow in a channel at friction Reynolds number $\text{Re}_{\tau,0} = 180$, which is the Reynolds number at the initial temperature T_0, with a heated wall at tempera-

[1] Computational resources provided by the Leibniz Supercomputing Center under the project pr83te are gratefully acknowledged.

ture T_H and a cooled wall at temperature T_C is studied first. A DNS study for this Reynolds number, Pr $= 0.76$ and various temperature ratios $T_\mathrm{H}/T_\mathrm{C}$ (i.e., $T_\mathrm{H}/T_\mathrm{C} = 1.01$, 2.00 and 4.00) was reported by Nicoud [229, 230]. Here, the temperature ratios $T_\mathrm{H}/T_\mathrm{C} = 1.01$ and 2.00 are investigated, since, particularly for these two temperature ratios, various DNS results are provided in Nicoud [229]. Hence, the results obtained with the AVM^4 are compared to results from Nicoud [229], marked by "DNS N98". While the temperature field remains almost uniform for the lower temperature ratio and the friction Reynolds numbers are almost identical at the hot and the cold wall as a result, the Reynolds number at the hot wall is expected to be notably smaller than the Reynolds number at the cold wall for the higher temperature ratio. In Nicoud [229], the Reynolds numbers for this case were given as $\mathrm{Re}_{\tau,\mathrm{H}} = 82$ at the hot wall and $\mathrm{Re}_{\tau,\mathrm{C}} = 200$ at the cold wall. Since the aforementioned DNS study did not provide any results for correlations of velocity and temperature fluctuations, LES results from turbulent variable-density flow at low Mach number provided in Lessani and Papalexandris [187] are also included for comparison. In that article, temperature ratios $T_\mathrm{H}/T_\mathrm{C} = 1.01$, 2.00 and 8.00 were examined at $\mathrm{Re}_{\tau,0} = 180$, and Pr was set to 0.7 for $T_\mathrm{H}/T_\mathrm{C} = 1.01$ and to 0.8 otherwise. For $T_\mathrm{H}/T_\mathrm{C} = 2.00$, the Reynolds numbers at the walls were given as $\mathrm{Re}_{\tau,\mathrm{H}} = 91$ and $\mathrm{Re}_{\tau,\mathrm{C}} = 224$. Results taken from that study are denoted by "LES LP06". Further LES results were reported, e.g., by Wang and Pletcher [328], where $T_\mathrm{H}/T_\mathrm{C} = 1.02$ and 3.00 were investigated at $\mathrm{Re}_{\tau,0} = 160$ and Pr $= 0.71$. The Reynolds numbers for $T_\mathrm{H}/T_\mathrm{C} = 3.00$ were $\mathrm{Re}_{\tau,\mathrm{H}} = 103$ as well as $\mathrm{Re}_{\tau,\mathrm{C}} = 187$ and thus relatively close to the present ones. The respective results are marked by "LES WP96". The discretizations used in both LES studies are comparable to the finer one of the present thesis, which will be described below. Compared to the present setup, the same number of grid points was used for a larger streamwise length by Lessani and Papalexandris [187] and smaller spanwise width by Wang and Pletcher [328]. Furthermore, the lower temperature ratio also enables a comparison to the velocity results of incompressible DNS given by Moser *et al.* [224] and denoted by "DNS MKM99".

Problem Setup. As given by Nicoud [229, 230], a gas constant $R = 1.0$ is assumed, and a scaled Sutherland law, where $T_\mathrm{ref} = 1.0$ and $S = 0.368$, is applied. The specific heat capacity at constant pressure is chosen to be $c_p = 1004.5$. The Prandtl number, which is assumed constant, is Pr $= 0.71$. Initially, a scaled thermodynamic pressure $p_{\mathrm{the},0} = 1.0$ is prescribed. As driving mechanism for the flow, a pressure gradient ∇p_drive is imposed in form of a non-density-weighted volume force in streamwise direction (i.e., $\rho\mathbf{f} = \nabla p_\mathrm{drive}$ in the momentum equation (6.3)). While μ_0 and ρ_0, i.e., μ_ref and T_0 in the present variable-density context, may be chosen for $T_\mathrm{H}/T_\mathrm{C} = 1.01$ such as for turbulent incompressible flow at a given friction Reynolds number, T_H and T_C as well as μ_ref and T_0 have to be set based on the targeted friction Reynolds numbers $\mathrm{Re}_{\tau,\mathrm{H}} = 82$ and $\mathrm{Re}_{\tau,\mathrm{C}} = 200$ as well as the initial one for $T_\mathrm{H}/T_\mathrm{C} = 2.00$. A randomly-perturbed parabolic velocity profile in streamwise direction constitutes the initial velocity field. Within several initial time steps, the lower wall is cooled down and the upper wall heated up such that the desired temperature ratio is achieved. The channel dimensions are $2\pi\delta_\mathrm{c} \times 2\delta_\mathrm{c} \times (4/3)\pi\delta_\mathrm{c}$ in streamwise, wall-normal and spanwise direction, respectively. Hence, the channel dimensions are chosen according to the respective dimensions of Nicoud [229], except for the streamwise length, which is reduced by a factor of two. The channel half-width δ_c is chosen to be 1.0. No-slip boundary conditions are applied at the top and the bottom wall. In homogeneous streamwise and spanwise direction, periodic boundary conditions for velocity and temperature are assumed.

Three different spatial discretizations with 32, 48 and 64 elements in each spatial direction are used. To obtain a better resolution of the near-wall region, the distribution of the elements is refined in wall-normal direction towards the wall using the hyperbolic mesh stretching function given in equation (4.61). The mesh stretching function yields a symmetric node distribution with respect to the x_1x_3-centerplane. Since $h^+_{2,\text{min}}$ (see below) is sufficiently small for LES, the symmetric distribution is maintained for both cases, and not specifically unsymmetrically adapted for the case with higher temperature ratio as, e.g., for the DNS by Nicoud [229]. Depending on the temperature ratio T_H/T_C and the resulting friction Reynolds numbers, the element lengths in non-dimensional form

$$h^+_{i,\text{W}} = \frac{h_i}{\delta_{\nu,\text{W}}} \tag{6.56}$$

are summarized in Table 6.1. They are evaluated with respect to the lower and upper wall (i.e., $\text{W} \in \{\text{C}, \text{H}\}$) using the corresponding viscous length scale

$$\delta_{\nu,\text{W}} = \frac{\mu_\text{W}}{\rho_\text{W} u_{\tau,\text{W}}}, \tag{6.57}$$

where ρ_W and μ_W denote the density and viscosity at the wall. The friction velocity is defined as

$$u_{\tau,\text{W}} = \sqrt{\frac{\tau_\text{W}}{\rho_\text{W}}}, \tag{6.58}$$

where τ_W denotes the wall-shear stress. A constant time-step length $\Delta t = 0.004$ is applied for both cases. Statistics are collected in homogeneous directions and in time during 5000 time steps, after the flow has reached a fully turbulent state and the thermodynamic pressure has converged, that is, the heat fluxes at both walls are equal.

Table 6.1: Mesh parameters for turbulent channel flow with a heated and a cooled wall at $T_\text{H}/T_\text{C} = 1.01$ and 2.00: number of elements, mesh stretching parameter C_G and non-dimensional element lengths $h^+_{i,\text{W}}$.

no. elements	C_G	$h^+_{1,\text{C}}$ $h^+_{1,\text{H}}$	$h^+_{2,\text{min,C}}$ $h^+_{2,\text{min,H}}$	$h^+_{2,\text{max,C}}$ $h^+_{2,\text{max,H}}$	$h^+_{3,\text{C}}$ $h^+_{3,\text{H}}$
lower temperature ratio: $T_\text{H}/T_\text{C} = 1.01$, $\text{Re}_{\tau,\text{C}} = \text{Re}_{\tau,\text{H}} = 180$					
32^3	2.15	35.34	1.50	24.70	23.56
48^3	1.95	23.56	1.28	15.20	15.71
64^3	1.85	17.67	1.09	10.92	11.78
higher temperature ratio: $T_\text{H}/T_\text{C} = 2.00$, $\text{Re}_{\tau,\text{C}} = 200$, $\text{Re}_{\tau,\text{H}} = 82$					
32^3	2.15	39.27	1.67	27.45	26.18
		16.10	0.68	11.25	10.73
48^3	1.95	26.18	1.42	16.88	17.45
		10.73	0.58	6.92	7.16
64^3	1.85	19.63	1.21	12.14	13.09
		8.05	0.50	4.98	5.37

Flow Description. The mean streamwise velocity and temperature profile, $\langle u_1 \rangle / U_\mathrm{c}$ and $(\langle T \rangle - T_\mathrm{C})/(T_\mathrm{H} - T_\mathrm{C})$, where U_c denotes the mean centerline velocity, are depicted in wall-normal direction in Figure 6.1 for both temperature ratios. In accordance with the increasing dynamic viscosity and the decreasing Reynolds number, which indicates a less turbulent flow, the velocity profile exhibits a smaller gradient at the hot wall for $T_\mathrm{H}/T_\mathrm{C} = 2.00$ than for 1.01. At $\mathrm{Re}_{\tau,\mathrm{H}} = 82$, relaminarization might even occur. Analogously, the thermal conductivity increases at the hot channel wall for $T_\mathrm{H}/T_\mathrm{C} = 2.00$, resulting in a smaller gradient of the temperature profile at the wall such that the heat fluxes at both walls are equal.

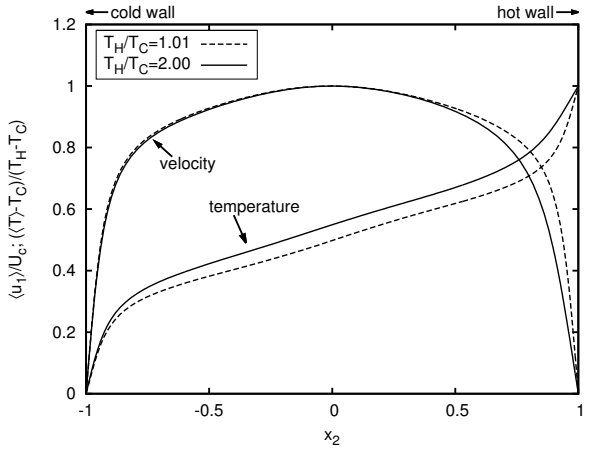

Figure 6.1: Mean streamwise velocity and temperature profiles, $\langle u_1 \rangle / U_\mathrm{c}$ and $(\langle T \rangle - T_\mathrm{C})/(T_\mathrm{H} - T_\mathrm{C})$, for turbulent channel flow with a heated and a cooled wall at $T_\mathrm{H}/T_\mathrm{C} = 1.01$ and 2.00. Results obtained with the AVM^4 using 64^3 elements are shown.

Figure 6.2 gives further insights into the influence of heating and cooling on the flow field. Therefore, instantaneous velocity fields as well as instantaneous temperature iso-contours at two streamwise and spanwise locations are displayed. For $T_\mathrm{H}/T_\mathrm{C} = 1.01$, the temperature iso-contours are strongly wrinkled at both channel walls, and isolated pockets of hot and cold fluid, respectively, are ejected outward from the wall. For $T_\mathrm{H}/T_\mathrm{C} = 2.00$, in contrast, the temperature iso-contours are hardly wrinkled in the vicinity of the hot channel wall. Almost no pockets of hot fluid are ejected, and large structures of hot fluid rather move towards the center of the channel. The first iso-contours away from the wall are almost parallel to it, giving further evidence that the flow locally relaminarizes. In accordance with Figure 6.1, the layer of hot fluid gets broader. The temperature iso-contours in the vicinity of the cold wall resemble the ones for the lower temperature ratio. Likewise, a comparison of the instantaneous velocity fields near the hot channel wall reveals larger flow structures and an almost uniform flow in streamwise direction for the higher temperature ratio.

Statistical Results for $\mathbf{T_H/T_C}$=1.01. All statistical results are normalized by the friction velocity $u_{\tau,\mathrm{W}}$ and the friction temperature

$$T_{\tau,\mathrm{W}} = \frac{q_\mathrm{W}}{\rho_\mathrm{W} c_p u_{\tau,\mathrm{W}}}, \tag{6.59}$$

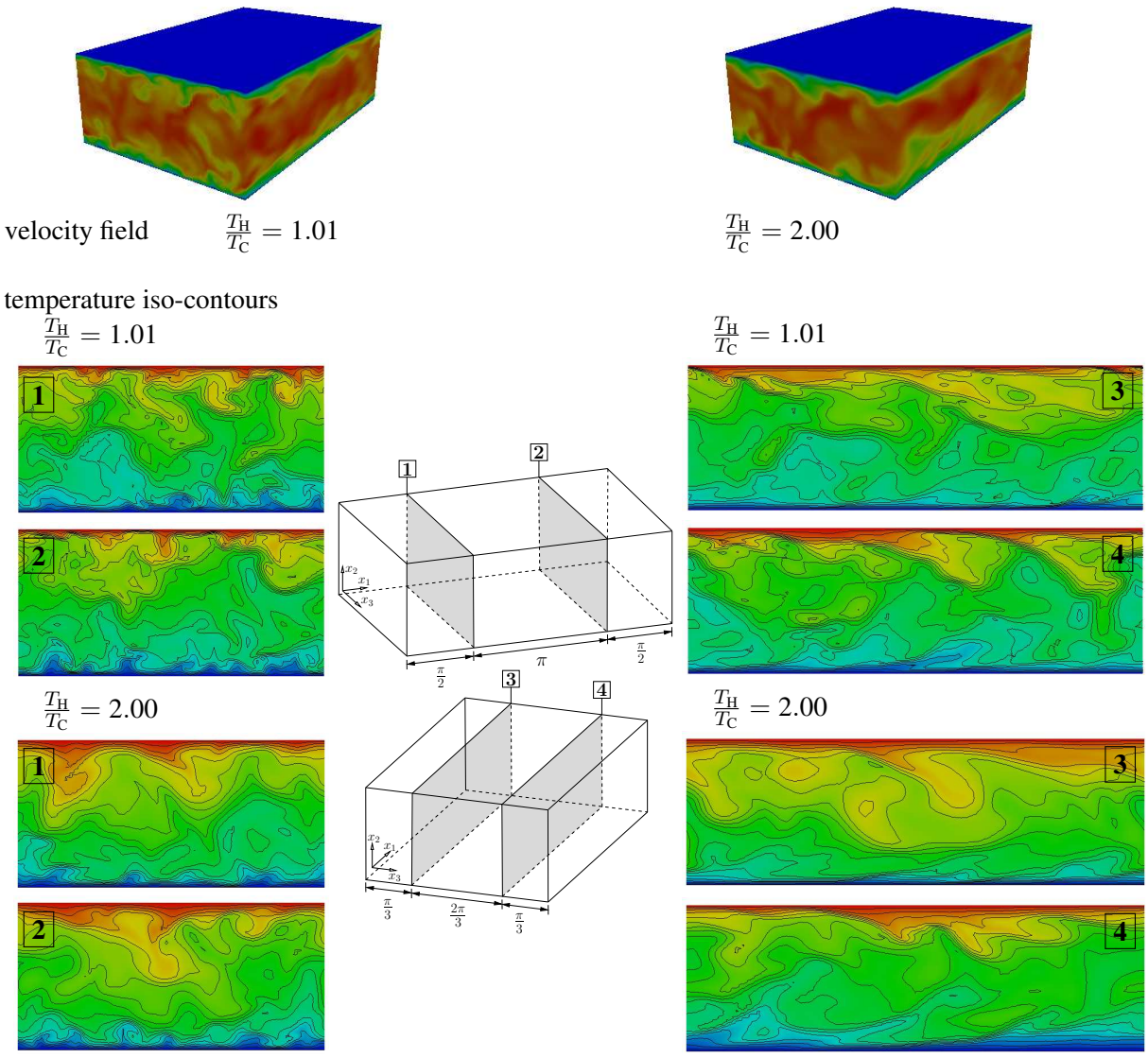

Figure 6.2: Instantaneous velocity magnitude distribution (top) as well as temperature iso-contours on colored temperature distribution at various locations (bottom) for turbulent channel flow with a heated and a cooled wall at $T_H/T_C = 1.01$ and 2.00 (red color indicates high velocity/temperature and blue color low velocity/temperature). Results obtained with the AVM^4 using 64^3 elements are shown at the end of the simulation.

where $q_W = \lambda_W(\partial\langle T\rangle/\partial x_2)|_W$ is the heat flux in wall-normal direction at the wall and λ_W the thermal conductivity at wall. As usual, statistical results are depicted in wall units x_2^+, i.e., as a function of the distance from the wall normalized by the respective viscous length scale $\delta_{\nu,W}$. For the lower temperature ratio, the temperature difference has almost no effect on the flow field. Therefore, only the most relevant velocity results are displayed, comparing them to the respective DNS data of incompressible flow. Since the lower temperature ratio does not induce a significant asymmetry in the mean quantities and turbulent fluctuations, the results of the upper channel half are merely depicted. The mean streamwise velocity u_1^+ and the mean temperature T^+ are

shown in Figure 6.3. For u_1^+ and T^+, the AVM^4 exhibits a notably better approximation than the RBVMM and DSM. Indeed, the results obtained with the AVM^4 are already for the medium discretization quite close to the DNS results, and the improvement due to further refinement is only of small amount. In contrast, the RBVMM provides results which substantially deviate from the DNS data using the coarser and the medium discretization. Even with the finer discretization, there are notable deviations from the DNS results, while the AVM^4 results match them almost exactly. For all discretizations, the largest deviations from DNS are observed for the DSM.

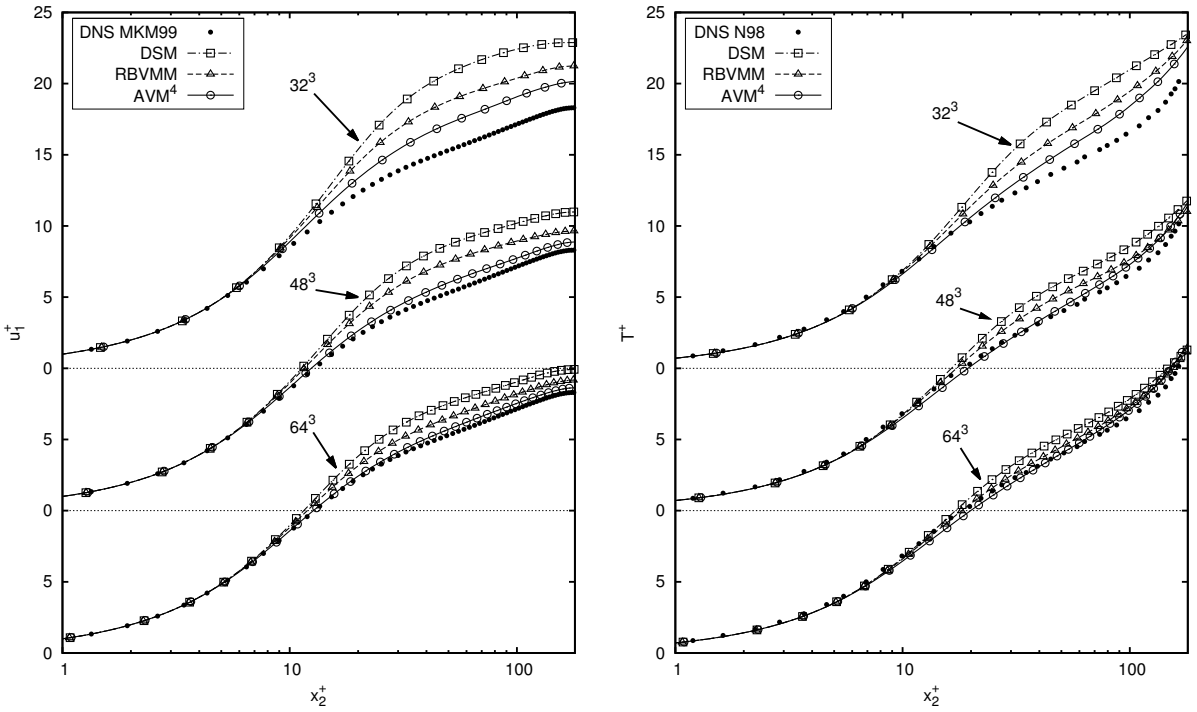

Figure 6.3: Convergence study of mean streamwise velocity u_1^+ and temperature T^+ for turbulent channel flow with a heated and a cooled wall at temperature ratio $T_\mathrm{H}/T_\mathrm{C} = 1.01$ in the hot channel half using 32^3, 48^3 and 64^3 elements.

The root-mean-square velocity and temperature, rms u_1^+ and rms T^+, as well as correlations of streamwise and wall-normal velocity and temperature fluctuations, $\langle u_1' T' \rangle^+$ and $\langle u_2' T' \rangle^+$, respectively, are depicted in Figure 6.4. For the root-mean-square velocity rms u_1^+, the AVM^4 provides significantly better predictions than the RBVMM and DSM. While the AVM^4 approximates rms u_1^+ exactly for the medium and finer discretization, the methods included for comparison overestimate rms u_1^+ for all discretizations. In particular, the result obtained with the coarser discretization using the AVM^4 is not attained by the RBVMM using the finer discretization. The DSM even overestimates the results of the RBVMM. Concerning rms T^+, the best approximation overall is again obtained with the AVM^4. In particular, the maximum value in the vicinity of the wall is captured more accurately by the AVM^4 than by the other two methods, since the RBVMM and most notable the DSM overpredict the small peak near the wall. Towards the channel center, the AVM^4 somewhat overestimates the DNS values, and results by the RBVMM

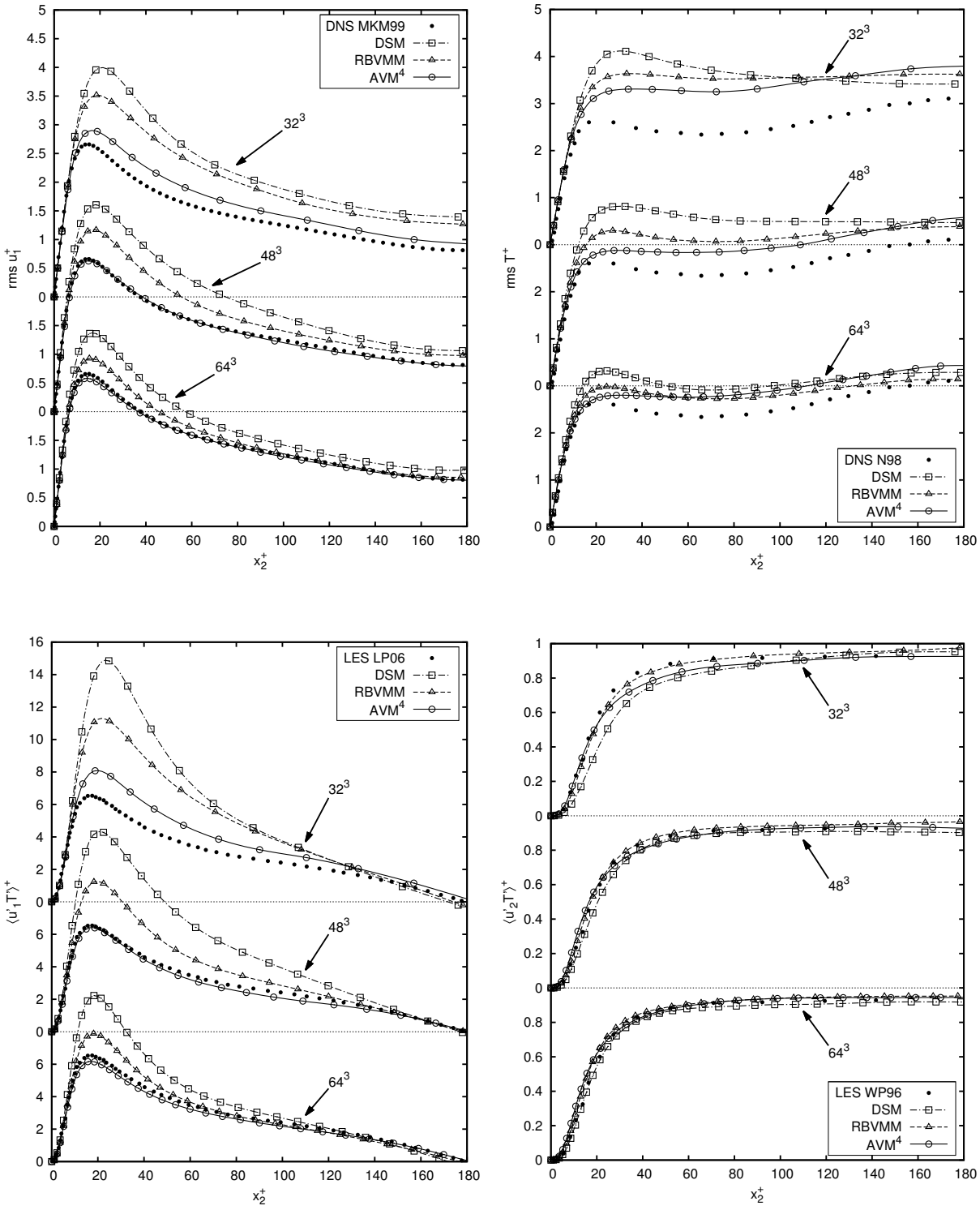

Figure 6.4: Convergence study of root-mean-square velocity rms u_1^+ and temperature rms T^+ as well as streamwise velocity-temperature fluctuations $\langle u_1' T' \rangle^+$ and wall-normal velocity-temperature fluctuations $\langle u_2' T' \rangle^+$ for turbulent channel flow with a heated and a cooled wall at temperature ratio $T_\mathrm{H}/T_\mathrm{C} = 1.01$ in the hot channel half using 32^3, 48^3 and 64^3 elements.

and DSM are slightly closer to DNS. As no reference DNS data for correlations of velocity and temperature fluctuations for variable-density flow at low Mach number appear to be available in literature, results taken from the LES studies by Lessani and Papalexandris [187] and by Wang and Pletcher [328] are included for comparison here. Due to the minor influence of the temperature ratio, the LES data for $\langle u_1' T' \rangle^+$, provided by Lessani and Papalexandris [187] only for the lower (cold) channel half, are mirrored to the upper channel half. Differences in the approximation quality between the AVM^4, RBVMM and DSM are again particularly pronounced for $\langle u_1' T' \rangle^+$. As already observed for u_1^+, T^+ and rms u_1^+, differences between the results obtained with the medium and finer discretization are marginal for the AVM^4, indicating with respect to the results observed for the aforementioned quantities for these discretizations, which match the DNS data almost exactly, that the solution is almost converged. Moreover, the LES data taken from Lessani and Papalexandris [187] are also quite close to these curves. Concerning the other methods included for comparison, the results provided by the AVM^4 using the finer discretization are thus taken as reference values. Using the finer discretization, the results obtained with the RBVMM provide an approximation comparable with the results obtained with the AVM^4 using the coarser discretization. The DSM shows by far the worst approximation for all discretizations. For $\langle u_2' T' \rangle^+$, differences between the AVM^4 and RBVMM are hardly observable. The DSM somewhat underestimates the steep increase of $\langle u_2' T' \rangle^+$ for the coarser and medium discretization. With respect to the results included from the LES study by Wang and Pletcher [328], the AVM^4, RBVMM and DSM yield a similar behavior, and the curves are located very close to each other.

Statistical Results for T_H/T_C=2.00. Next, the higher temperature ratio is investigated. This case constitutes a rather challenging example for turbulent variable-density flow at low Mach number. On the one hand, a temperature ratio $T_H/T_C = 2.00$ already includes notable density and viscosity variations. On the other hand, as aforementioned, relaminarization may occur near the hot channel wall due to the rather low friction Reynolds number. For this setup, the RBVMM became unstable after a certain number of time steps; and oscillations in the temperature solution were observed, even yielding unphysical negative temperature values. These instabilities were caused by the residual-based subgrid-scale modeling of the second cross-stress term and the subgrid-scale Reynolds-stress term in the energy equation. Closer investigations revealed that the second cross-stress term was responsible for the observed instabilities. According to Hughes and Wells [151], this cross-stress term has the form of a convective term and needs to be stabilized, as a result. Analogously to the stabilization of the convective (Galerkin) term by the SUPG term, which is the first cross-stress term, the subgrid-scale Reynolds-stress term might be interpreted as the corresponding stabilization of the second cross-stress term, as done by Hughes and Wells [151]. A comprehensive investigation of the residual-based multiscale form of the cross- and subgrid-scale Reynolds-stress terms with respect to the subgrid-scale energy transfer in turbulent incompressible flow may also be found in Wang and Oberai [329]. Therein, the authors showed based on an *a priori* analysis that the contribution of the subgrid-scale Reynolds-stress term was substantially underpredicted. Hence, it seems that the subgrid-scale Reynolds-stress term does not sufficiently stabilize the second cross-stress term in a complete residual-based variational multiscale formulation for the present case. Therefore, a reduced version of the RBVMM without modeling of the second cross-stress term and the subgrid-scale Reynolds-stress term of the energy equation is used here for comparison. Hence, merely the SUPG term is included

in the modeled formulation of the energy equation. The residual-based variational multiscale formulation of the continuity and momentum equation is not modified.

Figure 6.5 depicts the mean streamwise velocity u_1^+ and the mean temperature T^+ for $T_\mathrm{H}/T_\mathrm{C} = 2.00$ for both channel halves. Convergence to DNS is observed for all methods. Owing to the low Reynolds number at the hot channel wall, all methods provide approximations close to the DNS data for u_1^+ and T^+ as well as for all discretizations. Differences between the methods, if ascertainable, are only of small amount. In the lower channel half, the situation is different. Concerning u_1^+, the AVM^4 provides results which are already for the medium discretization quite close to the DNS data and match them almost exactly for the finer one. The results provided by the AVM^4 for the coarser discretization are comparable to the ones by the RBVMM and DSM using the medium discretization. For the coarse discretization, the RBVMM and DSM yield comparable approximations. For T^+, the results obtained with the AVM^4 using the finer discretization again approximate the DNS data very accurately, while the results provided by the other two methods still significantly deviate from the DNS data. Also for the other two discretizations, the AVM^4 provides the best approximation compared to the RBVMM and DSM. As already observed for u_1^+, the RBVMM and DSM perform similar when using the coarser and medium discretization.

The root-mean-square values of the velocity components and the temperature as well as correlations of velocity and temperature fluctuations are summarized in Figures 6.6 to 6.8. Differences in the approximation quality are particularly pronounced for rms u_1^+. Despite the low friction Reynolds number in the hot channel half and the observed good approximations for u_1^+ and T^+ by all methods, differences are observable on both sides. Again, the AVM^4 provides results for the medium discretization that are already close to the DNS data and capture them quite accurately for the finer one. The other two methods provide results which deviate even for the finer discretization considerably from the reference data. In the cold channel half, the AVM^4 using the coarser discretization provides results that are closer to the DNS data than the results shown by the RBVMM and DSM using the finer discretization. Moreover, the RBVMM yields somewhat better results than the DSM. All methods underestimate rms u_2^+ in the lower channel half, with the AVM^4 showing again the best approximations for all discretizations. In the upper channel half, the DSM also underpredicts rms u_2^+ for all discretizations. The AVM^4 again provides the overall best results, although the RBVMM likewise captures the DNS data quite accurately. For rms u_3^+, the AVM^4 shows results which are quite close to the DNS data in the cold channel half for all discretizations, while the DSM and RBVMM underestimate the maximum value and also significantly deviate from the DNS data towards the middle of the channel. All methods provide reliable approximations in the hot channel half. Concerning rms T^+, the AVM^4 shows again the overall best approximation in both channel halves. In particular in the cold channel half, the AVM^4 captures rms T^+ significantly better than the other two methods. All methods somewhat deviate from the DNS data in the middle of the channel. Since there are no DNS or LES reference data for $\langle u_1' T' \rangle^+$ and $\langle u_2' T' \rangle^+$ for this temperature ratio and friction Reynolds numbers, results shown by Wang and Pletcher [328] for the temperature ratio $T_\mathrm{H}/T_\mathrm{C} = 3.00$, which is relatively close to the present one, are included for a qualitative comparison. Again, differences in the results provided by the different methods are particularly pronounced for $\langle u_1' T' \rangle^+$. Due to the overall good performance of the AVM^4 and the marginal differences between the results obtained with the medium and finer discretization when using this method, results provided by

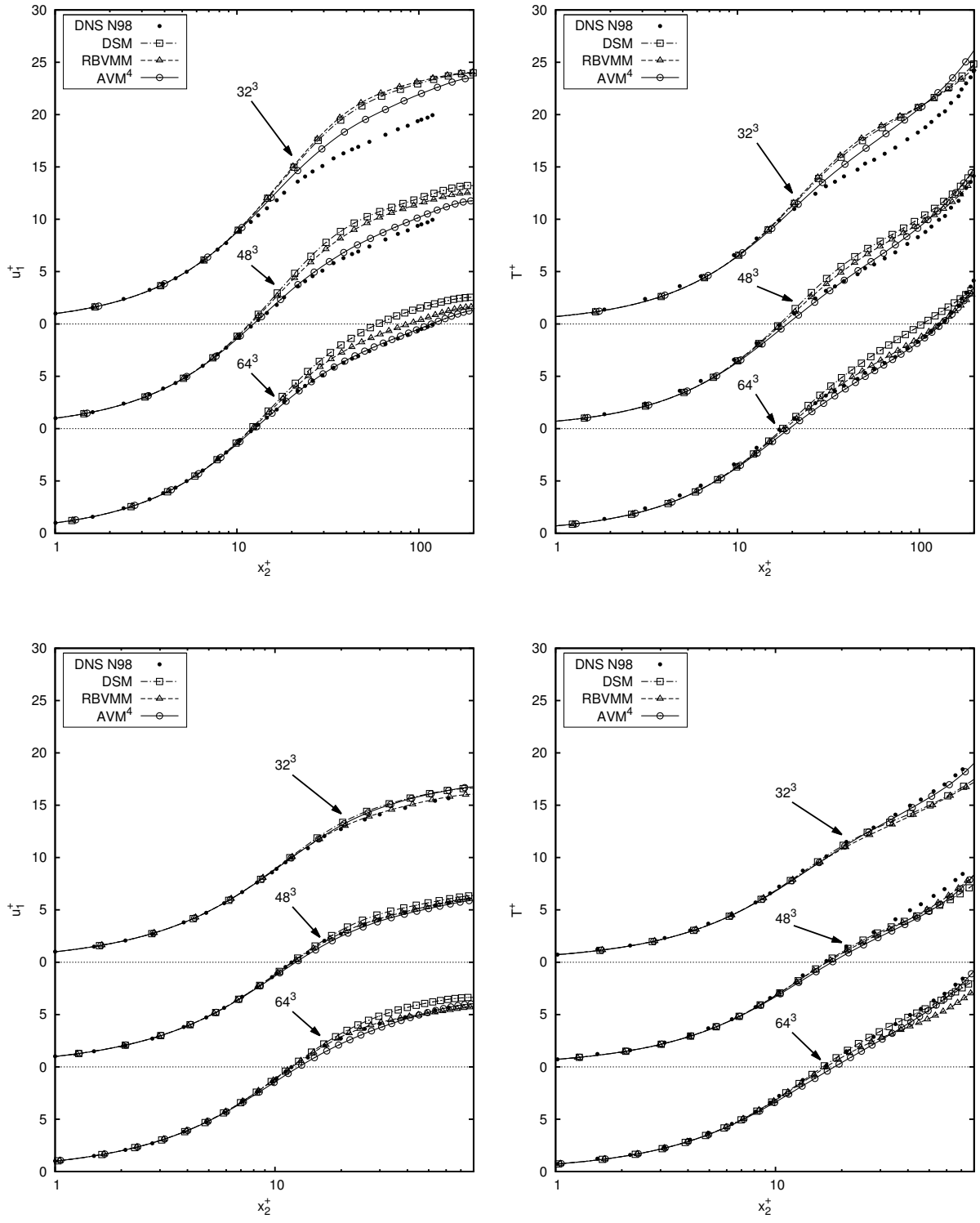

Figure 6.5: Convergence study of mean streamwise velocity u_1^+ and temperature T^+ for turbulent channel flow with a heated and a cooled wall at temperature ratio $T_\mathrm{H}/T_\mathrm{C} = 2.00$ in the cold (top) and hot (bottom) channel half using 32^3, 48^3 and 64^3 elements.

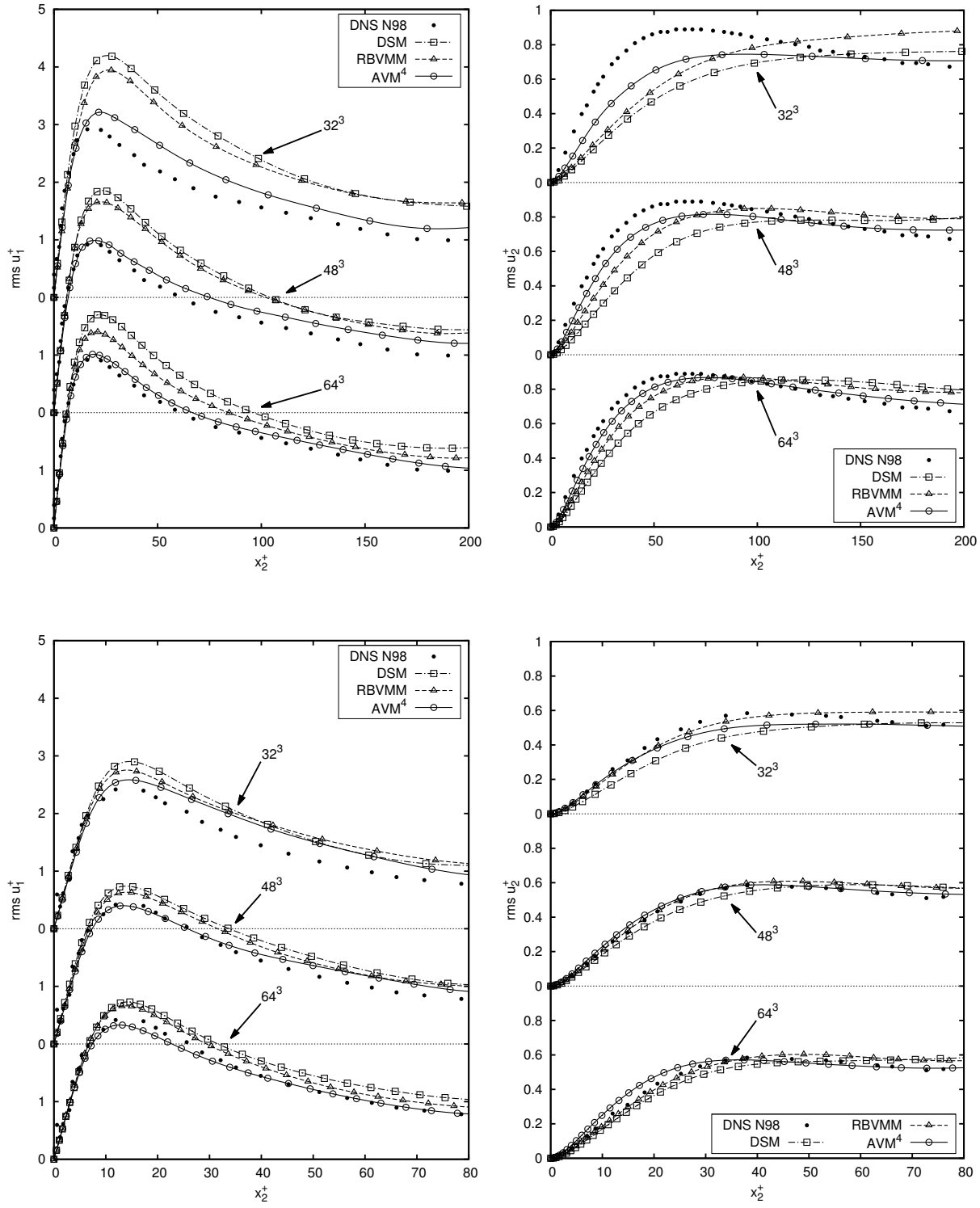

Figure 6.6: Convergence study of root-mean-square velocities $\mathrm{rms}\, u_1^+$ and $\mathrm{rms}\, u_2^+$ for turbulent channel flow with a heated and a cooled wall at temperature ratio $T_\mathrm{H}/T_\mathrm{C} = 2.00$ in the cold (top) and hot (bottom) channel half using 32^3, 48^3 and 64^3 elements.

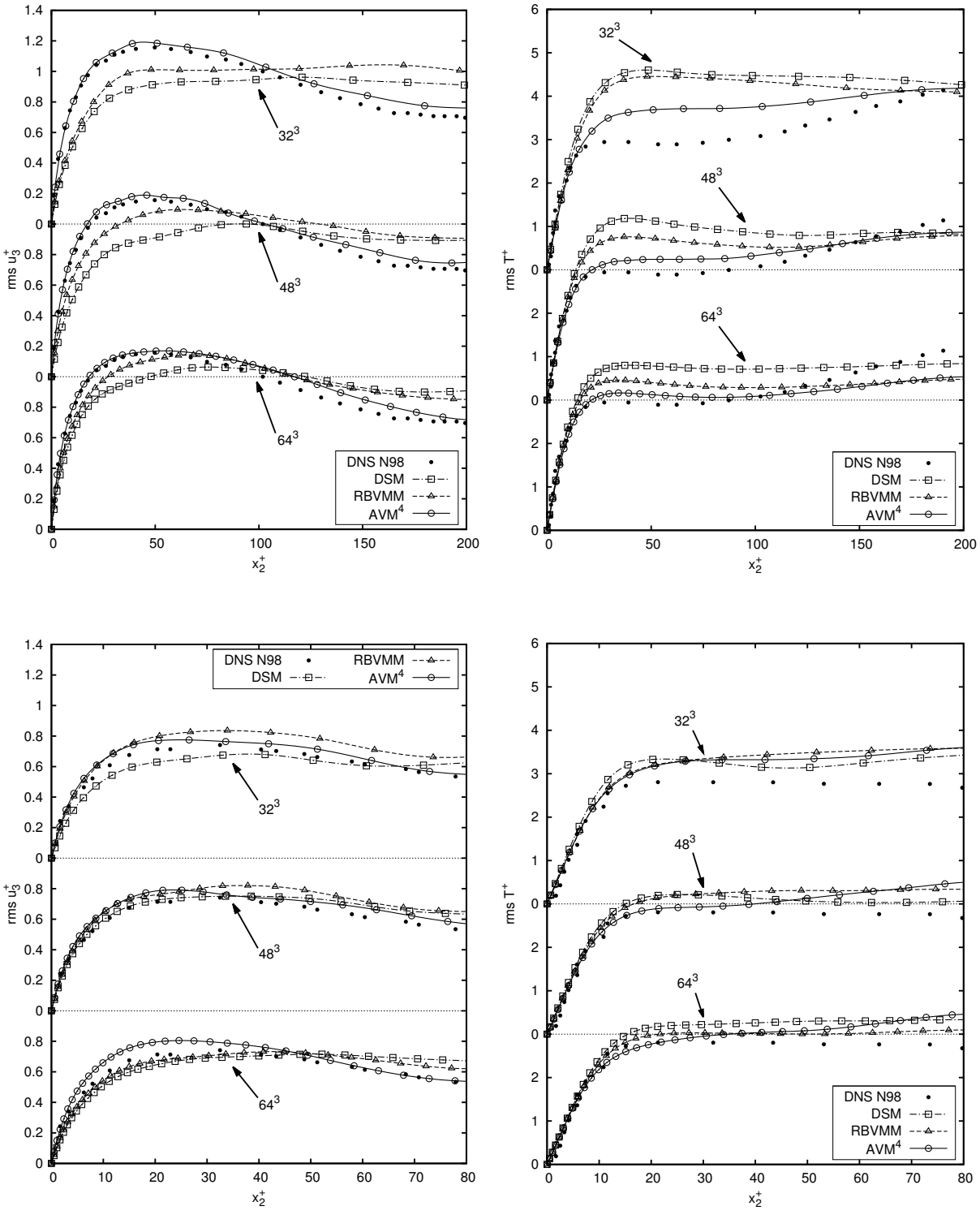

Figure 6.7: Convergence study of root-mean-square velocity rms u_3^+ and temperature rms T^+ for turbulent channel flow with a heated and a cooled wall at temperature ratio $T_\mathrm{H}/T_\mathrm{C} = 2.00$ in the cold (top) and hot (bottom) channel half using 32^3, 48^3 and 64^3 elements.

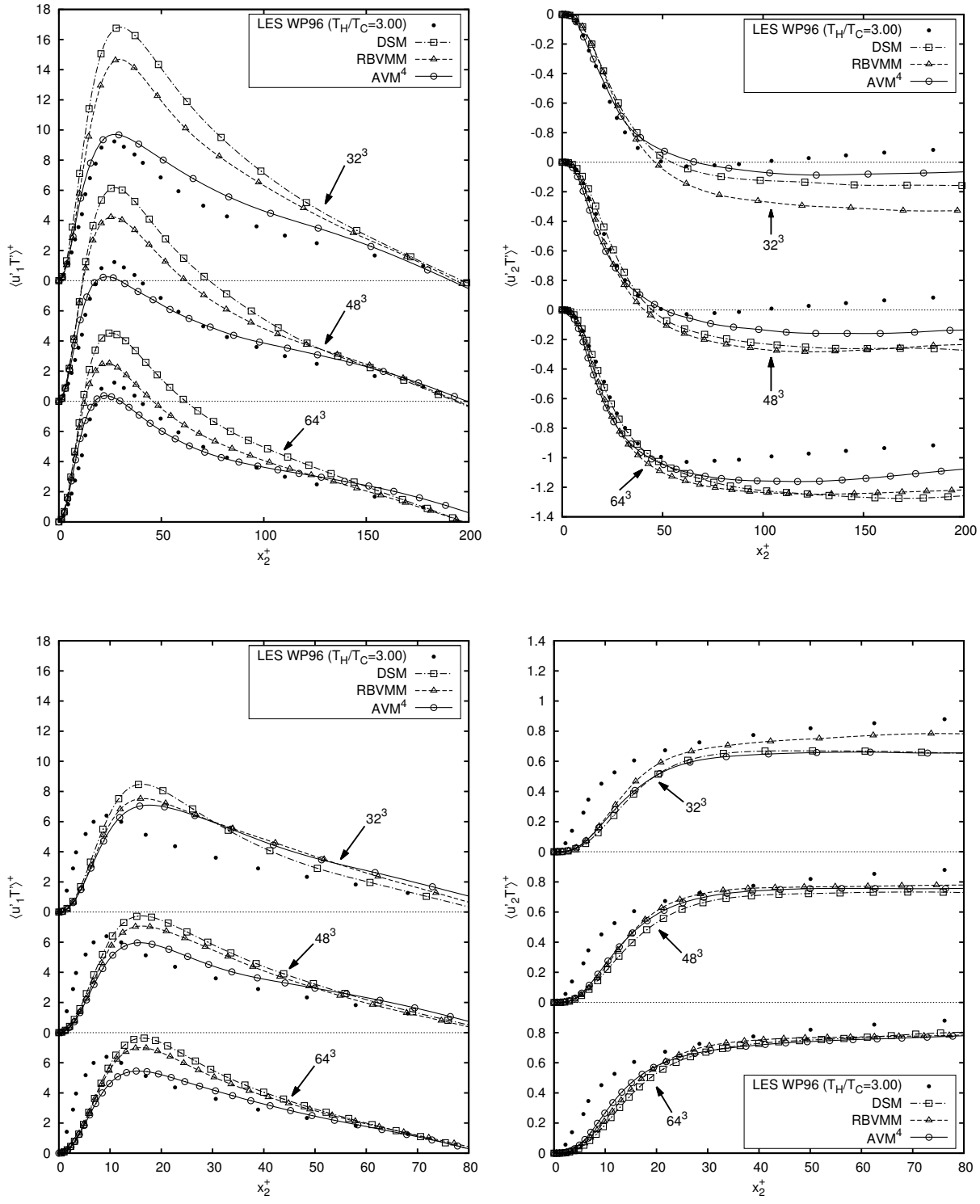

Figure 6.8: Convergence study of streamwise velocity-temperature fluctuations $\langle u_1'T'\rangle^+$ and wall-normal velocity-temperature fluctuations $\langle u_2'T'\rangle^+$ for turbulent channel flow with a heated and a cooled wall at temperature ratio $T_\mathrm{H}/T_\mathrm{C} = 2.00$ in the cold (top) and hot (bottom) channel half using 32^3, 48^3 and 64^3 elements.

the AVM^4 using the finer discretization are again taken as reference values. The results obtained with the coarser discretization in the cold channel half are not achievable for the RBVMM and DSM when using the finer discretization. Moreover, the RBVMM provides better approximations than the DSM. Also in the hot channel half, significant differences between the AVM^4 and the other two methods occur in particular for the medium and finer discretization. For $\langle u_2' T' \rangle^+$, the qualitative behavior of all methods is in good agreement with the included data from LES of $T_\mathrm{H}/T_\mathrm{C} = 3.00$.

6.5.2 Backward-Facing Step with Heating

Flow Description. Separation and reattachment of turbulent flow are of great importance for many engineering devices such as combustion chambers and airfoils. Among the various configurations to investigate these phenomena, the backward-facing step belongs to the simplest possible types of geometry and provides a well-defined separation point. However, turbulent flow over a backward-facing step is complex, since it incorporates several canonical flows. Turbulent flow over a backward-facing step combines the dynamics of near-wall regions and free shear layers. At the edge of the step, a boundary layer separates. The resulting shear layer gives rise to spanwise Kelvin-Helmholtz vortices, which undergo complex processes. Owing to the reattachment of the shear layer at the wall behind the step, fluid is entrained, and a recirculation zone evolves. Behind the reattachment region, the boundary layer redevelops. If heat transfer is additionally involved, separation and reattachment provoke large variations in the heat-transfer coefficient and significantly increase the heat-transfer rates. Moreover, turbulent flow over a backward-facing step in general is comprehensively documented, both experimentally and numerically.

Overview and Problem Setup. Based on the step height H and the mean centerline velocity U_c at the inlet, the Reynolds number

$$\mathrm{Re} = \frac{\rho_0 U_\mathrm{c} H}{\mu_0} \tag{6.60}$$

is defined. The expansion ratio ER, which is the ratio of the channel height downstream and upstream of the step, characterizes the geometry of the backward-facing step. A problem configuration similar to the one in Avancha and Pletcher [9] is chosen. Therein, ER $= 1.5$ was in accordance with the geometry of the isothermal experiment reported by Kasagi and Matsunaga [168]. The step height $H = 0.041\mathrm{m}$ and the Reynolds number Re $= 5540$ used here are also similar to that study. The geometry of the problem domain as well as the channel used to generate turbulent flow fields to extract velocity profiles, which are then prescribed as Dirichlet boundary conditions at the inlet of the backward-facing step, are depicted in Figure 6.9. According to Avancha and Pletcher [9], a wall heat flux q_W is prescribed at the bottom wall behind the step, as indicated in Figure 6.9. Three different heat fluxes were examined by Avancha and Pletcher [9]. Using the AVM^4, wall heat fluxes of $q_\mathrm{W} = 1000\,\mathrm{W/m^2}$ and $3000\,\mathrm{W/m^2}$, which are the lowest and highest value discussed by Avancha and Pletcher [9], are examined. To keep the number of results within reasonable bounds, the subsequent presentations are restricted to the investigations of a wall heat flux of $q_\mathrm{W} = 3000\,\mathrm{W/m^2}$. The data obtained for the lower wall heat flux are summarized in Appendix A in form of supplementary material. With respect to the subgrid-scale modeling approaches, all findings from $q_\mathrm{W} = 3000\,\mathrm{W/m^2}$ are valid for $q_\mathrm{W} = 1000\,\mathrm{W/m^2}$ as

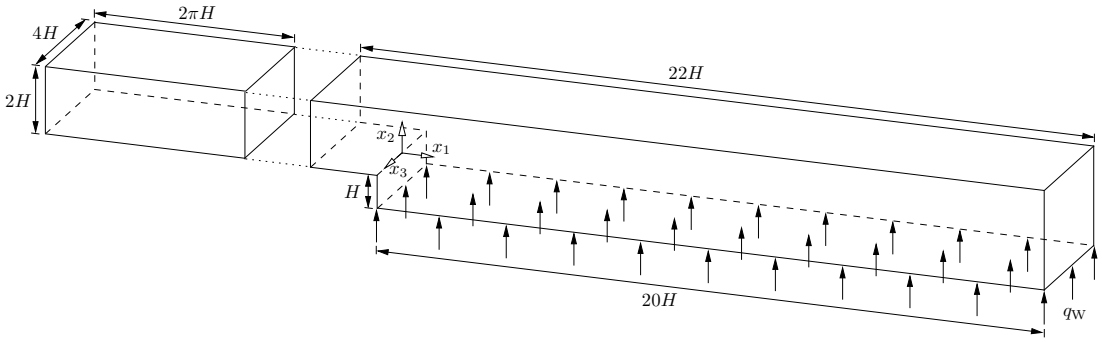

Figure 6.9: Geometry of backward-facing step and inflow channel.

well. Results for the medium wall heat flux $q_\mathrm{W} = 2000\,\mathrm{W/m^2}$, obtained with the predecessor method AVM^3, may be found in Gravemeier and Wall [122]. LES data taken from Avancha and Pletcher [9] for comparison are denoted by "LES AP02" in the following.

A comprehensive experimental study of a backward-facing step with heating at a higher Reynolds number of 28 000 and with an expansion ratio of 1.25 was conducted by Vogel and Eaton [323]. LES of that configuration, considering it as an incompressible flow problem with the temperature coupled as a passive scalar, may be found, e.g., in Keating *et al.* [170] and You and Moin [336]. Consequently, effects due to density and viscosity variations were not taken into account in those studies. Therefore, they were restricted to substantially lower wall heat fluxes. While a maximum overheating of approximately 15 K was considered in those studies, an overheating of several hundred Kelvin is expected for the present configuration. Considerably more investigations of flow over a backward-facing step without heating have been published to date. For example, a DNS study was presented by Le *et al.* [179], where a Reynolds number of 5100, which is relatively close to the present one, and ER $= 1.2$ were used. The corresponding experiment was conducted by Jovic and Driver [165]. Various LESs of turbulent flow over a backward-facing step without heating may also be found in literature, an early one, e.g., in Friedrich and Arnal [98] and more recent ones, e.g., in Aider *et al.* [2], where the DNS setup of Le *et al.* [179] was considered, and in Toschi *et al.* [310], which was based on the geometry of Kasagi and Matsunaga [168].

The initial temperature field is set to $T_0 = 293.0\,\mathrm{K}$, which also represents the reference temperature T_ref. The thermodynamic pressure, which remains constant during the simulation due to the open outflow boundary, is $p_\mathrm{the} = 100\,405\,\mathrm{N/m^2}$. With the gas constant $R = 287.0\,\mathrm{J/(kgK)}$ and T_0, the initial density amounts to $\rho_0 = 1.194\,\mathrm{kg/m^3}$. The viscosity at the reference temperature is $\mu_\mathrm{ref} = \mu_0 = 1.823 \cdot 10^{-5}\,\mathrm{kg/(ms)}$, and the Sutherland constant is $S = 110.4\,\mathrm{K}$. The Prandtl number is assumed to be $\mathrm{Pr} = 0.71$ and the specific heat capacity at constant pressure $c_p = 1006.0\,\mathrm{J/(kgK)}$. No-slip boundary conditions are prescribed on all upper and lower walls, including the vertical step wall. At all walls except for the bottom wall behind the step, adiabatic boundary conditions are prescribed for the temperature. At the bottom wall behind the step, the aforementioned wall heat flux q_W is applied. Periodic boundary conditions are assumed for both velocity and temperature in spanwise x_3-direction. At the outlet, a zero-traction Neumann

boundary condition $\mathbf{h_u} = \mathbf{0}$ and a zero-flux Neumann boundary condition $h_T = 0$, respectively, are applied. At the inflow boundary, T_0 is prescribed as Dirichlet boundary condition.

Inflow Generation. An important aspect of spatially developing turbulent flow problems is the choice of an appropriate inflow velocity profile. Overviews of the generation of such inflow data are provided, e.g., by Keating *et al.* [169] and in form of a review article by Tabor and Baba-Ahmadi [305]. Usually, two different approaches are distinguished in literature: precursor simulation and synthetic inflow generation. In precursor simulation, turbulent flow is pre-computed and then introduced in the main simulation at the inflow boundary, as done, e.g., by Li *et al.* [192] and Lund *et al.* [201]. Prescribed mean velocity profiles superimposed by some sort of fluctuations form the class of synthetic methods as used, e.g., by Lee *et al.* [183] and Pamiès *et al.* [242]. Precursor simulation and random fluctuations were compared, e.g., by Aider *et al.* [2] for flow over a backward-facing step, and it was shown that turbulent structures upstream of the step strongly influence the flow downstream. Here, a precursor approach is used, and precursor as well as main simulation are run simultaneously, after the flow in the inflow section has reached a fully turbulent state. As a consequence, both the storage of a large amount of data and the periodicity introduced due to a potentially repeated application of the same results are avoided. Therefore, the problem domain consists of two spatially separated parts, a domain to generate the inflow velocity profile, which results from a canonical flow such as a turbulent channel flow, and the main problem domain, for instance, the backward-facing step. The resulting velocity profile at the outlet of the channel is transferred to the inlet of the main problem domain and prescribed as Dirichlet boundary condition. The same initial and boundary conditions for the velocity field as described in Section 6.5.1 are used for the inflow channel. Since the temperature in the inflow channel is constant and equal to T_0, variable-density flow reduces to incompressible flow therein. In Kasagi and Matsunaga [168], a friction Reynolds number $\mathrm{Re}_\tau = 290$ was evaluated upstream of the step. Based on the step height, which equals the channel half-width, the streamwise component of the prescribed pressure gradient ∇p_{drive} in the inflow section is $0.3396\,\mathrm{N/m^3}$.

Space and Time Discretization. The discretization consists of 2 714 112 elements (resulting in ca. 13.9 million degrees of freedom overall). The mesh is hence finer than the rather coarse one used by Avancha and Pletcher [9]. In wall-normal direction, 64 elements, refined towards the upper wall and a horizontal line defined by the upper corner of the step, are arranged above the step. This discretization is maintained in the channel. Below the step, 64 elements, which are refined towards the lower wall and the horizontal line such that $(h_2/\delta_\nu)_{\text{min}} = 1.05$ based on the viscous length scale of the inflow section, are used. In streamwise direction, 64 uniformly-distributed elements are arranged in the channel. Another 45 elements, refined towards the step, are included in the backward-facing step domain in front of the step. Between $x_1/H = 0$ and $x_1/H = 10$, 180 elements are used, again refined towards the step such that $(h_1/H)_{\text{min}} = 0.029$ based on the step height. Another 60 uniformly distributed elements are used between $x_1/H = 10$ and $x_1/H = 20$. In spanwise direction, 72 uniformly distributed elements are used. The hyperbolic function f applied to stretch the mesh is given as $f : [0, L_i] \rightarrow [0, L_i]$:

$$x_i \mapsto f(x_i) = C_{\mathrm{C}} x_{\mathrm{G}} \left(1 - \frac{\tanh\left(C_{\mathrm{G}}\left(x_{\mathrm{G}} - x_i\right)\right)}{\tanh\left(C_{\mathrm{G}} x_{\mathrm{G}}\right)} \right),$$

where x_G is the location of the inflection point and C_G the degree of refinement. The scaling factor $C_\mathrm{C} = C_\mathrm{C}(x_\mathrm{G}, C_\mathrm{G})$ is necessary to satisfy $f(L_i) = L_i$. A summary of the discretization details is given in Table 6.2.

Table 6.2: Mesh parameters for turbulent flow over a backward-facing step with heating: number of elements, mesh stretching parameters x_G, C_G and C_C as well as non-dimensional element lengths h_1/H and h_2/δ_ν.

x_i	no. elements	x_G	C_G	C_C	$(h_1/H)_\mathrm{min}$ $(h_1/H)_\mathrm{max}$	$(h_2/\delta_\nu)_\mathrm{min}$ $(h_2/\delta_\nu)_\mathrm{max}$
backward-facing step						
$-2H \leq x_1 \leq 0$	45	$-3H$	8.3	1.160	0.028 0.061	-
$0 \leq x_1 \leq 10H$	180	$15H$	2.0	1.237	0.029 0.085	-
$10H \leq x_1 \leq 20H$	60	uniform				
$-H \leq x_2 \leq 0$	64	$-0.5H$	84.0	1.0	-	1.05 8.31
$0 \leq x_2 \leq 2H$	64	H	53.6	1.0	-	1.05 20.38
$-2H \leq x_3 \leq 2H$	72	uniform				
inflow channel						
$-(2\pi+4)H \leq x_1 \leq -4H$	64	uniform				
$0 \leq x_2 \leq 2H$	64	H	53.6	1.0	-	1.05 20.38
$-2H \leq x_3 \leq 2H$	72	uniform				

A constant time-step length $\Delta t = 0.0008$ s is applied. After a sufficient number of time steps for the heated flow to develop, statistics are collected during another 5000 time steps, representing approximately nine flow-through times based on the mean centerline velocity at the inlet of the backward-facing step and the length of the backward-facing-step geometry. Statistics are collected in homogeneous direction and in time.

A Remark on the RBVMM. As already observed for turbulent channel flow with higher temperature ratio, the RBVMM turned out to be unstable. Hence, the reduced version merely using the SUPG term in the modeled formulation of the energy equation is also used for this example. Similar observations concerning the stability of (complete) residual-based variational multiscale methods for the energy equation for the present problem were made by Gravemeier and Wall [122].

Discussion of the Results. A visualization of the instantaneous velocity and temperature field at the end of the simulation is provided in Figure 6.10. Additionally, Figure 6.11 displays the mean temperature T_W at the bottom wall. Hot areas at the heated bottom wall near the step and

an overall higher temperature in the recirculation zone are clearly observable from Figure 6.10. While heat is piled up in the recirculation zone, hot fluid is transported downstream behind the recirculation zone, resulting in a significantly lower temperature of the fluid. Moreover, the development of a thin temperature boundary layer is observable in this region. As seen from Figure 6.11, a maximum overheating of about 800 K arises for $q_{\mathrm{W}} = 3000\,\mathrm{W/m^2}$. Compared to Avancha and Pletcher [9], all methods used in this study predict higher temperatures in the recirculation zone and lower ones further downstream.

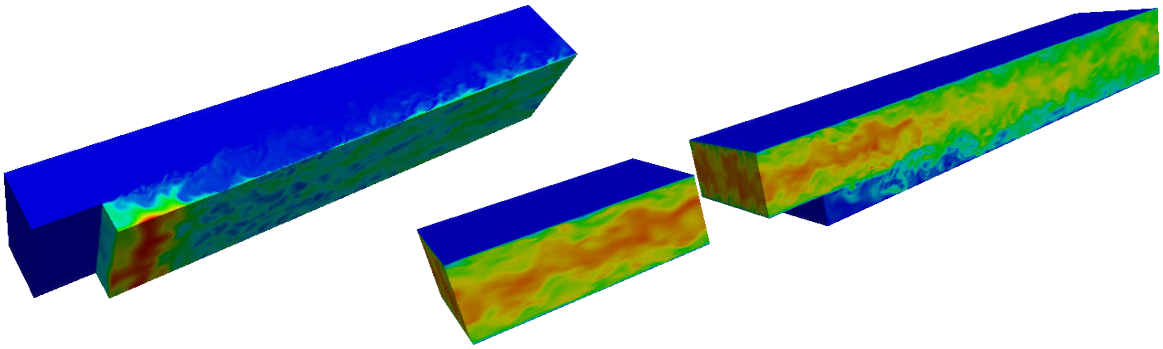

Figure 6.10: Instantaneous temperature (left) and velocity magnitude (right) distribution in inflow channel and over backward-facing step (red color indicates high velocity/temperature and blue color low velocity/temperature). Results obtained with the AVM^4 are shown at the end of the simulation.

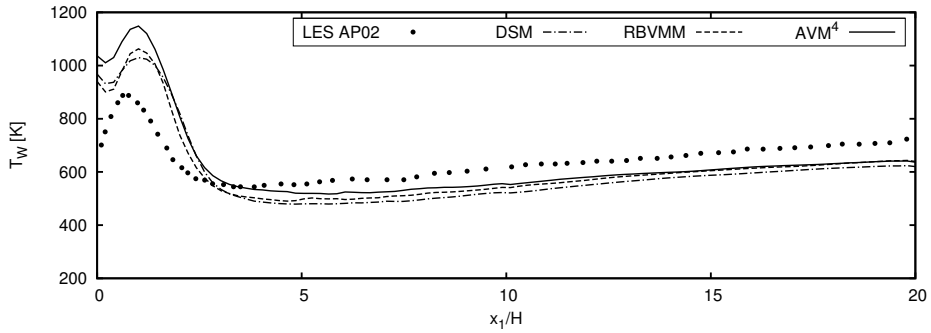

Figure 6.11: Mean temperature T_{W} at the bottom wall of the backward-facing step.

All velocity results are normalized by the mean centerline velocity U_{c} at the inlet of the backward-facing step. Velocity profiles as well as root-mean-square velocities are plotted against the isothermal experimental results from Kasagi and Matsunaga [168], denoted by "Exp KM95", which were also used by Avancha and Pletcher [9] as reference results and allow for a qualitative comparison over the complete domain. As already indicated by the instantaneous temperature distribution, and as will be seen below in the discussion of the mean temperature profiles, mainly the domain from the bottom wall up to the horizontal line defined by the upper corner of the step

is affected by heating. Downstream of the recirculation zone, the influence of heating is even more restricted to the near-wall region. Therefore, the isothermal experimental values may be considered as reliable reference results for the upper domain above the step as well as large parts behind the recirculation zone. Figure 6.12 illustrates the mean streamwise velocity $\langle u_1 \rangle$ at various locations behind the step. Despite the relatively high heating, the overall results do not notably deviate from the isothermal data. All models provide results that are in good agreement with the experimental data, and differences between the various models are hardly observable. Overall, the AVM^4 performs slightly better than the RBVMM and DSM. Figure 6.13 displays all root-mean-square velocities rms u_i. Here, differences between the methods are clearly observable. Near the upper wall, where the flow is unaffected by heating, the AVM^4 provides results well matching the ones from the experiment, whereas the results obtained with the RBVMM and DSM notably deviate from them. As already observed for turbulent channel flow, the AVM^4 captures rms u_1 very accurately, while the RBVMM and in particular the DSM overestimate rms u_1. The AVM^4 and RBVMM yield good results for rms u_2 and rms u_3, which are both underestimated by the DSM. Bearing in mind the aforementioned restrictions, the results obtained with the AVM^4 are also in the lower domain significantly closer to the experimental data than the ones provided by the other two methods. Except for the first three locations, the RBVMM and DSM show similar behavior.

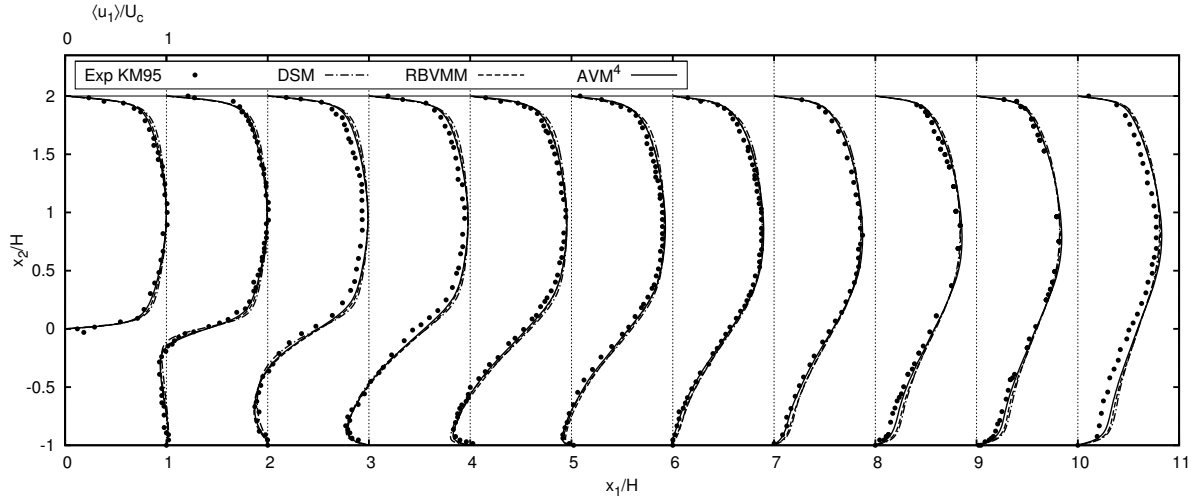

Figure 6.12: Mean streamwise velocity $\langle u_1 \rangle / U_\mathrm{c}$ at various locations x_1/H for turbulent flow over a backward-facing step with heating.

Figure 6.14 shows mean temperature profiles at various locations behind the step. A closeup view of the near-wall region is also included. All temperature results are normalized by the initial temperature T_0 and only shown for the lower part of the problem domain, i.e., up to $x_2/H = 1$. As aforementioned, the temperature undergoes substantial variations near the step. Above the step and further downstream, the temperature almost equals the initial temperature. Behind the recirculation zone, significant temperature variations are restricted to a thin boundary layer. Except for the first two sampling locations, differences between the methods are only of small amount. At $x_1/H = 1$ and 3, the present simulations reveal higher temperatures than the

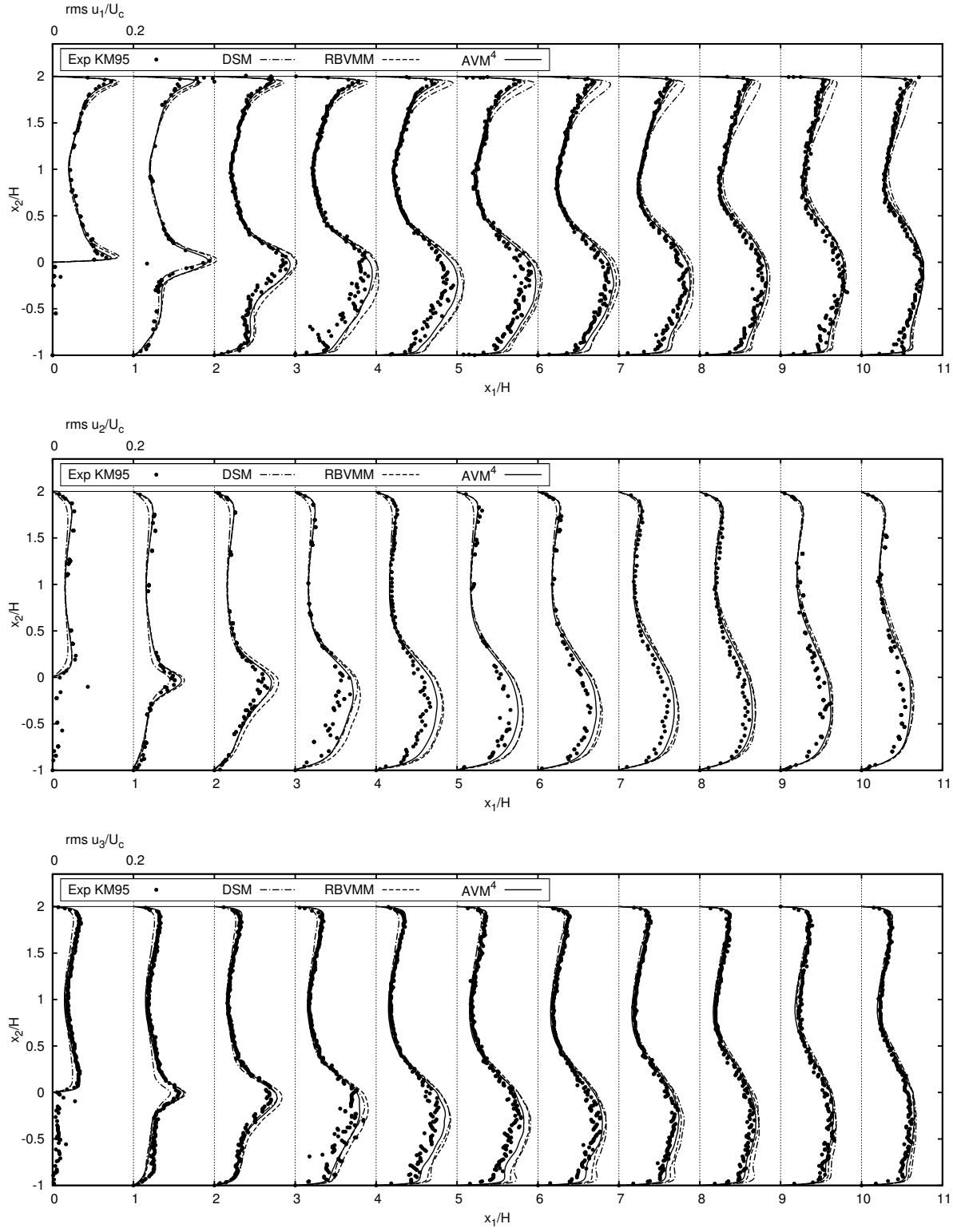

Figure 6.13: Root-mean-square velocities rms u_i/U_c at various locations x_1/H for turbulent flow over a backward-facing step with heating.

LES presented by Avancha and Pletcher [9], while somewhat lower values compared to Avancha and Pletcher [9] are obtained at the locations $x_1/H = 5, 7$ and 9. With respect to the present methods, the AVM^4 predicts higher values than the RBVMM, which, in turn, yields higher ones than the DSM. The differences between the methods decrease with increasing distance from the step. Figure 6.15 shows the root-mean-square temperature rms T as well as correlations of

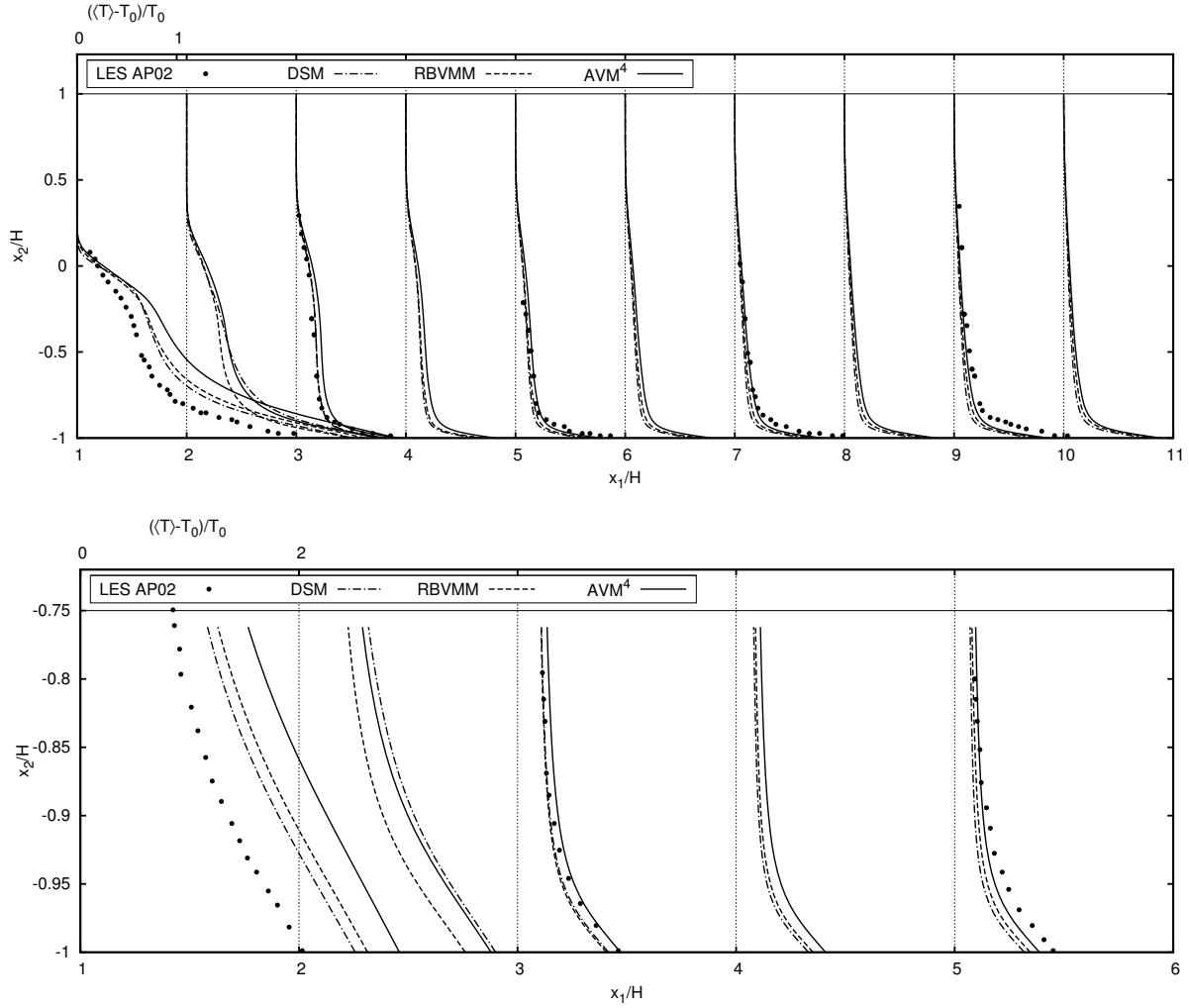

Figure 6.14: Mean temperature $(\langle T \rangle - T_0)/T_0$ at various locations x_1/H for turbulent flow over a backward-facing step with heating including a closeup view of the near-wall region.

streamwise and wall-normal velocity and temperature fluctuations, $\langle u_1' T' \rangle$ and $\langle u_2' T' \rangle$, respectively. Compared to the results shown for rms T by Avancha and Pletcher [9], higher values are obtained at $x_1/H = 1$ with the present methods, while lower values are observed at the remaining locations. No data for a direct comparison are available from Avancha and Pletcher [9] for correlations of velocity and temperature fluctuations. A qualitative comparison with the corresponding data shown in Keating *et al.* [170] (see Figure 16 therein for $\langle u_1' T' \rangle$ and Figure 17 for $\langle u_2' T' \rangle$) for a somewhat different configuration, as described above, reveals that the behavior of the present data is in agreement with the one given by Keating *et al.* [170]. Pronounced

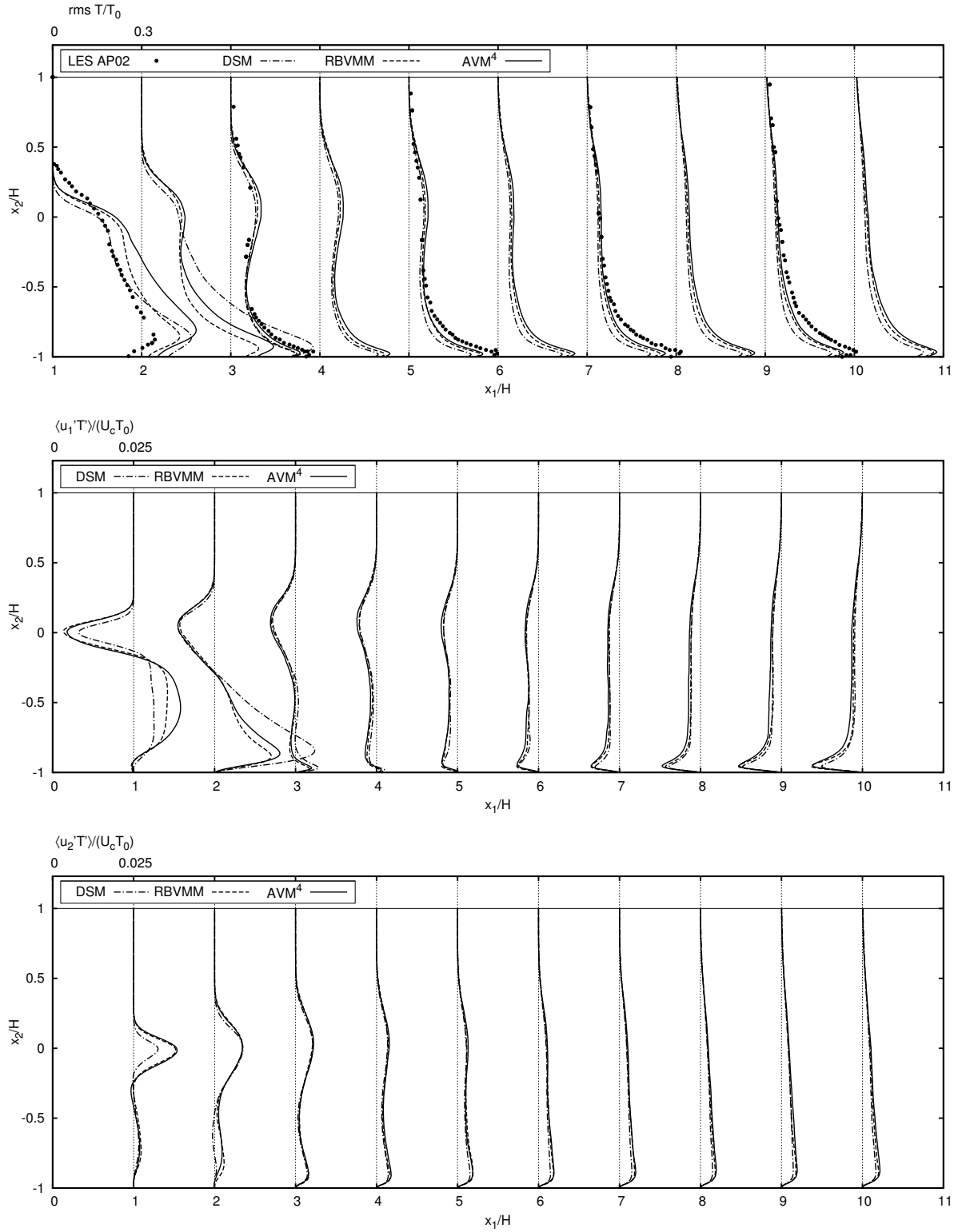

Figure 6.15: Root-mean-square temperature $\mathrm{rms}\, T/T_0$, streamwise velocity-temperature fluctuations $\langle u_1' T' \rangle / (U_\mathrm{c} T_0)$ and wall-normal velocity-temperature fluctuations $\langle u_2' T' \rangle / (U_\mathrm{c} T_0)$ at various locations x_1/H for turbulent flow over a backward-facing step with heating.

differences between the present methods are restricted to the locations $x_1/H = 1$ and 2 and are particularly observable for the rather demanding rms T and $\langle u_1' T' \rangle$. Again, differences between them decrease with increasing distance from the step. While the results obtained with the AVM^4 and RBVMM are quite close to each other, the DSM tends to somewhat deviating values.

The skin-friction coefficient is defined as

$$C_\mathrm{f} = \frac{\tau_\mathrm{W}}{\frac{1}{2}\rho_0 U_\mathrm{c}^2}, \tag{6.61}$$

where τ_W

$$\tau_\mathrm{W} = \left\langle \mu_\mathrm{W} \frac{\partial u_1}{\partial x_2}\bigg|_\mathrm{W} \right\rangle \tag{6.62}$$

denotes the wall-shear stress. Figure 6.16 shows the skin-friction coefficient at the bottom wall. Again, LES data taken from Avancha and Pletcher [9] are included. With respect to those data, it is remarked that (i) the wall-shear stress τ_W does not go to zero at the corner, which is however mandatory due the vertical step wall and the resulting zero velocity gradient in bottom-wall-normal direction, and (ii) C_f is defined as $C_\mathrm{f} = (2/\mathrm{Re})(\mu_\mathrm{W}/\rho_\mathrm{W})\,(\partial u_1/\partial x_2)\,|_\mathrm{W}$ in Avancha and Pletcher [9], which is a dimensional quantity. Therefore, the values from Avancha and Pletcher [9] should be taken with caution. Due to the lack of other variable-density data for this problem configuration, those values are nevertheless added to the diagrams. Additionally, results for incompressible flow over a backward-facing step obtained with the AVM^4 and provided in Rasthofer and Gravemeier [258] are included. Therein, a coarser discretization with about 1.9 million elements was used. The respective results are marked by "AVM^4 RG13". Apart from those LES data, isothermal DNS data reported by Le *et al.* [179] are also incorporated for a qualitative comparison. They are denoted by "LMK 97". In contrast to the questionable results given in Avancha and Pletcher [9], the present results are in good agreement with the isothermal data. The negative peak value is obtained at almost the same location as in the isothermal case. Except for a somewhat more negative peak value predicted by the RBVMM and DSM, differences between the methods are only of small amount. Due to the increase of μ_W in the heated

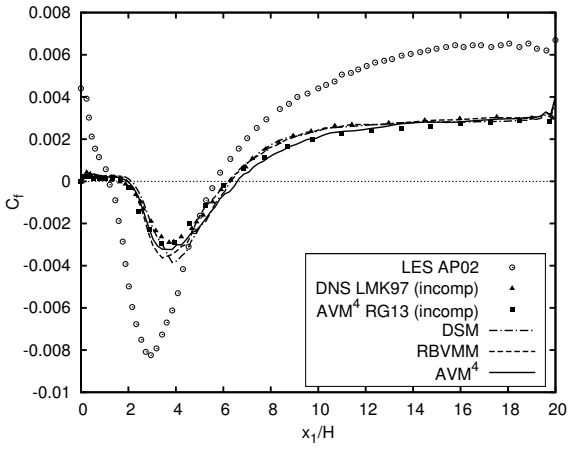

Figure 6.16: Skin-friction coefficient C_f at the bottom wall of the backward-facing step.

configuration, the flow at the bottom wall behind the step becomes less turbulent resulting in a lower gradient of $\mathbf{u}$ in wall-normal direction, which counterbalances higher viscosity values such that the wall-shear stress remains nearly unaffected. The mean reattachment length X_r/H is defined by the location of zero wall-shear stress, which is equivalent to $C_\mathrm{f} = 0$. Table 6.3 summarizes the predicted mean reattachment length for all methods as well as results from several isothermal studies. All present values of the heated configuration are within the range of the isothermal reference data, but tend to the higher end of the spectrum.

Table 6.3: Mean reattachment length X_r/H of turbulent flow over a backward-facing step with heating from present simulations as well as isothermal numerical and experimental results from other studies.

	$q_\mathrm{W} = 3000\ \frac{\mathrm{W}}{\mathrm{m}^2}$	isothermal
present results		
AVM^4	6.59	-
RBVMM	6.23	-
DSM	6.31	-
numerical results		
DNS LMK95 [179]	-	6.28
LES ADL07 [2]	-	5.29-5.80
AVM^4 RG13 [258]	-	6.18
experimental results		
Exp KM95 [168]	-	6.51
Exp JD94 [165]	-	6$\pm$0.15

II

XAVM^4 - The EXtended Algebraic Variational Multiscale-Multigrid-Multifractal Method for Two-Phase Flows

7

Fluid Dynamics with Interfaces

This chapter aims at providing the framework for the subsequent two-phase-flow simulations, both from a physical as well as a computational point of view. Based on three general physical principles, which are (i) the continuum hypothesis, (iii) the assumption of infinitely thin interfaces and (iii) the consideration of intermolecular forces by modeling them as surface tension, a mathematical description of the incompressible flow of two immiscible fluids is presented. Computational strategies for two-phase flows are reviewed, and fixed-grid methods are identified as an adequate approach for their numerical simulation.

7.1 Physics of Two-Phase Flows

Taking the continuum hypothesis (see also Section 2.1) as a basis for treating the involved fluids, the smooth transition from one fluid to another occurs at very small scales, i.e., within a layer which is only a few molecules in size, such that the interface thickness may be considered as infinitely thin; see, e.g., the textbook by Levich [189]. At the macroscopic level of two contiguous bulk fluids separated by an infinitely thin interface, the effect of cohesive forces between the individual molecules amounts to a stress concentrated at the interface and referred to as surface tension.

For each fluid, the velocity field $\mathbf{u}(\mathbf{x},t) = (u_1(\mathbf{x},t), u_2(\mathbf{x},t), u_3(\mathbf{x},t))^{\mathrm{T}}$ is governed by the incompressible Navier-Stokes equations as

$$\rho\frac{\partial \mathbf{u}}{\partial t} + \rho\nabla\cdot(\mathbf{u}\otimes\mathbf{u}) + \nabla p - 2\mu\nabla\cdot\boldsymbol{\varepsilon}(\mathbf{u}) = \rho\mathbf{g}, \tag{7.1}$$

$$\nabla\cdot\mathbf{u} = 0, \tag{7.2}$$

where $p(\mathbf{x},t)$ denotes the pressure. Density ρ and dynamic viscosity μ are assumed constant. Moreover, $\boldsymbol{\varepsilon}(\mathbf{u})$ is the rate-of-deformation tensor, defined in equation (2.3), and $\mathbf{g}$ the gravity force vector. To derive the interface conditions coupling the motions of the fluids, the conservation principles of mass and momentum are applied to a control volume including a portion of the interface. The control volume follows the movement of the interface, which is described by its normal velocity u_{int}. The thickness of the control volume is assumed to go to zero. Balance

of mass and momentum across the interface leads to

$$\rho_- \left(\mathbf{u}_- \cdot \mathbf{n}_{\text{int}} - u_{\text{int}}\right) = \rho_+ \left(\mathbf{u}_+ \cdot \mathbf{n}_{\text{int}} - u_{\text{int}}\right) = \dot{m}, \tag{7.3}$$

$$\begin{aligned}\rho_- \mathbf{u}_- \left(\mathbf{u}_- \cdot \mathbf{n}_{\text{int}} - u_{\text{int}}\right) - \boldsymbol{\sigma}(\mathbf{u}_-, p_-) \cdot \mathbf{n}_{\text{int}} = {} & \rho_+ \mathbf{u}_+ \left(\mathbf{u}_+ \cdot \mathbf{n}_{\text{int}} - u_{\text{int}}\right) - \boldsymbol{\sigma}(\mathbf{u}_+, p_+) \cdot \mathbf{n}_{\text{int}} \\ & + \gamma \kappa \mathbf{n}_{\text{int}} + \nabla_\Gamma \gamma,\end{aligned} \tag{7.4}$$

where $\boldsymbol{\sigma}(\mathbf{u}, p)$ denotes the Cauchy-stress tensor, defined as

$$\boldsymbol{\sigma}(\mathbf{u}, p) = -p\mathbf{I} + 2\mu\boldsymbol{\varepsilon}\left(\mathbf{u}\right). \tag{7.5}$$

Variables corresponding to the first and second fluid are labeled by $(\cdot)_+$ and $(\cdot)_-$, respectively. By definition, the unit normal vector $\mathbf{n}_{\text{int}}$ on the interface points from the domain occupied by the fluid marked by $(\cdot)_+$ to the domain filled with the fluid denoted by $(\cdot)_-$. The first equation is the Rankine-Hugoniot condition. Since phase change is not considered, implying $\dot{m} = 0$ for the mass flux across the interface, the interface velocity as well as the normal velocities on both sides have to be equal, i.e., $u_{\text{int}} = \mathbf{u}_+ \cdot \mathbf{n}_{\text{int}} = \mathbf{u}_- \cdot \mathbf{n}_{\text{int}}$. This result may be transferred into a jump condition for the velocity:

$$[\![\mathbf{u}]\!] \cdot \mathbf{n}_{\text{int}} = 0, \tag{7.6}$$

using the jump operator $[\![\cdot]\!] := (\cdot)_- - (\cdot)_+$. Mass conservation does not introduce any restriction on the tangential velocities. For viscous fluids, the tangential velocities are continuous, that is, a no-slip condition is assumed:

$$[\![\mathbf{u}]\!] \cdot \mathbf{t}_{\text{int}}^{(i)} = 0, \tag{7.7}$$

where $\mathbf{t}_{\text{int}}^{(i)}$ with $i = 1, 2$ are the unit tangential vectors on the interface. Concerning momentum conservation (7.4), the first term on the left and right-hand side vanishes owing to the results from mass conservation. The surface force given by the third and fourth term on the right-hand side represent surface tension. The surface-tension coefficient, which depends in general on the involved fluids and the temperature, is denoted by γ, and $\nabla_\Gamma(\cdot) := (\mathbf{I} - \mathbf{n}_{\text{int}} \otimes \mathbf{n}_{\text{int}})\nabla(\cdot)$ is the tangential derivative operator at the interface. The curvature κ of the interface is defined as

$$\kappa = -\nabla \cdot \mathbf{n}_{\text{int}}. \tag{7.8}$$

Expressed in terms of jump conditions, momentum conservation across the interface yields

$$\mathbf{n}_{\text{int}} \cdot [\![\boldsymbol{\sigma}(\mathbf{u}, p)]\!] \cdot \mathbf{n}_{\text{int}} = -\gamma\kappa, \tag{7.9}$$

$$\mathbf{t}_{\text{int}}^{(i)} \cdot [\![\boldsymbol{\sigma}(\mathbf{u}, p)]\!] \cdot \mathbf{n}_{\text{int}} = -\mathbf{t}_{\text{int}}^{(i)} \cdot \nabla_\Gamma \gamma \tag{7.10}$$

in normal and tangential directions, respectively. For constant surface-tension coefficients, the normal stress exhibits a jump, while the tangential stresses are continuous. Variable surface-tension coefficients emanate, for instance, from temperature variations or surface-active substances with varying concentrations. Such cases are not considered here, and γ is assumed constant in the remainder of this thesis. Combining conditions (7.6) and (7.7) as well as (7.9)

and (7.10), the following set of interface conditions is obtained:

$$[\![\mathbf{u}]\!] = 0, \tag{7.11}$$

$$[\![\boldsymbol{\sigma}(\mathbf{u}, p)]\!] \cdot \mathbf{n}_{\text{int}} = -\gamma\kappa\mathbf{n}_{\text{int}}; \tag{7.12}$$

see, e.g., the textbook by Tryggvason *et al.* [316] for further details on the derivation.

Since two-phase flows exhibit a wide variety of phenomena, a more detailed presentation of some further physical aspects, for instance, instabilities occurring in stratified fluids, bubble dynamics as well as issues related to turbulence, are postponed to the respective applications in the subsequent chapters.

7.2 Simulating Flows with Moving Interfaces

The interface separating the two fluids usually undergoes large and complex deformations including break-up processes and reconnections. Moreover, the interface manifests itself as a discontinuity in the flow field. On the one hand, the physical parameters change discontinuously across the interface. On the other hand, the traction interface condition describes discontinuities in the velocity gradient and pressure field. Most of the methods and issues addressed in the following are presented in a more thorough form, e.g., in the introductory textbook by Tryggvason *et al.* [316] and the review article by Scardovelli and Zaleski [275].

Moving-grid methods, where the interface is represented by element or cell boundaries, facilitate the treatment of discontinuities and allow for a direct imposition of interface conditions. However, as soon as the interface is subject to a complex evolution, remeshing of the domain, which is a computationally expensive task and also comes along with the transfer of the solution fields from the old grid to the new one, is usually unavoidable. The Arbitrary Lagrangian-Eulerian (ALE) approach, frequently applied in the context of fluid dynamics and reviewed, e.g., by Donea *et al.* [86], aims at combining the advantages of the Lagrangian and Eulerian description.

In contrast, the interface somehow cuts across the grid in fixed-grid methods; that is, the interface is not aligned with element or cell boundaries. Numerical methods for governing the evolving interface can be grouped into Lagrangian and Eulerian approaches. Front-tracking methods, which describe the interface explicitly, are among the first category. The method by Unverdi and Tryggvason [317], for instance, advects connected marker points, which represent a moving interface grid. For large interface deformations as well as topological changes, the marker particles and their connectivity need to be rearranged. Approaches based on an Eulerian description such as the Volume-Of-Fluid (VOF) method and the level-set method provide the interface in an implicit way and are commonly classified as interface-capturing methods. The VOF was first introduced by Hirt and Nichols [148], but dates back to early works, e.g., by Noh and Woodward [232]. A scalar function describes the volume fraction corresponding to one of the two fluids for each grid cell and is advected in a conservative way. The VOF naturally accounts for topological changes, but the interface has to be reconstructed based on the discrete volume

fractions. The VOF was recently reviewed with a focus on applications to two-phase flows by Fuster *et al.* [105]. A comprehensive description of the VOF, including many significant contributions as well as implementation aspects, may be found, e.g., in the textbook by Tryggvason *et al.* [316]. The level-set method was introduced by Osher and Sethian [241] and first applied to incompressible two-phase flows by Sussman *et al.* [301]. Introductory textbooks are Osher and Fedkiw [240] as well as Sethian [283]. A review article was written, e.g., by Losasso *et al.* [199]. In the level-set method, the interface is represented by the zero iso-contour of a smooth function, which is positive in one fluid domain and negative in the other one. Usually, the smooth function is defined as a signed distance function to interface. The transport equation for the level-set function can in principle be solved with any standard method for hyperbolic equations. The level-set method is known for not properly preserving volume or mass, respectively, and usually requires recovering the signed distance property during simulation, referred to as reinitialization. Similar to the VOF, the level-set method handles topological changes without additional provisions. The main advantage commonly attributed to the level-set method is the straightforward evaluation of geometrical interface quantities, for instance, curvature and normal vectors.

When using interfaces embedded into an unfitted grid, additional numerical effort is required to cope with discontinuities at the interface and to apply interface conditions. The regularization of the discontinuities in the solution fields constitutes a straightforward way. Physical parameters may also be smoothly blended from one fluid to the other. The continuum surface force model of Brackbill *et al.* [36], which incorporates surface tension via a local volume force, or similar approaches are frequently used. In doing so, the interface is numerically thickened over several elements or grid cells. Other strategies consider sharp interfaces. The ghost fluid method, originally introduced by Fedkiw *et al.* [94] and further developed for multiphase incompressible flow by Kang *et al.* [167], is among the most popular techniques of this category. Alternative methods for application to incompressible two-phase flow were devised, e.g., by Sussman *et al.* [304] and Wang and Tong [330]. In FEMs, sharp interfaces may be dealt with using the XFEM, which is adopted in this thesis in conjunction with the level-set method.

8

A Computational Framework for the Level-Set Method

Level-set methods enable a convenient description of complex interface evolutions. However, level-set methods demand specifically devised numerical frameworks to prevent excessive mass/volume loss, to recover the signed distance property and to remain computationally efficient, among other things. In this respect, this chapter does not only provide the (basic) level-set method used for capturing the interface in the two-phase-flow simulations carried out in the next chapters, but also addresses further progress towards a more advanced and comprehensive framework for the level-set field in the context of FEMs. A novel elliptic reinitialization equation, recently proposed by Basting and Kuzmin [18] and specifically devised for FEMs, is introduced to some extent. In particular, the idea of a hybrid particle-level-set method, originally developed by Enright *et al.* [91], is transferred to a finite element approach for the level-set field and thoroughly studied.[1] At the beginning of this chapter, the level-set equation is introduced, and a stabilized finite element formulation is presented. Thereafter, reinitialization of the level-set function is addressed. Next, it is focused on the hybrid particle-level-set method, including a survey of mass/volume-conservation issues in level-set approaches. Eventually, the proposed hybrid particle-level-set method is validated for classical level-set test cases and applied to the impact of a drop on a quiescent water surface. Supportive results obtained with the basic level-set method are additionally considered.

8.1 The Level-Set Equation

The level-set method uses a smooth scalar function $\phi(\mathbf{x}, t)$ whose zero iso-contour implicitly represents the interface in a considered domain Ω:

$$\Gamma_{\text{int}}(t) := \{\mathbf{x} \in \Omega \mid \phi(\mathbf{x}, t) = 0\}. \tag{8.1}$$

[1] This method has been realized during the final stage of the author's PhD studies to overcome deficiencies in terms of accuracy and mass/volume conservation observed for the originally available level-set approach. At the time of computing the examples shown in Chapters 9 and 10, this improvement had not yet been devised to its full extent and had thus not be applied. Likewise, the elliptic reinitialization equation has only recently been implemented in BACI (see Section 4.6) by the author of this thesis.

Moreover, two subdomains, $\Omega_+(t)$ and $\Omega_-(t)$, with $\Omega_+ \cap \Omega_- = \emptyset$ and $\Omega_+ \cup \Omega_- = \Omega$, can be identified by the sign of the level-set function, i.e.,

$$\phi(\mathbf{x},t) \begin{cases} > 0 & \text{if } \mathbf{x} \text{ in } \Omega_+(t) \\ = 0 & \text{if } \mathbf{x} \text{ on } \Gamma_{\text{int}}(t) \\ < 0 & \text{if } \mathbf{x} \text{ in } \Omega_-(t). \end{cases} \tag{8.2}$$

The unit normal vector $\mathbf{n}(\phi)$ to the iso-contours of ϕ and their curvature $\kappa(\phi)$ can be directly calculated from the level-set function as

$$\mathbf{n}(\phi) = \frac{\nabla\phi}{\|\nabla\phi\|} \tag{8.3}$$

and

$$\kappa(\phi) = \nabla \cdot \frac{\nabla\phi}{\|\nabla\phi\|}, \tag{8.4}$$

respectively. In level-set methods, it is common to define $\phi(\mathbf{x})$ equal to the signed distance to the interface Γ_{int}:

$$\phi(\mathbf{x}) = \begin{cases} - \min\limits_{\mathbf{x}_{\Gamma_{\text{int}}} \in \Gamma_{\text{int}}} (\|\mathbf{x} - \mathbf{x}_{\Gamma_{\text{int}}}\|) & \text{if } \operatorname{sign}((\mathbf{x} - \mathbf{x}_{\Gamma_{\text{int}}}) \cdot \mathbf{n}_{\text{int}}) > 0 \\ \min\limits_{\mathbf{x}_{\Gamma_{\text{int}}} \in \Gamma_{\text{int}}} (\|\mathbf{x} - \mathbf{x}_{\Gamma_{\text{int}}}\|) & \text{if } \operatorname{sign}((\mathbf{x} - \mathbf{x}_{\Gamma_{\text{int}}}) \cdot \mathbf{n}_{\text{int}}) \leq 0 \end{cases} \tag{8.5}$$

for all $\mathbf{x} \in \Omega$, implying

$$\|\nabla\phi\| = 1. \tag{8.6}$$

The unit normal vector $\mathbf{n}_{\text{int}}$ on the interface is assumed to point into Ω_-; i.e., $\mathbf{n}_{\text{int}} = -\mathbf{n}(\phi = 0)$. The level-set function is advected by a velocity field $\mathbf{a}(\mathbf{x},t)$, which may, for instance, be externally prescribed, dependent on the geometry of the interface itself or be the solution $\mathbf{u}(\mathbf{x},t)$ of the Navier-Stokes equations as for two-phase flows. The evolution of $\phi(\mathbf{x},t)$ in the domain Ω is mathematically governed by the advection equation as

$$\frac{\partial\phi}{\partial t} + \mathbf{a} \cdot \nabla\phi = 0 \qquad \text{in } \Omega \times]0, t_{\text{end}}[, \tag{8.7}$$

$$\phi = \phi_0 \qquad \text{in } \Omega \times \{0\}, \tag{8.8}$$

where t_{end} marks the end of the considered time period. Equation (8.7) is also referred to as the level-set equation. The level-set field is initialized as a signed distance function.

The stabilized finite element formulation of the level-set equation (8.7) reads: find $\phi^h \in \mathcal{S}_\phi^h$ such that

$$\left(w^h, \frac{\partial\phi^h}{\partial t}\right)_\Omega + \left(w^h, \mathbf{a} \cdot \nabla\phi^h\right)_\Omega + \left(\mathbf{a} \cdot \nabla w^h, \tau_{\text{LS}} r_{\text{LS}}^h\right)_{\Omega^*} = 0 \tag{8.9}$$

for all $w^h \in \mathcal{V}_\phi^h$. Here, $\mathcal{S}_\phi^h$ and $\mathcal{V}_\phi^h$ denote appropriate finite dimensional solution and weighting functions spaces for the discrete solution function ϕ^h and the discrete scalar weighting function w^h, respectively; see also Section 5.2. As introduced in Section 3.2, $(\cdot,\cdot)_\Omega$ denotes the usual L_2-

inner product in Ω. For further general notations, it is referred to Chapter 3. The last term on the left-hand side constitutes the SUPG term, which provides convective stabilization. The discrete residual r_{LS}^h of the level-set equation is given by

$$r_{\mathrm{LS}}^h = \frac{\partial \phi^h}{\partial t} + \mathbf{a} \cdot \nabla \phi^h. \tag{8.10}$$

The stabilization parameter introduced by Taylor *et al.* [306] is adapted to pure convection, i.e., vanishing diffusivity. Hence, stabilization parameter τ_{LS} is defined as

$$\tau_{\mathrm{LS}} = \frac{1}{\sqrt{\frac{4}{\Delta t^2} + \mathbf{a} \cdot \mathbf{G}\mathbf{a}}}, \tag{8.11}$$

using tensor $\mathbf{G}$ as given in equation (3.42). According to the derivations provided in Sections 5.2 and 5.4, formulation (8.9) may also be interpreted as a form of a residual-based variational multiscale formulation. For time integration, the one-step-θ scheme with $\theta = 0.5$ (i.e., the Crank-Nicolson scheme) is applied.

For incorporation of surface tension in two-phase flow simulations, the computation of the curvature κ of the interface is required. According to equation (8.4), this computation involves second derivatives of the discrete solution function ϕ^h. Since trilinearly-interpolated hexahedral elements are used in this thesis, the required second derivatives partially vanish in the element interior. Therefore, continuous gradients are reconstructed based on an L_2-projection, as applied, e.g., by Jansen *et al.* [158]. For each spatial direction $i = 1, 2$ and 3, it is solved for

$$\left(w^h, (\mathbf{b}^h)_i\right)_\Omega = \left(w^h, (\nabla \phi^h)_i\right)_\Omega, \tag{8.12}$$

where the continuous gradient field is given in a usual finite element expansion (see also Section 3.2) as

$$\mathbf{b}^h = \sum_{A \in \mathcal{E}} N_A \mathbf{b}_A. \tag{8.13}$$

The second derivatives are then evaluated by differentiating $\mathbf{b}^h$ at points in the element interior, where κ has to be evaluated. A similar procedure was used, e.g., by Nagrath *et al.* [228].

8.2 Reinitialization

As the interface evolves in time, the level-set function may drift away from a signed distance function. The development of disturbing features such as too flat or too steep gradients, which may result in numerical artifacts or instabilities, has to be prevented, though. Moreover, some approaches incorporating the level-set method strongly rely on ϕ being a signed distance function, for instance, those defining a constant interface thickness to smooth discontinuities and impose surface tension. Therefore, periodic reinitialization of the level-set function to restore the signed distance property is commonly applied. After providing an overview of major approaches to reinitialization, a geometric reinitialization procedure, which is used in this thesis, as well as an

elliptic reinitialization equation, which is particularly tailored to application within FEMs, are presented in detail.

8.2.1 Common Techniques for Reinitization

The most straightforward way to rebuild a signed distance function is the explicit computation of the distance of each node or grid point to the interface or an approximation thereof, respectively. From a computational point of view, however, geometric reinitialization is a quite expensive task. Fast marching methods, originally introduced by Sethian [282], solve the Eikonal equation $\|\nabla\phi\| = 1$ to reinitialize the level-set field. Therefore, fast marching methods step though the grid points in a specific order starting from the interface outward. Elias *et al.* [90], for instance, proposed an extension of the fast marching method for computing distance fields in a finite element context with unstructured grids. A finite-element-based level-set method for two-phase flows including a variant of the fast marching method was introduced by Groß *et al.* [132]. Sussman *et al.* [301] derived a partial differential equation which is solved to steady state in pseudo time τ to redistance ϕ. The so-called reinitialization equation is given by

$$\frac{\partial\phi}{\partial\tau} + \text{sign}(\phi_0)\,(\|\nabla\phi\| - 1) = 0 \quad \text{in } \Omega. \tag{8.14}$$

and can be reformulated to

$$\frac{\partial\phi}{\partial\tau} + \mathbf{w}(\phi)\cdot\nabla\phi = \text{sign}(\phi_0) \quad \text{in } \Omega, \tag{8.15}$$

where the velocity $\mathbf{w}$ depends on ϕ as

$$\mathbf{w}(\phi) = \text{sign}(\phi_0)\frac{\nabla\phi}{\|\nabla\phi\|}. \tag{8.16}$$

The initial (disturbed) level-set field is denoted by ϕ_0. For numerical reasons, Sussman *et al.* [301] replaced the discontinuous sign-function $\text{sign}(\phi_0)$ by a smoothed form $S(\phi_0)$, which is defined as

$$S(\phi_0) = \frac{\phi_0}{\sqrt{\phi_0^2 + h^2}} \tag{8.17}$$

based on the grid size h. Equation (8.15) is a non-linear hyperbolic equation. The velocity vector $\mathbf{w}$ is a unit vector normal to the iso-contours of the level-set function and points away from the interface. This reinitialization procedure avoids explicitly determining the interface. Since the information propagates from the interface to the far field, only a few pseudo time steps have to be performed to restore the signed distance property in a band around the interface. Solving the reinitialization equation numerically may lead to a movement of the interface and, hence, to a change of volume. Therefore, Sussman and Fatemi [299] suggested a constraint which is evaluated locally and aims at preserving the subdomain volumes in each grid cell during reinitialization. Nagrath *et al.* [228] used an SUPG-stabilized finite element formulation for the level-set equation, similar to the present approach, as well as for the reinitialization equation. Additionally, the volume constraint according to Sussman and Fatemi [299] was realized within an FEM.

Characteristic Galerkin FEMs to solve for the level-set equation and the reinitialization equation were applied, e.g., by Lin *et al.* [194], who validated their method for established level-set test cases as well as two-phase-flow problems, and Quecedo and Pastor [257], who also investigated two-phase flows. To enhance stability, Akkerman *et al.* [3] considered the SUPG term together with a discontinuity-capturing term for the level-set and the reinitialization equation. Additionally, a term penalizing movements of the interface during reinitialization was included in the latter. A so-called convected level-set method which embeds the reinitialization equation into the transport equation for the level-set field, was presented by Ville *et al.* [321]. An SUPG-stabilized FEM was applied to the resulting equation.

8.2.2 Geometric Reinitialization

In this thesis, a discrete representation of the interface by surface patches is used for a geometric reinitialization. For each node of the discretization, the distance from the interface is determined based on the minimal distance to the surface patches, their edges or vertices. When applying this approach in the context of two-phase-flow simulations based on the XFEM, the surface patches are obtained without additional effort as they have to be constructed for the purpose of evaluating interface terms. This reinitialization strategy is exclusively applied in this thesis. For further details as well as evaluations, the reader is referred to the accompanying thesis by Henke [140].

As observed for most reinitialization procedures, the interface position is not preserved. In order to improve mass/volume conservation, an issue which is also particularly addressed in the next section, a relatively simple correction to the level-set field, which can be optionally applied after reinitialization, is additionally considered in this thesis. Global mass conservation may be enforced by shifting the zero iso-contour of the level-set function by a small increment estimated via

$$\phi_{n+1} \longleftarrow \phi_{n+1} + C_{\mathrm{M}} \left(V(\Omega_-(t_{n+1})) - V(\Omega_-(t_0)) \right), \tag{8.18}$$

using the volume $V(\Omega_-(t_{n+1}))$ of subdomain Ω_- at the current time level t_{n+1} as well as its initial one. Owing to the signed distance property after reinitialization, the interface is homogeneously moved by a distance of the increment. Here, coefficient C_{M} is estimated based on the area $A(\Gamma_{\mathrm{int}}(t_{n+1}))$ of the current interface as

$$C_{\mathrm{M}} = \frac{1}{A(\Gamma_{\mathrm{int}}(t_{n+1}))}. \tag{8.19}$$

Although several iterations are conceivable for correcting ϕ_{n+1} based on equation (8.18), one step turned out to be sufficiently accurate. Analogous techniques were applied, e.g., by Croce *et al.* [75] and Lee *et al.* [181]. As further explained below, global mass conservation has to be used with caution. This procedure is thus only applied if appropriate and necessary. Therefore, its inclusion is explicitly indicated in the remainder of this thesis.

In summary, the finite element formulation for the level-set equation presented in Section 8.1 together with the present geometric reinitialization procedure constitutes the basic level-set method applied to all two-phase-flow examples in this thesis. For its application within an XFEM, which

treats the interface separating the two fluids in a sharp fashion, reinitialization may just be performed as frequently as necessary to maintain a well-behaved level-set field.

8.2.3 Elliptic Reinitialization

As aforementioned, this chapter does not only provide the level-set method used for the two-phase-flow simulations performed in the subsequent chapters, but also aims at outlining further progress towards a more advanced framework for the level-set field. In this respect, another recently proposed reinitialization technique is briefly introduced here. Based on ideas introduced by Li *et al.* [191] in the context of level-set methods for image segmentation, Basting and Kuzmin [18] recently devised a minimization-based partial differential equation for reinitialization, which allows for application of standard FEMs for elliptic partial differential equation. This reinitialization procedure, which is referred to as elliptic reinitialization, preserves the signed distance property in a variationally consistent manner. As discussed by Basting and Kuzmin [18], the applied approach also allows for recovering modified signed distance functions, for instance, truncated fields which represent a signed distance function in the vicinity of the interface and exhibit constant values in the far field. Such modifications are not considered in the following, and the reader is referred to Basting and Kuzmin [18] for elaboration.

To restore the signed distance property of the level-set function, it is generally solved for the Eikonal equation

$$\|\nabla\phi\| = 1 \quad \text{in } \Omega \tag{8.20}$$

subject to the interface condition

$$\phi = 0 \quad \text{on } \Gamma_{\text{int}} \tag{8.21}$$

in some way. The least-squares solution to the Eikonal equation (8.20) is given by

$$\Pi_{\text{E}}(\phi) = \frac{1}{2}\int_{\Omega} \left(\|\nabla\phi\| - 1\right)^2 \mathrm{d}\Omega. \tag{8.22}$$

To enforce the interface condition (8.21), the energy functional Π_{E} is extended by an additional penalty term:

$$\Pi_{\text{P}}(\phi) = \frac{\alpha_{\text{P}}}{2}\int_{\Gamma_{\text{int}}} \phi^2 \mathrm{d}\Gamma, \tag{8.23}$$

where α_{P} denotes the penalty parameter. Minimization of the total energy functional $\Pi(\phi) = \Pi_{\text{E}}(\phi) + \Pi_{\text{P}}(\phi)$ leads to the variational formulation: find $\phi \in \mathcal{S}_\phi$ such that

$$\left(\nabla w, \left(1 - \frac{1}{\|\nabla\phi\|}\right)\nabla\phi\right)_{\Omega} + \left(\alpha_{\text{P}} w, \phi\right)_{\Gamma_{\text{int}}} = 0. \tag{8.24}$$

for all $w \in \mathcal{V}_\phi$, where $\mathcal{S}_\phi$ and $\mathcal{V}_\phi$ denote appropriate solution and weighting function spaces. The first term represents a diffusive term with diffusivity $(1 - 1/\|\nabla\phi\|)$. The diffusivity is positive for $\|\nabla\phi\| > 1$ such that these gradients in the level-set field get reduced and the signed distance function is recovered. For $\|\nabla\phi\| < 1$, the diffusivity is negative, and the level-set field becomes

steeper in the respective regions to likewise rebuild the signed distance function. The second term is the penalty term, which aims at preserving the zero iso-contour Γ_{int} of the original level-set field during the redistancing procedure. Therefore, α_{P} has to be chosen sufficiently large.

To solve the non-linear formulation (8.24), Basting and Kuzmin [18] suggested the application of a simple fixed-point iteration:

$$\left(\nabla w^h, \nabla \phi^{h,i+1}\right)_\Omega + \left(\alpha_{\text{P}} w^h, \phi^{h,i+1}\right)_{\Gamma_{\text{int}}} = \left(\nabla w, \frac{\nabla \phi^{h,i}}{\|\nabla \phi^{h,i}\|}\right)_\Omega , \tag{8.25}$$

where w and ϕ are replaced by their discrete counterparts $w^h \in \mathcal{V}_\phi^h$ and $\phi^h \in \mathcal{S}_\phi^h$. For initialization, $\phi^{h,0}$ is set to the original level-set field. This procedure leads to the repeated solution of a diffusion equation with source term and a weakly enforced Dirichlet-type condition at the interface. The source term on the right-hand side contains $\nabla \phi^h$. With respect to trilinearly-interpolated hexahedral elements, as considered in this thesis, a continuous approximation of the gradient, calculated via an L_2-projection (see equation (8.12)), may be considered, as also suggested by Basting and Kuzmin [18] for their linearly-interpolated triangular elements. For stability reasons, Basting and Kuzmin [18] further recommended to replace the consistent mass matrix resulting from the left-hand-side term of equation (8.12) by a lumped one. A lumped mass matrix is obtained, for instance, via a row-sum technique (see, e.g., Hughes [149]). The evaluation of the penalty term requires a discrete representation of the interface. To construct surface patches for integration on the interface, the same algorithm as used in the geometric reinitialization is applied.

For a first illustration of the performance of this reinitialization technique, the reinitialization of a one-dimensional level-set function $\phi(\mathbf{x}) = 0.2x_1$ is considered. The penalty parameter is set to $\alpha_{\text{P}} = 10^5$. A projection of $\nabla \phi^h$ is not applied for this simple configuration. The domain $\Omega = [-7.5, 7.5]$ is discretized using five elements. The elliptic reinitialization requires one iteration to exactly restore the signed distance function without shifting the interface. The result of this simple test is also displayed in Figure 8.1. Black values correspond to the initial field and colored ones to the restored signed distance field.

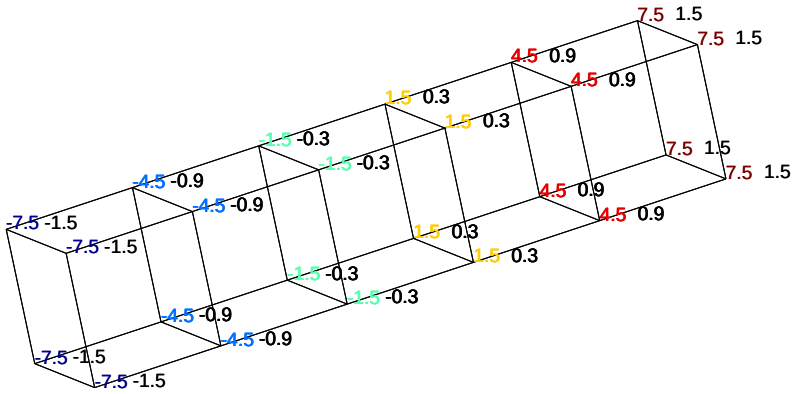

Figure 8.1: Elliptic reinitialization of one-dimensional function.

The elliptic reinitialization equation constitutes an interesting alternative to the established procedures, as also preliminary examinations based on classical benchmark examples for level-set methods indicate, and thus is worth further consideration. A more detailed discussion of this novel reinitialization technique, taking into account its application to the aforementioned test cases, which, to the best of the author's knowledge, has not yet been reported in literature, is however beyond the scope of the present thesis.

8.3 A Hybrid Particle-Level-Set Method

The level-set framework, presented so far and applied in this form to two-phase flows in Chapters 9 and 10, is further developed in this section in order to improve accuracy and mass/volume conservation. Potential sources of mass loss or gain, i.e., volume changes of the reference subdomain, and respective remedies are reviewed, and the hybrid particle-level-set method is identified as an adequate extension to the present framework to tackle this issue. The hybrid particle-level-set method and its realization within an FEM solver for the level-set field is then outlined step by step.

8.3.1 Mass Loss: Sources and Remedies

Generally, level-set methods conserve mass or volume, respectively, only insufficiently. Various aspects of level-set methods may contribute to this issue. The interface may locally exhibit, for instance, thin filaments or sharp corners, which can not be adequately represented on the grid. These underresolved regions manifest themselves in a loss of mass. Diffusion incorporated by the underlying numerical scheme may also influence mass/volume conservation. Moreover, as aforementioned, reinitialization does not preserve the position of the zero-isocontour of the level-set function in most cases. Various remedies, addressing the different sources of mass loss or gain, have been proposed in literature. Some approaches aiming at improving mass/volume conservation during reinitialization have been mentioned in Section 8.2.1 in the context of the reinitialization equation. However, these methods obviously do not account for other sources of mass loss or gain. Higher order (Weighted) Essentially Non-Oscillatory (ENO/WENO) schemes (see, e.g., Osher and Fedkiw [240] and references therein) are frequently used for discretizing the spatial derivatives of the advection and reinitialization equation; see, e.g., Sussman *et al.* [302] and Gaudlitz and Adams [110]. Global mass conservation techniques such as the one presented in Section 8.2.2 preserve mass independent of the origin of mass loss or gain, but implicitly assume that mass is homogeneously lost or gained over the entire interface region. Consequently, mass is not necessarily restored in the regions where it has been lost or gained. In the conservative level-set method, originally introduced by Olsson and Kreiss [238] and further developed by Olsson *et al.* [239] within an FEM, the signed distance function is replaced by a smeared Heaviside function and the conservative form of the level-set equation is used. Building on the level-set method to provide more accurate geometric interface quantities and the VOF to better conserve mass or volume, respectively, Sussman and Puckett [300] coupled the level-set method and the VOF. Another hybrid method was suggested by Enright *et al.* [91]. Their hybrid

particle-level-set method aims at combining the advantages of an Eulerian level-set method and a Lagrangian marker-particle approach. Lagrangian schemes inherently preserve information in regions underresolved by the grid and are therefore particularly appropriate to tackle the resulting mass losses in the level-set description. In the hybrid particle-level-set method, marker particles are placed near the interface. The particles are identified by the sign of the level-set function at the location of their initial position and then advected by the same velocity as the level-set field. Hence, particles are expected to only cross the interface when the level-set method fails to accurately represent the interface position. Inaccuracies of the level-set description are indicated by particles inserted on one side of the interface but later recovered on the opposite side. The information provided by these particles allows for locally correcting the level-set field. Enright *et al.* [91] further demonstrated that the inclusion of particles also permits to correct movements of the interface during reinitialization. As the particles are at rest during the reinitialization procedure, movements of the interface, which should likewise remain at its position, may be handled in a similar manner. In a further study, Enright *et al.* [92] argued that low-order numerical schemes for the level-set transport are sufficient for accurately capturing the interface in hybrid particle-level-set methods, since this approach can also cope with excessive numerical diffusion. A comprehensive parameter study on the hybrid particle-level-set method was conducted, e.g., by Gaudlitz and Adams [110] in the context of two-phase-flow simulations. All listed aspects of the hybrid particle-level-set method render it particularly appropriate for application within a low-order FEM as considered in this thesis. The following elaborations basically follow the suggestions by Enright *et al.* [91], which are here adapted to the present FEM using trilinearly-interpolated hexahedral elements. The extension to other element types is straightforward.

8.3.2 Initialization Procedure

Initially, particles are placed on both sides of the interface within a band of a predefined thickness. Particles introduced into the subdomain Ω_+ form the set of positive particles, whereas particles inserted into the subdomain Ω_- belong to the set of negative particles. Hence, particles P are identified by their sign, which is denoted by $\text{sign}(P)$. Moreover, they possess a radius r_P. The radius of the particles is bounded by a minimum value r_{min} and a maximum value r_{max}, which depend on the element length h (i.e., h_1, h_2 and h_3 for a three-dimensional Cartesian grid) as

$$r_{\text{min}} = c_{\text{min}} \min(h_1, h_2, h_3), \tag{8.26}$$

$$r_{\text{max}} = c_{\text{max}} \min(h_1, h_2, h_3). \tag{8.27}$$

Enright *et al.* [91] suggested $c_{\text{min}} = 0.1$ and $c_{\text{max}} = 0.5$. The location of the center of the particle is denoted by $\mathbf{x}_P$. Furthermore, the particles are allowed to overlap. The level-set value $\phi(\mathbf{x}_P)$ at the position of the particle is calculated from the level-set field via interpolation using the nodal values and shape functions of the element containing the particle.

In the first step of the initialization procedure, particles of both signs are placed in all elements that have at least one corner, i.e., node A, within a band of size

$$b_{\text{max}} = c_{\text{band}} \max(h_1, h_2, h_3) \tag{8.28}$$

on both sides of the interface; that is, the value ϕ_A associated with any node A of the element has to satisfy

$$|\phi_A| < b_{\text{max}}, \tag{8.29}$$

assuming that ϕ is a signed distance function. Enright *et al.* [91] choose $c_{\text{band}} = 3$. In each element sufficiently close to the interface, a predefined number n_{P} of particles are then randomly positioned. In this process, the same number of positive and negative particles is seeded per element. Enright *et al.* [91] used $4^{n_{\text{sd}}}$ particles per cell, where n_{sd} is the number of space dimensions. This step, which is referred to as initial seeding, is depicted in the first subfigure of Figure 8.2. Negative particles are colored in blue and positive particles in red.

Next, the particles are attracted to the correct side of the interface. Positive particles are moved to Ω_+ and negative ones to Ω_- in this step. All particles are placed in a band between a distance of $b_{\text{min}} = r_{\text{min}}$ and b_{max} of the interface. Therefore, all particles are shifted from their current level-set iso-contour $\phi(\mathbf{x}_P)$, which is equal to the signed distance from the interface, along the direction of the normal vector to a target iso-contour ϕ_{target} (i.e., a target signed distance from the interface), which is again chosen at random from the interval $[\text{sign}(P)b_{\text{min}}, \text{sign}(P)b_{\text{max}}]$. As a result, the final particle distribution is generated randomly both with respect to the tangential directions of the interface and its normal direction. The new particle position $\mathbf{x}_P^{\text{new}}$ is calculated via

$$\mathbf{x}_P^{\text{new}} = \mathbf{x}_P + \lambda \left(\phi_{\text{target}} - \phi(\mathbf{x}_P)\right) \mathbf{n}(\phi(\mathbf{x}_P)), \tag{8.30}$$

where the normal vector $\mathbf{n}(\phi)$ is defined as given in equation (8.3) and $\lambda = 1$. Parameter λ allows for handling situations in which a particle can not be placed into the desired band owing to a degenerated level-set function, for instance, in underresolved regions. If equation (8.30) predicts a particle position outside of the desired band, λ is halved, and an intermediate particle position $\mathbf{x}_P^*$ is determined from equation (8.30). In doing so, the affected particle is moved closer to the interface, where the normal vector should be more appropriate. Starting from this intermediate position, the process is repeated with λ reset to 1 and $\mathbf{x}_P = \mathbf{x}_P^*$. Particles that are not within the desired band after a given number of iterations are deleted. The particle distribution after the attraction step is illustrated in the second subfigure of Figure 8.2.

Finally, the particle radius is adjusted as

$$r_P = \begin{cases} r_{\text{max}} & \text{if } \text{sign}(P)\phi(\mathbf{x}_P) > r_{\text{max}} \\ \text{sign}(P)\phi(\mathbf{x}_P) & \text{if } r_{\text{min}} \leq \text{sign}(P)\phi(\mathbf{x}_P) \leq r_{\text{max}} \\ r_{\text{min}} & \text{if } \text{sign}(P)\phi(\mathbf{x}_P) < r_{\text{min}}. \end{cases} \tag{8.31}$$

For particles sufficiently close to the interface, the interface is thus tangential to the sphere defined by the particle position and its radius. As the particles are allowed to overlap, the interface is exactly reproduced in the limit of an infinite number of particles. This final step of the setup of the particle field is displayed in the last subfigure of Figure 8.2, where the circles representing the particles, are colored according to their radius. Red color corresponds to r_{max} and blue color to r_{min}. Additionally, a closeup view of the region near the interface is included below.

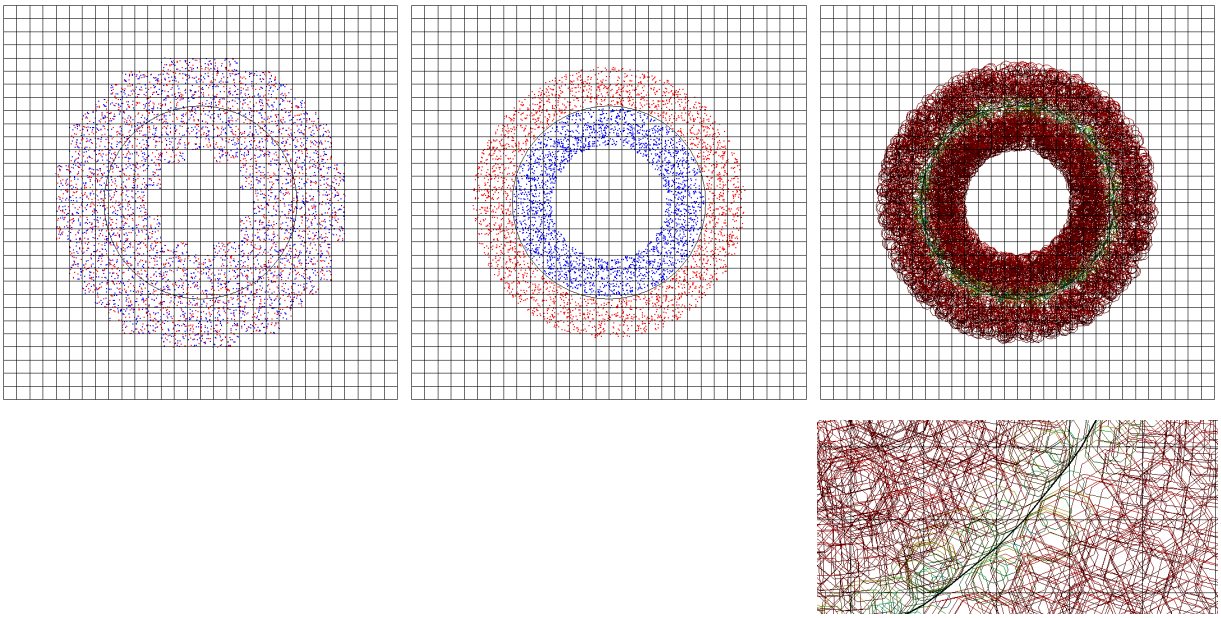

Figure 8.2: Setup of particles: initial seeding, attraction and radii adjustment.

8.3.3 Particle Transport

Particles are advected by the local velocity as

$$\frac{\mathrm{d}\mathbf{x}_P}{\mathrm{d}t} = \mathbf{a}(\mathbf{x}_P, t). \tag{8.32}$$

In the present FEM, the velocity at the particle position is interpolated from the nodal velocity values of the underlying element using the shape functions. Owing to the present trilinear interpolation, second-order accuracy is obtained for the particle transport, as also considered by Enright *et al.* [91]. For time integration, a second-order Runge-Kutta scheme is applied, similar to Enright *et al.* [92]:

$$\begin{aligned} \mathbf{x}_{P,n+\frac{1}{2}} &= \mathbf{x}_{P,n} + \frac{\Delta t}{2}\mathbf{a}(\mathbf{x}_{P,n}, t_n), \\ \mathbf{x}_{P,n+1} &= \mathbf{x}_{P,n} + \Delta t\mathbf{a}(\mathbf{x}_{P,n+\frac{1}{2}}, t_{n+\frac{1}{2}}). \end{aligned} \tag{8.33}$$

8.3.4 Correction by Particles

In case of discrepancies between the interface location predicted by the level-set function and its description by the particles, the information contained in the particle field serves for a correction of the level-set function. Following Enright *et al.* [91], a reconstruction of the level-set function based on the information from the particles is only performed in regions where the level-set function shows an error of the order of the element length, i.e., a clear deviation. As long as

the particles do not drift an appreciable distance across the interface, the level-set function is assumed to be sufficiently accurate. This approach is thus consistent with the second-order accuracy of the particle evolution. Particles that contribute to the correction of the level-set function are classified as escaped. As a criterion, Enright *et al.* [91] considered particles which are on the wrong side of the interface by more than their radius to have escaped. As the radius of the particles is of the order of the element length, any (non-zero) multiple of r_P is also conceivable as an escape condition according to Enright *et al.* [91]. Particles satisfying

$$\operatorname{sign}(P)\phi\left(\mathbf{x}_P\right) < 0, \tag{8.34}$$

are marked as escaped in this thesis.

For each escaped particle, a local level-set function is defined as

$$\phi_P\left(\mathbf{x}\right) = \operatorname{sign}(P)\left(r_P - \|\mathbf{x} - \mathbf{x}_P\|\right), \tag{8.35}$$

which is zero at the boundary of the sphere associated with the particle, of the sign of the particle inside of the sphere and of opposite sign outside. The particle-based level-set value is then evaluated at all nodes of the element containing the escaped particle. If $\phi_P(\mathbf{x}_A)$, where $\mathbf{x}_A$ denotes the coordinates of node A, differs from the nodal value ϕ_A of the level-set field, the level-set function may have to be corrected. The escaped positive particles are used to rebuild the subdomain Ω_+ and the escaped negative ones to rebuild Ω_-. Using the set of escaped positive particles $\mathcal{P}_+$ as well as the set of escaped negative ones $\mathcal{P}_-$ corresponding to an element, a corrected level-set value ϕ_A^{corr} is determined for each node A of the element. A potentially corrected level-set value $\phi_{A,+}$ is estimated from the escaped positive particles via

$$\phi_{A,+} = \max_{\forall P \in \mathcal{P}_+} \left(\phi_P(\mathbf{x}_A), \phi_{A,+}\right), \tag{8.36}$$

where $\phi_{A,+}$ is initialized by ϕ_A. Analogously, the level-set value $\phi_{A,-}$, determined based on the escaped negative particles, is calculated as

$$\phi_{A,-} = \min_{\forall P \in \mathcal{P}_-} \left(\phi_P(\mathbf{x}_A), \phi_{A,-}\right), \tag{8.37}$$

where $\phi_{A,-}$ is likewise initially set to ϕ_A. Eventually, the corrected level-set value is determined by

$$\phi_A^{\text{corr}} = \begin{cases} \phi_{A,+} & \text{if } |\phi_{A,+}| \leq |\phi_{A,-}| \\ \phi_{A,-} & \text{if } |\phi_{A,+}| > |\phi_{A,-}|. \end{cases} \tag{8.38}$$

In summary, escaped positive particles, which are located in Ω_-, are used to correct negative level-set values. Analogously, escaped negative particles are able to shift the interface towards Ω_+ by modifying positive level-set values. For correcting values, the described procedure gives priority to the escaped particle whose sphere is closest to the node. Recently, Wang *et al.* [331] suggested a modified correction procedure by which level-set values on both sides of the interface can be corrected by the same escaped particle. The modified strategy is not further considered in this thesis.

8.3.5 Reseeding

While evolving the interface and the particles by the velocity field, the particle concentration may change. Regions which do not possess a sufficient number of particles may form, for instance, due to a stretching of the interface. Likewise, particles may be agglomerated in other regions. To ensure an approximately homogeneous particle distribution along the interface throughout the simulation, repeated reseeding of particles has to be performed. Simply deleting all particles and then seeding new ones would discard the information on the interface position provided by particles that are resided very close to the interface or are escaped. Similar to the initial placement of the particles, new particles are placed at least at a distance of b_{min} to the interface. Therefore, the reseeding procedure should maintain all particles whose distance to the interface, given by $|\phi(\mathbf{x}_P)|$, is smaller than r_{min}. These particles may contribute to the correction in the time steps following immediately after the reseeding, whereas particles placed at least in a distance of b_{min} of the interface may not be able to account for errors of the order of the element length in the interface description, leading to a deterioration of mass/volume conservation. Furthermore, escaped particles should not be removed, since they exhibit information that cannot be represented on the grid in the current instant of time. However, this information may be recovered in a future instant of time. All these particles, which are referred to as critical ones in the following, are kept during reseeding. In order to ensure an appropriate particle distribution, the following three tasks are performed by the reseeding procedure:

1. All particles which drifted too far away from the interface to contribute to the correction are deleted, i.e., all particles satisfying $\text{sign}(P)\phi(\mathbf{x}_P) > b_{\text{max}}$.
2. Particles are added to elements which are at least partially located within a distance of b_{max} of the interface and possess less than n_{P} particles. New particles of the appropriate type (i.e., positive particles in Ω_+ and negative ones in Ω_-) are randomly positioned in the respective element until the number of particles again equals n_{P}. Afterwards, they are attracted to the interface as described in Section 8.3.2. As a result of the attraction step, all newly seeded particles are placed within a band between b_{min} and b_{max} of the interface. Their radius is set by equation (8.31).
3. Particles are deleted from elements which are at least partially located within a distance of b_{max} of the interface and possess more than n_{P} particles. Therefore, all non-critical particles in an affected element are sorted according to the criterion $\text{sign}(P)\phi(\mathbf{x}_P) - r_P$. The particle with the largest value is deleted until the number of particles equals n_{P}, keeping the particles closest to the interface.

Elements intersected by the interface usually contain positive and negative particles and, therefore, require a particular treatment. Based on an estimation of the volume fraction v_-^e corresponding to Ω_-, the number of positive and negative particles for these elements is determined as $n_{\text{P},+} = (1 - v_-^e)n_{\text{P}}$ and $n_{\text{P},-} = v_-^e n_{\text{P}}$, respectively; see Gaudlitz [109]. Using these numbers, positive and negative particles are either added or removed as explained in item 2 and 3.

The reseeding frequency is generally problem-dependent. Apart from a periodic reseeding after a certain number of time steps, reseeding according to a criterion taking into account the change

of the interface area is also conceivable (see, e.g., Enright *et al.* [91] for considerations) but not further pursued in the present thesis.

8.3.6 Overview of the Algorithm

Algorithm 8.1 summarizes the sequence of the steps of the hybrid particle-level-set method. The particle method relies on the level-set field being a signed distance function. Therefore, reinitialization is performed in every time step. In contrast to what was suggested by Enright *et al.* [91], the level-set values are corrected only once in each time step. Enright *et al.* [91] evolved the level-set function and the particles forward in time, corrected the level-set field based on the particles, applied reinitialization, corrected the level-set field once again and adjusted the particle radii. Here, the particle-correction step is performed after reinitialization only, as also applied, e.g., by Gaudlitz and Adams [110]. Preliminary investigations showed that correcting the level-set field also before reinitialization does not further improve the results. Moreover, less computational work is required. After the correction step, the particle radii are adjusted according to the current interface position using equation (8.31). All particles which remain escaped exhibit a radius set to r_{min}. A potential reseeding is arranged at the end of the time step.

Algorithm 8.1: hybrid particle-level-set algorithm

```
initialize level-set field and particles

while time loop not finished: t < t_end

    solve level-set equation for φ^h_{n+1}

    reinitialize φ^h_{n+1}

    advect particles to x_{P,n+1}

    correct φ^h_{n+1} using particles

    adjust r_P

    if reseeding
        remove useless particles and seed new ones
    end if

    update time step: φ^h_n = φ^h_{n+1}, x_{P,n} = x_{P,n+1}

end while
```

8.4 Numerical Test Cases and Applications

The hybrid particle-level-set method is validated in this section. For comparison, results obtained with the basic approach are additionally included. The hybrid particle-level-set method is applied to established benchmark examples as well as to one two-phase-flow problem, since it is not further used in the next chapters for reasons given at the beginning of the present one. Results obtained with the Hybrid Particle-Level-Set method are abbreviated by "HPLS" in the remainder of this section. Results provided by a pure advection of the level-set function, i.e., by merely solving the Level-Set equation (8.7), are marked by "LS" and the ones by a level-set approach including REINITialization via a geometric distance computation in every time step, as also applied in the HPLS, by "REINIT". Two-dimensional problems are computed using one layer of hexahedral elements. In this case, the location of the particles is restricted to the centerplane of the element layer. Consequently, coordinates of element nodes are projected into the centerplane, when estimating corrected level-set values (see equations (8.36) and (8.37)). Parameters based on the element length h, such as r_{min}, are determined without the contribution of the third dimension. Unless otherwise specified, the parameters of the HPLS are set to $r_{\text{min}} = 0.1h$, $r_{\text{max}} = 0.5h$, $b_{\text{max}} = 3h$ and $n_{\text{P}} = 4^{n_{\text{sd}}}$. Reseeding of the particles is performed periodically for all examples. For all level-set test cases, the Courant-Friedrichs-Lewy number is set to CFL ≈ 0.5.

8.4.1 Zalesak's Disk

First, Zalesak's disk [337], which denotes the rigid body rotation of a slotted disk in a constant velocity field, is considered. At the beginning, the slotted disk is centered at $(0.5,\ 0.75)$ in a square domain of size $\Omega = [0, 1] \times [0, 1]$. The radius of the circle is given by $R = 0.15$. The slot has a size of $d_{\text{w}} = 0.05$ in width and of $d_{\text{l}} = 0.25$ in length. The velocity field is given as

$$\mathbf{a}(\mathbf{x}) = \begin{pmatrix} \frac{\pi}{3.14}(0.5 - x_2) \\ \frac{\pi}{3.14}(x_1 - 0.5) \end{pmatrix}. \tag{8.39}$$

Figure 8.3 displays the shape of the disk, which should be preserved during rotation, after one revolution of the disk. Using 100×100 elements, the shape obtained with the HPLS is compared to the zero iso-contours recovered by the LS and the REINIT. As a reference, the initial shape of the disk on 200×200 elements is included. The HPLS retains the interface accurately. The rounding of the corners is mainly related to the limited resolution of the grid, since sharp corners of the interface cannot be represented inside elements and hence remain subgrid. In contrast, the LS leads to a slight distortion of the upper part of the disk and a stronger smoothing of the corners. The REINIT fails to preserve the shape of the disk and yields a significant loss of area. Moreover, Figure 8.3 illustrates a grid refinement study for the HPLS using 50×50, 100×100 and 200×200 elements. Even for the coarser discretization, the HPLS provides a good approximation of the disk. An almost exact preservation of the interface is achieved with the HPLS on the finer discretization. A more detailed insight into area conservation is obtained from Figure 8.4, which provides the area of the disk, given in terms of the initial area $A(\Omega_-(t = 0))$ as $A(\Omega_-(t))/A(\Omega_-(t = 0))$, as a function of time. The aforementioned three grids are considered

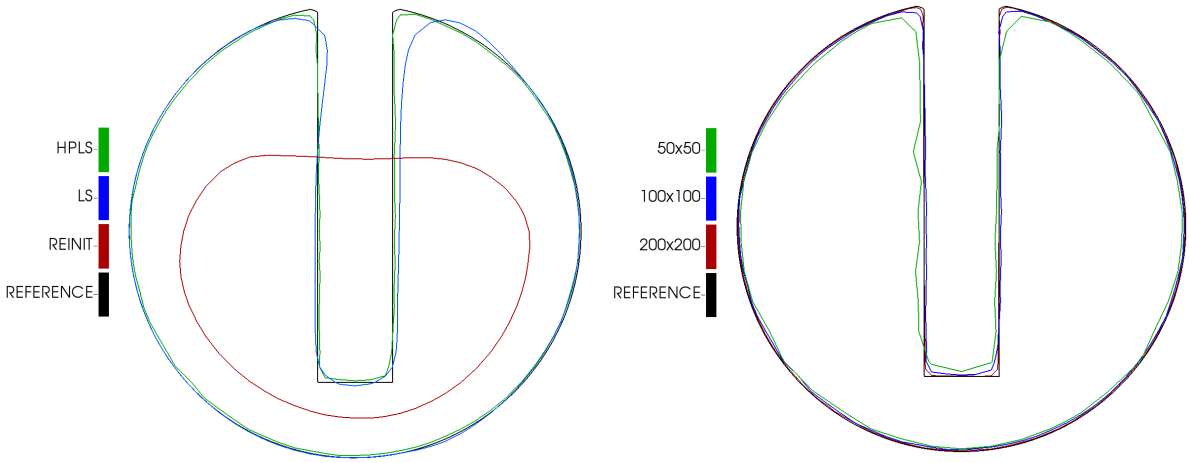

Figure 8.3: Comparison of the shape of Zalesak's disk after one rotation for various methods using 100^2 elements (left) and for the HPLS using 50^2, 100^2 and 200^2 elements (right). The initial shape of the disk on 200^2 elements is taken as a reference.

for all methods. Even with the coarser grid, the loss of area in the HPLS remains below 5%. The loss of area decreases with grid refinement. A comparable change of area is stated for the LS. The REINIT exhibits an excessive loss of area for all discretizations. With respect to the overall behavior of the REINIT, the excellent area and shape conservation properties of the HPLS, which also includes reinitialization in every time step, is remarkable. In addition, Figure 8.4 illustrates

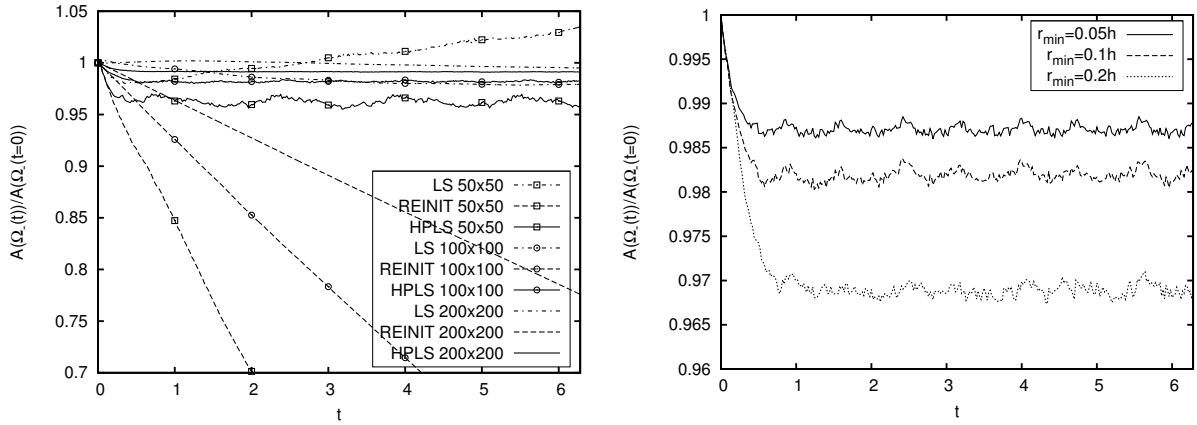

Figure 8.4: Area $A(\Omega_-(t))/A(\Omega_-(t=0))$ of Zalesak's disk over time t for various methods as well as 50^2, 100^2 and 200^2 elements and influence of the minimal particle radius $r_{\min}$ on the HPLS using 100^2 elements. The diagram for $r_{\min}$ incorporates every 2nd time step.

the influence of the minimal particle radius $r_{\min}$ on area conservation using 100×100 elements. Therefore, $r_{\min} = 0.05h, 0.1h$ and $0.2h$ are investigated. For this example, increasing $r_{\min}$ leads to an increased loss of area with respect to the disk.

8.4.2 Single Vortex Stretching

The second example aims at investigating the ability of an interface capturing method to accurately handle thin structures of the size of the elements. Therefore, a circle stretched by the velocity field such that it is wrapped towards the center of the domain $\Omega = [0,1] \times [0,1]$ is considered. A circle with radius $R = 0.15$ is placed at $(0.5,\ 0.75)$. The velocity field is given via the stream function

$$\Psi = \frac{1}{\pi} \sin^2(\pi x_1) \sin^2(\pi x_2) \tag{8.40}$$

(see Bell *et al.* [29]) such that

$$\mathbf{a}(\mathbf{x}) = \begin{pmatrix} \frac{\partial \Psi}{\partial x_2} \\ -\frac{\partial \Psi}{\partial x_1} \end{pmatrix} = \begin{pmatrix} \sin^2(\pi x_1) \sin(2\pi x_2) \\ -\sin(2\pi x_1) \sin^2(\pi x_2) \end{pmatrix}. \tag{8.41}$$

By multiplying $\mathbf{a}$ by $\cos((\pi t)/t_{\text{end}})$, the velocity field is inverted after half of the simulation time, which is set to $t_{\text{end}} = 8$, and the problem becomes reversible; see also LeVeque [188]. The domain is discretized using 128×128 elements. Figure 8.5 illustrates the behavior of the HPLS. The interface as well as the particle distribution are shown at time $t = 4$, and iso-contours of the level-set function, which remains a signed distance function due to reinitialization, are indicated. Furthermore, a comparison of the shape of the zero iso-contour, which should return

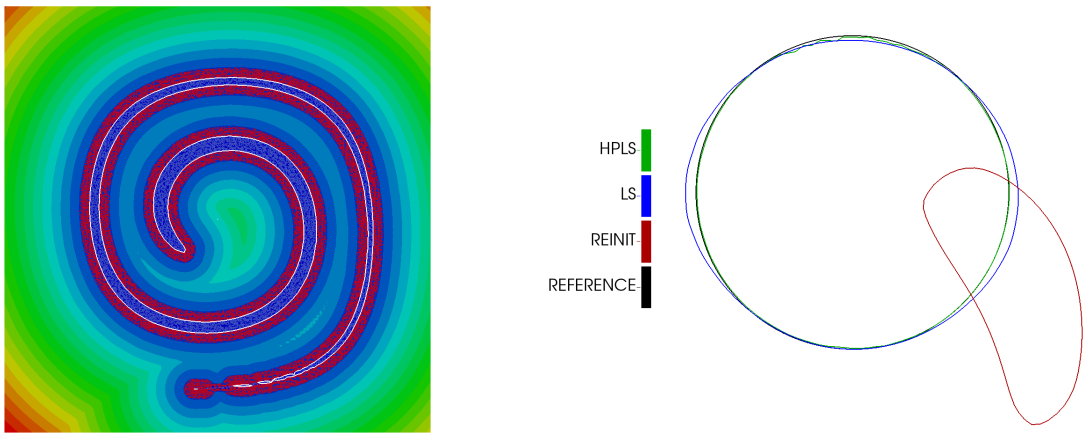

Figure 8.5: Level-set iso-contours (red color indicates high level-set values and blue color low level-set values), interface (colored in white) and particles (red color identifies positive particles and blue color negative particles) for single vortex stretching at time $t = 4$ using 128^2 elements for the HPLS (left) and comparison of the final shape of the interface for various methods using 128^2 elements (right). The initial shape of the circle on 256^2 elements is taken as a reference.

to a circle at the end of the simulation, is displayed for the considered methods. Again, the REINIT fails to recover the expected interface, while the LS yields a somewhat deformed circle. Merely the HPLS is able to well capture the interface at the end of the simulation, although some disturbances are observable at the upper arc of the circle, where particles that have been escaped

during stretching of the underresolved outer filament are located. Concerning the HPLS, the influence of the number of particles n_{P} and the minimal particle radius r_{min} on area conservation is further examined. Therefore, Figure 8.6 displays the area of the (stretched) circle normalized by its initial area, $A(\Omega_{-}(t))/A(\Omega_{-}(t=0))$, as a function of time for $n_{\mathrm{P}} = 16, 32$ and 64 as well as $r_{\mathrm{min}} = 0.05h, 0.1h$ and $0.2h$. For each series, only the parameter of interest, i.e., n_{P} or r_{min}, is varied, while the default values are kept for the remaining ones. Increasing n_{P} improves area

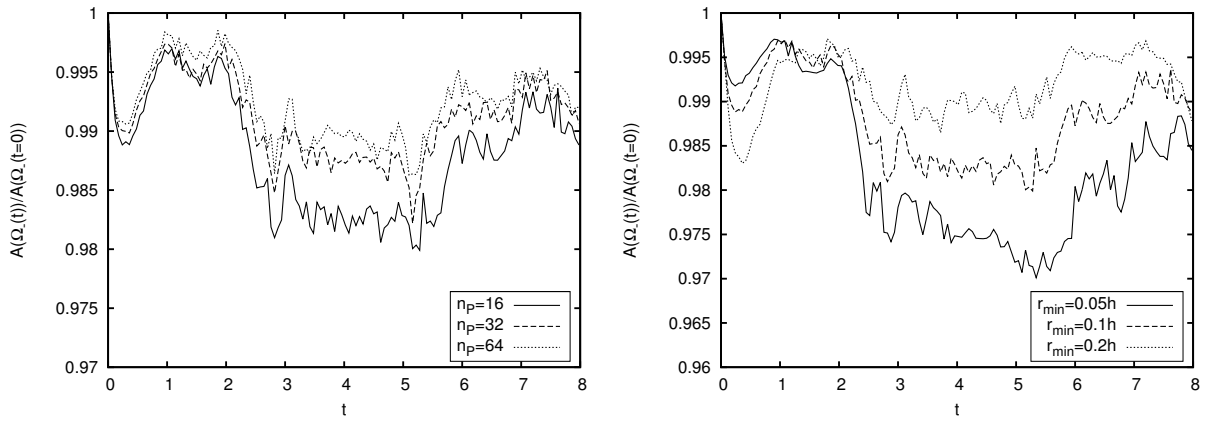

Figure 8.6: Influence of the number of particles n_{P} and the minimal particle radius r_{min} on the HPLS for single vortex stretching based on the area $A(\Omega_{-}(t))/A(\Omega_{-}(t=0))$ over time t using 128^2 elements. The diagrams incorporate every 15th time step.

conservation, although the gain in accuracy decreases with an augmenting number of particles. In contrast to what is observed for Zalesak's disk, lowering r_{min} degrades area conservation for this example, which exhibits an underresolved elongated filament, i.e., the outer end of the spiral-like interface. In this regard, Zalesak's disk mainly suffers from numerical diffusion and shifting of the interface during reinitialization.

8.4.3 Deformation of a Sphere

The deformation of a sphere with radius $R = 0.15$, centered at (0.35,0.35,0.35) of the domain $\Omega = [0,1] \times [0,1] \times [0,1]$, is considered next for evaluating the HPLS. LeVeque [188] extended the velocity field of the previous example to three dimensions such that the deformation of the sphere in the x_1x_2-plane is superimposed by another deformation in the x_1x_3-plane:

$$\mathbf{a}(\mathbf{x},t) = \begin{pmatrix} 2\sin^2(\pi x_1)\sin(2\pi x_2)\sin(2\pi x_3)\cos((\pi t)/t_{\mathrm{end}}) \\ -\sin(2\pi x_1)\sin^2(\pi x_2)\sin(2\pi x_3)\cos((\pi t)/t_{\mathrm{end}}) \\ -\sin(2\pi x_1)\sin(2\pi x_2)\sin^2(\pi x_3)\cos((\pi t)/t_{\mathrm{end}}) \end{pmatrix}. \tag{8.42}$$

Again, the velocity field is reversed at time $t_{\mathrm{end}}/2$. The simulation time is set to $t_{\mathrm{end}} = 3$. A uniform discretization with $100 \times 100 \times 100$ elements is used, and the HPLS is applied. Figure 8.7

shows the zero iso-contour of the level-set field at times $t = 0$, 0.25, 1, 1.5, 2.5 and 3. After returning to the initial state, only 2.3% of the initial volume of the sphere is lost for this three-dimensional problem when using the HPLS.

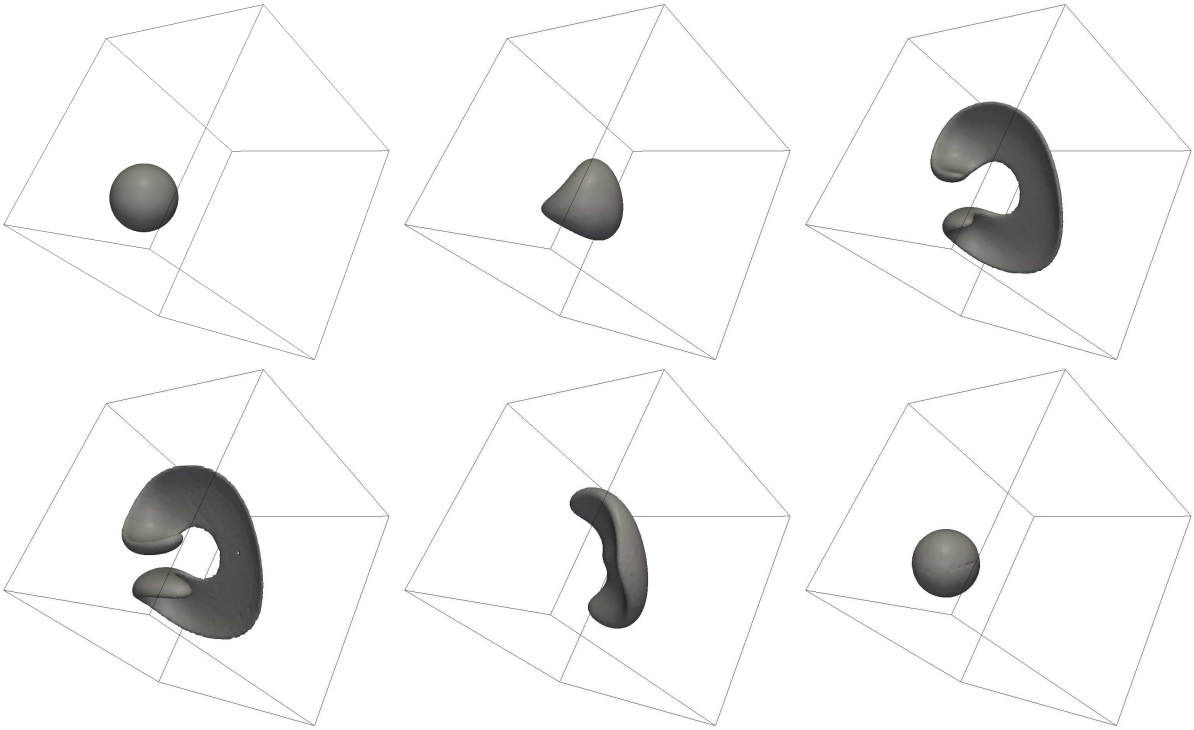

Figure 8.7: Three-dimensional deformation of a sphere at times $t = 0$, 0.25, 1, 1.5, 2.5 and 3.

8.4.4 Impact of a Drop

In order to demonstrate the applicability of the present HPLS to two-phase-flow simulations, the impact of a water drop on the surface of a pool filled with water is investigated. A similar flow problem was examined by Wang *et al.* [331]. Here, a domain of size $\Omega = [0, L] \times [0, L] \times [0, L]$, where $L = 2.0\,\mathrm{m}$, is considered and discretized using $80 \times 80 \times 80$ elements. A drop at rest is initially positioned at $(0.5L, 0.61L, 0.5L)^{\mathrm{T}}$. The radius of the drop is chosen to be $R = L/12$. The water pool is $d = 0.5L$ in depth. Density and viscosity of the water are taken to be $\rho_+ = 1000\,\mathrm{kg/m^3}$ and $\mu_+ = 0.001137\,\mathrm{kg/(ms)}$, respectively. For the air, $\rho_- = 1.226\,\mathrm{kg/m^3}$ and $\mu_- = 0.0000178\,\mathrm{kg/(ms)}$ are assumed. The surface-tension coefficient is set to $\gamma = 0.0728\,\mathrm{kg/s^2}$. Gravitation acts in vertical x_2-direction as $\mathbf{g} = (0.0, -9.81, 0.0)^{\mathrm{T}}\,\mathrm{m/s^2}$. Slip conditions are prescribed at all boundaries of the domain. The time-step length is $\Delta t = 0.001$ s. Concerning the HPLS, $r_{\min}$ is set to $0.05h$, since this value ensures a smooth interface also for rather coarse discretizations and thus works best for two-phase-flow problems. For two-phase flow, the method derived in the next chapter is used. Figure 8.8 illustrates the drop impinging on the water surface. Therefore, the interface is depicted at times

$t = 0$, 0.2, 0.4, 0.6, 0.7 and 1 s. The drop plunges into the pool, pushing water away. As the water returns, an upward pointing jet forms.

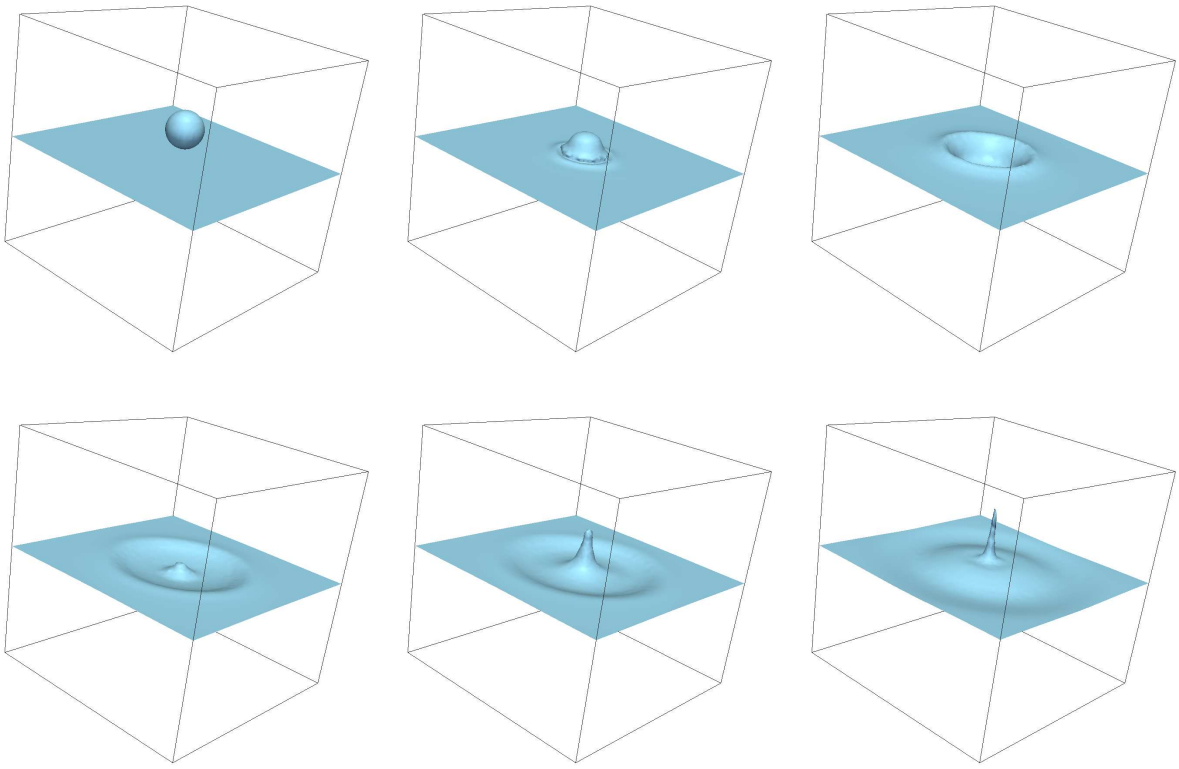

Figure 8.8: Impact of drop at times $t = 0$, 0.2, 0.4, 0.6, 0.7 and 1 s.

9

A Nitsche-Type Extended Variational Multiscale Method for Two-Phase Flow

The interface separating the two fluids appears as a discontinuity in the flow field. The eXtended Finite Element Method (XFEM) is able to treat a discontinuity in the solution field for arbitrary interface locations in a sharp fashion. In this chapter, a novel approach based on the XFEM is derived for incompressible two-phase flows. First, the underlying problem statement is briefly described. Then, the applied XFEM-based representation of discontinuities in elements intersected by the interface is reviewed. Next, the weak imposition of the Dirichlet-type interface condition for two-phase flow using Nitsche's method [231] is shown. Moreover, appropriate accompanying face-oriented ghost-penalty as well as fluid stabilization terms, ensuring the stability of the numerical method in the enriched interface region, are introduced. In particular, Nitsche's method as well as the face-oriented stabilization terms are further extended to account for viscous- and convection-dominated transient flows. After summarizing the complete formulation for two-phase flow, the coupled fluid-level-set algorithm is also briefly addressed. Finally, the novel approach is validated for various two- and three-dimensional numerical examples of increasing complexity, rigorously demonstrating the excellent accuracy and robustness of the proposed method. The present chapter is based on work published in Rasthofer and Schott *et al.* [262].

9.1 Problem Statement

Two-phase flow in the domain Ω is considered. The time-dependent moving interface $\Gamma_{\text{int}}(t)$, captured by the level-set method as introduced in Section 8.1, divides the domain Ω into two subdomains $\Omega_+(t)$ and $\Omega_-(t)$, representing the two fluids; see also Figure 9.1. The unit normal vector $\mathbf{n}_{\text{int}}$ on Γ_{int} is defined to point into the domain Ω_-. Moreover, $\mathbf{n}_k$ denotes the outward

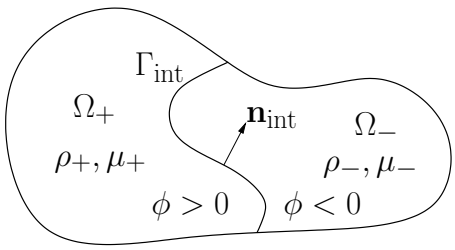

Figure 9.1: Domain Ω of two-phase-flow problem.

pointing unit normal vector on the boundary $\partial\Omega_k$ of each subdomain Ω_k, where $k \in \{+,-\}$; that is, $\mathbf{n}_{\text{int}} = \mathbf{n}_+ = -\mathbf{n}_-$ at the interface. The strong form of the two-phase-flow problem reads as

$$\rho_k \frac{\partial \mathbf{u}_k}{\partial t} + \rho_k \mathbf{u}_k \cdot \nabla \mathbf{u}_k + \nabla p_k - 2\mu_k \nabla \cdot \boldsymbol{\varepsilon}(\mathbf{u}_k) = \rho_k \mathbf{g} \qquad \text{in } \Omega_k \times]0, t_{\text{end}}[\,, \tag{9.1}$$

$$\nabla \cdot \mathbf{u}_k = 0 \qquad \text{in } \Omega_k \times]0, t_{\text{end}}[\,, \tag{9.2}$$

$$[\![\mathbf{u}]\!] = 0 \qquad \text{on } \Gamma_{\text{int}} \times]0, t_{\text{end}}[\,, \tag{9.3}$$

$$[\![\boldsymbol{\sigma}(\mathbf{u}, p)]\!] \cdot \mathbf{n}_{\text{int}} = -\gamma\kappa\mathbf{n}_{\text{int}} \qquad \text{on } \Gamma_{\text{int}} \times]0, t_{\text{end}}[\,, \tag{9.4}$$

$$\mathbf{u}_k = \mathbf{u}_{\text{D},k} \qquad \text{on } \Gamma_{\text{D},\mathbf{u},k} \times]0, t_{\text{end}}[\,, \tag{9.5}$$

$$\boldsymbol{\sigma}(\mathbf{u}_k, p_k) \cdot \mathbf{n}_k = \mathbf{h}_{\mathbf{u},k} \qquad \text{on } \Gamma_{\text{N},\mathbf{u},k} \times]0, t_{\text{end}}[\,, \tag{9.6}$$

$$\mathbf{u}_k = \mathbf{u}_{0,k} \qquad \text{in } \Omega_k \times \{0\} \tag{9.7}$$

for $k \in \{+,-\}$. The momentum equation is given in convective form; and t_{end} denotes the considered time period. Appropriate initial conditions in Ω_k as well as boundary conditions on the outer part of $\partial\Omega_k$, belonging to the boundary $\partial\Omega$ of the entire domain Ω, are defined as usual. Initially, a divergence-free velocity field $\mathbf{u}_{0,k}$ is prescribed. Dirichlet and Neumann boundary conditions are imposed on $\Gamma_{\text{D},\mathbf{u},k}$ and $\Gamma_{\text{N},\mathbf{u},k}$, respectively. For the boundary $\partial\Omega_k$ of subdomain Ω_k, it is assumed that $\Gamma_{\text{D},\mathbf{u},k} \cap \Gamma_{\text{N},\mathbf{u},k} \cap \Gamma_{\text{int}} = \emptyset$ and $\Gamma_{\text{D},\mathbf{u},k} \cup \Gamma_{\text{N},\mathbf{u},k} \cup \Gamma_{\text{int}} = \partial\Omega_k$.

Assuming appropriate solution function spaces $\mathcal{S}_{\mathbf{u},k}$ for $\mathbf{u}_k$ and $\mathcal{S}_{p,k}$ for p_k as well as weighting function spaces $\mathcal{V}_{\mathbf{u},k}$ for the velocity weighting function $\mathbf{v}_k$ and $\mathcal{V}_{p,k}$ for the pressure weighting function q_k, momentum equation (9.1) and continuity equation (9.2) are multiplied by $\mathbf{v}_k \in \mathcal{V}_{\mathbf{u},k}$ and $q_k \in \mathcal{V}_{p,k}$ and integrated over the subdomains Ω_k. Moreover, viscous and pressure term are integrated by parts, with boundary conditions (9.5) and (9.6) applied to the resulting boundary integrals on the outer boundary parts $\Gamma_{\text{D},\mathbf{u},k}$ and $\Gamma_{\text{N},\mathbf{u},k}$, respectively. For each subdomain Ω_k, the variational formulation of the incompressible Navier-Stokes equations is thus obtained as: find $(\mathbf{u}_k, p_k) \in \mathcal{S}_{\mathbf{u},k} \times \mathcal{S}_{p,k}$ such that

$$\begin{aligned} &\left(\mathbf{v}_k, \rho_k \frac{\partial \mathbf{u}_k}{\partial t}\right)_{\Omega_k} + (\mathbf{v}_k, \rho_k \mathbf{u}_k \cdot \nabla \mathbf{u}_k)_{\Omega_k} - (\nabla \cdot \mathbf{v}_k, p_k)_{\Omega_k} + (\boldsymbol{\varepsilon}(\mathbf{v}_k), 2\mu_k \boldsymbol{\varepsilon}(\mathbf{u}_k))_{\Omega_k} \\ &+ (q_k, \nabla \cdot \mathbf{u}_k)_{\Omega_k} - (\mathbf{v}_k, \boldsymbol{\sigma}(\mathbf{u}_k, p_k) \cdot \mathbf{n}_k)_{\Gamma_{\text{int}}} = (\mathbf{v}_k, \rho_k \mathbf{g})_{\Omega_k} + (\mathbf{v}_k, \mathbf{h}_{\mathbf{u},k})_{\Gamma_{\text{N},\mathbf{u},k}} \end{aligned} \tag{9.8}$$

for all $(\mathbf{v}_k, q_k) \in \mathcal{V}_{\mathbf{u},k} \times \mathcal{V}_{p,k}$ and $k \in \{+,-\}$. Here, $(\cdot,\cdot)_{\Omega_k}$ and $(\cdot,\cdot)_{\Gamma_{\text{N},\mathbf{u},k}/\Gamma_{\text{int}}}$ denote the usual L_2-inner product in Ω_k and on $\Gamma_{\text{N},\mathbf{u},k}/\Gamma_{\text{int}}$, respectively; see also Section 3.2. In the following, the short notations $(\cdot,\cdot)_{\Omega_\pm} := (\cdot,\cdot)_{\Omega_+} + (\cdot,\cdot)_{\Omega_-}$ as well as $(\cdot,\cdot)_{\Gamma_{\text{N},\mathbf{u},\pm}} := (\cdot,\cdot)_{\Gamma_{\text{N},\mathbf{u},+}} + (\cdot,\cdot)_{\Gamma_{\text{N},\mathbf{u},-}}$ will also be used. The assumed solution and weighting function spaces for each subdomain can be adopted from equations (3.6) to (3.9).

To sum up the variational formulations for the two fluids, weighted average operators are defined as

$$\{\cdot\}_w := w_+(\cdot)_+ + w_-(\cdot)_-, \tag{9.9}$$

$$\langle\cdot\rangle_w := w_-(\cdot)_+ + w_+(\cdot)_- \tag{9.10}$$

based on the weights w_+ and w_-, with $w_+, w_- \in [0,1]$ and $w_+ + w_- = 1$. Furthermore, the identity

$$[\![\mathsf{ab}]\!] = [\![\mathsf{a}]\!]\{\mathsf{b}\}_w + \langle \mathsf{a} \rangle_w [\![\mathsf{b}]\!] \tag{9.11}$$

is introduced, where a and b denote arbitrary functions which are sufficiently smooth in the subdomains and potentially discontinuous at the interface. Hence, the sum of the interface terms can be expressed as

$$\begin{aligned} &- (\mathbf{v}_+, \boldsymbol{\sigma}(\mathbf{u}_+, p_+) \cdot \mathbf{n}_+)_{\Gamma_{\text{int}}} - (\mathbf{v}_-, \boldsymbol{\sigma}(\mathbf{u}_-, p_-) \cdot \mathbf{n}_-)_{\Gamma_{\text{int}}} = \\ &([\![\mathbf{v}]\!], \{2\mu\boldsymbol{\varepsilon}(\mathbf{u})\}_w \cdot \mathbf{n}_{\text{int}})_{\Gamma_{\text{int}}} - ([\![\mathbf{v}]\!] \cdot \mathbf{n}_{\text{int}}, \{p\}_w)_{\Gamma_{\text{int}}} - (\langle \mathbf{v} \rangle_w, \gamma\kappa\mathbf{n}_{\text{int}})_{\Gamma_{\text{int}}} , \end{aligned} \tag{9.12}$$

where $\mathbf{u} = (\mathbf{u}_+, \mathbf{u}_-) \in \mathcal{S}_{\mathbf{u},+} \times \mathcal{S}_{\mathbf{u},-}$, $p = (p_+, p_-) \in \mathcal{S}_{p,+} \times \mathcal{S}_{p,-}$, $\mathbf{v} = (\mathbf{v}_+, \mathbf{v}_-) \in \mathcal{V}_{\mathbf{u},+} \times \mathcal{V}_{\mathbf{u},-}$ as well as $q = (q_+, q_-) \in \mathcal{V}_{p,+} \times \mathcal{V}_{p,-}$. The traction interface condition (9.4) is incorporated naturally, resulting in the surface-tension term (last term on the right-hand side). In addition, two further terms, a viscous and a pressure consistency term, arise (first and second term).

Furthermore, the following compact forms are introduced for the sum of the variational formulations (9.8) for the two fluids. The bulk terms on the left-hand side are summarized as

$$\begin{aligned} \mathcal{B}_{\text{NS}}(\mathbf{v}, q; \mathbf{u}, p) := &\left(\mathbf{v}, \rho\frac{\partial \mathbf{u}}{\partial t}\right)_{\Omega_\pm} + (\mathbf{v}, \rho\mathbf{u} \cdot \nabla\mathbf{u})_{\Omega_\pm} - (\nabla \cdot \mathbf{v}, p)_{\Omega_\pm} \\ &+ (\boldsymbol{\varepsilon}(\mathbf{v}), 2\mu\boldsymbol{\varepsilon}(\mathbf{u}))_{\Omega_\pm} + (q, \nabla \cdot \mathbf{u})_{\Omega_\pm} , \end{aligned} \tag{9.13}$$

where all terms are evaluated with respect to Ω_+ and Ω_- using ρ_+ and μ_+ or ρ_- and μ_-, respectively, i.e., $\rho = \rho_k$ and $\mu = \mu_k$ for all $\mathbf{x} \in \Omega_k$. The surface-tension term of equation (9.12) is included in the linear form

$$\ell_{\text{NS}}(\mathbf{v}) := (\mathbf{v}, \rho\mathbf{g})_{\Omega_\pm} + (\mathbf{v}, \mathbf{h}_{\mathbf{u}})_{\Gamma_{\text{N},\mathbf{u},\pm}} + (\langle \mathbf{v} \rangle_w, \gamma\kappa\mathbf{n}_{\text{int}})_{\Gamma_{\text{int}}} , \tag{9.14}$$

which comprises all terms on the right-hand side. The remaining interface terms of equation (9.12) are treated separately in the following.

9.2 The Extended Finite Element Method

This section first provides a brief overview of the XFEM in general as well as its application to two-phase flows. Afterwards, an enrichment strategy based on jump functions is presented.

9.2.1 The Extent of the XFEM

Owing to the implicit capturing of the interface by means of the level-set method, elements may be intersected by the interface, and the related discontinuities may thus occur inside them. Using a standard finite element method with polynomial shape functions, as, e.g., done by Nagrath

et al. [228] and Quecedo and Pastor [257] for incompressible two-phase flows, the discontinuities in the solution fields cannot be represented explicitly. The XFEM, originally proposed by Belytschko and Black [31] and by Moës *et al.* [219] for crack-propagation problems in solid mechanics, however, allows for reproducing arbitrary discontinuities in the solution fields inside elements by providing an enhanced shape function basis. Up to now, the XFEM has been applied to various other problem configurations, among them fluid-structure interaction (see, e.g., Gerstenberger and Wall [117] and Zilian and Legay [340]), premixed combustion (see, e.g., van der Bos and Gravemeier [318] and Henke [140]), solidification processes (see, e.g., Chessa *et al.* [63] and Ji *et al.* [161]) and convection-dominated problems involving high gradients (see, e.g., Abbas *et al.* [1]). A comprehensive overview of the XFEM may be found, e.g., in the review articles by Belytschko *et al.* [33] and by Fries and Belytschko [99]. The XFEM is based on the partition-of-unity concept (see, e.g., Melenk and Babuška [211]). A partition of unity is a set of functions $N_i(\mathbf{x})$ satisfying $\sum_i N_i(\mathbf{x}) = 1$. For instance, the shape functions used in FEMs, as already implied by the previous notation, build a partition of unity. The essential property exploited by the XFEM is that any (enrichment) function $\Psi(\mathbf{x})$ can be recovered by multiplying it with the partition-of-unity functions.

In general, strong and weak discontinuities are distinguished. Problems with strong discontinuities exhibit a jump in the solution field, whereas, for weak discontinuities, the jump occurs in the derivative of the solution field. In the latter, the solution field is continuous, but shows a kink. With respect to two-phase flows, both types are present. Due the no-slip condition together with the different viscosities of the involved fluids, the velocity field exhibits a discontinuous gradient across the interface. Surface tension leads to a strongly discontinuous pressure field, which may additionally show a discontinuous gradient in gravitation fields owing to the different densities. Also for negligible surface-tension effects, a jump in the pressure field may occur owing to different viscosities. To incorporate these discontinuities into the numerical solution fields, various XFEMs have been proposed in literature. Chessa and Belytschko [61, 64] merely took into account gradient discontinuities of the velocity field by using a kink enrichment. In contrast, only the pressure field was enhanced, e.g., by Groß and Reusken [131] and Sauerland and Fries [272]. The application of kink enrichments for the velocity field and jump enrichments for the pressure field was suggested, e.g., by Rasthofer *et al.* [259]. In that study, the kink enrichment function according to Moës *et al.* [220] was applied, which differs from the one used by Chessa and Belytschko [61] and is exclusively non-zero in intersected elements. Zlotnik and Díez [341] further extended the XFEM in conjunction with the level-set method for n-phase flows involving more than two fluids. Therefore, an enrichment function accounting for several interfaces within one element was derived. Furthermore, various methods similar to the XFEM, following an analogous strategy to account for the discontinuities inherent in two-phase flows, were developed, e.g., by Ausas *et al.* [8], Coppola-Owen and Codina [73] and Minev *et al.* [216].

9.2.2 Enrichment Strategy

In the XFEM, the standard finite element expansion is extended by using a properly chosen enrichment function $\Psi(\mathbf{x}, t)$, which allows for reproducing the desired discontinuity inside the

element. An enriched approximation for the velocity and the pressure field is defined as

$$\mathbf{u}^h(\mathbf{x},t) = \sum_{A\in\mathcal{E}} N_A(\mathbf{x})\mathbf{u}_A(t) + \sum_{\tilde{A}\in\mathcal{E}_{\text{enr}}} N_{\tilde{A}}(\mathbf{x})\Psi_{\tilde{A}}(\mathbf{x},t)\tilde{\mathbf{u}}_{\tilde{A}}(t), \tag{9.15}$$

$$p^h(\mathbf{x},t) = \sum_{A\in\mathcal{E}} N_A(\mathbf{x})p_A(t) + \sum_{\tilde{A}\in\mathcal{E}_{\text{enr}}} N_{\tilde{A}}(\mathbf{x})\Psi_{\tilde{A}}(\mathbf{x},t)\tilde{p}_{\tilde{A}}(t), \tag{9.16}$$

where

$$\Psi_{\tilde{A}}(\mathbf{x},t) = \Psi(\mathbf{x},t) - \Psi(\mathbf{x}_{\tilde{A}},t) \tag{9.17}$$

represents a shifted enrichment function as suggested by Belytschko *et al.* [32]. The weighting functions $\mathbf{v}^h$ and q^h are given analogously. Here, $\mathcal{E}$ denotes the set of all nodes and $\mathcal{E}_{\text{enr}}$ a subset of enriched nodes, which contains all nodes corresponding to the elements intersected by the interface. The enrichment distribution is also displayed in Figure 9.2, where all nodes are marked by dots and enriched nodes are identified by an additional square. The first part of the finite

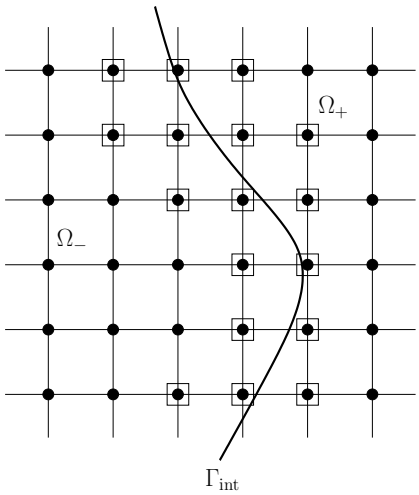

Figure 9.2: Enrichment distribution.

element expansions (9.15) and (9.16) represents the standard continuous finite element approximation, where N_A is the shape function and $\mathbf{u}_A$ and p_A are the standard velocity and pressure degrees of freedom at node A. To accurately represent discontinuities across the interface, the second term expands the standard continuous solution space. In accordance with the partition-of-unity concept, an appropriate enrichment function $\Psi_{\tilde{A}}$ that represents the problem-dependent discontinuity is multiplied by the standard polynomial shape function $N_{\tilde{A}}$. The resulting enriched shape functions $N_{\tilde{A}}\Psi_{\tilde{A}}$ are multiplied by additional velocity and pressure degrees of freedom $\tilde{\mathbf{u}}_{\tilde{A}}$ and $\tilde{p}_{\tilde{A}}$, respectively. The shifting of Ψ, given in equation (9.17), where $\mathbf{x}_{\tilde{A}}$ denotes the coordinates of an enriched node $\tilde{A}$, may be applied optionally to retain the nodal interpolation property for standard degrees of freedom, i.e., $\mathbf{u}^h(\mathbf{x}_A,t) = \mathbf{u}_A(t)$. Since the extended finite element expansion for fully-enriched (i.e., intersected) elements is still able to reproduce the enrichment function Ψ exactly, shifting does not deteriorate this fundamental property.

A so-called jump enrichment allows for recovering a discontinuity in the solution field as well as in its gradient. A symmetric Heaviside function, which depends on the underlying level-set field for the present application, defines the associated jump enrichment function as

$$\Psi(\mathbf{x},t) = \begin{cases} +1 & \text{if } \phi^h(\mathbf{x},t) \geq 0 \\ -1 & \text{if } \phi^h(\mathbf{x},t) < 0. \end{cases} \tag{9.18}$$

As usual, the jump enrichment function is applied together with the shifting given in equation (9.17). Due to the shifting, the enriched shape functions are non-zero only in elements intersected by the interface, thus avoiding any problems in elements adjacent to fully-enriched intersected elements, so-called partially-enriched elements, where the partition-of-unity concept is formally violated (see, e.g., Fries and Belytschko [99] for further discussion). For illustration, Figure 9.3 displays the enriched shape functions $N_{\tilde{A}}\Psi_{\tilde{A}}$ for a two-dimensional bilinearly-interpolated quadrilateral element with the interface being located at $\xi_1 = 0$ (i.e., $\phi(\boldsymbol{\xi}) = \xi_1$).

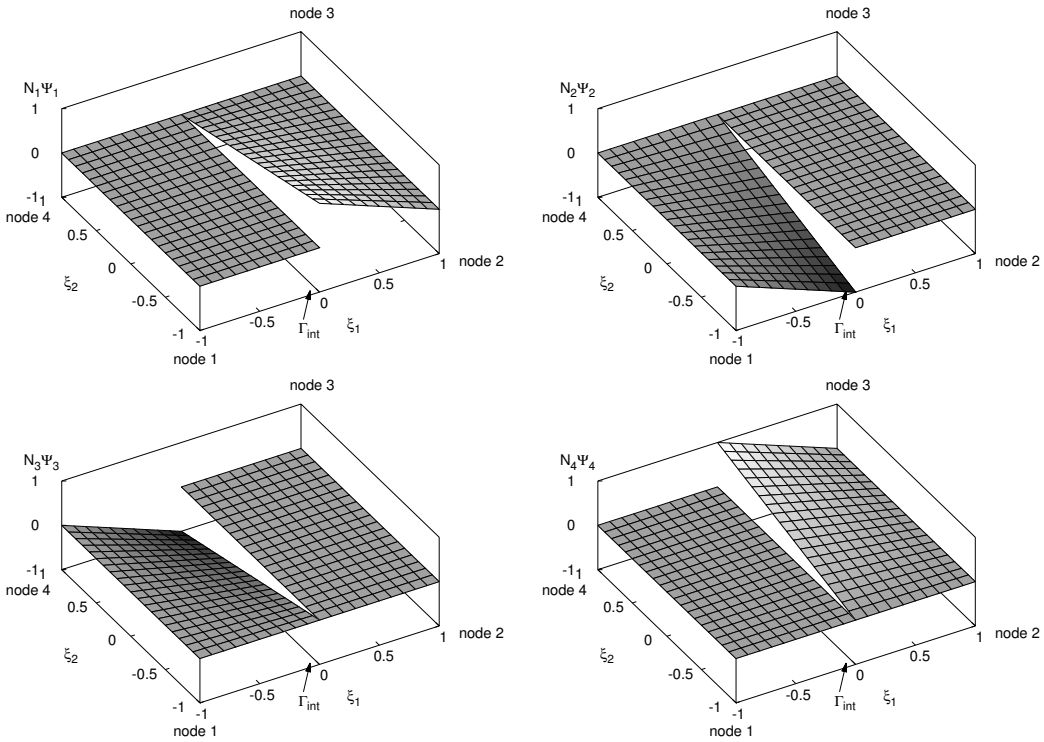

Figure 9.3: Enriched shape functions.

In this thesis, the jump enrichment is not only applied to the pressure field, where strong and weak discontinuities may occur, but also to the velocity field, which is continuous at the interface and merely exhibits a kink. Hence, additional means, such as Nitsche's method, to incorporate the velocity interface condition, i.e., to enforce a continuous velocity field at the interface, are required. Nevertheless, several advantages may be identified for the present choice. In contrast

to the kink enrichment function according to Moës *et al.* [220], the present jump enrichment function retains the polynomial order of the shape function N_A also for the enriched shape function $N_{\tilde{A}}\Psi_{\tilde{A}}$ instead of increasing it. Moreover, the applied equal-order interpolation for velocity and pressure is also upheld in the enriched elements by this choice. As a result of these aspects, the extended discrete function spaces are inherently consistent. In addition, this enrichment strategy leads to a method that is equivalent to the approach suggested by Hansbo and Hansbo [136], where the nodes of intersected elements as well as their associated degrees of freedom are doubled, formally leading to two overlapping meshes; see also Areias and Belytschko [7]. Within that framework, the theoretical foundation towards a robust formulation, among other things, with respect to stability issues arising from the application of the XFEM, has already been established in literature. This aspect will be further addressed in the next section.

9.3 A Face-Oriented Stabilized Nitsche-Type Formulation

Since the discontinuous enrichment function is not only used for the pressure field but also for the velocity field, an appropriate numerical technique, such as Nitsche's method, is additionally required to enforce a continuous velocity field at the interface. An overview of Nitsche's method including a brief classification of this method within other frequently used techniques to impose interface constraints is given first. Then, Nitsche's method is further developed for instationary two-phase flow problems governed by the incompressible Navier-Stokes equations. Furthermore, appropriate face-oriented ghost-penalty and fluid stabilization terms are introduced to guarantee the stability of the overall method independent of the flow regime.

9.3.1 "Nitsche's method is the most straightforward method to use"

(Stenberg [294])

To enforce coupling constraints at interfaces embedded in a non-matching grid, techniques originally developed to weakly apply Dirichlet conditions at boundaries represented by the grid have been extended to such configurations. Two fundamental approaches to weakly impose Dirichlet boundary conditions are Lagrange multiplier methods, as originally suggested by Babuška [11], and Nitsche's method [231], which may be classified as a variationally consistent penalty method among other interpretations. In Lagrange multiplier methods, an additional multiplier field, representing the fluxes at the boundary, is introduced. Owing to the related unknowns, the computational cost increases. Moreover, the function space for the primary field and the function space for the multiplier field are subject to an inf-sup condition (see, e.g., Brezzi and Fortin [39]) and, therefore, cannot be chosen independently from each other. Based on the formulation of Babuška [11], Barbosa and Hughes [13] proposed a stabilized Lagrange multiplier method to circumvent the inf-sup condition. The Lagrange multiplier method by Babuška [11] was reviewed by Stenberg [294], who emphasized the close relation between Nitsche's method and the stabilized Lagrange multiplier method by Barbosa and Hughes [13]. In spite of their potential drawbacks, several Lagrange multiplier methods for embedded interfaces have been developed.

For instance, Béchet *et al.* [26] suggested a stable Lagrange multiplier method satisfying the aforementioned inf-sup condition and Mourad *et al.* [225] a stabilized formulation.

In the aforementioned review article, Stenberg [294] classified Nitsche's method as the most straightforward method to impose Dirichlet-type conditions in general. The application of Nitsche's method to elliptic problems with embedded interfaces was first recognized by Hansbo and Hansbo [136]. A juxtaposition of Nitsche's method and a stable Lagrange multiplier method was later given by Hautefeuille *et al.* [139] for three-dimensional elliptic problems. Recently, Burman and Zunino [47] reviewed Nitsche's method for the enforcement of Dirichlet-type interface conditions in diffusion problems. In particular, stability issues related to elements intersected by the interface, the treatment of large differences between the involved diffusivites as well as the extension of Nitsche's method to convection-diffusion problems were addressed in comprehensive form.

Nitsche's method for problems with embedded interfaces is prone to instabilities related to pathological intersections of the elements; that is, the interface cuts off tiny corners and edges or small slices. To ensure stability and robustness, which is mathematically expressed in terms of coercivity (see, e.g., the textbook by Braess [37]), an inverse inequality has to be satisfied, leading to a constraint on the involved penalty parameter (see, e.g., Dolbow and Harari [82] for derivation). In simple terms, the penalty parameter has to depend on how the interface intersects the element to ensure coercivity. For the aforementioned pathological intersections, this can in turn result in an unbounded penalty parameter and, hence, in an unbounded condition number for the resulting matrix system. While it was shown, e.g., by Annavarapu *et al.* [6] and Barrau *et al.* [16], that Nitsche's method incorporating the volume fractions of intersected elements is adequate for linearly-interpolated tetrahedral elements to overcome this lack of robustness, alternative measures are needed for higher-order elements. To stabilize Nitsche's method for embedded interfaces independent of the order of the elements, Burman [44] and Burman and Hansbo [45] suggested the incorporation of a so-called ghost-penalty stabilization term, which is active in the interface region and penalizes degrees of freedom outside of the physical subdomain but contributing to the solution inside. While Burman [44] considered a local projection-based ghost-penalty stabilization, Burman and Hansbo [45] investigated a face-oriented ghost-penalty stabilization evaluated on selected faces of intersected elements. The face-oriented ghost-penalty stabilization was first presented for elliptic problems and then further developed for problems governed by the Stokes equations by Burman and Hansbo [45, 46]. The face-oriented ghost-penalty stabilization is closely related to the respective fluid stabilization. Similar to the SUPG, PSPG and grad-div term of the residual-based fluid stabilization (see Section 3.3), face-oriented fluid stabilization terms, as, e.g., proposed by Burman *et al.* [48] for the Oseen equations, were derived as a means to stabilize FEMs for flow problems. These terms penalize jumps in the gradient of the solution fields across element boundaries to stabilize numerical schemes and have their origin in an early work by Douglas and Dupont [87]. For further details on stabilization techniques in FEMs for flow problems, the reader is referred, e.g., to the review article by Braack *et al.* [35]. Applications of the face-oriented fluid stabilization to two-dimensional flow problems may be found, e.g., in Burman [43].

Discontinuous diffusivites or viscosities constitute a further issue that demands proper consideration. For two-phase flow problems, for instance, dynamic-viscosity ratios of the order of one

hundred have to be expected. For linearly-interpolated tetrahedral elements, both the intersection of the element as well as different diffusivities can be directly introduced into Nitsche's method in an appropriate manner as shown, e.g., in the aforementioned works by Annavarapu *et al.* [6] and Barrau *et al.* [16]. As a general framework, Burman and Zunino [47] proposed using a ghost-penalty stabilization to ensure the robustness of the method irrespective of the intersection of the elements and merely incorporating the different diffusivities into Nitsche's method. Originally, Nitsche's method was developed for elliptic problems. When applying Nitsche's method to problems with convection, the convective flux across the interface has also to be considered. In the hyperbolic limit, Dirichlet-type conditions can only be prescribed at the inflow part of an interface, i.e., $\Gamma_{\text{int},+}^{\text{in}} := \{\mathbf{x} \in \Gamma_{\text{int}} | (\mathbf{u}_+ \cdot \mathbf{n}_{\text{int}} - u_{\text{int}}) < 0\}$ with respect to Ω_+ and $\Gamma_{\text{int},-}^{\text{in}} := \{\mathbf{x} \in \Gamma_{\text{int}} | (\mathbf{u}_- \cdot \mathbf{n}_{\text{int}} - u_{\text{int}}) > 0\}$ with respect to Ω_-, where u_{int} denotes the interface velocity as introduced in Section 7.1. Therefore, a term accounting for the convective flux has also to be restricted to $\Gamma_{\text{int},+}^{\text{in}}$ and $\Gamma_{\text{int},-}^{\text{in}}$, respectively. Concerning the present two-phase flows, the interface moves with the convective velocity of the fluids. Hence, a respective convective flux term is not considered in the formulation derived in the following. A thorough discussion of this issue may be found in the review article by Burman and Zunino [47].

Becker *et al.* [28] showed the first extension of the approach by Hansbo and Hansbo [136] to incompressible elasticity problems described by the Stokes equations. D'Angelo and Zunino [77], for instance, applied Nitsche's method to couple Stokes and Darcy flow. Henke [140] combined the XFEM with Nitsche's method and the G-function approach to premixed combustion. In particular, Henke elaborately analyzed convective flux terms at the interface. Face-oriented stabilization terms were not considered in that work. Schott and Wall [276] further extended the formulation of Burman and Hansbo [46] for embedded boundaries arbitrarily intersecting the grid to flow problems governed by the incompressible Navier-Stokes equations by incorporating the convective face-oriented fluid stabilization term. A convective flux term was also discussed in that study. Shahmiri [284] embedded an ALE discretization aligned with the boundary of a moving structure into a fixed background grid, thus coupling two fluid domains. The combination of face-oriented ghost-penalty stabilization terms in the vicinity of an embedded boundary and a residual-based stabilization term in the interior of the domain was particularly investigated by Massing *et al.* [209] for problems described by the Stokes equations. Recently, Hansbo *et al.* [137] applied Nitsche's method to two-phase flow problems governed by the stationary Stokes equations.

The aforementioned intersections splitting an element into extremely unevenly sized parts also affect the XFEM. The support of the enriched shape functions introduced in Section 9.2.2 is confined to elements parts only and hence goes to zero for such intersections. The resulting matrix system gets ill-conditioned. Although this aspect is not directly related to Nitsche's method, it is discussed in this section for reasons which will become obvious below. This issue is frequently tackled by *ad hoc* measures such as the manipulations of the enrichments. As, e.g., suggested by Reusken [264] as well as Sauerland and Fries [273], enrichments are removed based on a certain criterion taking into account the size of the support of their associated enriched shape function. Recently, Babuška and Banerjee [12] introduced a concept referred to as stable XFEM. By expanding the support of the enrichment function to the entire element, condition numbers of the XFEM matrix system which are in the order of the ones of standard FEM systems are enabled, as shown by Babuška and Banerjee [12]. Since these enrichment functions incorporate

the standard shape functions, the resulting enriched shape functions involve polynomials of a higher order than the applied standard ones. For instance, the kink enrichment function, originally introduced by Moës *et al.* [220] and applied to two-phase-flow problems, e.g., by Rasthofer *et al.* [259], belongs to this particular group of enrichment functions. However, several deficiencies were observed, e.g., by Henke [140] and Sauerland and Fries [273] for the respective jump enrichment function. By inclusion of the aforementioned face-oriented stabilization terms in the interface region, this issue is accounted for in a mathematically rigorous way, allowing for the conventional jump enrichment without further provisions. All the reviewed strategies have in common that they somehow aim at providing a sufficiently large support of the enriched shape function for evaluation. For the sake of completeness, it is therefore also referred to a recent work by Gerstenberger and Tuminaro [116] who focused on the application of established algebraic multigrid methods (see also Section 4.3) to matrix systems arising from XFEMs. Gerstenberger and Tuminaro [116] reported that the tolerance for removing enrichments could be reduced by about two orders of magnitude compared to the respective values provided elsewhere in literature. This observation may be traced back to the restriction of the matrix system onto a coarser level, which likewise comes along with an increase of the support.

9.3.2 Enforcement of the Dirichlet-Type Interface Condition

The application of Nitsche's method to flow problems governed by the incompressible Navier-Stokes equations introduces three further terms to weakly impose the velocity interface condition (9.3). Together with the viscous and pressure consistency term (see equation (9.12)), they are given by

$$\begin{aligned}\mathcal{B}_{\text{Nit}}(\mathbf{v}^h, q^h; \mathbf{u}^h, p^h) := &\left(\llbracket \mathbf{v}^h \rrbracket, \{2\mu\boldsymbol{\varepsilon}(\mathbf{u}^h)\}_w \cdot \mathbf{n}_{\text{int}}\right)_{\Gamma_{\text{int}}} - \left(\llbracket \mathbf{v}^h \rrbracket \cdot \mathbf{n}_{\text{int}}, \{p^h\}_w\right)_{\Gamma_{\text{int}}} \\ &+ \left(\{2\mu\boldsymbol{\varepsilon}(\mathbf{v}^h)\}_w \cdot \mathbf{n}_{\text{int}}, \llbracket \mathbf{u}^h \rrbracket\right)_{\Gamma_{\text{int}}} + \left(\{q^h\}_w, \llbracket \mathbf{u}^h \rrbracket \cdot \mathbf{n}_{\text{int}}\right)_{\Gamma_{\text{int}}} \\ &+ \left(\alpha_{\text{NP}} \left(\frac{\{\mu\}_w}{h} + \frac{\{\rho \|\mathbf{u}^h\|_\infty\}_w}{6} + \frac{\{\rho\}_w h}{12\theta\Delta t} \right) \llbracket \mathbf{v}^h \rrbracket, \llbracket \mathbf{u}^h \rrbracket \right)_{\Gamma^*_{\text{int}}},\end{aligned} \tag{9.19}$$

where $(\cdot,\cdot)_{\Gamma^*_{\text{int}}} := \sum_{e \in \mathcal{G}^h} (\cdot,\cdot)_{\Gamma^e_{\text{int}}}$ based on the interface Γ^e_{int} within the element and the set $\mathcal{G}^h$ of intersected elements. The third and fourth term are the viscous and the pressure adjoint consistency term. As introduced by Becker *et al.* [28], a symmetric (i.e., the same sign as the first term) viscous adjoint consistency term is used, reflecting the symmetry of the viscous term. To balance instabilities related to the pressure consistency term, a skew-symmetric pressure adjoint consistency term is added. While the viscous adjoint consistency term weakly enforces continuity of the velocity field across the interface (i.e., condition (9.3)) for viscous fluids, the pressure adjoint consistency term imposes mass conservation (i.e., $\llbracket \mathbf{u}^h \rrbracket \cdot \mathbf{n}_{\text{int}} = 0$; see also equation (7.6)) at the interface also in the inviscid limit. To account for large viscosity ratios of the two fluids, a

viscosity-based harmonic average weighting is applied in definitions (9.9) and (9.10), that is,

$$w_+ = \frac{\mu_-}{\mu_+ + \mu_-}, \tag{9.20}$$

$$w_- = \frac{\mu_+}{\mu_+ + \mu_-}, \tag{9.21}$$

as suggested, e.g., by Burman and Zunino [47]. The last term of $\mathcal{B}_{\text{Nit}}(\mathbf{v}^h, q^h; \mathbf{u}^h, p^h)$ constitutes a penalty term. Further following, e.g., Burman and Zunino [47], the definition of the weights also enters the scaling of the penalty term. Therein, h denotes the characteristic element length, which is defined as the longest element diameter. The viscous part $\{\mu\}_w/h$ only represents the classical Nitsche penalty term which is added to stabilize the viscous consistency and adjoint consistency term. In contrast to Becker *et al.* [28] and Hansbo *et al.* [137], who restricted their derivations to stationary problems described by the Stokes equations, two further contributions are additionally included here for application of Nitsche's method to two-phase-flow problems governed by the incompressible Navier-Stokes equations. The convective and transient part, $\{\rho\|\mathbf{u}^h\|_\infty\}_w/6$ and $(\{\rho\}_w h)/(12\theta\Delta t)$, respectively, extend the penalty-term scaling for non-viscous-dominated flows based on considerations from the enforcement of mass conservation as further explained below. A temporal discretization based on a one-step-θ scheme is assumed for the third part, where Δt denotes the time-step length. Similar forms merely taking into account two of the three contributions may be found, e.g., in D'Angelo and Zunino [77] and Schott and Wall [276]. Formally, the second and third part have to be restricted to the direction normal to the interface, i.e., $(\alpha_{\text{NP}}(\{\rho\|\mathbf{u}^h\|_\infty\}_w/6 + (\{\rho\}_w h)/(12\theta\Delta t))[\![\mathbf{v}^h]\!] \cdot \mathbf{n}_{\text{int}}, [\![\mathbf{u}^h]\!] \cdot \mathbf{n}_{\text{int}})_{\Gamma_{\text{int}}}$, since, in the inviscid limit, the no-slip condition at the interface has to be replaced by a slip condition, that is, merely the imposition of zero mass transfer across the interface (i.e., $[\![\mathbf{u}^h]\!] \cdot \mathbf{n}_{\text{int}} = 0$) is allowed in this case; see also, e.g., Becker [27] for similar considerations in the context of Dirichlet boundary conditions. However, for viscous fluids and an interface thickness that goes to zero, as considered in this thesis, anything but a no-slip condition at the interface would physically result in infinitely high stresses; see, e.g., the textbook by Tryggvason *et al.* [316]. For better satisfying the no-slip condition for non-viscous-dominated flows, the weak application of condition (9.3) is strengthened by not restricting the convective and transient part of the penalty-term scaling to the direction normal to the interface. The coefficient α_{NP} is set to 50 in this thesis.

9.3.3 Face-Oriented Ghost-Penalty Stabilization

Without additional provisions, the Nitsche-type formulation introduced so far as well as the XFEM are not stable for interface positions that cut off tiny corners and edges or thin slices from elements. On the one hand, the weak imposition of the velocity interface condition with respect to these intersection configurations would demand a penalty parameter that tends to infinity, which in turn would result in an ill-conditioning of the resulting matrix system. On the other hand, the support of the enriched shape function goes to zero, and the matrix system likewise becomes ill-conditioned. Therefore, face-oriented ghost-penalty stabilization terms, which allow for tackling both issues at once, are additionally included in the interface region. Moreover, classical fluid instabilities related to convection-dominated flows and a violation of the inf-sup condition (see,

e.g., Brezzi and Fortin [39]) due to equal-order interpolation for velocity and pressure have to be balanced not only in the physical subdomains Ω_+ and Ω_- but also in the natural extrapolation of the flow field onto the entire intersected element. This issue is addressed by further incorporating face-oriented fluid stabilization terms in the interface region as well.

For interface problems, face-oriented ghost-penalty and fluid stabilization terms have to be applied for both subdomains separately. Here, a face f denotes the surface shared by two adjacent elements. The characteristic length associated with the face is denoted by h_f and defined as the maximal distance to the opposite surface of the adjacent elements. As illustrated in Figure 9.4, face-oriented stabilization terms are evaluated only on faces that belong to intersected elements and lie at least partially within the considered subdomain. These faces are marked by thick lines in Figure 9.4. The set $\mathcal{F}_k$ with $k \in \{+,-\}$ contains the considered faces corresponding to the

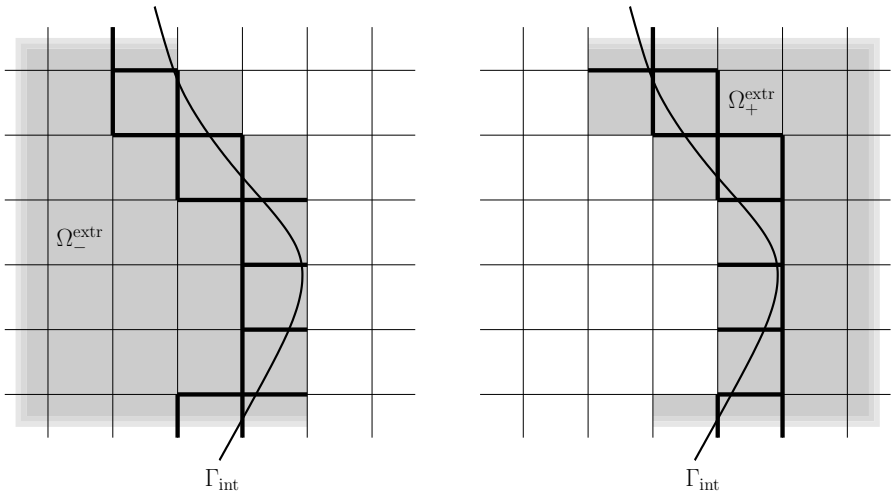

Figure 9.4: Extended subdomains Ω_-^{extr} and Ω_+^{extr} as well as corresponding faces considered for face-oriented stabilization.

subdomain Ω_k. Faces intersected by the interface are taken into account twice, once with respect to Ω_+ and once with respect to Ω_-. Since face-oriented stabilization terms are always evaluated on the entire surface Γ_f of the face and not only on the part belonging to the physical domain, extrapolated velocity and pressure fields are required for faces intersected by the interface. Here, $\mathbf{u}_k^{h,\text{extr}}$ and $p_k^{h,\text{extr}}$ denote extrapolations of the physical solution fields $\mathbf{u}_k^h$ and p_k^h of the respective subdomain Ω_k onto an extended subdomain Ω_k^{extr}. The extended subdomains Ω_+^{extr} and Ω_-^{extr} are defined by incorporating all intersected elements completely and depicted in Figure 9.4 via shaded regions. The respective extrapolations are defined as

$$\mathbf{u}_k^{h,\text{extr}}(\mathbf{x},t) = \sum_{A\in\mathcal{E}_k} N_A(\mathbf{x})\mathbf{u}_A(t) + \sum_{\tilde{A}\in\mathcal{E}_{\text{enr},k}} N_{\tilde{A}}(\mathbf{x})\Psi_{\tilde{A},k}^{\text{extr}}(\mathbf{x},t)\tilde{\mathbf{u}}_{\tilde{A}}(t), \tag{9.22}$$

$$p_k^{h,\text{extr}}(\mathbf{x},t) = \sum_{A\in\mathcal{E}_k} N_A(\mathbf{x})p_A(t) + \sum_{\tilde{A}\in\mathcal{E}_{\text{enr},k}} N_{\tilde{A}}(\mathbf{x})\Psi_{\tilde{A},k}^{\text{extr}}(\mathbf{x},t)\tilde{p}_{\tilde{A}}(t), \tag{9.23}$$

using the extrapolated enrichment function

$$\Psi^{\text{extr}}_{\bar{A},k}(\mathbf{x},t) = \begin{cases} +2 & \text{for } k = + \\ -2 & \text{for } k = -. \end{cases} \tag{9.24}$$

Here, $\mathcal{E}_k$ denotes set of all nodes contained in Ω_k^{extr} and $\mathcal{E}_{\text{enr},k}$ the set of enriched nodes whose associated (enriched) shape functions and degrees of freedom contribute to the solution in Ω_k (i.e., all enriched nodes outside of Ω_k). The extrapolated weighting functions $\mathbf{v}_k^{h,\text{extr}}$ and $q_k^{h,\text{extr}}$ are defined analogously. Figure 9.5 exemplifies the extrapolation of the solution field onto the entire element domain Ω^e. Therefore, a one-dimensional discontinuous solution field u^h is considered on a two-dimensional bilinearly-interpolated quadrilateral element with jump enrichment. The element is intersected by the interface at $\xi_1 = 0$. Below the depiction of u^h, both the extrapola-

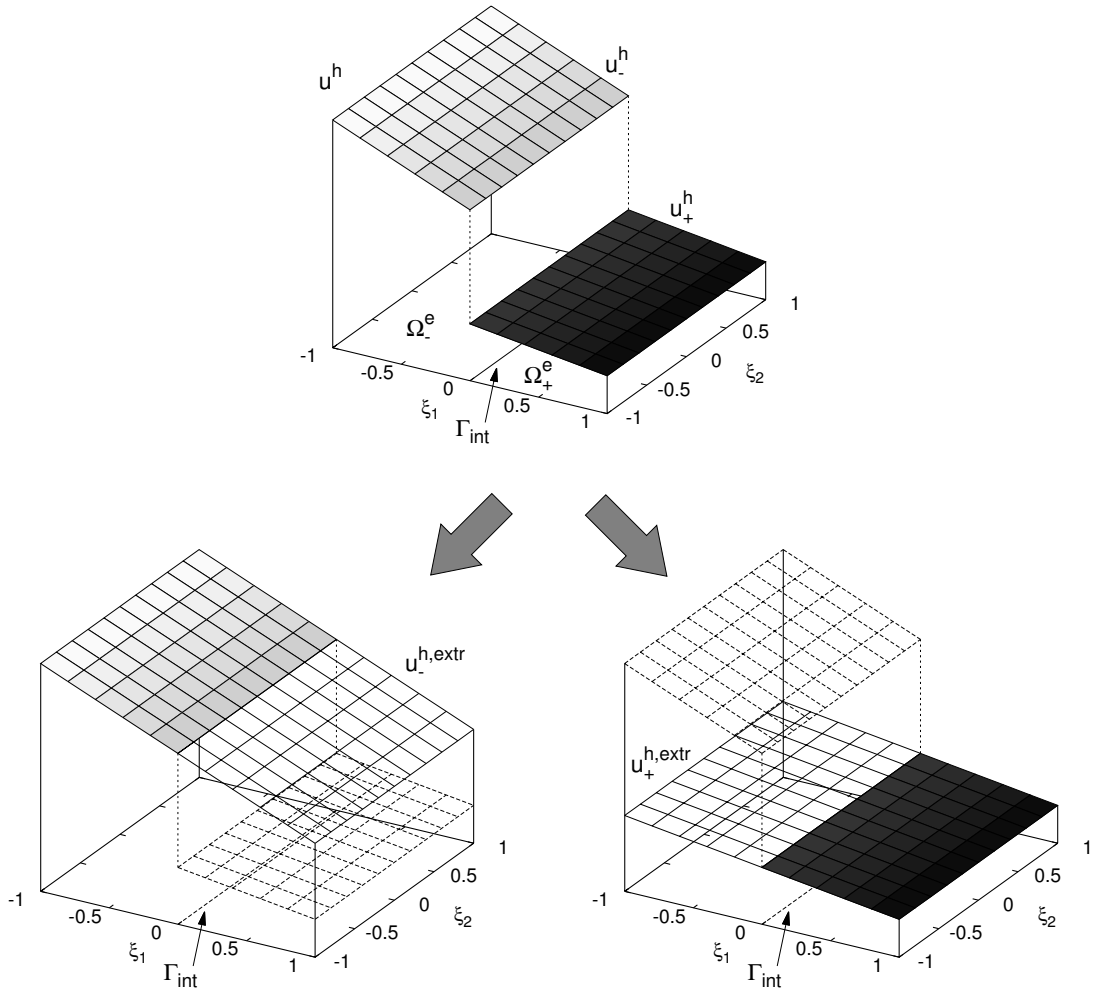

Figure 9.5: Extrapolation of solution field.

tion $u_-^{h,\text{extr}}$ of u_-^h from the element subdomain Ω_-^e onto Ω^e as well as the extrapolation $u_+^{h,\text{extr}}$ of u_+^h from Ω_+^e onto Ω^e are provided.

To guarantee the robustness of the overall method and to sufficiently stabilize the two-phase flow formulation, the following face-oriented ghost-penalty and fluid stabilization terms are additionally incorporated in the interface region:

$$
\begin{aligned}
&\mathcal{B}_{\text{FOStab}}(\mathbf{v}^h, q^h; \mathbf{u}^h, p^h) := \\
&\qquad \sum_{k\in\{+,-\}} \sum_{f\in\mathcal{F}_k} \sum_{i=1}^{l} \left(\gamma_{\text{gp}}^{\mu} \mu_k h_f^{2(i-1)+1} [\![D^i \mathbf{v}_k^{h,\text{extr}}]\!], [\![D^i \mathbf{u}_k^{h,\text{extr}}]\!] \right)_{\Gamma_f} \\
&\quad + \sum_{k\in\{+,-\}} \sum_{f\in\mathcal{F}_k} \sum_{i=1}^{l} \left(\frac{\gamma_{\text{gp}}^{t} \rho_k h_f^{2(i-1)+3}}{\theta \Delta t} [\![D^i \mathbf{v}_k^{h,\text{extr}}]\!], [\![D^i \mathbf{u}_k^{h,\text{extr}}]\!] \right)_{\Gamma_f} \\
&\quad + \sum_{k\in\{+,-\}} \sum_{f\in\mathcal{F}_k} \sum_{i=1}^{l} \left(\frac{\gamma_{\text{gp}}^{p} h_f^{2i}}{\frac{\mu_k}{h_f} + \frac{\rho_k \|\mathbf{u}_k^{h,\text{extr}}\|_\infty}{6} + \frac{\rho_k h_f}{12\theta\Delta t}} [\![D^i q_k^{h,\text{extr}}]\!], [\![D^i p_k^{h,\text{extr}}]\!] \right)_{\Gamma_f} \\
&\quad + \sum_{k\in\{+,-\}} \sum_{f\in\mathcal{F}_k} \left(\gamma^{\mathbf{u}} \rho_k |\mathbf{u}_k^{h,\text{extr}} \cdot \mathbf{n}_f| h_f^2 [\![\nabla \mathbf{v}_k^{h,\text{extr}}]\!], [\![\nabla \mathbf{u}_k^{h,\text{extr}}]\!] \right)_{\Gamma_f} \\
&\quad + \sum_{k\in\{+,-\}} \sum_{f\in\mathcal{F}_k} \left(\gamma^{\text{div}} \rho_k \|\mathbf{u}_k^{h,\text{extr}}\|_\infty h_f^2 [\![\nabla \cdot \mathbf{v}_k^{h,\text{extr}}]\!], [\![\nabla \cdot \mathbf{u}_k^{h,\text{extr}}]\!] \right)_{\Gamma_f} .
\end{aligned}
\tag{9.25}
$$

The first and the third term are the viscous and pressure face-oriented ghost-penalty stabilization terms as suggested by Burman and Hansbo [46] for stationary problems governed by the Stokes equations. For viscous-dominated problems and independent of the order of the elements, the viscous face-oriented ghost-penalty stabilization term controls the instability of Nitsche's method arising from pathological intersections of the elements and thus enables the convenient choice of an intersection-independent penalty parameter. Consequently, the penalty parameter remains bounded and an ill-conditioning of the system is prevented. For viscous-dominated problems, this term leads to robust and stable enrichment values for the velocity. According to, e.g., Burman and Hansbo [46] as well as Burman and Zunino [47], face-oriented ghost-penalty stabilization terms have to address all polynomial orders contained in the finite element interpolation space. Here, l denotes the highest polynomial order and $D^i(\cdot)$ the normal derivative of order i on the face. For the used trilinearly-interpolated hexahedral elements, l is set to 2, including contributions of mixed derivatives. In contrast to the pressure face-oriented ghost-penalty stabilization term presented by Burman and Hansbo [46], which merely scales as h_f^{2i+1}/μ_k, the present term accounts for problems governed by the incompressible Navier-Stokes equations by enhancing its scaling with a convective and a transient contribution. Definitions for the pressure stabilization term scaling merely taking into account two of the aforementioned three contributions may be found, e.g., in D'Angelo and Zunino [77] as well as in Burman *et al.* [48]. The present set of coefficients for the three constituents is inspired by stabilization parameters used in the corresponding PSPG term of the residual-based fluid stabilization (see Franca and Valentin [96] and Barrenechea and Valentin [17]). The same switching between the different regimes is applied for the extended penalty term based on mass conservation (see last term

of equation (9.19)), which is related to the pressure. Furthermore, penalizing not only jumps in the gradient (i.e., $i = 1$), as required to balance the inf-sup instability due to the equal-order interpolation for velocity and pressure, but also controlling all higher-order derivatives $D^i p_h$ with $i \geq 1$ yields well-behaved pressure enrichment values. Furthermore, the inclusion of a reactive face-oriented ghost-penalty stabilization term (second term) for transient problems is proposed here. Potential benefits owing to an inclusion of this term were already recognized by Schott and Wall [276], but not further considered. Again, a one-step-θ scheme for temporal discretization is assumed. Similar to the viscous face-oriented ghost-penalty stabilization term, this term controls the velocity enrichment values for transient problems when discretized with a small time-step length Δt. To provide convective stability on the extended domain, a convective face-oriented fluid stabilization term, as also applied by Schott and Wall [276] for embedded boundaries arbitrarily intersecting the grid, is presented in the fourth term. Here, $\mathbf{n}_f$ denotes the unit normal vector on the face f. For high-Reynolds-number flows, additional stability can be obtained on the extended domain by adding a face-oriented fluid stabilization term penalizing jumps of $\nabla \cdot \mathbf{u}_k^{h,\text{extr}}$ across element faces (fifth term). Alternatively, the scaling in the fourth term can be extended to $(\gamma^{\mathbf{u}} \rho_k |\mathbf{u}_k^{h,\text{extr}} \cdot \mathbf{n}_f| + \gamma^{\text{div}} \rho_k \|\mathbf{u}_k^{h,\text{extr}}\|_\infty) h_f^2$. The fourth and fifth term come along with an additional ghost-penalty effect for convection-dominated problems and contribute to the ghost-penalty stabilization terms by ensuring stable velocity enrichment values for arbitrarily intersected elements. Independent of the position of the interface, all these terms improve the conditioning of the matrix system. As a consequence, a manipulation of the enrichment based on a user-defined tolerance is neither required nor applied. In accordance with the values provided in literature for face-oriented ghost-penalty and fluid stabilization terms (see, e.g., Burman [43] and Schott and Wall [276]), the corresponding coefficients are chosen to be $\gamma_{\text{gp}}^{\mu} = \gamma_{\text{gp}}^{t} = \gamma^{\mathbf{u}} = 20\gamma^{\text{div}} = 10\gamma_{\text{gp}}^{p} = 0.05$.

9.4 The Final Coupled Formulation

Equipping the standard Galerkin terms for both subdomains as well as the interface, given in equations (9.13) and (9.14), with the interface terms (9.19) related to Nitsche's method as well as the face-oriented ghost-penalty and fluid stabilization terms (9.25) and additionally incorporating appropriate residual-based multiscale terms in the interior domain of the fluids, the final coupled variational multiscale formulation for incompressible two-phase flow in the entire domain Ω reads: find $(\mathbf{u}^h, p^h) \in \mathcal{S}_{\mathbf{u}}^{h,\text{enr}} \times \mathcal{S}_p^{h,\text{enr}}$ such that

$$\begin{aligned} &\mathcal{B}_{\text{NS}}(\mathbf{v}^h, q^h; \mathbf{u}^h, p^h) + \mathcal{B}_{\text{RBStab}}(\mathbf{v}^h, q^h; \mathbf{u}^h, p^h) \\ &+ \mathcal{B}_{\text{Nit}}(\mathbf{v}^h, q^h; \mathbf{u}^h, p^h) + \mathcal{B}_{\text{FOStab}}(\mathbf{v}^h, q^h; \mathbf{u}^h, p^h) = \ell_{\text{NS}}(\mathbf{v}^h) \end{aligned} \tag{9.26}$$

for all $(\mathbf{v}^h, q^h) \in \mathcal{V}_{\mathbf{u}}^{h,\text{enr}} \times \mathcal{V}_p^{h,\text{enr}}$. The enriched finite dimensional subspaces are given by

$$\mathcal{S}_{\mathbf{u}}^{h,\text{enr}} := \mathcal{S}_{\mathbf{u}}^{h} \oplus \text{span}\left\{ [N_{\tilde{A}}(\mathbf{x}) \boldsymbol{\Psi}_{\tilde{A}}(\mathbf{x}, t)]^3 \;\; \forall \tilde{A} \in \mathcal{E}_{\text{enr}} \right\}, \tag{9.27}$$

$$\mathcal{S}_{p}^{h,\text{enr}} := \mathcal{S}_{p}^{h} \oplus \text{span}\left\{ N_{\tilde{A}}(\mathbf{x}) \boldsymbol{\Psi}_{\tilde{A}}(\mathbf{x}, t) \; \forall \tilde{A} \in \mathcal{E}_{\text{enr}} \right\}, \tag{9.28}$$

$$\mathcal{V}_{\mathbf{u}}^{h,\text{enr}} := \mathcal{V}_{\mathbf{u}}^{h} \oplus \text{span}\left\{ [N_{\tilde{A}}(\mathbf{x})\boldsymbol{\Psi}_{\tilde{A}}(\mathbf{x},t)]^3 \ \forall \tilde{A} \in \mathcal{E}_{\text{enr}} \right\}, \tag{9.29}$$

$$\mathcal{V}_{p}^{h,\text{enr}} := \mathcal{V}_{p}^{h} \oplus \text{span}\left\{ N_{\tilde{A}}(\mathbf{x})\boldsymbol{\Psi}_{\tilde{A}}(\mathbf{x},t) \ \forall \tilde{A} \in \mathcal{E}_{\text{enr}} \right\}, \tag{9.30}$$

where $\mathcal{S}_{\mathbf{u}}^{h}$, $\mathcal{S}_{p}^{h}$, $\mathcal{V}_{\mathbf{u}}^{h}$ and $\mathcal{V}_{p}^{h}$ are given according to equations (3.31) to (3.34). The compact from $\mathcal{B}_{\text{RBStab}}(\mathbf{v}^h, q^h; \mathbf{u}^h, p^h)$ is defined as

$$\begin{aligned}\mathcal{B}_{\text{RBStab}}(\mathbf{v}^h, q^h; \mathbf{u}^h, p^h) := &\left(\rho\mathbf{u}^h \cdot \nabla\mathbf{v}^h, \tau_{\text{M}}\mathbf{r}_{\text{M}}^h\right)_{\Omega_{\pm}^*} + \left(\nabla\cdot\mathbf{v}^h, \tau_{\text{C}} r_{\text{C}}^h\right)_{\Omega_{\pm}^*} \\ &+ \left(\nabla q^h, \tau_{\text{M}}\mathbf{r}_{\text{M}}^h\right)_{\Omega_{\pm}^*},\end{aligned} \tag{9.31}$$

where $(\cdot,\cdot)_{\Omega_{\pm}^*} := \sum_{e\in\mathcal{T}^h}((\cdot,\cdot)_{\Omega_{+}^e} + (\cdot,\cdot)_{\Omega_{-}^e})$, and comprises, in this order, an SUPG, grad-div and PSPG term. These stabilization terms account for instabilities of the standard Galerkin method when applied to the incompressible Navier-Stokes equations and lead to a stabilized method within both subdomains; see Section 3.3 for elaboration. Residual-based stabilization terms may be derived within the framework of the variational multiscale method as shown in Chapter 3 for one fluid. For a step-by-step derivation of formulation (9.26) as a residual-based variational multiscale formulation for two-phase flow, the reader is referred to Rasthofer and Schott *et al.* [262].

In $\mathcal{B}_{\text{RBStab}}(\mathbf{v}^h, q^h; \mathbf{u}^h, p^h)$, the discrete residuals of continuity and momentum equation for each subdomain Ω_k read

$$r_{\text{C},k}^h = \nabla\cdot\mathbf{u}_k^h, \tag{9.32}$$

$$\mathbf{r}_{\text{M},k}^h = \rho_k\frac{\partial\mathbf{u}_k^h}{\partial t} + \rho_k\mathbf{u}_k^h\cdot\nabla\mathbf{u}_k^h + \nabla p_k^h - 2\mu_k\nabla\cdot\boldsymbol{\varepsilon}(\mathbf{u}_k^h) - \rho_k\mathbf{g}. \tag{9.33}$$

The stabilization parameters $\tau_{\text{M},k}$ and $\tau_{\text{C},k}$ as presented for incompressible single-phase flow in Section 3.3 are adopted for two-phase flow. Hence, $\tau_{\text{M},k}$ reads as

$$\tau_{\text{M},k} = \frac{1}{\sqrt{\left(\frac{2\rho_k}{\Delta t}\right)^2 + (\rho_k\mathbf{u}_k^h)\cdot\mathbf{G}(\rho_k\mathbf{u}_k^h) + C_{\text{I}}(\mu_k)^2\mathbf{G}:\mathbf{G}}}. \tag{9.34}$$

The calculation of $\tau_{\text{C},k}$ from $\tau_{\text{M},k}$ as given in equation (3.41) remains unaffected. The splitting of these quantities according to Ω_k implies their evaluation with respect to the subdomains, i.e., $\mathbf{r}_{\text{M}}^h = \mathbf{r}_{\text{M},k}^h$, $r_{\text{C}}^h = r_{\text{C},k}^h$, $\tau_{\text{M}} = \tau_{\text{M},k}$ and $\tau_{\text{C}} = \tau_{\text{C},k}$ for all $\mathbf{x}\in\Omega_k$ with $k\in\{+,-\}$.

9.5 The Fluid-Level-Set Coupling Algorithm

In this section, the fluid-level-set coupling algorithm is summarized. Additionally, two further specific issues, i.e., numerical integration and time discretization, are briefly addressed. These issues, which are also relevant for the successful application of the present approach, were thoroughly discussed in the accompanying thesis by Henke [140] and therefore do not constitute a particular subject of the present one.

Owing to the discontinuities of the physical properties and the enriched shape functions in intersected elements, the quadrature of the variational formulation deserves further considerations. Since quadrature rules for numerical integration commonly rely on the assumption of sufficiently smooth functions, they can not be applied straightforwardly to the present situation. For trilinearly-interpolated hexahedral elements as used in this thesis, the interface usually subdivides an element into two parts assigned to the subdomains Ω_+ and Ω_-, although some special configurations with multiple parts may also be encountered. Consequently, domain integrals are evaluated separately for each part of an intersected element. As suggested in early works on the XFEM (see, e.g., Moës *et al.* [219]), a procedure, usually referred to as tessellation, is used in this thesis. In doing so, all parts of an intersected element are further subdivided into integration cells of simple geometric shape, such as hexahedra or tetrahedra, for which standard quadrature rules can be applied. More sophisticated integration techniques bypassing any further volume decomposition of arbitrarily shaped element parts have been proposed in the meantime, for instance, by Sudhakar *et al.* [298], who recently developed an efficient strategy by utilizing the divergence theorem. Concerning further details on the construction of the domain integration cells as well as the simultaneous construction of boundary integration cells, which provide a discrete representation of the interface and are used for evaluating interface integrals, the reader is referred to the thesis by Henke [140]. Moreover, a thorough presentation of the numerical integration in domain integration cells and on boundary integration cells is likewise contained therein.

When using a pure Eulerian description together with moving interfaces or boundaries, additional difficulties are encountered, which manifest themselves as soon as discretization in time is considered. This issue has been elaborately addressed in the accompanying thesis by Henke [140] and is therefore only briefly summarized here. Since the subdomains Ω_k with $k \in \{+, -\}$ evolve with time, they incorporate new parts of the domain Ω, while releasing other parts. As claimed by Chessa and Belytschko [62] for the XFEM, merely a space-time ansatz enables a consistent formulation for moving interfaces, since it allows for fully resolving the interface with respect to space and time. Discretizing such problems in time using finite difference schemes gives rise to solution fields defined on subdomains assigned to the different involved time levels, and special care is thus required. Since the solution at the current time level $n+1$ is computed with respect to $\Gamma_{\text{int}}(t_{n+1})$, values for the previous time levels have to be initialized in an appropriate way in the newly captured parts of $\Omega_k(t_{n+1})$. Concerning the present XFEM, this issue is not only reflected by nodes which change sides with respect to the interface but also by time-dependent enriched shape functions as well as a continuously changing map of enriched nodes, that is, there are nodes which have been enriched at the previous time level but are not enriched at the current one and vice versa. For temporal discretization, a one-step-θ time-integration scheme is applied to the incompressible Navier-Stokes equations. Hence, solution fields at time level n and $n+1$ are involved in the time-discrete formulation. The finite element approximation of the velocity field for time level $n+1$ is given by

$$\mathbf{u}^h_{n+1}(\mathbf{x}) = \sum_{A \in \mathcal{E}} N_A(\mathbf{x})\, \mathbf{u}_{A,n+1} + \sum_{\tilde{A} \in \mathcal{E}_{\text{enr}}(t_{n+1})} N_{\tilde{A}}(\mathbf{x})\, \Psi_{n+1}(\mathbf{x})\, \tilde{\mathbf{u}}_{\tilde{A},n+1}, \tag{9.35}$$

$$\mathbf{v}^h_{n+1}(\mathbf{x}) = \sum_{A \in \mathcal{E}} N_A(\mathbf{x})\, \mathbf{v}_{A,n+1} + \sum_{\tilde{A} \in \mathcal{E}_{\text{enr}}(t_{n+1})} N_{\tilde{A}}(\mathbf{x})\, \Psi_{n+1}(\mathbf{x})\, \tilde{\mathbf{v}}_{\tilde{A},n+1}. \tag{9.36}$$

and for the time level n as

$$\mathbf{u}_n^{h,\Gamma_{\text{int}}(t_{n+1})}(\mathbf{x}) = \sum_{A\in\mathcal{E}} N_A(\mathbf{x})\,\mathbf{u}_{A,n}^{\Gamma_{\text{int}}(t_{n+1})} + \sum_{\tilde{A}\in\mathcal{E}_{\text{enr}}(t_{n+1})} N_{\tilde{A}}(\mathbf{x})\,\Psi_{n+1}(\mathbf{x})\,\tilde{\mathbf{u}}_{\tilde{A},n}^{\Gamma_{\text{int}}(t_{n+1})}. \tag{9.37}$$

The solution and weighting functions for the pressure are defined analogously. Since the strong form is discretized in space with respect to $\Gamma_{\text{int}}(t_{n+1})$, the weighting function is chosen accordingly as given in equation (9.36); see also, e.g., Chessa and Belytschko [62] as well as Gerstenberger [115]. Since $\mathbf{u}_{n,k}^h$ with $k \in \{+,-\}$ has been computed with respect to $\Omega_k(t_n)$, it does not fit to $\Omega_k(t_{n+1})$, as aforementioned. For proper time integration, the complete solution $\mathbf{u}_n^h$ has to be adapted to the current interface position $\Gamma_{\text{int}}(t_{n+1})$ in an appropriate way, indicated by the additional superscript $\Gamma_{\text{int}}(t_{n+1})$ in equation (9.37).

Two strategies to estimate $\mathbf{u}_n^{h,\Gamma_{\text{int}}(t_{n+1})}$ are used in the present thesis. In Rasthofer *et al.* [259], a quasi-static enrichment strategy was proposed for weak discontinuities, assuming that the differences in the solution field between each side of the interface are sufficiently small. Merely retaining the standard finite element part and omitting the enrichment of the previous time level leads to a smeared discontinuity when evaluating contributions of the previous time level:

$$\mathbf{u}_n^{h,\Gamma_{\text{int}}(t_{n+1})}(\mathbf{x}) = \sum_{A\in\mathcal{E}} N_A(\mathbf{x})\,\mathbf{u}_{A,n}^{\Gamma_{\text{int}}(t_n)}. \tag{9.38}$$

Application of this approach assumes that the pressure, which exhibits a strong discontinuity, is exclusively evaluated at the current time level $n+1$. The approach suggested by Henke *et al.* [141] consists of two parts and may be applied to both strong and weak discontinuities. The standard degrees of freedom of all nodes that change sides with respect to the interface are adapted by a semi-Lagrangian approach. To transfer the standard degrees of freedom to the current interface position, a virtual Lagrangian particle is assumed at the location $\mathbf{x}_A$ of an affected node. This particle is then tracked back in time to its location $\mathbf{x}_A^{\text{Lagr}}$ at the previous time level:

$$\mathbf{x}_A^{\text{Lagr}} = \mathbf{x}_A - \Delta t\,\mathbf{u}_n^h(\mathbf{x}_A^{\text{Lagr}}). \tag{9.39}$$

After having found the origin, the solution at the previous time level is advanced to the current position of the virtual particle, i.e., the position of node A:

$$\mathbf{u}_{A,n}^{\Gamma_{\text{int}}(t_{n+1})} = \mathbf{u}_n^h(\mathbf{x}_A^{\text{Lagr}}) + \Delta t\,\mathbf{u}_n^h(\mathbf{x}_A^{\text{Lagr}})\cdot\nabla\mathbf{u}_n^h(\mathbf{x}_A^{\text{Lagr}}). \tag{9.40}$$

Enrichment degrees of freedom $\mathbf{u}_{\tilde{A},n}^{\Gamma_{\text{int}}(t_{n+1})}$ are treated differently. All newly created enrichment degrees of freedom are recovered in a node-wise manner by exploiting the jump in the primary variable and its gradient. Other approaches to time integration in the context of the XFEM may be found, e.g., in Fries and Zilian [100] and Gerstenberger [115]. For further discussion and references, the reader is once more referred to the thesis by Henke [140].

The two-way coupling between the fluid and the level-set field is accounted for by a partitioned approach as illustrated in Algorithm 9.1. At the beginning of each time step, it is first solved for the level-set equation (8.9) and then for the continuity and momentum equation (9.26). Depending on a prescribed number of iterations n_{it} or on whether a given tolerance criterion has not

Algorithm 9.1: fluid-level-set coupling algorithm

initialize fluid and level-set solver

while time loop not finished: $t < t_{\text{end}}$

  while fluid-level-set iteration not finished: not converged / $i + 1 \leq \text{n}_{\text{it}}$

    fluid solver $\rightarrow$ level-set solver: transfer $\mathbf{u}_{n+1}^{h,i}$

    level-set solver:
      solve for $\phi_{n+1}^{h,i+1}$
      compute $\nabla\phi_{n+1}^{h,i+1}$

    level-set solver $\rightarrow$ fluid solver: transfer $\phi_{n+1}^{h,i+1}$, $\nabla\phi_{n+1}^{h,i+1}$

    fluid solver:
      construct domain and boundary integration cells
      update distribution of enrichment degrees of freedom
      adapt $\mathbf{u}_n^h$ to $\Gamma_{\text{int}}^{i+1}(t_{n+1})$
      solve for $\mathbf{u}_{n+1}^{h,i+1}$ and $p_{n+1}^{h,i+1}$

  end while

  fluid solver $\rightarrow$ level-set solver: transfer $\mathbf{u}_{n+1}^h$

  level-set solver:
    solve for ϕ_{n+1}^h
    if reinitialization
      reinitialize ϕ_{n+1}^h
    end if
    if particles
      solve for $\mathbf{x}_{\text{P},n+1}$
      perform particle correction
    end if

  update time step: $\mathbf{u}_n^h = \mathbf{u}_{n+1}^h$, $p_n^h = p_{n+1}^h$, $\phi_n^h = \phi_{n+1}^h$

end while

yet been achieved, further iterations between the fields may be performed. At the end of each time step, it is finally solved for the level-set equation another time. This procedure turned out instrumental in coupled fluid-scalar-transport problems in general by improving the accuracy of the approach, while providing an efficient computational method (see, e.g., Gravemeier and Wall [122]).

In addition to the overall cycle, quantities transferred between the fluid and the level-set solver are explicitly indicated in Algorithm 9.1. Since the same spatial discretization (i.e., grid and trilinearly-interpolated hexahedral elements) is used for both the fluid and the level-set field, node-based velocity and level-set values can easily be transferred between the two fields, and projections from the velocity space to the level-set space and vice versa are not necessary. Moreover, the aforementioned specific issues of the present approach are included. Before it is solved for $\mathbf{u}_{n+1}^{h,i+1}$ and $p_{n+1}^{h,i+1}$, domain and boundary integration cells are constructed. This step is followed by an update of the distribution of the enrichment degrees of freedom and the applied algorithm that transfers the velocity solution of the previous time step to the current interface position. As already explained in Section 8.1, a continuous gradient of ϕ^h is computed and transferred to the fluid solver for the purpose of evaluating the curvature in the surface-tension term (see right-hand-side form (9.14)). Corrections of the level-set field via reinitalization and particles are arranged at the end of the time step. In practice, $n_{\text{it}} = 1$ is usually chosen. Again, all implementations have been realized in BACI (see Section 4.6).

9.6 Numerical Examples for Laminar Two-Phase Flows

The proposed method is validated for various two- and three-dimensional numerical examples of increasing complexity: two-dimensional Rayleigh-Taylor instabilities at a lower and a higher Atwood number, a two-dimensional collapsing water column, three-dimensional rising bubbles at various shape regimes as well as a three-dimensional bubble coalescence. Since hexahedral elements are used for the fluid and the level-set field, two-dimensional configurations are computed with one element layer in the third dimension. Slip and no penetration boundary conditions are applied for the velocity at the surfaces orthogonal to the respective two-dimensional computational domain, i.e., to the third dimension. For the fluid field, the parameter θ of the time integration scheme is set to 1.0, that is, a backward Euler scheme is applied. The movement of the interface as well as the related enrichments are taken into account by the semi-Lagrangian approach, as described in Section 9.5. For the subsequent investigations of laminar flows, the face-oriented fluid-stabilization term related to the incompressibility constraint (i.e., the last term of $\mathcal{B}_{\text{FOStab}}(\mathbf{v}^h, q^h; \mathbf{u}^h, p^h)$) is omitted. Reinitialization of the level-set field is applied periodically throughout the simulation and performed by explicitly calculating the distance of each node from the interface.

9.6.1 Two-Dimensional Rayleigh-Taylor Instability

An important example of a hydrodynamic instability is the mixing of two fluids of different densities owing to opposite directions of density and pressure gradient, which is usually referred to

as Rayleigh-Taylor instability. If a heavier fluid is placed on top of a lighter one in a gravitational field, an initial perturbation of the interface separating the two fluids starts to grow. Stratified fluids at rest under the influence of gravitation were first investigated by Rayleigh [297] at the end of the 19th century. In the 1950s, Taylor [307] renewed this problem by considering accelerated fluids. Both scientists theoretically predicted a linear growth stage of the perturbation of the interface, which was then experimentally confirmed by Lewis [190]. While Rayleigh and Taylor assumed inviscid fluids, their stability analysis has been extended to take into consideration other physical effects such as viscosity and surface tension in the meantime (see, e.g., Bellman and Pennington [30] as well as the textbook by Chandrasekhar [58]).

A perturbation of the interface leads to a misalignment of the pressure and density gradient, which in turn causes baroclinic torques that set the system into motion. According to the review article by Sharp [285], the subsequent growth of the instability can be roughly divided into four stages. If the initial perturbations are sufficiently small, their amplitudes grow exponentially with time. In the first stage, the evolution of the Rayleigh-Taylor instability can therefore be mathematically described using linear stability theory. After the amplitude has grown to 10% to 40% of its wave length, the second stage is reached. During the second stage, the amplitudes of the perturbations grow non-linearly. Heavy fluid falls as spikes into the lighter fluid, while the lighter fluid rises as bubbles into the heavier fluid. Moreover, the development strongly depends on the Atwood number, which is defined as

$$\mathrm{At} = \frac{\rho_+ - \rho_-}{\rho_+ + \rho_-}, \tag{9.41}$$

where ρ_+ denotes the density of the heavier fluid and ρ_- the density of the lighter one. Three-dimensional effects may also come into play. The development of secondary structures on the spikes as well as interactions among the bubbles characterize the third stage. The Kelvin-Helmholtz instability at the side of the spike may cause the fluids to roll up, leading to the typical “mushroom”-like shape of the interface. According to Sharp [285], this effect is more pronounced at lower density ratios. Eventually, chaotic or turbulent mixing is encountered, which constitutes the last stage of the evolution of the Rayleigh-Taylor instability.

For further analysis, a semi-infinite configuration of two stratified fluids in a gravitational field $\mathbf{g}$, acting perpendicular to the interface, is assumed. The heavier fluid with density ρ_+ is placed on top of the lighter fluid with ρ_- (i.e., $\rho_- < \rho_+$). Considering a single-mode perturbation of the planar interface with wave number k, the asymptotic exponential growth of its amplitude $A(t)$ in the linear regime, i.e., $Ak \ll 1$, is given by

$$A(t) \sim A_0 \mathrm{e}^{\varsigma t}, \tag{9.42}$$

where ς denotes the growth rate and A_0 the initial amplitude. For inviscid fluids, the growth rate ς depends on the Atwood number At, the gravitational acceleration $g = \|\mathbf{g}\|$, the surface-tension coefficient γ and the wave number k as

$$\varsigma = \sqrt{\mathrm{At} g k - \frac{\gamma k^3}{\rho_+ + \rho_-}}; \tag{9.43}$$

see, e.g., Piriz *et al.* [249] and Sharp [285] for derivation. Surface tension stabilizes perturbations with wave numbers $k > k_\mathrm{c}$, where

$$k_\mathrm{c} = \sqrt{\frac{(\rho_+ - \rho_-)\, g}{\gamma}} \tag{9.44}$$

denotes the critical wave number. For vanishing surface-tension effects, the growth rate increases unbounded with k. An analytical relation for the growth rate of the amplitude of the perturbation also taking into account viscous fluids may be found, e.g., in the textbook by Chandrasekhar [58]. Assuming $\nu = \nu_+ = \nu_-$ for the kinematic viscosity, defined as $\nu = \mu/\rho$, and considering wave number k, growth rate ς and surface-tension coefficient γ in non-dimensional form, marked by $\tilde{(\cdot)}$ in this section, as

$$\tilde{k} = \left(\frac{\nu^2 k^3}{g}\right)^{\frac{1}{3}}, \tag{9.45}$$

$$\tilde{\varsigma} = \left(\frac{\nu \varsigma^3}{g^2}\right)^{\frac{1}{3}}, \tag{9.46}$$

$$\tilde{\gamma} = \frac{\gamma}{(\rho_+ + \rho_-)\,(g\nu^4)^{\frac{1}{3}}}, \tag{9.47}$$

the non-dimensional growth rate $\tilde{\varsigma}$ is obtained via

$$\tilde{\varsigma} = \left[\left(y(\tilde{k})\right)^2 - 1\right] \tilde{k}^2, \tag{9.48}$$

where $y(\tilde{k})$ is the solution of the fourth-order polynomial

$$y^4 + 4\rho^* y^3 + (2 - 12\rho^*)y^2 - (4 - 12\rho^*)y + (1 - 4\rho^*) - \tilde{k}^{-3}\mathrm{At} + \tilde{k}^{-1}\tilde{\gamma} = 0 \tag{9.49}$$

with non-dimensional coefficient $\rho^* = (\rho_+\rho_-)/(\rho_- + \rho_+)^2$. Apart from equation (9.49), which may be numerically solved for $y(\tilde{k})$ to finally obtain ς from equations (9.48) and (9.46), an approximate analytical form for ς may also be found in literature (see, e.g., Piriz *et al.* [249]). However, that expression is only accurate to within 11% and thus inappropriate for the subsequent investigations. Concerning the stabilization of perturbations by surface tension, equation (9.44) also holds true in the considered viscid case; that is, the wave numbers stabilized by surface tension are independent of viscosity

The Rayleigh-Taylor instability has also become a widely-used test case to validate numerical methods developed for two-phase-flow problems; see, e.g., Nourgaliev *et al.* [233], Pochet *et al.* [250], Popinet and Zaleski [253] as well as Puckett *et al.* [256]. Furthermore, Tryggvason [315] presented a comprehensive numerical study of the Rayleigh-Taylor instability examining Atwood numbers ranging from $\mathrm{At} = 0.0$ to 1.0 as well as two-dimensional single and multi-mode simulations. Investigations of the XFEM using kink enrichments may be found, e.g., in Rasthofer *et al.* [259]. To demonstrate the ability of the proposed method to accurately simulate two-phase flows, numerical predictions for the growth rate are examined comparing them to the respective analytical values. Therefore, Rayleigh-Taylor instabilities at two Atwood

numbers are investigated including the effect of surface tension to some extent. A rectangular domain of size $\Omega = [-0.5L, 0.5L] \times [-0.5H, 0.5H]$, where $L = 1.0\,\mathrm{m}$ and $H = 4.0\,\mathrm{m}$, is considered and discretized using 64×256 elements. The initial interface is described by a cosine function as

$$x_2 = A_0 \cos(kx_1) - \frac{h}{2}, \tag{9.50}$$

where $k = (2\pi)/L$ is the wave number of this single-mode perturbation. As usual, h denotes the element length. Shifting the interface by $-h/2$ ensures that interface and element boundaries are separated in an appropriate manner such that the interface is protected against further potentially disturbing influences. In vertical direction, gravitation is applied as $\mathbf{g} = (0.0, -10.0)^{\mathrm{T}}\,\mathrm{m/s^2}$. Periodic boundary conditions at the vertical walls and no-slip boundary conditions at the top and bottom wall are assumed. Initially, a zero-velocity field is prescribed, and the time-step length is chosen to be $\Delta t = 0.005\,\mathrm{s}$ for all simulations. Density ratios $\rho_+/\rho_- = 1.5$ and $\rho_+/\rho_- = 1000$ are examined. The densities are set to $\rho_+ = 1.5\,\mathrm{kg/m^3}$ and $\rho_- = 1.0\,\mathrm{kg/m^3}$ for the lower density ratio and to $\rho_+ = 1.0\,\mathrm{kg/m^3}$ and $\rho_- = 0.001\,\mathrm{kg/m^3}$ for the higher one, resulting in $\mathrm{At} = 0.2$ and 0.998, respectively. The initial amplitude is chosen to be $A_0 = 0.005\,\mathrm{m}$ for the lower density ratio and $A_0 = 0.0001\,\mathrm{m}$ for the higher density ratio. In accordance with the analytical expression presented above, the kinematic viscosities ν_+ and ν_- are assumed to be equal for both cases, that is, $\nu_+ = \nu_- = \nu$.

First, the non-dimensional growth rate $\tilde{\varsigma}$ is estimated for various $\tilde{k}$ in the absence of surface tension (i.e., $\gamma = 0$). To change $\tilde{k}$, the kinematic viscosity ν is varied. In Figure 9.6, the evolution of the hydrodynamic instability is exemplarily shown for the lower density ratio and $\tilde{k} = 0.1$. Defining the Reynolds number as

$$\mathrm{Re} = \frac{\sqrt{Hg}L}{\nu}, \tag{9.51}$$

it amounts to 1000 for this configuration. For $t = 1.5\,\mathrm{s}$, the development of the Rayleigh-Taylor instability is about to leave the linear regime. After entering the non-linear regime, secondary Kelvin-Helmholtz instabilities are created at the flanks of the perturbation, and the fluids start to roll up as observed for $t = 2.0\,\mathrm{s}$. Eventually, the interface forms a "mushroom"-like shape. Figure 9.7 displays the evolution of the amplitude of the perturbation as a function of time as well as the analytical relation between $\tilde{k}$ and $\tilde{\varsigma}$ together with the computed growth rates in non-dimensional form for the lower density ratio $\rho_+/\rho_- = 1.5$. The growth rate ς is determined by a linear least-squares approximation of the transformed amplitude $\ln(A(t)/A_0)$ in the time interval of exponential growth. The respective results for the higher density ratio $\rho_+/\rho_- = 1000$ are shown in Figure 9.8. For both density ratios, an excellent agreement between analytical solution and numerical results is observed for a wide range of wave numbers.

Second, the accuracy of the proposed method for two-phase flows including surface tension is investigated. Therefore, the effect of surface tension on the evolution of the hydrodynamic instability is considered for a fixed non-dimensional wave number $\tilde{k} = 1.0$ and the lower density ratio. Rearranging equation (9.44), it follows that the critical surface-tension coefficient, stabilizing the present case, amounts to $\gamma_{\mathrm{c}} = 0.1267\,\mathrm{kg/s^2}$. The non-dimensional growth rates obtained for various surface-tension coefficients γ, with $\gamma < \gamma_{\mathrm{c}}$, are displayed in Figure 9.9 and compared

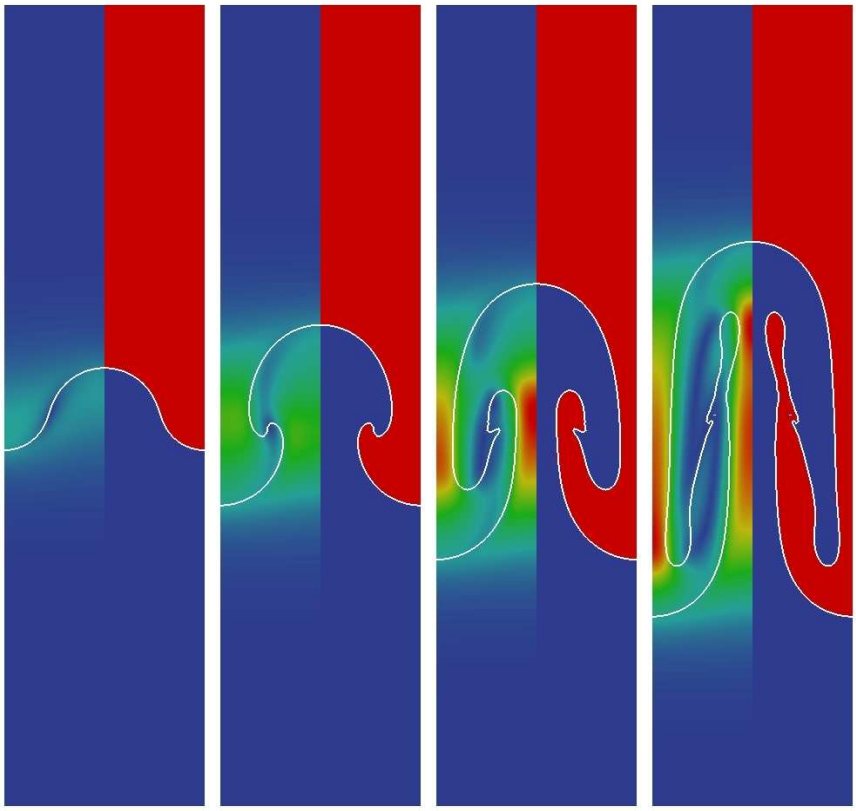

Figure 9.6: Velocity magnitude distribution (red color indicates high velocity and blue color low velocity) visualized on the left half of each subfigure as well as subdomains Ω_+ (colored in red) and Ω_- (colored in blue) visualized on the right half of each subfigure at (from left to right) times $t = 1.5, 2.0, 2.5$ and $3.0\,\mathrm{s}$ for the Rayleigh-Taylor instability at $\mathrm{At} = 0.2$ and $\mathrm{Re} = 1000$.

to the analytical solution. Again, the predicted results perfectly match the analytical values. As expected, surface tension damps the evolution of the hydrodynamic instability.

9.6.2 Two-Dimensional Collapsing Water Column

A two-dimensional column of water collapsing under the influence of gravity is considered as the second numerical example. This flow problem has not only frequently served as a numerical test case for two-phase flows (see, e.g., Elias and Coutinho [89], Greaves [128], Kees *et al.* [171] and Sauerland and Fries [272]), but was also studied experimentally many times (see, e.g., Martin and Moyce [208] for an early work). Analogously to Kees *et al.* [171], the dimensions of the domain, representing a tank in which the water column breaks down, are $\Omega = [0, 4L] \times [0, 2.4L]$, where $L = 0.146\,\mathrm{m}$. The dimensions of the water column, located at the left-hand side of the tank, are $\Omega_+ = [0, L] \times [0, 2L]$. Slip boundary conditions are prescribed at the side walls and the bottom of the tank. A zero-traction Neumann boundary condition is prescribed at the top of the tank. As a result, reverse flow may locally occur. Since the total momentum flux has to be prescribed at inflow parts $\Gamma^{\mathrm{in}}_{\mathrm{N},\mathbf{u}}$ of the Neumann boundary (i.e., where $\mathbf{u}^h \cdot \mathbf{n} < 0$), a term

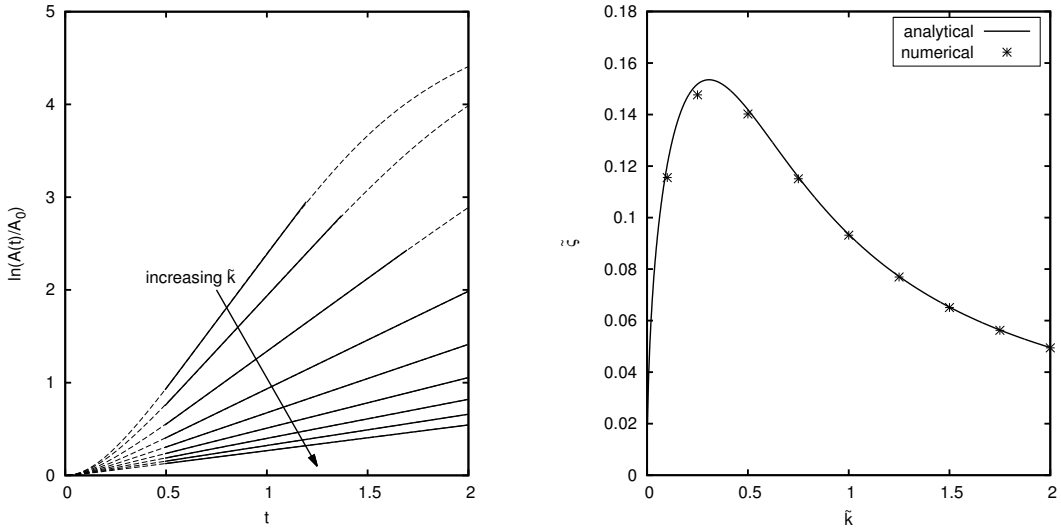

Figure 9.7: Transformed amplitudes $\ln(A(t)/A_0)$ over time t for non-dimensional wave numbers $\tilde{k} = 0.10, 0.25, 0.50, 0.75, 1.00, 1.25, 1.50, 1.75$ and 2.00 and comparison of non-dimensional growth rates $\tilde{\varsigma}$ obtained from simulations to the analytical solution for the Rayleigh-Taylor instability at $\mathrm{At} = 0.2$. The solid lines in the left diagram mark the interval of the linear least-squares approximation.

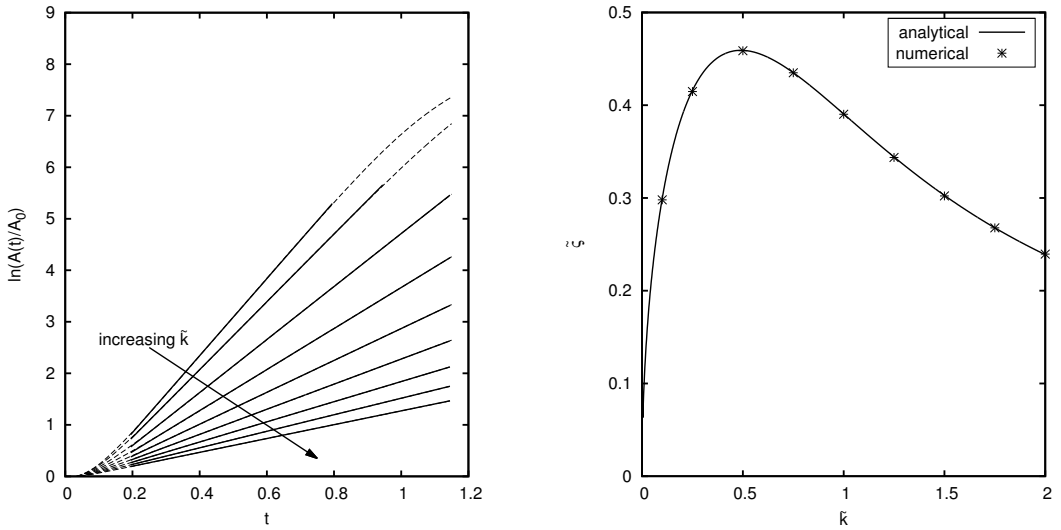

Figure 9.8: Transformed amplitudes $\ln(A(t)/A_0)$ over time t for non-dimensional wave numbers $\tilde{k} = 0.10, 0.25, 0.50, 0.75, 1.00, 1.25, 1.50, 1.75$ and 2.00 and comparison of non-dimensional growth rates $\tilde{\varsigma}$ obtained from simulations to the analytical solution for the Rayleigh-Taylor instability at $\mathrm{At} = 0.998$. The solid lines in the left diagram mark the interval of the linear least-squares approximation.

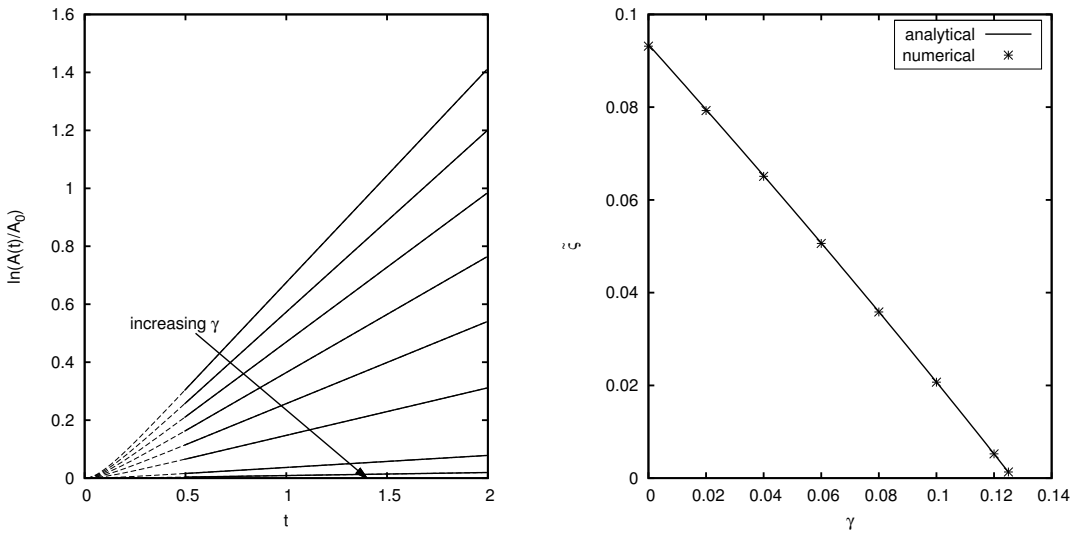

Figure 9.9: Transformed amplitudes $\ln(A(t)/A_0)$ over time t for surface-tension coefficients $\gamma = 0.000$, 0.020, 0.040, 0.060, 0.080, 0.100, 0.120 and $0.125\,\mathrm{kg/s^2}$ and comparison of non-dimensional growth rates $\tilde{\zeta}$ obtained from simulations to the analytical solution for the Rayleigh-Taylor instability at $\mathrm{At} = 0.2$. The solid lines in the left diagram mark the interval of the linear least-squares approximation.

as $-(\mathbf{v}^h, \rho\mathbf{u}^h(\mathbf{u}^h \cdot \mathbf{n}))_{\Gamma^{\mathrm{in}}_{\mathrm{N},\mathbf{u}}}$ has to be added to the left-hand side of formulation (9.26); see Section 3.2 for further details. To replicate a combination of water and air, as usually considered in the experimental setups, the liquid density is set to $\rho_+ = 1000.0\,\mathrm{kg/m^3}$ and the gas density to $\rho_- = 1.0\,\mathrm{kg/m^3}$. The corresponding dynamic viscosities are chosen to be $\mu_+ = 0.001\,\mathrm{kg/(ms)}$ and $\mu_- = 0.00001\,\mathrm{kg/(ms)}$, respectively. Surface tension is not included in this example. The gravitation vector, acting in vertical direction, is $\mathbf{g} = (0.0,\ -9.81)^{\mathrm{T}}\,\mathrm{m/s^2}$. Three different discretizations, defined such that the elements are not aligned with the interface at the beginning of the simulation, are considered for this example. For the coarser discretization, 62×38 elements are used. The medium and finer discretizations consist of 122×74 and 246×147 elements, respectively. Hence with each refinement step, the number of elements in each spatial direction is approximately doubled. The time-step length, which is set to $\Delta t = 0.0006\,\mathrm{s}$ for the coarser discretization, is successively halved.

Figure 9.10 illustrates the break-down process. Results obtained with the medium discretization are shown. The various interface positions may be compared to the respective results presented by Kees *et al.* [171] (see Figure 14 therein), which agree exactly with the present ones. The corresponding pressure and velocity fields at time $t = 0.2\,\mathrm{s}$ are shown in Figure 9.11. While the pressure field mainly exhibits a hydrostatic distribution, the velocity field experiences large gradients in the interface region. Moreover, the tip of the water front moves at the maximal speed, and a vortex emerges on top of the water column. The propagation of the water front, i.e., the position x_1^{w} of its tip, measured are the bottom wall, as well as the height x_2^{w} of the column, measured at the left wall, as a function of time are depicted in non-dimensional form in Figure 9.12. Numerical results extracted from other studies are included in addition. Data taken from Kees

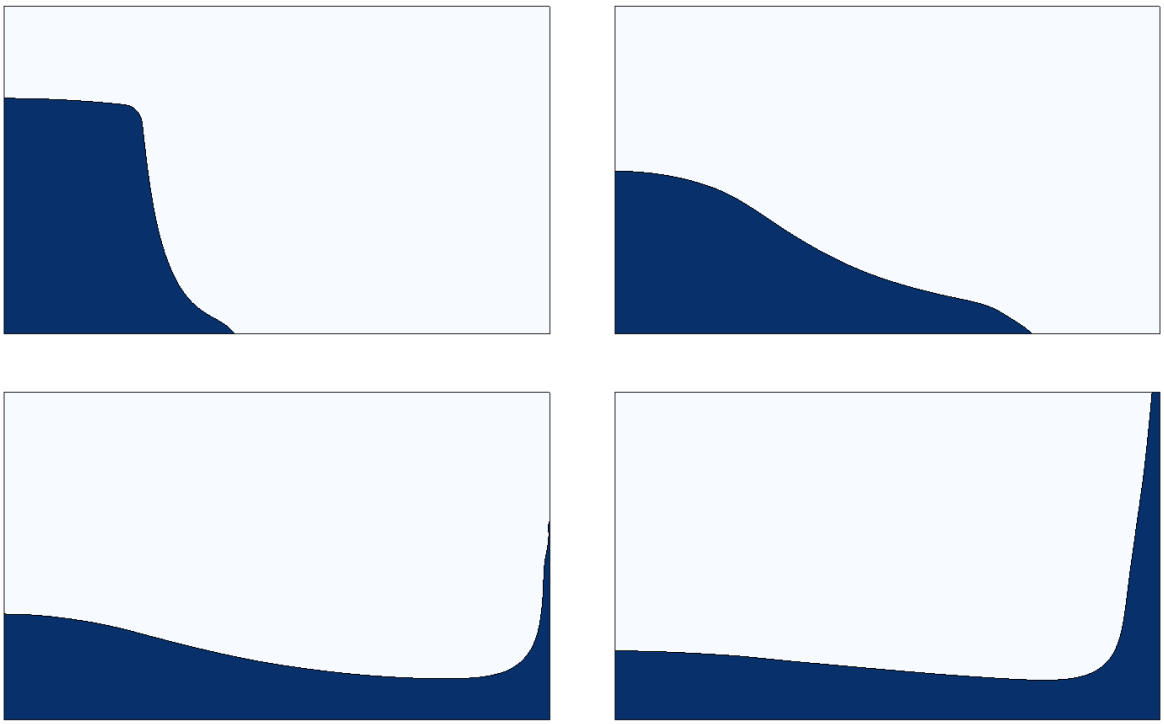

Figure 9.10: Collapsing water column at (from left to right and from top to bottom) times $t = 0.1, 0.2, 0.3$ and $0.4\,\mathrm{s}$ using 122×74 elements.

et al. [171] are marked by "KAFB11" and from Greaves [128] by "G06". In Kees *et al.* [171], several discretizations were used. Here, two of the respective data sets are taken into account. To distinguish between them, their notation is extended by the respective resolution. Experimental

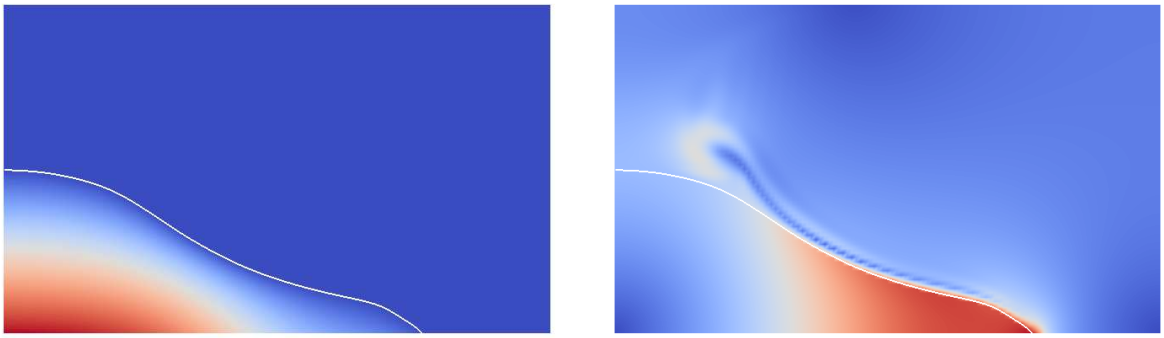

Figure 9.11: Pressure (left) and velocity magnitude (right) distribution for the collapsing water column at time $t = 0.2\,\mathrm{s}$ using 122×74 elements (red color indicates high velocity/pressure and blue color low velocity/pressure).

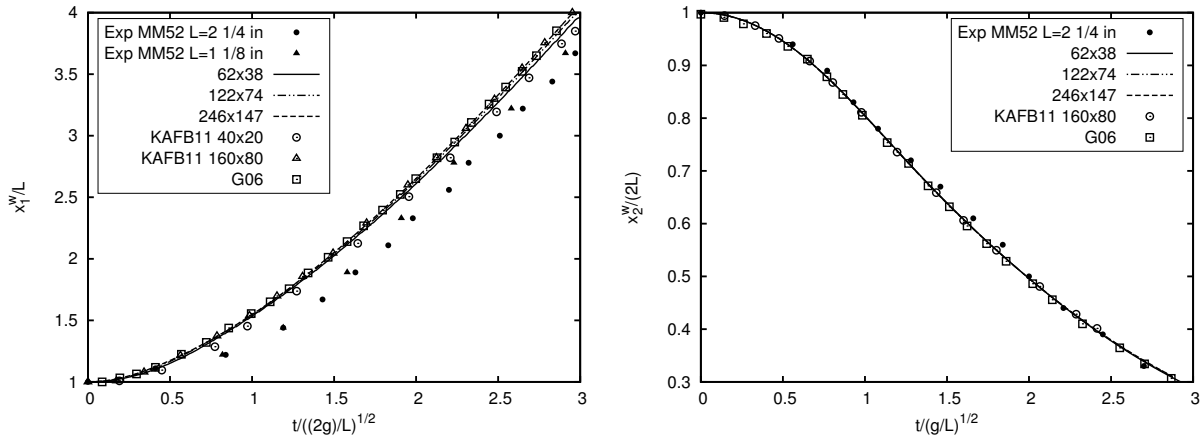

Figure 9.12: Non-dimensional width x_1^{w}/L and height $x_2^{\mathrm{w}}/(2L)$ of the collapsing water column as a function of time in non-dimensional form using 62×38, 122×74 and 246×147 elements.

data presented in Martin and Moyce [208] and denoted by "Exp MM52" are likewise considered for comparison. Since two experimental data sets are available in Martin and Moyce [208], the respective column width is additionally indicated. Similar to the included numerical reference data, the results obtained with the proposed method capture the experimentally predicted evolution of the height of the column on all discretizations. In contrast, the development of its width is overestimated by all simulations. However, also the experimental data somewhat deviate from each other. The observed discrepancy between experiment and simulation may be attributed to the slip boundary condition prescribed at the bottom of the numerical test setup. Analogously, small differences between the results obtained on the different discretizations considered in this work are merely observable for the width of the water column. While the water front propagates slightly slower for the coarser discretization, the curves obtained with the medium and finer discretization are hardly distinguishable, and convergence can be stated.

9.6.3 Three-Dimensional Rising Bubbles

Three-dimensional gas bubbles rising in a container filled with liquid are studied next. Due to buoyancy, the bubble starts to move upwards, and a flow field evolves. Under the influence of this flow field, the bubble deforms until the stresses at the interface are in equilibrium. Following Clift *et al.* [67], rising bubbles may be characterized by three non-dimensional numbers, Eötvös number Eo, Morton number Mo and Reynolds number Re, which are defined as

$$\mathrm{Eo} = \frac{g(\rho_+ - \rho_-)D^2}{\gamma}, \tag{9.52}$$

$$\mathrm{Mo} = \frac{g(\mu_+)^4(\rho_+ - \rho_-)}{(\rho_+)^2\gamma^3}, \tag{9.53}$$

$$\mathrm{Re} = \frac{\rho_+ U D}{\mu_+}, \tag{9.54}$$

where D is the diameter of the bubble and $g = \|\mathbf{g}\|$. For rising bubbles, the characteristic velocity U of Re may be identified as the terminal rise velocity. Depending on these non-dimensional numbers, three regimes are usually distinguished for the bubble shapes; see, e.g., Clift *et al.* [67]. Almost spherical bubbles define the first regime. Ellipsoidal bubbles, which are summarized in the second regime, are somewhat oblate, while keeping a convex interface. Bubbles belonging to the third regime are characterized by a cap-like shape. If the rear of the cap-like bubble exhibits an indentation, the shape may also be denoted as dimpled. Cap-like bubbles that tail thin filaments at the border of a flat base are also named skirted. The correlation between the bubble shape and the non-dimensional numbers Eo, Mo and Re is illustrated in the diagram displayed in Figure 9.13 (see Clift *et al.* [67]), which is commonly referred to as Grace' diagram. This diagram, which is based on experimental data, may be used to predict terminal rise velocities and shape regimes.

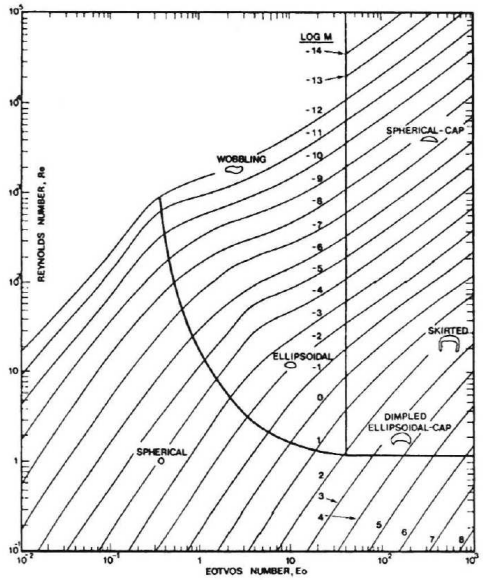

Figure 9.13: Grace' diagram (extracted from Clift *et al.* [67]).

Three-dimensional rising bubbles are frequently examined in literature as a numerical test case for two-phase flows; see, e.g., Ausas *et al.* [8], Marchandise *et al.* [207], Nagrath *et al.* [228] and Sussman *et al.* [303]. Here, the setup presented by Ausas *et al.* [8] is considered. Accordingly, the dimensions of the container are $\Omega = [0, L] \times [0, H] \times [0, L]$, where $L = 2.25\,\mathrm{m}$ and $H = 4.0\,\mathrm{m}$. Initially, the bubble is at rest and has a spherical shape with diameter $D = 1.0\,\mathrm{m}$. The bubble center is positioned at $(0.5L, 0.25H, 0.5L)^{\mathrm{T}}$. Gravitation acts in vertical x_2-direction as $\mathbf{g} = (0.0, -10.0, 0.0)^{\mathrm{T}}\,\mathrm{m/s^2}$. The density of the liquid is assumed to be $\rho_+ = 1.0\,\mathrm{kg/m^3}$ and of the gas to be $\rho_- = 0.001\,\mathrm{kg/m^3}$, resulting in a density ratio of $\rho_+/\rho_- = 1000$. The dynamic viscosity μ_+ of the liquid is chosen such that the various regimes, defined in terms of Eötvös and Morton number, are reached. The dynamic viscosity μ_- of the gas is determined by keeping the

viscosity ratio $\mu_+/\mu_- = 1000$ fixed. Table 9.1 summarizes the physical parameters and resulting non-dimensional numbers of all investigated bubbles. The parameters of the spherical and skirted bubble are identical to the ones given by Ausas *et al.* [8], except for the lower viscosity μ_- in case of the skirted bubble. In contrast to Ausas *et al.* [8], where μ_- was chosen to be $0.001\,\mathrm{kg/(ms)}$, it is set to $\mu_- = 0.0001\,\mathrm{kg/(ms)}$ here to retain a constant viscosity ratio for all examples. Following Clift *et al.* [67], μ_- does only marginally influence the reached rise velocity as well as the shape. Hence, notable differences compared to Ausas *et al.* [8] are not expected. The setup of the remaining two regimes is defined such that the non-dimensional numbers given by Marchandise *et al.* [207] are matched. The time-step length is set to $\Delta t = 0.003\,\mathrm{s}$, except for the skirted bubble. Due to the higher Reynolds number, Δt is reduced to $0.001\,\mathrm{s}$ for this case. The domain is discretized using $45 \times 80 \times 45$ equally spaced elements. Slip boundary conditions are prescribed at the side walls and the bottom of the container. At the top, a zero-traction Neumann boundary condition is assumed. As explained for the preceding example, a convective inflow term on the Neumann boundary has to be added to the formulation to account for potentially recirculating flow at the top of the container.

Table 9.1: Physical parameters for three-dimensional rising bubbles depending on the regime: liquid density ρ_+, gas density ρ_-, liquid dynamic viscosity μ_+, gas dynamic viscosity μ_-, surface-tension coefficient γ, Eötvös number Eo and Morton number Mo.

regime	$\rho_+\ [\frac{\mathrm{kg}}{\mathrm{m}^3}]$	$\rho_-\ [\frac{\mathrm{kg}}{\mathrm{m}^3}]$	$\mu_+\ [\frac{\mathrm{kg}}{\mathrm{ms}}]$	$\mu_-\ [\frac{\mathrm{kg}}{\mathrm{ms}}]$	$\gamma\ [\frac{\mathrm{kg}}{\mathrm{s}^2}]$	Eo	Mo
spherical	1.0	0.001	0.3	0.0003	10	1.0	$8.1 \cdot 10^{-5}$
skirted	1.0	0.001	0.1	0.0001	0.1	100	1.0
ellipsoidal	1.0	0.001	0.3	0.0003	1.0	10	$8.1 \cdot 10^{-2}$
dimpled	1.0	0.001	0.56	0.00056	0.1	100	982

In Figures 9.14 and 9.15, the developed shapes of the four bubbles are shown together with velocity streamlines in the x_1x_2-centerplane. While the shape at time $t = 2.2\,\mathrm{s}$ is displayed for the slowly-rising dimpled bubble, the shape at time $t = 1.1\,\mathrm{s}$ is depicted for the remaining ones. All aforementioned characteristics of the different shape regimes are clearly identifiable from Figures 9.14 and 9.15. Figure 9.16 illustrates the vertical position x_2^{c} of the center of mass for the different bubbles as a function of time. In addition, results extracted from Ausas *et al.* [8] and marked by "ABI12" are included. Compared to those data, the present method predicts slightly higher values. As displayed in Figure 9.16, a terminal rise velocity, i.e., a constant gradient, is reached after an initial transient. Starting from $t = 0.4\,\mathrm{s}$ to $1.2\,\mathrm{s}$, the rise velocity is determined via a linear least-squares approximation comprising about 60% of the overall simulation time. Based on this velocity, the Reynolds number can be calculated. Table 9.2 juxtaposes the Reynolds numbers obtained with the proposed method and various reference data taken from literature. Apart from the aforementioned data taken from Ausas *et al.* [8], Reynolds numbers reported by Marchandise *et al.* [207] are also included to some extent. These values are denoted by "MGCR07". For all shape regimes, the Reynolds numbers obtained with the present method are within the range of values reported in other numerical studies and close to the expected values extracted from Grace' diagram (see Figure 9.13). In summary, good agreement with the expected physical behavior of rising bubbles is obtained.

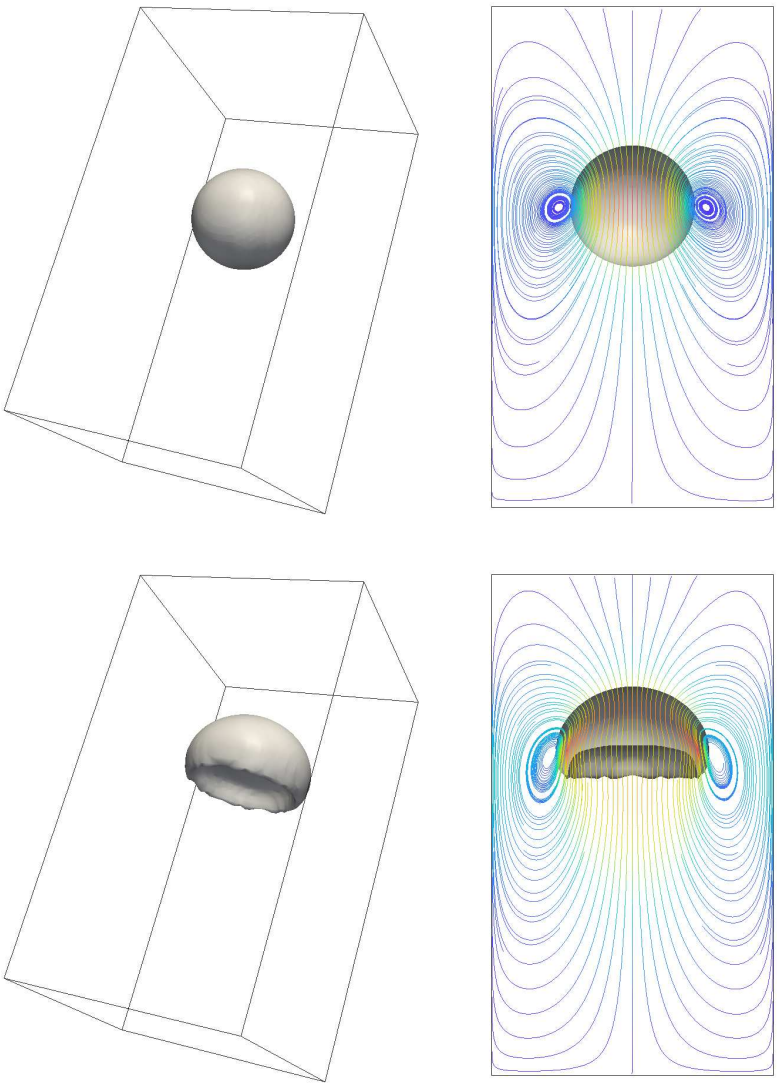

Figure 9.14: Developed bubble shapes for the spherical regime (top) and the skirted regime (bottom) at time $t = 1.1$ s including velocity streamlines in the x_1x_2-centerplane colored by the velocity magnitude (red color indicates high velocity and blue color low velocity).

9.6.4 Three-Dimensional Bubble Coalescence

Finally, the coalescence of two three-dimensional rising bubbles is considered. Numerical investigations of merging bubbles may be found, e.g., in Marchandise *et al.* [207], Nagrath *et al.* [228] and Sussman *et al.* [303]. Due to the interface connection, this example exhibits a particular challenge on the robustness of the presented method. A setup analogue to the one presented by Nagrath *et al.* [228] is used, except for a slight modification of the initial positions of the bubbles, which is necessary since the values given in that study result in touching bubbles at the beginning. Two bubbles of the same density and viscosity are considered in a cubic domain of size

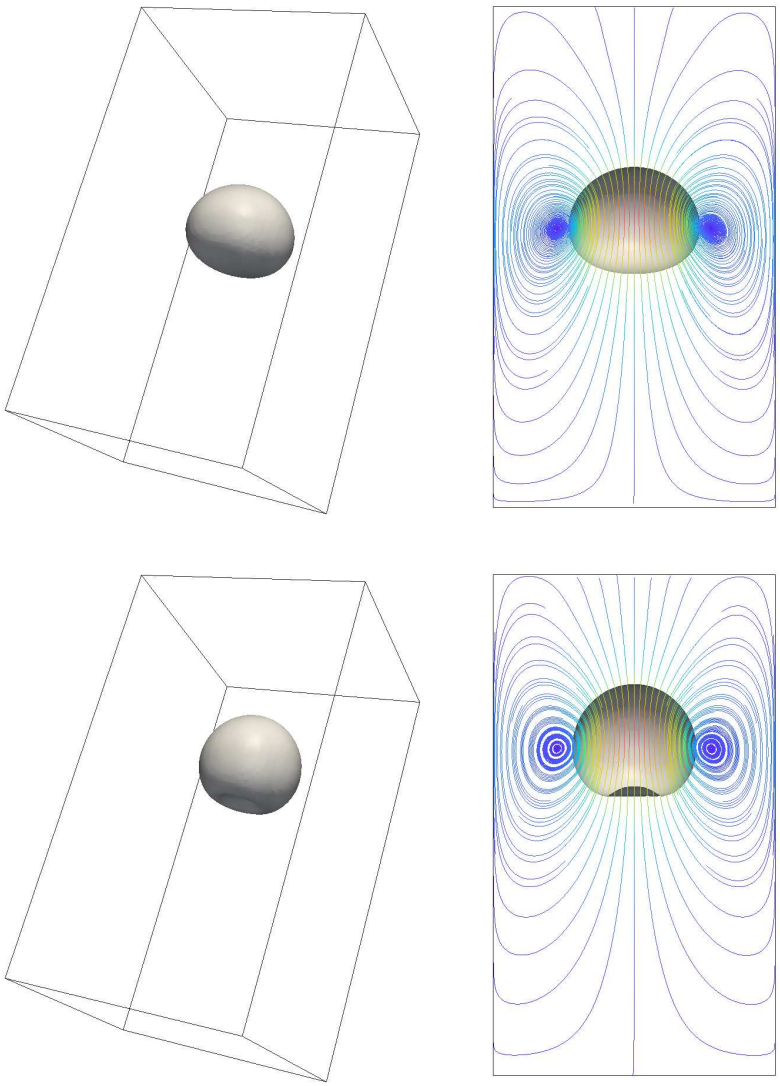

Figure 9.15: Developed bubble shapes for the ellipsoidal regime (top) at time $t = 1.1\,\mathrm{s}$ and for the dimpled regime (bottom) at time $t = 2.2\,\mathrm{s}$ including velocity streamlines in the x_1x_2-centerplane colored by the velocity magnitude (red color indicates high velocity and blue color low velocity).

$\Omega = [0, L] \times [0, L] \times [0, L]$, where $L = 1.0\,\mathrm{m}$. A larger bubble is centered at $(0.5L, 0.58L, 0.5L)^{\mathrm{T}}$ on top of a smaller one, which is located at $(0.5L, 0.3L, 0.5L)^{\mathrm{T}}$; see also Figure 9.17. The radius of the upper bubble is set to $R_1 = 0.15L$ and the one of the lower bubble to $R_2 = 0.10L$. The density of the bubbles is $\rho_- = 1.0\,\mathrm{kg/m^3}$. The density of the surrounding fluid is assumed to be $\rho_+ = 10.0\,\mathrm{kg/m^3}$. The dynamic viscosities of the bubbles and the surrounding fluid are chosen to be $\mu_- = 0.00025\,\mathrm{kg/(ms)}$ and $\mu_+ = 0.0005\,\mathrm{kg/(ms)}$, respectively. Surface-tension effects are not considered for this example. A gravitational force $\mathrm{g} = (0.0, -9.81, 0.0)^{\mathrm{T}}\,\mathrm{m/s^2}$ is applied in vertical x_2-direction. Initially, the two bubbles as well as the surrounding fluid are at rest. Pe-

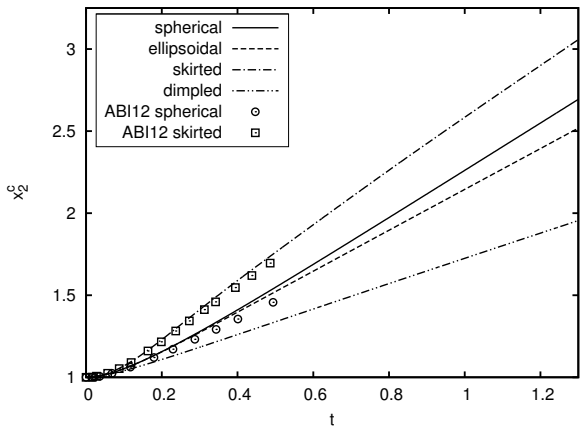

Figure 9.16: Vertical position x_2^c of the center of mass as a function of time t for three-dimensional rising bubbles at various shape regimes.

Table 9.2: Reynolds numbers Re of three-dimensional rising bubbles at various shape regimes from present simulations, other numerical studies as well as values extracted from Grace' diagram.

regime	present results	ABI12 [8]	MGCR07 [207]	Grace' diagram [67]
spherical	4.76	3.93	-	5
skirted	16.37	16.22	22.25	20
ellipsoidal	4.15	-	4.25	4
dimpled	1.38	-	1.9	1.5

riodic boundary conditions are prescribed in all three spatial directions. Therefore, an additional volume force term representing the pressure gradient, which would adjust itself in the presence

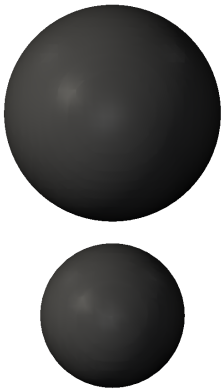

Figure 9.17: Initial position of bubbles for coalescence.

of a bottom wall, has to be enforced. This volume force term prevents the vertical acceleration of the whole system and is defined as $\mathbf{f} = -\rho_{\mathrm{m}}\mathbf{g}$, where

$$\rho_{\mathrm{m}} = \alpha\rho_{-} + (1-\alpha)\rho_{+} \tag{9.55}$$

is the density of the mixture. For bubbly flow, the void fraction α is given as

$$\alpha = \sum_{i=1}^{n_{\mathrm{B}}} \frac{\frac{4\pi R_i^3}{3}}{V(\Omega)} \tag{9.56}$$

where n_{B} is the number of bubbles, which is equal to 2 here, and R_i their radius. The volume of the domain is denoted by $V(\Omega)$ and amounts to $V(\Omega) = L^3$ for the present configuration. The domain is discretized using $80 \times 80 \times 80$ elements, and the time-step length is set to $\Delta t = 0.00025$ s.

Figures 9.18 to 9.21 display the shapes of the bubbles during the merging process. The initial stage, where the upper bubble captures the lower one, is shown in Figure 9.18 for time $t = 0.05$ s and in Figure 9.19 for a somewhat later time $t = 0.1$ s. In addition to the shapes of the bubbles,

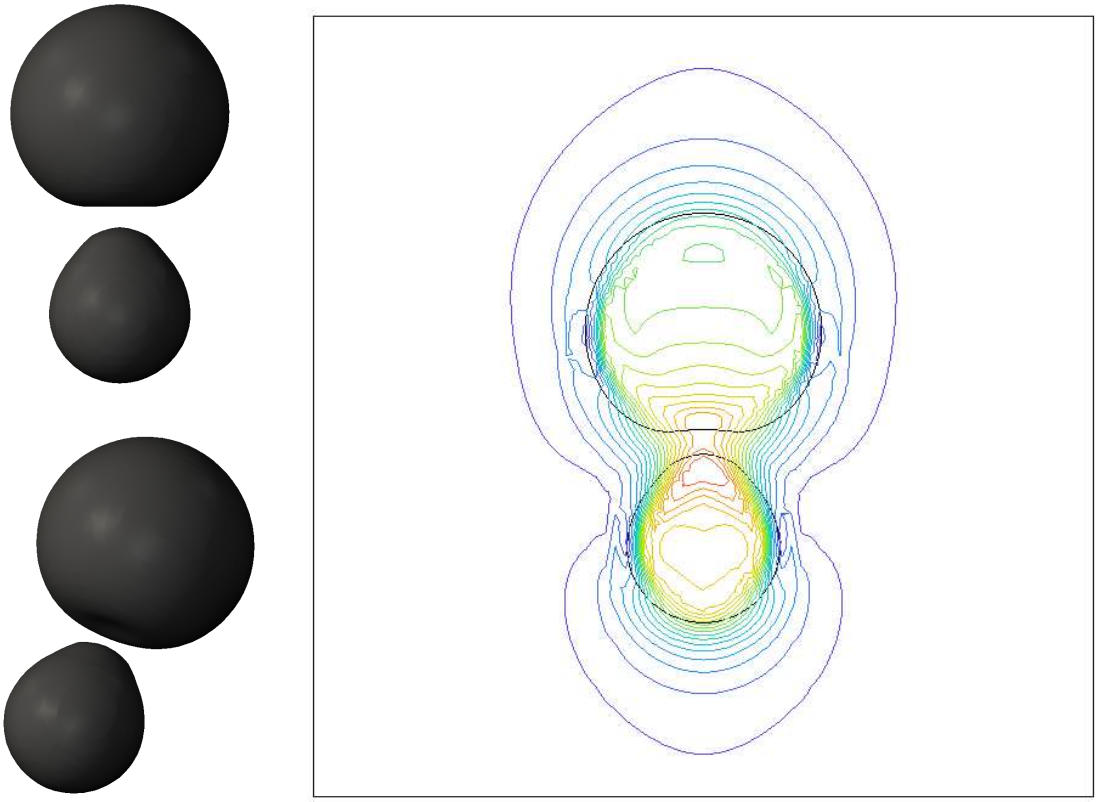

Figure 9.18: Position of bubbles (left) and velocity magnitude iso-contours in the x_1x_2-centerplane (right) at time $t = 0.05$ s of the coalescence (red color indicates high velocity and blue color low velocity).

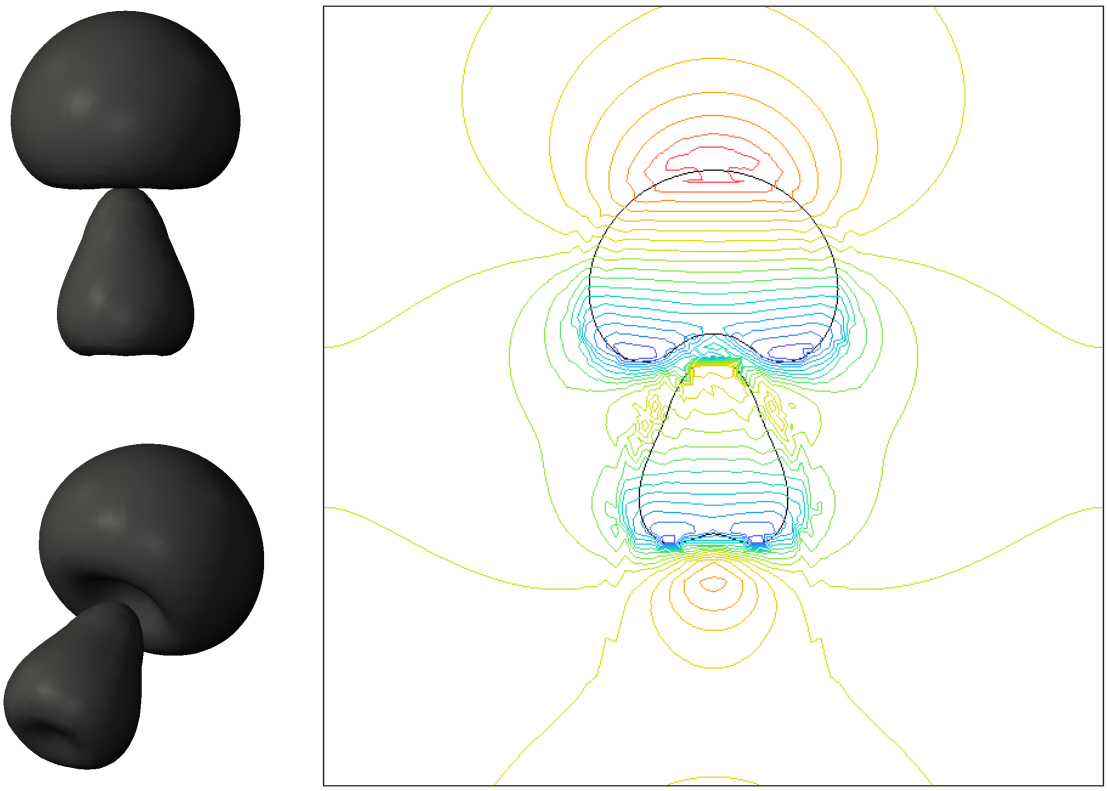

Figure 9.19: Position of bubbles (left) and pressure iso-contours in the x_1x_2-centerplane (right) at time $t = 0.1$ s of the coalescence (red color indicates high pressure and blue color low pressure).

velocity magnitude iso-contours in the x_1x_2-centerplane are presented in Figure 9.18, and pressure iso-contours in the same plane are depicted in Figure 9.19. Due to the emerging upward-pointing jet in the wake of the bubbles, their bases start to move. While the upper bubble behaves similar to an isolated bubble at the beginning of the process, the lower bubble, which is located in the wake of the upper one, also exhibits a moving front; see Figure 9.18. As shown in Figure 9.19, the jets on the bases of the bubbles are caused by the lower pressure values immediately behind them. In particular, the strong jet of the larger bubble also affects the smaller bubble by attracting it. Together with the wake at its base, the lower bubble is thus substantially deformed. Due to the increasing narrowing of the lower bubble, it finally enters the cap formed by the upper bubble. At time $t = 0.15$ s, the front of the lower bubble almost catches the upper bubble, as shown in Figure 9.20, and the coalescence of the bubbles is initiated. The merged bubbles at time $t = 0.2$ s are then shown in Figure 9.21. For illustration of the coalescence, Figures 9.20 and 9.21 also provide the interface in the x_1x_2-centerplane. The complete process notably conforms with the respective simulation presented by Nagrath *et al.* [228] (see Figures 12 to 20 therein).

Figure 9.20: Position of about to merge bubbles (left and middle) and interface in the x_1x_2-centerplane (right) at time $t = 0.15$ s of the coalescence.

Figure 9.21: Position of merged bubbles (left and middle) and interface in the x_1x_2-centerplane (right) at time $t = 0.2$ s of the coalescence.

10 Turbulent Two-Phase Flows

Starting from the fundamental concept of the VMM established in Chapter 3, the AVM^4 is developed as a novel and promising approach to LES of turbulent incompressible single-phase flow in Chapter 4. Resuming the mathematical description for two-phase flow introduced in Chapter 7, the interface separating the two fluids is assumed infinitely thin, and surface-tension effects as well as different physical parameters for both fluids give rise to strong and weak discontinuities in the solution fields at the interface. To accurately represent an arbitrary evolution of the interface, the level-set method, which allows for capturing the interface on a fixed grid, is addressed in Chapter 8. The face-oriented stabilized Nitsche-type extended VMM, devised in Chapter 9, enables the appropriate incorporation of the involved discontinuities at the interface into the finite element approximation and constitutes a novel and robust approach applicable to transient convection-dominated problems. All listed ingredients are finally combined into an eXtended Algebraic Variational Multiscale-Multigrid-Multifractal Method, referred to as the XAVM^4, for LES of turbulent two-phase flow in this chapter. Before the XAVM^4 is discussed, an overview of previous attempts towards LES of turbulent two-phase flow is provided, followed by the investigation of an idealized bubble-vortex interaction. Finally, the XAVM^4 is applied to turbulent channel flow carrying a bubble of the size of the channel half-width, demonstrating its high potential.

10.1 Towards New Challenges for Modeling Subgrid-Scale Features

In the case of two contiguous bulk fluids separated by a deformable interface, the flow in both subdomains may be turbulent, and turbulent structures may interact with the interface. The ratio of inertia to surface-tension forces is given by the Weber number, defined as

$$\mathrm{We} = \frac{\rho U^2 \ell}{\gamma}, \tag{10.1}$$

where U and ℓ are a characteristic velocity and length.

In LES of these situations, both fluid domains are covered by the computational grid, and the interface is resolved as far as possible, but not necessarily perfectly. Hence, the same modeling situation as described for turbulent single-phase flow in Section 2.3 is encountered for the flow in each subdomain. In addition to the small-scale turbulent structures, which are unresolved in LES by definition, further subgrid-scale structures related to the interface may occur in two-phase

flow. For interfaces of highly complex or wrinkled shape, fine structures such as thin fingers and small bubbles or droplets may remain unresolved. Subgrid-scale modeling issues emanating from underresolved interfaces, which bring in additional physics, demand specifically devised closures. Respective developments constitute a field of active research, as the references provided below illustrate. Such developments are beyond the scope of the present thesis, since the interface is assumed fully resolved.

Labourasse *et al.* [177] discussed filtering of the governing equations for two-phase flows and conduced an *a priori* analysis to evaluate the order of magnitude of the various subgrid-scale contributions arising from their procedure. For investigation, two-dimensional problems were taken into account by Labourasse *et al.* [177]. Similar *a priori* investigations were carried out, e.g., by Toutant *et al.* [311], who evaluated DNS data of a deformable bubble in decaying turbulence, Larocque *et al.* [178], who considered phase inversion in a closed cubic box as well as Chesnel *et al.* [60], who investigated DNS data of jet atomization. Modeling issues stemming from underresolved interfaces, for instance, related to surface-tension effects, were addressed, e.g., by Herrmann [144] as well as Liovic and Lakehal [196]. Another concept to deal with underresolved interfaces was proposed, e.g., by Toutant *et al.* [312, 313].

Up to now, only a few studies dealing with LES of two-phase flows may be found in literature. Liovic and Lakehal [195], for instance, performed LES of a turbulent bubbling flow driven by the downward injection of air into a pool filled with water. Aniszewski *et al.* [5] suggested a subgrid-scale model accounting for surface-tension effects, which was then applied to LES of phase inversion in a closed cubic box. DNS of this flow problem was presented, e.g., by Vincent *et al.* [322]. Recently, Xiao *et al.* [334] conducted LES of a liquid jet in a coaxial air flow. All the aforementioned LESs included a form of the Smagorinsky model (see also Section 2.3.2). Eventually, some further DNS studies, which may serve as a reference for future LES of turbulent two-phase flow with two bulk fluids, are provided. Fulgosi *et al.* [103] investigated countercurrent air-water flow in a rectangular domain. Also in the context of stratified fluids, Lee *et al.* [182] examined turbulent open-channel flow with an air-water interface. Kim *et al.* [173] recently introduced turbulent two-phase Couette flow as a canonical problem. Aiming at evaluating the skin-friction drag reduction by air injection, Kim and Moin [172] investigated a two-phase backward-facing step configuration, which represents a simplified geometry for examining Air Layer Drag Reduction (ALDR) and may also be considered as a canonical flow. Based on the backward-facing step geometry used, e.g., by Le *et al.* [179] for turbulent single-phase flow, a modified configuration was set up, exhibiting a slot in the step, where air was injected. Both the turbulent flow with and without air injection were considered and compared to each other.

10.2 Bubble-Vortex Interaction

With respect to the intended investigation of turbulent two-phase bubbly channel flow via LES in this chapter, the interaction between turbulent structures and interfaces separating two fluids is of particular relevance. In bubbly flows, a significant portion of turbulence is generated by the wake of the bubbles and, hence, the associated scales are of a size only slightly smaller than the bubbles themselves. To illustrate the involved dynamics, a simplified two-dimensional setup, as

introduced by Labourasse *et al.* [177], is examined. Labourasse *et al.* [177] idealized the turbulent structures by two vortices, which interact with an initially circular bubble. This example is thus closely related to the flame-vortex-interaction problem originally considered by Poinsot *et al.* [251]. That configuration, which evolved into a widely-used example for validating proposed approaches for (turbulent) premixed combustion (see, e.g., Lessani and Papalexandris [187] as well as Henke [140]), consists of an isolated pair of vortices interacting with a flame front in a laminar flow.

Following Labourasse *et al.* [177], a bubble at rest is approached by two counter-rotating vortices, which are advected by their self-induced velocity fields. The velocity induced by each of the vortices is given by

$$\mathbf{u}_\mathrm{v} = C_\mathrm{v} \mathrm{e}^{\frac{1}{2}\left(1-\frac{\left(x_1-x_{\mathrm{v},1}\right)^2+\left(x_2-x_{\mathrm{v},2}\right)^2}{R_\mathrm{v}^2}\right)} \begin{pmatrix} x_{\mathrm{v},2}-x_2 \\ x_1-x_{\mathrm{v},1} \end{pmatrix}, \tag{10.2}$$

where $\mathbf{x}_\mathrm{v}$ is the position of the center of the vortex, $R_\mathrm{v} = 8.0 \cdot 10^{-4}\,\mathrm{m}$ its associated radius and C_v a coefficient, which characterizes its strength and is positive for the right vortex and negative for the left one, i.e., $C_\mathrm{v}^\mathrm{right} = -C_\mathrm{v}^\mathrm{left} = 962.5\,\mathrm{s}^{-1}$. The distance between the centers of the vortices is set to $d_\mathrm{v} = 1.855 \cdot 10^{-3}\,\mathrm{m}$ such that the velocity induced at the center of the other vortex amounts to $U_\mathrm{v} = 0.2\,\mathrm{m/s}$. The size of the considered domain is $\Omega = [-0.5L, 0.5L] \times [-0.5L, 0.5L]$, where $L = 8.1 \cdot 10^{-3}\,\mathrm{m}$. The domain is uniformly discretized using 405×405 elements. This relatively high resolution is required here to shield the interface from spurious velocities, which may disturb the vorticity field. The bubble with radius $R_\mathrm{b} = 1.5 \cdot 10^{-3}\,\mathrm{m}$ is centered at $(0, -0.2L)^\mathrm{T}$ and the vortices at $\mathbf{x}_\mathrm{v}^\mathrm{left} = (-0.5d_\mathrm{v}, 0.2L)^\mathrm{T}$ and $\mathbf{x}_\mathrm{v}^\mathrm{right} = (0.5d_\mathrm{v}, 0.2L)^\mathrm{T}$, respectively. Analogously to Labourasse *et al.* [177], the two fluids considered here are water and air, such that $\rho_+ = 1000\,\mathrm{kg/m^3}$ and $\mu_+ = 1.0 \cdot 10^{-3}\,\mathrm{kg/(ms)}$ for the liquid, $\rho_- = 1.3\,\mathrm{kg/m^3}$ and $\mu_- = 2.0 \cdot 10^{-5}\,\mathrm{kg/(ms)}$ for the gas as well as $\gamma = 0.07\,\mathrm{kg/s^2}$ for the surface-tension coefficient. No-slip conditions are assumed at all boundaries of the domain. The time-step length is chosen to be $\Delta t = 1.0 \cdot 10^{-5}\,\mathrm{s}$, and the general statements provided at the beginning of Section 9.6 also hold true for this example. Figure 10.1 provides a sketch of the setup together with a visualization of the velocity vectors and the pressure distribution at the beginning of the simulation.

Figure 10.2 illustrates the generation of vorticity inside the bubble. Therefore, the vorticity distribution, i.e., its component ω_3, which is the only non-zero entry of the vorticity vector for two-dimensional problems, is shown for two instants of time. As soon as the interface starts to interact with the vortices, vorticity is generated inside the bubble. For the present configuration, two pairs of counter-rotating vortices emerge. An amplification of the strength and an increase of the size of the vortices inside the bubble is observed with time. As displayed in Figure 10.2, the two vortices are also able to strongly deform the bubble. The present result for the bubble-vortex-interaction problem conforms well with the respective simulation of Labourasse *et al.* [177] (see Figure 4 for case N1 therein). Labourasse *et al.* [177] additionally investigated another configuration (case N0 in that article), where the impact of stronger but smaller vortices on the bubble was examined. In that case, the vortices only slightly distorted the shape of the interface.

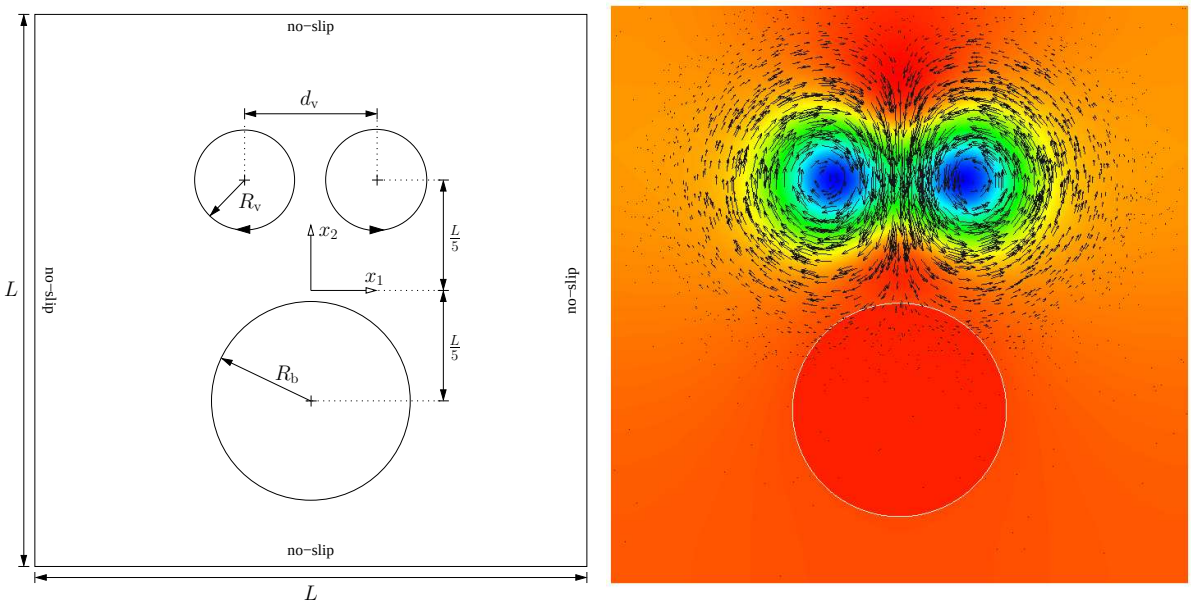

Figure 10.1: Setup of bubble-vortex interaction (left) and velocity vectors on the pressure distribution (red color indicates high pressure and blue color low pressure) visualized after two time steps (right).

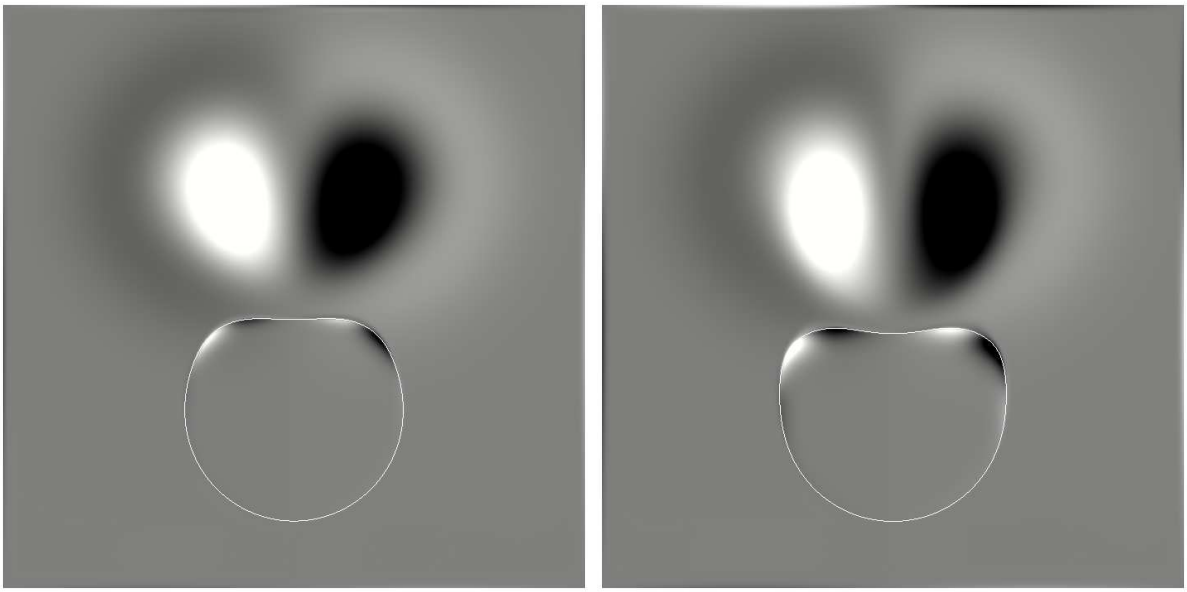

Figure 10.2: Bubble-vortex interaction at times $t = 1.0 \cdot 10^{-3}$ s (left) and $1.8 \cdot 10^{-3}$ s (right) visualized via its vorticity distribution (white color indicates high negative vorticity and black color high positive vorticity).

10.3 Extending the AVM^4

The present section brings together the face-oriented stabilized Nitsche-type extended VMM developed in Chapter 9 and the AVM^4 derived in Chapter 4. To close the cross- and subgrid-scale Reynolds-stress terms arising in the variational multiscale formulation of the incompressible Navier-Stokes equations for the flow in each subdomain Ω_k, with $k \in \{+,-\}$ (see Section 3.2 for one fluid), the multifractal subgrid-scale modeling approach is applied, yielding the following approximation of the subgrid-scale velocity $\hat{\mathbf{u}}_k$:

$$\hat{\mathbf{u}}_k = B\delta\mathbf{u}_k^h, \tag{10.3}$$

where the coefficient B is defined as given in equation (4.27). The smaller resolved velocity $\delta\mathbf{u}_k^h$ is obtained by explicitly decomposing the resolved velocity $\mathbf{u}_k^h$ using level-transfer operators from PA-AMG; see Section 4.3. The enrichment of the velocity is entirely assigned to the larger resolved scales. For application to turbulent bubbly channel flow, the near-wall limit introduced in Section 4.8.1 is applied. All parameters of the multifractal subgrid-scale modeling approach are chosen as discussed in the aforementioned section. Depending on whether $\mathrm{Re}_{h,k}$ is based on the resolved velocity or the strain rate tensor, it reads as

$$\mathrm{Re}_{h,k}^{\mathrm{R}} = \frac{\rho_k \|\mathbf{u}^h\| h}{\mu_k} \tag{10.4}$$

or

$$\mathrm{Re}_{h,k}^{\mathrm{S}} = \frac{\rho_k \left(\boldsymbol{\varepsilon}(\mathbf{u}^h) : \boldsymbol{\varepsilon}(\mathbf{u}^h)\right)^{\frac{1}{2}} h^2}{\mu_k} \tag{10.5}$$

for the present two-phase flows, which is annotated for the sake of completeness.

Taking the effect of the subgrid scales into account in the extended variational multiscale formulation (9.26) gives rise to the following modeled formulation for LES: find $(\mathbf{u}^h, p^h) \in \mathcal{S}_{\mathbf{u}}^{h,\mathrm{enr}} \times \mathcal{S}_p^{h,\mathrm{enr}}$ such that

$$\begin{aligned}
&\mathcal{B}_{\mathrm{NS}}(\mathbf{v}^h, q^h; \mathbf{u}^h, p^h) \\
&+ \left(\mathbf{v}^h, \rho\left(\mathbf{u}^h \cdot \nabla\left(B\delta\mathbf{u}^h\right) + B\delta\mathbf{u}^h \cdot \nabla\mathbf{u}^h\right)\right)_{\Omega_\pm^*} + \left(\mathbf{v}^h, \rho B\delta\mathbf{u}^h \cdot \nabla\left(B\delta\mathbf{u}^h\right)\right)_{\Omega_\pm^*} \\
&+ \mathcal{B}_{\mathrm{RBStab}}(\mathbf{v}^h, q^h; \mathbf{u}^h, p^h) + \mathcal{B}_{\mathrm{Nit}}(\mathbf{v}^h, q^h; \mathbf{u}^h, p^h) + \mathcal{B}_{\mathrm{FOStab}}(\mathbf{v}^h, q^h; \mathbf{u}^h, p^h) = \ell_{\mathrm{NS}}(\mathbf{v}^h)
\end{aligned} \tag{10.6}$$

for all $(\mathbf{v}^h, q^h) \in \mathcal{V}_{\mathbf{u}}^{h,\mathrm{enr}} \times \mathcal{V}_p^{h,\mathrm{enr}}$. The multifractal forms of the cross- and subgrid-scale Reynolds-stress terms are depicted in the second line. Formulation (10.6) constitutes a **V**ariational **M**ulti-scale **M**ethod including **M**ultifractal subgrid-scale modeling, scale separation by level-transfer operators from plain aggregation **A**lgebraic **M**ultigrid methods and an e**X**tended finite element approach based on Nitsche's method to accurately represent the involved discontinuities and is introduced here as the XAVM^4.

For the subsequent LES, the interface, which is treated in a sharp fashion in this thesis, is assumed to be fully resolved; that is, it is captured in a DNS-like manner. Moreover, the subgrid-scale velocity is taken to be hardly able to notably deform the interface in the considered case.

As a consequence, the stabilized formulation (8.9) of the level-set equation remains unchanged, and the subgrid-scale velocity is not considered therein.

10.4 Turbulent Two-Phase Bubbly Channel Flow

Overview. Bubble columns in chemical processes or rising bubbles in the ocean emanating from enclosed air within breaking waves represent only two situations among a multitude of examples for turbulent bubbly flows. Owing to their essential role in industrial systems, turbulent bubbly flows in channels and pipes are extensively studied both experimentally and numerically. In an early experimental study, for instance, Serizawa *et al.* [280, 281] investigated bubbly flow in a vertical pipe. Recently, Oishi and Murai [236] examined a single large bubble of a size comparable to the thickness of the boundary layer in a horizontal turbulent channel flow at $\mathrm{Re}_\tau = 260$. Only a few numerical works on turbulent two-phase bubbly channel flow, where both fluids are resolved and the interface is allowed to deform, have been published to date. Recently, Dabiri *et al.* [76] studied bubbles with varying deformability in initially turbulent channel flow using DNS. Friction Reynolds numbers of $\mathrm{Re}_\tau = 127$ and 90 were considered. In a parallel work, Lu and Tryggvason [200] investigated a higher friction Reynolds number of $\mathrm{Re}_\tau = 250$. In that study, small and almost spherical bubbles of equal size were considered as a first setup. Then, several small bubbles were replaced by one large bubble for a second configuration. While the small bubbles drifted towards the walls, the large bubble remained in the middle of the channel. In Dabiri *et al.* [76] and Lu and Tryggvason [200], the density of the bubbles was assumed to be one tenth of the liquid density, and the dynamic viscosities of the fluids were taken to be equal. Moreover, flow direction and gravitation pointed into opposite directions. Bolotnov *et al.* [34] performed detached DNS, as further explained below, of turbulent bubbly channel flows using an FEM. The interface was captured by a level-set approach. Their simulations took into account a realistic water-to-air density ratio of 858.3 and were based on a friction Reynolds number of $\mathrm{Re}_\tau = 180$ for a turbulent single-phase channel flow using the liquid only. Bolotnov *et al.* [34] investigated three different configurations: a single small bubble, multiple small bubbles and a single large bubble. For the present LES,[1] merely the large bubble case is considered, since it allows for resolving the flow in the sense of an LES. In contrast, the resolution requirements are determined by the bubble size rather than by the turbulent structures in the small bubble cases. Bolotnov *et al.* [34] used a uniform mesh such that the initial diameter of the small bubbles was resolved by 18 elements throughout the domain. A similar number of elements has to be expected when using the present approach. Hence, there would not be any necessity for further subgrid-scale modeling owing to the resulting overall high resolution.

Problem Setup. Following Bolotnov *et al.* [34], the channel dimensions are chosen to be $2\pi\delta_\mathrm{c} \times 2\delta_\mathrm{c} \times (2/3)\pi\delta_\mathrm{c}$ in streamwise, wall-normal and spanwise direction, respectively, where δ_c denotes the channel half-width. A spherical bubble, whose diameter is set equal to the channel half-width, i.e., $D = \delta_\mathrm{c}$, is initially placed at the center of the channel. The void fraction (see

[1] Computational resources provided by the Leibniz Supercomputing Center under the project pr83te are gratefully acknowledged.

equation (9.56)) thus amounts to $\alpha = 2.0\%$. Gravitation $\mathbf{g}$ acts against the flow direction. No-slip boundary conditions are applied at the side walls. In homogeneous streamwise and spanwise direction, periodic boundary conditions are assumed for the flow and level-set field. A schematic drawing of the setup is depicted in Figure 10.3. As also illustrated in Figure 10.3, a precomputed fully-developed turbulent single-phase channel flow using the liquid constitutes the initial flow field, into which the bubble is inserted. All physical parameters are compiled in Table 10.1 to-

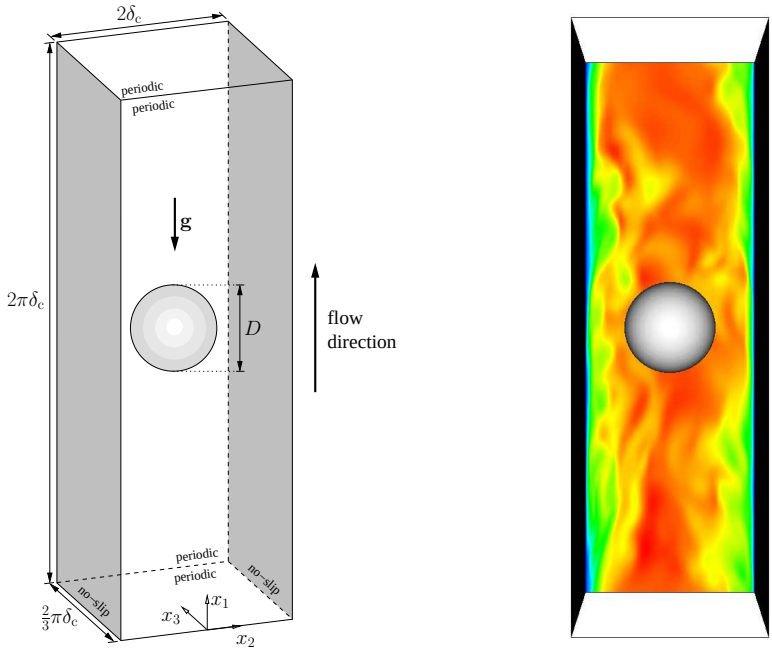

Figure 10.3: Setup of turbulent two-phase bubbly channel flow (left) and insertion of spherical bubble into precomputed turbulent single-phase channel flow (right) visualized via its velocity magnitude distribution in the x_1x_2-plane at $x_3 = (2/3)\pi\delta_c$ (red color indicates high velocity and blue color low velocity).

gether with the most important geometrical characteristics and the driving forces. Variables and parameters associated with the liquid and the gas are labeled by $(\cdot)_+$ and $(\cdot)_-$, respectively. The flow is pushed upward by a pressure gradient working against the gravity. Based on the provided values, Eötvös and Morton number (see equations (9.52) and (9.53)) are obtained as $\mathrm{Eo} = 6.689$ and $\mathrm{Mo} = 1.06 \cdot 10^{-10}$, respectively. Bolotnov *et al.* [34] defined the Weber number based on the superficial velocity $U_{\mathrm{sf},+}$ of the liquid (see, e.g., the textbook by Brennen [38] for definition) and the diameter of the bubble D as

$$\mathrm{We} = \frac{\rho_+ U_{\mathrm{sf},+}^2 D}{\gamma} \tag{10.7}$$

and reported $\mathrm{We} = 41.181$ for their investigations.

Non-dimensional values, which are also given in Table 10.1, are used for the simulation. Following Bolotnov *et al.* [34], the reference values for density, viscosity and length are given by $\rho_{\mathrm{ref}} = 996.5\,\mathrm{kg/m^3}$, $\mu_{\mathrm{ref}} = 2.3279\,\mathrm{kg/(ms)}$ and $L_{\mathrm{ref}} = 0.005\,\mathrm{m}$. Since non-dimensional values

Table 10.1: Overview of all quantities for turbulent two-phase bubbly channel flow.

	dimensional value	non-dimensional value
geometry		
channel half-width δ_c	0.005 m	1.0
bubble diameter D	0.005 m	1.0
physical parameters of fluids		
liquid density ρ_+	996.5 kg/m^3	1.0
liquid dynamic viscosity μ_+	0.0008514 kg/(ms)	0.00036574
gas density ρ_-	1.1610 kg/m^3	0.0011651
gas dynamic viscosity μ_-	0.00001827 kg/(ms)	0.0000078483
surface-tension coefficient γ	0.0365 kg/s^2	0.03356
driving forces		
x_1-component of gravity vector $\mathbf{g}$	-9.8 m/s^2	-0.22448
x_1-component of pressure gradient ∇p	-9954 Pa/m	-0.22881

are exclusively considered in the following, dimensional and non-dimensional values are not specifically distinguished via an additional sub- or superscript. For single-phase flow using the liquid only, the resulting parameters match the ones for turbulent channel flow at $\mathrm{Re}_\tau = 180$ with bulk velocity $U_\mathrm{b} = 1.0$ and $\delta_\mathrm{c} = 1.0$.

For LES, a discretization with $151 \times 56 \times 50$ trilinearly-interpolated hexahedral elements is used. This discretization is particularly tailored to present needs and consists of three blocks: a center block in the core of the channel and two outer blocks each attached to a wall. While a homogeneous distribution of elements is used for the center block, the distribution of elements is refined in wall-normal direction towards the wall for the outer blocks. The distribution of the elements is realized by first taking a basic discretization with 48 uniformly distributed elements in wall-normal direction. The first four layers of elements from the walls representing the outer blocks are then replaced by eight layers of elements obeying the refinement towards the walls. This discretization thus unifies an increased resolution in the vicinity of the walls and a homogeneous resolution of the domain occupied by the bubble. The characteristics of the present discretization, i.e., the element lengths h_i^+ in non-dimensional form (4.62) based on the parameters of the turbulent single-phase channel flow at $\mathrm{Re}_\tau = 180$ as well as the initial resolution of the bubble in terms of the number of elements corresponding to its diameter, are itemized in Table 10.2 and juxtaposed with the respective values of the discretization applied by Bolotnov *et al.* [34], which likewise consisted of hexahedral elements. The time-step length is set to $\Delta t = 0.015$ in non-dimensional form. A Crank-Nicholson scheme (i.e., $\theta = 0.5$) is applied together with a quasi-static enrichment strategy as described in Section 9.5. The level-set field is reinitialized periodically throughout the simulation. To ensure mass conservation for several tens of thousand time steps, global mass conservation in the form presented in Section 8.2.2 is applied. In the following, statistical averages are denoted by $\langle\cdot\rangle$ and fluctuations by $(\cdot)'$.

Table 10.2: Mesh parameters for turbulent two-phase bubbly channel flow: number of elements, non-dimensional element lengths h_i^+ and bubble resolution.

	no. elements	h_1^+	$h_{2,\text{min}}^+$	$h_{2,\text{max}}^+$	h_3^+	bubble resolution (no. elements)
present LES	$151 \times 56 \times 50$	7.49	1.50	7.50	7.54	24
DDNS Bolotnov et al. [34]	$452 \times 144 \times 151$	2.5	2.5	2.5	2.5	72

At this point, several differences compared to the simulations performed by Bolotnov *et al.* [34] have to be mentioned:

- A (residual-based) stabilized (standard) FEM together with a level-set approach to capture the interface was applied in that study. Bolotnov *et al.* [34] did not explicitly resolve the discontinuities at the interface but used the continuum surface force model of Brackbill *et al.* [36] in conjunction with a smooth transition of the physical properties from one fluid to the other within a predefined interface thickness.
- The uniform mesh used by Bolotnov *et al.* [34] (see Table 10.2) was chosen to adequately resolve the bubbles everywhere in the channel for all the investigated cases and, hence, already contained quite a large number of elements. Owing to the still insufficient resolution of the viscous sublayer (i.e., $h^+ = 2.5$), Bolotnov *et al.* [34] applied a boundary condition to which they referred to as a "friction-type" one instead of a no-slip condition.
- Bolotnov *et al.* [34] observed bubbles attaching to the walls. According to them, such an effect was not expected for the investigated two-phase flows. Therefore, they introduced a repellent lubrication-like force only acting on the interface in the near-wall region and preventing the bubbles from touching the walls. Bolotnov *et al.* [34] interpreted this force as a subgrid force.

By analogy to Detached Eddy Simulation (DES) for turbulent single-phase flows (see, e.g., the textbook by Sagaut *et al.* [271] for an introduction and further references), they referred to their approach as Detached Direct Numerical Simulation (DDNS). The aforementioned repellent lubrication-like force is not required for the present simulation. Since the near-wall region is appropriately resolved and the no-slip condition strongly imposed, the physical interaction between the bubble and the wall is naturally captured such that the bubble is able to directly respond to the presence of the wall.

From Single-Phase to Two-Phase Flow. As aforementioned, the velocity solution obtained from turbulent single-phase channel flow at $\text{Re}_\tau = 180$ using the liquid serves as initial field for the two-phase-flow simulation. Figure 10.4 summarizes the mean streamwise velocity u_1^+ and the root-mean-square velocities $\text{rms}\, u_i^+$ of the precursor single-phase-flow simulation. The velocity results are normalized by the friction velocity $u_\tau = \sqrt{\tau_\text{W}/\rho_+}$, where τ_W denotes the wall-shear stress, and plotted in wall units x_2^+, i.e., the distance from the wall normalized by the viscous length scale $\delta_\nu = \mu_+/(\rho_+ u_\tau)$, as usual. All values are in agreement with the DNS data provided by Moser *et al.* [224] for turbulent single-phase channel flow at $\text{Re}_\tau = 180$ and marked by "DNS MKM99".

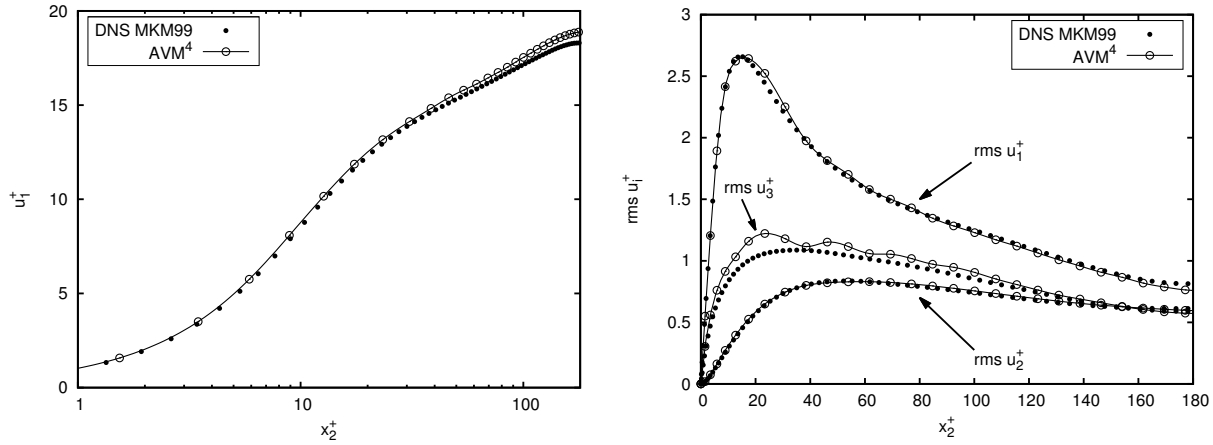

Figure 10.4: Mean streamwise velocity u_1^+ and root-mean-square velocities rms u_i^+ for turbulent single-phase channel flow at $\mathrm{Re}_\tau = 180$ using $151 \times 56 \times 50$ elements.

The initial level-set field is defined by the analytical expression for a spherical interface centered at a prescribed position. While surface tension is immediately enforced to provide a certain resistance against disproportional deformation of the interface in a turbulent flow, the physical parameters of the liquid are initially assumed also for the fluid in the subdomain Ω_-. During the subsequent transition period $[t_0^{\mathrm{tpf}}, t_1^{\mathrm{tpf}}]$, density and viscosity of the fluid in Ω_- are smoothly blended from the values of the liquid to the values of the gas via

$$\rho_-(t) = H_{t^{\mathrm{tpf}}}(t)\rho_+ + (1 - H_{t^{\mathrm{tpf}}}(t))\,\rho_-, \tag{10.8}$$

$$\mu_-(t) = H_{t^{\mathrm{tpf}}}(t)\mu_+ + (1 - H_{t^{\mathrm{tpf}}}(t))\,\mu_-, \tag{10.9}$$

where

$$H_{t^{\mathrm{tpf}}}(t) = \begin{cases} 1 & \text{if } t < t_0^{\mathrm{tpf}} \\ \frac{1}{2}\left(1 + \cos\left(\frac{\pi\left(t - t_0^{\mathrm{tpf}}\right)}{t_1^{\mathrm{tpf}} - t_0^{\mathrm{tpf}}}\right)\right) & \text{if } t_0^{\mathrm{tpf}} \leq t \leq t_1^{\mathrm{tpf}} \\ 0 & \text{if } t > t_1^{\mathrm{tpf}} \end{cases} \tag{10.10}$$

denotes a smoothed Heaviside function in time. A transition period comprising 500 time steps is used, which corresponds to roughly two flow-through cycles of the periodic domain.

The friction velocity u_τ for turbulent two-phase bubbly channel flow is defined based on the wall-shear stress τ_{W} and the density ρ_+ of the liquid as

$$u_\tau = \sqrt{\frac{\tau_{\mathrm{W}}}{\rho_+}}; \tag{10.11}$$

see, e.g., Bolotnov *et al.* [34] and Lu and Tryggvason [200]. Analogously, the friction Reynolds number is given as

$$\mathrm{Re}_\tau = \frac{\rho_+ u_\tau \delta_{\mathrm{c}}}{\mu_+}, \tag{10.12}$$

using the physical parameters of the liquid. The balance of mean forces in streamwise direction for steady state leads to the relation between wall-shear stress, pressure gradient and gravity (see, e.g., Lu and Tryggvason [200]):

$$\frac{\tau_{\mathrm{W}}}{\delta_c} = -\frac{\partial \langle p \rangle}{\partial x_1} + \rho_{\mathrm{m}} g_1, \tag{10.13}$$

where ρ_{m} denotes the density of the mixture (see equation (9.55)). Using the values given in Table 10.1, the friction Reynolds number amounts to $\mathrm{Re}_\tau = 257$. This increase of Re_τ also affects the resolution in the vicinity of the walls, which somewhat decreases as a result (i.e., $h^+_{2,\mathrm{min}} \approx 2$).

Flow Description. Figure 10.5 displays the shape of the bubble together with the vortical structures. Snapshots are taken from about two flow-through cycles of the periodic domain during the sampling period. In each snapshot, the left and right boundaries are the walls. Additionally, closeup views of the bubble shapes corresponding to the snapshots from the first of the two flow-through cycles are provided in Figure 10.6. In these closeup views, the bubble moves towards the observer, and, as before, the left and right boundaries are the walls. The bubble undergoes a continuous deformation. In some more detail, the bubble gets stretched in the plane perpendicular to the streamwise direction and possesses a highly irregular shape. The bubble mainly rises in the core of the channel. Vortical structures are identified by the Q-criterion (see Jeong and Hussain [160]). As for turbulent single-phase channel flow, vortical structures, characterized by their typical hairpin-like shape, evolve at the channel walls. The bubble exhibits a toroidal vortical structure in its equatorial plane, which was also described, e.g., by Lu and Tryggvason [200]. Moreover, elongated vortical structures occur in the wake of the bubble. This flow configuration essentially represents a chain of large bubbles rising in a turbulent channel flow.

Statistical Results. For obtaining statistical data, 10 000 steps are considered after the flow has reached a fully-developed state. Overall, the two-phase-flow simulation comprises 40 000 time steps. Averaging in x_1- and x_3-direction as well as in time is performed. Therefore, a phase-indicator function χ_k with $k \in \{+, -\}$ is introduced:

$$\chi_k(\mathbf{x}, t) = \begin{cases} 1 & \text{if } \mathbf{x} \text{ in } \Omega_k(t) \\ 0 & \text{else.} \end{cases} \tag{10.14}$$

The local mean void fraction $\langle \alpha \rangle$, i.e., the void fraction as a function of x_2, is calculated via integration of the phase-indicator function χ_- corresponding to the gas as

$$\langle \alpha \rangle = \frac{1}{N_{\mathrm{s}}} \sum^{N_{\mathrm{s}}} \frac{\int \chi_- \mathrm{d}x_1 \mathrm{d}x_3}{\int \mathrm{d}x_1 \mathrm{d}x_3}, \tag{10.15}$$

where N_{s} denotes the number of considered time steps. For the present XFEM-based approach, this evaluation is realized by summing up the volumes of the domain integration cells (see Section 9.5) belonging to Ω_- in each wall-parallel layer of elements and dividing by the volume of the layer itself. All remaining statistical data are evaluated based on nodal values. For each

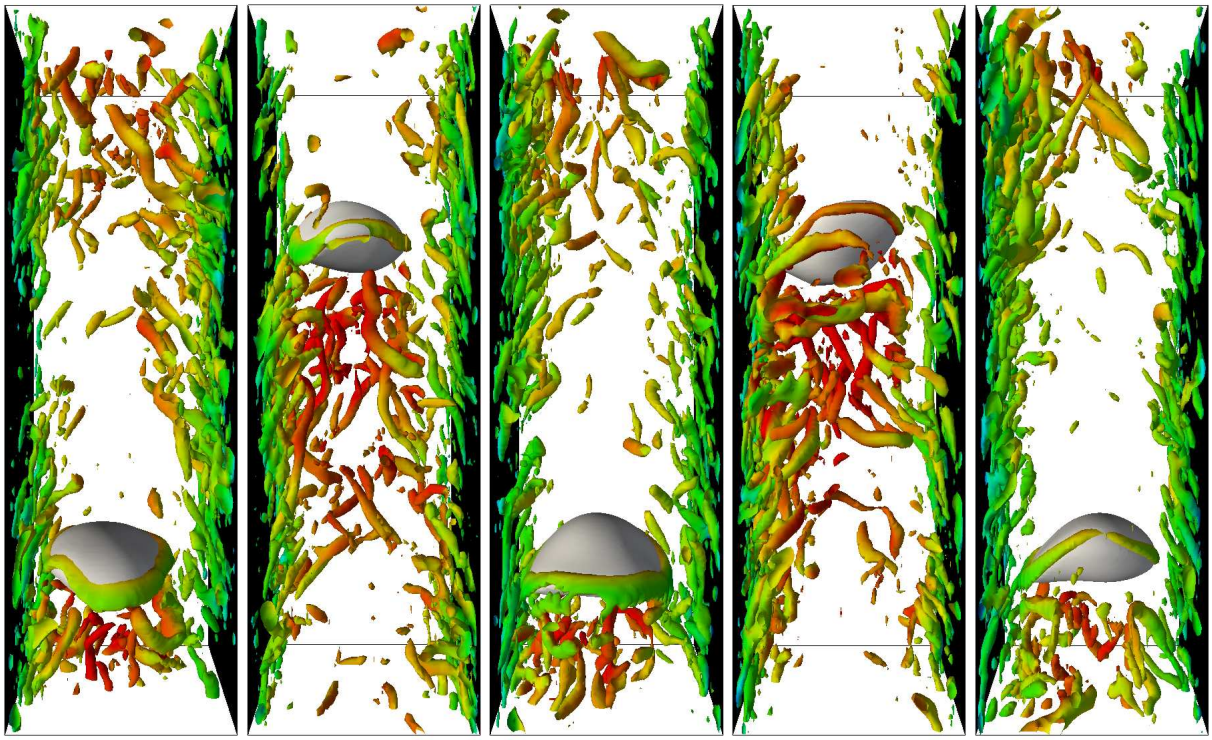

Figure 10.5: Instantaneous bubble shapes and vortical structures visualized via the Q-criterion and colored by the velocity magnitude (red color indicates high velocity and blue color low velocity) for turbulent two-phase bubbly channel flow.

Figure 10.6: Top view of instantaneous bubble shapes for turbulent two-phase bubbly channel flow.

phase, the averaged value $\langle \mathsf{X}_k \rangle$ of an arbitrary (velocity) value X is determined as

$$\langle \mathsf{X}_k \rangle = \frac{\sum_{N_\mathrm{s}} \sum_{N_\mathrm{n}} \chi_k \mathsf{X}}{\sum_{N_\mathrm{s}} \sum_{N_\mathrm{n}} \chi_k}, \tag{10.16}$$

where N_n is the number of nodes in each layer of nodes parallel to the walls. To determine the wall-shear stress from simulation for the present turbulent two-phase bubbly channel flow, the nodal forces in streamwise direction at the walls are summed up, divided by the total wall area and averaged in time. A value of $\mathrm{Re}_\tau = 260$, almost matching the theoretical one, is obtained from the simulation.

Figure 10.7 shows the mean streamwise velocity for both fluids, $\langle u_{1,+} \rangle$ and $\langle u_{1,-} \rangle$, together with the local mean void fraction $\langle \alpha \rangle$. Additionally, the mean streamwise velocity $\langle u_1^{\mathrm{sfp}} \rangle$ of the single-phase flow simulation is displayed. Values extracted from Bolotnov *et al.* [34] are marked by "DDNS BJDOLP11". As expected, the bubble moves faster than the liquid. Moreover, the bubble remains in the core of the channel, as already observed. Compared to the present single-phase-flow case, the mean streamwise velocity of the liquid increases. The DDNS of Bolotnov *et al.* [34] suggests notably lower mean values for $\langle u_{1,+} \rangle$ and $\langle u_{1,-} \rangle$. From Bolotnov *et al.* [34], it seems that the DDNS data are based on an earlier statistical period and a considerably smaller number of flow-through cycles. The LES curves are close to the DDNS curves for the equivalent statistical period, but further ascend until a converged statistical state is reached. After the flow has fully developed, one flow-through cycle of the bubble takes about 210 time steps in the LES. The peak of the void fraction occurs at the centerline of the channel. Compared to the data taken from Bolotnov *et al.* [34], the peak is higher in accordance to the fact that the bubble never enters the immediate vicinity of the wall, as also seen from $\langle u_{1,-} \rangle$. In contrast, the DDNS result for $\langle \alpha \rangle$ exhibits non-zero values almost up to $x_2 = 1$ and -1. This difference may be traced back to the present no-slip boundary conditions and the related resolution of the near-wall region, allowing for directly incorporating the physical interaction between the bubble and the wall.

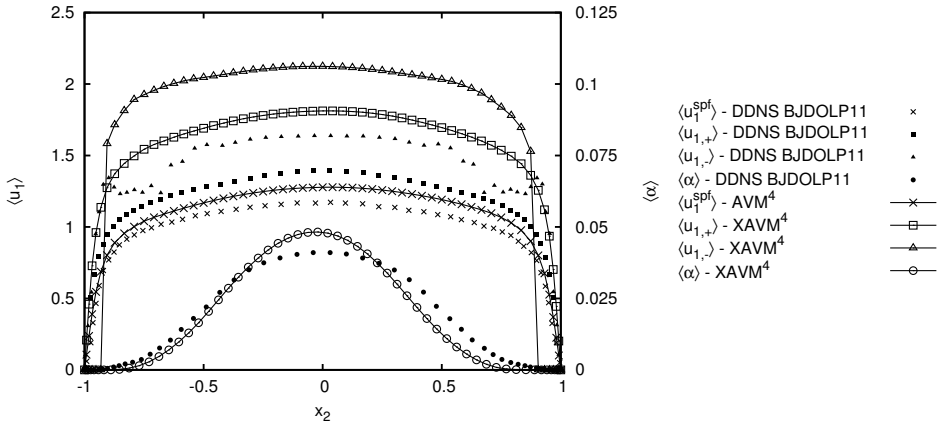

Figure 10.7: Mean streamwise velocity profiles $\langle u_1 \rangle$ and mean local void fraction $\langle \alpha \rangle$ for turbulent two-phase bubbly channel flow.

Figure 10.8 displays the distribution of the turbulent kinetic energy $k_{\text{tke},+}$ corresponding to the liquid. The turbulent kinetic energy k_{tke} is defined as

$$k_{\text{tke}} = \frac{1}{2}\langle \mathbf{u}' \cdot \mathbf{u}' \rangle. \tag{10.17}$$

The presence of the bubble notably alters the distribution of the turbulent kinetic energy compared to $k_{\text{tke}}^{\text{spf}}$ of the turbulent single-phase channel flow. This behavior is related to the wake of the bubble which occupies a significant portion of the channel domain, as also observable from Figure 10.5. The resulting intensification of velocity fluctuations, in particular in the core of the channel, contributes to the notable increase of $k_{\text{tke},+}$.

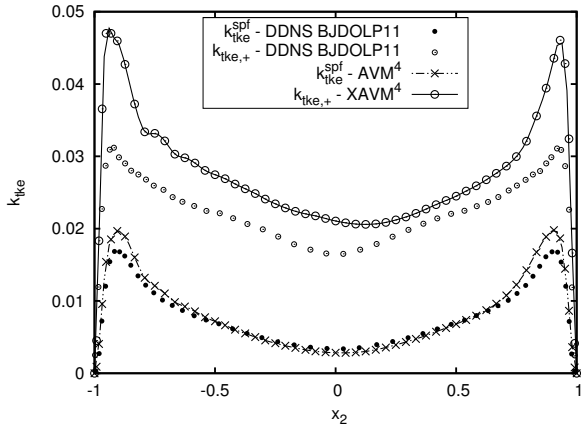

Figure 10.8: Comparison of turbulent kinetic energy k_{tke} for turbulent two-phase bubbly channel flow and turbulent single-phase channel flow.

11
Summary and Outlook

In this thesis, computational multiscale methods for large-eddy simulation of turbulent single- and two-phase flows have been developed. The variational multiscale method constitutes the framework for all these approaches.

For large-eddy simulation of turbulent incompressible single-phase flow, an algebraic variational multiscale-multigrid-multifractal method (AVM^4) has been proposed. In the multifractal subgrid-scale modeling approach, the subgrid-scale velocity is evaluated via integration based on the law of Biot-Savart using a multifractal reconstruction procedure for the subgrid-scale vorticity. Level-transfer operators from plain aggregation algebraic multigrid methods have been used for further separating the resolved scales. The multifractal subgrid-scale modeling approach has been embedded into a variational multiscale formulation, including appropriate residual-based multiscale terms to control the stability of the numerical method. A near-wall limit of the multifractal subgrid-scale modeling has been derived, which allows for particularly taking into account the near-wall effects of turbulent flow. Furthermore, passive-scalar mixing in turbulent incompressible flow has been considered. Both low- and high-Schmidt-number mixing has been naturally incorporated into the multifractal modeling procedure for the subgrid-scale scalar quantity. Moreover, the AVM^4 has been further developed for large-eddy simulation of turbulent variable-density flow at low Mach number. Various important benchmark examples have been examined to evaluate the AVM^4 for turbulent incompressible flow as well as its extensions to passive-scalar mixing and variable-density flow at low Mach number. For turbulent incompressible channel flow, the AVM^4 has produced results significantly closer to reference results from direct numerical simulation than the results obtained with the dynamic Smagorinsky model and the complete residual-based variational multiscale method or the basic stabilized finite element method, particularly regarding substantially improved results for both mean and root-mean-square velocity in streamwise direction. The dissipative properties of the AVM^4 have also been thoroughly investigated for this example, revealing a pronounced subgrid-scale dissipation in the buffer layer and approximately no dissipation in the core of the channel. The observation concerning the statistical values also holds true for the mean scalar quantity, its root-mean-square value as well as correlations of velocity and scalar fluctuations in the context of the respective channel flow configurations examined for passive-scalar mixing and variable-density flow. Considering turbulent flow past a square-section cylinder and over a backward-facing step with heating, the convenient applicability of the AVM^4 to substantially more complex flow configurations has been shown. Evaluations of computing times have revealed notably reduced computational cost compared to the dynamic Smagorinsky model, while the cost has only been marginally enhanced compared to the basic stabilized finite element method. Eventually, linking this outcome to the demands outlined in the introduction, the building blocks of the AVM^4, that is, the variational multiscale method, multifractal subgrid-scale modeling and scale separation based

on level transfer operators from plain aggregation algebraic multigrid methods, enable a method that promises to match these demands.

For incompressible two-phase flow, a face-oriented stabilized Nitsche-type extended variational multiscale method has been devised. An extended finite element method based on jump enrichments for both the velocity and pressure field has allowed for adequately capturing strong and weak discontinuities at the interface, which has been described by the level-set method. Using Nitsche's method, the variational multiscale formulations for each fluid have been coupled. While appropriate residual-based multiscale terms have ensured the stability of the numerical method inside each fluid domain, additional face-oriented ghost-penalty as well as fluid stabilization terms have been introduced to also provide a stable formulation in the vicinity of the interface. In particular, both the Nitsche-penalty term as well as the face-oriented stabilization terms have been enhanced to account for viscous- and convection-dominated transient flows. Various two- and three-dimensional numerical examples have been investigated to demonstrate the excellent performance of the proposed method in terms of accuracy and stability. Two-dimensional Rayleigh-Taylor instabilities have been examined. A comparison of the predicted growth rate for various physical parameter configurations with and without surface tension has revealed excellent agreement with analytical solutions. Three-dimensional rising bubbles have been studied using density and viscosity ratios of 1000. For all four investigated bubble shapes, the resulting Reynolds numbers based on the final rise velocity have well matched the available experimental values. The robustness of the proposed method for substantially more complex two-phase flow situations has been particularly demonstrated for the coalescence of two bubbles. As an add-on, level-set methods have been reviewed in the context of finite element methods, and a hybrid particle level-set method has been realized as a further improvement for the level-set field. Its applicability to two-phase flow simulations has been shown for the impact of a drop on a quiescent water surface.

Eventually, the AVM^4 and the face-oriented stabilized Nitsche-type extended variational multiscale method have been unified leading to the extended variational multiscale-multigrid-multifractal method (XAVM^4). To demonstrate the high potential of the XAVM^4 for large-eddy simulation, turbulent channel flow carrying a single large bubble of the size of the channel half-width has been investigated. The XAVM^4 has shown very good performance both with respect to robustness as well as the ability to capture the expected flow features and the statistical results.

The developed computational multiscale methods for single- and two-phase flows enable various promising future research directions. Concerning two-phase-flow simulations using the present framework, the development of a reliable numerical description of the contact line between the interface and a solid wall or the incorporation of a variable surface-tension coefficient resulting from a locally varying surfactant concentration or temperature distribution opens the field to a variety of demanding industrial applications. Owing to the practical importance of wall-bounded turbulent flow at very high Reynolds number, the development of a consistent wall-layer modeling approach to be integrated into the AVM^4 constitutes a further possible research direction. Large-eddy simulation of turbulent two-phase flow composed of two bulk fluids is likewise still at the beginning and gives rise to new challenges concerning subgrid-scale modeling in the vicinity of interfaces. Furthermore, the XAVM^4 also allows for further development towards large-eddy simulation of turbulent premixed combustion.

A

Supplementary Data for Backward-Facing Step Flow with Heating

In this appendix, supplementary data for LES of turbulent flow over a backward-facing step with heating are summarized. The provided data correspond to a wall heat flux of $q_\mathrm{W} = 1000\,\mathrm{W/m^2}$ and are not explicitly discussed. Figure A.1 displays the skin-friction coefficient C_f, Figure A.2 the mean temperature T_W at the bottom wall of the backward-facing step, Figure A.3 the normalized mean temperature $(\langle T \rangle - T_0)/T_0$ and Figure A.4 the normalized root-mean-square temperature $\mathrm{rms}\,T/T_0$, streamwise velocity-temperature fluctuations $\langle u_1' T' \rangle/(U_\mathrm{c} T_0)$ as well as wall-normal velocity-temperature fluctuations $\langle u_2' T' \rangle/(U_\mathrm{c} T_0)$. The mean reattachment lengths are $X_\mathrm{r}/H = 6.21$ for the AVM^4, 6.30 for the RBVMM and 6.15 for the DSM.

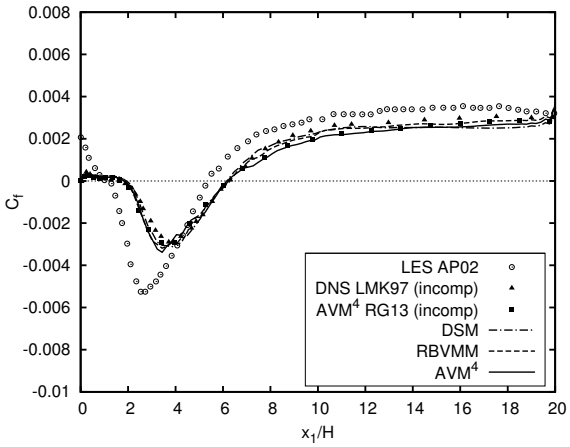

Figure A.1: Skin-friction coefficient C_f at the bottom wall of the backward-facing step for $q_\mathrm{W} = 1000\,\mathrm{W/m^2}$.

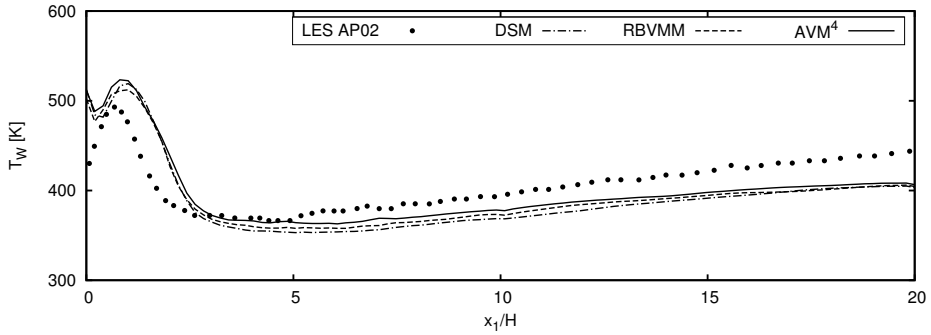

Figure A.2: Mean temperature T_W at the bottom wall of the backward-facing step for $q_\mathrm{W} = 1000\,\mathrm{W/m^2}$.

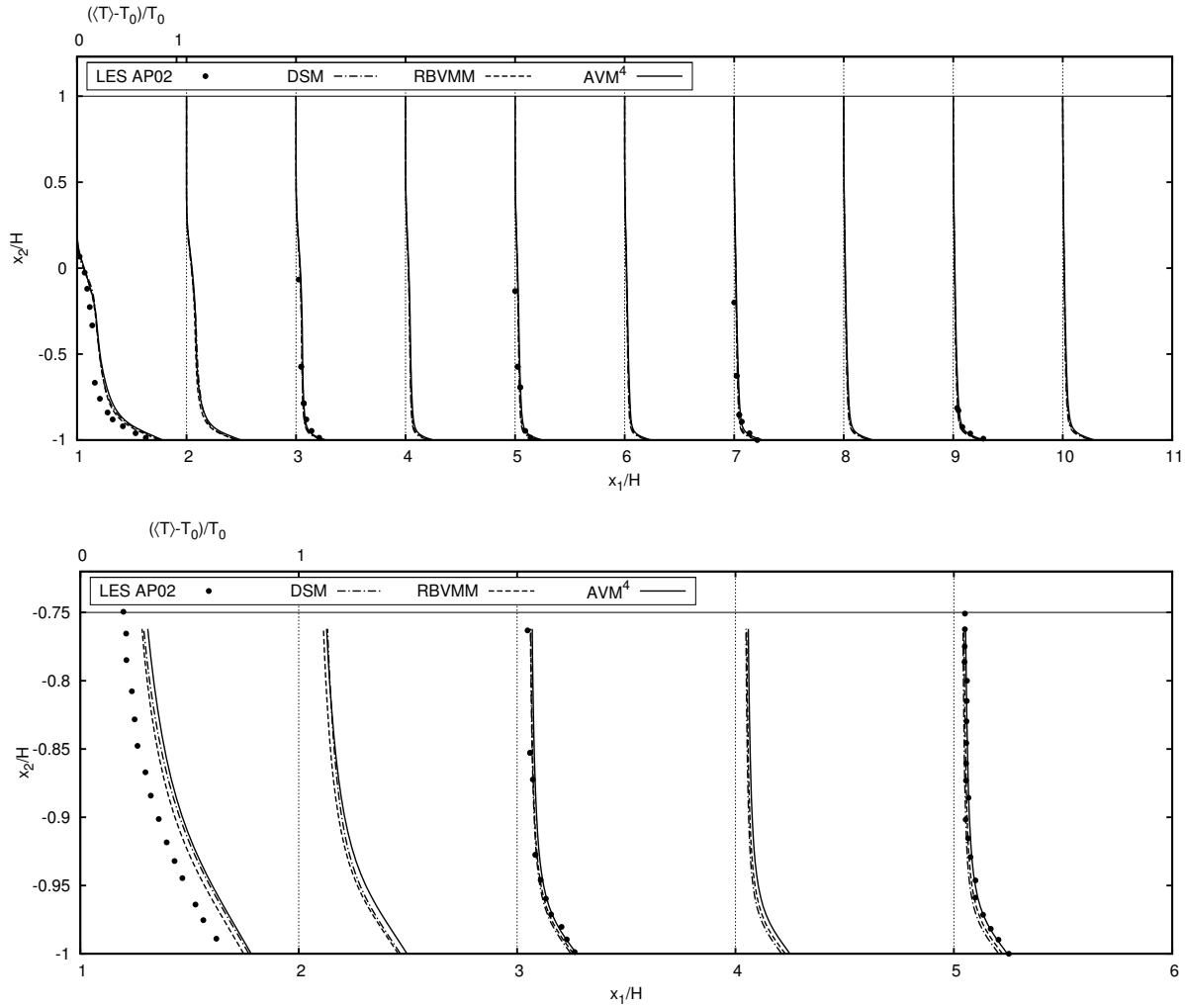

Figure A.3: Mean temperature $(\langle T\rangle - T_0)/T_0$ at various locations x_1/H for turbulent flow over a backward-facing step with heating at $q_\mathrm{W} = 1000\,\mathrm{W/m^2}$ including a closeup view of the near-wall region.

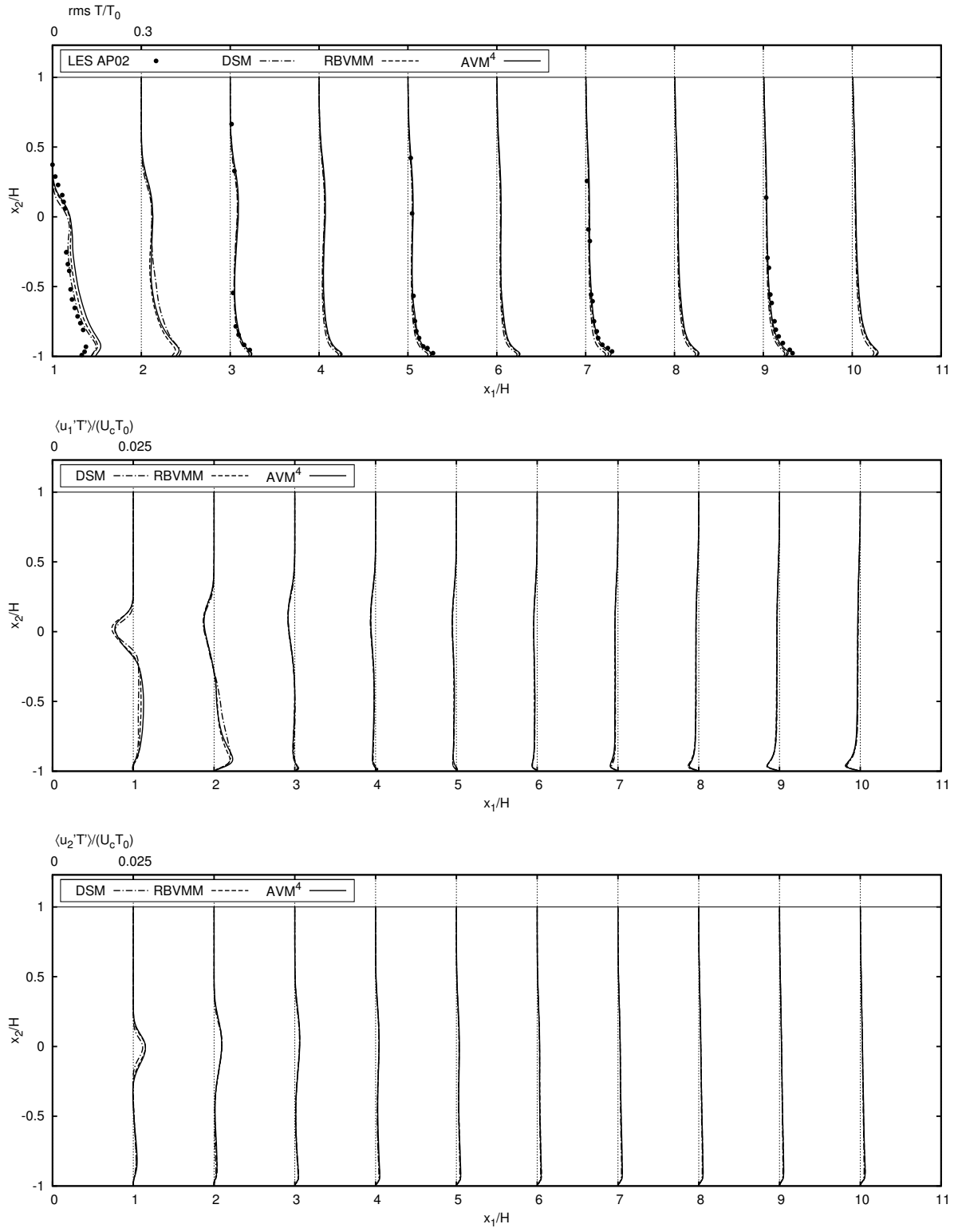

Figure A.4: Root-mean-square temperature $\mathrm{rms}\, T/T_0$, streamwise velocity-temperature fluctuations $\langle u_1' T' \rangle / (U_\mathrm{c} T_0)$ and wall-normal velocity-temperature fluctuations $\langle u_2' T' \rangle / (U_\mathrm{c} T_0)$ at various locations x_1/H for turbulent flow over a backward-facing step with heating at $q_\mathrm{W} = 1000\,\mathrm{W/m^2}$.

Bibliography

[1] S. Abbas, A. Alizada, and T.-P. Fries, The XFEM for high-gradient solutions in convection-dominated problems, *International Journal for Numerical Methods in Engineering* **82**, 1044–1072, 2010.

[2] J.-L. Aider, A. Danet, and M. Lesieur, Large-eddy simulation applied to study the influence of upstream conditions on the time-dependent and averaged characteristics of a backward-facing step flow, *Journal of Turbulence* **8**, N51, 2007.

[3] I. Akkerman, Y. Bazilevs, C. E. Kees, and M. W. Farthing, Isogeometric analysis of free-surface flow, *Journal of Computational Physics* **230**, 4137–4152, 2011.

[4] B. W. Anderson and J. A. Domaradzki, A subgrid-scale model for large-eddy simulation based on the physics of interscale energy transfer in turbulence, *Physics of Fluids* **24**, 065104, 2012.

[5] W. Aniszewski, A. Bogusławski, M. Marek, and A. Tyliszczak, A new approach to subgrid surface tension for LES of two-phase flows, *Journal of Computational Physics* **231**, 7368–7397, 2012.

[6] C. Annavarapu, M. Hautefeuille, and J. Dolbow, A robust Nitsche's formulation for interface problems, *Computer Methods in Applied Mechanics and Engineering* **225–228**, 44–54, 2012.

[7] P. M. A. Areias and T. Belytschko, A comment on the article a finite element method for simulation of strong and weak discontinuities in solid mechanics by A. Hansbo and P. Hansbo [Comput. Methods Appl. Mech. Engrg. 193 (2004) 3523–3540], *Computer Methods in Applied Mechanics and Engineering* **195**, 1275–1276, 2006.

[8] R. F. Ausas, G. C. Buscaglia, and S. R. Idelsohn, A new enrichment space for the treatment of discontinuous pressures in multi-fluid flows, *International Journal for Numerical Methods in Fluids* **70**, 829–850, 2012.

[9] R. V. R. Avancha and R. H. Pletcher, Large eddy simulation of the turbulent flow past a backward-facing step with heat transfer and property variations, *International Journal of Heat and Fluid Flow* **23**, 601–614, 2002.

[10] M. Avila, R. Codina, and J. Principe, Large eddy simulation of low Mach number flows using dynamic and orthogonal subgrid scales, *Computers & Fluids* **99**, 44–66, 2014.

[11] I. Babuška, The finite element method with Lagrangian multipliers, *Numerische Mathematik* **20**, 179–192, 1973.

[12] I. Babuška and U. Banerjee, Stable generalized finite element method (SGFEM), *Computer Methods in Applied Mechanics and Engineering* **201–204**, 91–111, 2012.

[13] H. J. C. Barbosa and T. J. R. Hughes, The finite element method with Lagrange multipliers on the boundary: Circumventing the Babuška-Brezzi condition, *Computer Methods in Applied Mechanics and Engineering* **85**, 109–128, 1991.

[14] J. Bardina, J. H. Ferziger, and W. C. Reynolds, Improved subgrid models for large eddy simulation, *AIAA Paper*, No. 80–1357, 1980.

[15] J. Bardina, J. H. Ferziger, and W. C. Reynolds, Improved turbulence models based on large eddy simulation of homogeneous, incompressible, turbulent flows, Technical Report TF-19, Thermosciences Division, Department of Mechanical Engineering, Stanford University, 1983.

[16] N. Barrau, R. Becker, E. Dubach, and R. Luce, A robust variant of NXFEM for the interface problem, *Comptes Rendus Mathematique* **350**, 789–792, 2012.

[17] G. R. Barrenechea and F. Valentin, An unusual stabilized finite element method for a generalized Stokes problem, *Numerische Mathematik* **92**, 653–677, 2002.

[18] C. Basting and D. Kuzmin, A minimization-based finite element formulation for interface-preserving level set reinitialization, *Computing* **95**, 13–25, 2013.

[19] G. K. Batchelor, Small-scale variation of convected quantities like temperature in turbulent fluid. Part 1. General discussion and the case of small conductivity, *Journal of Fluid Mechanics* **5**, 113–133, 1959.

[20] G. K. Batchelor, *An introduction to fluid dynamics*, Cambridge University Press, Cambridge, 1967.

[21] G. Bauer, P. Gamnitzer, V. Gravemeier, and W. A. Wall, An isogeometric variational multiscale method for large-eddy simulation of coupled multi-ion transport in turbulent flow, *Journal of Computational Physics* **251**, 194–208, 2013.

[22] Y. Bazilevs, V. M. Calo, J. A. Cottrell, T. J. R. Hughes, A. Reali, and G. Scovazzi, Variational multiscale residual-based turbulence modeling for large eddy simulation of incompressible flows, *Computer Methods in Applied Mechanics and Engineering* **197**, 173–201, 2007.

[23] Y. Bazilevs, C. Michler, V. M. Calo, and T. J. R. Hughes, Isogeometric variational multiscale modeling of wall-bounded turbulent flows with weakly enforced boundary conditions on unstretched meshes, *Computer Methods in Applied Mechanics and Engineering* **199**, 780–790, 2010.

[24] P. Bearman and E. Obasaju, An experimental study of pressure fluctuations on fixed and oscillating square-section cylinders, *Journal of Fluid Mechanics* **119**, 279–321, 1982.

[25] A. Beccantini, E. Studer, S. Gounand, J.-P. Magnaud, T. Kloczko, C. Corre, and S. Kudriakov, Numerical simulations of a transient injection flow at low Mach number regime, *International Journal for Numerical Methods in Engineering* **76**, 662–696, 2008.

[26] E. Béchet, N. Moës, and B. Wohlmuth, A stable Lagrange multiplier space for stiff interface conditions within the extended finite element method, *International Journal for Numerical Methods in Engineering* **78**, 931–954, 2009.

[27] R. Becker, Mesh adaptation for Dirichlet flow control via Nitsche's method, *Communications in Numerical Methods in Engineering* **18**, 669–680, 2002.

[28] R. Becker, E. Burman, and P. Hansbo, A Nitsche extended finite element method for incompressible elasticity with discontinuous modulus of elasticity, *Computer Methods in Applied Mechanics and Engineering* **198**, 3352–3360, 2009.

[29] J. B. Bell, P. Colella, and H. M. Glaz, A second-order projection method for the incompressible Navier-Stokes equations, *Journal of Computational Physics* **85**, 257–283, 1989.

[30] R. Bellman and R. H. Pennington, Effects of surface tension and viscosity on Taylor instability, *Quarterly of Applied Mathematics* **12**, 151–162, 1954.

[31] T. Belytschko and T. Black, Elastic crack growth in finite elements with minimal remeshing, *International Journal for Numerical Methods in Engineering* **45**, 601–620, 1999.

[32] T. Belytschko, N. Moës, S. Usui, and C. Parimi, Arbitrary discontinuities in finite elements, *International Journal for Numerical Methods in Engineering* **50**, 993–1013, 2001.

[33] T. Belytschko, R. Gracie, and G. Ventura, A review of extended/generalized finite element methods for material modeling, *Modelling and Simulation in Materials Science and Engineering* **17**, 043001, 2009.

[34] I. A. Bolotnov, K. E. Jansen, D. A. Drew, A. A. Oberai, R. T. Lahey Jr., and M. Z. Podowski, Detached direct numerical simulation of turbulent two-phase bubbly channel flow, *International Journal of Multiphase Flow* **37**, 647–659, 2011.

[35] M. Braack, E. Burman, V. John, and G. Lube, Stabilized finite element methods for the generalized Oseen problem, *Computer Methods in Applied Mechanics and Engineering* **196**, 853–866, 2007.

[36] J. U. Brackbill, D. B. Kothe, and C. Zemach, A continuum method for modeling surface tension, *Journal of Computational Physics* **100**, 335–354, 1992.

[37] D. Braess, *Finite Elemente: Theorie, schnelle Löser und Anwendungen in der Elastizitätstheorie*, 4th Edition, Springer, Berlin, 2007.

[38] C. E. Brennen, *Fundamentals of multiphase flows*, Cambridge University Press, New York, 2005.

[39] F. Brezzi and M. Fortin, *Mixed and hybrid finite element methods*, Springer, New York, 1991.

[40] W. L. Briggs, V. E. Henson, and S. F. McCormick, *A multigrid tutorial*, 2nd Edition, SIAM, Philadelphia, 2000.

[41] A. N. Brooks and T. J. R. Hughes, Streamline Upwind/Petrov-Galerkin formulations for convection dominated flows with particular emphasis on the incompressible Navier-Stokes equations, *Computer Methods in Applied Mechanics and Engineering* **32**, 199–259, 1982.

[42] K. A. Buch and W. J. A. Dahm, Experimental study of the fine-scale structure of conserved scalar mixing in turbulent shear flows. Part 2. Sc $\approx$ 1, *Journal of Fluid Mechanics* **364**, 1–29, 1998.

[43] E. Burman, Interior penalty variational multiscale method for the incompressible Navier-Stokes equation: Monitoring artificial dissipation, *Computer Methods in Applied Mechanics and Engineering* **196**, 4045–4058, 2007.

[44] E. Burman, Ghost penalty, *Comptes Rendus Mathematique* **348**, 1217–1220, 2010.

[45] E. Burman and P. Hansbo, Fictitious domain finite element methods using cut elements: II. A stabilized Nitsche method, *Applied Numerical Mathematics* **62**, 328–341, 2012.

[46] E. Burman and P. Hansbo, Fictitious domain methods using cut elements: III. A stabilized Nitsche method for Stokes' problem, *ESAIM: Mathematical Modelling and Numerical Analysis* **48**, 859–874, 2014.

[47] E. Burman and P. Zunino, Numerical approximation of large contrast problems with the unfitted Nitsche method, In J. Blowey and M. Jensen (eds.), *Frontiers in numerical analysis - Durham 2010*, Volume 85 of *Lecture Notes in Computational Science and Engineering*, pages 227–282, Springer, Berlin, 2012.

[48] E. Burman, M. A. Fernández, and P. Hansbo, Continuous interior penalty finite element method for Oseen's equations, *SIAM Journal on Numerical Analysis* **44**, 1248–1274, 2006.

[49] G. C. Burton, *A multifractal subgrid-scale model for large-eddy simulation of turbulent flows*, Dissertation, The University of Michigan, 2003.

[50] G. C. Burton, The nonlinear large-eddy simulation method applied to Sc $\approx$ 1 and Sc $\gg$ 1 passive-scalar mixing, *Physics of Fluids* **20**, 035103, 2008.

[51] G. C. Burton, Scalar-energy spectra in simulations of Sc $\gg$ 1 mixing by turbulent jets using the nonlinear large-eddy simulation method, *Physics of Fluids* **20**, 071701, 2008.

[52] G. C. Burton, Study of ultrahigh Atwood-number Rayleigh-Taylor mixing dynamics using the nonlinear large-eddy simulation method, *Physics of Fluids* **23**, 045106, 2011.

[53] G. C. Burton and W. J. A. Dahm, Multifractal subgrid-scale modeling for large-eddy simulation. I. Model development and a priori testing, *Physics of Fluids* **17**, 075111, 2005.

[54] G. C. Burton and W. J. A. Dahm, Multifractal subgrid-scale modeling for large-eddy simulation. II. Backscatter limiting and a posteriori evaluation, *Physics of Fluids* **17**, 075112, 2005.

[55] I. Calmet and J. Magnaudet, Large-eddy simulation of high-Schmidt number mass transfer in a turbulent channel flow, *Physics of Fluids* **9**, 438–455, 1997.

[56] V. M. Calo, *Residual-based multiscale turbulence modeling: Finite volume simulations of bypass transition*, Dissertation, Stanford University, 2004.

[57] R. S. Cant and E. Mastorakos, *An introduction to turbulent reacting flows*, Imperial College Press, London, 2008.

[58] S. Chandrasekhar, *Hydrodynamic and hydromagnetic stability*, Dover Publications, New York, 1981.

[59] P. Chassaing, The modeling of variable density turbulent flows. A review of first-order closure schemes, *Flow, Turbulence and Combustion* **66**, 293–332, 2001.

[60] J. Chesnel, T. Ménard, J. Réveillon, and F.-X. Demoulin, Subgrid analysis of liquid jet atomization, *Atomization and Sprays* **21**, 41–67, 2011.

[61] J. Chessa and T. Belytschko, An extended finite element method for two-phase fluids, *Journal of Applied Mechanics* **70**, 10–17, 2003.

[62] J. Chessa and T. Belytschko, Arbitrary discontinuities in space-time finite elements by level sets and XFEM, *International Journal for Numerical Methods in Engineering* **61**, 2595–2614, 2004.

[63] J. Chessa, P. Smolinski, and T. Belytschko, The extended finite element method (XFEM) for solidification problems, *International Journal for Numerical Methods in Engineering* **53**, 1959–1977, 2002.

[64] J. Chessa and T. Belytschko, An enriched finite element method and level sets for axisymmetric two-phase flow with surface tension, *International Journal for Numerical Methods in Engineering* **58**, 2041–2064, 2003.

[65] H. Choi and P. Moin, Effects of the computational time step on numerical solutions of turbulent flow, *Journal of Computational Physics* **113**, 1–4, 1994.

[66] J. Chung and G. M. Hulbert, A time integration algorithm for structural dynamics with improved numerical dissipation: The generalized-α method, *Journal of Applied Mechanics* **60**, 371–375, 1993.

[67] R. Clift, J. R. Grace, and M. W. Weber, *Bubbles, drops, and particles*, Academic Press, New York, 1978.

[68] R. Codina, J. Principe, O. Guasch, and S. Badia, Time dependent subscales in the stabilized finite element approximation of incompressible flow problems, *Computer Methods in Applied Mechanics and Engineering* **196**, 2413–2430, 2007.

[69] R. Codina, J. Principe, and M. Avila, Finite element approximation of turbulent thermally coupled incompressible flows with numerical sub-grid scale modelling, *International Journal of Numerical Methods for Heat and Fluid Flow* **20**, 492–515, 2010.

[70] S. S. Collis, Monitoring unresolved scales in multiscale turbulence modeling, *Physics of Fluids* **13**, 1800–1806, 2001.

[71] S. S. Collis, Multiscale methods for turbulence simulation and control, MEMS Preprint 2002–034, Department of Mechanical Engineering and Material Science, Rice University, 2002.

[72] A. Comerford, V. Gravemeier, and W. A. Wall, An algebraic variational multiscale-multigrid method for large-eddy simulation of turbulent pulsatile flows in complex geometries with detailed insight into pulmonary airway flow, *International Journal for Numerical Methods in Fluids* **71**, 1207–1225, 2013.

[73] A. H. Coppola-Owen and R. Codina, Improving Eulerian two-phase flow finite element approximation with discontinuous gradient pressure shape functions, *International Journal for Numerical Methods in Fluids* **49**, 1287–1304, 2005.

[74] S. Corrsin, On the spectrum of isotropic temperature fluctuations in isotropic turbulence, *Journal of Applied Physics* **22**, 469–473, 1951.

[75] R. Croce, M. Griebel, and M. A. Schweitzer, Numerical simulation of bubble and droplet deformation by a level set approach with surface tension in three dimensions, *International Journal for Numerical Methods in Fluids* **62**, 963–993, 2009.

[76] S. Dabiri, J. Lu, and G. Tryggvason, Transition between regimes of a vertical channel bubbly upflow due to bubble deformability, *Physics of Fluids* **25**, 102110, 2013.

[77] C. D'Angelo and P. Zunino, Numerical approximation with Nitsche's coupling of transient Stokes'/Darcy's flow problems applied to hemodynamics, *Applied Numerical Mathematics* **62**, 378–395, 2012.

[78] P. A. Davidson, *Turbulence: An introduction for scientists and engineers*, Oxford University Press, New York, 2004.

[79] T. De Mulder, The role of bulk viscosity in stabilized finite element formulations for incompressible flow: A review, *Computer Methods in Applied Mechanics and Engineering* **163**, 1–10, 1998.

[80] J. C. del Álamo, J. Jiménez, P. Zandonade, and R. D. Moser, Scaling of the energy spectra of turbulent channels, *Journal of Fluid Mechanics* **500**, 135–144, 2004.

[81] O. Desjardins, G. Blanquart, G. Balarac, and H. Pitsch, High order conservative finite difference scheme for variable density low Mach number turbulent flows, *Journal of Computational Physics* **227**, 7125–7159, 2008.

[82] J. Dolbow and I. Harari, An efficient finite element method for embedded interface problems, *International Journal for Numerical Methods in Engineering* **78**, 229–252, 2009.

[83] J. A. Domaradzki and N. A. Adams, Direct modeling of subgrid-scales of turbulence in large eddy simulation, *Journal of Turbulence* **3**, 024, 2002.

[84] J. A. Domaradzki and K. Loh, The subgrid-scale estimation model in the physical space respresentation, *Physics of Fluids* **11**, 2330–2342, 1999.

[85] J. Donea and A. Huerta, *Finite element methods for flow problems*, Wiley, Chichester, 2003.

[86] J. Donea, A. Huerta, J. P. Ponthot, and A. Rodríguez-Ferran, Arbitrary Lagrangian-Eulerian methods, In E. Stein, R. de Borst, and T. J. R. Hughes (eds.), *Encyclopedia of Computational Mechanics*, pages 1–25, Wiley, Chichester, 2004.

[87] J. Douglas and T. Dupont, Interior penalty procedures for elliptic and parabolic Galerkin methods, In R. Glowinski and J. Lions (eds.), *Computing methods in applied sciences*, Volume 58 of *Lecture Notes in Physics*, pages 207–216, Springer, Berlin, 1976.

[88] D. F. G. Durão, M. V. Heitor, and J. C. F. Pereira, Measurements of turbulent and periodic flows around a square cross-section cylinder, *Experiments in Fluids* **6**, 298–304, 1988.

[89] R. N. Elias and A. L. G. A. Coutinho, Stabilized edge-based finite element simulation of free-surface flows, *International Journal for Numerical Methods in Fluids* **54**, 965–993, 2007.

[90] R. N. Elias, M. A. D. Martins, and A. L. G. A. Coutinho, Simple finite element-based computation of distance functions in unstructured grids, *International Journal for Numerical Methods in Engineering* **72**, 1095–1110, 2007.

[91] D. Enright, R. Fedkiw, J. Ferziger, and I. Mitchell, A hybrid particle level set method for improved interface capturing, *Journal of Computational Physics* **183**, 83–116, 2002.

[92] D. Enright, F. Losasso, and R. Fedkiw, A fast and accurate semi-Lagrangian particle level set method, *Computers & Structures* **83**, 479–490, 2005.

[93] K. Falconer, *Fractal geometry: Mathematical foundations and applications*, 2nd Edition, Wiley, Chichester, 2003.

[94] R. P. Fedkiw, T. Aslam, B. Merriman, and S. Osher, A non-oscillatory Eulerian approach to interfaces in multimaterial flows (the ghost fluid method), *Journal of Computational Physics* **152**, 457–492, 1999.

[95] A. T. Fedorchenko, A model of unsteady subsonic flow with acoustics excluded, *Journal of Fluid Mechanics* **334**, 135–155, 1997.

[96] L. P. Franca and F. Valentin, On an improved unusual stabilized finite element method for the advective-reactive-diffusive equation, *Computer Methods in Applied Mechanics and Engineering* **190**, 1785–1800, 2000.

[97] R. D. Frederiksen, W. J. A. Dahm, and D. R. Dowling, Experimental assessment of fractal scale similarity in turbulent flows. Part 3. Multifractal scaling, *Journal of Fluid Mechanics* **338**, 127–155, 1997.

[98] R. Friedrich and M. Arnal, Analysing turbulent backward-facing step flow with the lowpass-filtered Navier-Stokes equations, *Journal of Wind Engineering and Industrial Aerodynamics* **35**, 101–128, 1990.

[99] T.-P. Fries and T. Belytschko, The extended/generalized finite element method: An overview of the method and its applications, *International Journal for Numerical Methods in Engineering* **84**, 253–304, 2010.

[100] T.-P. Fries and A. Zilian, On time integration in the XFEM, *International Journal for Numerical Methods in Engineering* **79**, 69–93, 2009.

[101] U. Frisch and G. Parisi, On the singularity structure of fully developed turbulence, In M. Ghil, R. Benzi, and G. Parisi (eds.), *Turbulence and predictability in geophysical fluid dynamics and climate dynamics*, pages 84–88, Elsevier, Amsterdam, 1985.

[102] J. Fröhlich and W. Rodi, Introduction to large eddy simulation of turbulent flows, In B. E. Launder and N. D. Sandham (eds.), *Closure strategies for turbulent and transitional flows*, pages 267–298, Cambridge University Press, Cambridge, 2002.

[103] M. Fulgosi, D. Lakehal, S. Banerjee, and V. De Angelis, Direct numerical simulation of turbulence in a sheared air-water flow with a deformable interface, *Journal of Fluid Mechanics* **482**, 319–345, 2003.

[104] C. Fureby, G. Tabor, H. G. Weller, and A. D. Gosman, Large eddy simulations of the flow around a square prism, *AIAA Journal* **38**, 442–452, 2000.

[105] D. Fuster, G. Agbaglah, C. Josserand, S. Popinet, and S. Zaleski, Numerical simulation of droplets, bubbles and waves: State of the art, *Fluid Dynamics Research* **41**, 065001, 2009.

[106] P. Gamnitzer, *Residual-based variational multiscale methods for turbulent flows and fluid-structure interaction*, Dissertation, Technische Universität München, 2010.

[107] P. Gamnitzer, V. Gravemeier, and W. A. Wall, Time-dependent subgrid scales in residual-based large eddy simulation of turbulent channel flow, *Computer Methods in Applied Mechanics and Engineering* **199**, 819–827, 2010.

[108] E. Garnier, N. Adams, and P. Sagaut, *Large eddy simulation for compressible flows*, Springer, 2009.

[109] D. Gaudlitz, *Numerische Untersuchung des Aufstiegsverhaltens von Gasblasen in Flüssigkeiten*, Dissertation, Technische Universität München, 2008.

[110] D. Gaudlitz and N. Adams, On improving mass-conservation properties of the hybrid particle-level-set method, *Computers & Fluids* **37**, 1320–1331, 2008.

[111] M. W. Gee, C. M. Siefert, J. J. Hu, R. S. Tuminaro, and M. G. Sala, ML 5.0 Smoothed aggregation user's guide, Technical Report SAND2006–2256, Sandia National Laboratories, 2006.

[112] N. J. Georgiadis, D. P. Rizzetta, and C. Fureby, Large-eddy simulation: Current capabilities, recommended practices, and future research, *AIAA Journal* **48**, 1772–1784, 2010.

[113] M. Germano, Turbulence: The filtering approach, *Journal of Fluid Mechanics* **238**, 325–336, 1992.

[114] M. Germano, U. Piomelli, P. Moin, and W. H. Cabot, A dynamic subgrid-scale eddy viscosity model, *Physics of Fluids A* **3**, 1760–1765, 1991.

[115] A. Gerstenberger, *An XFEM based fixed-grid approach to fluid-structure interaction*, Dissertation, Technische Universität München, 2010.

[116] A. Gerstenberger and R. S. Tuminaro, An algebraic multigrid approach to solve extended finite element method based fracture problems, *International Journal for Numerical Methods in Engineering* **94**, 248–272, 2013.

[117] A. Gerstenberger and W. A. Wall, An extended finite element method/Lagrange multiplier based approach for fluid-structure interaction, *Computer Methods in Applied Mechanics and Engineering* **197**, 1699–1714, 2008.

[118] V. Gravemeier, Scale-separating operators for variational multiscale large eddy simulation of turbulent flows, *Journal of Computational Physics* **212**, 400–435, 2006.

[119] V. Gravemeier, The variational multiscale method for laminar and turbulent flow, *Archives of Computational Methods in Engineering* **13**, 249–324, 2006.

[120] V. Gravemeier and U. Rasthofer, A variational multiscale method with multifractal subgrid-scale modeling for large-eddy simulation of turbulent flow, In J. Eberhardtsteiner et al. (ed.), *Proceedings of the European Congress on Computational Methods in Applied Sciences and Engineering (ECCOMAS 2012)*, pages 4525–4543, Vienna, Austria, 2012.

[121] V. Gravemeier and U. Rasthofer, A variational multiscale method with multifractal subgrid-scale modeling for large-eddy simulation of turbulent flow, In *Proceedings of the Tenth World Congress on Computational Mechanics (WCCM X)*, Sao Paulo, Brazil, 2012.

[122] V. Gravemeier and W. A. Wall, An algebraic variational multiscale-multigrid method for large-eddy simulation of turbulent variable-density flow at low Mach number, *Journal of Computational Physics* **229**, 6047–6070, 2010.

[123] V. Gravemeier and W. A. Wall, Residual-based variational multiscale methods for laminar, transitional and turbulent variable-density flow at low Mach number, *International Journal for Numerical Methods in Fluids* **65**, 1260–1278, 2011.

[124] V. Gravemeier, S. Lenz, and W. A. Wall, Towards a taxonomy for multiscale methods in computational mechanics: Building blocks of existing methods, *Computational Mechanics* **41**, 279–291, 2008.

[125] V. Gravemeier, M. W. Gee, and W. A. Wall, An algebraic variational multiscale-multigrid method based on plain aggregation for convection-diffusion problems, *Computer Methods in Applied Mechanics and Engineering* **198**, 3821–3835, 2009.

[126] V. Gravemeier, M. W. Gee, M. Kronbichler, and W. A. Wall, An algebraic variational multiscale-multigrid method for large-eddy simulation of turbulent flow, *Computer Methods in Applied Mechanics and Engineering* **199**, 853–864, 2010.

[127] V. Gravemeier, M. Kronbichler, M. W. Gee, and W. A. Wall, An algebraic variational multiscale-multigrid method for large-eddy simulation: Generalized-α time integration, Fourier analysis and application to turbulent flow past a square-section cylinder, *Computational Mechanics* **47**, 217–233, 2011.

[128] D. M. Greaves, Simulation of viscous water column collapse using adapting hierarchical grids, *International Journal for Numerical Methods in Fluids* **50**, 693–711, 2006.

[129] P. M. Gresho and R. L. Sani, *Incompressible flow and the finite element method, Volume 1, Advection-diffusion*, Wiley, Chichester, 2000.

[130] P. M. Gresho and R. L. Sani, *Incompressible flow and the finite element method, Volume 2, Isothermal laminar flow*, Wiley, Chichester, 2000.

[131] S. Groß and A. Reusken, An extended pressure finite element space for two-phase incompressible flows with surface tension, *Journal of Computational Physics* **224**, 40–58, 2007.

[132] S. Groß, V. Reichelt, and A. Reusken, A finite element based level set method for two-phase incompressible flows, *Computing and Visualization in Science* **9**, 239–257, 2006.

[133] J.-L. Guermond, J. T. Oden, and S. Prudhomme, Mathematical perspectives on large eddy simulation models for turbulent flows, *Journal of Mathematical Fluid Mechanics* **6**, 194–248, 2004.

[134] W. Hackbush, *Multigrid methods and applications*, Springer, Berlin, 1985.

[135] T. C. Halsey, M. H. Jensen, L. P. Kadanoff, I. Procaccia, and B. I. Shraiman, Fractal measures and their singularities: The characterization of strage sets, *Physical Review A* **33**, 1141–1151, 1986.

[136] A. Hansbo and P. Hansbo, An unfitted finite element method, based on Nitsche's method, for elliptic interface problems, *Computer Methods in Applied Mechanics and Engineering* **191**, 5537–5552, 2002.

[137] P. Hansbo, M. G. Larson, and S. Zahedi, A cut finite element method for a Stokes interface problem, *Applied Numerical Mathematics* **85**, 90–114, 2014.

[138] C. Härtel, L. Kleiser, F. Unger, and R. Friedrich, Subgrid-scale energy transfer in the near-wall region of turbulent flows, *Physics of Fluids* **6**, 3130–3143, 1994.

[139] M. Hautefeuille, C. Annavarapu, and J. E. Dolbow, Robust imposition of Dirichlet boundary conditions on embedded surfaces, *International Journal for Numerical Methods in Engineering* **90**, 40–64, 2012.

[140] F. Henke, *An extended finite element method for turbulent premixed combustion*, Dissertation, Technische Universität München, 2012.

[141] F. Henke, M. Winklmaier, V. Gravemeier, and W. A. Wall, A semi-Lagrangean time-integration approach for extended finite element methods, *International Journal for Numerical Methods in Engineering* **98**, 174–202, 2014.

[142] H. G. E. Hentschel and I. Procaccia, The infinite number of generalized dimensions of fractals and strange attractors, *Physica D: Nonlinear Phenomena* **8**, 435–444, 1983.

[143] M. A. Heroux, R. A. Bartlett, V. E. Howle, R. J. Hoekstra, J. J. Hu, T. G. Kolda, R. B. Lehoucq, K. R. Long, R. P. Pawlowski, E. T. Phipps, A. G. Salinger, H. K. Thornquist, R. S. Tuminaro, J. M. Willenbring, A. Williams, and K. S. Stanley, An overview of the Trilinos project, *ACM Transactions on Mathematical Software* **31**, 397–423, 2005.

[144] M. Herrmann, A sub-grid surface dynamics model for sub-filter surface tension induced interface dynamics, *Computers & Fluids* **87**, 92–101, 2013.

[145] S. Hickel and N. A. Adams, On implicit subgrid-scale modeling in wall-bounded flows, *Physics of Fluids* **19**, 105106, 2007.

[146] S. Hickel, N. A. Adams, and J. A. Domaradzki, An adaptive local deconvolution method for implicit LES, *Journal of Computational Physics* **213**, 413–436, 2006.

[147] S. Hickel, N. A. Adams, and N. N. Mansour, Implicit subgrid-scale modeling for large-eddy simulation of passive-scalar mixing, *Physics of Fluids* **19**, 095102, 2007.

[148] C. W. Hirt and B. D. Nichols, Volume of fluid (VOF) method for the dynamics of free boundaries, *Journal of Computational Physics* **39**, 201–225, 1981.

[149] T. J. R. Hughes, *The finite element method: Linear static and dynamic finite element analysis*, Prentice-Hall, Englewood Cliffs, 1987.

[150] T. J. R. Hughes, Multiscale phenomena: Green's functions, the Dirichlet-to-Neumann formulation, subgrid scale models, bubbles and the origins of stabilized methods, *Computer Methods in Applied Mechanics and Engineering* **127**, 387–401, 1995.

[151] T. J. R. Hughes and G. N. Wells, Conservation properties for the Galerkin and stabilised forms of the advection-diffusion and incompressible Navier-Stokes equations, *Computer Methods in Applied Mechanics and Engineering* **194**, 1141–1159, 2005.

[152] T. J. R. Hughes, L. P. Franca, and M. Balestra, A new finite element formulation for computational fluid dynamics: V. Circumventing the Babuška-Brezzi condition: A stable Petrov-Galerkin formulation of the Stokes problem accommodating equal-order interpolation, *Computer Methods in Applied Mechanics and Engineering* **59**, 85–99, 1986.

[153] T. J. R. Hughes, G. R. Feijóo, L. Mazzei, and J.-B. Quincy, The variational multiscale method - a paradigm for computational mechanics, *Computer Methods in Applied Mechanics and Engineering* **166**, 3–24, 1998.

[154] T. J. R. Hughes, L. Mazzei, and K. E. Jansen, Large eddy simulation and the variational multiscale method, *Computing and Visualization in Science* **3**, 47–59, 2000.

[155] T. J. R. Hughes, L. Mazzei, A. A. Oberai, and A. A. Wray, The multiscale formulation of large eddy simulation: Decay of homogeneous isotropic turbulence, *Physics of Fluids* **13**, 505–512, 2001.

[156] T. J. R. Hughes, A. A. Oberai, and L. Mazzei, Large eddy simulation of turbulent channel flows by the variational multiscale method, *Physics of Fluids* **13**, 1784–1799, 2001.

[157] K. E. Jansen and A. E. Tejada-Martínez, An evaluation of the variational multiscale model for large-eddy simulation while using a hierarchical basis, *AIAA Paper*, No. 02–0283, 2002.

[158] K. E. Jansen, S. Collis, C. Whiting, and F. Shakib, A better consistency for low-order stabilized finite element methods, *Computer Methods in Applied Mechanics and Engineering* **174**, 153–170, 1999.

[159] K. E. Jansen, C. H. Whiting, and G. M. Hulbert, A generalized-α method for integrating the filtered Navier-Stokes equations with a stabilized finite element method, *Computer Methods in Applied Mechanics and Engineering* **190**, 305–319, 2000.

[160] J. Jeong and F. Hussain, On the identification of a vortex, *Journal of Fluid Mechanics* **285**, 69–94, 1995.

[161] H. Ji, D. Chopp, and J. E. Dolbow, A hybrid extended finite element/level set method for modeling phase transformations, *International Journal for Numerical Methods in Engineering* **54**, 1209–1233, 2002.

[162] V. John, On large eddy simulation and variational multiscale methods in the numerical simulation of turbulent incompressible flows, *Applications of Mathematics* **51**, 321–353, 2006.

[163] V. John and S. Kaya, A finite element variational multiscale method for the Navier-Stokes equations, *SIAM Journal on Scientific Computing* **26**, 1485–1503, 2005.

[164] V. John and A. Kindl, A variational multiscale method for turbulent flow simulation with adaptive large scale space, *Journal of Computational Physics* **229**, 301–312, 2010.

[165] S. Jovic and D. M. Driver, Backward-facing step measurement at low Reynolds number, $\mathrm{Re_h} = 5000$, NASA Technical Memorandum 108807, 1994.

[166] B. A. Kader and A. M. Yaglom, Heat and mass transfer laws for fully turbulent wall flows, *International Journal of Heat and Mass Transfer* **15**, 2329–2351, 1972.

[167] M. Kang, R. P. Fedkiw, and X.-D. Liu, A boundary condition capturing method for multiphase incompressible flow, *Journal of Scientific Computing* **15**, 323–360, 2000.

[168] N. Kasagi and A. Matsunaga, Three-dimensional particle-tracking velocimetry measurement of turbulence statistics and energy budget in a backward-facing step flow, *International Journal of Heat and Fluid Flow* **16**, 477–485, 1995.

[169] A. Keating, U. Piomelli, E. Balaras, and H.-J. Kaltenbach, A priori and a posteriori tests of inflow conditions for large-eddy simulation, *Physics of Fluids* **16**, 4696–4712, 2004.

[170] A. Keating, U. Piomelli, K. Bremhorst, and C. Nešić, Large-eddy simulation of heat transfer downstream of a backward-facing step, *Journal of Turbulence* **5**, 020, 2004.

[171] C. E. Kees, I. Akkerman, M. W. Farthing, and Y. Bazilevs, A conservative level set method suitable for variable-order approximations and unstructured meshes, *Journal of Computational Physics* **230**, 4536–4558, 2011.

[172] D. Kim and P. Moin, Direct numerical study of air layer drag reduction phenomenon over a backward-facing step, In *Annual Research Briefs 2010*, Center for Turbulence Research, Stanford University and NASA Ames Research Center, pages 351–363, 2010.

[173] D. Kim, A. Mani, and P. Moin, Numerical simulation of wave breaking in turbulent two-phase couette flow, In *Annual Research Briefs 2012*, Center for Turbulence Research, Stanford University and NASA Ames Research Center, pages 171–178, 2012.

[174] A. N. Kolmogorov, The local structure of turbulence in incompressible viscous fluid for very large Reynolds numbers, *Proceedings of the Royal Society of London A: Mathematical, Physical & Engineering Sciences* **434**, 9–13, 1991 (republished English translation of *Doklady Akademii Nauk SSSR* **30**, 299–303, 1941 in Russian).

[175] B. Koobus and C. Farhat, A variational multiscale method for the large eddy simulation of compressible turbulent flows on unstructured meshes - application to vortex shedding, *Computer Methods in Applied Mechanics and Engineering* **193**, 1367–1383, 2004.

[176] P. K. Kundu and I. M. Cohen, *Fluid mechanics*, 4th Edition, Academic Press, Burlington, 2008.

[177] E. Labourasse, D. Lacanette, A. Toutant, P. Lubin, S. Vincent, O. Lebaigue, J.-P. Caltagirone, and P. Sagaut, Towards large eddy simulation of isothermal two-phase flows: Governing equations and a priori tests, *International Journal of Multiphase flow* **33**, 1–39, 2007.

[178] J. Larocque, S. Vincent, D. Lacanette, P. Lubin, and J.-P. Caltagirone, Parametric study of LES subgrid terms in a turbulent phase separation flow, *International Journal of Heat and Fluid Flow* **31**, 536–544, 2010.

[179] H. Le, P. Moin, and J. Kim, Direct numerical simulation of turbulent flow over a backward-facing step, *Journal of Fluid Mechanics* **330**, 349–374, 1997.

[180] B. E. Lee, The effect of turbulence on the surface pressure field of square prisms, *Journal of Fluid Mechanics* **69**, 263–282, 1975.

[181] C. Lee, J. Dolbow, and P. J. Mucha, A narrow-band gradient-augmented level set method for multiphase incompressible flow, *Journal of Computational Physics* **273**, 12–37, 2014.

[182] J. Lee, J. Suh, H. J. Sung, and B. Pettersen, Structures of turbulent open-channel flow in the presence of an air-water interface, *Journal of Turbulence*, N18, 2012.

[183] S. Lee, S. Lele, and P. Moin, Simulation of spatially evolving compressible turbulence and application of Taylor's hypothesis, *Physics of Fluids* **4**, 1521–1530, 1992.

[184] S. K. Lele, Compressibility effects on turbulence, *Annual Review of Fluid Mechanics* **32**, 211–254, 1994.

[185] A. Leonard, Energy cascade in large eddy simulation of turbulent fluid flow, *Advances in Geophysics A* **18**, 237–248, 1974.

[186] M. Lesieur and O. Métais, New trends in large-eddy simulations of turbulence, *Annual Review of Fluid Mechanics* **28**, 45–82, 1996.

[187] B. Lessani and M. V. Papalexandris, Time-accurate calculation of variable density flows with strong temperature gradients and combustion, *Journal of Computational Physics* **212**, 218–246, 2006.

[188] R. J. LeVeque, High-resolution conservative algorithms for advection in incompressible flow, *SIAM Journal on Numerical Analysis* **33**, 627–665, 1996.

[189] V. G. Levich, *Physicochemical hydrodynamics*, Prentice-Hall, Englewood Cliffs, 1962.

[190] D. J. Lewis, The instability of liquid surfaces when accelerated in a direction perpendicular to their planes. II, *Proceedings of the Royal Society of London A: Mathematical, Physical & Engineering Sciences* **202**, 81–96, 1950.

[191] C. Li, C. Xu, C. Gui, and M. D. Fox, Distance regularized level set evolution and its application to image segmentation, *IEEE Transactions on Image Processing* **19**, 3243–3254, 2010.

[192] N. Li, E. Balaras, and U. Piomelli, Inflow conditions for large-eddy simulations of mixing layers, *Physics of Fluids* **12**, 935–938, 2000.

[193] D. K. Lilly, A proposed modification of the Germano subgrid-scale closure method, *Physics of Fluids* **4**, 633–635, 1992.

[194] C.-L. Lin, H. Lee, T. Lee, and L. J. Weber, A level set characteristic Galerkin finite element method for free surface flows, *International Journal for Numerical Methods in Fluids* **49**, 521–547, 2005.

[195] P. Liovic and D. Lakehal, Interface-turbulence interactions in large-scale bubbling processes, *International Journal of Heat and Fluid Flow* **28**, 127–144, 2007.

[196] P. Liovic and D. Lakehal, Subgrid-scale modelling of surface tension within interface tracking-based large eddy and interface simulation of 3D interfacial flows, *Computers & Fluids* **63**, 27–46, 2012.

[197] S. Liu, C. Meneveau, and J. Katz, On the properties of similarity subgrid-scale models as deduced from measurements in a turbulent jet, *Journal of Fluid Mechanics* **215**, 83–119, 1994.

[198] R. Löhner, Improved error and work estimates for high-order elements, *International Journal for Numerical Methods in Fluids* **72**, 1207–1218, 2013.

[199] F. Losasso, R. Fedkiw, and S. Osher, Spatially adaptive techniques for level set methods and incompressible flow, *Computers & Fluids* **35**, 995–1010, 2006.

[200] J. Lu and G. Tryggvason, Dynamics of nearly spherical bubbles in a turbulent channel upflow, *Journal of Fluid Mechanics* **732**, 166–189, 2013.

[201] T. S. Lund, X. Wu, and K. D. Squires, Generation of turbulent inflow data for spatially-developing boundary layer simulations, *Journal of Computational Physics* **140**, 233–258, 1998.

[202] S. C. Luo, M. G. Yazdani, Y. T. Chew, and T. S. Lee, Effects of incidence and afterbody shape on flow past bluff cylinders, *Journal of Wind Engineering and Aerodynamics* **53**, 375–399, 1994.

[203] D. A. Lyn and W. Rodi, The flapping shear layer formed by flow separation from the forward corner of a square cylinder, *Journal of Fluid Mechanics* **267**, 353–376, 1994.

[204] D. A. Lyn, S. Einav, W. Rodi, and J.-H. Park, A laser-doppler-velocimetry study of ensemble-averaged characteristics of the turbulent near wake of a square cylinder, *Journal of Fluid Mechanics* **304**, 285–319, 1995.

[205] A. Majda and J. Sethian, The derivation and numerical solution of the equations for zero Mach number combustion, *Combustion Science and Technology* **42**, 185–205, 1985.

[206] B. B. Mandelbrot, Intermittent turbulence in self-similar cascades: Divergence of high moments and dimension of the carrier, *Journal of Fluid Mechanics* **62**, 331–358, 1974.

[207] E. Marchandise, P. Geuzaine, N. Chevaugeon, and J.-F. Remacle, A stabilized finite element method using a discontinuous level set approach for the computation of bubble dynamics, *Journal of Computational Physics* **225**, 949–974, 2007.

[208] J. C. Martin and W. J. Moyce, An experimental study of the collapse of liquid columns on a rigid horizontal plane, *Philosophical Transactions of the Royal Society of London* **224**, 312–324, 1952.

[209] A. Massing, M. G. Larson, A. Logg, and M. E. Rognes, A stabilized Nitsche fictitious domain method for the Stokes problem, *Journal of Scientific Computing* **61**, 604–628, 2014.

[210] A. Masud and R. Calderer, A variational multiscale method for incompressible turbulent flows: Bubble functions and fine scale fields, *Computer Methods in Applied Mechanics and Engineering* **200**, 2577–2593, 2011.

[211] J. M. Melenk and I. Babuška, The partition of unity finite element method: Basic theory and applications, *Computer Methods in Applied Mechanics and Engineering* **39**, 289–314, 1996.

[212] C. Meneveau, Germano identity-based subgrid-scale modeling: A brief survey of variations on a fertile theme, *Physics of Fluids* **24**, 121301, 2012.

[213] C. Meneveau and J. Katz, Scale-invariance and turbulence models for large-eddy simulation, *Annual Review of Fluid Mechanics* **32**, 1–32, 2000.

[214] C. Meneveau and K. R. Sreenivasan, Simple multifractal cascade model for fully developed turbulence, *Physical Review Letters* **59**, 1424–1427, 1987.

[215] C. Meneveau and K. R. Sreenivasan, The multifractal nature of turbulent energy dissipation, *Journal of Fluid Mechanics* **224**, 429–484, 1991.

[216] P. D. Minev, T. Chen, and K. Nandakumar, A finite element technique for multifluid incompressible flow using Eulerian grids, *Journal of Computational Physics* **187**, 255–273, 2003.

[217] M. Minguez, C. Brun, R. Pasquetti, and E. Serre, Experimental and high-order LES analysis of the flow in near-wall region of a square cylinder, *International Journal of Heat and Fluid Flow* **32**, 558–566, 2011.

[218] A. Misra and D. I. Pullin, A vortex-based subgrid stress model for large-eddy simulation, *Physics of Fluids* **9**, 2443–2454, 1997.

[219] N. Moës, J. Dolbow, and T. Belytschko, A finite element method for crack growth without remeshing, *International Journal for Numerical Methods in Engineering* **46**, 131–150, 1999.

[220] N. Moës, M. Cloirec, P. Cartraud, and J.-F. Remacle, A computational approach to handle complex microstructure geometries, *Computer Methods in Applied Mechanics and Engineering* **192**, 3163–3177, 2003.

[221] P. Moin, Advances in large eddy simulation methodology for complex flows, *International Journal of Heat and Fluid Flow* **23**, 710–720, 2002.

[222] P. Moin and J. Kim, Tackling turbulence with supercomputers, *Scientific American*, 62–68, January 1997.

[223] P. Moin, K. Squires, W. Cabot, and S. Lee, A dynamic subgrid-scale model for compressible turbulence and scalar transport, *Physics of Fluids* **3**, 2746–2757, 1991.

[224] R. D. Moser, J. Kim, and N. N. Mansour, Direct numerical simulation of turbulent channel flow up to $\mathrm{Re}_\tau = 590$, *Physics of Fluids* **11**, 943–945, 1999.

[225] H. M. Mourad, J. Dolbow, and I. Harari, A bubble-stabilized finite element method for Dirichlet constraints on embedded interfaces, *International Journal for Numerical Methods in Engineering* **69**, 772–793, 2007.

[226] B. Müller, Low-Mach-number asymptotics of the Navier-Stokes equations, *Journal of Engineering Mathematics* **34**, 97–109, 1998.

[227] J. A. Mullin and W. J. A. Dahm, Dual-plane stereo particle image velocimetry measurements of velocity gradient tensor fields in turbulent shear flow. II. Experimental results, *Physics of Fluids* **18**, 035102, 2006.

[228] S. Nagrath, K. E. Jansen, and R. T. Lahey Jr., Computation of incompressible bubble dynamics with a stabilized finite element level set method, *Computer Methods in Applied Mechanics and Engineering* **194**, 4565–4587, 2005.

[229] F. Nicoud, Numerical study of a channel flow with variable properties, In *Annual Research Briefs 1998*, Center for Turbulence Research, Stanford University and NASA Ames Research Center, pages 289–310, 1998.

[230] F. Nicoud, Conservative high-order finite difference schemes for low-Mach number flows, *Journal of Computational Physics* **158**, 71–97, 2000.

[231] J. Nitsche, Über ein Variationsprinzip zur Lösung von Dirichlet-Problemen bei Verwendung von Teilräumen, die keinen Randbedingungen unterworfen sind, *Abhandlungen aus dem Mathematischen Seminar der Universität Hamburg* **36**, 9–15, 1971.

[232] W. F. Noh and P. Woodward, SLIC (simple line interface calculation), In A. I. van der Vooren and P. J. Zandbergen (eds.), *Proceedings of the Fifth International Conference on Numerical Methods in Fluid Dynamics*, Volume 59 of *Lecture Notes in Physics*, pages 330–340, Springer, Enschede, Netherlands, 1976.

[233] R. R. Nourgaliev, M. S. Liou, and T. G. Theofanous, Numerical prediction of interfacial instabilities: Sharp interface method, *Journal of Computational Physics* **227**, 3940–3970, 2008.

[234] A. A. Oberai, J. Liu, D. Sondak, and T. J. R. Hughes, A residual based eddy viscosity model for the large eddy simulation of turbulent flows, *Computer Methods in Applied Mechanics and Engineering* **282**, 54–70, 2014.

[235] A. M. Obukhov, Structure of the temperature field in turbulent flow, *Izvestiia Akademii Nauk SSSR* **13**, 58–69, 1949 (in Russian).

[236] Y. Oishi and Y. Murai, Horizontal turbulent channel flow interacted by a single large bubble, *Experimental Thermal and Fluid Science* **55**, 128–139, 2014.

[237] M. Olshanskii, G. Lube, T. Heister, and J. Löwe, Grad-div stabilization and pressure models for the incompressible Navier-Stokes equations, *Computer Methods in Applied Mechanics and Engineering* **198**, 3975–3988, 2009.

[238] E. Olsson and G. Kreiss, A conservative level set method for two phase flow, *Journal of Computational Physics* **210**, 225–246, 2005.

[239] E. Olsson, G. Kreiss, and S. Zahedi, A conservative level set method for two phase flow II, *Journal of Computational Physics* **225**, 785–807, 2007.

[240] S. Osher and R. Fedkiw, *Level set methods and dynamic implicit surfaces*, Springer, New York, 2003.

[241] S. Osher and J. A. Sethian, Fronts propagating with curvature-dependent speed: Algorithms based on Hamilton-Jacobi formulations, *Journal of Computational Physics* **79**, 12–49, 1988.

[242] M. Pamiès, P.-É. Weiss, E. Garnier, S. Deck, and P. Sagaut, Generation of synthetic turbulent inflow data for large eddy simulation of spatially evolving wall-bounded flows, *Physics of Fluids* **21**, 045103, 2009.

[243] R. L. Panton, *Incompressible flow*, 3rd Edition, Wiley, Hoboken, 2005.

[244] D. Papavassiliou and T. J. Hanratty, Transport of a passive scalar in a turbulent channel flow, *International Journal of Heat and Mass Transfer* **40**, 1303–1311, 1997.

[245] H.-O. Peitgen, H. Jürgens, and D. Saupe, *Chaos and fractals: New frontiers of science*, 2nd Edition, Springer, New York, 2004.

[246] N. Peters, *Turbulent combustion*, Cambridge University Press, Cambridge, 2000.

[247] U. Piomelli, Large-eddy simulation: Achievements and challenges, *Progress in Aerospace Sciences* **35**, 335–362, 1999.

[248] U. Piomelli, W. H. Cabot, P. Moin, and S. Lee, Subgrid-scale backscatter in turbulent and transitional flows, *Physics of Fluids A* **3**, 1766–1771, 1991.

[249] A. R. Piriz, O. D. Cortázar, J. J. López Cela, and N. A. Tahir, The Rayleigh-Taylor instability, *American Journal of Physics* **74**, 1095–1098, 2006.

[250] F. Pochet, K. Hillewaert, P. Geuzaine, J.-F. Remacle, and E. Marchandise, A 3D strongly coupled implicit discontinuous Galerkin level set-based method for modeling two-phase flows, *Computers & Fluids* **87**, 144–155, 2013.

[251] T. Poinsot, D. Veynante, and S. Candel, Quenching processes and premixed turbulent combustion diagrams, *Journal of Fluid Mechanics* **228**, 561–606, 1991.

[252] S. B. Pope, *Turbulent flows*, Cambridge University Press, Cambridge, 2000.

[253] S. Popinet and S. Zaleski, A front-tracking algorithm for accurate representation of surface tension, *International Journal for Numerical Methods in Fluids* **30**, 775–793, 1999.

[254] R. R. Prasad, C. Meneveau, and K. R. Sreenivasan, Multifractal nature of the dissipation field of passive scalars in fully turbulent flows, *Physical Review Letters* **61**, 74–77, 1988.

[255] J. Principe, R. Codina, and F. Henke, The dissipative structure of variational multiscale methods for incompressible flows, *Computer Methods in Applied Mechanics and Engineering* **199**, 791–801, 2010.

[256] E. G. Puckett, A. S. Almgren, J. B. Bell, L. M. Marcus, and W. J. Rider, High-order projection method for tracking fluid interfaces in variable density incompressible flows, *Journal of Computational Physics* **130**, 269–282, 1997.

[257] M. Quecedo and M. Pastor, Application of the level set method to the finite element solution of two-phase flows, *International Journal for Numerical Methods in Engineering* **50**, 645–663, 2001.

[258] U. Rasthofer and V. Gravemeier, Multifractal subgrid-scale modeling within a variational multiscale method for large-eddy simulation of turbulent flow, *Journal of Computational Physics* **234**, 79–107, 2013.

[259] U. Rasthofer, F. Henke, W. A. Wall, and V. Gravemeier, An extended residual-based variational multiscale method for two-phase flow including surface tension, *Computer Methods in Applied Mechanics and Engineering* **200**, 1866–1876, 2011.

[260] U. Rasthofer, G. C. Burton, W. A. Wall, and V. Gravemeier, Multifractal subgrid-scale modeling within a variational multiscale method for large-eddy simulation of passive-scalar mixing in turbulent flow at low and high Schmidt numbers, *Physics of Fluids* **26**, 055108, 2014.

[261] U. Rasthofer, G. C. Burton, W. A. Wall, and V. Gravemeier, An algebraic variational multiscale-multigrid-multifractal method (AVM^4) for large-eddy simulation of turbulent variable-density flow at low Mach number, *International Journal for Numerical Methods in Fluids* **76**, 416–449, 2014.

[262] U. Rasthofer*, B. Schott*, V. Gravemeier, and W. A. Wall, A face-oriented stabilized Nitsche-type extended variational multiscale method for incompressible two-phase flow, *International Journal for Numerical Methods in Engineering*, 2014, available online, DOI: 10.1002/nme.4789 (*co-first authorship).

[263] R. G. Rehm and H. R. Baum, The equations of motion for thermally driven, buoyant flows, *Journal of Research of the National Bureau of Science* **83**, 297–308, 1978.

[264] A. Reusken, Analysis of an extended pressure finite element space for two-phase incompressible flows, *Computing and Visualization in Science* **11**, 293–305, 2008.

[265] L. F. Richardson, *Weather prediction by numerical process*, Cambridge University Press, Cambridge, 1922.

[266] W. Rodi, J. H. Ferziger, M. Breuer, and M. Pourquié, Status of large eddy simulation: Results of a workshop, *ASME Journal of Fluids Engineering* **119**, 248–262, 1997.

[267] R. S. Rogallo, Numerical experiments in homogeneous turbulence, NASA Technical Memorandum 81315, 1981.

[268] R. S. Rogallo and P. Moin, Numerical simulation of turbulent flows, *Annual Review of Fluid Mechanics* **16**, 99–137, 1984.

[269] L. Röhe and G. Lube, Analysis of a variational multiscale method for large-eddy simulation and its application to homogeneous isotropic turbulence, *Computer Methods in Applied Mechanics and Engineering* **199**, 2331–2342, 2010.

[270] P. Sagaut, *Large eddy simulation for incompressible flows*, Springer, Berlin, 2006.

[271] P. Sagaut, S. Deck, and M. Terracol, *Multiscale and multiresolution approaches in turbulence*, Imperial College Press, London, 2006.

[272] H. Sauerland and T.-P. Fries, The extended finite element method for two-phase and free-surface flows: A systematic study, *Journal of Computational Physics* **230**, 3369–3390, 2011.

[273] H. Sauerland and T.-P. Fries, The stable XFEM for two-phase flows, *Computers & Fluids* **87**, 41–49, 2013.

[274] C. Scalo, U. Piomelli, and L. Boegman, High-Schmidt-number mass transport mechanisms from a turbulent flow to absorbing sediments, *Physics of Fluids* **24**, 085103, 2012.

[275] R. Scardovelli and S. Zaleski, Direct numerical simulation of free-surface and interfacial flow, *Annual Review of Fluid Mechanics* **31**, 567–603, 1999.

[276] B. Schott and W. A. Wall, A new face-oriented stabilized XFEM approach for 2D and 3D incompressible Navier-Stokes equations, *Computer Methods in Applied Mechanics and Engineering* **276**, 233–265, 2014.

[277] U. Schumann, Subgrid scale model for finite difference simulations of turbulent flows in plane channels and annuli, *Journal of Computational Physics* **18**, 376–404, 1975.

[278] F. Schwertfirm and M. Manhart, DNS of passive scalar transport in turbulent channel flow at high Schmidt numbers, *International Journal of Heat and Fluid Flow* **28**, 1204–1214, 2007.

[279] A. Scotti and C. Meneveau, A fractal model for large eddy simulation of turbulent flow, *Physica D: Nonlinear Phenomena* **127**, 198–232, 1999.

[280] A. Serizawa, I. Kataoka, and I. Michiyoshi, Turbulence structure of air-water bubbly flow - I. Measuring techniques, *International Journal of Multiphase Flow* **2**, 221–233, 1975.

[281] A. Serizawa, I. Kataoka, and I. Michiyoshi, Turbulence structure of air-water bubbly flow - II. Local properties, *International Journal of Multiphase Flow* **2**, 235–246, 1975.

[282] J. A. Sethian, A fast marching level set method for monotonically advancing fronts, *Proceedings of the National Academy of Sciences* **93**, 1591–1595, 1996.

[283] J. A. Sethian, *Level set methods and fast marching methods: Evolving interfaces in computational geometry, fluid mechanics, computer vision, and materials science*, Cambridge University Press, New York, 1999.

[284] S. Shahmiri, *A hybrid ALE-fixed-grid approach for fluid-structure interaction*, Dissertation, Technische Universität München, 2014.

[285] D. H. Sharp, An overview of Rayleigh-Taylor instability, *Physica D: Nonlinear Phenomena* **12**, 3–18, 1984.

[286] D. A. Shaw and T. J. Hanratty, Turbulent mass transfer rates to a wall for large Schmidt numbers, *AIChE Journal* **23**, 28–37, 1977.

[287] S. Singh and D. You, A dynamic global-coefficient mixed subgrid-scale model for large-eddy simulation of turbulent flow, *International Journal of Heat and Fluid Flow* **42**, 94–104, 2013.

[288] J. Smagorinsky, General circulation experiments with the primitive equations. I. The basic experiment, *Monthly Weather Review* **91**, 99–164, 1963.

[289] A. Sohankar, L. Davidson, and C. Norberg, Large eddy simulation of flow past a square cylinder: Comparison of different subgrid scale models, *ASME Journal of Fluids Engineering* **122**, 39–47, 2000.

[290] K. R. Sreenivasan, Fractals and multifractals in fluid turbulence, *Annual Review of Fluid Mechanics* **23**, 539–600, 1991.

[291] K. R. Sreenivasan and R. A. Antonia, The phenomenology of small-scale turbulence, *Annual Review of Fluid Mechanics* **29**, 435–472, 1997.

[292] K. R. Sreenivasan and R. R. Prasad, New results on the fractal and multifractal structure of the large Schmidt number passive scalars in fully turbulent flows, *Physica D: Nonlinear Phenomena* **38**, 322–329, 1989.

[293] K. R. Sreenivasan and G. Stolovitzky, Turbulent cascades, *Journal of Statistical Physics* **78**, 311–333, 1995.

[294] R. Stenberg, On some techniques for approximating boundary conditions in the finite element method, *Journal of Computational and Applied Mathematics* **63**, 139–148, 1995.

[295] S. Stolz and N. A. Adams, An approximate deconvolution procedure for large-eddy simulation, *Physics of Fluids* **11**, 1699–1701, 1999.

[296] S. Stolz, N. A. Adams, and L. Kleiser, An approximate deconvolution model for large-eddy simulation with application to incompressible wall-bounded flows, *Physics of Fluids* **13**, 997–1015, 2001.

[297] J. W. Strutt, Lord Rayleigh, Investigation of the character of the equilibrium of an incompressible heavy fluid of variable density, *Proceedings of the London Mathematical Society* **s1–14**, 170–177, 1882.

[298] Y. Sudhakar, J. P. Moitinho de Almeida, and W. A. Wall, An accurate, robust, and easy-to-implement method for integration over arbitrary polyhedra: Application to embedded interface methods, *Journal of Computational Physic* **273**, 393–415, 2014.

[299] M. Sussman and E. Fatemi, An efficient, interface-preserving level set redistancing algorithm and its application to interfacial incompressible fluid flow, *SIAM Journal on Scientific Computing* **20**, 1165–1191, 1999.

[300] M. Sussman and E. G. Puckett, A coupled level set and volume-of-fluid method for computing 3d and axisymmetric incompressible two-phase flows, *Journal of Computational Physics* **162**, 301–337, 2000.

[301] M. Sussman, P. Smereka, and S. Osher, A level set approach for computing solutions to incompressible two-phase flow, *Journal of Computational Physics* **114**, 146–159, 1994.

[302] M. Sussman, E. Fatemi, P. Smereka, and S. Osher, An improved level set method for incompressible two-phase flows, *Computers & Fluids* **27**, 663–680, 1998.

[303] M. Sussman, A. S. Almgren, J. B. Bell, P. Colella, L. H. Howell, and M. L. Welcome, An adaptive level set approach for incompressible two-phase flows, *Journal of Computational Physics* **148**, 81–124, 1999.

[304] M. Sussman, K. M. Smith, M. Y. Hussaini, M. Ohta, and R. Zhi-Wei, A sharp interface method for incompressible two-phase flows, *Journal of Computational Physics* **221**, 469–505, 2007.

[305] G. R. Tabor and M. H. Baba-Ahmadi, Inlet conditions for large eddy simulation: A review, *Computers & Fluids* **39**, 553–567, 2010.

[306] C. A. Taylor, T. J. R. Hughes, and C. K. Zarins, Finite element modeling of blood flow in arteries, *Computer Methods in Applied Mechanics and Engineering* **158**, 155–196, 1998.

[307] G. I. Taylor, The instability of liquid surfaces when accelerated in a direction perpendicular to their planes. I, *Proceedings of the Royal Society of London A: Mathematical, Physical & Engineering Sciences* **201**, 192–196, 1950.

[308] A. E. Tejada-Martínez and K. E. Jansen, On the interaction between dynamic model dissipation and numerical dissipation due to streamline upwind/Petrov-Galerkin stabilization, *Computer Methods in Applied Mechanics and Engineering* **194**, 1225–1248, 2005.

[309] H. Tennekes and J. L. Lumley, *A first course in turbulence*, MIT Press, Cambridge, 1972.

[310] F. Toschi, H. Kobayashi, U. Piomelli, and G. Iaccarino, Backward-facing step calculations using the shear improved Smagorinsky model, In *Proceedings of the 2006 Summer Program*, Center for Turbulence Research, Stanford University and NASA Ames Research Center, pages 87–97, 2006.

[311] A. Toutant, E. Labourasse, O. Lebaigue, and O. Simonin, DNS of the interaction between a deformable buoyant bubble and a spatially decaying turbulence: A priori tests for LES two-phase flow modelling, *Computers & Fluids* **37**, 877–886, 2008.

[312] A. Toutant, M. Chandesris, D. Jamet, and O. Lebaigue, Jump conditions for filtered quantities at an under-resolved discontinuous interface. Part 1: Theoretical development, *International Journal of Multiphase Flow* **35**, 1100–1118, 2009.

[313] A. Toutant, M. Chandesris, D. Jamet, and O. Lebaigue, Jump conditions for filtered quantities at an under-resolved discontinuous interface. Part 2: A priori tests, *International Journal of Multiphase Flow* **35**, 1119–1129, 2009.

[314] U. Trottenberg, C. Oosterlee, and A. Schüller, *Multigrid*, Academic Press, London, 2001.

[315] G. Tryggvason, Numerical simulations of the Rayleigh-Taylor instability, *Journal of Computational Physics* **75**, 253–282, 1988.

[316] G. Tryggvason, R. Scardovelli, and S. Zaleski, *Direct numerical simulations of gas-liquid multiphase flows*, Cambridge University Press, New York, 2011.

[317] S. O. Unverdi and G. Tryggvason, A front-tracking method for viscous, incompressible, multi-fluid flows, *Journal of Computational Physics* **100**, 25–37, 1992.

[318] F. van der Bos and V. Gravemeier, Numerical simulation of premixed combustion using an enriched finite element method, *Journal of Computational Physics* **228**, 3605–3624, 2009.

[319] P. Vaněk, J. Mandel, and M. Brezina, Algebraic multigrid by smoothed aggregation for second and fourth order elliptic problems, *Computing* **56**, 179–196, 1996.

[320] R. W. C. P. Verstappen and A. E. P. Veldman, Direct numerical simulation of turbulence at lower costs, *Journal of Engineering Mathematics* **32**, 143–159, 1997.

[321] L. Ville, L. Silva, and T. Coupez, Convected level set method for the numerical simulation of fluid buckling, *International Journal for Numerical Methods in Fluids* **66**, 324–344, 2011.

[322] S. Vincent, J. Larocque, D. Lacanette, A. Toutant, P. Lubin, and P. Sagaut, Numerical simulation of phase separation and a priori two-phase LES filtering, *Computers & Fluids* **37**, 898–906, 2008.

[323] J. C. Vogel and J. K. Eaton, Combined heat transfer and fluid dynamic measurements downstream of a backward facing step, *Journal of Heat Transfer* **107**, 922–929, 1985.

[324] P. R. Voke, Flow past a square cylinder: Test case LES2, In J.-P. Chollet, P. R. Voke, and L. Kleiser (eds.), *Direct and large eddy simulation II*, pages 355–374, Kluwer, Dordrecht, 1997.

[325] A. W. Vreman, The filtering analog of the varaitional multiscale method in large-eddy simulation, *Physics of Fluids* **15**, L61–L64, 2003.

[326] W. A. Wall and M. W. Gee, BACI: A multiphysics simulation environment, Technical Report, Institute for Compuational Mechanics, Technische Universität München, 2012.

[327] P. Wang, J. Fröhlich, V. Michelassi, and W. Rodi, Large-eddy simulation of variable-density turbulent axisymmetric jets, *International Journal of Heat and Fluid Flow* **29**, 654–664, 2008.

[328] W. P. Wang and R. H. Pletcher, On the large-eddy simulation of a turbulent channel flow with significant heat transfer, *Physics of Fluids* **8**, 3354–3366, 1996.

[329] Z. Wang and A. A. Oberai, Spectral analysis of the dissipation of the residual-based variational multiscale method, *Computer Methods in Applied Mechanics and Engineering* **199**, 810–818, 2010.

[330] Z. Wang and A. Y. Tong, A sharp surface tension modeling method for two-phase incompressible interfacial flows, *International Journal for Numerical Methods in Fluids* **64**, 709–732, 2010.

[331] Z. Wang, J. Yang, and F. Stern, An improved particle correction procedure for the particle level set method, *Journal of Computational Physics* **228**, 5819–5837, 2009.

[332] Z. Warhaft, Passive scalars in turbulent flows, *Annual Review of Fluid Mechanics* **32**, 203–240, 2000.

[333] C. H. Whiting and K. E. Jansen, A stabilized finite element method for the incompressible Navier-Stokes equations using a hierarchical basis, *International Journal for Numerical Methods in Fluids* **35**, 93–116, 2001.

[334] F. Xiao, M. Dianat, and J. J. McGuirk, LES of turbulent liquid jet primary breakup in turbulent coaxial air flow, *International Journal of Multiphase Flow* **60**, 103–118, 2014.

[335] A. Yoshizawa, Statistical theory for compressible turbulent shear flows, with the application to subgrid modeling, *Physics of Fluids* **29**, 2152–2164, 1986.

[336] D. You and P. Moin, A dynamic global-coefficient subgrid-scale model for large-eddy simulation of turbulent scalar transport in complex geometries, *Physics of Fluids* **21**, 045109, 2009.

[337] S. T. Zalesak, Fully multidimensional flux-corrected transport algorithms for fluids, *Journal of Computational Physics* **31**, 335–362, 1979.

[338] Y. Zang, R. L. Street, and J. R. Koseff, A dynamic mixed subgrid-scale model and its application to turbulent recirculating flows, *Physics of Fluids* **5**, 3186–3196, 1993.

[339] O. C. Zienkiewicz and R. L. Taylor, *The finite element method set*, 7th Edition, Butterworth-Heinemann, Oxford, 2013.

[340] A. Zilian and A. Legay, The enriched space-time finite element method (EST) for simultaneous solution of fluid-structure interaction, *International Journal for Numerical Methods in Engineering* **75**, 305–334, 2008.

[341] S. Zlotnik and P. Díez, Hierarchical XFEM for n-phase flow (n>2), *Computer Methods in Applied Mechanics and Engineering* **198**, 2329–2338, 2009.